Identification and Characterization of Young Stars in Star Forming Regions

A

THESIS SUBMITTED

To

Pt. Ravishankar Shukla University, Raipur

For

The Degree of Doctor of Philosophy

in

PHYSICS

under the Faculty of Science

2021

Supervisor :
Dr. Maheswar Gopinathan
(Associate Professor)
IIA, II Block, Koramangala
Bengaluru, Karnataka 560 034

Investigator :
Piyali Saha
(Senior Research Fellow)
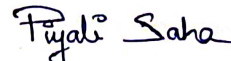ARIES, Manora Peak,
Nainital 263 001

Declaration by Candidate

I declare that the thesis entitled *Identification and Characterization of Young Stars in Star Forming Regions* is my own work conducted under the supervision of *Dr. Maheswar Gopinathan* at *Aryabhatta Research Institute of observational sciencES (ARIES), Manora Peak, Nainital 263 001, India*, approved by the Research Degree Committee. I have put in more than 300 days of attendance with the supervisor at the center, *excluding coursework.*

I further declare that to the best of my knowledge the thesis does not contain any part of any work, which has been submitted for the award of any degree either in this University or in any other University/Deemed university without proper citation.

Dr. Maheswar Gopinathan
Signature of the Supervisor

भारतीय तारामौतिकी संस्थान
INDIAN INSTITUTE OF ASTROPHYSICS
विज्ञान और पौद्यागिक विभाग
DEPARTMENT OF SCIENCE & TECHNOLOGY
भारत सरकार GOVT OF INDIA
कोरमंगला KORAMANGALA
बेंगलूर BANGALORE-560 034
भारत INDIA

D. Banerjee

निदेशक / Director
आर्यभट्ट प्रेक्षण विज्ञान शोध संस्थान (एरीज)
Aryabhatta Research Institute of Observational Sciences (ARIES)
मनोरा पीक, नैनीताल - 263 001
Manora Peak, Nainital-263 001

Piyali Saha
Signature of the Candidate

01/2021

Signature of the Chairman, DRC
CHAIRMAN
SOS in Physics & Astrophysics,
Pt. R.S. University, RAIPUR. (CG.)

Certificate by the Supervisor

This is to certify that the work entitled *Identification and Characterization of Young Stars in Star Forming Regions* is a piece of research work done by *Ms. Piyali Saha* under my guidance and supervision for the degree of Doctor of Philosophy in *PHYSICS* of Pt. Ravishankar Shukla University, Raipur, Chhattisgarh, India. That the candidate has put in an attendance of 300 days, excluding attendance of course-work, in the research centre.

To the best of my knowledge and belief this thesis

1. Embodies the work of the candidate herself.

2. Has duly been completed.

3. Fulfills the requirements of the Ordinance relating to the Ph.D. degree of the University;
   and

4. Is up to the standard both in respect of contents and language for being referred to the examiner.

D. Banerjee

निदेशक / Director
आर्यभट्ट प्रेक्षण विज्ञान शोध संस्थान (एरीज)
Aryabhatta Research Institute of Observational Sciences (ARIES)
मनोरा पीठ, नैनीताल – 263 001
Manora Peak, Nainital-263 001

Dr. Maheswar Gopinathan
Signature of the Supervisor

भारतीय खगोलभौतिकी संस्थान
INDIAN INSTITUTE OF ASTROPHYSICS
विज्ञान और प्रौद्योगिकि विभाग
DEPARTMENT OF SCIENCE & TECHNOLOGY
भारत सरकार GOVT. OF INDIA
कोरमंगला KORAMANGALA
बेंगलूर BANGALORE-560 034
भारत INDIA

Forwarded
11/01/2021

Signature of the Chairman, DRC

CHAIRMAN,
Deptt. Research Committee,
SOS In Physics & Astrophysics,
Pt. R.S. University, RAIPUR (CG)

Declaration on Plagiarism

I declare that all materials in my thesis entitled *Identification and Character-ization of Young Stars in Star Forming Regions* are my own work and do not involve plagiarism. I also certify that

    a. No sentence, equation, diagram, table, paragraph or section has been copied verbatim from previous work unless it is placed under quotation marks and duly referenced.

    b.   The work presented is original and my own work. No ideas, processes, results or words of others have been presented as my own work.

    c. Report on Plagiarism check is appended.

Piyali Saha

Date 11-01-2021

Place Raipur

Piyali Saha

Signature of the Candidate

D. Banerjee

11/01/2021

Signature of the Chairman, DRC

CHAIRMAN;
Deptt. Research Committee;
SOS In Physics & Astrophysics,
Pt. R.S. University, RAIPUR (C.G.)

URKUND

Urkund Analysis Result

Analysed Document: Identification and Characterizations of Young Stars in Star Forming Regions (Piyali Saha).pdf (D90872432)

Submitted: 1/4/2021 10:39:00 AM

Submitted By: library_prsu@rediffmail.com

Significance: 9 %

Sources included in the report:

15772f.pdf (D50934536)
2012-04-16_0408170.pdf (D5630399)
2012-04-11_0408170.pdf (D5601946)
thesis_ekta_correct.pdf (D86561266)
thesis_ekta.pdf (D86478703)
Raksha_MphilThesis_final.pdf (D76887103)
Nayana_George_MPhilthesis.pdf (D63566870)
Nayana_George_MPhilthesis.pdf (D63568602)
TFG-Guasch-Estevez-Daniel.pdf (D75178074)
GAIA.pdf (D40878561)
GCJ_Photo_Thesis.pdf (D36684711)
Thesis_all_chapters.pdf (D78384319)
Thesis_all_chapters (1).pdf (D78694816)
thesis_chapters_sapna.pdf (D78640409)
thesis_all_chapters.pdf (D88887298)
sapna_thesis_all_chapters.pdf (D78694770)
fbd85f35-e59f-4c30-aeef-3ef0292e15e3
http://general-tools.cosmos.esa.int/iso/meetings/isopeaks/burgdorf/burgdorf.ps
https://www.researchgate.net/
publication/231007808_The_Taurus_Spitzer_Survey_New_Candidate_Taurus_Members_Selected
_Using_Sensitive_Mid-Infrared_Photometry
https://zenodo.org/record/889068/files/dissertation.pdf
https://www.researchgate.net/publication/230925315_The_Structure_of_the_Star-
forming_Cluster_RCW_38

Instances where selected sources appear:

224

University Librarian
Pt. Ravishankar Shukla University
Raipur (C.G.)

Copy Right Transfer Approval Form

Copy Right Transfer Approval Form
(Clause 14e of the Ordinance - 45)

Name of the Candidate: Piyali Saha

Department: School of Studies in Physics and Astrophysics

Degree :   Doctor or Philosophy in Physics

University: Pt. Ravishankar Shukla University, Raipur

Supervisor: Dr. Maheswar Gopinathan

Thesis Title: Identification and Characterization of Young Stars in Star Forming Regions

Year of Award: . . . .

Agreement

1. I hereby declare that, if appropriate, I have obtained and attended hereto a written permission/statement from owner(s) of each third party copyrighted matter to be included in my thesis/dissertation, allowing distribution as specified below.

2. I hereby grant to the university and its agents the non-exclusive license to archive and make accessible, under the condition specified below, my thesis/dissertation, in whole or in part in all forms of media, now or hereafter known. I retain all other ownership rights to the copyright of the thesis/dissertation. I and my Supervisor, also retain the right to use in future works (such as articles or books) all or part of this thesis, dissertation, or project report.

Condition:

1. Release the entire work for access worldwide   ☑

Signature of the Candidate   **Signature and Seal of the Supervisor**

Place Raipur

Date 11.01.2021

ARIES/AC/CC/2015/03

ARYABHATTA RESEARCH INSTITUTE OF OBSERVATIONAL SCIENCES

(An autonomous institute under the Department of Science & Technology)

Manora Peak, Nainital

Pre-PhD Course work - 2014 - 15

It is certified that **Ms. Piyali Saha** attended and successfully completed the pre–PhD course work conducted at ARIES during the session August 2014 – July 2015.

Her performance in the course work was found to be satisfactory and she has obtained an aggregate of 72.2%.

Widi:

Dr. Wahab Uddin

(Acting Director)

Dr. Manish Naja

(Academic Committee Chairman)

Dr. D. P. Bisen
M. Phil, Ph. D.
Profess & Head

Phone : (M) 9406201131, 7987186589
        (O) (0771) 2262864
Email : hodphysics98@gmail.com
       : dpbisen@rediffmail.com

Ref. : 1416/Phy /2021 ,   Raipur   Date : 07.01.2021

CERTIFICATE

This is to certify that **Piyali Saha** has given Pre-Ph.D. seminar on her thesis entitled **"Identification and Characterization of Young Stars in Star Forming Regions"** on **05.01.2021** at School of Studies in Physics & Astrophysics, Pt. Ravishankar Shukla University, Raipur (C. G.). **Piyali Saha's** presentation has been very satisfactory and DRC members have recommended for the submission of her Ph. D. Thesis.

Chairman
Departmental Research Committee
SoS in Physics & Astrophysics
Pt. Ravishankar Shukla University, Raipur (C. G.)

PLAGIARISM VERIFICATION REPORT

This is to certify that plagiarism check of the Ph.D. thesis submitted by **Piyali Saha** entitled **"Identification and Characterization of Young Stars in Star Forming Regions"** has been carried out by **Pt. Sunder Lal Sharma Library of Pt. Ravishankar Shukla University, Raipur (C.G.) India**. On the basis of this report it has been found that the percentage of similarity is 9%; within acceptable limit (less than 10%). Therefore almost no plagiarism was found.

Hence DRC recommends the thesis may be dispatched to the reviewers for further action.

07/01/2021

Chairman CHAIRMAN;
Departmental Research Committee
SoS in Physics & Astrophysics
Pt. Ravishankar Shukla University, Raipur (C.G)

Dr. D. P. Bisen
M. Phil, Ph. D.
Profess & Head

Phone : (M) 9406201131, 7987186589
(O) (0771) 2262864
Email : hodphysics98@gmail com
: dpbisen@rediffmail.com

Ref. : 1417 / Phy / 2021   Raipur   Date : 07-01-2021

CERTIFICATE OF PUBLICATION

This is to certify that Piyali Saha has published her research work in various reputed international journals having **Science Citation Index (SCI) with IMPACT FACTOR** as listed in Thomson Reuters which are given below:

List of Publications:

Publications in refereed journal:

1. A census of young stellar population associated with the Herbig Be star HD 200775
   Saha Piyali; Maheswar. G.; Kamath. U. S.; Lee. C. W; Manoj. P.; Blesson Mathew; Ekta Sharma, 2020. Monthly Notices of the Royal Astronomical Society. **(MNRAS)**. 494, 5851 **(Impact factor: 5.536)**
2. Distance, magnetic field, and kinematics of the filamentary cloud LDN 1157
   Ekta Sharma; Maheswar G.; Archana Soam; Lee. C. W.; Shinyoung Kim; Tuhin Ghosh; Anandmayee Tej; Gwanjeong Kim; Neha Sharma; **Saha Piyali**, 2020. Astronomy and Astrophysics **(A&A)**. 639, A133 **(Impact factor: 5.636)**
3. Tracing the magnetic field morphology of LDN 1172/1174 cloud complex
   Saha Piyali; Maheswar. G.; Ekta Sharma; Lee. C. W; Tuhin Ghosh; Kim. Shinyoung. 2020. Astronomy and Astrophysics **(A&A)**. under revision. **(Impact factor: 5.636)**
4. Star formation around three comoving HAeBe stars in the Cepheus Flare
   Saha Piyali; Maheswar. G.; Blesson Mathew; U. S. Kamath. 2020. Astronomy and Astrophysics **(A&A)**. under revision. **(Impact factor: 5.636)**
5. Investigation of Rocket Effect in Bright Rimmed Clouds using Gaia DR2
   Saha Piyali; Maheswar. G.; D K Ojha; Neha. S., To be submitted in Astronomy and Astrophysics **(A&A)**, **(Impact factor: 5.636)**
6. Characterization of young intermediate-mass stars associated with Perseus OB2
   Saha Piyali; Maheswar. G.. To be submitted in Monthly Notices of the Royal Astronomical Society. **(MNRAS), (Impact factor: 5.536)**

Conference Proceedings

1. A highly embedded protostar in SFO 18: IRAS 05417+0907
   Piyali Saha; Maheswar. G.; Manoj P.; Neha Sharma; Archana Soam. 2018. Bulletin de la Societe Royale des Sciences de Liege. Vol. 87. p. 257 – 261. presented at an International BINA workshop. held in ARIES. Nainital, 15-18 November 2016
2. Distance to LDN 1172/1174 based on Gaia parallax measurements
   Piyali Saha; Maheswar G.; Lee. C. W; Manoj. P., 2018. presented at an International conference Exploring the Universe: Near Earth Space Science to Extra-Galactic Astronomy (EXPUNIV2018). held in Kolkata (India). 14-17 November 2018
3. Spectroscopic Study of Young Stars towards NGC 7023
   Piyali Saha; Maheswar G.. U S Kamath. 2020. presented at a National conference 20 Years of HCT (HCT 20). held at IIA. Bengaluru. 29-30 September 2020

Circulars

1. GRB 190114C: Optical detection from HCT
   Brajesh Kumar; S. B. Pandey; Avinash Singh; D. K. Sahu; G. C. Anupama and **Piyali Saha**. 2019. GCN Circular. Number: 23742

Chairman,
CHAIRMAN,
Departmental Research Committee
SoS in Physics & Astrophysics
Pt. Ravishankar Shukla University, Raipur (C. G.)

Dedicated to

My Family....

"I have loved the stars too fondly to be fearful of the night."

—Sarah Williams

ACKNOWLEDGEMENTS

*"**If you have the courage to start, you have the courage to succeed.**"*
−by Mel Robbins

Abstract

Star formation is a chain of processes in which molecular clouds get converted to a compact stellar systems, which are the potential platforms of life. Although, numerous observations and simulations have been performed over few decades to understand these processes and evolutionary sequences, many questions remain unanswered. Several factors are found to regulate the star formation processes, e.g. magnetic field and turbulence of the molecular clouds, supernova explosions, high stellar winds and so on. The formation and interaction of low and high mass stars can be constructive as well as destructive in small and large scale environments. In the very early stage of its formation, the young stellar object (YSO) shows emission in millimeter and sub-millimeter. Accretion of circumstellar material and outflow are the signatures of interaction of YSOs with the surroundings. Being associated with the circumstellar disks, YSOs are often found to have infrared (IR) excess. Due to presence of accretion, YSOs show emission in $H\alpha$, $H\beta$, Bracketγ, Paschenβ etc. in their spectra. Due to accretion shocks, YSOs can be associated with X-ray and ultraviolet emission also. Being formed together, YSOs share similar kinematic properties as they form together in molecular clouds. Based on these ways, YSOs can be identified to study the star formation history in the molecular clouds. In this thesis, we identified and characterized young stars in star forming regions.

We made a detailed study of an elongated cloud named LDN 1172/1174, showing "head-tail" structure which is located in the Cepheus constellation. LDN 1174 (NGC 7023) is illuminated by a Herbig Be star HD 200775. At first we made an attempt to estimate the distance to this cloud as it is not well estimated in previous literature. Based on the latest *Gaia* DR2 distances of the YSOs associated with LDN 1172/1174

we computed its distance as 335 ± 11 pc. We further confirm the estimated distance to this cloud complex based on the polarization measurements of the stars projected background to the cloud. In the polarizaion vs. distance (obtained from *Gaia* DR2) plot of these observed stars we found a hike in polarization at ~ 335 pc. Now, based on the median absolute deviation of the distance and proper motion values of the YSOs we found 20 additional sources having similar kinematics as the YSOs. These sources could possibly be YSOs missed in the earlier studies. They are having little or no near-IR excess and some of them are associated with X-ray emission. Optical spectroscopic observations of four of them show signature of Hα in emission. We classify them based on their IR spectral index. We found that these comoving sources are of $1 - 2$ Myr in age. Finally, we made a census of YSOs towards HD 20075, which is a Herbig Be star responsible to ionize LDN 1174. We also made near-IR spectoscopic study towards 10 YSOs to obtain a detailed knowledge of star formation in LDN 1172/1174. We estimated their physical properties and found that star formation in this cloud complex started prior to the birth of the central ionzing source HD 200775.

Magnetic field plays a significant role in evolution of molecular clouds and regulation of star formation in them. Therefore, we estimated the orientation and strength of the projected magnetic field B_{POS} towards LDN 1172/1174 complex by optical R-band polarimetric observations. We found that B_{POS} follows the cloud structure. We compared our findings with the *Planck* results also and found that the inferred (B_{POS}) is well corelated in optical R-band and *Planck* observations.

We extend the work done in LDN 1172/1174 on a wider scale in the Cepheus Flare. There are two more Herbig AeBe stars (BD+68°1118 and PV Cep) within 1.5° radius of HD 200775 which share similar kinematics. We found an age sequence in the stellar associations from BD+68°1118 (~ 10 Myr), HD 200775 (~ 1 Myr) and PV Cep (~ 0.1 Myr). Based on the distance and proper motion distribution of the previously known YSOs from *Gaia* DR2, we found a loosely bound cluster surrounding BD+68°1118 which contains relatively older cluster members whereas PV Cep is not associated with any cluster. The comoving sources are

mainly low-mass M-type sources and have lack of IR excess which is consistent with their ages.

The young intermediate-mass sources located in the Perseus OB2 region were observed spectroscopically with high resolution for investigating their spectral types with more accuracy. These sources don't have near-IR excess and emission in Balmer lines. Most of their ages are lying within $2 - 4$ Myr and yet they are having lack of circumstellar disks. The typical disk dispersal timescale for intermediate-mass stars ($3 - 7$ Myr) is comparable with their ages due to which it is suspected that these sources have aleady shreaded their surrounding disks. We present temperature, extinction, mass, age, and other properties of the observed sources. We also explain their kinematic properties using the latest *Gaia* DR2 and have found these sources are widely scattered across the region. Some of these sources are kinematically asscoiated with the low-mass YSOs.

The intermediate-mass Herbig Ae and Be (HAeBe) stars bridge the gap between low-mass stars, whose formation is fairly well understood and high mass stars, whose formation still poses challenges. Lower mass stars are formed through magnetospheric accretion, whereas high mass stars are thought to form through disk accretion. Linear spectropolarimetry is an excellent tool to probe the circumstellar disks around stars on scales of order stellar radii, i.e. the accretion region of young stars. Now, in case of HBe stars one can observe a depolarization indicaing disk accretion while in HAe stars line polarization can be seen signifying magnetospheric accretion. We acquired spectropolarimetric data of six HAeBe stars and investigated about their accretion mechansims.

Based on the optical polarimetric study of the YSOs associated with BRC 18, we found that polarization measurements of these sources are quite random with respect to the cloud's projected magnetic field. This finding indicates that the circumstellar disks of the YSOs are also oriented arbitrarily. Based on the kinematic properties of the associated YSOs using the latest *Gaia* DR2, we showed that BRC 18 and most of the other BRCs are moving away from the direction of ionization, which is a signature of the "Rocket Effect". We have found a strong correlation between the angle of ionizing source with the *IRAS* source and

the proper motion of the YSOs with respect to the celestial north-south axis. In addition, we searched for sources having projected motion similar to the YSOs and could possibly be young sources not detected in earlier surveys. A fraction of them show near-IR excess and similar age distribution as the known YSOs and candidates.

List of Publications

Publications in refereed journal

1. A census of young stellar population associated with the Herbig Be star HD 200775
   Piyali, Saha; Maheswar, G.; Kamath, U. S.; Lee, C. W; Manoj, P.; Blesson Mathew; Ekta Sharma, 2020, **MNRAS**, 494, 5851 **(Impact factor: 5.536)**

2. Distance, magnetic field, and kinematics of the filamentary cloud LDN 1157
   Ekta Sharma; Maheswar G.; Archana Soam; Lee, C. W.; Shinyoung Kim; Tuhin Ghosh; Anandmayee Tej; Gwanjeong Kim; Neha Sharma and Piyali, Saha, 2020, **A&A**, 639, A133 **(Impact factor: 5.636)**

3. Tracing the magnetic field morphology of LDN 1172/1174 cloud complex
   Piyali, Saha; Maheswar, G.; Ekta Sharma; Lee, C. W; Tuhin Ghosh; Kim, Shinyoung, 2020, under revision, **A&A**, **(Impact factor: 5.636)**

4. Star formation around three comoving HAeBe stars in the Cepheus Flare
   Piyali, Saha; Maheswar, G.; Blesson Mathew; U. S. Kamath, 2020, under revision, **A&A**, **(Impact factor: 5.636)**

5. Investigation of Rocket Effect in Bright Rimmed Clouds using *Gaia* DR2
   Piyali, Saha; Maheswar, G.; D K Ojha; Neha, S., To be submitted in **A&A**

6. Characterization of young intermediate-mass stars associated with Perseus OB2
   Piyali, Saha; Maheswar, G., To be submitted in **MNRAS**

Conference Proceedings

1. A highly embedded protostar in SFO 18: IRAS 05417+0907
   Piyali, Saha; Maheswar, G.; Manoj P.; Neha Sharma; Archana Soam, 2018, Bulletin de la Societe Royale des Sciences de Liege, Vol. 87, p. 257-261, presented at an International BINA workshop, held in ARIES, Nainital, 15-18 November 2016

2. Distance to LDN 1172/1174 based on Gaia parallax measurements
   Piyali, Saha; Maheswar G.; Lee, C. W; Manoj, P., 2018, presented at an International conference Exploring the Universe: Near Earth Space Science to Extra-Galactic Astronomy (EXPUNIV2018), held in Kolkata (India), 14-17 November 2018

3. Spectroscopic Study of Young Stars towards NGC 7023
   Piyali, Saha; Maheswar G., U S Kamath, 2020, presented at a National conference 20 Years of HCT (HCT 20), held at IIA, Bengaluru, 29-30 September 2020

Circulars

1. GRB 190114C: Optical detection from HCT
   Brajesh Kumar; S. B. Pandey; Avinash Singh; D. K. Sahu; G. C. Anupama and **Piyali, Saha**, 2019, GCN Circular, Number: 23742

NOTATIONS AND ABBREVIATIONS

The most commonly used notations and abbreviations in the thesis are given below. If a symbol has been used in a different connection than listed here, it has been explained at the appropriate place.

Notations

Å	Angstrom
α, RA	Right Ascension
A_V	Visual extinction
d	Distance to the star/cluster from earth in parsec (pc)
°, deg	Degree
δ, Dec	Declination
$E(B-V)$	Color excess in $(B-V)$
I_e, I_o	Extraordinary and ordinary intensities
I_{pol}, I_{unpol}	Polarized and unpolarized intensities
J, H, K	Apparent standard magnitude in J, H, and K filters respectively
$(J-K), (H-K)$	Apparent standard colors
$J2000$	Epoch of observation
Jy	Jansky
K	Wdth parameter
kpc	Kiloparsec(unit of distance)
λ	Wavelength
λ_{max}	Wavelength at which maximum polarization observed
l, b	Galactic longitude and latitude
L_{acc}	Accretion luminosity
m	Apparent visual magnitude
$(m-M)_o$	True distance modulus
$M_\odot$	Mass of the Sun
$\dot{M}_{acc}$	Mass accretion rate
M_V	Absolute visual magnitude
Myr	Million Years
pc	Parsec (unit of distance)
′, arcmin	Arc minute

$''$, arcsec	Arc second
μG	Micro Gauss
μm	Micro meter
$M_\star$, $T_\star$	Mass and Temperature of a star
$n(H_2)$	H_2 column density
q_{fg}, u_{fg}	Normalized Stokes parameters for the foreground
q, u, q_1, u_1	Normalized Stokes parameters at four positions of HWP
R_V	Ratio of total to selective extinction
sr	Steradian
τ	Optical depth
V_{LSR}	Velocity of observer relative to local standard of rest
yr	Year/Years
Z	Solar metallicity

Abbreviations

AIMPOL	ARIES IMaging POLarimeter
ARIES	Aryabhatta Research Institute of observational SciencES
B	Barnard
Be	Berkeley
BRC	Bright Rimmed Cloud
CB	Clemens & Barvainis
CC	Color-Color (diagram)
CCD	Charge-Couple Device
CLASS	Continuum and Line Analysis Single Dish Software
CMD	Color-Magnitude Diagram
CREST	Centre for Research and Education in Science and Technology
CTTs	Classical T-Tauri star (or Class II source)
DAOPHOT	Domanian Astrophysical Observatory PHOTometry
DIBs	Diffuse Interstellar Bands
DSS	Digitized Sky Survey
EUV	Extreme Ultraviolet
ESO	European Southern Observatory
EW	Equivalent Width
FIR	Far Infrared

FOV	Field of view
FUV	Far Ultraviolet
FWHM	Full Width at Half Maximum
GAIA	Global Astrometric Interferometer for Astrophysics
GHz	Giga Hertz
GMCs	Giant Molecular Clouds
GP	Galactic Parallel
GUI	Graphical User Interface
HAeBe	Herbig Ae Be
HCT	Himalayan Chandra Telescope
HD	Henry Draper Catalogue
HFOSC	Hanle Faint Object Spectrograph and Camera
HFI	High Frequency Instrument
HR	Hertzsprung-Russell
HWP	Half Wave Plate
IAO	Indian Astronomical Observatory
IBL	Ionized Boundary Layer
ICM	Intra Cluster Medium
IF	Ionization Front
IIA	Indian Institute of Astrophysics
IMF	Initial Mass Function
IR	Infra-Red
IRAC	Infra Red Array Camera
IRAF	Image Reduction and Analysis Facility
IRAS	Infrared Astronomical Satellite
IRS	Infrared Spectrograph
IRSF	Infra-Red Survey Facility
IRTF	Infrared Telescope Facility
ISM	Interstellar Matter/Medium
K-S	Kolmogorov-Smirnov
LDN	Lynd's Dark Nebula
LF	Luminosity Function
LFI	Low Frequency Instrument
mag	magnitude (stellar)

MF	Mass Function
MIPS	Multiband Imaging Photometer for *Spitzer*
MIR	Mid-infrared
mm	millimeter
MS	Main-Sequence
MSX	Midcourse Space Experiment
Myr	Million year
NGC	New General Catalogue
nm	nano meter
PAH	Polycyclic Aromatic Hydrocarbons
Pan-STARRS	Panoramic Survey Telescope and Rapid Response System
PDR	Photo Dissociation Region
PMS	Pre-Main Sequence
PSC	Point Source Catalog
PSF	Point Spread Function
RDI	Radiation Driven Implosion
RGB	Red Green Blue
SAAO	South African Astronomical Observatory
SALT	Southern African Large Telescope
SED	Spectral Energy Distribution
SFR	Star Forming Region
SIMBAD	Set of Identifications, Measurements, and Bibliography for Astronomical Data
SNR	Signal to noise ratio
SPIRE	Spectral and Photometric Imaging Receiver
SSC	*Spitzer* Science Center
ST	Sampurnanand Telescope
2MASS	Two Micron All-Sky Survey
TRAO	Taeduk Radio Astronomy Observatory
TTS	T Tauri Star
UV	Ultraviolet
WISE	Wide-field Infrared Survey Explorer
WTTs	Weak-line T-Tauri star (or Class III source)
XMM	X-ray Multi-Mirror Mission
YSO	Young Stellar Object

Contents

List of Figures

LIST OF FIGURES

List of Tables

LIST OF TABLES

Chapter 1

Introduction

In the early history of observational astronomy, the appearance of the night sky filled with stars influenced human beings to know about them. Since then, the improved telescope technology and various advanced numerical simulations have made the astronomical study more progressive. The processes through which stars form have taken many years for astronomers to understand. Stars are born within highly obscured maternal clouds and grow through rapid contractions and violent ejections. They further evolve with others with whom they interact. Finally, they die often in isolation after living their lives. Although being inanimate objects, stars are worthy of scientific endeavour. In order to unlock the star formation mysteries, we require vigorous use of advanced techniques and the opening of various wavelength regimes.

1.1   Interstellar medium and star formation

A deeper understanding of the stellar evolution can be acquired by investigating the rarefied medium from which stars are born. The interstellar medium (ISM) is a vast name for all that exists in-between the stars inside galaxies. ISM consists of diverse clouds of gas, composed mainly of molecules, atoms, and ions of hydrogen, electrons, and a small quantity of other heavier elements and solid dust grains. Approximately 1% of the ISM mass is in the form of solid microscopic dust grains (Li & Mann, 2012). Various regions of ISM have different physical properties, e.g., diffuse clouds, molecular clouds, cold and warm clouds. A wide range of temperature ($10 - 10^4$ K) and density ($100 - 10^8$ hydrogen atoms cm^{-3}) can be seen in these clouds.

Star formation is a chain of processes through which the diffuse interstellar clouds are converted into isolated stars or star clusters. In general, stars are born deep inside the highly dense cores within the gravitationally bound molecular clouds. Stars are formed in different molecular clouds, e.g. Bok Globules (BGs), Dark Molecular Clouds (DMCs), Giant Molecular Clouds (GMCs), etc. A huge assemble of molecular gas having a mass of approximately $10^3 - 10^7$ M$_\odot$ is called GMC, of extent around $5-200$ pc. Considering as separate entities, the clumps located within GMCs are classified as the individual DMCs. They have mass close to 10^4 M$_\odot$ and very high extinction A$_V$ (e.g. ρ Ophiuchi complex have peak A$_V \sim 100$). BGs are relatively isolated clouds of low-mass star formation. These clouds are of size $0.1-2$ pc and mass $2-100$ M$_\odot$. Based on the appearance, BGs have been classified into different structures, for example, elephant trunk, speck globules, bright-rimmed clouds and cometary globules (Leung, 1985).

1.2 Modes of Star Formation

Mainly in two different modes star formation occurs; (1) spontaneous mode, that is without influence of any external force, (2) triggered mode, which is affected by external forces, for e.g., supernova explosions, feedback from ionization, and winds from massive stars.

1.2.1 Spontaneous Star Formation

Different mechanisms perform a significant role on star formation on different scales. Since gravity provides a direct impact on star formation, the strength of the opposing forces is also crucial. On the larger scales, for example, galactic scales, galactic tidal forces resist the condensation of interstellar matter under gravity into star-forming molecular clouds. In the spiral arms, there is a possibility of gas becoming dense enough so that its self gravity can overcome these tidal forces. On the intermediate scales, magnetic fields and turbulence can resist further collapse of the molecular cloud due to gravity, hence dissipation of magnetic fields and turbulence may lead to star formation. On the small-scales, for example, the prestellar cloud cores, the self-gravity is opposed by the thermal pressure, thus setting a minimum mass which is required by a cloud core to collapse under self-gravity for star formation (Larson, 2003).

It is believed that in spontaneous star formation, the molecular cloud becomes unstable and starts collapsing under its own gravity, by falling towards the center which would become a protostar with time. In the beginning, the cloud has relatively lower gravitational binding energy with other energies resisting the gravity, such as, kinematic, magnetic and thermal energy, which dissipate with time. According to the virial theorem, the gravitational binding energy becomes stronger as the other opposing energies dissipate, thus, dissipation-collapse scenarios mainly lead to spontaneous star formation. So, the time scale in which the spontaneous star formation happens is the dissipation time scale (i.e., free-fall time scale or the ambipolar diffusion time scale), which is the slowest process in the star formation. Hence in a simpler way, the two extreme scenarios that lead to spontaneous star formation are magnetically dominated and turbulence dominated scenarios (Myers & Lazarian, 1998; Mouschovias & Ciolek, 1999).

1.2.1.1   Magnetically Dominated Star Formation

As it is believed that magnetic fields put significant impact on the star formation, various authors devoted numerous efforts to study the evolution of magnetically supported cloud cores (e.g. Nakano, 1984; Shu et al., 1987; Mouschovias, 1991; McKee et al., 1993; Mouschovias & Ciolek, 1999). Such cloud cores condense slowly by ambipolar diffusion with an estimated time scale of $\sim 10^7$ years. Being about an order of magnitude longer than free-fall time scale, the ambipolar diffusion time scale makes the cloud evolution to become quasi-static. During slow contraction of the central part of magnetically supported cloud cores, the cloud flattens gradually along the magnetic field lines due to its increasing self-gravity. Eventually, gravity acquires enough strength to suppress the magnetic support near the central region, which directs the cloud to a runaway collapse. Basu & Mouschovias (1994) estimated that the typical central density has to reach $\sim 10^5$ cm^{-3} to initiate the runaway collapse, which is found to be similar to observed prestellar cloud cores (Ciolek & Basu, 2000). As the ambipolar diffusion continues to reduce the magnetic flux from the contracting region, the collapse accelerates and eventually reaches the non-magnetic phase. Since the flattened collapsing region retains some magnetic support, the collapse velocity is less than that in the non-magnetic case, and the maximum speed it acquires is the sound speed.

1.2.1.2   Turbulence Dominated Star Formation

The ambipolar diffusion model was questioned by Nakano (1998), raising a fact that the prestellar cloud cores can not have a strong support of magnetic field as they would not then exhibit the vast enhancement in the column density which is often found while analyzing the observed data. Also, it is hard to explain the observed level of turbulence in the prestellar cloud cores. In the mode of turbulence dominated star formation, the highly turbulent gas produces large density inhomogeneities in the cloud, some of which eventually become gravitationally unstable and starts to collapse to form stars (Ward-Thompson, 2002). Nakano (1998) further suggested that turbulence plays a more significant role than magnetic fields in supporting prestellar cloud cores against the collapse because of gravity. Most importantly, the dissipation of turbulence may catalyze the dynamical collapse of prestellar cloud cores more than the ambipolar diffusion (Goodman et al., 1998; Myers & Lazarian, 1998; Williams & Myers, 2000). Thus magnetic fields play less important role throughout the whole collapse phase, mainly slowing it down compared to the non-magnetic case (Indebetouw & Zweibel, 2000; Heitsch et al., 2001a). Also, the observed molecular abundances in the prestellar cloud cores are found to be consistent with those computed for rapidly collapsing cloud cores (Aikawa et al., 2003). This argument worsens if the collapse gets retarded by magnetic fields.

1.2.2   Triggered Star Formation

Massive early type stars have a profound impact on their neighboring molecular clouds through their highly energetic radiation, which can evaporate away the nearby clouds and eventually end the star formation process. On the other way, they can act as catalysts in star formation processes through stellar winds or ionization fronts, which compress the dense molecular clouds to form stars (Elmegreen & Lada, 1977). There are other several triggering mechanisms which induce the star formation activity, such as, supernova explosion, cloud-cloud collision. In a small scale, triggering can happen in bright rimmed clouds (BRCs) or cometary globules (CGs) usually located at the edge of HII region, due to higher external pressure, which compresses the pre-exsiting cloud cores. Triggering can also take place in the intermediate scale by compression from one side of a nearby cloud, which leads to a dense layer of moving gas that eventually collects more material and collapses into denser cores resulting formation of star clusters. Also, on the large scale, triggering

can happen during accumulation of material into an expanding ring which surrounds the pressure source. Star formation happening in ring can presumably be triggered by gravitational collapse of the swept up gas.

Massive ionizing sources, having luminosity higher than 10^5 L$_\odot$, emit extreme ultraviolet (EUV) and far ultraviolet (FUV) radiation. EUV ionizes the adjacent area of the star while FUV probes deeper into the area occupied by neutral gas. The ionized gaseous region centering the massive ionizing star is commonly known as HII region as the primary component here is ionized hydrogen. When a massive star begins radiating, the surrounding medium becomes ionized rapidly and temperature reaches to $\sim 10^4$ K. Eventually, the pressure increases, and as a result, this region starts expanding into the surrounding molecular gas with roughly the speed of sound. At a similar time, new atomic hydrogen is produced due to the recombination of protons and electrons in the plasma. As each ionization event removes a photon, a star having a fixed amount of UV photons is able to only ionize a limited region of the surrounding. If the density of the surrounding is uniform, then the ionization expands isotropically and occupies a volume commonly known as 'Stromgren sphere'. Star formation thus triggered can be classified into two categories, collect and collapse model and radiation driven implosion.

1.2.2.1 Collect and Collapse Model

Elmegreen & Lada (1977) first proposed the collect and collapse model of star formation, an illustration of which is shown in Fig. 1.1. During expansion of an HII region, the ionization-front produced by the massive ionizing source/s, moves with supersonic speed, which is preceded by shock-front generated on the neutral side of molecular cloud. This results in the accumulation of neutral cloud material between the two fronts, forming a dense layer of shocked cloud material. Along the length of the shocked layer, gravitational instabilities can develop over a long time scale, which results in the formation of very massive fragments of the compressed layer. The presence of a layer of higher concentration and massive condensations by the side of an HII region provides the observational signature of collect and collapse process (Deharveng et al., 2003).

1.2.2.2 Radiation Driven Implosion Model

The mode of triggered star formation in which the molecular clouds are compressed by ionization or shock front is known as 'radiation driven implosion' (RDI; Bertoldi,

1. INTRODUCTION
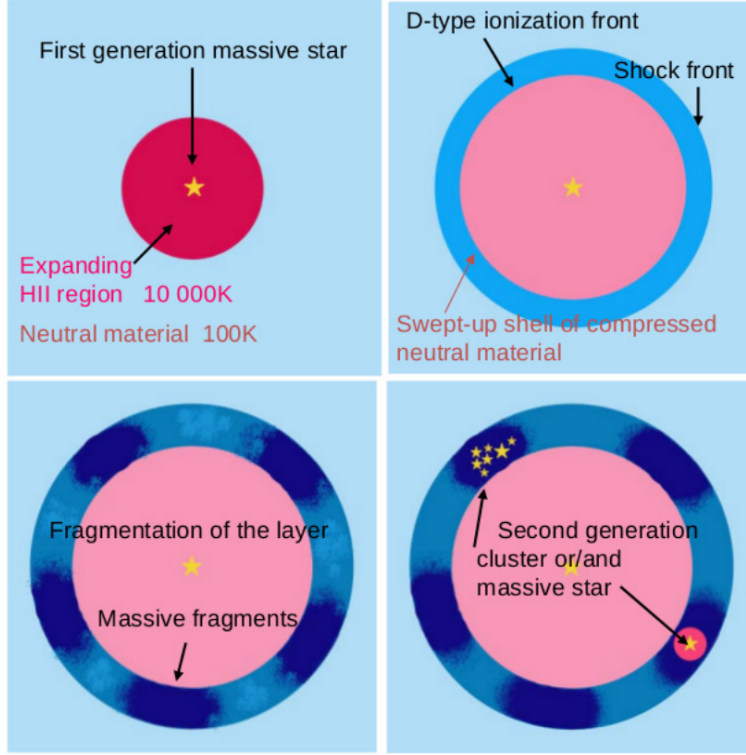
Figure 1.1: An illustration of the collect and collapse model. Figure credit: A. Zavagno.

1989; Lefloch & Lazareff, 1994; Miao et al., 2006). An illustration of RDI mode is presented in Fig. 1.2. Massive early type stars form HII regions by joint effects of their powerful wind and ionizing radiation. In the early phase of expansion of HII region, when the strong UV photons impinge a dense cloud, the neutral hydrogen atoms become ionized near the surface and this ionized surface layer eats its ways into the neutral cloud. The temperature of the gas rises to $\sim$ 10,000 K as the ionization completes (Bertoldi, 1989). Evidently, the temperature rises by a factor of 100, leading to an increase in pressure by the same factor as well. As an effect, the gas tends to expand into the cloud material vigorously, which is soon stopped by the dense neutral material there. A shock thus created compresses the pre-existing cloud cores or triggers the formation of new ones and thus forms a new generation of stars. By the appearance, the observed clumps are classified as speck globules, elephant trunks, BRCs, or CGs (Leung, 1985). Now towards the massive ionizing sources, away from the direction of the cloud, the heated gas experiences a lower density medium and expands into it. So, the material starts moving preponderantly towards the direction of the ionizing stars. Due to an equal and opposite reaction of
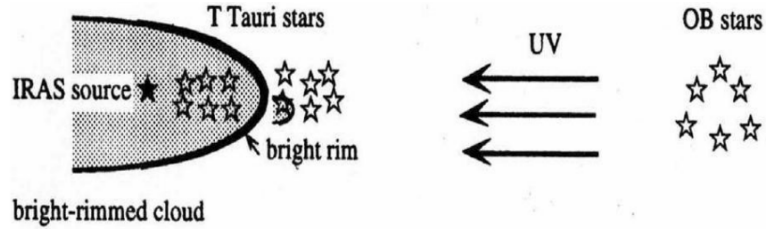
Figure 1.2: An illustration of RDI mode of triggered star formation. Image credit: Ogura (2006).

the escaping material, the cloud accelerates away from the source of ionization. The whole phenomenon resembles to a jet emission from a rocket, and so it is commonly known as 'Rocket Effect' (Bertoldi, 1989).

Bertoldi (1989) and Bertoldi & McKee (1990) computed analytical solution to the photo-evaporation process of the cloud. Based on axisymmetry, they found that the imploded cloud becomes elongated, thus gains a shape similar to comets during the late phase of RDI process. The evolution of the is found to be highly dependent on the orientation of magnetic field (B-field) with respect to the direction of propagation of ionization front (Henney et al., 2009; Mackey & Lim, 2011). The shape of the post imploded cloud deviates from the cylindrical symmetry and it will reach maximum deviation when B-field is perpendicular.

Various studies suggest that in triggered star formation, the external compression can increase the rate of accretion and luminosity of protostars. Motoyama & Yoshida (2003) studied core collapse by external shock waves and found enhanced accretion rate in them. In support of these results, Belloche et al. (2006) observationally found evidence of a high accretion rate in the Class 0 protostar IRAS 4A towards the star forming cloud NGC 1333, whose formation is thought to be triggered by strong molecular outflows (Sandell & Knee, 2001).

1.2.3 Low-mass Stars

In order to classify the low-mass protostars ($0.2 - 2M_\odot$), Lada (1987) defined the infrared (IR) spectral index (α) as the slope of the spectral energy distribution (SED) of these objects in $\log(\lambda F_\lambda)$ versus $\log(\lambda)$, where λ is the wavelength and F_λ implies the flux density at that wavelength:

$$\alpha = \frac{d\log(\lambda F_\lambda)}{d\log(\lambda)} \tag{1.1}$$

1. INTRODUCTION

In Fig. 1.3, we have shown different evolutionary classes of a low-mass protostar, starting from a prestellar cloud core to an evolved Class III source.

Class 0 and I: Low-mass protostars having $0 < \alpha \lesssim 3$ belong to this group. A positive value of α indicates the rising of SED with an increase in wavelength. SEDs of these protostars are found to be much broader compared to that of a single temperature black body. Most of the derived luminosity is an outcome of the accretion process ongoing in these sources. Class I sources are more evolved than Class 0 sources as the later are surrounded by an envelope of significantly higher mass than the former. The Class 0 sources are often found to be associated with highly collimated and powerful bipolar jets and outflows. Their SEDs peak at wavelength higher than 100 μm with faint near-IR emission. Class 0 protostars mainly emit in FIR, sub- millimeter and millimeter. The Class I protostars have higher 'IR excess' due to the presence of circumstellar disk and envelope system. These sources have SED, which peaks in FIR and has a strong absorption at 10 μm for silicate dust grain. Class I sources are also found to emit bipolar jets and outflows, which are less energetic compared to those associated with Class 0 sources.

Class II: Young stars in this group have $-2 \lesssim \alpha \leq 0$ and their SEDs peak at comparatively shorter wavelengths (in general NIR) than Class 0 and I stars. Their SEDs are also broader as they are still surrounded by dense gas and dust in form of an optically thick disk. The envelope mass gets reduced in Class II sources due to strong stellar wind and also due to the transfer of a significant amount of cloud material from envelope with time.

Class III: These sources are the most evolved YSOs having $-3 < \alpha \lesssim -2$. They have no or optically thin circumstellar disk, which results in a lack of IR excess. SEDs of Class III sources fit well with reddened blackbody functions and these sources are located very near or on zero age main sequence (ZAMS), approaching towards a normal MS star.

While proposing the IR classification of YSOs, Lada (1987) pointed out a set of young sources with SEDs varying almost continuously with $-3 > \alpha > 3$, being an intermediate phase between Class I and II sources.

Later, Greene et al. (1994) proposed a revised classification of the YSOs based on α obtained by least square fitting of all the available data between $2.2 - 10 \mu$m. They grouped sources having $\alpha > 0.3$ as Class I, $0.3 > \alpha > -0.3$ as Flat spectrum, $-0.3 > \alpha > -1.6$ as Class II and $\alpha < -1.6$ as Class III YSOs. This revised scheme
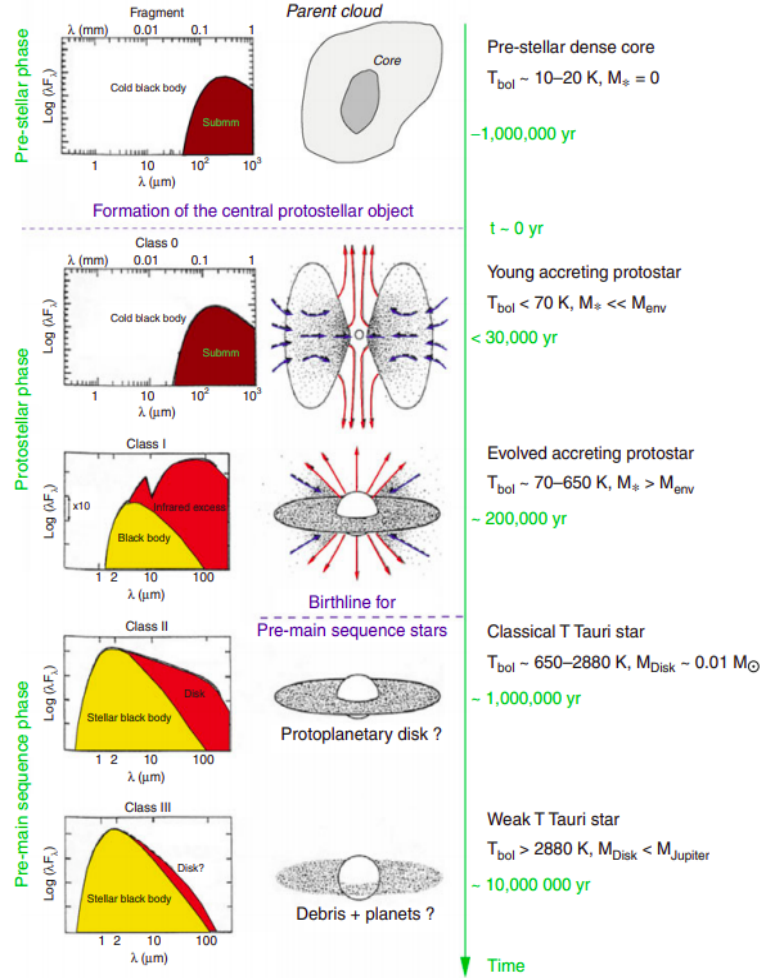
Figure 1.3: An illustration representing the star formation scenario in a molecular cloud from a prestellar cloud core to an evolved Class III YSO. By accreting cloud material from the surroundings as a form of optically thick disk, the core then forms a protostar having size of a few solar radii. The protostar is also associated with bipolar jets and outflows. Once the amount of surrounding dust and gas material dies down, the accretion mechanism ceases, leaving behind an optically thin disk and the central protostar, which is called a pre-main sequence star. On the left, the SEDs of the YSO in different evolutionary stages are shown. The mass of circumstellar (disk+envelope) material and bolometric temperature are shown in the right end. Figure credit: André (2011).

was adopted by Greene et al. (1994) because this work refined the SED classes to

correspond different evolutionary stages of YSOs in a better way.

1.2.4 Intermediate-mass Herbig Ae/Be Stars

Herbig Ae/Be (HAeBe) stars are more massive analog of the low-mass TT stars, optically visible PMS stars having mass range $2 - 8$ M$\odot$. George Herbig (Herbig, 1960) first identified a group of higher mass counterparts of the TTS in 1960. These stars met the following conditions:

1. They are of spectral type earlier than F0, having emission lines in their spectra.
2. They are located inside an obscured region or molecular cloud.
3. These objects illuminate a fairly bright reflection nebula in the vicinity.

But these membership criteria were not sufficient for the selection of the HAeBe stars. Based on later studies (e.g. Hu et al., 1989; Hillenbrand et al., 1992; Oudmaijer et al., 1992; The et al., 1994) it was confirmed that not all HABes are located within a molecular cloud, they could be present in isolated regions also. So, there came a necessity to set a modified selection criteria (Davies et al., 1990; van den Ancker et al., 1997a; Malfait et al., 1998; Waters & Waelkens, 1998) of HAeBe stars which are the following:

1. Stars of spectral type A or B having emission lines in their spectra.
2. Stars that show IR excess, due to the presence of hot or cool circumstellar dust or both.
3. Stars that belong to luminosity class III to V.

Hillenbrand et al. (1992) classified the HAeBes into three groups based on their SED.

Group I: HAeBes in this group are having large IR excess at wavelengths $\lambda \geq 2.2$ μm with the spectral slope given by $\lambda F_\lambda \sim \lambda^{-4/3}$. The SED is similar to that of TT stars, which harbor optically thick flattened accretion disks. With an increase in wavelength, the HAeBes in this group exhibit a decrease in IR excess.
Group II: These HAeBes can be explained best as a disk+envelope system. The HAeBes show large IR excess with flattened or rising spectra with a sharp rise of IR excess between $1 - 2$ μm. This wavelength range corresponds to temperature range 3000-1500 K. The approximate dust evaporation temperature is ~ 1500 K.
Group III: HAeBes belonging to this group have very little IR excess, similar to Classical Be stars. It suggests that the excess is because of the free free emission

from the gaseous circumstellar disk. These HAeBes could possibly be disk-less TT stars of higher-mass (Hillenbrand et al., 1992).

Again, Fuente et al. (1998a) proposed three types of HAeBes based on their gas dispersal efficiency. They found the efficiency to be very different for the "late-type" (B5-A5) and the "early-type" (B0-B5) stars. Early-type stars have more efficiency in the dispersal of the circumstellar cloud material than late-type stars. Due to this difference, no correlation was found between the stellar ages and the Hillenbrands' IR groups. As the morphology of the natal molecular cloud seems to depend highly on the stellar ages, Fuente et al. (1998a) presented classification for both early- and late-type HAeBes.

According to the classification by Fuente et al. (1998a), the Type I stars are those embedded in a dense clump. These sources are of age $\sim 10^5$ years and they generally show bipolar outflows. The Type III stars are of age $> 10^6$ years and they have completely dispersed the surrounding cloud material. They are not associated with any bipolar outflow and are found to be located inside a cavity of the parental cloud. Now, the Type II stars are the intermediate analog of the previous two types. They are not located at the dense clump but immersed in the molecular cloud.

Additionally, based on extended SED emission, Meeus et al. (2001) made additional classification of HAeBes.

Group I: SED of the stars in this group shows a rising or strong emission in the far-IR ($420 - 100\ \mu$m) region.
Group II: In this group stars have flux which falls off sharply in the far-IR region in the SED.

HAeBes inherit gas and dust from the natal molecular clouds while they are still undergoing the formation of the process of main sequence (MS) stars. Eventually, the gas and dust settle down to a flattened circumstellar disk. Being intermediate analog of the low- and high-mass stars, HAeBes have convective cores with radiative envelopes (Alecian et al., 2009). They might produce core fields for having convective cores, but still such fields do not seem to appear on the stellar surface. So the magnetic fields found in HAeBes could possibly be large scale fossil fields. In the survey of intermediate-mass (IM) stars, less than 10% of HAeBes show magnetic fields (Alecian et al., 2009, 2013a), so it is relevant to conclude that HAeBes may not accrete cloud material via magnetic field lines (Alecian et al., 2009). Whether

or not the HAeBes accrete magnetospherically is still one of the greatest mysteries in this group of stars.

Based on linear spectropolarimetry across Hα emission, Vink et al. (2002, 2003) first indicated that the formation mechanisms of Herbig Ae (HAe) stars are similar to the TT stars but different from Herbig Be (HBe) stars. The application of spectropolarimetry was first employed while studying classical Be stars (Clarke & McLean, 1974; Poeckert, 1975). Based on the assumption that Hα photons emerge from a much larger volume than the continuum photons of the star. For this, the Hα photons suffer less scattering and as a consequence, the spectral emission-line flux would be less polarized than the continuum emission. This change in polarization across the spectral line profile is referred as "depolarization", or the classical line effect as this scenario first appears while studying classical Be stars. The technique of spectropolarimetry was first applied on nine HBes by Oudmaijer & Drew (1999). They found the line effect in about half of the whole sample. It is now well established that HAes exhibit intrinsic linear polarization, which is consistent with magnetospheric accretion, while HBes show line-depolarization, which indicates the presence of classical disk accretion Vink et al. (2002, 2005b). In the classical disk accretion scenario, the cloud material is supplied to the regions very close to the star through gravitational instability or viscous heating (Lynden-Bell & Pringle, 1974) in the disk. The cloud material finally settles down onto the star's equatorial area through sporadic accretion.

However, to validate the distinction in accretion mechanism between HAe and HBe stars, a large number of samples is needed. Already, a good number of HAeBes has been studied using spectropolarimetry (Vink et al., 2002; Hubrig et al., 2013; Alecian et al., 2013a; Alecian et al., 2013b; Ababakr et al., 2016; Ababakr et al., 2017). Additionally, we observed 6 more HAeBes and presented the results in chapter 6.

1.2.5   High mass stars

Recent studies provide evidence that the formation process of massive ($> 8\text{M}_\odot$) stars differ from that of low-mass stars (e.g. Zinnecker & Yorke, 2007) in many respects. The estimated mass accretion rate is usually $\geqslant 10^{-4}\text{M}_\odot \text{ yr}^{-1}$ for high mass stars (Hosokawa et al., 2010) which is much higher than the typical value of the low-mass stars ($\sim 10^{-8}\text{M}_\odot \text{ yr}^{-1}$). Because of their rarity, most of such massive stars are located at a distance of a few kpc or greater. In recent literature, three

different concepts of the origin of high mass stars have been discussed, which may occur depending on the environmental conditions of the molecular clouds. These are (1) monolithic collapse and disk accretion (e.g. McKee & Tan, 2002, 2003; Yorke & Sonnhalter, 2002), (2) competitive accretion and runaway growth (Bonnell et al., 1997, 1998, 2004), and (3) stellar collisions and mergers (Zinnecker & Yorke, 2007). The strength of the magnetic field in the parent molecular clouds plays a significant role in determining whether high mass stars form in isolation or clustered (Shu et al., 1987; Crutcher & Troland, 2007).

(a) Monolithic Collapse and Disk Accretion:

McKee & Tan (2002, 2003) initially proposed the monolithic core accretion theory, in which the high mass stars form massive cores supported by internal turbulence against self-gravity, having accretion rates high enough to overpower the radiation pressure. In this mechanism, the massive cores collapse monolithically and eventually produce individual massive stars, rather than numerous low-mass stars (Krumholz, 2006; Krumholz et al., 2009). In monolithic collapse, it is assumed that the mass is gathered before the beginning of the star formation process. According to this scenario, high-mass stars should form in isolation or with other massive stars, unlike a dense cluster of low-mass stars inside the core. Although this theory could be able to explain the observed small fraction of isolated high-mass stars (de Wit et al., 2004), it failed to explain the existence of low-mass star clusters with the high-mass star cradles in Orion, and in most star clusters (Clarke et al., 2000; Lada & Lada, 2003). Additionally, the massive cores embedded in the infrared dark clouds (IRDCs), are believed to exhibit the initial conditions for the formation of massive stars and also star clusters. Also, these cores usually show fragmentation into smaller clumps of low- to intermediate-masses (e.g. Wang et al., 2011), which contradicts the idea of the birth of a massive star from a single massive core.

Nakano et al. (1995) and Jijina & Adams (1996) mentioned that the radiation pressure from massive stars could blow away the polar regions but not the equatorial zone where the massive disk lies. Based on numerical simulations, Yorke & Bodenheimer (1999) and Yorke & Sonnhalter (2002) found that though the central protostar may radiate isotropically, the radiation field becomes anisotropic further from the center. Therefore the radiative flux near the equatorial plane is much lower than the component along the rotation axis. This is known as 'flashlight effect' and it happens whenever a circumstellar disk forms. This allows the gas material to enter into the central regions through accretion. Some disk material can be removed,

which lies at the interface between the HII disk and the outflow region. But the inward radial flow of disk material is allowed along the disk's equatorial plane.

(b) Competitive accretion and runaway growth:

Bonnell et al. (1997, 2001) presented 3D simulations of the increase in stellar masses in small young star clusters by competitive accretion for the first time. The growth of a protostar mainly depends on the size of the accreting area, i,e, the domain from which gas is gathered. The central area of a protostellar cluster is relatively beneficial, as gas flowing into the cluster center increases the gas reservoir for an individual star.

Consider a large, dense molecular cloud having a number of protostellar seeds that are already created by the initial condensation of some denser regions of the cloud. These condensed cores would grow in mass by accreting gas from their individual accretion area (Larson, 1978; Zinnecker, 1982). The accretion domains are relatively larger for higher mass cores and the gravitational spheres of influence would also grow with increasing mass. The external environment of the individual accretion domain is also equally important as it regulates the amount of gas being accumulated in each prostostellar core. The accretion domain of a protostar located at the edge of the cloud is tidally limited by the cloud mass of the inner part. On the other hand, for a protostar located at the center of the cloud is associated with an accretion domain of the whole cloud. Now, as the cloud mass is limited, the protostellar cores start to compete for the cloud gas, especially when the accretion domains begin to overlap. The action of the protostellar cluster to accumulate gas material from longer distances and focus it towards the accreting protostars, in combination with their increasing action radii due to their mass growth, is what makes the competitive accretion process a powerful mechanism for massive star formation.

(c) Stellar Collisions and Mergers:

Stellar mergers are rare and relevant for the highly massive stars located in the rich young clusters, for example, young globular clusters. One reason to invoke this fact is that ongoing competitive accretion of the protostellar cluster members leads to an increase in the stellar density at the cluster center, potentially to the region where grazing collisions become unavoidable. Stellar collisions might be the process by which rapidly rotating massive stars form. If a merger does happen, there could be three distinct phases (Bally et al., 2005). (1) An 'inspiral' phase, during which the encountered system evolves towards a more compact order, (2) the 'merger'

phase, when a bulk of the gravitational energy is released and (3) the 'outflow' phase, when a part of circumstellar matter is ejected by gravitational energy and the collision products settle into a new configuration.

1.3 Pre-main-sequence accretion

The low-mass ($1 \lesssim M_\odot$) young ($1-10$ Myr) stars grow their mass by accreting material from the circumstellar disks of dust and gas. In a very close vicinity (~ 0.1 AU) of the star, disk temperature increases above $\sim 1,000$ K due to heating by stellar radiation and the dust grains start to sublimate. The inner edge of the dust wall re-emits the stellar energy it absorbs, accounting for a substantial amount of the observed near-IR excess. At a few stellar radii, the stellar magnetosphere truncates the circumstellar disk and the matter flows onto the star, following the magnetic field lines in funnel flows or accretion columns. The temperature of the gas material in these columns rises to ~ 8000 K or above, resulting the observed broad emission lines (e.g., Hα, Hβ, Paschen β, Bracket γ etc.). In order to study the objects having high extinction, we need to consider the emission lines at longer wavelengths (e.g. Paschen β, Bracket γ), rather than shorter wavelengths (e.g. Hα, Hβ etc.), so that the line fluxes are not heavily affected by the extinction caused by the contribution from gas and dust.

The infalling gas material moves with free-fall velocities (~ 300 km s^{-1}) when it shocks the stellar photosphere. The shock heats the gas to a temperature of order of 10^6 K, producing X-ray emission. Most of this X-ray emission gets absorbed and re-emitted at lower temperatures, resulting in strong ultraviolet (UV) and optical continuum excess along with some other relatively narrow emission lines. The typical accretion rate for low-mass stars is $\sim 10^{-8}$ M$_\odot$ yr^{-1} lasting for $\sim 2-3$ Myr (Hartmann et al., 2016).

Koenigl (1991) stated that disk truncation radii can be expected to be larger for weaker mass accretion rate ($\dot{M}$) and stronger dipole components (B$_{dip}$), as R$_t \propto$ B$_{dip}^{4/7}\dot{M}^{-2/7}$. Now low-mass TT stars have strong B$_{dip}$, having smaller radiative cores and larger outer convective zones, they possess axisymmetric magnetic fields of the order of kGauss. Such strong magnetic fields can destroy circumstellar disks upto a few stellar radii. On the other hand, high-mass stars possess more complex magnetic fields with many higher order components. The fields are found to be highly non-axisymmetric and B$_{dip}$ is also weak. In principle, the drop in B$_{dip}$ will allow the

circumstellar disk to push closer to the star. For some HAeBe stars, the disk could be able to reach the stellar surface and accrete through a boundary layer (Hartmann et al., 2016).

1.4   Magnetic fields in Molecular clouds

Though Hall (1949a) and Hiltner (1949b) discovered the presence of magnetic fields in the ISM around seven decades ago. But how the ISM magnetic field originated is still not clear. In general, the galactic-scale dynamo is thought to be responsible for generation of the magnetic field, which converts mechanical energy into magnetic energy (e.g., Beck et al., 1996; Brandenburg & Subramanian, 2005). In astronomical objects, such as, galaxies, stars and planets, the alpha-Omega dynamo generates large-scale regular fields. The impact of magnetic fields on the process of star formation is a major topic of discussion (e.g., Pudritz et al., 2014; Seifried & Walch, 2015). Additionally, magnetic fields influence in reshaping the structure of cloud fragments and coupling between the gas and dust particles in molecular clouds (Henning et al., 2001). Internal magnetic fields support the molecular clouds against the gravity, the phenomenon known as 'flux freezing' is considered to be responsible for this support in them. The magnetic field lines behave as being tethered to the gas in clouds. So, any clumping in the clouds brings together the adjacent magnetic field lines, which increases the magnetic field value. Flux freezing implies both that the magnetic fields are tied with fluid motion and the cloud is constrained by the magnetic field configuration. When a spherical cloud of radius 'R' is threaded by a uniform magnetic field, the magnetic flux would be:

$$\phi_B = area \times B = \pi R^2 B \tag{1.2}$$

which remains constant due to flux-freezing. For a uniform density ρ and constant mass M$= \frac{4}{3}\pi\rho$R^3, the flux freezing indicates that B $\propto \rho^{3/2}$. So the magnetic field increases sharply with density than that found by the observations. A detailed study of magnetic fields is always necessary as they affect the evolution of molecular clouds and also star formation, both in spontaneous and triggered modes.

   Various techniques are employed to probe the interstellar magnetic field, such as (i) polarization of stellar radiation, (ii) polarized emission from dust grains at the longer wavelengths (sub-millimeter and millimeter), (iii) Zeeman effect of the spectral lines and (iv) Faraday rotation of the background radio sources. First three

methods are usually opted to estimate the magnetic fields towards the star forming regions while the later is used for the fields in the diffuse medium.

In the thesis, we have used the modified Chandrasekhar-Fermi (CF) relation (Chandrasekhar & Fermi, 1953) to estimate the projected magnetic field strength (B_{POS}). This relation assumes an equipartition between the perturbed magnetic and kinetic energies. B_{POS} can be calculated using the following relation (Chandrasekhar & Fermi, 1953; Crutcher, 2005; Ostriker et al., 2001):

$$B_{POS} = 9.3\sqrt{n(H_2)}\frac{\Delta v}{\Delta \theta} \tag{1.3}$$

where $n(H_2)$ is the volume density of hydrogen gas in molecular clouds. Δv is the full width at half maximum obtained from the velocity dispersion δv ($\sqrt{8ln2}\ \delta v$). The dispersion in position angles ($\Delta \theta$) can be obtained from polarimetric measurements of the stars projected background to the clouds. The CF method is applicable only when $\Delta \theta < 25°$.

1.5 Interstellar Polarization

Interstellar polarization was first discovered over 70 years ago (Hall, 1949b; Hiltner, 1949a) at visible wavelengths. In a short while, Hiltner (1949b) suggested this scenario to be an outcome of the dichroic extinction of unpolarized starlight by aspherical dust grains aligned with the ambient magnetic field. Stein (1966) predicted polarized emission from the dust and it was first observed by Cudlip et al. (1982) in the far-IR (FIR). The polarization of interstellar medium (ISM) by aligned dust grains can be traced from UV (e.g. Anderson et al., 1996) to highly obscured region in the near-IR emission (Clemens et al., 2012) and into heavily dense cloud with highly embedded sources using FIR emission (Dotson et al., 2000). These observations imply that the ISM is magnetized and also provide a tool to infer the strength and geometry of the magnetic fields (e.g. Davis & Greenstein, 1951; Chandrasekhar & Fermi, 1953).

When the unpolarized starlight gets absorbed and scattered by a series of interstellar dust grains present along the line-of-sight, the absorbed starlight by dust grains re-emits in IR (see Fig. 1.4). The absorption is maximum along the major axes of the dust grains, which are aligned by the interstellar magnetic fields with their minor axes parallel to the field lines. So, the transmitted radiation would be polarized along the direction of the magnetic field. Davis & Greenstein (1951,

hereafter DG mechanism) proposed that the mechanism responsible for the alignment of dust grains involves an interaction between the magnetic fields and the spin of dust grains. This principle states that the spinning grains have a tendency to align with their major axes perpendicular to the direction of angular momentum vector. The orientation of the spinning dust grains is predicted by paramagnetic dissipation of their rotational kinetic energy. The external magnetic field induces an internal field within the dust grains. In case of a spinning grain, it is difficult for the internal field to align along the external field. This misalignment leads to a dissipative torque that gradually eliminates components of rotation perpendicular to the ambient magnetic field, tending to align the angular momentum along the direction of the field lines. Gas-grain collisions oppose this alignment, which tends to restore their random orientations.

Till date, several mechanisms have been proposed to explain the dust grain alignments, among which the radiative torque alignment mechanism is the most successful one (Lazarian, 2007). In this mechanism, irregularly shaped dust grains differentially scatter anisotropic radiation, making them spinning preferentially about their short axes. The precision of this spin axis in this mechanism is the local magnetic field. In the diffuse ISM, outer regions of the cloud and the vicinity of star forming regions, the dust grains are aligned by radiative torques due to the external radiation field. On the other hand, dust grains located deep inside clouds could possibly be aligned by the radiation from prestellar and protostellar objects (Crutcher, 2012).

1.6 Thesis outline

The thesis consists of eight chapters, and its structure is as follows:

Chapter 1: This chapter presents a comprehensive view of the star formation processes with a general introduction of ISM, which exists between the stars. Different modes of star formation are discussed, along with the evolution of protostars with different ranges of masses. It also describes the impact of the magnetic fields on the evolution of molecular clouds and star formation. The interstellar polarization and estimation of magnetic fields using polarimetry as a tool are also discussed.

Chapter 2: This chapter describes various telescopes and instruments used for acquiring data in this thesis. In order to trace the projected magnetic field geometry towards the star forming regions, we used the technique known as polarimetry. Optical polarimetric observations were carried out using the polarimeter
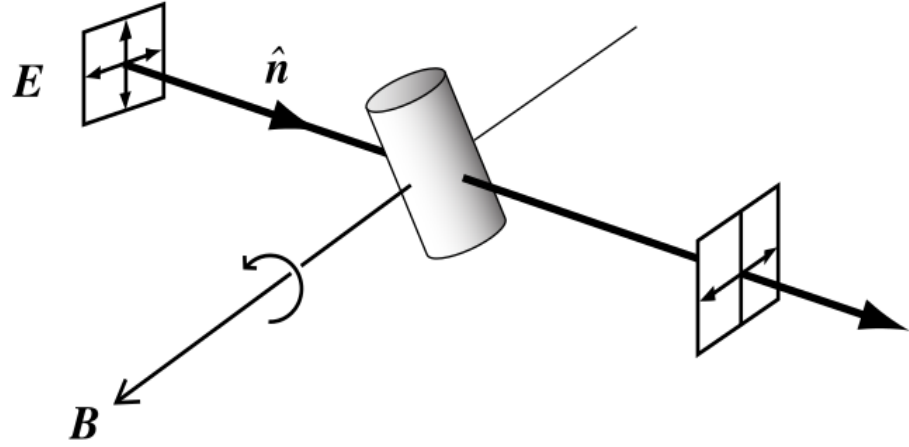
Figure 1.4: An illustration of polarization through dichroic extinction by dust grains. Unpolarized radiation propagating along $\hat{n}$ impinges on an asymmetric dust grain rotating with its minor axis parallel to the ambient magnetic field **B**. The radiation would be absorbed maximum along the longer axis of the grain and the transmitted radiation gets polarized in the direction of **B**. Figure credit: Stahler & Palla (2005).

attached with 1-m Sampurnanand Telescope (ST) at ARIES, Nainital, India. We also performed optical and near-IR spectroscopic observations towards YSOs using 2-m Himalayan Chandra Telescope (HCT) at IIA, Bengaluru, India and 3-m Infrared Telescope Facility (IRTF) at Mauna Kea Observatory (MKO), Honolulu, USA. Optical spectropolarimetric observations towards HAeBe stars were carried out using 10-m South African Large Telescope (SALT), South African Astronomical Observatory, South Africa. Different software and processes of data reduction are also explained in detail. In addition, the archival data used in this thesis are also briefly described.

Chapter 3: This chapter presents a detailed study of LDN 1172/1174. After a general introduction of the cloud complex, we estimated the distance to this cloud using the latest *Gaia* DR2 of the YSOs associated with LDN 1172/1174 and polarimetric measurements of the stars projected background to this cloud complex. The distance to this cloud complex is estimated to be 335±11 pc. Using the distance and proper motion of the previously identified YSOs, we have found 20 sources kinematically associated with the YSOs, which are characterized in this chapter. We acquired spectroscopic observations of 4 of these newly found comoving sources to obtain their spectral types. We made a census of YSOs towards HD 200775, the star which is considered to be responsible for ionizing LDN 1174. We estimated the magnetic field orientation and strength towards this cloud complex to know its

impact on star formation. The magnetic field lines are found to follow the cloud's elongated structure. The strength of the projected magnetic field is estimated as $\sim$20 μG. We compare our results with the same obtained from *Planck* data and found a good correlation in the results. We found that LDN 1172/1174 is having a higher star formation rate per unit solar mass, consistent with the clouds where the magnetic field lines are parallel to the cloud elongation, compared to that for the perpendicular orientation. We also made near-IR spectroscopic study towards 10 YSOs distributed towards LDN 1172/1174 and characterized them. A majority of them do not show Bracket-γ in emission.

Chapter 4: In this chapter, we explain the kinematic properties of three HAeBes in the Cepheus Flare. This is an extension of the work done in Chapter 2 on a wider scale in the cloud complexes LDN 1147/1158, LDN 1172/1174 and LDN 1177. A number of YSOs are found to be distributed towards these cloud complexes along with the HAeBe stars PV Cep, HD 200775 and BD+68°1118. Based on the distances and proper motions of all the known YSOs and HAeBe candidates from *Gaia* DR2, a total of 74 additional comoving sources are found in this region of which 39 form a loose association surrounding BD+68°1118 and 17 sources are distributed in a more compact manner towards HD 200775. These sources are characterized using optical and near-IR color-color and color-magnitude diagrams. The comoving sources around BD+68°1118 are predominantly of $\sim$10 Myr age with no or very little near-IR excess emission, while sources surrounding HD 200775 are younger (1−3 Myr), showing comparatively higher near-IR excess emission. The positive expansion coefficients obtained for the systems of BD+68°1118 and HD 200775 indicate that they are in the expanding phase. A spatio-temporal gradient of these associations towards the center of the Cepheus Flare Shell supports the concept of triggered star formation due to external impacts.

Chapter 5: Perseus is another star forming region located diagonally opposite to the Cepheus Flare, at a similar distance from the Galactic plane. Here we present high resolution spectroscopic study of 12 young intermediate-mass stars located in the Perseus OB2 region. We also explain their kinematic properties using the latest *Gaia* DR2 and have found that a fraction of these sources are kinematically associated with the low-mass YSOs, though the intermediate-mass stars are relatively more scattered in the distance and proper motion planes. Absorption in Balmer lines in all the observed spectra signifies the absence of circumstellar disks surrounding these sources. A majority of these sources are found to be of 2−4 Myr age, which is

comparable with the typical disk dispersal timescale of the intermediate-mass stars. We obtained EWs of four DIBs in the observed spectra and found a trend of increase of EW with the color excess. Presence of interstellar components of sodium (Na) lines along with stellar Na lines in the spectra of two observed sources indicates higher relative velocities between the stars and interstellar clouds.

Chapter 7: Here, we present spectropolarimetric study of six HAeBe stars to know their accretion mechanism. We computed the continuum degree of polarization and position angle of each star across the Hα and Hβ lines. The QU behaviour for each target is also noted. For A-type stars, we obtained the line polarizations and loop in the QU plots, signifying ongoing magnetospheric accretion in these sources. We also can notice depolarization for the B-type stars, indicating disk accretion. We added our results to the previous spectropolarimetric studies of 56 HAeBe stars, thus increasing the statistics by $\sim$9%.

Chapter 5: We made R-band polarimetric observations of 12 YSOs identified in the vicinity of BRC 18 to infer their disk orientations. Using the distance and the proper motion measurements obtained from the *Gaia* DR2 of the sources identified as YSOs in the vicinity of BRC 18, we determined projected motion of the YSOs and hence BRC 18 on sky plane by assuming that both are kinematically coupled. We found that the disk orientations of the YSOs are oriented randomly with respect to the projected magnetic field towards BRC 18. The relative proper motions of the YSOs associated with the BRC 18 are found to show a trend of them moving away from the direction of ionizing sources. Using BRC 18 as a prototype, we made our analysis for other BRCs also which showed the similar trend. We computed the offset between the angle of direction of ionization and relative proper motion of YSOs and found it to lie close to being parallel to each other. The Pearsons correlation coefficient of these two angles is found to be 0.961 with pnull 3.072e-09. The Spearman's correlation coefficient is estimated as 0.940, with pnull as 6.115e-08. Along with these, we also performed k-s test on these angles. The computed statistic is 0.125 and the pvalue is 0.999. All these results indicate that the YSOs and hence the BRCs are most likely accelerating away from the ionizing source due to the "Rocket Effect". In addition to these, we also found several sources lying in the vicinity of several BRCs, which are kinematically associated with the previously known YSO candidates and therefore, could be YSO candidates unidentified in earlier studies.

Chapter 8: In the final chapter, we have summarized all the main results obtained from the various aforesaid studies we carried out in this thesis. We presented the conclusion based on the key findings and briefly explained the future work.

Chapter 2

Telescopes, Instruments, Observations, Software & Data Reduction

2.1 Introduction

Magnetic field plays a vital role in the evolution of molecular clouds and the star formation processes in them. Magnetic field lines at different extinction scales can be probed by acquiring polarimetric observations in different wavelengths. When unpolarized starlight passes through the aspherical dust grains aligned with their shorter axis parallel to the ambient magnetic field associated with the molecular clouds, the starlight gets polarized. The polarization vectors, produced by selective extinction, trace the plane-of-sky component of the magnetic fields of the molecular clouds. We mapped the magnetic field geometry prevailed in the molecular clouds by performing optical polarimetric observations. We have used ARIES IMaging POLarimeter (AIMPOL) attached with 104-cm Sampurnanand Telescope.

The young stellar objects (YSOs) associated with the molecular clouds are found to accrete mass at an early evolutionary stage. It begins with a short period ($\sim 10^5$ yr, Class 0 phase) of strong accretion, during which the star gains most of its mass. The circumstellar material continues to get channeled from the inner disk onto the stellar photosphere following the magnetic field lines. The processes involved in these early stages of evolution play a significant role in removing material from the circumstellar disk, influencing the disk dissipation timescales, and eventually settling the final stellar mass. The processes may also affect the formation of planets

2. TELESCOPES, INSTRUMENTS, OBSERVATIONS, SOFTWARE & DATA REDUCTION

in the disk. We obtained the optical and near-IR spectroscopic data to obtain the spectral types and mass accretion rates of the YSOs using the Hanle Faint Object Spectrograph and Camera (HFOSC) attached with 2-m Himalayan Chandra Telescope (HCT).

The YSOs, being embedded in the parental cloud during its early stage of evolution, lack emission in the optical regime. For this, the luminosities of commonly used optical traces like Hα and CaII could get contaminated due to the emission from jets and winds, making the measurement of mass accretion rate highly uncertain (Rigliaco et al., 2012). As Brγ (2.165 μm) and Paβ (1.281 μm) are higher excitation lines than Hα and CaII, they are less likely to get contaminated by winds and jets. Also, near-IR lines are less affected by extinction than optical tracers making them particularly suitable to derive the properties of more embedded younger sources. We performed near-IR spectroscopic observations using SpeX attached with 3.2-m InfraRed Telescope Facility (IRTF) to obtain the spectral properties of the YSOs.

Intermediate-mass (IM) stars form an important link between the reasonably well understood formation of low-mass stars to the rarer, more deeply embedded high mass stars. Investigations in the Herbig Ae/Be (HAeBe) stars (M = 2$-$8 M$_\odot$) suggest that their circumstellar disks may be dispersed within a shorter timescale $\sim$3 Myr (Hernández et al., 2005; Carpenter et al., 2006; Manoj et al., 2006). Hydrogen lines are found to be in emission in HAeBe stars. As they evolve, Hα goes into absorption, but the possibility of filling of the absorption core is observed in some of the sources which are found to be associated with star forming regions (Manoj et al., 2006). Hence the hydrogen line widths that are usually used to determine the luminosity class, cannot be used. This necessitates the observations of gravity sensitive lines, for example, NII (3995 Å), SiII (4128 and 4131 Å), CII (4267 Å), SiIII (4553 and 4561 Å), and OII lines (4070 and 4976 Å). But, these lines are relatively weak and are hardly visible in low-resolution spectra. Therefore to accurately estimate the spectral type and luminosity class of IM stars, observations at high spectral resolution are essential. To obtain the spectral types of the IM young stars, we acquired high resolution spectroscopic data using Hanle Echelle Spectrograph (HESP) attached with HCT.

It is now well established that HAeBes are associated with circumstellar disks (e.g. Matter et al., 2014) and a significant number of them are actively accreting material through these disks (e.g. Mendigutía et al., 2012). Many questions, for example, whether massive stars are formed through disk accretion, and issues related

to the role of magnetic fields during their formation, are not answered properly. For this, the region of few stellar radii from the stellar surface is a crucial area to investigate the accretion mechanism. For this, we carried out spectro-polarimetric data of six HAeBe stars using RSS spectropolarimeter attached with 10-m South African Large Telescope (SALT).

In addition, we also used the archival data available in optical (*Gaia*, Pan-STARRS), near-IR (2MASS), mid-IR (*Spitzer* and *WISE*) and X-ray (*XMM-Newton*) wavelengths in our research work.

In this chapter, we describe the telescopes used in this thesis in section 2.2 and discuss the back-end instruments used during our observations in section 2.3. The details of observations are described in section 2.4 and information about the software used for data reduction along with methods obtained are discussed in section 2.5. Finally, we provide the details of the archival data used in our research in section 2.6.

2.2 Telescopes

- **104-cm Sampurnanand Telescope (ST):** This is an optical observing facility located at Aryabhatta Research Institute of observational SciencES (ARIES), Manora Peak, Nainital, India. This telescope is commonly called as 40-inch by ARIES people. It is installed at Manora Peak by Veb Carl Zeiss, Jena, East Germany in 1972. This facility has an Ritchey-Chretien (RC) reflector with a f/13 Cassegrain and f/31 Coude foci with plate scales $15.5''$/mm and $6.5''$/mm, respectively. At the cassegrain end of the telescope, there is a field of $\sim 45'$ with corrector. It has an equatorial 2-pier English mount. An ST4 camera attached with 8-inch guider telescope is used for guiding. It has a tracking accuracy $\sim 7''$/hr without guider and $\sim 0.7\ ''$/hr with guider. Sagar et al. (2013) provided a detailed description of the telescope. It is equipped with a 1K×1K CCD camera. Field-of-view (FOV) of the ARIES Imaging Polarimeter (AIMPOL) is $\sim8'$.

- **201-cm Himalayan Chandra Telescope (HCT):** This is an optical and IR observing facility, located at the Indian Astronomical Observatory (IAO), Mt. Saraswati, Hanle, Ladakh, India. It was installed by Indian Institute of Astrophysics (IIA), Bangalore, in 2000. This telescope is remotely operated

through a satellite communication link from the Centre for Research & Education in Science & Technology (CREST), IIA, Hosakote. It has a tracking accuracy (without guiding) of 1.38″ (mean) over 10 minutes. The telescope is equipped with three science instruments which are mounted on an instrument mount cube at the Cassegrain focus. The Cassegrain F-ratio is f/9 with a plate scale $\sim$ 11.5″/mm. It has a FOV $\sim$ 7′ and 30′ with corrector. The instrument mount cube has an on-axis port and four side ports, which makes all the available instruments mounted on the telescope. The instruments currently available are the near-IR Imaging Spectrograph (TIRSPEC), Hanle Faint Object Spectrograph Camera (HFOSC), the near-IR imager, the optical CCD imager, and the Hanle Echelle Spectrograph (HESP). A detailed information about the telescope is provided in Prabhu & Anupama (2010).

- **3.2-m NASA InfraRed Telescope Facility (IRTF):** This telescope is optimized for IR observations. It was established by NASA in 1979 and located in the Mauna Kea Observatory in Hawaii, operated by University of Hawaii Institute for Astronomy, Mauna Kea, Honolulu, USA. The Cassegrain f/ratio is f/38 with a plate scale 1.95″/mm. The telescope is mounted on a large English yoke equatorial mount. Observations can be remotely done through a VNC software. Two displays Bigdog and Guidedog are assigned to instruments at this time. The IRTF hosts four instruments: SpeX, iSHELL, MORIS, MIRSI, MOC. Further details of this facility are provided in http://irtfweb.ifa.hawaii.edu/.

- **10-m South African Large Telescope (SALT):** SALT is the largest optical telescope in the southern hemisphere. It is located at the South African Astronomical Observatory (SAAO) field station near Sutherland, in the Northern Cape province, about 400 km from Cape Town. The primary mirror is configured with 91 hexagonal mirror segments, each of 1-m wide, resulting in a whole mirror of 11.1 m × 9.8 m. The primary mirror is tilted at a constant zenith distance (37°), with azimuthal rotation only for the target. The target is tracked by shifting the instrument payload located at the primary focus. The first light of SALT was announced on 1st September, 2005. SALT provides four instruments: RSS, SALTICAM, BVIT and HRS. Details of each instrument is explained in https://astronomers.salt.ac.za/instruments/.

Table 2.1 presents the main specifications of the telescopes used for our observations.

Table 2.1: Details of the telescopes used for observations:

	Sampurnanand Telescope (ST)	Himalayan Chandra Telescope (HCT)	Infra-red Telescope Facility (IRTF)	South-African Large Telescope (SALT)
Place	ARIES, Nainital, India	IAO, Hanle, India Operated by IIA, Bangalore	Hawaii, Mauna Kea, Honululu, US	Sutherland, Northern Cape, South Africa
Longitude	$79°27'24''$ (E)	$78°57'51''$ (E)	$155°28'23''$ (E)	$20°48'38''$ (E)
Latitude	$29°21'42''$ (N)	$32°46'46''$ (N)	$19°49'35''$ (N)	$32°22'34''$ (S)
Altitude (m)	1951	4250	4145	1759
Focus	Cassegrain	Cassegrain	Cassegrain	Segmented
F-ratio	f/13	f/9	f/2.5	f/4.2
Diameter of the primary mirror (m)	1.04	2.01	3.2	11.1×9.8
Plate-scale	$15.5''$/mm	$11.5''$/mm		$4.5''$/mm
Mount	Equatorial	Alt-Azimuth	Equatorial	Alt-Azimuth

2.3 Instruments

2.3.1 ARIES Imaging Polarimeter (AIMPOL)
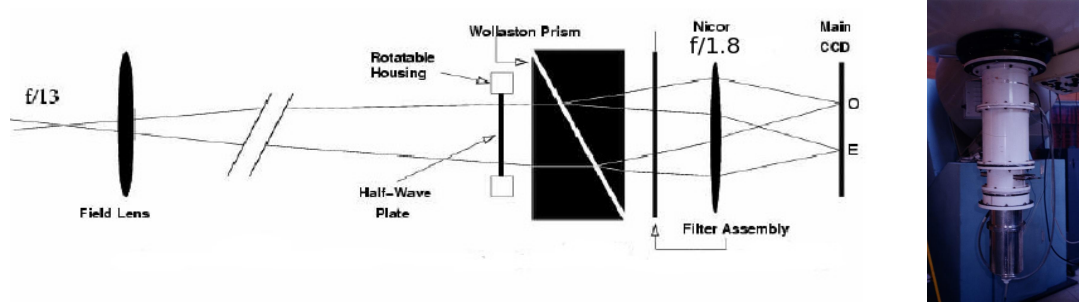
Figure 2.1: (Left panel:) Optical design of the ARIES Imaging Polarimeter (AIMPOL). Credit: Rautela et al. 2004. (Right panel): AIMPOL is mounted as back-end instrument to the 104-cm telescope during the observations. The white-coated suit contains the polarimeter. Filters holder and 1024×1024 CCD are also attached.

Linear optical polarimetric observations were acquired using the ARIES IMaging POLarimeter (AIMPOL; Rautela et al., 2004), mounted as a back-end instrument at the Cassegrain focus of the 104-cm Sampurnanand telescope of ARIES, Nainital, India. The optical design of AIMPOL is shown in Fig. 2.1. It consists of a field lens (50mm, f/6) in combination with the camera lens (85mm, f/1.8). Along with the lens combinations, there is an achromatic, rotatable half-wave plate (HWP), which acts as a modulator and a Wollaston prism beam-splitter, which is used as analyzer. Wollaston prism splits the infalling light into ordinary and extraordinary polarized rays separated by ∼28 pixels along the north-south direction on the plane of sky. The optic axis of the HWP is kept along the north-south axis of the telescope. AIMPOL is attached with TK 1024×1024 pixel^2 CCD camera of which the central 325×325 pixel^2 are used for the observations. The plate scale of the CCD is $1.48''$/pixel

(pixel size $\sim$ 24 μm) and the FOV is $\sim$ 8$'$ in diameter. The read-out noise and the gain are 7.0 e^{-1} and 11.98 e^{-1}/ADU, respectively. The instrumental polarization is $\sim$0.1%. Details of the instrument and the polarization measurement techniques can be found in Rautela et al. 2004.

2.3.2 Hanle Faint Object Spectrograph Camera (HFOSC)
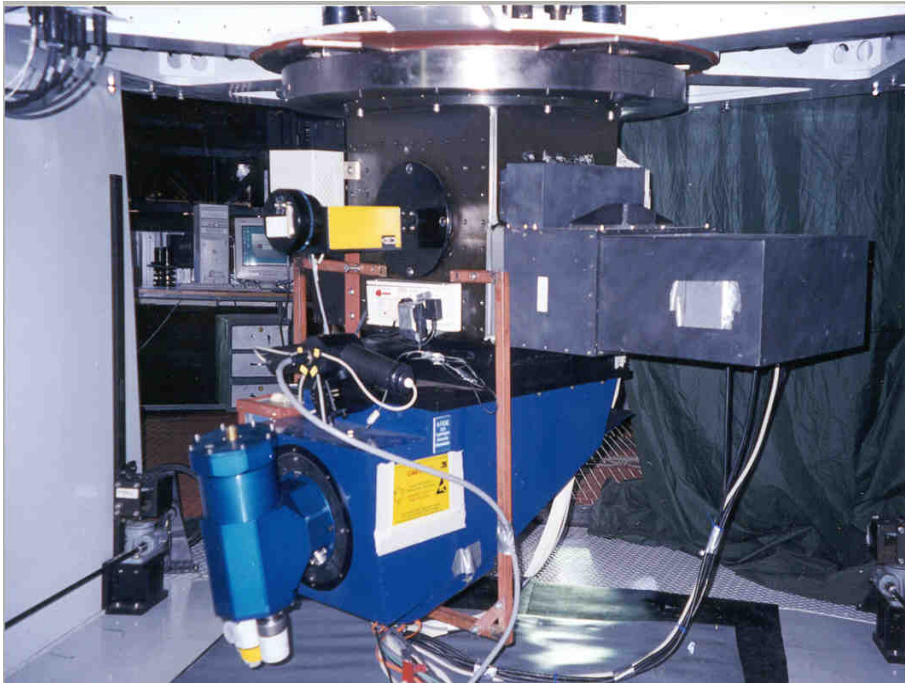
Figure 2.2: Image of the HFOSC. Credit: "https://www.iiap.res.in/iao/hfosc.html".

HFOSC is an optical imager and spectrograph which was built collaboratively at the Copenhagen University Observatory. It covers wavelength from 350-900 nm. HFOSC is attached with a 2048$\times$4096 pixels^2 SiTe CCD with pixel size 15$\times$15 microns. The plate scale of the CCD is 0.296$''$/pixel and the FOV is 10$'\times$10$'$. The read-out noise and the gain are 4.8 e^{-1} and 1.22 e^{-1}/ADU, respectively. Low to intermediate spectral resolution (R = 205-4500) can be achieved using a set of 10 grisms. In imaging mode Bessell UBVRI broad-band filters and narrow-band filters OII, OIII, Hα, SII etc. are available. HFOSC consists of an optical bench collimator and camera. Three wheels are present: an aperture/slit wheel, a filter wheel and a grism wheel. All wheels have 8 positions. The converging beam from

the telescope passes through the Filter and Spectral lamp Unit (FASU) and comes to focus of the aperture wheel. After that the beam passes through the collimator and forms a parallel beam which is imaged by the camera on the CCD. An image of the HFOSC is shown in Fig. 2.2. One can get details of the instrument at "http://www.iiap.res.in/iao/hfosc.html".

2.3.3 Hanle Echelle Spectrograph (HESP)
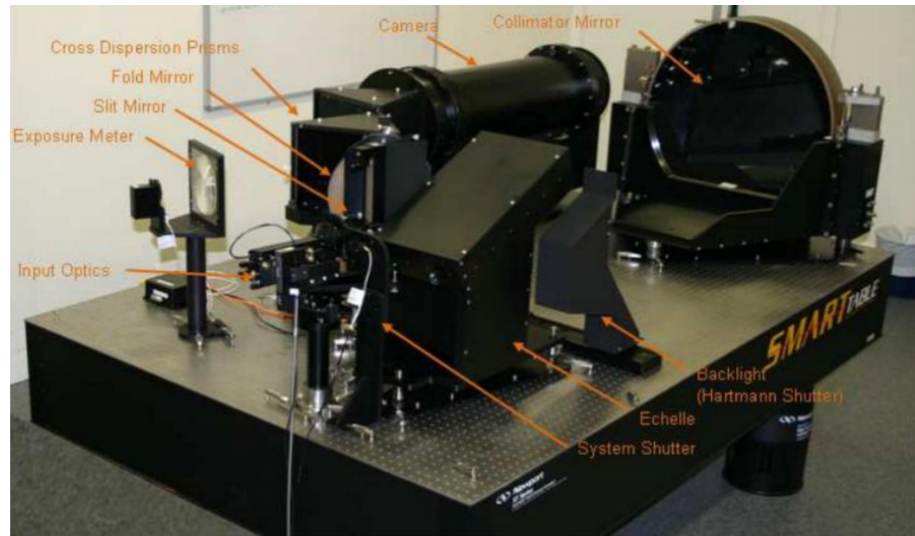
Figure 2.3: Image of the Hanle Echelle Spectrograph (HESP). Credit: Sriram et al. 2018.

Hanle echelle spectrograph is a bench mounted, fibre-fed, high resolution (R = 30,000 and 60,000), spectrograph attached with the 2-m HCT. HESP was built and designed by Kiwi Star Optics, Callaghan Innovation, New Zealand. The system control including acquisition and guiding unit, CCD system, spectral data reduction pipeline were developed at IIA. A 100 micron fiber as a input slit is used to achieve the low resolution mode (30,000) and an image slicer is used for the high resolution mode (60,000). An R2 echelle grating, along with two cross dispersing prisms, produces a wavelength coverage of 350-1000nm in a single CCD frame. HESP has E2V CCD231-84 4K×4K 15 micron square pixel CCD. The spectrograph is kept in a thermally controlled environment and provides a mechanical stability of 200 m/s during an observing run. A simultaneous ThAr calibration can achieve a radial velocity accuracy of 20m/s. The minimum inter-order separation on the detector is

400 μm. The faintest star one can observe using HESP is with $\sim$12 mag (R=60000, S/N $\sim$15). An image of the instrument is shown in Fig. 2.3. A detailed description of HESP can be found in Anantha et al. (2013); Sriram et al. (2018).

2.3.4 Spex
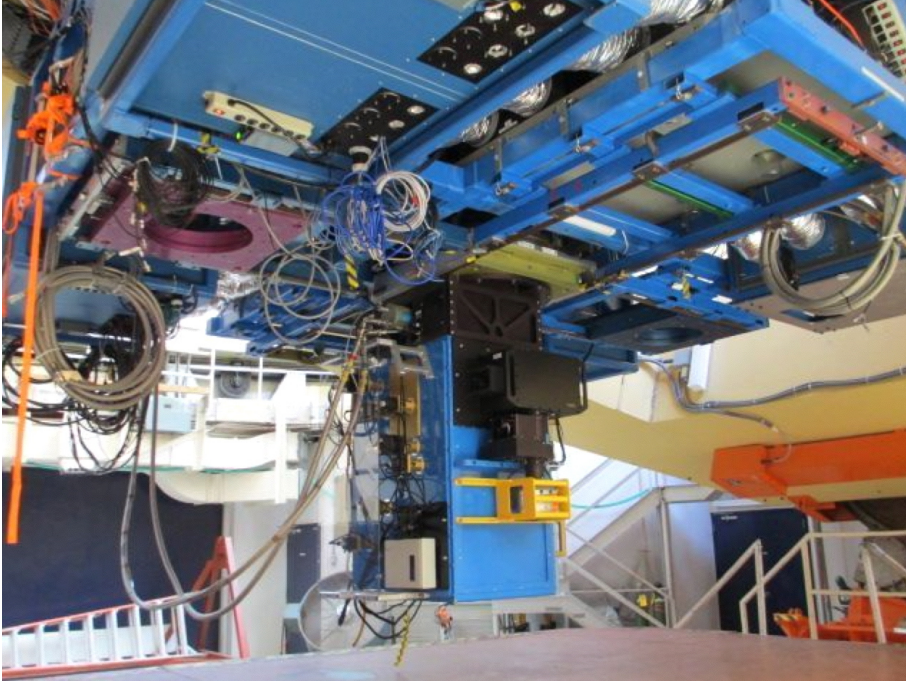
Figure 2.4: Image of the Spex. Credit: "http://irtfweb.ifa.hawaii.edu/~spex/".

SpeX is a medium-resolution ($\lambda/\triangle\lambda \simeq 2000$), cross-dispersed spectrograph built at the Institute for Astronomy (IfA), for the NASA IRTF on Mauna Kea. The operating wavelength range of Spex is $0.7-5.3$ μm. The wavelength range $0.7-5.3$ μm is covered with two cross-dispersed modes, the short-wavelength cross-dispersed mode (SXD), and the long wavelength cross-dispersed mode (LXD), along with a 15″ long slit. Spex is also having single-order long slit (60″) modes and a low-resolution prism mode (covering $0.7-2.5$ μm wavelength range) with 15″ or 60″ long slit. Rayner et al. (2003) provided a detailed description of SpeX. Since 2012, an additional CCD imager known as MORIS (MIT Optical Rapid Imaging System; Gulbis et al., 2011), is installed to the side of SpeX. MORIS can be used simultaneously for optical guiding and optical photometry with SpeX. The plate scale for SpeX is 0.1″/pixel. A

Table 2.2: Wavelength Coverage with SXD Mode in SpeX

Order	Wavelength Coverage (μm)
9	0.69−0.85
8	0.71−0.96
7	0.78−1.10
6	0.92−1.28
5	1.11−1.54
4	1.37−1.92
3	1.83−2.56

combination of $0.5''\times15''$ slit was used during observations at a spectroscopic resolution of R=1200 in the short cross-dispersed mode (SXD) which covers 0.7−2.56 μm. Table 2.2 lists wavelength coverage with SXD mode in SpeX. Gain is 1.5 e$^-$/DN and RON is 5e$^-$RMS (3 μs/pixel) with 32 NDR and 12 e$^-$ RMS (3 μs/pixel). An image of Spex is provided in Fig. 2.4.

2.3.5   Robert Stobie Spectrograph (RSS)

The main workhorse instrument working in SALT is the Robert Stobie Spectrograph (RSS), a complex multi-mode instrument having a wide range of capabilities. RSS was designed uniquely to have a number of rapidly and remotely reconfigurable observing modes. The facilities available with RSS are described below:

1. Narrow-band imaging: Sensitivity from 320−900 nm, i.e., down to the UV atmospheric cut-off.

2. Long-slit spectroscopy (LS): A fully articulating camera/detector along with Volume Phase Holographic transmission gratings (VPHGs), allowing for a broader choice of wavelength coverage and spectral resolutions. Low to medium resolution spectroscopy can be achieved (upto R $\sim$5000 with $1''$ slits; R $\sim$9000 with $0.6''$ slits).

3. Multi-object spectroscopy (MOS) using laser-cut carbon composite focal plane slit masks, to obtain upto $\sim$50 objects at a time. For achieving more accurate background subtraction, a "nod and shuffle" mode will be eventually employed, but is not available yet.

4. Fabry-Prot imaging spectroscopy and tunable filter imaging in the range of 430−860 nm, using 3 etalons providing 3 resolution regimes of R = 320−770, 1250−1650, and 9000.

5. Long-slit spectropolarimetry: It provides linear, circular and all-Stokes mode spectropolarimetry and also imaging polarimetry can be obtained, using either one

2. TELESCOPES, INSTRUMENTS, OBSERVATIONS, SOFTWARE & DATA REDUCTION

Table 2.3: RSS grating complement

Grating Name	Wavelength Coverage (nm)	Usable Angles (deg)	Bandpass per tilt (nm)	Resolving Power (1.25″ slit)
PG0300	370-900		390/440	250-600
PG0900	320-900	12-20	∼300	600-2000
PG1300	390-900	19-32	∼200	1000-3200
PG1800	450-900	28.5-50	150-100	2000-5500
PG2300	380-700	30.5-50	100-80	2200-5500
PG3000	320-540	32-50	80-60	2200-5500

or both 1/2- and 1/4-waveplate retarders, along with a large Wollaston beam-splitter mosaic, providing two completely off-set O- and E-images on the detector.

6. High time-resolution spectroscopy: The use of fast frame-transfer CCDs, allowing for the high-speed observations (upto 0.05 s exposures) in all observing modes.

The pixel scale of the detector is $0.1267''$/unbinned pixel. The positional accuracy and repeatability is $0.3'' - 0.5''$ RMS while guiding. RSS has a complement of 6 transmission gratings: 1 standard surface-relief grating (PG0300) and 5 volume phase holographic (VPH) gratings. We have used PG2300 and PG3000 for our observations (see Table 2.3).

2.4 Observations

2.4.1 Optical Polarimetric observations

We carried out optical linear polarimatric observations using ARIES IMaging POLarimeter (AIMPOL) coupled with TK 1024×1024 pixels^2 CCD camera. Only the central 325×325 pixels^2 was used out of these 1024×1024 pixels^2. The total intensity of the incoming light (I) is represented by the Stokes parameters: $I^2 = Q^2 + U^2 + V^2$, where Q and U provide the information regarding linearly polarized light and V provides the same about the circularly polarized light. Using the Stokes parameters, Q and U, the degree of polarization (P) and polarization position angle (θ) can be estimated. We measure the intensity of light at four different position angles of HWP to estimate the stokes parameters Q and U.

Aligning polarimeter with N-S axis of telescope: Before starting the observations, we align the optic axis of the polarimeter with the North-South (N-S) axis of the telescope to measure the polarization angles in the equatorial coordinate

system. The polarization angle is conventionally measured from the north, increasing towards the east. Thus it is 0° in the north, while it is 90° in the east. For the alignment, at first, the telescope is pointed towards any bright star. Then we move the telescope either in the north or south direction while the exposure is on. If the optic axis of the polarimeter is misaligned with the NS direction of the telescope, in the CCD frame, the elongated images of ordinary and extraordinary rays will be separated based on the angle between the optic axis and NS direction. To reduce the separation we rotate the telescope dial in a proper direction and again move the telescope in the manner mentioned before. This procedure is repeated until we get the elongated images of ordinary and extraordinary rays perfectly overlapped.

After we obtain the aligned position of the polarimeter, we carry out observations at four positions (i.e. $\alpha = 0.0^{\circ}$, 22.5°, 45.0°, 67.5°) of the HWP. α is the angle of the HWP with respect to the N-S direction of the telescope. A number of observing frames have been acquired at each plate position of the HWP to get a good SNR. Along with the object frames, bias frames also have been taken. The data processing and reduction steps have been explained in details in section 2.5.1.

2.4.2   Optical Spectroscopic observations using HFOSC

We carried out optical spectroscopic observations using HFOSC attached with 2-m HCT. During observations, Grism 7 was used, which has a spectral resolution $\sim$ 1330, in combination with a slit of $11'$ length and $1.92''$ width (slit 167l) providing a wavelength range of $3800-6840$ Å. Data acquisition using HFOSC CCD is done remotely through the VNC viewer and by the commands issued in BIAS command line window. In spectroscopic mode, first, we select the desired slit then the Grism we need for observations. We also set the spectral image area and center the target star in the slit. To obtain bias frames, we give a command 'dark0'. For wavelength calibration Fe-Ar and Fe-Ne hollow cathode and Hg-Cd lamps are available. After completion of exposure of a target, we obtain calibration data using Fe-Ar lamp during our observations. The output files are automated to be named according to the month and year of observation. The steps of data reduction are discussed in section 2.5.2.

2.4.3 Optical Spectroscopic observations using HESP

We carried out high resolution optical spectroscopic observations using HESP attached with 2-m HCT. During observations, star-sky mode was used, with spectral resolution $\sim$60,000 with a slit width of 0.14 mm, providing a wavelength range $350-1000$ nm. Several bias frames has been acquired in the beginning and the end of the observing night. The image is obtained using the HESP autoguider with a FOV of 100″. During a good pointing, the position of the target is within 10″ from the center. The telescope is slightly shifted to central position of the star onto one of the pinholes, usually pinhole-1. The choice of pinhole is based on the throughput of the fibers 1 and 2. However, it is possible to use any pinhole for the target. In the star-sky mode, one of the pinholes is pointed to the star and the other is illuminated by the surrounding sky. Data acquisition is done remotely through the VNC viewer. For wavelength calibration Th-Ar lamp is available. The output files are automated to be named according to the month and year of observation. The steps of data reduction are discussed in section 2.5.3.

2.4.4 Near-IR Spectroscopic observations using SpeX

During near-IR spectroscopic observation using SpeX, data acquisition and guiding is performed using the IR guider/slit viewer, which is commonly known as Guidedog. Guidedog is operated from the Guidedog X-windows User Interface (GXUI) and the observed data can be seen in the Guidedog Data Viewer (GDV). The SpeX foreoptics system reimage the telescope's focal plane onto the slit mirrors. Images are acquired with Guidedog in Basic mode. The Basic mode window can be selected by clicking the 'Obs' in GXUI. Observers acquire images by clicking the GO button in the GXUI window. Observation can be stopped anytime by clicking the 'STOP' button. The spectrograph is generally known as Bigdog. Observers access Bigdog from the Bigdog X-windows User Interface (BXUI) and show observed data in the Bigdog Data Viewer (BDV). The BXUI and BDV are found in the VNC session #1 (Stefan.ifa.hawaii.edu:1).

At the starting of observation, after the slit and spectroscopic mode selection, the next step is to acquire the science frame, fix rotator angle and start guiding. A test exposure can be taken with Bigdog to establish the necessary integration time. The observer follows the same procedure to observe the telluric standard star in close air mass and angle. The flat and wavelength calibration frames are also

acquired after the observation of the target star. The steps of data reduction for the near-IR spectroscopic data are discussed in detail in section 2.5.4.

2.4.5 Optical Spectropolarimetric observations using RSS:

The optical Spectropolarimetric observations were carried out remotely with help of liaison astronomer Encarni Romero-Colmenero. One needs to provide the observing block for each target, which contains the basic information about the target, for example, position (right ascension and declination), spectral type, magnitude, finding chart, etc. Also, the instrument, which will be used during the observations and its basic configurations have to be mentioned. The filters and exposure time also have to be provided in the observing block. After the completion of the observations, information about the observed data would be provided at the observer's account in the salt webpage. The data can be downloaded through an ftp link, after sending a request to download the data.

Table 2.4: Table of observations performed towards the objects studied for this thesis using various telescopes.

Object	No. of fields	No. of stars	Time on each field (Hours)	Total time
104-cm Sampurnanand telescope				
LDN 1172/1174	42	545	1	42
YSOs in λ-Ori				
Region	23	28	1	23
Total hours				65
2-m Himalayan Chandra telescope Optical				
YSOs	4	4	1	4
IM stars	12	12	1	12
Total hours				16
3-m InfraRed Telescope Facility				
YSOs	10	10	1	10
Total hours				10
10-m South African Large Telescope				
HAeBes	6	6		6
Total hours				6
Total observation hours with all the telescopes				97

Note: Some supplementary observations were also performed, that are not listed in this Table.

2.5 Software & Data Reduction

2.5.1 Optical Polarimetric data reduction

The data reduction steps of the optical polarimteric observations are given below:

- **Change of Data Format**

  In general, the astronomical data are recorded in Flexible Image Transport System (FITS). But, for different telescopes, the format of the recorded data can vary for different technical reasons. In 104-cm ST, the observed data are archived in .pmi format. There is a script named as 'pmi2fits' written in the fortran language, which converts these pmi files into FITS files.

- **Data Reduction Steps**

  We have used the Image Reduction and Analysis Facility (IRAF) to preprocess and reduce the observed data and obtain the flux and magnitudes of the sources. Along with the available packages in IRAF, we have also used a number of programs written in IDL language to estimate the percentage of polarization and position angle.

- **Subtraction of bias frames:**

  Bias frames allow the observer to estimate the zero noise level of the CCD being used during observations. Now, an unexposed pixel of the CCD would provide a mean value of zero with a Gaussian distribution upon readout and analog-to-digital conversion (ADC) of the photoelectrons created at zero level. It implies that some of the pixels contain negative counts which is nonphysical as the ADC cannot provide numbers less than zero. In order to avoid the negative numbers, the CCD electronics are provided an offset value, ensuring that ADC receives a positive signal. This offset level is called as bias level. Usually poor stability of CCD electronics with time, temperature, also higher readout noise values require the bias level. At regular intervals during the observing run, one should acquire a number of bias frames and these frames can be median combined to create a master bias frame of that observing night. In IRAF one can perform this using the task named "zerocombine". In order to extract the flat and science frames from the positive DC bias, one should subtract these frames by the master bias frame. One can perform the task called "imarith" or "ccdproc" for this step.

- **Aligning & Combining the images:**

In the next step, we have to align all the observed frames with respect to a reference frame using "imalign" in IRAF. Here, the central coordinates (in pixels) of the common sources in every frame are provided and then the "imalign" task calculates the transformation coefficients using the shifts of the central coordinates of the sources in each frame. Now, these transformation coefficients are used in all frames to get them aligned with respect to the reference frame. Then, these aligned frames are combined for every position of the HWP to increase the signal-to-noise ratio (SNR). This task can be performed using "imcombine" in IRAF.

- **Astrometry of the images:**

In this step, we have executed the astrometry of the frames using the tasks named as"ccmap" and "ccsetwcs" in IRAF. Here, a list of world coordinates of some sources has to be provided with their corresponding pixel coordinates. The "ccmap" task computes the plate solution using this list. Then the "ccsetwcs" generates an output image with world coordinate system using this plate solution.

- **Aperture photometry to extract flux:**

We can extract the flux of the sources by two techniques: (1) Aperture photometry and (2) Point-spread-function (PSF) photometry. The first technique can not be used in case of faint stars or over-crowded fields, in that case, we have to use the second method. Here, we have used the aperture photometry as the fields we observed are not crowded. We have used the task '*phot*' routine from the '*daophot*' package to perform the aperture photometry. This is basically the measurement of the stellar photon count in the given aperture. We have to be careful about choosing the aperture size as the bigger aperture can increase the noise level due to contribution from the background sky and the smaller aperture can reduce the counts from the star. A solution to this is to check the curve-of-growth. So, the aperture we provide has to enclose the entire stellar profile to collect the photon count from the whole star. The measured flux is the result of the integration of the flux in all the pixels residing in the given aperture. We also have made a similar measurement in a region without stars to compute the background sky flux. The apparent stellar flux can be estimated from the difference between these two flux values. The

flux can be used to calculate the instrumental magnitude from the relation: m=-2.5log(I), (I: the stellar flux). A set of IDL routines and IRAF tasks were used to reduce the polarimetric data and obtain the percentage of polarization and position angle of the stars.

We have identified the ordinary and extraordinary images of each star in each position of HWP using a program written in IDL. This program takes four combined images in each plate position with filename format '$comalip[1,2,3,4].fits$' and gives four output files with the filename '$phot-coord-p[1,2,3,4].list$'. The ordinary and extraordinary images of each star are identified using red and green open circles. After this, we have selected the stars which are common in all the four plate position of the HWP using another program written in IDL. This gives the pixel coordinates of the ordinary (O) and extraordinary (E) positions of the common stars which can be used for photometry. We have shown an image of O and E rays of stars in Fig. 2.5. FWHM of the stars were usually $2-3$ pixels. Flux of the stars were extracted at 25 apertures ranging from 1 to 6 pixels with a 0.2 pixel aperture width. Then we have examined at which aperture the χ^2 is minimum and the percentage of polarization does not vary.

- **Estimation of the percentage of polarization and position angle:**

The wollaston prism divides the incoming starlight into two orthogonal light rays, and as a result, we can estimate the percentage of polarization (p) and position angle (θ) of the orthogonal O and E rays from their intensities. The intensities of these O and E rays can be written as,

$$I_e = I_{unpol} + I_{pol} \times cos^2(\theta - 2\alpha) \tag{2.1}$$

$$I_o = I_{unpol} + I_{pol} \times sin^2(\theta - 2\alpha) \tag{2.2}$$

I_o and I_e are the measured intensities of the ordinary and extraordinary images, respectively. I_{pol} and I_{unpol} represent the polarized and unpolarized intensities, respectively. θ and α are the position angle and the angle of the fast axis of the HWP, which are measured with respect to the axis of the beam-splitter. As already mentioned, the aperture photometry from the available packages in IRAF was used to extract the values of I_e and I_o. The ration R(α) is expressed
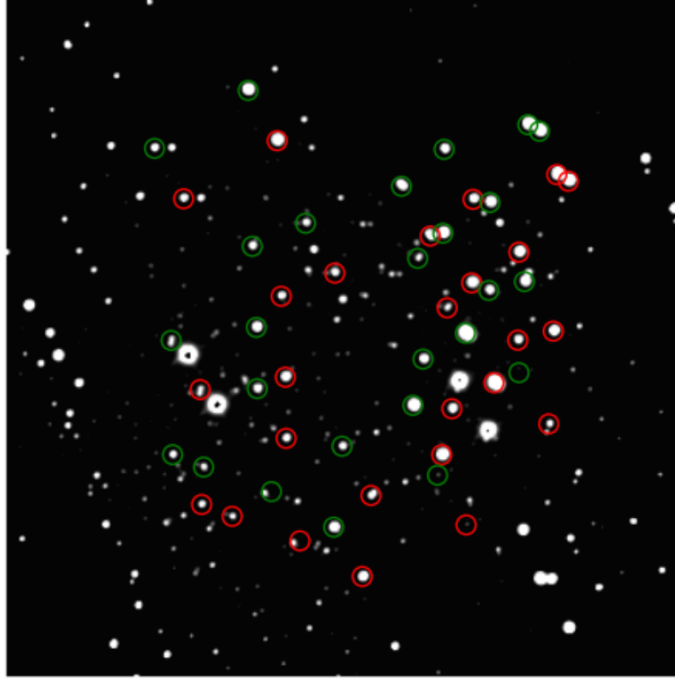
Figure 2.5: Ordinary (red open circles) and extraordinary (green open circles) images of stars selected by set of IDL codes. Image taken from the thesis by Neha Sharma, ARIES.

as:

$$R(\alpha) = \frac{\left(\frac{I_e}{I_o} - 1\right)}{\left(\frac{I_e}{I_o} + 1\right)} = P \times cos(2\theta - 4\alpha) \qquad (2.3)$$

P represents the degree of polarization (i.e. the fraction of the linearly polarized light). θ corresponds to the position angle of the polarization plane. α is the angle of the fast axis of HWP in four plate positions: 0°, 22.5°, 45° and 67.5°. These four positions correspond to four normalized Stoke's parameters: q[R(0°)], u[R(°)], q_1 [R(45.0°)], and u_1 [R(67.5°)] respectively.

Observations for at least two positions of the HWP are necessary to compute the three unknown parameters: total intensity (I), P, and θ. But, the only two positions are not enough as (i) the system can respond differently for the two orthogonal components, and (ii) the CCD response on its surface may vary as it is a function of the position. As a result, the measurement in I_e and I_o can be corrected (as I'_e and I'_o) using the following relation:

$$\frac{I'_e(\alpha)}{I'_o(\alpha)} = \frac{I_e(\alpha)}{I_o(\alpha)} \times \frac{F_o}{F_e} \qquad (2.4)$$

2. TELESCOPES, INSTRUMENTS, OBSERVATIONS, SOFTWARE & DATA REDUCTION

where,

$$\frac{F_o}{F_e} = \left[\frac{I_o(0°)}{I_e(45°)} \times \frac{I_o(45°)}{I_e(0°)} \times \frac{I_o(22.5°)}{I_e(67.5°)} \times \frac{I_o(67.5°)}{I_e(22.5°)}\right]^{\frac{1}{4}} \quad (2.5)$$

For the flat-field correction, we have used the equations mentioned above (Ramaprakash et al., 1998).

The percentage of polarization (p) and position angle (θ) have been estimated by fitting the four Stoke's parameters (q, u, q_1, u_1) with the relation of $R(\alpha)$ = P×cos($2\theta - 4\alpha$). We have used the IDL function '$mpfitfun$' for fitting. The errors in the four Stoke's parameters (σ_q, σ_u, σ_{q1} and σ_{u1}) are given by Ramaprakash et al. (1998),

$$\sigma_R(\alpha) = \frac{\sqrt{N_e + N_o + 2N_b}}{N_e + N_o} \quad (2.6)$$

N_o and N_e are the number of photon counts in the ordinary and extraordinary rays. N_b (=($N_{bo}+N_{be}$)/2) is the average background photon count in the ordinary and extraordinary images of the source.

Consider q_1 = R(0°) and u_1 = R(22.5°)

$$p_1 = \sqrt{q_1^2 + u_1^2}, \; \theta_1 = 0.5tan^{-1}(u_1/q_1) \quad (2.7)$$

$$\sigma_{p_1} = \sqrt{q_1^2\sigma_{q_1}^2 + u_1^2\sigma_{u_1}^2}/p_1 \quad (2.8)$$

$$\sigma_{\theta_1} = \sqrt{q_1^2\sigma_{u_1}^2 + u_1^2\sigma_{q_1}^2}/2p_1^2 \quad (2.9)$$

And q_2 = R(45°) and u_2 = R(67.5°)

$$p_2 = \sqrt{q_2^2 + u_2^2}, \; \theta_2 = 0.5tan^{-1}(u_2/q_2) \quad (2.10)$$

$$\sigma_{p_2} = \sqrt{q_2^2\sigma_{q_2}^2 + u_2^2\sigma_{u_2}^2}/p_2 \quad (2.11)$$

$$\sigma_{\theta_2} = \sqrt{q_2^2\sigma_{u_2}^2 + u_2^2\sigma_{q_2}^2}/2p_2^2 \quad (2.12)$$

These set of equations result in P=(p_1 + p_2)/2 and $\sigma_p = \sqrt{\sigma_{p_1}^2 + \sigma_{p_2}^2}/2$ and $\theta = (\theta_1 + \theta_2)/2$ and $\sigma_\theta = \sqrt{\sigma_{\theta_1}^2 + \sigma_{\theta_2}^2}/2$.

Where P is in % and θ is in radian. The computed polarization position angles are corrected according to the signs of the Stokes parameters presented in the

Table 2.5: Corrections implemented in the position angles:

q(%)	u(%)	q_1(%)	u_1(%)	θ(°)
-	-	+	+	θ $(\theta > 0)$
-	+	+	-	$90°+\theta$ $(\theta < 0)$
+	+	-	-	$90°+\theta$ $(\theta > 0)$
+	-	-	+	$180°+\theta$ $(\theta < 0)$

Table 2.5.

- **Calibration of the computed degree of polarization and position angle:**

In an ideal case, after the alignment of the optic axis with respect to the N-S direction of the telescope, the estimated polarization position angle of the observed polarized standard star should match with the value provided in the literature. But usually, there is a small offset value in the position angle from its original value, which is called as 'Zero-point Polarization Angle (ZPA)'. The reference direction of the polarizer have been estimated by observing a number of polarized standard stars mentioned in Schmidt et al. (1992) in every observing run. The zero point offset was corrected by computing the difference between the standard position angle values given in Schmidt et al. (1992) and those obtained by our observations. To estimate the instrumental polarization, we have observed some unpolarized standard stars during each run, which are listed in Schmidt et al. (1992). Typically the instrumental polarization is $<\sim$ 1%. The degree of polarization and position angles for the standard stars given in Schmidt et al. (1992) were obtained using the Kron-Cousins R filter. We have observed the standard stars with R_{Kc} filter.

After the estimation of P and θ for a number of stars in an observed frame, we have over-plotted them on the corresponding fits image using codes written in IDL.

2.5.2 Optical Spectroscopic data reduction

Spectroscopy is the key tool used in astronomy for the investigation of the Universe beyond the Earth's atmosphere. By the analysis of electromagnetic radiation emitted from celestial objects, spectroscopy enables us to assess their kinematics, chemical composition, distance, temperature, mass, luminosity, and more physical

2. TELESCOPES, INSTRUMENTS, OBSERVATIONS, SOFTWARE & DATA REDUCTION

properties. Spectroscopy of any astronomical body can be performed using an instrument called as spectrograph. Spectrograph consists of the following elements: a slit on which the incoming light gets focused; a collimator which turns the diverging light in the parallel mode, a disperser which splits the light into component wavelengths; and a camera on which the dispersed light gets focused onto the CCD. In a majority of astronomical spectrographs, the dispersers are diffraction gratings rather than prisms, and ruled with thousands of narrow lines as per requirement. We have performed the following steps for optical spectroscopic data reduction using HFOSC.

1. Bias level subtraction: As explained in the optical polarimetric data reduction, we subtracted the master bias (obtained by median combining the bias frames taken with zero exposure) from the science and flat frames.

2. Flat Fielding: Every pixel of the CCD may have dissimilar sensitivity to the incoming photons. If the response of every pixel is identical, each of them is expected to show a constant value, but practically it does not happen. In order to remove this variation, the flat frames were taken using arc lamp, and the master bias was subtracted from these frames. Master flat frame was generated by median combining these flat frames using the IRAF task "flatcombine". In order to normalize the flat frame, one can use the median value of the central dispersion row. We calculated the response of the flat frame using the task "response" and applied it to every arc lamp and on-source exposure. The response function computes a polynomial fit to the average flat frame along the dispersion axis and provides the deviation from this fit in each pixel. All science frames were then divided by the normalized master flat to remove the non-uniform response of the pixels. For this, we used the IRAF task "ccdproc".

3. Cosmic ray Removal: In the object frames, there are a few very bright spots along with the stars distributed on one or two pixels, created by cosmic rays. Their intensity profiles are different from the stellar profiles and this property is used to remove them from each frame by performing the task "cosmicrays" in IRAF.

4. Aligning and combining: In order to increase the SNR, we aligned and combined the science frames using the IRAF tasks "imalign" and "imcombine" respectively.

5. Wavelength Calibration: The spectra can be extracted from the flat-fielded frames using the task "apall" in IRAF. In order to obtain the pixel-to-wavelength solution of the frames, we have extracted a 1-D spectrum from the arc lamp for every slit using the slit tracing. This 1-D spectrum is a function of CCD pixels. The wavelength calibration has been made using the comparison spectra (arc lamp spectra), acquired with the same setup of the instrument as used for the object frames. The known laboratory wavelengths of individual spectral lines of the arc lamp are marked using the task "identify" and the wavelength solution is estimated by fitting a polynomial to these identified lines. Then the wavelength solution has been applied to each object spectrum using the tasks "refspec" and "dispcor" in IRAF.

6. Flux Calibration: In the next step we apply flux calibration to the science spectra using the spectra of standard star to obtain the actual flux of the stellar spectra. Here, we use the task "standard" and "sensfunc" in IRAF.

7. At the end, the ascii format of the 1-D spectra can be obtained using the task "wspectext" from "Onedspec" package in IRAF to plot using Python programming language.

2.5.3 Optical High Resolution Spectroscopic data reduction

We have used a set of scripts written in Python language by Arun Surya. The following are the commands we need to type in the terminal to process the observed data.

1. hesp_createlist
It creates 'files.txt' with the list of observed and calibration frames and related info for the reduction based on classification and information of each file.

2. hesp_preproc
It preprocesses the files including, creating master bias and bias subtraction from all the files, overscan correction, trimming and cosmic ray correction of the observed frames sequentially. After processing, the command creates output files with extension '_pp.fit'.

3. hesp_extract/hesp_extract_file

This step extracts the spectra from all the orders of the processed files and creates intermediate 'ec.fits' files. If we need to extract only a single file, then we have to use the command 'hesp_extract_file'.

4. hesp_traceview

It helps to examine the trace curves of the orders used by the pipeline. For optimal extraction, these lines should be following the middle section of each order. We can see the trace overplotted on the image file using this command.

5. hesp_traceshift

hesp_traceshift can be called similar to hesp_traceview with a file argument and a keyword for the trace used ('low'/'high'). We can interactively shift the traces vertically to align with the order positions on the data file. There is a slider using which the traces can be shifted. After confirming the alignment, we can save it using the 'Save' button on the interface. This updates the global traces in the bin directory.

6. hesp_extract/hesp_extract_file

To extract the orders from the preprocessed files, these two routines are available. 'hesp_extract' extracts the orders from the processed files of all objects and calibration files listed in the 'files.txt'. Whereas, 'hesp_extract_file' extracts orders for a single processed file given as an argument. The extracted files are saved as 'filename_fiber1_ec.fit' and 'filename_fiber2_ec.fit' for each fiber of each datafile. The '_ec.fit' at the end of the filenames indicates the extracted spectra.

7. hesp_addwave

It is the routine for wavelength calibration of the extracted spectra. The routine will create output files as 'filename_fiber1/2_wc.fit' for each extracted calibrated spectra. The '_wc.fit' files created have wavelength information encoded into their header in IRAF compatible format. Hence we can use IRAF tools like 'splot' to further process the file.

8. hesp_recalib

It allows calibrating the wavelength solution using a ThAr calibration file in the directory. The routine will cross-correlate a sample of orders to find a global shift

in the ThAr spectra and use it to adjust the wavelength solution accordingly.

9. hesp_view

It allows us to view the full wavelength calibrated spectra with an interactive Matplotlib GUI.

Along with these, there is also another script 'hesp_median' to create a median combined image from the list of images given as input.

2.5.4   Near-IR Spectroscopic data reduction (Spex)

Spextool was designed to reduce data taken with a $15''$ -long slit in the SXD, LXD, and prism modes. Cushing et al. (2004) elaborated the procedures incorporated into the Spextool. A detailed description of the telluric correction procedures is provided in Vacca et al. (2003). Spextool is developed to reduce the observed data obtained with SpeX. The latest version of Spextool uses a set of IDL scripts. The Spextool package includes multiple Graphical User Interfaces (GUIs) which allow us to process, extract and calibrate the data. Below are the steps we need to type at the IDL command line in order to reduce the data.

1. xspextool

- generates normalized flat field and wavelength calibrated files

- applies non-linearity correction and flat field correction on the raw image files

- subtracts A and B images in pair

- defines the extraction aperture positions

- traces object spectra

- subtracts the background contribution with the defined apertures

- extracts object spectra with the defined apertures and performs wavelength calibration

2. xcombspec

45

- scales, prunes and corrects the shape of the individual extracted multi-order spectra and then combines them

3. **xtellcor (and xtellcor_basic and xtellcor_finish)**

   - performs telluric correction and also flux calibration on the extracted multi-order object spectra.

4. **xmergeorders**

   - merges the telluric-corrected, multi-order object spectra into one single continuous spectrum

5. **xmergexd**

   - combines the SXD and LXD spectra of an object

6. **xcleanspec**

   - cleans the continuous spectrum by fixing or removing bad pixels and smooths the spectrum

7. **spex2text**

   - converts the reduced FITS file to an ASCII file for further analysis

In addition to the GUIs described above, there are three additional GUIs that we can interact with, 'ximgtool', 'xvspec', 'xzoomplot'.

2.5.5 Near-IR *Spitzer* Photometric data reduction

MOPEX (MOsaicker and Point source EXtractor) is a widely used package to reduce and analyze imaging data. MOPEX also includes the point source extraction package named APEX. One can download the data from the *Spitzer* space telescope at *Spitzer* Heritage Archive (SHA)[1]. *Spitzer* Infrared Array Camera observed sources in four different wavelengths, so the data have to be stored in 4 separate directories, namely ch1-4, which are 3.6, 4.5, 5.8 and 8.0 μm. There 4 directories will be within the main directory named bcd (basic calibrated data). Observed frames in IR are dithered as at this wavelength, the background sky is relatively brighter compared to the observed sources. Therefore, we have a large number of images that we have to combine to produce a mosaicked image, which will be analyzed further for science.

In order to run mopex, we have to type 'mopex' at the command line. Then, a GUI will appear where we will start the reduction procedures.

---

[1] https://sha.ipac.caltech.edu/applications/Spitzer/SHA/

- The first step is to select a new' overlap pipeline'. Then, we need to select the channel from which the data will be reduced.

- Next, we have to click on 'insert mosaic' and select from the template and the proper channel.

- Then, we go for 'create image stack'.

- We have to select 'bcd' in every image stack directory, sigma directory and mask directory tabs.

- The search criteria for image and sigma need to be changed to *_cbcd.fits and *_cbunc.fits, respectively. We have to click on the 'create and preview lists' for all tab, and then 'ok'.

- Next, we need to create an output directory.

- The Pmask fits file has to be changed to the relevant mask file for the date of observations. These files can be found in the cal directory of the location of mopex.

- Then, we have to click the 'Mosaic settings' box, go for 'Array Correction Frame', which is already saved in the cal directory and named as '_photcorr_rj.fits', beginning with the channel name. Alternatively, we need to click the 'cryo default' button.

- Next, we have to add in the 'PixArea Frame' by using the relpixarea.fits frame, which begins with the channel name.

- Then, we will click 'Make Array Correction Files' and 'Make Array Correction Mosaic' to add them. Till this part of the pipeline generates the mosaicked images. Now we have to process the photometric data so that aperture photometry can be performed on these images.

- Then, we have to click the 'Insert APEX single frame' tab, select from the template, and add the appropriate channel.

- In the next step, we need to change the 'Settings' of the Apex Single Frame. We have to enter the PRF (Point Response Function) filename as 'apex_sh_IRAC* _col129_row129_x100.fits' where the * has to be replaced by the proper channel number.

2. TELESCOPES, INSTRUMENTS, OBSERVATIONS, SOFTWARE & DATA REDUCTION

Table 2.6: The zeropoint and aperture correction values for 4 channels in *Spitzer*.

Channel	Zeropoint	Aperture Correction
Ch1	280.9	1.112
Ch2	179.7	1.113
Ch3	115.0	1.125
Ch4	64.9	1.218

- Then we have to click the green play button to run the process. This will run the pipeline and generate an array correction mosaicked image, as well as a list of sources. The mosaicked image will be stored in the Combinemosaic directory and named as mosaic.fits.

We need to repeat the whole steps 4 times for 4 different channels/wavelengths. The apex routine extracts sources with a signal to noise ratio (SNR)> 6. These data are stored in a file named as 'mosaic_extract.tbl'.

- First, we have to select the source on which we will perform the photometry. Coordinates of this source in pixels will be stored as x and y, and other numbers such as flux, uncertainty in flux will be saved in the ap and ap_unc columns of the mosaic_extract.tbl.

- Then we have to divide the measured flux $23.5044 \times$ pixelsize^2 to convert it into MJy/sr unit. One can find the pixel sizes in the image header.

- We also have to determine the array location value. For this, we need to open the array location frame, and based on the X, Y for the target, we will determine the value. We will multiply the measured flux (MJy/sr) by this value. This will account for the detector sensitivity.

- Next, we have to multiply the data by $23.5044 \times$ pixelsize^2 to convert it into μJy.

- For the relevant channel we have to multiply the data by the aperture correction value.

- Finally, we have to use the zeropoint for the applicable channel to obtain the magnitude using m=$2.5\log(Zp/(\text{flux}/10^6))$.

The zeropoint and aperture correction for all the 4 channels are listed in Table 2.6.

2.5.6 Spectropolarimetric data reduction using PySALT and PolSALT

Spectropolarimetry is a powerful tool to study the near-stellar environment of PMS stars and estimate their immediate geometries. The concept of spectropolarimetry is: free electrons in the ionized region scatter and polarize stellar continuum photons. If the near-stellar geometry is non-circular on the plane-of-sky, a net polarization can be detected. The emission line photons and stellar continuum photons originate from different regions and are scattered differently by free electrons, which in turn results in a different polarization across the continuum and line. Mostly Hα emission line is observed in spectropolarimetric mode as this line can probe very close to the central star.

RSS spectropolarimetric data can be reduced with PolSALT and PySALT, written in python language. Both PolSALT and PySALT are available in https://github.com/saltastro/polsalt and https://github.com/saltastro/pysalt respectively. We have used the Python based graphical user interface (GUI) developed by Enrico Kotze, which uses all the packages of PolSALT and PySALT.

The main code for reduction is reducepoldataGUI.py, which opens the GUI and executes the results. When the main window appears, we have to click the 'Select' button for the appropriate directories, e.g., where the PolSALT codes reside, the data for a specific observation date which we want to reduce. All codes require the data directory format to be 'CCYYMMDD' (i.e., the observing date) and a subdirectory named as 'raw' containing all the raw data taken on that observation date. The steps are as follows:

1. Raw image reduction: In this step, we have to click 'Raw image reduction' in the drop down box named 'Data reduction step'. Then we have to click the 'show files' key to select the raw files which will be used for reduction. We can select all the files by clicking the 'Select all' button. Optionally, one can select the files individually by putting ticks in the check boxes next to the file names. Once we are done with the selection of raw image files, we have to click the 'OK' button to run the 'Raw image reduction' step. While execution, the main GUI disappears, and the results obtained from the imred package in polsalt codes are displayed in the terminal. This step creates files with a prefix of 'mxgbp'. After completion of the execution, the main GUI reappears again.

2. Wavelength calibration: Again, we have to click the 'Data reduction step' box and then select the second option named 'Wavelength calibration'. Similar to the previous step, again we have to click the 'Show files' button to select the files for wavelength calibration. Then we have to hit the 'OK' button for the execution of this step. While running the specpolwavmap module, the main window again disappears, and the output files are shown in the terminal. This time, a separate interactive window appears for wavelength calibration of O and E beams. After the usual wavelength calibration processes, we have to close this window. The specpolwavmap package starts running again and after execution, the main GUI again reappears. This step creates files with a prefix of 'wmxgbp'.

3. Spectra extraction: Similar to the previous steps, we need to click the 'Data reduction step' first and then select the option named 'Spectra extraction'. Again we have to click the 'Show files' key to pick the necessary files to extract the spectra. As previously explained, one can use 'Select all' to select all the files or mark the files by putting ticks in the checkboxes of the files. Once this selection gets finished, we have to click the 'OK' button. The main window disappears, and a separate interactive window appears to choose the extraction width for the target and the background for O and E beams.

By default, the interactive spectra extraction window shows images of O and E beams of the first image file selected for extraction in a tab view. The bottom-left axes of each image are presented in pixels, and the top-right axes are displayed in angstroms and arcseconds, respectively. We can see any of the selected files by clicking it from the drop down box named 'Fits'. In the interactive window, the default values for the science window and the spectral extraction width are displayed. The science window is the range which is used by the spectral extraction process to detect the brightest spectrum as the spectrum of the target. The extraction width is set to be centered on the spectrum of the target to establish the spectral extraction window.

After selecting all the required windows as needed, we have to click the button named as 'Show tilt correction and windows' and then the images are modified with the tilt correction and windows according to the default values. The science window is displayed in green, the spectral extraction window in red and also the two windows for background in blue. By default the background windows are set to the same width as the spectral extraction window. They are at an offset (generally

20 pixels) above and below this extraction window. The default offset is computed as a function of the spectral extraction width. The image presented with the tilt correction is actually a temporary image and the final extraction process applies the correction before the spectral extraction.

We need to toggle the check box named as 'Override background window values' to override the background windows already set by default. After changing window values as needed, we have to click the 'Update background windows' option. For the override of the background window for one beam, is set to be 'mirrored' for the other beam also.

For the execution of the 'Spectra extraction' step we have to click the 'OK' button. The interactive window disappears and the results from the specpolextract_dev codes are shown in the terminal. This step creates files with a prefix of 'ecwmxgbp'. After the execution, the main window again appears.

4. Raw Stokes calculation: In this step, again we have to click the 'Data reduction step' box and choose the option named 'Raw Stokes calculation' and then click the button named 'Show files'. The necessary files for raw Stokes calculation are then shown and can be selected similarly as previous steps by clicking the 'Select all' button. If required, we can individually toggle the check boxes located next to the file names similar to the earlier steps. After the selection of files, we need to click the 'OK' button for the execution of the 'Raw Stokes calculation' step. The main window disappears then, and the results from specpolrawstokes_dev package is presented in the terminal. The main window reappears after the completion of this step.

5. Final Stokes calculation: Similar to the previous steps, we have to select the 'Data reduction step' box and choose the option named 'Final Stokes calculation' and then hit the 'Show files' button. The necessary files for calculation of final Stokes parameters are shown and these files can be selected if we click the 'Select all' button or we can individually select them by toggling the check boxes. Once all the applicable files are selected, we have to click the 'OK' button to execute this step. Again during execution main window disappears and the results from the specpolfinalstokes module are shown in the terminal. After the execution gets completed, the main window again appears.

6.   Results visualization: To visualize the results, we have to click 'Data reduction step' box and choose the 'Results visualization' option. Then we have to click the 'Show files' button to pick the applicable file(s) for visualization is/are displayed, and these files can be selected by hitting the 'Select all' button or by toggling their check box/es. After selection of the required file(s), we have to click the 'OK' button for the execution of the 'Results visualization' step. Similar to the previous steps, the main window disappears, and then an interactive window appears to select the results visualization output options.

Through the interactive output options window, we can select the plot type. If needed, one can also set the binning type as well as the binning width. There is also an indicator for showing the error bars.

Once all options for the plot type are set as per our requirements, we have to click the 'OK' button for the execution of the 'Results visualization' step. Then the interactive window disappears and results (depending to the values we set) from the specpolview_dev module is displayed in the terminal. After the completion of this step, the main window reappears.

7. Results visualization - interactive: In this step again, we have to click the 'Data reduction step' box, and choose the last option named 'Results visualization -interactive', and then select the 'Show files' button. The required file(s) is/are displayed, and these can be selected by clicking the button named 'Select all'. We can also toggle the check box/es next to the file name(s). After the selection of the file(s), we have to click the 'OK' button to carry out the 'Results visualization - interactive' step. Similar to the previous steps, the main window disappears, and an interactive window for results visualization appears.

Similar to the last step, here also the interactive window allows us to set the plot type, binning type, binning width, also an indicator to show the error bars. In this window, there is also an option for creating a custom plot (if we select the unbinned option).

Once we set all the options as per our requirements, we have to click the button named 'Plot results' for the execution of the 'Results visualization - interactive' step. Here also, the specpolview_dev module is used to obtain the spectropolarimetric results from the selected file(s), and these results are displayed on the interactive window as well as written to text file(s).

One can save all the plots as 'pdf' files by toggling the applicable check boxes and clicking the button named 'Save .pdf'. There is an option to click the 'Cancel' button to close the interactive window and appearance of the main window.

2.6 Other archival data used

2.6.1 *Gaia* Data Release-2

Gaia (Global Astrometric Interferometer for Astrophysics) is a space based observatory of the European Space Agency (ESA). It was launched on 19 December, 2013 and is expected to continue till 2022. The spacecraft is designed especially for astrometry: measurements of the positions, parallaxes, and motions of stars in the plane of sky with excellent precision. It consists of two three-mirror anastigmat each of size 1.45 m×0.5 m, and three instruments for astrometry, photometry, and spectroscopy. The spacecraft will monitor each target about 70 times over five years to estimate the precise position and proper motion of the target. *Gaia*'s photometer consists of three different passbands (G, G_{BP} and G_{RP}). The wavelength coverage of G passband ranges roughly from the near-ultraviolet to the near-IR ($\sim$330−1050 nm) region. The other 2 passbands, G_{BP} and G_{RP}, cover narrower wavelength ranges, from $\sim$330−680 nm, and $\sim$630−1050 nm, respectively. *Gaia* DR2 includes photometric measurements over a billion objects in a magnitude range G =3−21. Typical uncertainty in position and parallax is 0.02−0.04 mas, and in proper motion is 0.07 mas yr^{-1} at G <15. For sources with G =21, typical uncertainty in position and parallax is 2 mas, and in proper motion is 3 mas yr^{-1}. This thesis has made extensive use of *Gaia* Data Release 2 (DR2). The *Gaia* Archive can be accessible from the *Gaia* home page at http://www.cosmos.esa.int/gaia and directly at http://archives.esac.esa.int/gaia.

2.6.2 Pan-STARRS1 data

The Pan-STARRS (Panoramic Survey Telescope and Rapid Response System; Kaiser et al., 2010) system was built at Haleakala Observatory, Hawaii, US, Haleakala. This survey provides optical and near-IR photometry in five filters of the whole sky north of $\delta = -30°$. It consists of two mirrors, each of 1.8 m diameter and has a large (3°) FOV. This system has CCD cameras with 1.4 billion pixels (Hodapp et al., 2004;

Onaka et al., 2008) providing broad band imaging in $grizy_{\mathrm{P1}}$ 5 filters, in the wavelength range $400-1000$ nm. The five filters are similar to the filters used in the survey by SDSS. The primary difference is that the z_{P1} has a cut off at 920 nm. Also, the u filter used in SDSS is traded for the y_{P1} filter that covers wavelength range $920-1030$ nm (Stubbs et al., 2010).

2.6.3 2MASS data

The 2MASS (2 Micron All Sky Survey; Skrutskie et al., 2006) is an all sky survey in the near-IR regime which was carried out between 1997 and 2001. 2MASS employed two highly-automated 1.3-m telescopes, one at U.S. Fred Lawrence Whipple Observatory at Mt. Hopkins, Arizona, and one at Cerro Tololo Inter-American Observatory (CTIO), Chile. Each telescope was capable of observing the sky simultaneously at J (1.25 μm), H (1.65 μm), and K$_S$ (2.17 μm) bands. The 2MASS catalog provides photometric data in J, H and K$_S$ to the limiting magnitude of 15.8, 15.1, and 14.3, respectively, with SNR = 10. Pixelsize of the CCD camera attached with 2MASS telescopes is $2''$. Gain is ~ 8 e$^-$ per ADU count and read out noise is 40 e$^-$. We used magnitudes in three bands of our sources from Cutri et al. (2003) to construct the near-IR color-color (CC) diagrams and estimate the extinction (A$_V$) values.

2.6.4 *WISE* data

The *WISE* (Wide-field Infrared Survey Explorer; Wright et al., 2010) mapped the sky at 3.4, 4.6, 12, and 22 μm (W1, W2, W3, W4) over ten months using a 40 cm diameter IR telescope in Earth orbit. The telescope was launched in December 2009. $WISE$ achieved 5σ point source sensitivities better than 0.08, 0.11, 1, and 6 mJy at W1, W2, W3, and W4, respectively. These sensitivities correspond to the Vega magnitudes 16.5, 15.5, 11.2, and 7.9. Pixelscale of fits image is $1.375''$/pixel. We have mainly used W1, W2 and W3 to plot CC diagrams and get evolutionary classes of the sources.

2.6.5 *Spitzer* data

The *Spitzer* Space Telescope, named in honor of astronomer Lyman Spitzer, was launched in 2003. It consists of a primary mirror of 85 cm in diameter and three

scientific instruments. These are Infrared Array Camera (IRAC), Infrared Spectrograph (IRS), and Multiband Imaging Photometer for Spitzer (MIPS). IRAC operates simultaneously on four wavelengths (3.6, 4.5, 5.8, and 8 μm). IRS contains four sub-modules which operate at the wavelengths 5.3-14 μm (low resolution), 10-19.5 μm (high resolution), 14-40 μm (low resolution), and 19-37 μm (high resolution). MIPS operates at three wavelengths (24, 70, and 160 μm). We have used IRAC and MIPS photometric data to get their classifications.

2.6.6   *XMM-Newton* data

The X-ray Multi-Mirror Mission (*XMM-Newton*) was launched on December 10, 1999. It consists of three X-ray telescopes, each of which contains 58 Wolter I grazing-incidence mirrors. Diameter of the largest mirror is 70 cm. The onboard instruments are three European Photon Imaging Cameras (EPIC), an Optical Monitor (OM), and two Reflection Grating Spectrometers (RGS). EPIC is composed of a single pn-CCD camera and two MOS-CCD cameras, and its FOV is $\sim$30$'$. RGS consists of two Focal Plane Cameras with their associated Reflection Grating Arrays. OM is a 30 cm optical/UV telescope which provides simultaneous observations alongside the X-ray instruments. The XMM-SSC catalogue gives hardness ratios, HR1 and HR2 also. These are X-ray colors defined as (H-S)/(H+S) where H and S for HR1 are flux values in the band $0.5-1.0$ keV and $0.2-0.5$ keV, respectively. For HR2, the H and S are flux values in the bands $1.0-2.0$ keV and $0.5-1.0$ keV, respectively. These hardness ratios are used to confirm the young nature of some sources.

2.6.7   *Planck* data

Planck (http://www.esa.int/Planck) is a space based telescope, operated by European Space Agency (ESA). It was launched on 14 May 2009, and was turned off on 23 October 2013. *Planck* worked for 30 months, completing five full-sky surveys. The first all-sky map of the polarized emission from dust grains at sub-millimeter wavelengths was produced by *Planck* (Planck Collaboration et al., 2016a). The primary mirror is 1.9×1.5 m in diameter. Two main instruments of *Planck*, the High Frequency Instrument (HFI) and the Low Frequency Instrument (LFI), are described in Planck HFI Core Team et al. (2011) and Mennella et al. (2011), respectively. LFI covers a wavelength range from $30-70$ GHz, while HFI operates within

2. TELESCOPES, INSTRUMENTS, OBSERVATIONS, SOFTWARE & DATA REDUCTION

$100-857$ GHz. The *Planck* maps of polarization angle, ψ, and fraction, p, encode information on the magnetic field structure (Planck Collaboration et al., 2015). The *Planck* data have an angular resolution of 4.8′ at 353 GHz.

Chapter 3

A detailed study on LDN 1172/1174

3.1 Introduction

Hubble (1934) first introduced the term 'Cepheus flare' (see Fig. 3.1), suggesting a notable amount of obscuration outside the main Galactic belt, spanned over latitude $b \gtrsim 10°$ and longitude $100° \lesssim l \lesssim 120°$ of the Galactic plane (Lynds, 1962; Kun, 1998; Kun et al., 2008). A large scale ^{13}CO survey was conducted by Yonekura et al. (1997) to reveal the structure of cloud complexes located at the Cepheus and Cassiopeia region with $8'$ grid spacing and $2.\!'7$ beam size. They identified 51 molecular clouds in the Cepheus Flare region. Based on the study of HI distribution, Heiles (1967) pointed out two kinematically separate cloud sheets in the region of $13° \lesssim b \lesssim 17°$ moving at a speed of ~ 15 km s^{-1} relative to each other. Heiles (1967) also noticed that these two sheets present an expanding or contracting system. Hu (1981) reported an HI shell at $l = 105°$, $b = 17°$ and indicated that this region is in an energetic motion state. At $l = 124°$, $b = 15.5°$, a giant radio continuum region, found by Berkhuijsen (1973), is stretched across $65°$ and is considered as a result of multiple supernova explosions. Based on Leiden-Dwingeloo HI data and Columbia Survey CO data, Olano et al. (2006) found broad and often double-peaked spectral line profiles in the Cepheus Flare suggesting that this region encloses an old supernova remnant. Assuming a distance of 300 pc for the center of the shell, they derived a radius of approximately 50 pc, expansion velocity of 4 km s^{-1} for the Cepheus Flare shell. Various observable aspects of the supernova explosions,

---

[1]**Part of the results presented on L1172/1174 in this chapter have been published in Saha et al. (2020).**

3. A DETAILED STUDY ON LDN 1172/1174
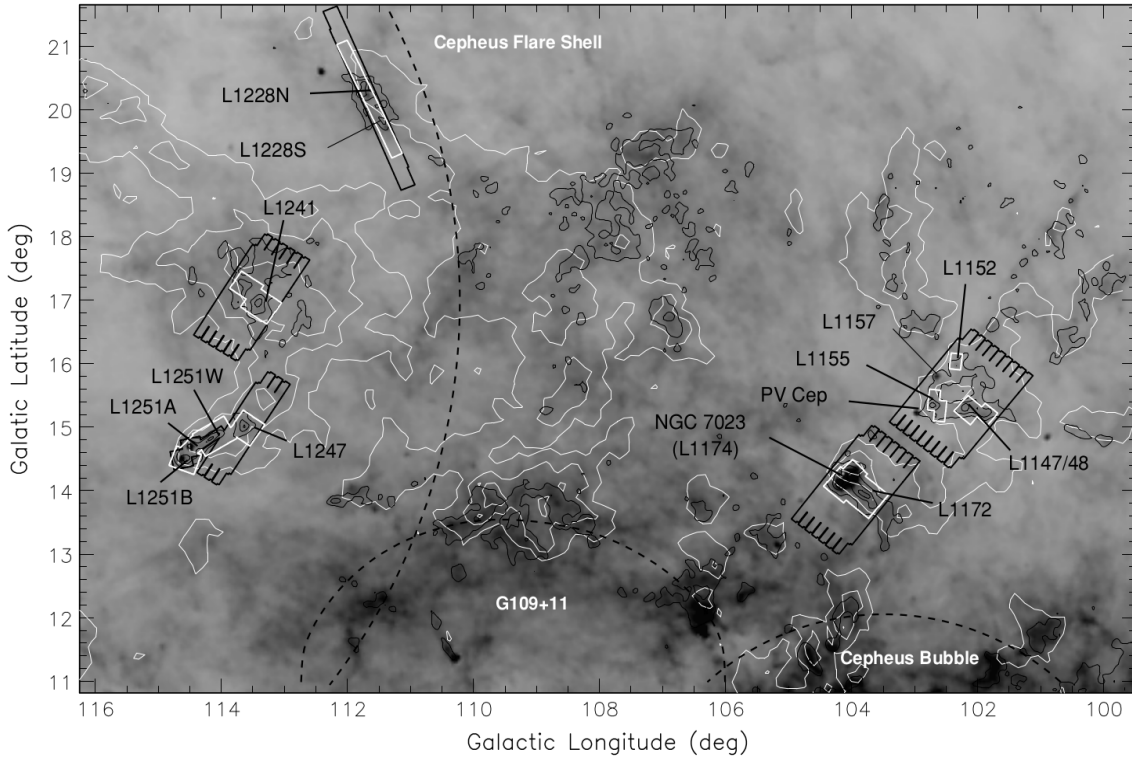
Figure 3.1: The Cepheus Flare region. Figure credit: Kirk et al. (2009)

such as the supernova bubble, radio continuum structure, and the Cepheus Flare Shell that shaped the structure of the interstellar medium, also found to trigger star formation in the Cepheus Flare in the last few million years (Kun et al., 2008).

Star formation studies in the Cepheus flare have been mainly conducted in a few smaller areas, such as dark cloud complexes that show signposts of formation of young stars (Kun, 1998; Kun et al., 2008; Kirk et al., 2009; Kun et al., 2009). In the Cepheus flare, the most thoroughly studied region is the reflection nebula NGC 7023 located in the cloud complex LDN 1172/1174 (hereafter L1172/1174; Lynds, 1962). This is an isolated star forming region located at $l \sim 104.1°$, $b \sim +14.2°$. The nebula is illuminated by a Herbig Be (B2/3Ve) star HD 200775 (The et al., 1994; Manoj et al., 2006). HD 200775 is identified as a double-line spectroscopic binary system having primary and secondary masses of 10.7 ± 2.5 M$_\odot$ and 9.3 ± 2.1 M$_\odot$ respectively (Alecian et al., 2008). Being associated with a single filament, the whole cloud system resembles a "head-tail" structure oriented at an angle of $\sim 50°$ to the Galactic plane (Elmegreen & Elmegreen, 1978). An outflow from HD 200775, currently inactive, is responsible for generating an asymmetric east-west biconical cavity that is filled with hot atomic gas (Fuente et al., 1998b). Rector & Schweiker (2013) discovered four new Herbig-Haro (HH) objects in NGC 7023 by wide-field

58

imaging. At least two distinct outflows were discovered in the northwestern "lobe" of NGC 7023. Kirk et al. (2009) identified a total of 50 YSO candidates in the vicinity of HD 200775 based on the *Spitzer* Infrared Array Camera (IRAC) and the Multiband Imaging Photometer for *Spitzer* (MIPS) study of the Cepheus Flare. HD 200775 is located at the center of a T association (Weston, 1953) which consists of about 14 stars showing Hα in emission and variability. At least 3 of the TTS are found to be in binary systems (Romano, 1975). Based on ^{13}CO observations, Yuan et al. (2013) suggested that strong winds from HD 200775 are blowing away ambient material, causing further compression of the matter around it, especially to the northern region where most of the YSOs are found to be distributed. They also found a systematic decrease in the age of YSOs as a function of distance from HD 200775, implying that at least some of them are possibly formed as a result of the feedback from HD 200775. The presence of a Herbig Be star, HH objects and low-mass YSOs makes L1172/1174 an excellent candidate to study star formation, possibly due to stellar feedback.

We have made a detailed study of L1172/1174 in parts I to IV. In part I, we estimated the distance to this cloud complex using the latest *Gaia* DR2. Then we searched for additional sources having distances and proper motions similar to the known YSOs located towards L1172/1174 in II. In part III, we present near-IR spectroscopic results of 10 YSOs associated with L1172/1174. Lastly, based on optical R-band polarimetric observations, we traced magnetic field morphology towards this cloud complex and then estimated the magnetic field strength in part IV. We also computed the star formation rate per unit mass to know the effect of magnetic field in star formation of L1172/1174.

Part I

Estimation of distance to LDN 1172/1174 using *Gaia* DR2

3.2   Introduction

Distance to any celestial object is one of the most important parameters. It is required to determine many of the physically relevant properties, such as the mass and the physical size of the molecular cloud. It is also required to determine the luminosity of YSOs that are embedded in the molecular cloud and the size of outflows, if present (Yun & Clemens, 1990; Clemens et al., 1991; Kauffmann et al., 2008). Distance estimation of molecular clouds has been and still is very tedious and difficult. Unfortunately, the estimated distances to many of the clouds are often plagued by very large uncertainties, and it is seen in the literature that measurements often differ by large factors, especially for those clouds that are isolated, sometimes by as much as a factor of two (Hilton & Lahulla, 1995).

Traditionally, the estimation of distances to molecular clouds employs the star count method (Bok & Bok, 1941) or Wolf diagrams (Wolf, 1923). One can also use the method of bracketing the cloud distance based on spectroscopic distances to stars (Hobbs et al., 1986) and equivalent widths of the Ca II H and K lines of stars located close in front and back of the molecular cloud (Megier et al., 2005). Additionally, distances to molecular clouds can be computed by bracketing them using the spectral classification of the stars projected on the cloud based on photometry obtained by Vilnius photometry system (Straizys, 1991; Straizys et al., 1992). Using the Stromgren $uvby-\beta$ intermediate-narrow-band photometric system, one can also determine distance and reddening for individual stars. These obtained parameters can be used to bracket the cloud distances (Nielsen et al., 2000; Franco, 2002). Peterson & Clemens (1998) developed a unique method to estimate the cloud distances by detecting M dwarfs located in front and back of the clouds, using their spectral types and reddening, which can be determined from the optical photometry alone as they populate a very distinct position in the $(V-I)$ versus $(B-V)$ color-color (CC) diagram. Maheswar et al. (2004) and Maheswar & Bhatt (2006) utilized 2MASS near-IR J, H and K_s and optical V, R, I photometry for spectral classification of the stars projected in front of and behind the clouds, to estimate their distances. Later, Maheswar et al. (2010) again presented a technique by which cloud distances can be determined using the 2MASS $(J - H)$, $(H - K_s)$ color indices of the main sequence stars in the spectral range from A0 to K7, projected on the clouds. Based on the Pan-STARRS1 photometry of the stars, Schlafly et al. (2014) simultaneously inferred their distances and reddening and bracketed the clouds between unreddened foreground stars and reddened background stars.

The distance to L1172/1174 is not firmly constrained. Several values of distances

have been quoted in the literature. The distance estimates made for the complex are compiled from literature and listed in Table 3.1. The estimated distances range from ~ 300 pc to ~ 700 pc. Based on the extinction and the absolute magnitude of HD 200775, Viotti (1969) made initial estimates of the distance to the star and obtained a value of 400±100 pc. Using photoelectric photometry and low resolution spectroscopy of 75 stars projected against L1172/1174, Shevchenko et al. (1989) reported a distance of 300±20 pc by producing a color-excess vs distance plot. Straizys et al. (1992) used Vilnius photometry, which gives two-dimensional classification, and interstellar reddening produced extinction vs. distance plot of 79 stars towards the cloud. They obtained a distance of 288±25 pc to L1172/1174. The parallax measurements of HD 200775 were used to calculate a distance of 430^{160}_{-90} pc to it (van den Ancker et al., 1998). However, based on a recomputed *Hipparcos* parallax value, van Leeuwen (2007) estimated a distance of 520^{+180}_{-110} pc to HD 200775. Maheswar et al. (2010), by using 2MASS JHK photometry obtained extinction and distances of sources projected against the cloud, estimated a distance of 408±76 pc. Benisty et al. (2013) obtained a revised distance of 320±51 pc to HD 200775 by combining radial velocity measurements and astrometric data. Using Wolf diagrams, Kun (1998) suggested that the Cepheus region above the Galactic latitude of $+10°$ consists of different cloud material partly projected against each other. They found evidence of absorbing clouds at ~ 200 and ~ 400 pc and assigned a distance of 450±45 pc to L1172/1174. Evidence for the presence of two layers of interstellar gas was found in neutral hydrogen (Heiles, 1967) and in CO molecular line (Grenier et al., 1989) observations. By applying the kinematical method to velocity profiles of the lines, Grenier et al. (1989) estimated the approximate distances of 300 pc and $800-900$ pc to the layers. Zdanavičius et al. (2009) investigated $1.5° \times 1.5°$ area centering at $l=104.1°, b=+14.2°$. This area was divided into five smaller subareas, and the dependence of extinction on distance was studied by using stars projected on these subareas. They suggested that the dust clouds in the vicinity of NGC 7023 are concentrated in at least two layers that are at ~ 280 pc and ~ 715 pc. However, in their analysis, the number of stars used to discern the hikes in extinction in different subareas is very small, making the distance estimates quite uncertain.

In this work, we estimated the distance to L1172/1174 using recently released *Gaia* DR2 data of the YSO candidates identified in the direction of the cloud and of the sources for which we have made optical R-band polarimetric observations. Use of YSOs associated with a cloud is one of the direct ways of finding distances to the cloud (e.g., Loinard et al., 2007, 2008). Polarization measurements of stars projected on a cloud can also be used as a technique to estimate distances to molecular

Table 3.1: List of previous distance estimation of L1172/1174 compiled from the literature.

Distance (pc)	Methods used to obtain the distance	Ref.
$282\pm42^{\dagger}$	Extinction vs distance	1
288 ± 25	Extinction vs distance	2
300 ± 20	Color-excess vs distance	3
320 ± 51	Radial velocity and astrometry of HD 200775	4
358 ± 31	Distances of YSOs in Cepheus flare region	5
408 ± 76	Extinction vs distance (JHK photometry)	6
430^{160}_{-90}	*Hipparcos* distance of HD 200775	7
440 ± 100	Extinction and absolute magnitude of HD 200775	8
450 ± 45	Wolf diagrams	9
510 ± 130	Star counts method	10
520^{180}_{-110}	Recomputed *Hipparcos* distance of HD 200775	11
$715\pm110^{\dagger}$	Extinction vs distance	1

1. Zdanavičius et al. (2009), 2. Straizys et al. (1992), 3. Shevchenko et al. (1989), 4. Benisty et al. (2013), 5. Dzib et al. (2018), 6 Maheswar et al. (2010), 7. van den Ancker et al. (1998), 8. Viotti (1969), 9. Kun (1998), 10. Armandroff & Herbst (1981), 11. van Leeuwen (2007)
† Zdanavičius et al. (2009) identified two layers of material towards the direction of L1172/1174 based on the jump in extinction seen in the extinction vs distance plot.

clouds (Straizys et al., 1992; Lombardi et al., 2008; Neha et al., 2016). While the foreground sources are expected to show a low degree of polarization (P%), sources that are located behind the cloud are expected to show a higher value of P% due to the aligned dust grains present in the cloud. Therefore the distance at which the P% values show a sudden hike is taken as the distance to the cloud (e.g., Straizys et al., 1992; Alves & Franco, 2007; Lombardi et al., 2008).

3.3 Observations and data reduction

3.3.1 Polarization measurements

The polarimetric observations of 42 fields covering the cloud L1172/1174 were carried out using ARIES Imaging POLarimeter (AIMPOL; Rautela et al., 2004) mounted at the Cassegrain focus of 1.04m Sampurnanand Telescope, ARIES, Nainital, India. Observations were performed on 26 nights spanning over three years from 2015 to 2017 (see Table 3.2). The frames were obtained using a 1024×1024 pixel^2 CCD chip (Tektronix TK1024), of which central 325×325 pixel^2 area was used for imaging polarimetry. The plate scale of the CCD is 1.48 arcsec pixel^{-1} and the FOV is $\sim8'$. The full width at half maximum (FWHM) of the observed stellar image profile is found to be ~ 3 pixels. The read-out noise and the gain of the CCD

Table 3.2: Log of polarimetric observations.

Year	Month (Date)
2015	Oct (11), Nov (2, 3, 15, 16, 17), Dec (15)
2016	Oct (23, 25, 26, 27, 28), Nov (22, 26, 27)
2017	May (22, 23), Oct (13, 14, 17, 18, 19, 20, 21, 26, 27)

were 7.0 e^{-1} and 11.98 e^{-1} per Analog to Digital Unit, respectively. An R-band filter, matching the Kron-Cousin passband ($\lambda_{eff} = 0.760$ μm), was used during the observations. AIMPOL provides only linear polarization and consists of an achromatic half wave plate (HWP) acting like a modulator and a Wollaston prism as a beam splitter. This set up provides two images (ordinary and extraordinary) of each target on the CCD frame. The HWP is rotated to obtain four normalized Stokes parameters, q[R(0°)], u[R(22.5°)], q1[R(45°)] and u1[R(67.5°)], corresponding to its four positions, i.e. 0°, 22.5°, 45° and 67.5°. We estimate the errors in normalized Stokes parameters $\sigma_R(\alpha)(\sigma_q, \sigma_u, \sigma_{q1}, \sigma_{u1})$ in per cent using the relation given by Ramaprakash et al. (1998). The average background counts have also been estimated around ordinary and extraordinary images of each star (Ramaprakash et al., 1998).

The contribution of instrumental polarization from the measurements was removed by observing a number of unpolarized standard stars from Schmidt et al. (1992). We also observed six polarized standard stars (HD 236633, BD+59°389, HD 19820, HD 204827, HD 25443, HD 15445) from the list given by Schmidt et al. (1992) to determine the reference direction of the polarizer during our observing runs. The measurements were used to obtain the zero-point offset with respect to the north, which was later applied to the position angles of the observed stars. After bias subtraction, flat correction of the images using the flux normalization formula from Ramaprakash et al. (1998), we aligned and combined multiple images of a given field. The selection of the ordinary and extraordinary pair of each star from a given field was automated using a program written in the Python language. We performed photometry of the selected pairs using the Image Reduction and Analysis Facility (IRAF) DAOPHOT package to obtain the P% and position angle (θ_P) of each star. The details of the instrument used and data reduction procedure are given in Soam et al. (2013, 2015b, 2017).

3.3.2 The *Gaia* DR2

Gaia DR2 provides accurate positions, parallaxes, and proper motions for more than a billion objects (Gaia Collaboration et al., 2018). However, the conversion from

parallax to distance is known to become non-trivial when the observed parallax is small compared to its uncertainty, especially in cases where $\sigma_\varpi/\varpi \gtrsim 20\%$ (Bailer-Jones, 2015). Recently, Bailer-Jones et al. (2018) calculated distances to 1.331 billion sources for which *Gaia* measured parallaxes by adopting an exponentially decreasing space density prior in the distance. The distances to the YSO candidates and the field stars for which we made polarization measurements are obtained from Bailer-Jones et al. (2018) and proper motions from Gaia Collaboration et al. (2018).

3.4 Results and Discussions

3.4.1 Distance estimation based on the known YSO candidates associated with L1172/1174

One of the direct ways of estimating distances to a molecular cloud is to use the stars that are associated with the cloud. Recently, using 47 YSO candidates identified by Kun et al. (2008), Dzib et al. (2018) estimated a distance of 358±32 pc to the whole Cepheus flare region. But as discussed by Kun (1998), the Cepheus flare region contains clouds that are located at different distances in projection. The distances of YSOs studied by Dzib et al. (2018) also show a large spread ranging from ~ 200 pc to ~ 400 pc. Therefore, in this work, we restricted our analysis to sources that are located within a $1° \times 1°$ region about the star HD 200775 and estimated the distance to L1174.

A total of 58 YSO candidates have been identified till now (after taking into account the common sources among various studies) in the vicinity of L1172/1174 (Kirk et al., 2009; Kun et al., 2009; Yuan et al., 2013). Table 3.3 presents the 58 YSOs located towards the cloud complex. Columns (1) and (2) provide the serial number and name of the YSOs and candidates. The positions of the sources are listed in columns (3) and (4). Sources detected in *Gaia* DR2 are marked with ticks in column (5).

Table 3.3: YSOs & candidates associated with the clouds.

No. (1)	Source Name (2)	RA (°) (3)	Dec (°) (4)	Detection by Gaia DR2 (5)	No. (1)	Source Name (2)	RA (°) (3)	Dec (°) (4)	Detection by Gaia DR2 (5)
sources associated with L1172/1174					30	[KWD 2009] 139	315.431700	68.160000	-
1	2MASS J20563311681481	314.137995	68.246719	-	31	2MASS J21014366750268	315.431874	67.840764	✓
2	FT Cep	314.845315	68.245467	-	32	2MASS J210143916814033	315.432926	68.234265	✓
3	2MASS J21001891811062	315.079042	68.185019	✓*	33	2MASS J210145376804208	315.439081	68.072427	✓
4	2MASS J21002024680268	315.084359	68.140777	✓	34	FU Cep	315.444875	68.145894	✓
5	2MASS J21002063681172	315.085994	68.221451	-	35	2MASS J210152656809520	315.469493	68.164419	✓
6	2MASS J21002149680452	315.089575	68.129233	-	36	2MASS J210154756806590	315.478284	68.116360	✓
7	2MASS J21002203681259	315.091806	68.216454	-	37	2MASS J210202426811587	315.510174	68.199649	✓
8	[KWD 2009] 100	315.093300	68.217800	-	38	FV Cep	315.553076	68.397116	✓*
9	2MASS J2100288968813024	315.120379	68.177339	✓	39	2MASS J21021402+6813594	315.558650	68.233141	✓
10	2MASS J2100320768812477	315.133839	68.213212	-	40	2MASS J210214046807306	315.558597	68.125207	✓
11	2MASS J2100366268803445	315.152600	68.062376	✓	41	EM* LkHα 275	315.584979	68.423341	-
12	2MASS J2100555068811273	315.231398	68.190892	✓	42	IRAS 21017+6742	315.588460	67.905610	-
13	2MASS J2100580868809382	315.242214	68.160613	-	43	2MASS J210222286812121	315.592850	68.203369	-
14	SSTgbs J21010306813072	315.262468	68.218646	✓	44	2MASS J210227446754186	315.614343	67.905190	✓
15	2MASS J2101036768813092	315.265512	68.219238	✓	45	2MASS J210228036808476	315.616830	68.146568	✓
16	2MASS J2101087068812525	315.286349	68.214588	✓	46	LkHα 428 N	315.617758	68.058287	✓
17	2MASS J2101101768811333	315.292436	68.192566	✓	46b	LkHα 428 S	315.618244	68.057669	✓
18	2MASS J2101125268810195	315.302195	68.172089	✓	47	2MASS J210229936754083	315.624731	67.902313	-
19	NGC 7023 RS 2	315.359984	68.177338	✓	48	FW Cep	315.637634	68.124746	✓
20	NGC 7023 RS 2 B	315.362884	68.177214	-	49	2MASS J210234926812024	315.645542	68.200670	✓*
21	2MASS J2101273468811383	315.363944	68.193993	✓	50	2MASS J210254846806210	315.728611	68.105833	✓
22	2MASS J2101277468808114	315.365645	68.136491	✓	51	NGC 7023 RS 10	315.747855	68.108939	✓
23	2MASS J2101296668813468	315.373607	68.229654	-	52	2MASS J210259636808119	315.748490	68.136670	✓
24	2MASS J2101328068811204	315.386675	68.189026	✓	53	2MASS J210307566808339	315.781610	68.142739	-
25	2MASS J2101358368813259	315.399297	68.223862	✓	54	IRAS 21025+6801	315.800400	68.216900	-
26	PW Cep	315.400352	68.139576	✓	55	EH Cep	315.851719	67.985134	✓
27	HD 200775	315.403923	68.163263	-	56	2MASS J210341546823456	315.923186	68.396032	✓
28	SX Cep	315.406537	68.191931	✓	57	2MASS J210359386749296	315.997496	67.824856	✓
29	NGC 7023 RS 5	315.427117	68.215960	✓	58	IRAS 21035+6730	316.065214	67.712884	✓*

* sources detected in Gaia DR2 but having distance ≳ 1 kpc, hence discarded in further analysis.

68
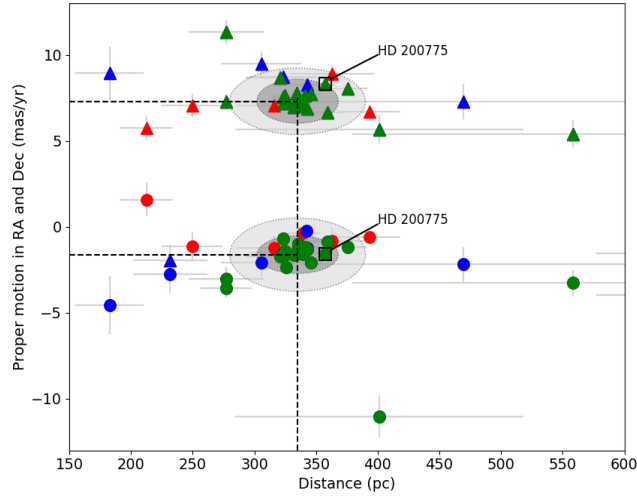
Figure 3.2: Proper motion values of the known YSO candidates associated with L1174 are plotted as a function of their distances obtained from *Gaia* DR2. The triangles and circles represent the distance-$\mu_{\alpha\star}$ and distance-μ_δ values respectively. Location of HD 200775 is also marked. The error ellipses corresponding to $3 \times$ MAD (darker shade) and $5 \times$ MAD (lighter shade) in proper motion and distance values are drawn. The dashed lines show the median values of distance, $\mu_{\alpha\star}$ and μ_δ. The ratios of distances and proper motion values with their respective errors $2 > (m/\sigma m) \geqslant 1$ are for red points, $3 > (m/\sigma m) \geqslant 2$ for blue points and $(m/\sigma m) \geqslant 3$ for green points.

Of the 58 YSO candidates, we found distance and proper motion values in the right ascension ($\mu_{\alpha\star} = \mu_\alpha \cos\delta$) and declination ($\mu_\delta$) for 37 sources in the Bailer-Jones et al. (2018) and in the *Gaia* DR2 (Gaia Collaboration et al., 2018) catalogues, respectively. For all the 37 sources, a *Gaia* counterpart was found well within $1''$ of the input coordinate of the YSO candidates and the ratio, $m/\sigma m$ (here m represents the distance, $\mu_{\alpha\star}$ and μ_δ values and the σ_m represents their respective errors) $\geqslant 1$. The *Gaia* DR2 results for the YSO candidates are shown in Fig. 3.2. The triangles and circles represent the distance-$\mu_{\alpha\star}$ and distance-μ_δ values respectively. Of the 37, 6 sources (red circles and triangles) are with $1 \leqslant m/\sigma_m < 2$; 8 sources (blue circles and triangles) are with $2 \leqslant m/\sigma_m < 3$; and 23 sources (green circles and triangles) with $m/\sigma_m \geqslant 3$. The distance-$\mu_{\alpha\star}$ and distance-μ_δ values for the HD 200775 are identified and marked separately. Three sources out of these 23 are found to be at a distance greater than 1 kpc. Thus, in this work, we selected only those sources for which $m/\sigma_m \geqslant 3$ and are at distances less than 1 kpc.

Table 3.4: Distance and proper motion values of the known YSO candidates identified towards L1172/1174 from *Gaia* DR2.

#	RA (°)	Dec (°)	Source ID	Distance (pc)	$\mu_{\alpha\star}$ ($\Delta\mu_{\alpha\star}$) (mas/yr)	μ_{δ} ($\Delta\mu_{\delta}$) (mas/yr)	G (eG) (mag)	RUWE	Spectral Type	Hα EW(Å)	2MASS	Spitzer	WISE	X − ray
(1)	(2)	(3)	(4)	(5)	(6)	(7)	(8)	(9)	(10)	(11)	(12)	(13)	(14)	(15)
1	314.845315	68.245467	2270256357606156160	339^{+5}_{-5}	7.333±0.087	-1.599±0.079	14.3789±0.0150	1.1	K1	-9.6	✓	✓	✓	-
2	315.084447	68.140772	2270240208529136128	341^{+10}_{-10}	7.630±0.147	-1.182±0.158	17.0301±0.0309	1.1	-	-	✓	✓	✓	-
3	315.231481	68.190885	2270240723925216640	333^{+12}_{-13}	7.205±0.184	-1.649±0.280	16.5545±0.0020	1.3	-	-	✓	✓	✓	-
4	315.359984	68.177338	2270245637367812352	325^{+7}_{-7}	7.652±0.104	-1.416±0.121	14.8691±0.0049	1.2	M0IV	-59.8	✓	✓	✓	✓
5	315.362884	68.177214	2270245637367812608	360^{+13}_{-13}	6.667±0.174	-0.865±0.189	16.3712±0.0266	1.5	M0	-63.9	✓	-	-	-
6*	315.399160	68.223752	2270246874315480960	277^{+27}_{-34}	11.343±0.673	-3.039±0.706	17.7558±0.0107	3.3	-	-	✓	✓	✓	-
7	315.400352	68.139576	2270245294110695808	332^{+6}_{-6}	6.971±0.106	-1.638±0.117	15.6235±0.0130	1.4	M0	-106.0	-	✓	✓	✓
8	315.403923	68.163263	2270245431209611776	357^{+5}_{-5}	8.336±0.079	-1.566±0.083	7.1592±0.0010	1.6	-	-	✓	-	✓	-
9	315.427117	68.215960	2270246146847658624	323^{+8}_{-9}	7.530±0.148	-0.668±0.164	15.6942±0.0033	1.5	M2	-28.8	✓	✓	✓	✓
10	315.444875	68.145894	2270057689598399360	335^{+4}_{-5}	7.770±0.071	-1.428±0.078	15.0363±0.0057	1.1	M1	-64.5	✓	✓	-	-
11	315.558650	68.233141	2270247492790812928	321^{+26}_{-31}	8.666±0.528	-1.736±0.568	19.1129±0.0059	1.1	-	-	✓	-	✓	✓
12*	315.584979	68.423341	2270276041439733504	277^{+19}_{-22}	7.262±0.483	-3.589±0.530	14.6337±0.0158	7.9	-	-	-	✓	✓	-
13	315.617758	68.058287	2270056246489398528	343^{+6}_{-6}	6.868±0.098	-1.319±0.107	15.3618±0.0053	1.1	K7	-56.0	-	-	✓	✓
13b	315.618244	68.057669	2270056246489398400	376^{+16}_{-15}	8.041±0.193	-1.202±0.215	15.5062±0.0010	1.5	M4.5IV	-7.5	✓	✓	-	-
14	315.637634	68.124746	2270056969804390928	336^{+3}_{-2}	7.054±0.044	-1.017±0.043	14.2794±0.0078	1.0	K5	-4.0	✓	-	✓	✓
15	315.747855	68.108939	2270053875667453056	323^{+4}_{-5}	7.174±0.079	-1.738±0.075	15.5766±0.0061	1.5	K4	-8.1	✓	✓	✓	-
16*	315.748555	68.136623	2270058303777440640	401^{+85}_{-149}	5.678±0.849	-11.026±1.196	16.5831±0.0108	4.7	-	-	✓	✓	✓	✓
17	315.851719	67.985134	2270052256462948736	326^{+8}_{-8}	7.269±0.140	-2.330±0.128	13.3182±0.0111	5.9	K2	-13.1	✓	✓	✓	-
18*	315.923249	68.396018	2270272330587968256	559^{+128}_{-230}	5.407±0.780	-3.269±0.752	17.4905±0.0045	4.1	-	-	✓	-	✓	✓
19	315.997585	67.824847	2270035287049455616	346^{+8}_{-9}	7.722±0.152	-2.061±0.133	16.3326±0.0041	1.4	-	-	✓	✓	✓	-

Columns 2 & 3: 2015.5 epoch Right Ascension & Declination of sources given by *Gaia* DR2.
Column 4: Distance taken from the Bailer-Jones et al. (2018) catalogue.
Column 9: Renormalised Unit Weight Error (RUWE) of the YSO candidates.
Columns 10 & 11: Spectral type and equivalent width of Hα taken from Kun et al. (2009).
Column 13: X-ray detection by *XMM-Newton*.
Stars #4 & #5 appear as double sources. Resolved by *Gaia* DR2, 2MASS and *Spitzer*. In *WISE* and *XMM-Newton*, they are detected as single source. *WISE* and X-ray are assigned to the brightest source in *Gaia*.
Stars #13 & #13b appear as double sources. Resolved only by *Gaia* DR2. 2MASS classified it as an extended source. Assigned X-ray detection to the brightest source in *Gaia*.
* Sources considered as outliers in our analysis.

The results of these 20 sources are shown in Table 3.4. Positions of the sources are provided in columns (2) and (3). *Gaia* DR2 source ID for each is source is listed in column (4). d, $\mu_{\alpha\star}$ and μ_δ values and *Gaia G* band magnitudes for the 20 sources are given in columns (5) to (8), respectively. In column 9 of Table 3.4, we give the renormalized unit weight error (RUWE[1]; Lindegren, 2018) for the YSO candidates. RUWE is a scaled unit weight error (UWE) with the scaling factor depending on the magnitude and color of the sources. Theoretically, the UWE is expected to be close to 1.0 for well-fitted solutions of single stars but can show larger values depending on the source environment and the geometric properties such as binarity. Practically, sources showing RUWE $\leq$ 1.4 are considered as having a good astrometric solution (Lindegren, 2018). Spectral types and equivalent widths of some YSOs are listed in column (10), which are obtained from Kun et al. (2009). Sources identified in 2MASS, *Spitzer*, *WISE* and *XMM-Newton* are marked with ticks in columns (12) to (15), respectively.

Based on the proper motion and the distance values, a clear clustering of sources are evident in Fig. 3.2. The median of $\mu_{\alpha\star}$, μ_δ and distance values are 7.301 mas yr^{-1}, -1.619 mas yr^{-1} and 335 pc, respectively. The variance and the standard deviation that are commonly used to measure spread in a data are more affected by the extreme (high and low) values. Therefore here we used median absolute deviation (MAD) to estimate statistical dispersion which is more resilient to outliers in a data set than the standard deviation. The estimated MAD in distance, $\mu_{\alpha\star}$ and μ_δ are 11 pc, 0.386 mas yr^{-1} and 0.427 mas yr^{-1}, respectively. A majority of the YSO candidates (14) are found to fall within the constraints of three times the MAD in proper motions and distances as shown in Fig 3.2 using the ellipses drawn with darker shade. Two more sources get included when we consider a constraint of five times the MAD in proper motions and distances (ellipses drawn in lighter shade). Remaining four sources show large scatter from the median values. We note that HD 200775 is showing a larger distance ($\sim 2\times$ MAD) with respect to the median value. As can be noticed in 3.4, of the 20 YSO candidates, 10 sources show RUWE>1.4. The four sources showing large scatter from the median values are the ones showing relatively high values of RUWE (>3.0). Of the remaining six, except one, the others show RUWE in the range of 1.5-1.6, including HD 200775 which shows a marginally higher value of 1.6. Thus we considered all the 16 sources that are lying within $5 \times$ MAD limit as part of L1174 and sources (four of them) that are located outside of the $5 \times$ MAD ellipses are considered as outliers.

---

[1]RUWE values are obtained from http://gaia.ari.uni-heidelberg.de/

3.4.2 Distance estimation based on R-band polarization and the *Gaia* DR2 distance measurements of field stars projected towards L1172/1174

Presence of interstellar dust grains along a given line of sight can be inferred by their effects on starlight coming from the background stars. Rotating non-spherical dust grains get aligned with their minor axis parallel to the ambient magnetic field (Crutcher, 2012; Davis & Greenstein, 1951). When the unpolarized starlight coming from a background star passes through regions containing such dust grains, the light gets polarized due to the selective absorption. Normally the value of P% increases gradually with the increase in the column of dust grains along the pencil-beam of a starlight. However, when it encounters a molecular cloud, a sudden increase in the values of P% occurs. Therefore, while the stars that are foreground to the cloud are expected to show low values of P%, the stars that are located behind the cloud are expected to show higher values of P%. The distance at which the sudden increase in the P% occurs is taken as the distance of the cloud (e.g. Alves & Franco, 2007; Knude & Hog, 1998; Straizys et al., 1992; Whittet et al., 1997). We examined the R-band polarization measurements of 569 sources that are projected on L1172/1174. The advantage of using polarization measurements to infer the presence of a molecular cloud is that the measured values are independent of the nature of the background stars.

The results of our polarization measurements for the stars are plotted in Fig. 3.3. The lengths of the vectors are proportional to the value of P%, and the orientations depend on the θ_P. The values of θ_P are measured from the north, increasing towards the east. We obtained *Gaia* DR2 distances for 545 sources from the Bailer-Jones et al. (2018) catalogue. In all the cases, we obtained a *Gaia* DR2 counterpart within $1''$ of our source positions. The results are presented in Fig. 3.4. The P% vs. distance and θ_P vs. distance plots are shown in Fig. 3.4 (a) and (b), respectively, using filled triangles in grey. We have shown only 301 sources for which the ratios of the P%, θ_P and distance and their corresponding error, P/σ_P, $\theta_P/\sigma_{\theta_P}$ and d/σ_d $\geqslant 3$, respectively. The mean values of P% and θ_P are found to be 2.5% and 142°. The closest star observed by us is at a distance of 306 pc. Therefore to investigate the foreground contribution to the polarization, we searched for additional sources in the Heiles (2000) catalogue with a search radius of 6° about HD 200775. The search gave a total of 26 sources, of which HD 200775, HD 203467, HD 208947, and HD 193533 were not considered in the analysis due to the following reasons. The polarization values of HD 200775 could be affected by the reflection nebulously
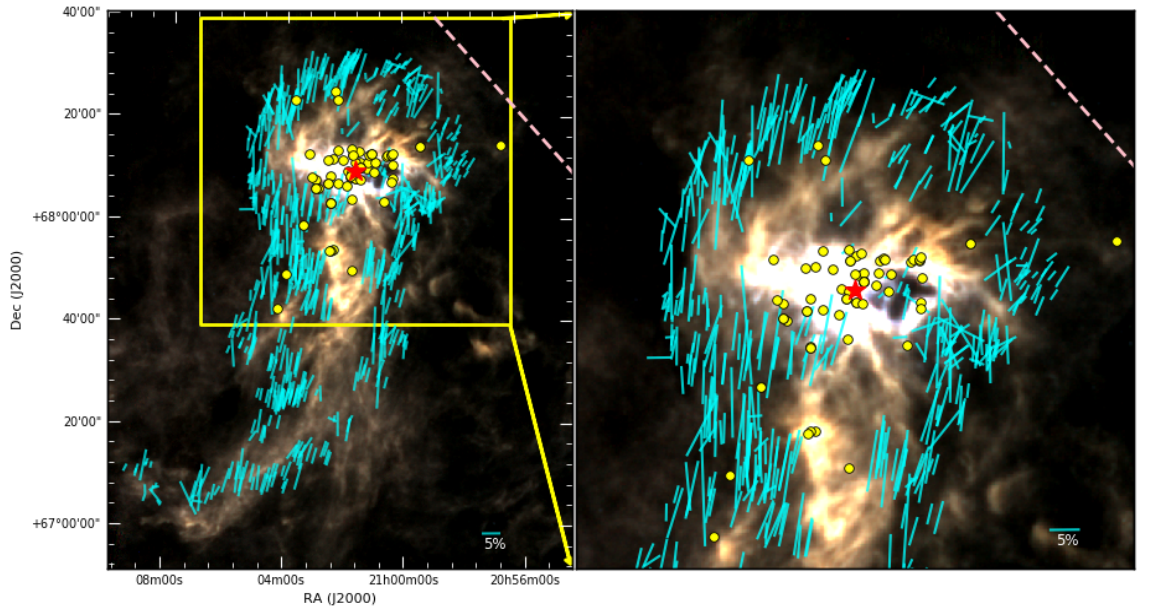
Figure 3.3: **LHS:** R-band polarization vectors (cyan lines), obtained from our observations, overplotted on *Herschel* color-composite diagram with 250, 350 and 500 μm images. Broken line in pink represents the galactic plane. Locations of the known YSO candidates (yellow circles) around the central star HD 200775 (red star) are also shown. A polarization vector corresponding to 5% is shown for reference. **RHS:** Enlarged view of the $1°\times1°$ region around HD 200775. Symbols represent the same as LHS.

around it. The HD 203467 is a Be type object, HD 208947 is an Algol variable, and HD 193533 is classified as a variable source in the Simbad database. Of the 22, we obtained the *Gaia* DR2 distance for 17 sources from the Bailer-Jones et al. (2018) catalogue. The degree of polarization (P_H%) and polarization position angles (θ_H) of the 17 sources are shown using filled circles in black in both (a) and (b) of Fig. 3.4 respectively. Because the foreground sources show relatively very low polarization, we set no constraints on the P_H/σ_H values while selecting them.

In Fig. 3.4 (a), the P_H% of the stars having distances less than ~ 335 pc (marked using dotted line in both upper and lower panels) show low values of polarization while the ones behind the cloud show relatively higher values. A significant increase in the P% values is seen at ~ 335 pc for the sources observed by us, which confirms the presence of the cloud at that distance, similar to what we obtained from the YSO candidates. From the Fig. 3.4 (b), as the distance increases from ~ 100 pc to ~ 335 pc, the θ_H values are found to change systematically from $\sim 0°$ to a value close to the mean value of $142°$ obtained for the sources observed by us. The mean value of the θ_H for the 4 sources lying beyond the distance of 335 pc is found to
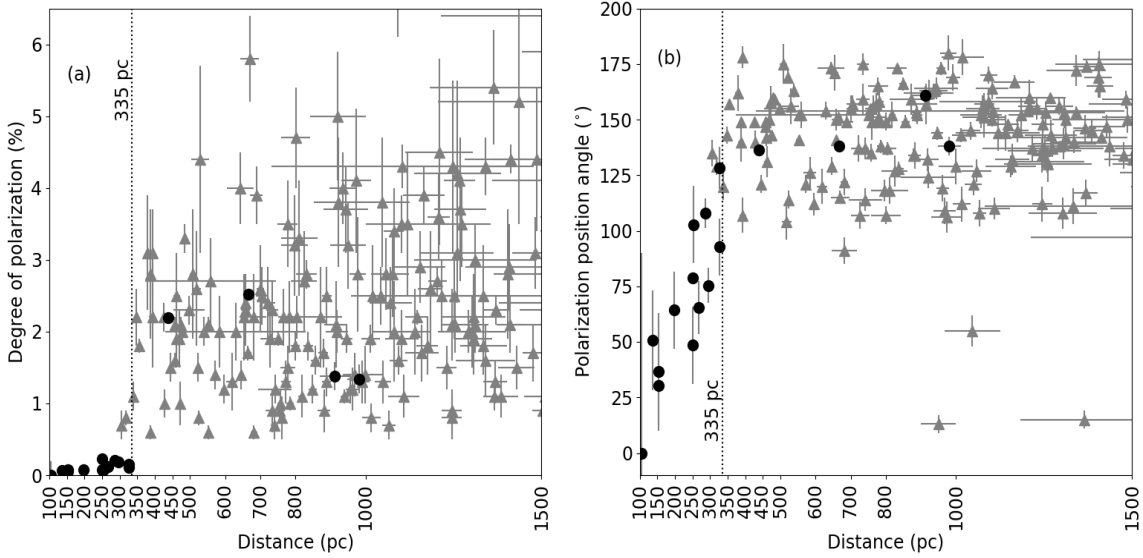
Figure 3.4: **(a)** Polarization (%) vs. distance plot for the stars projected towards the direction of L1172/1174 (filled triangles in grey). The filled circles in black are the sources for which the P% is obtained from the Heiles (2000) catalogue. **(b)** Polarization position angle vs. distance plot for the stars projected in the periphery of L1172/1174. The symbols are same as above.

be $\sim 143°$. Based on an abrupt increase in the values of the P% and the change in the θ_P for stars projected on the cloud, we confirm the distance of the entire L1172/1174 cloud complex at ~ 335 pc.

The distance of 335 ± 11 pc (the MAD is taken as the uncertainty in the distance) to L1174 implies that L1174 is at a height of ~ 80 pc above the galactic mid-plane. This is higher when compared to the scale-heights of ~ 45 pc estimated for the OB stars in the local galactic disk (Reed, 2000) and for the molecular gas (e.g. Heyer & Dame, 2015). Thus, L1174 is an example of a sparse cluster of young stars (which contains one or two intermediate-mass stars) forming at a relatively high galactic latitude. Based on the distance ~ 335 pc, the spatial extent of L1172/1174 cloud complex is estimated as ~ 9 pc$\times 4$ pc.

3.5 Conclusions

The region surrounding the well-known reflection nebula, NGC 7023, illuminated by a Herbig Be star, HD 200775, located in the dark cloud L1174, is known for low to intermediate-mass star formation activity. Distance to L1172/1174 complex, of which L1174 is a part, is not very well constrained. In this work, using *Gaia* DR2 distances and proper motion values, we determined distance to the cloud using the

known YSO candidates. We also used polarization measurements of 545 stars that are projected on the cloud to estimate the same. The main results of this study are summarized below:

- Based on the distances and proper motion values of 20 previously known YSO candidates associated with L1172/1174 we obtained a distance of 335±11 pc to the cloud.

- The distance estimated for the entire cloud using the polarization measurements of the foreground and background stars was also found to be consistent with the ~ 335 pc distance.

- Based on the distance ~ 335 pc, the spatial area of L1172/1174 cloud complex is estimated as ~ 9 pc×4 pc.

Part II

Comoving sources around HD 200775 identified using *Gaia* DR2

3.6   Introduction

A complete census of young stars and sub-stellar objects in the nearby star forming regions is essential to improve our understanding of the global properties of the younger population like disk fraction, initial mass function, star formation efficiency, and the star formation history. Low-mass sources (spectral type later than F) that are young and have not yet reached the main sequence are generally called as T Tauri stars (TTS). Observationally, TTS are identified based on their association with regions of high extinction and presence of Balmer lines of hydrogen in emission (Appenzeller & Mundt, 1989), which are found to be highly variable often in short time scales. The presence of Hα in emission in TTS is considered to be a sign of active accretion of material from the surrounding circumstellar disk. Based on the equivalent width of Hα emission line, EW(Hα), the TTS are further classified into classical T Tauri stars (CTTS) and weak-line T Tauri stars (WTTS). In WTTS, EW(Hα) is often low ($\lesssim$10 Å) or absent (naked T Tauri stars), which shows a low degree of accretion or that accretion has ceased completely. However, no particular value of EW(Hα) can be used to distinguish CTTS and WTTS because of the 'contrast effect' of the photosphere (Basri & Marcy, 1995; Martín, 1998; White & Basri, 2003; Barrado y Navascués & Martín, 2003; Mathew et al., 2017).

The YSOs are also classified on an empirical sequence based on the spectral slope of their spectral energy distribution (SED) in the near- to submillimeter wavelengths. The YSOs that are deeply embedded in their birth places are classified as "Class 0" objects, more evolved but still embedded in their envelope are "Class I' objects. Sources showing excess IR emission due to the presence of circumstellar material in a flattened geometry are "Class II" objects, and sources having little or no IR excess emission are "Class III" objects (Lada, 1987; Andre et al., 1993; Greene et al., 1994). A fifth class of "flat spectrum" was introduced by Greene et al. (1994) to represent sources that are relatively more evolved than "Class I" YSOs but are still embedded in the parental cloud showing excess in near- and mid-IR region. Though refinements to the above classification scheme were suggested in subsequent studies (e.g., Robitaille et al., 2007; Evans et al., 2009; McClure et al., 2010), it adequately presents an evolutionary sequence of YSOs. The Class II and Class III objects generally correspond to CTTS and WTTS, respectively.

Based on the Hα emission, near-IR and mid-IR observations, a total of 58 YSO candidates have been identified so far in NGC 7023 (Kirk et al., 2009; Kun et al., 2009; Yuan et al., 2013). Because WTTSs show low EW(Hα) and less IR excess emission, it is difficult to distinguish them from the unrelated field stars, and they

Table 3.5: Log of spectroscopic observations.

Year	Month (Date)
2018	Oct (11)
	Nov (30)

may fail detection in Hα and IR surveys. Thus a complete census of Class III sources in a star forming region may not always be complete. Using proper motion and parallax measurements from *Gaia* DR2, numerous kinematically coherent associations of stars have been recognized within a few hundred parsec of the Sun (e.g., Dzib et al., 2018; Faherty et al., 2018; Luhman et al., 2018). A detailed study of the nearest of these associations has revealed the presence of a large number of low-mass stars and sub-stellar objects (Luhman, 2018; Luhman et al., 2018). Thus, an alternative way to get a census of disk-less young members, if present, in a star forming region is to look for additional sources that are kinematically associated with the known YSOs of the region. We made a search for any additional sources that may be comoving with the known YSO candidates and may have been missed detection in the earlier studies of L1172/1174 (Kirk et al., 2009; Kun et al., 2009; Yuan et al., 2013), using distance and proper motion values from *Gaia* DR2.

3.7 Observation and data reduction

3.7.1 Spectroscopic Observations

We carried out spectroscopic observations of 4 of the 20 newly identified comoving sources discussed in this work using the Hanle Faint Object Spectrograph Camera (HFOSC) mounted on the 2-m Himalayan Chandra Telescope (HCT) of the Indian Astronomical Observatory (IAO). We selected sources based on their relative brightness. The HFOSC is equipped with a 2K×4K SITe CCD chip. We used a combination of slit 167l (slit width $1.92'' \times 11'$) and grism 7, covering the wavelength range 3500-7500 Å. This slit and grism combination gives a spectral resolution of $\Delta\lambda \sim 8$ Å. All the pre-processing and data reduction were performed in the standard manner using various tasks available with the IRAF. We used "splot" task to obtain the equivalent width of our observed sources. The log of the observations is given in Table 3.5.

3.7.2 *Spitzer* photometry of point sources

The *Spitzer* photometry of the known YSO candidates is obtained from the literature (Kirk et al., 2009). For the newly identified comoving sources, we calculated the *Spitzer* IRAC (3.6, 4.5, 5.8, 8.0 μm) magnitudes by carrying out photometry on the images obtained from the *Spitzer* Space Observatory archive with Program ID: 30574 (Kirk et al., 2009). The basic calibrated data (BCD) frames were co-added and mosaic images were created using the SSC mosaicing and point-source extraction software (MOPEX; Makovoz & Marleau, 2005). Sources were extracted from the final images using MOPEX. Photometry was performed by extracting the flux using an aperture of 7 pixels wide box centered on each source using the APEX tool developed by the *Spitzer* Science Center. For the sources for which APEX failed to detect in automated mode at one or more wavelengths, we used the user list option to supply the coordinates of the source to obtain the flux values. We adopted 280.9, 179.7, 115.0, and 64.1 Jy in the 3.6, 4.5, 5.8, and 8.0 μm bands, respectively as the zero points for conversion between flux densities to the magnitudes as provided by Kirk et al. (2009).

3.8 Results and Discussions

With the knowledge of the precise values of position, proper motion, and distance from the *Gaia* DR2 measurements, we looked for additional, probably young, sources that are comoving with the already known YSO candidates associated with L1172/1174. For this, we obtained proper motions and distances of sources that are located within a region of $1° \times 1°$ centered around HD 200775 from the *Gaia* DR2 (Gaia Collaboration et al., 2018), and Bailer-Jones et al. (2018) catalogues, respectively. For the reason that the majority of the known YSO candidates are distributed within a region of $1° \times 1°$ centered around HD 200775, we conducted our search for the comoving objects also within the same area. As in the case of the YSO candidates, here again, we selected only those sources for which m/σm$\geqslant$ 3. Considering that a majority of the previously known YSO candidates are found within 5 $\times$ MAD with respect to the median values of the distance and the proper motions, the same criteria are used to select the comoving sources also. That is, all sources falling within the range of 5 $\times$MAD with respect to the median values of the distance and the proper motions are regarded as comoving sources and included for further analysis.

The selected sources are shown on the proper motion $-$ distance plot presented
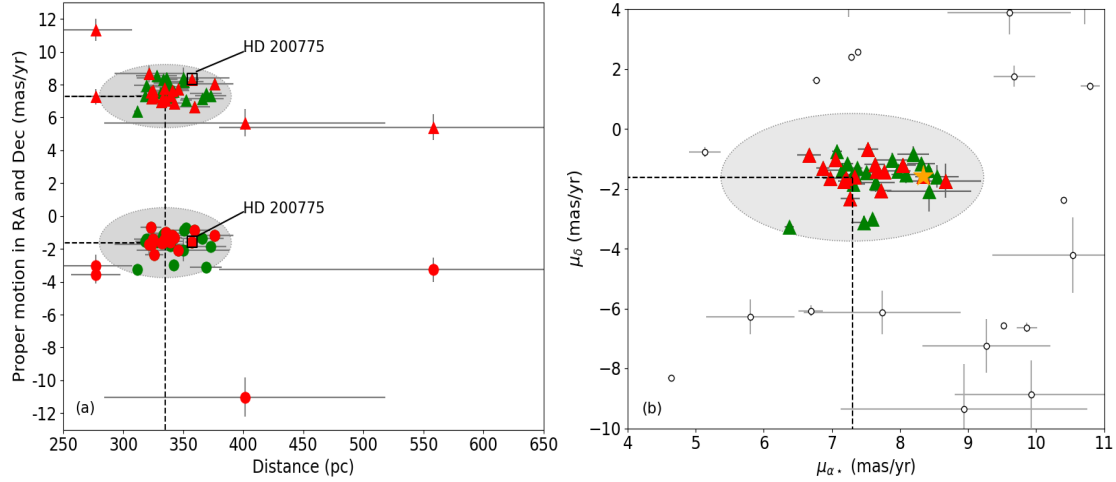
Figure 3.5: **(a)** Proper motion vs. distance plot for the known YSO candidates (triangles and circles in red) and for the 20 newly identified comoving sources (triangles and circles in green). The triangles (red and green) and circles (red and green) represent the distance-$\mu_{\alpha\star}$ and distance-μ_δ values of the known YSO candidates and comoving sources respectively. Locations of HD 200775 are identified by square boxes. The grey ellipses represent the boundary of the proper motion values and the distance ranges used to identify the new comoving sources. The dashed lines show the median values of distance, $\mu_{\alpha\star}$ and μ_δ. **(b)** μ_δ vs. $\mu_{\alpha\star}$ plot for the known YSO candidates and for the comoving sources. Red triangles represent proper motion values of known YSO candidates and green triangles represent that of the comoving sources. The grey ellipse represents the boundary of the proper motion values considered to select the comoving sources. The orange star symbol indicates the location of HD 200775. The open circles represent sources not satisfying the $5 \times$ MAD conditions in distance and proper motion values. The dashed lines show the median values of $\mu_{\alpha\star}$ and μ_δ.

in Fig. 3.5 (a) and results are tabulated in Table 3.6. The distance-$\mu_{\alpha\star}$ and distance-μ_δ values of the known YSO candidates are shown using filled triangles and filled circles in red, respectively. The same for the comoving sources are presented using filled triangles and filled circles in green, respectively. The ellipses drawn in grey in Fig. 3.5 (a) represent the constraint of $5 \times$ MAD drawn at the median values of $\mu_{\alpha\star}$, μ_δ and distances of the known YSO candidates. Here again, the distance-$\mu_{\alpha\star}$ and distance-μ_δ values of HD 200775 are marked. We found a total of 20 additional sources that are located within the grey ellipses. The distance-$\mu_{\alpha\star}$ and distance-μ_δ values of these 20 additional sources are shown using filled triangles and filled circles in green respectively in Fig. 3.5 (a). In Fig. 3.5 (b) we show the $\mu_{\alpha\star}$ and μ_δ values of the known YSO candidates and the 20 additional sources using filled triangles in red and green respectively. HD 200775 is indicated by an orange star symbol. The
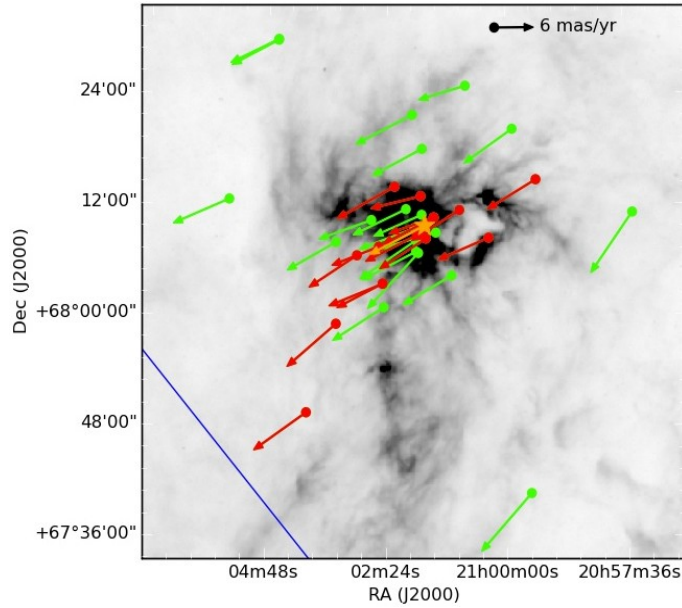
Figure 3.6: Proper motion plot for the YSO candidates (red arrows) associated with L1174 overplotted on the *Herschel* SPIRE 250 μm image. The green arrows represent the same for the newly identified comoving source. HD 200775 is indicated by a star symbol and an arrow in orange. The blue solid line represents the galactic plane.

grey ellipse indicates the range of $5 \times$ MAD in $\mu_{\alpha\star}$ and μ_δ about the median values obtained for the known YSO candidates. The kinematic association of the newly found 20 sources with the known YSO candidates is clearly evident in Fig. 3.5 (a) and (b). The proper motion values of other sources (open circles) in the field are found to be very different. The positions of the known YSO candidates and the 20 additional sources that are comoving are identified on the *Herschel* SPIRE 250 μm image as shown in Fig. 3.6 using red and green circles, respectively. The position of HD 200775 is shown using an orange star symbol. The arrows in red, green, and orange show the proper motion directions of the known YSO candidates, newly identified comoving sources, and HD 200775, respectively. The spatial locations of the comoving sources are very similar to those of the known YSO candidates. The distance and the proper motion values of the comoving sources are listed in Table 3.6. The RUWE values for the comoving sources are also shown in Table 3.6. Of the 20 comoving sources, only one source (c12) show RUWE of 1.5, which is marginally greater than the value of 1.4 considered as a criterion for good solution.

To investigate whether the sources with similar proper motions as that of the known YSO candidates from a given 1° square area are a chance projection of field stars or are really the comoving sources associated with the region, we selected 1°

square area from three reference fields lying towards the direction of the southern (tail) part of L1172/1174 having similar declination but differing in right ascension (field 1: 318.79282°, 67.174828°; field 2: 316.21048°, 67.206136°; field 3: 313.56081°, 67.197843°). Here also, we selected only those sources that are with $m/\sigma_m \geqslant 3$. We found only one source (in field 1), HD 202461 (distance = 309^{3}_{-2} pc, $\mu_{\alpha\star} = 7.317\pm0.060$ mas yr^{-1} and μ_δ = -1.724$\pm$0.050 mas yr^{-1}), which satisfies the above constraints (marked with a square box in the ellipses). Information pertaining to this source is not available in the literature. Thus, on an average, we expect at most one source in a given 1° square area in the direction close to L1172/1174 that could be a chance projection of field stars having proper motions and distances similar to those of the known YSO candidates. This confirms the presence of an over-density of stars within 1 square degree around HD 200775.

3.8.1 Properties of the sources identified around HD 200775

3.8.1.1 X-ray sources in the vicinity of HD 200775

The physics of star formation, as we understand now, indicates that the magnetic activity, accretion, and outflow are sources of the high-energy excess of the pre-main sequence (PMS) sources (Montmerle et al., 1983; Preibisch, 2004). This excess could be associated with an enhancement of the magnetic activity caused by the deep convective layers of the TTS prior to them getting settled onto the main sequence (Giampapa et al., 1981; Calvet et al., 1985). On the other hand, the accretion mechanism itself could be the source of high energy where both UV and X-ray excesses are produced by accretion shocks, material free-falling along the stellar field lines onto a shock front at the stellar surface (e.g., Lamzin, 1998; Gomez de Castro & Lamzin, 1999; Gullbring et al., 2000; Guenther et al., 2007). The shock front temperature may reach a few $\times10^6$ K, resulting in the production of soft X-ray, which is generally absorbed by the shocked material and thermalized at 10^4 K (Calvet & Gullbring, 1998). This emits like blackbody that peaks in UV (see Calvet & Gullbring, 1998). While X-ray emission in CTTS is believed to be either due to magnetic star-disk interaction or in accretion shocks or in shocks at the base of outflows and jets (e.g., Lamzin, 1999; Montmerle et al., 2000; Güdel et al., 2005), in WTTS, the X-ray emission mechanism is believed to be similar to that seen in active main sequence stars (e.g., Preibisch et al., 2005).

The field containing HD 200775 was observed by the *XMM-Newton* telescope to investigate X-ray properties of early type stars (Nazé et al., 2014). We searched for additional X-ray sources in the region around HD 200775 in the XMM-SSC, 2018
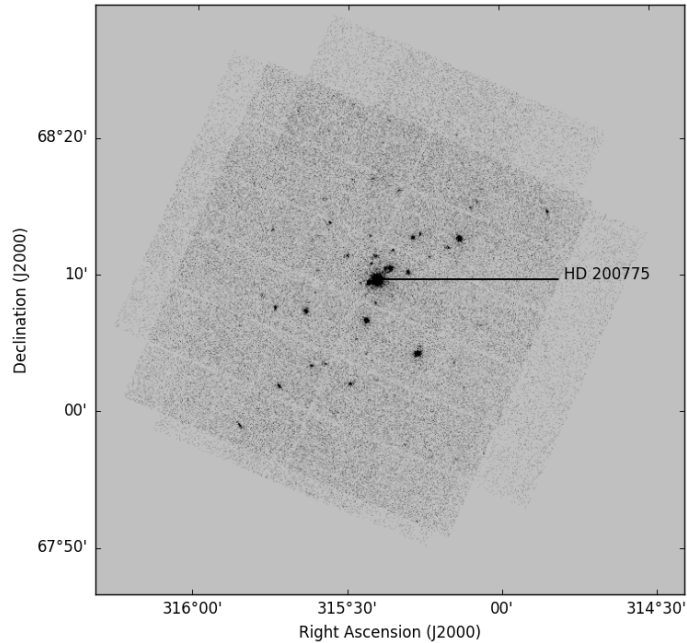
Figure 3.7: X-ray sources detected in the $XMM - Newton$ observations of HD 200775 (Nazé et al., 2014). The image is obtained from the $XMM - Newton$ Science Archive (XSA).

catalogue (Rosen et al., 2016). Within the FOV of the *XMM-Newton*, we found a total of 35 X-ray emitting sources. The maximum likelihood parameter is set at $\geqslant 15$ (which gives the maximum likelihood of the source detection, López-Santiago & Caballero, 2008), and the detection quality flag set at 0 or 1. The exposure time of the observations was 11.9 ks. Out of 35, 19 sources are found to have the ratio of the flux in 0.2-12 keV and the corresponding error $\geqslant 3$. Of these, 10 known YSO candidates (including HD 200775) and 4 newly identified comoving sources are found to spatially coincide within $5''$ from the positions of the X-ray detection. Based on the study conducted by Getman et al. (2011) on the Carina Nebula using the Chandra telescope and scaling for the survey coverage, approximately $\sim 10 - 20$ foreground and background and 30 extragalactic sources could be detected within the FOV of *XMM-Newton*. The foreground and background stars may have detection in *WISE*, but extragalactic sources may not have a *WISE* counterpart, because they are below its sensitivity limit. Out of 10 known YSO candidates, 8 of them have *WISE* counterparts. All the 4 newly identified comoving sources emitting in X-ray, have *WISE* counterparts.

The XMM-SSC catalogue provides hardness ratios, HR1 and HR2 also. These are X-ray colors defined as (H-S)/(H+S) where H and S for HR1 are flux values in the
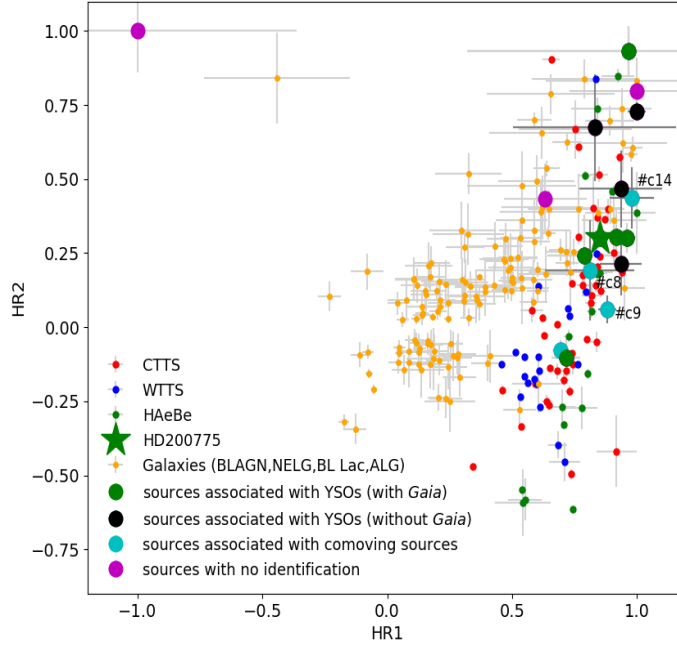
Figure 3.8: Hardness ratio plot for the X-ray sources detected by the *XMM-Newton* telescope in the vicinity of HD 200775. Known YSO candidates (with and without reliable *Gaia* data) and the newly identified comoving sources are identified. The comoving sources which are observed by us spectroscopically are marked. The hardness ratios of CTTS (red dots), WTTS (blue dots), HAeBe (green dots) and galaxies (orange dots) are also shown.

band 0.5-1.0 keV and 0.2-0.5 keV respectively. For HR2, the H and S are flux values in the bands 1.0-2.0 keV and 0.5-1.0 keV, respectively. Fig. 3.8 shows the HR2 vs HR1 plot for our YSO candidates (filled circles in green and black), 4 newly identified comoving sources (filled circles in cyan), and HD 200775 (star symbol in green). We obtained *XMM-Newton* data for the CTTS and WTTS, taken from Wahhaj et al. (2010), which are shown using red and blue filled dots respectively. Herbig AeBe (HAeBe) sources taken from The et al. (1994) catalogue are shown using dots in green. As mentioned already, some of the X-ray detection found in the vicinity of HD 200775 could be background galaxies. To differentiate the background galaxies from the PMS stars based on their hardness ratios, we obtained *XMM-Newton* data around a 5″ search radius of the galaxy samples of Barcons et al. (2007). This includes broad line active galactic nuclei, narrow emission line galaxies, absorption line galaxies, BL Lacertae. These sources are shown using orange dots in Fig. 3.8. The HAeBe, CTTS and WTTS (The et al., 1994; Wahhaj et al., 2010) are found to occupy a distinct region in Fig. 3.8. However, the distribution of the galaxy sample is noticeably different from that of the HAeBe, CTTS, and WTTS. The HR1 colors

of CTTS range between 0.5 - 1.0, while for WTTS, it is mostly close to ~ 0.6. The HR2 colors for CTTS show large range (0.5 to -0.5), while WTTS predominantly show HR2 $\lesssim 0.5$. The known YSO candidates and the comoving sources found associated with the X-ray detection are distributed in a similar manner as that of HAeBe, CTTS, and WTTS. Here our aim is not to characterize their X-ray properties but to show that X-ray sources found in the vicinity of HD 200775 show X-ray colors similar to those of CTTS and WTTS. Of the 5 X-ray detections that are not associated with any of the known YSO candidates or the comoving sources, 2 of them, namely, #x1 and #x5 (the identification numbers are as given in Table 3.7), do not have 2MASS, *Spitzer* and *WISE* counterparts within 5″ search radius. The location of #x1 at (-1.0, 1.0) is conspicuously different from the rest of the sources in Fig. 3.8 while the source #x5, located at (1.0, 0.8), could possibly be an extragalactic source due to the lack of *WISE* detection. Among the 3 sources with *WISE* counterparts, #x2 which is located at (0.63, 0.43) in Fig. 3.8 shows hardness ratios consistent with those of the extragalactic sources. The sources #x3 and #x4, based on the *Gaia* DR2 distances, are foreground sources and hence not shown in the figure. Two *Gaia* counterparts are found within our search radius of 5″ for #x3. The high proper motions ($\mu_{\alpha\star}$= -2.492 mas yr^{-1} and -4.615 mas yr^{-1} and μ_{δ}= -34.948 mas yr^{-1} and -34.931 mas yr^{-1}) confirm that they are foreground. #x4 with $\mu_{\alpha\star}$= 8.628 mas yr^{-1} and μ_{δ}= 5.798 mas yr^{-1}, confirms that this source is kinematically not associated with the region. Therefore we did not consider any of the X-ray sources other than those associated with the known YSO candidates and the comoving sources in further analysis.

3.8.1.2 Spectroscopy of four comoving sources

Of the 20 newly identified comoving sources, we obtained spectroscopic observations for four of them during our recent observing run. The objective was, as a first step, to look for emission lines in them. Spectral types of the four sources were determined by comparing the features in the spectrum of our sources with those in the templates of main sequence stars from the stellar library provided by Jacoby et al. (1984). Before performing the comparison, we normalized the spectra of our sources and took the templates to a common resolution. The uncertainty in our spectral classification is found to be of two spectral subclasses. The stars #c8 and #c18 (star identification numbers are as given in Table 3.6) are found to be of M1 spectral type while #c14 is found to be of M3 spectral type. The observed spectra of star #c8, #c14 and #c18 are shown in Fig. 3.9 (a). All the three are found to be X-ray emitters.
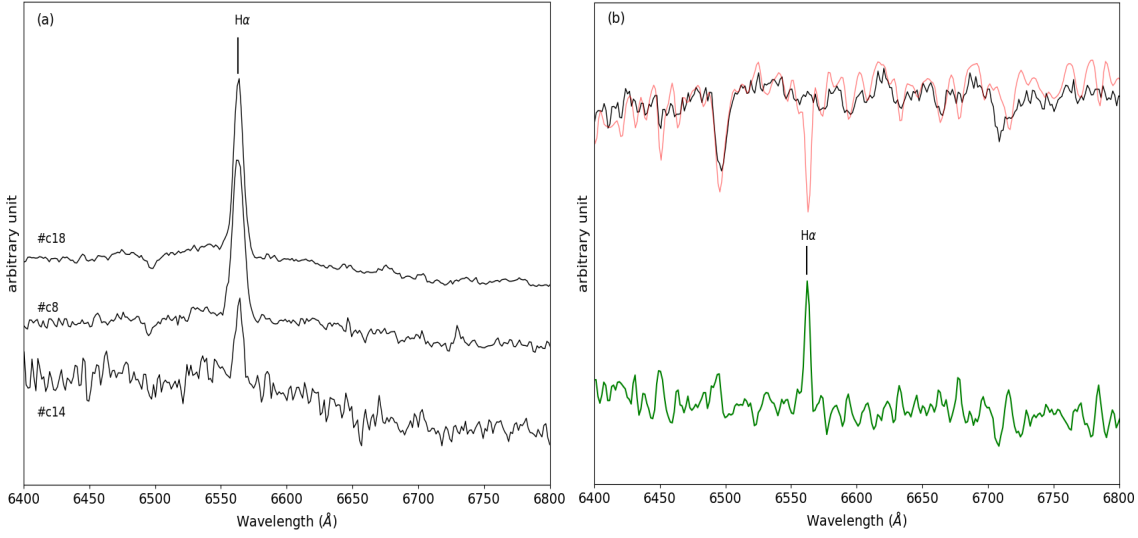
Figure 3.9: **(a)** Spectra of 3 of the 4 newly identified comoving sources found around HD 200775. The source identification numbers are also given. Wavelengths corresponding to Hα lines are marked with dashed vertical lines. **(b)** Spectrum of the comoving source #c9 (black) overplotted with a K2 spectral type spectrum (red) from Jacoby et al. (1984). The subtracted spectrum (#c9-K2) shown in green reveals the filled-in emission in the observed spectrum of #c9.

We detected Hα in emission in all three of them. We used the SPLOT task in the IRAF to obtain EW(Hα) of our observed sources. The EW(Hα) of #c8 and #c18 are found to be -15.03±1.52 Å and -13.01±1.30 Å, respectively. According to Barrado y Navascués & Martín (2003), these two sources can be classified as CTTS. However, it is surprising that these sources were not detected in any of the earlier surveys for Hα emission stars. Variability of Hα emission in #c8 and #c18 could be a plausible reason. The EW(Hα) of #c14 is found to be -4.06±0.41 Å which could possibly be a WTTS as mentioned in Barrado y Navascués & Martín (2003). The fourth star, #c9, is having Hα in filled-in emission. This star is found to be of a K2 spectral type. To reveal its Hα emission, we have subtracted the spectrum of a main sequence K2 spectrum (red) from that of the source #c9 (black) as shown in Fig. 3.9 (b). The resultant spectrum is shown in green. The EW(Hα) obtained from the resultant spectrum is found to be -0.69±0.08 Å.

3.8.1.3 Near-IR and Mid-IR properties

To understand the nature of the newly identified comoving sources based on their near- and mid-infrared colors, we obtained their 2MASS and *Spitzer* magnitudes. The 2MASS magnitudes are obtained from Cutri et al. (2003). Sources having pho-

tometric quality 'A' (SNR$\geqslant$10) in J, H and K_S are selected. Out of 20 comoving sources, we found a 2MASS counterpart for 19 of them. Of the 20 known YSO candidates having reliable *Gaia* DR2 data (Table 3.4), we found a 2MASS counterpart for 17 of them. We used a search radius of 1″ for getting the 2MASS counterparts. The comoving sources and the known YSO candidates are shown in the (J-H) vs. (H-K_S) color-color (CC) diagrams in Fig. 3.10 using filled circles in cyan and green, respectively and listed in Table 3.8. Also shown are the positions of Class I, II, and III (red, maroon, and blue dots, respectively) sources taken from Rebull et al. (2010) for comparison. The four sources for which we made optical spectroscopic observations (discussed in section 3.8.1.2), are identified and labeled. Of the remaining 38 known YSO candidates lacking reliable data or detection by the *Gaia*, we obtained the 2MASS magnitudes for 28 sources. The results are presented in Table 3.9 and shown in Fig. 3.10 using filled circles in black. The known YSO candidates and the newly identified comoving sources that are spatially associated with the X-ray detection made by the *XMM-Newton* satellite are identified using open square symbols in magenta.

The distribution of the known YSO candidates in the (J-H) vs. (H-K_S) CC diagram as shown in Fig. 3.10 is found to be similar to that of the Class I and Class II (red and maroon dots, respectively) sources taken from Rebull et al. (2010). A few of these known YSO candidates show relatively high amount of extinction. In contrast, the majority of the newly identified comoving sources are distributed to the left and lying below the known YSO candidates identified around HD 200775. This suggests that the comoving sources suffer relatively less extinction and exhibit a small amount of near-IR excess emission compared to the known YSO candidates. A notable number of them fall in a space between the region occupied by the Class II and Class III (maroon and blue dots, respectively) sources (Rebull et al., 2010) which indicates that a significant number of them may have some amount of circumstellar material. The *Spitzer* IRAC (3.6, 4.5, 5.8, and 8.0 μm) flux values given in Kirk et al. (2009) for the known YSO candidates are converted to their respective magnitudes and are shown in the [3.6]-[4.5] vs. [5.8]-[8.0] CC diagram in Fig. 3.11 using filled circles in green (with reliable *Gaia* DR2 data) and black (without reliable *Gaia* DR2 data). Of the 20 YSO candidates with reliable *Gaia* DR2 data, we obtained *Spitzer* IRAC magnitudes for 15 sources. Of the remaining 38 YSO candidates, 28 are associated with reliable *Spitzer* IRAC magnitudes. Since the IRAC magnitudes for the comoving sources are not available in the literature, we obtained their magnitudes by performing photometry using MOPEX. Nine comoving sources are found to lie outside the *Spitzer* FOV. Four comoving sources do
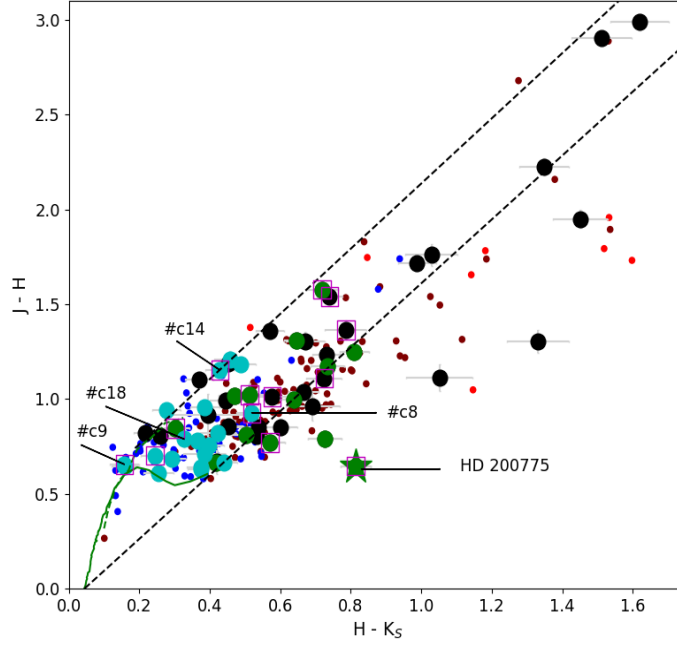
Figure 3.10: The (J-H) vs. (H-K_S) CC diagram for the newly identified comoving sources shown using filled cyan circles. The known YSO candidates having reliable *Gaia* data (green circle) and those without reliable *Gaia* data or no detection (black circle) are also shown. The solid and dashed curves in green represent the locii of the unreddened main sequence stars and the giants. The Class I, II, and III sources taken from Rebull et al. (2010) are shown in red, maroon, and blue dots, respectively. The known YSO candidates and the comoving sources spatially found to be associated with the *XMM-Newton* X-ray detection are identified using square boxes in magenta. The 4 sources observed by us spectroscopically are identified and marked.

not have reliable photometric flux in 8.0 μm band. None of the comoving sources show emission in MIPS 24 μm. Therefore we show only IRAC magnitudes in Table 3.8. The remaining seven sources for which we have reliable data are shown in Fig. 3.11 using filled circles in cyan. We show the boundaries of Class I, II, and III sources adopted from Fang et al. (2009) and Choudhury et al. (2010) in Fig. 3.11. The three new comoving sources are found to occupy the region generally occupied by the Class III sources.

The *WISE* magnitudes for the sources are also obtained from the Cutri & et al. (2014) catalogue by making a search around each of them with a search radius of 3″. The sources having photometric quality 'A' (SNR$\geqslant$10) in *W1*, *W2* and *W3* bands are selected as for a majority of the sources, the magnitudes given in the *W4* band are only upper limits. We confirmed the detection of the sources in each band by making a visual inspection of the *WISE* images in all the bands. We noticed that
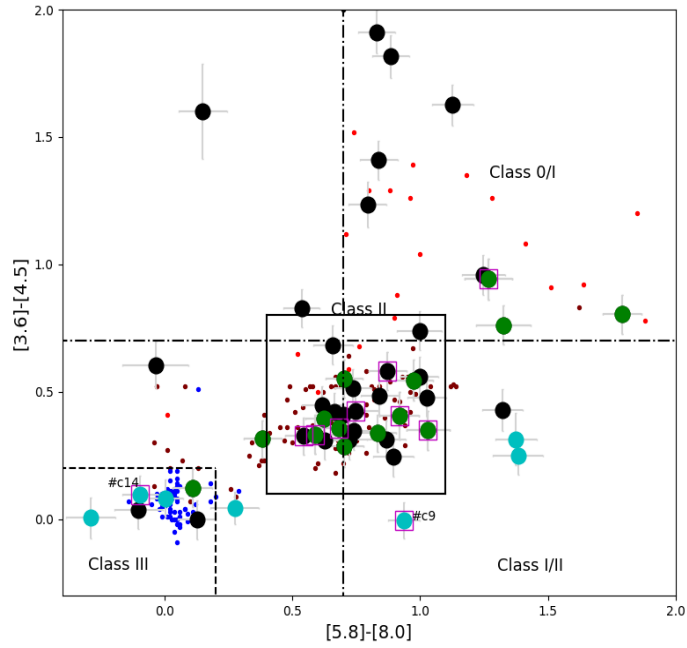
Figure 3.11: The *Spitzer* CC diagram for the newly identified comoving sources shown using filled cyan circles. The known YSO candidates having reliable *Gaia* data (green circle) and those without reliable *Gaia* data or no detection by the *Gaia* (black circle) are also shown. The Class I, II, and III sources taken from Rebull et al. (2010) are shown in red, maroon, and blue dots, respectively. The known YSO candidates and the comoving sources spatially found to be associated with the *XMM-Newton* X-ray detection are marked using square boxes in magenta. The 2 sources which are spectroscopically observed by us and have *Spitzer* colors are marked. The boundaries within which Class I, II and III sources generally occupy are also shown (Fang et al., 2009; Choudhury et al., 2010).

for a notable number of sources, though the catalogue provides magnitude values in 11.6 and 22.1 μm bands, on visual inspection, no detection was found on the images. The search results are shown in the $[3.4]-[4.6]$ vs. $[4.6]-[11.6]$ CC diagram (Fig. 3.12). The meanings of the symbols are the same as in Fig. 3.11. Of the 20 comoving sources, we found a counterpart for 7 in the *WISE* database. Among these, one source is common with those shown in Fig. 3.11. Six additional sources, including #c18, are found in the *WISE* database. Of 20 YSO candidates with reliable *Gaia* DR2 data, we obtained *WISE* magnitudes for 11 sources. Both, the known YSO candidates having reliable *Gaia* DR2 data and the comoving sources are presented in Table 3.8. Of the remaining known YSO candidates having no reliable data or the *Gaia* detection, we obtained *WISE* magnitudes for 10 sources, which are presented in Table 3.9. In both Fig. 3.11 and Fig. 3.12 we again show Class I, II, and III (red, maroon, and blue dots, respectively) sources, taken from
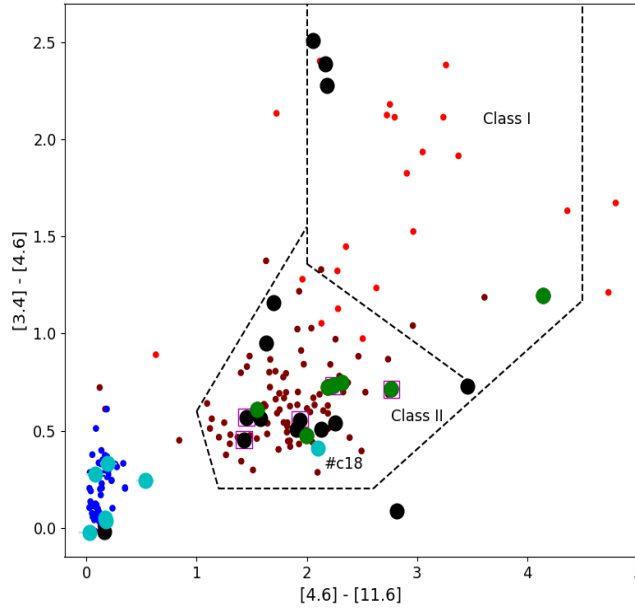
Figure 3.12: The *WISE* CC diagram for the newly identified comoving sources shown using filled cyan circles. The known YSO candidates detected (green circle) and not detected or without reliable detection (black circle) by the *Gaia* are also shown. The Class I, II, and III sources taken from Rebull et al. (2010) are shown in red, maroon, and blue dots, respectively. The known YSO candidates and the comoving sources spatially found to be associated with the *XMM-Newton* X-ray detection are marked using square boxes in magenta. The 4 sources observed by us spectroscopically are marked. The dashed lines are the criteria used by Koenig & Leisawitz (2014) to separate the regions occupied by the Class I and Class II sources.

Rebull et al. (2010) for comparison.

The difference in the distribution of the known YSO candidates and the comoving sources is more prominent in Fig. 3.11 and in Fig. 3.12. It is evident that the known YSO candidates fall in a region generally occupied by Class I and Class II objects. The sources showing spatial association with X-ray detection are marked with square boxes in magenta. A number of the newly identified comoving sources fall in a region populated by the Class III sources. The comoving source #c18 is located in a region occupied by the Class II sources in *WISE* CC diagram. This is the source which shows the second highest EW(Hα). The source #c9, which shows a filled-in emission in Hα, is located in the Class I/II region and the source #c14, which shows the smallest EW(Hα), occupies Class III region in *Spitzer* CC diagram. The source #c8, which shows highest EW(Hα), is not shown in both Fig. 3.11 and Fig. 3.12 because of its non-detection by the *Spitzer* IRAC and the *WISE*.

Owing to the lack of reliable photometry in all the bands, we were unable to classify a significant number of comoving sources into various classes based on the CC diagrams. Thus we made an attempt to classify them by calculating their spectral index values. The spectral index, α, is defined as, $\alpha = \frac{dlog(\lambda F_\lambda)}{dlog(\lambda)}$; where F_λ denotes the flux density at wavelength λ. We calculated the index by a least-squares fit to all the available data from 2MASS K_s (2.2 μm) to *WISE* 22 μm/MIPS 24 μm. Greene et al. (1994) proposed the following criteria to classify sources into different evolutionary classes: Class I: $\alpha \geq 0.3$, Flat Spectrum: $0.3 > \alpha \geq$ -0.3, Class II: $-0.3 > \alpha \geq$ -1.6, and Class III: $\alpha \leq$ -1.6. A decrease in the value of α implies that the amount of the circumstellar material around the sources decreases as they evolve. The SEDs and the spectral index values of the "flat" spectrum sources are intermediate between those of deeply embedded "Class I" and those of more evolved Class II YSOs. We obtained spectral index values of the known YSO candidates from Kirk et al. (2009) shown in Tables 3.8 and 3.9. For five YSO candidates that are not listed in the catalogue by Kirk et al. (2009), we calculated their α values from the available photometric data in various bands. Thus, based on the α values, of the 58 YSO candidates, 7 are classified as Class I, 4 as flat spectrum sources, 35 as Class II, and 6 as Class III sources. Of the 20 comoving sources, 4 are classified as Class II, and 12 as Class III sources. The remaining 6 YSO candidates and 4 comoving sources are unclassified due to the lack of reliable photometric data.

3.8.1.4 Optical and near-IR color-magnitude diagrams

Using G and $G_{\rm RP}$ magnitudes of 20 YSO candidates and 20 comoving sources from the *Gaia* DR2, we constructed M_G vs. (G-$G_{\rm RP}$) color-magnitude diagram (CMD). We converted the G magnitudes into absolute magnitudes using the expression M_G = G + 5 - 5 $\log(d)$, where d is the distance taken from Bailer-Jones et al. (2018). Out of 20 YSO candidates for which we have reliable distances from the *Gaia* DR2 (Table 3.4), extinction values for 11 sources are available in Kun et al. (2009). Based on our spectral type determination, only 4 of the 20 comoving sources have extinction values. As the individual extinction values for most of the sources are unknown, we constructed M_G vs. (G-$G_{\rm RP}$) CMD without correcting for the extinction. We did not use extinction values provided by the *Gaia* DR2 catalogue as these values are not accurate at the individual star level (Andrae et al., 2018). The effective temperatures and extinctions listed in *Gaia* DR2 are based on a naked stellar model where the contribution from the dust in the star forming region and/or the protoplanetary disk is ignored.

In Fig. 3.13 (a) we show the M_G vs. (G-G_{RP}) CMD for the known YSO candidates (filled circles in green) and the newly identified comoving sources (filled circles in cyan) found in the vicinity of HD 200775. The known YSO candidates and the comoving sources that are showing X-ray emission are also marked using magenta square boxes. Also shown are HAeBe (The et al., 1994), CTTS and WTTS (Wahhaj et al., 2010) using dots in green, red and blue, respectively. A reddening vector corresponding to a median extinction of 1.6 magnitude estimated by Kun et al. (2009) for NGC 7023 is shown in Fig. 3.13 (a) and (b). The reddening vector is computed based on Bossini et al. (2019). The PMS isochrones corresponding to 0.1 Myr, 0.5 Myr, 1 Myr, and 10 Myr are also shown. We used two grids of models, the CIFIST 2011_2015[1] models for low-mass stars (thick curves in black, Baraffe et al., 2015), and the PADOVA tracks Parsec 3.3[2] for the higher-mass stars (dashed curves in black, Marigo et al., 2017). Also shown are the positions of HAeBe, CTTS, and WTTS sources taken from The et al. (1994) and Wright et al. (2010). The four comoving sources for which we have carried out optical spectroscopy are identified and labeled.

In Fig. 3.13 (a), a number of known YSO candidates and comoving sources are lying on or above the 1 Myr isochrone. HD 200775 is found to be of $\sim$ 0.5 Myr old, which is consistent with the previous studies (Alecian et al., 2008; Arun et al., 2019; Vioque et al., 2018). In Fig. 3.13 (b) we show M_G vs. (G-G_{RP}) CMD of the sources that are classified as Class I, II, III and flat spectrum sources in red, orange, cyan, and blue filled circles, respectively. Also shown are the locations of Class I, II, III ,and the flat spectrum sources, taken from Rebull et al. (2010), using filled square boxes in red, orange, cyan, and blue colors, respectively. These are the identified members of the Taurus molecular cloud whose average age is estimated to be $\sim$ 1 Myr (Gomez et al., 1992). A total of 187 out of 257 sources have a *Gaia* DR2 counterpart found within a search radius of 3″. M_G values of these sources are corrected for their distances obtained from the *Gaia* DR2. All but two sources identified in the vicinity of HD 200775 show a well defined sequence roughly following the 1 Myr isochrone, which is consistent with the median age of the YSO candidates ($\sim$1.6 Myr) obtained by Kun et al. (2009). The distribution is found to be similar to the sources found in the Taurus molecular cloud. As the extinction vector is parallel to the isochrones for the sources having $M_G \lesssim 8$ magnitude, the extinction will not affect their distribution. However, for sources having $M_G \gtrsim 8$ magnitude, the effect of extinction can cause erroneous age estimates of the sources

---

[1] phoenix.ens-lyon.fr/Grids/BT-Settl/CIFIST2011_2015/ISOCHRONES/
[2] stev.oapd.inaf.it/cmd
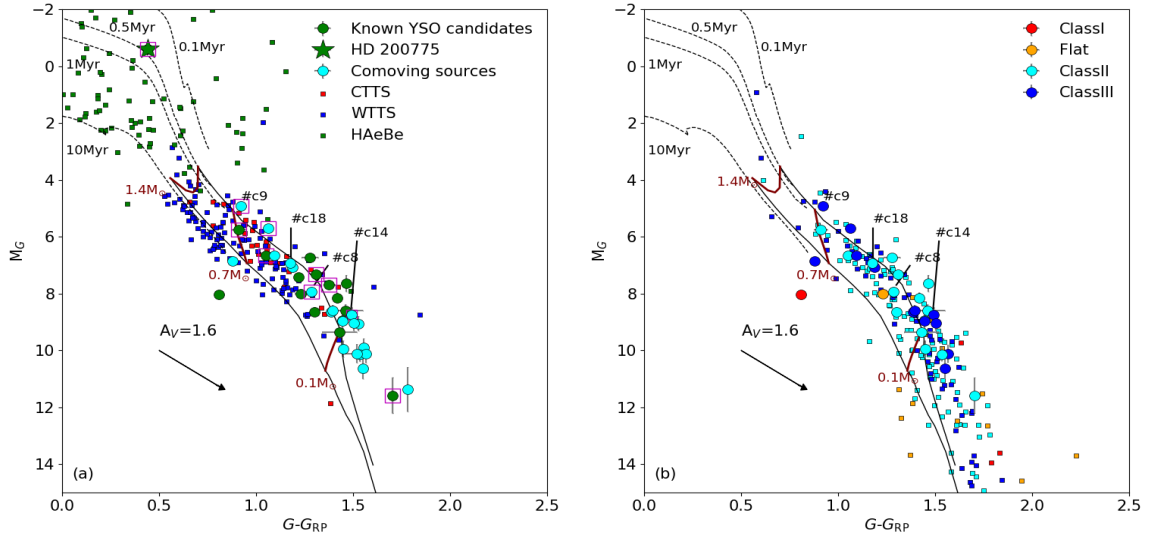
Figure 3.13: **(a)** The M$_G$ vs. (G-G_{RP}) color-magnitude plot of the YSO candidates and the comoving sources in the vicinity of HD 200775. The dashed lines indicate the isochrones from PARSEC models (Marigo et al., 2017) and solid curves represent the same from CIFIST models (Baraffe et al., 2015). Green circles: known YSO candidates, cyan circles: newly identified comoving sources, magenta square boxes: X-ray sources. The comoving sources observed spectroscopically are marked. The arrow represents extinction of 1.6 magnitude (the average extinction toward NGC 7023 estimated by Kun et al., 2009). **(b)** Same as above but the sources are shown according to their classifications. Red square boxes: Class I, orange square boxes: Flat spectrum, cyan square boxes: Class II and blue square boxes: Class III sources.

as can be noticed in Fig. 3.13 (b). The source falling below the 10 Myr isochrone is classified by us as a Class I source. This is the only Class I source that shows reliable data in *Gaia* DR2. This source, #15 (Table 3.4), is identified by Kun et al. (2009) as NGC 7023 RS 10 and they classified it as a variable source. They also found this source to be peculiar as it was showing an age older than 10^8 year. This source is at a distance of 323^{+4}_{-5} pc, and the proper motion values (7.174±0.079 mas yr^{-1} in RA and -1.738±0.075 mas yr^{-1} in Dec) are quite consistent with those of other known YSO candidates. As suggested by Kun et al. (2009), this source could be highly variable.

In Fig. 3.14 (a) and (b) we show M$_H$ vs. ($H - K_S$) CMD for the sources seen in the vicinity of HD 200775. Considering that a significant number of known YSO candidates and the comoving sources have 2MASS data, it is possible to compare the properties of the comoving and the known YSO candidates, including those having no reliable or no *Gaia* DR2 data. The symbols are identical as in Fig. 3.13 (a) and (b), respectively, except that the known YSO candidates without reliable or no *Gaia*
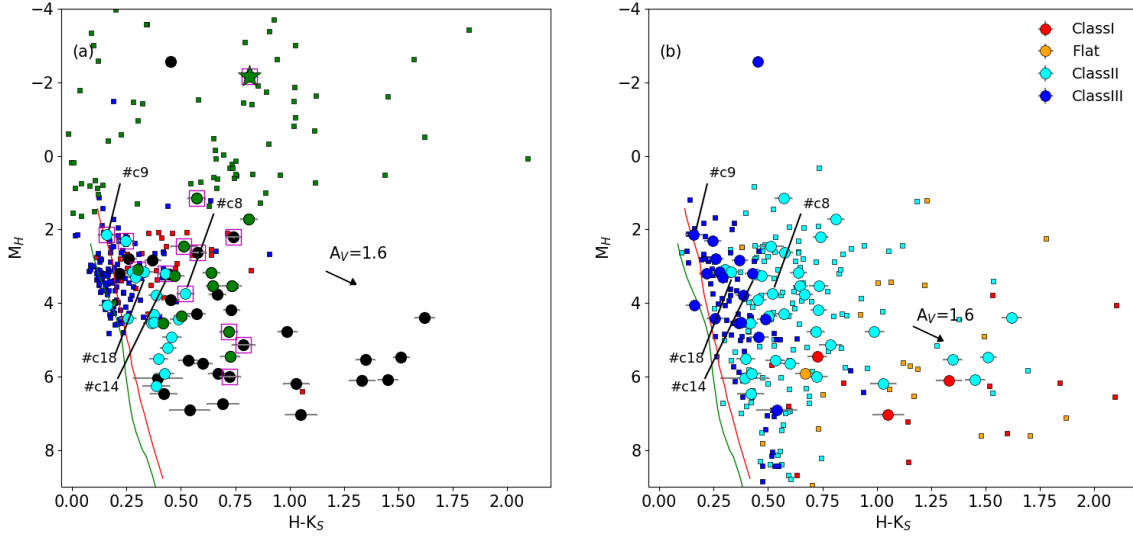
Figure 3.14: **(a)** M_H vs. $(H - K_S)$ color-magnitude plot for sources identified in the vicinity of HD 200775. The PMS isochrones corresponding to 1 Myr (red curve) and 10 Myr (green curve) taken from CIFIST models are drawn. Cyan filled circles: newly identified comoving sources, green filled circles: known YSO candidates having reliable *Gaia* DR2 detection, black filled circles: known YSO candidates without reliable or no *Gaia* DR2 detection, green dots: HAeBe, red dots: CTTS, blue dots: WTTS, green star: HD 200775, magenta square boxes: X-ray sources. The comoving sources observed spectroscopically are marked. **(b)** Same as above but sources are shown according to their classifications. Red square boxes: Class I, orange square boxes: Flat spectrum, cyan square boxes: Class II and blue square boxes: Class III sources.

DR2 data are shown using filled circles in black. The known YSO candidates and the comoving sources found associated with the X-ray sources are also marked using magenta square boxes. The PMS isochrones corresponding to 1 Myr and 10 Myr, taken from the CIFIST models are drawn as red and green curves, respectively. A reddening vector corresponding to A_V=1.6 magnitude is drawn. In Fig. 3.14 (a) we also show the HAeBe (The et al., 1994), CTTS, and WTTS (Wahhaj et al., 2010) using squares in green, red, and blue, respectively. Evidently, the known YSOs having no reliable or no *Gaia* DR2 data are relatively fainter and show higher values of $(H - K_S)$ colors. The faintness of these sources could be because of the extinction suffered by them due to the presence of both interstellar and circumstellar material along the line of sight.

In Fig. 3.14 (b) we show the sources classified based on their spectral index values. As in Fig. 3.13 (b), here also we show the Class I, II, III, and Flat spectrum sources obtained from Rebull et al. (2010). These sources, associated with the

Taurus molecular clouds, show a sequence with the Class I sources lying relatively far away from the 1 Myr isochrone and the Class III sources lying closer to it. The flat spectrum and the Class II sources are found to occupy a region between Class I and Class III sources. Except for the 4 sources that are classified as Class II but showing relatively large $(H - K_S)$ colors, other sources classified as Class I, II, III, and Flat spectrum sources in the vicinity of HD 200775 are also found to follow the sequence shown by the YSOs in the Taurus molecular cloud. Of the 55 sources for which we made the classification, we found 3 Class I (5%), 34 Class II (62%), 1 flat spectrum (2%), and 17 Class III (31%) sources towards HD 200775. Based on the classification made by Rebull et al. (2010) for the sources associated with the Taurus molecular cloud, there are 14 Class I (6%), 122 Class II (53%), 20 flat spectrum (8%), and 76 Class III (33%) sources. These are the 232 sources out of 257, for which we obtained 2MASS counterparts within 3" search radius (following the strategy used by Rebull et al. (2010) to get the 2MASS counterparts) and photometric quality of 'A' in all the bands. Based on the statistics of the sources found in different categories, it is apparent that the nature of the sources found in the vicinity of HD 200775 and those in the Taurus molecular cloud are very much similar.

3.8.1.5   Spatial distribution of the sources with respect to HD 200775

Now that the distances to a number of sources towards the direction of HD 200775 are known, we constructed a 3-D distribution of the known YSO candidates and the comoving sources in cartesian coordinate system as shown in Fig. 3.15. The known YSO candidates and the comoving sources are shown using filled circles in green and cyan, respectively. The projection of the distribution on the X-Y, Y-Z and X-Z planes are also shown (plus sign for the comoving and square boxes for the known YSO candidates). The X-, Y- and Z-positives are towards the Galactic center, the Galactic east, and the Galactic north, respectively. The location of HD 200775 is shown using a star symbol. We find a significant ($\sim 2\sigma$) shift in the distance of HD 200775 with respect to the distances of other known YSO candidates. Assuming a distance of 335 pc to all the sources (both with and without *Gaia* DR2 data) found in the vicinity of HD 200775, we calculated the projected separation (in parsec) of them with reference to the position of HD 200775. The 2D distribution of 58 sources (both known YSO candidates and comoving sources having good quality data from 2MASS) thus obtained is shown in Fig. 3.16. The distribution shows that the maximum projected extent of the sources on the sky plane is ~ 6 pc in diameter. If we assume a similar depth along the line of sight direction also, then
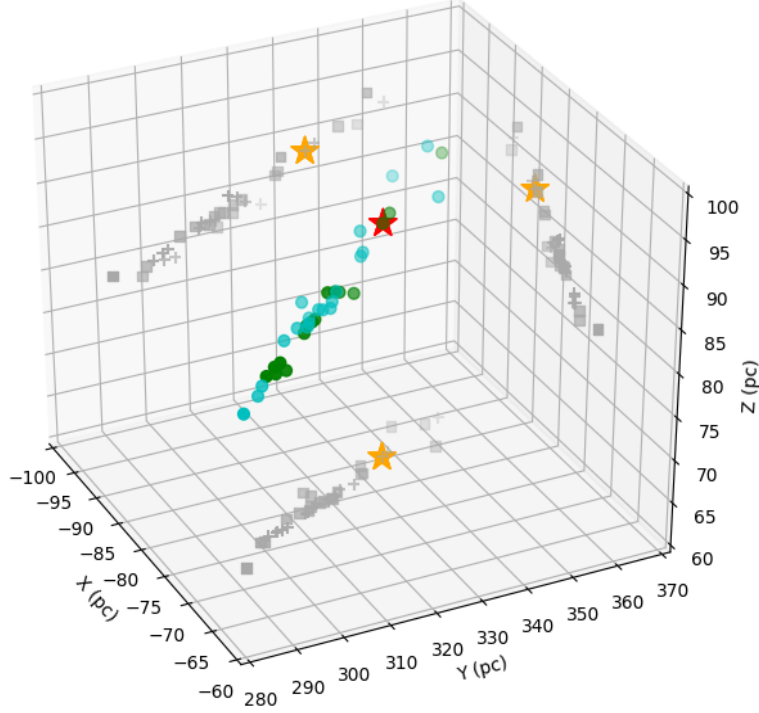
Figure 3.15: The 3D distribution of the known YSO candidates (filled circles in green) and the comoving (filled circles in cyan) sources having *Gaia* DR2 distances. Their respective projections on the X, Y and Z planes are shown using plus and square symbols in black (X positive towards the Galactic center, Y positive towards the Galactic east, and Z positive towards the Galactic north. HD 200775 is identified using a star symbol in red. Its projection in all the three planes is shown using a star in orange.

HD 200775 will lie outside the cloud. This is inconsistent with the fact that the nebulosity, NGC 7023, is illuminated by HD 200775.

The *Gaia* DR2 distance of 357^{+6}_{-7} pc to HD 200775, though is found to be consistent with the 430^{+160}_{-90} pc estimated using the *Hipparcos* parallax measurements (van den Ancker et al., 1998), the value is found to be significantly different from the recomputed distance of 520^{+180}_{-110} pc made by van Leeuwen (2007). HD 200775 is a triple system composed of a double-lined spectroscopic binary at ~ 18 mas separation (Millan-Gabet et al., 2001) and a third companion at $6''$ separation (Li et al., 1994). Based on the radial velocity measurements and the astrometric data, Benisty et al. (2013) estimated a dynamical distance of 320 ± 51 pc. We note that binarity was not worked into the astrometric solution for the *Gaia* DR2. The astrometric excess noise (ϵ_i; Lindegren et al., 2012) which measures the disagreement between the observations of a source and the best-fitting standard astrometric model is found to be 0.185 milli-arcsec for HD 200775. A positive value of ϵ_i signifies that the residuals
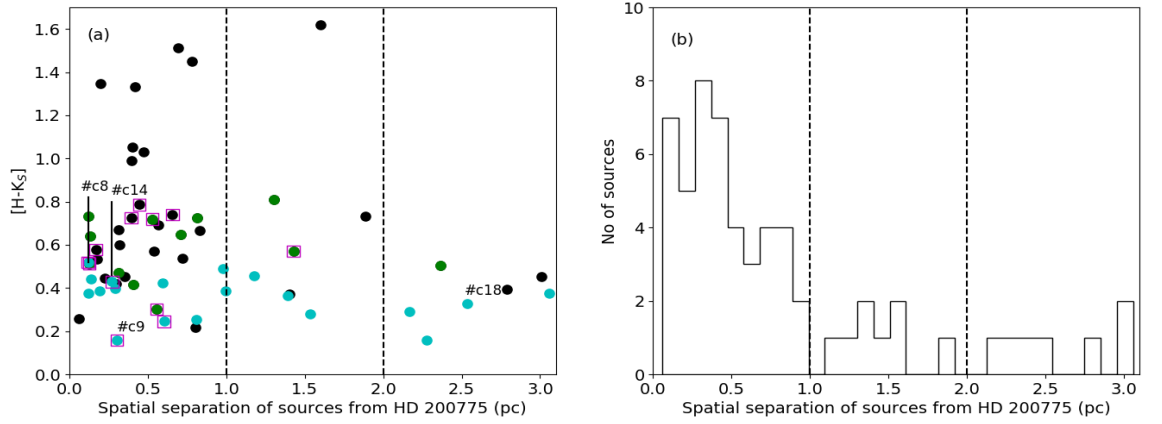
Figure 3.16: (**a**) The 2D spatial distribution of the known YSO candidates (filled circles in green: sources having reliable *Gaia* data, filled circles in black: sources without *Gaia* data) and the newly identified comoving sources (filled circles in cyan) with respect to the star HD 200775. Their $(H\text{-}K_S)$ values are shown in the vertical axis. Sources having X-ray emission are marked with magenta square boxes. The sources observed by us using HFOSC are also marked. (**b**) Histogram of the distribution of the known YSO candidates and the newly identified comoving sources with respect to the star HD 200775.

are statistically larger than expected. The significance of ϵ_i depends on the value of a dimensionless parameter, D ("astrometric_excess_noise_sig"; Lindegren et al., 2012)[1], which if is greater than 2, implies that ϵ_i is significant. The value of D for HD 200775 is 12.3, suggesting that there is a disagreement between the observations and the standard astrometric model. In addition, the RUWE value of HD 200775 is 1.6, indicating that the astrometric solution is not well-behaved. The presence of unresolved binaries is believed to be one of the reasons for such deviations (Gaia Collaboration et al., 2018). Therefore the present *Gaia* DR2 parallax measurement of HD 200775 is possibly inaccurate.

In Fig. 3.16 (a), along the vertical axis, we show the $(H\text{-}K_S)$ color of the sources considering it to be a proxy for the amount of circumstellar material present around each source. The objects identified as X-ray sources are marked with square boxes in magenta. Evidently, the comoving sources show the lowest of the $(H\text{-}K_S)$ color and are spatially well correlated with the known YSO candidates. A majority of the sources (44 or 75%) are distributed within ~ 1 pc distance from HD 200775, 8 ($\sim 13\%$) are distributed between 1 and 2 pc, and only 7 ($\sim 12\%$) are located beyond 2 pc. Both the known YSO candidates and the comoving sources are among the

---

[1]https://gea.esac.esa.int/archive/documentation/GDR2/Gaia_archive/chap_datamodel/

sources distributed within 1 pc from HD 200775. The distribution of the sources presented in Fig. 3.16 shows an enhancement in the vicinity of HD 200775 but, instead of a high density clustering, we detect a loose association. Dynamical dissipation was suggested as one of the possible reasons for the lack of clustering in HD 200775 (Fuente et al., 2001). The distribution of the proper motions of the young stars associated with a region can yield the velocity dispersion provided the distance is well known. Using the distance of 335 pc and the dispersion in the proper motion values in RA and Dec for the known YSO candidates and the comoving sources combined, we calculated a velocity dispersion of ~ 1 km s^{-1} for the sources found in the vicinity of HD 200775. Given the velocity dispersion and an age of ~ 1 Myr, the sources around HD 200775 could have moved by ~ 1 pc from where they were born. If we assume that they were all born very close to HD 200775, the distribution seen in Fig. 3.16 is quite consistent. But in such a case, we expect the distribution of the known YSO candidates and the comoving sources around HD 200775 to be symmetrical.

In Fig. 3.17 (a) we show the distribution of 59 sources (YSO candidates + comoving sources) that fall within the *Herschel* dust column density map. The known YSO candidates are identified using red square symbols. Of these, the sources having no reliable *Gaia* DR2 data are identified with red square + white dot. The comoving sources are shown using circles in yellow. Both the known YSO candidates and the comoving sources associated with X-ray detection are identified using cross symbols. The contours shown in thick lines represent the source distribution around HD 200775 (white star symbol). The distribution of the sources is not symmetrical with respect to HD 200775. At immediate surroundings of HD 200775, source distribution is concentrated more towards the north, and as we move further out, sources are sparsely distributed more in the east-west direction. Testi et al. (1999) found a correlation between the spectral type of HAeBe stars and the stellar density surrounding them. However, HD 200775 was shown as an exception due to the lack of clustering around it. Testi et al. (2001) discussed the results in connection with two competing models, namely, physical (Bonnell et al., 1998) and random sampling models (Elmegreen, 1999) which are advocated to explain the formation of high-mass stars. According to the physical models, the presence of clustering is a pre-requisite for the formation of massive stars, but on the other hand, they are unrelated according to the random models. In fact, the presence of a few of the massive stars (like HD 200775) not surrounded by an enhanced stellar density was shown as a support to the random models. Even with the identification of 20 additional comoving sources in the vicinity of HD 200775, because these sources
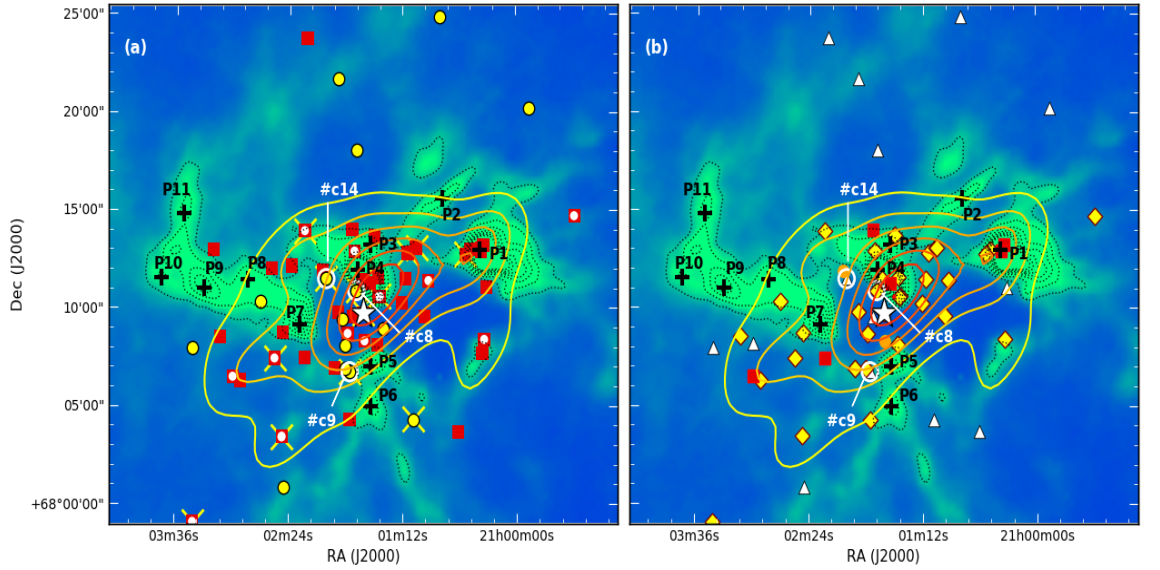
Figure 3.17: **(a)** The spatial distribution of the YSO candidates and the comoving sources overplotted on the *Herschel* column density map of the region surrounding HD 200775. The position of HD 200775 is identified using a white star symbol. Peak emission regions are shown in black '+' symbols. Red square: known YSO candidates; Red square + white dot: known YSO candidates with reliable *Gaia* DR2 data; Yellow filled circle: comoving sources identified in this work; Yellow filled circle + open circle in white: comoving sources observed by us spectroscopically; Yellow cross: X-ray detection by the *XMM-Newton* satellite. Black Plus: Column density peaks. The contours shown in thick lines represent the source distribution around HD 200775. **(b)** Represents the same as (a) but with the classifications of the sources. Red square box: Class I, Orange filled circle: Flat spectrum, Yellow diamond: Class II, White filled triangle: Class III sources.

are more sparsely distributed compared to the known YSO candidates, the stellar density around HD 200775 is still very low and hence favours the random sampling models.

HD 200775 is residing inside a biconical cavity, which is believed to have been carved out in an earlier evolutionary stage by a currently inactive bipolar outflow (Fuente et al., 1996). The outflow axis runs along the east-west direction. Fuente et al. (1998a), based on the morphology of the parent cloud, classified HAeBe stars into three groups. They classified HD 200775 as Type III, which implies that the source has completely dispersed the surrounding dense gas and is currently located inside a cavity of the molecular cloud. The expulsion of gas from the vicinity of OB stars could limit the amount of molecular material available for the formation of additional stars, which could be a possible reason for the lack of clustering around HD 200775. Using the CLUMPFIND (Williams et al., 1994) task on the dust column

density map made using the *Herschel* images, we found a total of 11 peak emission regions (P1 - P11), which are shown in Fig. 3.17. The contours are plotted from 3.2×10^{21} to 1.1×10^{22} cm^{-2} in steps of 1.3×10^{21} cm^{-2}. While two peak emission regions are located to the north and two to the south of HD 200775, the rest of the peaks are distributed mostly along the east-west direction. This roughly coincides with the orientation of the biconical cavity (Fuente et al., 1996). The velocity-intensity map of ^{13}CO J=2-1 gas emission (Yuan et al., 2013) and the dust emission (Fig. 3.17) surrounding HD 200775 show a large intensity gradient along the sides facing HD 200775. It is possible that the bipolar outflow and the stellar wind from HD 200775 might have been responsible for shaping the geometry of the material seen around it.

A significant number of the sources are found to be associated with the peaks towards P1, P3, and P4. Evidence of current star formation is seen towards P1 (e.g., Rector & Schweiker, 2013). Using ^{12}CO J=3$-$2 observations, Yuan et al. (2013) detected a non-Gaussian line profile with the peak skewed to the blue indicative of infall motions. The presence of infall motions suggests that star formation is still active. In Fig. 3.17 (b), we show the distribution of sources classified as Class I, II, III, and flat spectrum sources. Of the six sources classified as Class I, five (squares in red) are located within the mapped area. Among these, three sources are located towards P1 and P4. Possibly, star formation in L1172/1174 complex might have begun roughly ~ 1 Myr ago, but the very young sources, particularly those of Class I type, which are associated with the P1 and P4 peaks, might have been formed as a result of positive feedback from HD 200775. P1 is found to be associated with two Class I sources and a number of outflows (Kirk et al., 2009; Rector & Schweiker, 2013). A dynamical age of $\sim$7500 yr is estimated by Rector & Schweiker (2013). This suggests that some of these young sources might have been formed very recently. The presence of infall motions in Core 1 (P1 in Fig. 3.17) and intensity gradient to the south of Core 3 (P3 and P4 in Fig. 3.17) shown by Yuan et al. (2013) supports this argument. Based on this and the shock features observed at 4.5μm, they suggested that star formation around HD 200775 could have been possibly triggered due to HD 200775. Star formation scenario in the Cepheus region was presented by Kun et al. (2009). However, to understand the history of star formation, it is important to study the true nature of the rest of the comoving sources and study the dynamical state of the gas surrounding HD200775.

3.9 Summary and Conclusions

With the knowledge of distance and proper motion values of the YSO candidates associated with the cloud, we searched for additional comoving sources in the vicinity ($1° \times 1°$ area) of HD 200775. We found a total of 20 sources, which are comoving with the known YSO candidates. The main results from this study are summarized below:

- Based on the near-IR color-color diagrams, we found that the comoving sources are found to show less IR excess compared to the known YSO candidates. From their locations on the CMDs (optical and near-IR) and by comparison with the PMS isochrone models, they are found to be young (~ 1 Myr) sources.

- Based on the *XMM-Newton* data, we found 19 reliable X-ray detection around HD200775. Of these, 10 are found to be associated with the known YSO candidates and 4 with the newly identified comoving sources.

- We made spectroscopic observations of 4 of the 20 comoving sources of which three are X-ray sources. We found Hα in emission in 3 of the 4 sources.

- We classified the YSO candidates and the comoving sources based on their spectral index values as Class I, II, III, and flat spectrum sources. A majority of the comoving sources are classified as Class III. About 80% of the known YSO candidates and the comoving sources are found to be distributed within ~ 1 pc distance from HD 200775.

- Spatial correlation of a number of Class I sources with the density peaks of dust identified from the *Herschel* map suggests that star formation is currently active in the vicinity of HD 200775 and some of these young sources could have been formed as a result of positive feedback from it.

A detailed study of all the identified sources, especially, the 20 newly identified comoving sources, is required to estimate their spectral type, extinction, and luminosity, to confirm their true characteristics.

Table 3.6: Distance and proper motion values of the comoving sources from *Gaia* DR2.

#	RA(2015.5) (°)	Dec(2015.5) (°)	Source ID	Distance (pc)	$\mu_{\alpha\star}$ ($\Delta\mu_{\alpha\star}$) (mas/yr)	μ_δ ($\Delta\mu_\delta$) (mas/yr)	G (eG) (mag)	RUWE	Spectral Type	Hα EW (Å)	2MASS	*Spitzer*	*WISE*	X-ray	Spectral Index (α)
(1)	(2)	(3)	(4)	(5)	(6)	(7)	(8)	(9)	(10)	(11)	(12)	(13)	(14)	(15)	(16)
c1	314.358914	68.184721	2270164445306098560	311^{+3}_{-2}	6.372±0.066	-3.263±0.000	14.321±0.000	1.0	-	-	✓	-	✓	-	-2.78
c2	314.877400	67.678993	2269947738436093696	369^{+13}_{-13}	7.472±0.183	-3.129±0.216	16.881±0.002	1.0	-	-	✓	-	✓	-	-2.41
c3	314.963955	68.336928	2270263092114875520	373^{+13}_{-13}	7.315±0.177	-1.844±0.166	16.825±0.002	1.0	-	-	✓	-	✓	-	-2.56
c4	315.201051	68.415148	2270265016260228608	352^{+5}_{-5}	7.073±0.074	-0.752±0.079	14.800±0.001	1.1	-	-	✓	-	✓	-	-2.66
c5	315.271845	68.072754	2270238795483033728	340^{+3}_{-3}	7.294±0.048	-1.576±0.006	13.363±0.006	1.2	-	-	✓	-	✓	✓	-2.52
c6	315.350786	68.150243	2270245289474206848	351^{+17}_{-17}	8.195±0.233	-0.846±0.271	17.622±0.003	1.3	-	-	✓	-	-	-	-
c7	315.420625	68.301379	2270248798463735808	331^{+9}_{-8}	7.510±0.142	-1.452±0.001	16.243±0.001	1.2	-	-	✓	✓	✓	-	-2.32
c8	315.422157	68.182326	2270245465569124608	337^{+6}_{-6}	7.222±0.096	-1.154±0.105	15.564±0.002	1.3	M1	-15.03	✓	✓	✓	✓	-0.73
c9	315.439309	68.113265	2270057483439969408	342^{+2}_{-3}	7.595±0.242	-3.004±0.046	12.600±0.002	1.0	K2	-0.69	✓	✓	✓	✓	-2.45
c10	315.450292	68.115938	2270057517799708032	338^{+13}_{-13}	8.084±0.206	-1.537±0.280	17.776±0.002	1.0	-	-	✓	✓	✓	-	-0.61
c11	315.452017	68.135740	2270057685302330240	350^{+43}_{-34}	8.426±0.623	-2.081±0.684	19.088±0.004	1.3	-	-	✓	-	-	-	-
c12	315.458232	68.158415	2270057723958137600	333^{+13}_{-12}	8.312±0.202	-1.153±0.219	16.674±0.001	1.5	-	-	✓	-	-	-	-
c13	315.470563	68.362746	2270252367759936768	328^{+18}_{-17}	8.544±0.324	-1.593±0.369	18.204±0.002	1.1	-	-	✓	✓	✓	-	-2.30
c14	315.501565	68.192440	2270245809166510080	319^{+11}_{-10}	7.975±0.177	-1.400±0.193	16.260±0.001	1.3	M3	-4.06	✓	✓	✓	✓	-1.98
c15	315.612647	68.015216	2270053081097108480	339^{+17}_{-14}	7.643±0.282	-1.804±0.294	17.782±0.002	1.0	-	-	✓	-	✓	-	-2.21
c16	315.675742	68.172632	2270058651671079808	334^{+15}_{-13}	7.885±0.231	-1.042±0.250	17.566±0.005	1.3	-	-	✓	✓	✓	-	-1.45
c17	315.853497	68.132781	2270055421855682688	318^{+8}_{-8}	7.334±0.146	-1.539±0.137	16.103±0.002	1.2	-	-	✓	✓	✓	-	-2.39
c18	316.150453	68.498418	2270280409423293952	336^{+5}_{-5}	7.372±0.078	-1.308±0.068	14.571±0.004	1.4	M1	-13.01	✓	✓	✓	-	-0.80
c19	316.151474	68.496975	2270280405127009024	366^{+19}_{-17}	7.148±0.242	-1.375±0.237	17.925±0.017	1.0	-	-	✓	-	-	-	-
c20	316.394054	68.209051	2270068512916332672	336^{+3}_{-3}	8.417±0.054	-1.372±0.053	14.290±0.003	1.2	-	-	✓	-	✓	-	-2.67

Columns 2 & 3: 2015.5 epoch Right Ascension & Declination of sources given by *Gaia* DR2.
Column 4: Distance taken from the Bailer-Jones et al. (2018) catalogue.
Column 9: Renormalised Unit Weight Error (RUWE) of the comoving sources.
Column 15: X-ray detection by *XMM-Newton*.

Table 3.7: X-ray sources detected by *XMM-Newton* around HD 200775.

#	RA (2000) (°)	Dec (2000) (°)	r (″)	HR1	e_HR1	HR2	e_HR2	2MASS	*Spitzer*	*WISE*
			X-ray sources associated with the known YSO candidates							
4	315.360137	68.177384	0.346	0.96	0.04	0.30	0.05	✓	✓	✓
8	315.403845	68.163229	0.079	0.85	0.01	0.30	0.01	✓	-	-
11	315.558856	68.232957	0.973	0.97	0.65	0.93	0.09	✓	✓	✓
13†	315.617351	68.058043	0.723	0.79	0.15	0.24	0.14	-	✓	✓
14	315.637078	68.124783	0.561	0.72	0.06	-0.10	0.06	✓	✓	✓
17	315.849525	67.984878	2.996	0.92	0.08	0.31	0.10	✓	✓	✓
27	315.133771	68.213195	0.324	1.00	0.04	0.73	0.03	✓	✓	✓
30	315.261981	68.218805	0.728	0.94	0.17	0.47	0.13	✓	✓	-
32	315.286172	68.214544	0.234	0.83	0.33	0.67	0.18	✓	✓	✓
39	315.406921	68.191929	0.646	0.94	0.08	0.21	0.11	✓	-	✓
			X-ray sources associated with the newly identified comoving sources							
c5	315.271092	68.072880	0.858	0.69	0.03	-0.08	0.03	✓	-	✓
c8	315.421356	68.182647	1.375	0.81	0.18	0.19	0.17	✓	-	✓
c9	315.439065	68.113329	0.081	0.88	0.04	0.06	0.05	✓	✓	✓
c14	315.501365	68.192470	0.123	0.98	0.09	0.44	0.10	✓	✓	✓

r is the separation of the position of sources detected in *XMM-Newton* and 2MASS.
† Star #13 is a double star (the second component is identified as 13b, see Table 3.4) of $\sim 2''$ separation as resolved by the *Gaia* DR2. However, in both *Spitzer* & *WISE*, they are detected as a single source. The *Spitzer* and the *WISE* values are assigned to the brightest of them.
‡ There are two sources within a search radius of $5''$ from the X-ray detection.

Table 3.8: 2MASS, *Spitzer* and *WISE* magnitudes for the known YSO candidates and newly identified comoving sources with photometric quality 'A' in all bands.

#	RA	Dec	J±eJ	H±eH	K±eK	I1±eI1	I2±eI2	I3±eI3	I4±eI4	W1±eW1	W2±eW2	W3±eW3	Class
						Previously known YSO candidates							
1	314.845315	68.245467	10.588±0.026	9.342±0.032	8.532±0.021	7.267±0.056	6.722±0.056	6.246±0.054	5.270±0.052	7.601±0.031	6.877±0.020	4.690±0.014	II
2	315.084447	68.140772	12.472±0.024	11.165±0.027	10.518±0.021	9.579±0.053	9.028±0.052	8.538±0.052	7.835±0.051	9.886±0.023	9.137±0.020	6.819±0.020	II
3	315.231481	68.190885	12.831±0.024	12.166±0.029	11.749±0.020	11.243±0.052	10.906±0.052	10.544±0.053	9.711±0.052	11.418±0.023	10.879±0.021	-	II
4†	315.359984	68.177338	11.107±0.042	10.084±0.046	9.571±0.039	9.192±0.059	8.250±0.053	7.874±0.053	6.607±0.075	8.360±0.020	7.647±0.018	4.880±0.015	II
5†	315.362884	68.177214	12.323±0.031	11.150±0.036	10.417±0.025	-	-	-	-	-	-	-	II
6‡	315.399160	68.223752	12.471±0.029	11.033±0.038	10.257±0.023	9.139±0.054	8.579±0.056	8.536±0.052	7.538±0.053	9.355±0.023	8.649±0.020	-	II
7	315.400352	68.139576	-	-	-	10.166±0.054	9.404±0.053	8.988±0.060	7.663±0.087	9.844±0.023	9.114±0.020	-	Flat
8	315.403923	68.163263	6.111±0.030	5.465±0.031	4.651±0.017	-	-	-	-	-	-	-	-
9	315.427117	68.215960	11.911±0.031	10.892±0.033	10.421±0.023	9.752±0.056	9.466±0.059	9.090±0.053	8.388±0.054	9.905±0.023	9.400±0.020	-	II
10	315.444875	68.145894	11.792±0.024	10.798±0.033	10.159±0.022	9.561±0.052	9.246±0.051	9.144±0.052	8.760±0.054	-	-	-	II
11	315.558650	68.233141	13.982±0.032	12.405±0.033	11.686±0.024	10.870±0.052	10.513±0.058	10.179±0.055	9.496±0.053	11.065±0.023	10.513±0.020	-	II
12‡	315.584979	68.423341	11.513±0.027	10.529±0.033	9.880±0.024	-	-	-	-	9.346±0.023	8.765±0.020	6.386±0.014	II
13*	315.617758	68.058287	-	-	-	9.350±0.055	9.001±0.053	8.526±0.066	7.495±0.054	9.103±0.022	8.630±0.020	6.637±0.016	II
13b*	315.618244	68.057669	-	-	-	-	-	-	-	-	-	-	-
14	315.637634	68.124746	11.559±0.027	10.713±0.029	10.411±0.021	9.614±0.054	9.282±0.053	8.937±0.053	8.347±0.052	9.905±0.023	9.452±0.020	8.021±0.028	II
15	315.747855	68.108939	13.871±0.035	13.083±0.033	12.357±0.028	10.772±0.055	9.968±0.053	9.069±0.052	7.279±0.054	11.302±0.023	10.105±0.023	5.962±0.015	I
16‡	315.748555	68.136623	12.414±0.029	11.440±0.031	11.066±0.023	10.748±0.054	10.626±0.054	10.559±0.052	10.449±0.057	10.866±0.023	10.643±0.020	10.175±0.086	III
17	315.851719	67.985134	9.538±0.027	8.767±0.032	8.196±0.02	7.393±0.053	6.988±0.076	6.534±0.055	5.615±0.054	7.632±0.030	6.900±0.020	4.662±0.014	II
18‡	315.923249	68.396018	13.762±0.029	13.020±0.037	12.603±0.030	-	-	-	-	12.189±0.023	11.762±0.020	10.090±0.035	II
19	315.997585	67.824847	12.789±0.029	11.981±0.031	11.478±0.019	10.618±0.055	10.225±0.052	9.909±0.052	9.284±0.053	10.838±0.023	10.231±0.020	8.685±0.021	II
						Newly identified comoving sources							
c1	314.358914	68.184721	12.338±0.024	11.695±0.029	11.535±0.023	-	-	-	-	11.437±0.023	11.464±0.020	11.434±0.096	III
c2	314.877400	67.678993	12.772±0.025	12.145±0.026	11.769±0.026	-	-	-	-	11.531±0.020	11.201±0.020	11.006±0.069	III
c3	314.963955	68.336928	12.954±0.026	12.173±0.030	11.808±0.025	-	-	-	-	11.674±0.023	11.397±0.020	11.316±0.082	III
c4	315.201051	68.415148	11.715±0.026	10.773±0.030	10.495±0.019	-	-	-	-	10.386±0.023	10.349±0.020	10.172±0.041	III
c5	315.271845	68.072754	10.630±0.024	9.928±0.032	9.683±0.022	-	-	-	-	9.567±0.023	9.472±0.020	-	III
c6	315.350786	68.150243	13.516±0.024	12.851±0.029	12.411±0.022	-	-	-	-	-	-	-	-
c7	315.420625	68.301379	12.662±0.027	12.051±0.033	11.796±0.021	11.498±0.051	11.455±0.039	11.851±0.086	11.576±0.037	11.643±0.023	11.410±0.020	-	III
c8	315.422157	68.182326	12.300±0.029	11.373±0.033	10.854±0.022	-	-	-	-	9.575±0.020	9.220±0.019	-	II
c9	315.439309	68.113264	10.426±0.026	9.771±0.032	9.613±0.022	9.601±0.050	9.606±0.051	9.553±0.048	8.616±0.040	9.374±0.024	9.362±0.020	-	III
c10	315.450292	68.115938	13.893±0.027	13.136±0.033	12.739±0.025	12.217±0.094	11.903±0.042	10.789±0.064	9.414±0.050	11.447±0.025	11.002±0.022	-	II
c11	315.452017	68.135740	14.588±0.035	13.876±0.048	13.491±0.042	-	-	-	-	-	-	-	-
c12	315.458232	68.158415	12.589±0.024	11.948±0.032	11.573±0.023	-	-	-	-	-	-	-	III
c13	315.470563	68.362746	13.771±0.029	12.561±0.035	12.104±0.026	11.866±0.056	11.861±0.056	11.751±0.081	12.039±0.053	11.941±0.022	11.700±0.020	11.168±0.075	III
c14	315.501565	68.192440	11.968±0.027	10.816±0.032	10.387±0.019	10.257±0.056	10.161±0.050	10.123±0.053	10.217±0.045	9.939±0.022	9.748±0.020	-	III
c15	315.612647	68.015216	13.258±0.030	12.073±0.032	11.585±0.024	-	-	-	-	11.396±0.023	11.107±0.020	-	III
c16	315.675742	68.172632	14.368±0.035	13.549±0.037	13.125±0.024	12.465±0.052	12.217±0.052	12.004±0.084	10.621±0.050	12.366±0.023	12.051±0.023	-	III
c17	315.853497	68.132781	12.364±0.029	11.410±0.030	11.024±0.021	10.885±0.051	10.803±0.051	10.689±0.050	10.683±0.044	10.881±0.022	10.699±0.020	-	III
c18	316.150453	68.498418	11.570±0.030	10.782±0.037	10.454±0.023	-	-	-	-	9.746±0.023	9.338±0.020	7.241±0.016	II
c19	316.151474	68.496975	-	-	-	-	-	-	-	-	-	-	-
c20	316.394054	68.209051	11.600±0.027	10.918±0.031	10.626±0.021	-	-	-	-	10.559±0.022	10.511±0.020	10.342±0.042	III

† Stars #4 and #5 are resolved as two sources in 2MASS, *Spitzer* and *Gaia* DR2, but *WISE* detected them as a single source. We assigned the *WISE* to the brightest of them in K_s.

* Stars #13 & #13b appear as double sources of ∼ 2″ in *Gaia* DR2. 2MASS classified it as an extended source. Visual inspection also show them as two sources. But detected as single source by 2MASS and *WISE*.

‡ Stars 6, 12, 16 and 18 are identified as outliers based on our distance estimation.

106

Table 3.9: 2MASS, *Spitzer* and *WISE* magnitudes for the rest of known YSO candidates with photometric quality 'A' in all bands.

#	RA	Dec	J±eJ	H±eH	K±eK	I1±eI1	I2±eI2	I3±eI3	I4±eI4	W1±eW1	W2±eW2	W3±eW3	Class
20	314.137917	68.246667	14.583±0.077	13.669±0.087	13.275±0.072	-	-	-	-	12.204±0.023	12.118±0.021	9.304±0.026	II
21	315.078827	68.185074	15.386±0.058	14.533±0.065	13.994±0.066	-	-	-	-	13.749±0.026	13.681±0.029	-	III
22	315.086250	68.221111	-	-	-	12.255±0.059	10.343±0.058	9.331±0.051	8.501±0.051	12.086±0.023	9.698±0.020	7.528±0.018	I
23	315.089576	68.129234	-	-	-	-	-	-	-	-	-	-	-
24	315.092083	68.216111	-	-	-	11.207±0.063	9.391±0.055	8.462±0.051	7.576±0.051	11.595±0.027	9.086±0.021	7.028±0.017	I
25	315.093333	68.217778	-	-	-	12.755±0.069	11.520±0.059	10.883±0.053	10.089±0.053	-	-	-	Flat
26	315.120417	68.217222	15.998±0.080	13.096±0.030	11.584±0.023	10.270±0.055	9.756±0.053	9.321±0.051	8.585±0.051	10.587±0.023	9.638±0.020	8.006±0.022	II
27	315.133750	68.213056	11.377±0.024	9.836±0.028	9.096±0.021	8.379±0.052	8.053±0.050	7.688±0.052	7.143±0.053	8.712±0.022	8.143±0.020	6.690±0.016	II
28	315.152500	68.062222	11.646±0.022	10.826±0.027	10.608±0.023	10.391±0.056	10.394±0.052	10.318±0.052	10.191±0.051	10.458±0.023	10.377±0.020	-	III
29	315.242083	68.160556	12.389±0.026	11.535±0.031	11.081±0.020	10.539±0.051	10.225±0.052	9.802±0.055	8.935±0.051	10.623±0.023	10.116±0.021	-	II
30	315.262500	68.218611	14.118±0.040	12.755±0.043	11.969±0.029	11.028±0.050	10.448±0.055	10.165±0.052	9.293±0.053	-	-	-	II
31	315.265417	68.219167	14.736±0.034	13.627±0.037	12.902±0.032	10.171±0.054	9.761±0.054	11.317±0.054	10.568±0.069	9.877±0.023	9.305±0.020	-	II
32	315.286250	68.214444	14.764±0.036	14.097±0.041	13.677±0.047	12.189±0.052	11.764±0.052	12.384±0.060	11.660±0.071	12.385±0.024	11.675±0.022	-	II
33	315.292500	68.192500	11.829±0.027	10.836±0.035	10.391±0.022	13.091±0.053	12.779±0.055	-	-	9.839±0.022	9.386±0.020	-	II
34	315.302083	68.171944	15.378±0.059	13.15±0.037	11.806±0.025	9.786±0.054	9.542±0.056	9.098±0.054	8.202±0.058	10.728±0.023	9.842±0.020	-	II
35	315.363750	68.193889	13.999±0.024	13.195±0.031	12.663±0.026	10.578±0.053	10.093±0.053	9.508±0.054	8.667±0.050	11.455±0.036	10.664±0.029	-	II
36	315.365622	68.136520	14.116±0.039	12.398±0.038	11.410±0.022	-	-	-	-	-	-	-	II
37	315.373750	68.229444	11.271±0.024	10.260±0.031	9.683±0.022	10.442±0.052	10.023±0.056	9.520±0.049	8.856±0.053	10.852±0.023	10.086±0.021	-	II
38	315.386667	68.188889	-	-	-	12.404±0.057	10.778±0.057	9.726±0.052	8.599±0.061	11.507±0.022	9.835±0.019	-	I
39	315.406537	68.191931	11.218±0.024	10.415±0.030	10.156±0.020	-	-	-	-	-	-	-	II
40	315.431667	68.160000	13.056±0.027	11.82±0.031	11.090±0.022	9.988±0.054	9.951±0.052	9.859±0.058	9.961±0.075	8.935±0.022	8.474±0.020	8.335±0.021	III
41	315.432083	67.840556	15.036±0.071	13.734±0.052	12.402±0.032	10.300±0.051	9.992±0.054	9.756±0.053	9.129±0.053	10.478±0.023	9.915±0.020	-	II
42	315.432917	68.234167	13.281±0.026	11.923±0.031	11.352±0.025	9.872±0.052	9.045±0.055	8.376±0.051	7.840±0.051	10.040±0.023	8.894±0.018	-	I
43	315.439167	68.072500	14.116±0.032	13.264±0.035	12.664±0.023	10.796±0.057	10.368±0.060	10.209±0.056	8.886±0.055	11.002±0.023	10.515±0.020	-	II
44	315.469583	68.164167	14.854±0.043	13.549±0.036	12.878±0.030	11.058±0.051	10.319±0.057	9.741±0.060	8.744±0.064	-	-	-	II
45	315.478158	68.116402	11.573±0.024	10.469±0.032	10.099±0.021	-	-	-	-	11.534±0.025	11.490±0.021	-	Flat
46	315.510417	68.199444	15.768±0.075	14.656±0.056	13.604±0.044	-	-	-	-	12.319±0.024	11.796±0.023	9.791±0.034	III
47	315.553036	68.397097	15.574±0.059	13.815±0.046	12.786±0.036	11.397±0.056	10.438±0.054	9.683±0.057	8.435±0.064	9.937±0.023	9.956±0.020	-	I
48	315.558750	68.125000	-	-	-	-	-	-	-	11.263±0.024	10.167±0.021	-	-
49	315.588333	67.905556	-	-	-	10.772±0.055	9.363±0.054	8.566±0.053	7.728±0.052	11.389±0.022	9.111±0.020	6.931±0.016	-
50	315.592848	68.203369	-	-	-	-	-	-	-	-	-	-	-
51	315.613750	67.905000	-	-	-	13.589±0.063	12.985±0.066	13.105±0.081	13.139±0.101	-	-	-	Flat
52	315.616667	68.146389	15.022±0.074	12.035±0.038	10.415±0.024	11.894±0.053	11.418±0.054	10.940±0.054	9.914±0.052	9.131±0.023	7.971±0.020	6.271±0.015	II
53	315.624583	67.902222	15.337±0.051	14.377±0.056	13.685±0.050	8.621±0.054	7.938±0.055	7.392±0.051	6.733±0.059	-	-	-	II
54	315.645524	68.200684	15.661±0.067	13.712±0.041	12.261±0.023	-	-	-	-	-	-	-	-
55	315.728750	68.105833	15.661±0.067	13.712±0.041	12.261±0.023	10.688±0.051	10.240±0.053	9.945±0.054	9.329±0.055	10.809±0.023	10.033±0.020	-	II
56	315.781667	68.142778	12.435±0.029	11.398±0.032	10.732±0.021	10.035±0.052	9.690±0.050	9.372±0.053	8.632±0.053	10.134±0.023	9.627±0.020	7.494±0.026	II
57	315.800417	68.216944	-	-	-	-	-	-	-	-	-	-	-
58	316.065000	67.712778	6.256±0.019	5.068±0.018	4.616±0.017	6.100±0.178	4.499±0.060	4.042±0.071	3.892±0.061	-	-	-	III

The classifications of the YSO candidates were taken from Kirk et al. (2009).

α for #21, #36, #39, #45 and #47 were calculated by us.

Part III

Spectroscopic studies of the YSOs towards LDN 1174

3.10   Introduction

A significant fraction of the mass of YSOs is accumulated during their early stages of evolution through accretion in which the material continues to get transported from the inner disk onto the central star channeled through the magnetic field lines. Mass accretion rate is an essential parameter to estimate as it enables us to understand the history of how the stars have built up their mass as a function of time. The processes involved in the accumulation of matter have serious implications not only on the evolution of the central source but also on the formation of planets in the disk. near-IR spectroscopy can reveal important new details as it is sensitive to the light from the protostellar photosphere, emission from the warm inner disk, and high excitation atomic and molecular transitions.

Located in L1174, the well known reflection nebula NGC 7023 is illuminated by the Herbig Be (B3) star HD 200775 (Kun et al., 2009) in the Cepheus constellation. Based on different identification methods in literature (Kirk et al., 2009; Kun et al., 2009; Yuan et al., 2013), we listed ~ 58 YSO candidates towards NGC 7023 which are mostly distributed around HD 200775 (see part I). The bulk motion of gas was detected in a large area around L1174 in ^{13}CO observations (Yuan et al., 2013) which suggests that strong winds from HD 200775 are blowing away ambient material causing further compression of the matter around it, especially to the north where most of the YSOs are found to be distributed. They also found a systematic decrease in the age of YSOs as a function of distance from the HD 200775, implying that at least some of them are possibly formed as a result of the feedback from HD 200775. In our polarization measurements of the stars projected around HD 200775 (described in detail in part IV), we found that the dispersion of polarization position angles is more towards the south-west of HD 200775, suggesting that magnetic fields are also affected by its presence. Thus HD 200775 has a profound effect on the environment around it.

Based on the infrared spectral index and bolometric temperature derived from the spectral energy distribution (SED), Kirk et al. (2009) classified YSOs identified towards NGC 7023 into Class I, flat, Class II disk, and Class III sources. The majority of the YSOs are of Class II type. Also, from the ratio $\frac{L_{disk}}{L_{star}}$ star which is used to characterize a disk as either accretion, passive reprocessing or debris-like, Kirk et al. (2009) suggested that majority of the disks around YSOs in NGC 7023 are of accreting type. However, to determine the degree of circumstellar material from SEDs, Kirk et al. (2009) assumed a K7 spectral type for all the YSOs to remove the stellar contribution. Though the results from such an approach are

Table 3.10: Log of spectroscopic observations.

Year	Month (Date)
2018	September (10, 11)

suited for statistical studies, a significant scatter is expected for individual sources due to possible spectral type mismatch. Therefore it is important to determine the spectral type of the sources from the spectral features using spectroscopy. But we don't have information of spectral types of a large fraction of these YSOs which are relatively fainter in optical. Kun et al. (2009) made spectroscopic studies of the sources relatively brighter in optical and obtained their spectral types and found that these sources are mainly low-mass of late K to M types. We carried out near-IR spectroscopic observations of 10 YSO candidates having K magnitude <12 using SpeX. The main aim of this work is to determine the spectral types of the sources using near-IR spectroscopy that are fainter in optical to ascertain their properties and evolutionary stages. We present the sources observed in our study in section 3.11 and discuss our findings in section 3.12. Finally we conclude our results in section 3.13.

3.11   Observation and Data Reduction

Spectroscopic observations of 10 YSO candidates were carried out using Spex attached with 4-m IRTF. The log of the spectroscopic observations is given in Table 3.10. Table 3.11 lists the observed sources. We additionally observed standard star 55 Dra for the removal of telluric lines. Details of the reduction of Spex data are discussed in Chapter 2. We acquired spectra of 10 sources using IRTF at spectroscopic resolution of ~1200. In the SXD mode, Spex covers the wavelength range from 0.7 to 2.56 μm. SNR of the sources observed using IRTF ~150. We show the spatial distribution of these sources as yellow filled circles in Fig. 3.18 (LHS). The central source HD 200775 is marked as red star symbol in this figure.

3.12   Results and Discussions

Fig. 3.18 (RHS) presents 41 sources (out of total 58 YSO candidates towards HD 200775) which are detected well within 1″ search radius about each source position and having photometric quality 'A' (SNR≥10) in J, H, and K_s bands. In Fig. 3.18 (RHS) we present the sources we observed using Spex (filled red circles) along with

Table 3.11: List of Sources observed in spectroscopic mode.

#	Name	RA(°) (2000)	Dec(°) (2000)	K (mag)	d (pc)	Sp. Type*	Age* (yr)
1	2MASS J21002024+6808268	315.084583	68.140833	10.52	341	-	-
2	FW Cep	315.637500	68.124722	10.41	336	K5	8.5
3	FU Cep	315.444583	68.145833	10.16	335	M1	1.6
4	NGC 7023 RS 5	315.427083	68.215833	10.42	323	M2	1.3
5	NGC 7023 RS 2 B	315.362917	68.177222	10.42	360	M0	2.0
6	HZ Cep	315.360000	68.177222	10.16	325	M0	1.5
7	2MASS J21030756+6808339	315.781667	68.142778	10.73	-	-	-
8	2MASS J21003662+6803445	315.152500	68.062222	10.61	342	-	-
9	2MASS J21005808+6809382	315.242083	68.160556	11.08	-	-	-
10	2MASS J21005550+6811273	315.231250	68.190833	11.75	333	-	-

* Spectral types are taken from Kun et al. (2009).
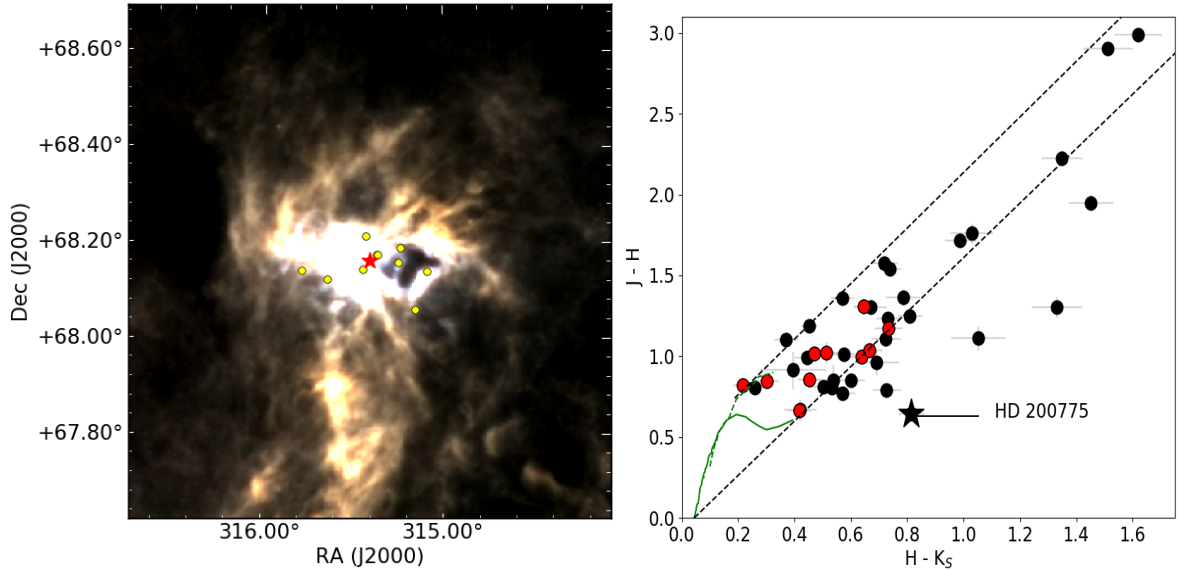
Figure 3.18: **(LHS)** Spatial distribution of the observed sources are shown using yellow filled circles overplotted on the *Herschel* colour-composite image with 250, 350 and 500 μm images. HD20775 is identified using red star symbol. **(RHS)** The (J-H) vs. (H-K_S) CC diagram for the known YSO candidates towards L1172/1174 is shown. The red filled circles are the sources observed by us while the black filled circles are the remaining sources from literature. The solid and dashed curves in green represent the locii of the unreddened main sequence stars and the giants.

other YSO candidates (filled black circles) located towards NGC 7023. From this figure, it is clear that our samples are of lower extinction and lower near-IR excess, compared to the other sources not observed by us. Five of our observed sources were studied by Kun et al. (2009) in optical, we made near-IR observations to find their Br-γ counterparts. The majority of our observed sources do not show Br-γ

emission, rather, we obtained filled-in emission. We found Br-γ emission in three of our samples, FU Cep, NGC 7023 RS 5, and 2MASS J21030756+6808339. The near-IR spectra of the 10 observed sources are shown in Fig. 3.19.

We estimated the effective temperatures (T_{eff}) of the observed sources using the 2.21 μm and the 2.26 μm features. Because of the low excitation energy, these lines appear as strong absorption features in M-type stars. For late-type objects, the 2.21 μm feature is mainly comprised of Na, Si, Sc, and V absorption lines and the 2.26 μm feature mainly consists of Ca, Ti and Si lines (Ramirez et al., 1997). Itoh et al. (2002) provided the EWs of the 2.21 μm and the 2.26 μm features as functions of T_{eff}, respectively. They also came up with the ratio of 2.26 μm/2.21 μm as a function of T_{eff}. Based on the EWs of 2.21 μm, 2.26 μm absorption features and the ratio of 2.26 μm/2.21 μm, we obtained three T_{eff} for each source. The final T_{eff} for each source is the mean of these three T_{eff}. The EWs of these lines are shown in columns 4 and 5 of Table 3.12. The extinction of each target was computed based on the difference between the observed color of the source and the intrinsic color of CTTSs, provided by Meyer et al. (1997), in the 2MASS color-color diagram (Fig. 3.18 (RHS)). Bolometric luminosity of the observed sources were estimated from the luminosity in J band. We applied the bolometric correction in J band from Pecaut & Mamajek (2013).

We constructed the Hertzsprung-Russell (HR) diagram for the observed sources as shown in Fig. 3.20. The Pisa pre-main sequence tracks and isochrones (Tognelli et al., 2011) were used in our analysis. Solar scaled models were obtained with Y = 0.2533, Z = 0.01377, mixing length parameter (α)= 1.68, initial deuterium abundance $X_D = 2.0 \times 10^{-5}$. The 10 YSO candidates are shown using black filled circles, respectively. We estimated the ages and the masses of the sources based on their positions with respect to the isochrones and tracks in the HR diagram. Typical errors in age and mass are $\sim$1 Myr and 0.05 $M_\odot$. Table 3.12 lists the estimated physical parameters of the 10 sources.

Brief description on individual observed sources are provided below:

- **2MASS J21002024+6808268:** This source is located at a distance 341^{+10}_{-10} pc (Bailer-Jones et al., 2018). It does not show emission in hydrogen lines. Strong absorption in CO band heads can be noted in the observed spectrum (see Fig. 3.19) Based on its location in the HR diagram (Fig. 3.20), this source is of age 1−2 Myr and its mass is 0.7 $M_\odot$. The T_{eff} of this target is estimated 4100 K.

- **FW Cep:** Kun et al. (2009) estimated A_V towards FW Cep as 1.52, T_{eff}
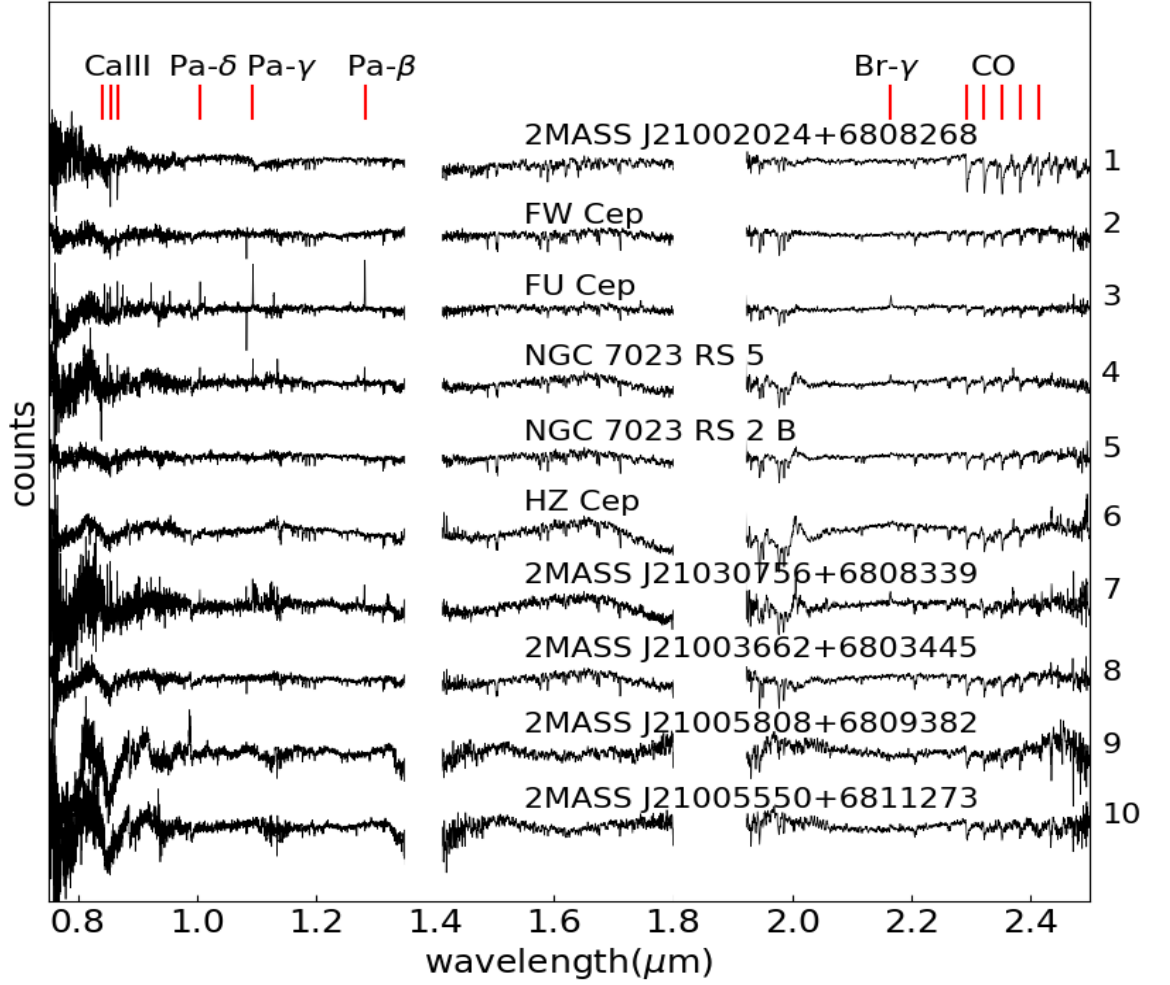
Figure 3.19: Near-infrared spectra of the observed targets using Spex.

as 4350 K, spectral type as K5, mass as 1 $M_\odot$, age as 8.5 Myr. Rosino & Romano (1962) identified it as a variable source. Distance to this source is 336^{+3}_{-2} pc (Bailer-Jones et al., 2018). It does not show any signature of emission in hydrogen lines. It is classified as a CTTS with EW of Hα as -4.0Å (Kun et al., 2009). Based on our analysis, we estimated the age of this source as 2 Myr and mass as 0.6 $M_\odot$.

- **FU Cep:** Kun et al. (2009) identified it as a variable source. They computed A_V towards FU Cep as 1.82, spectral type as M1, T_{eff} as 3720 K. The estimated mass and age of this source is 0.48 $M_\odot$ and 1.6 Myr (Kun et al., 2009), respectively. We can notice emission in Br-γ in the observed spectrum of this source. Emission in Br-γ, Pa-β, Pa-γ and Pa-δ and CaII triplet lines are clearly visible in the observed spectrum. EW of Br-γ line is -3.0±0.4 Å,
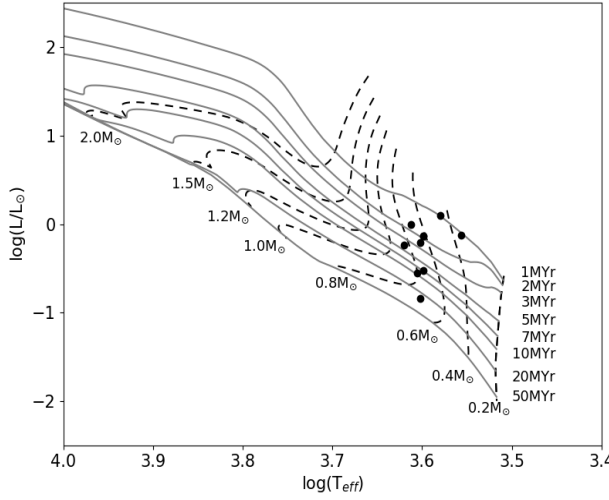
Figure 3.20: HR diagram of the YSO candidates (black filled circles) observed by us. Thin solid lines indicate the isochrones as labeled, and dashed lines show the evolutionary tracks for the masses indicated at the lower end of the tracks from the Pisa pre-main sequence tracks and isochrones (Tognelli et al., 2011).

EW of Pa-β line is -4.73±0.2 Å, EW of Pa-γ line is -3.2±0.2 Å, EW of Pa-δ line is -3.2±0.2 Å. The EWs of CaII triplet lines are also obtained. EW of CaII (8662Å) is -2.3±0.2 Å, CaII (8542Å) is -2.8±0.3 Å, CaII (8498Å) is -2.8±0.2 Å. EW of He absorption line is 4.7±0.3 Å. Kun et al. (2009) classified it as a CTTS with EW of Hα as -64.5Å. They also found emission in CaII triplet in their observations. Based on our observations, we estimated the T$_{eff}$ of this source as 4170 K. We estimated the age and mass of this source as 4 Myr and 0.85 M$_\odot$, respectively.

- **NGC 7023 RS 5:** Based on the analysis by Kun et al. (2009), A$_V$ towards FW Cep is 2.83, T$_{eff}$ is 3580 K. It is of spectral type M2, mass 0.38 M$_\odot$ and age of 1.3 Myr (Kun et al., 2009). This source is also classified as a variable source (Rosino & Romano, 1962; Sellgren, 1983). We can notice a weak Br-γ emission in the observed spectrum of this source. EW of Br-γ line is -3.9±0.3 Å. Also, emission lines in Pa-β, Pa-γ and Pa-δ and CaII triplet are noticeable in the spectrum. EW of Pa-β line is -4.7±0.3 Å, EW of Pa-γ line is -1.9±0.2 Å, EW of Pa-δ line is -2.2±0.2 Å. It is classified as a CTTS with EW of Hα as -28.8Å (Kun et al., 2009). But they did not find any emission in the CaII triplet lines. We estimated the T$_{eff}$ of this source as 3970 K. Based on its position on the HR diagram, this source is of age 2 Myr and mass 0.6 M$_\odot$.

- **NGC 7023 RS 2 B:** This source is also classified as a variable source (Rosino

& Romano, 1962). Kun et al. (2009) estimated A_V towards FW Cep as 4.41, T_{eff} as 3850 K, spectral type as M0, mass as 0.6 $M_\odot$ and age as 2.0 Myr. A very weak emission in Br-γ line is visible in the observed spectrum, almost in the level of continuum. Other hydrogen lines do not show any signature of emission, along with CaII triplet lines. Distance to this YSO is 360^{+13}_{-13} pc (Bailer-Jones et al., 2018). Kun et al. (2009) classified it as a CTTS with EW of Hα as -63.9Å. No emission in CaII triplet lines were found in their observations. We estimated the T_{eff} of NGC 7023 RS 2 B as 4000 K. The age and mass of this source are 2-3 Myr and 0.7 $M_\odot$, respectively.

- **HZ Cep:** This source is classified as a variable source (Rosino & Romano, 1962; Sellgren, 1983). According to Kun et al. (2009), A_V towards FW Cep as 1.74, T_{eff} is 3850 K, spectral type as M0. They estimated the mass as 0.6 $M_\odot$, age as 1.5 Myr. Bailer-Jones et al. (2018) estimated the distance to this YSO as 325^{+7}_{-6} pc. It is a WTTS with EW of Hα as -3.9Å (Kun et al., 2009). Similar to NGC 7023 RS 5 and NGC 7023 RS 2 B, they did not find any emission in CaII triplet lines. Based on our observations, we obtained the T_{eff} as 3800 K and spectral type as M0. The estimated mass and age of HZ Cep are 0.45 $M_\odot$ and 1 Myr, respectively.

- **2MASS J21030756+6808339:** This target shows a very weak Brγ emission line in its spectrum. Also, emission in Pa-β and Pa-γ can be noted. Kirk et al. (2009) identified this source as a YSO candidate based on the 5-Band method with a 24 micron detection, the IRAC, and the 2MASS/MIPS color-magnitude methods. It is a Class II source with A_V =1.2 magnitude. *Gaia* DR2 did not detect this source. Therefore, we considered the estimated distance to L1172/1174 (335±11 pc, part I) as the distance to this source. We can see the Br-γ, Pa-β, Pa-γ, and Pa-δ emission lines. Also, CaII triplet emission lines are also visible in the observed spectrum. EW of Br-γ line is -3.6±0.2 Å. Also, relatively weak emission lines in Pa-β, Pa-γ and Pa-δ and CaII triplet are noticeable in the spectrum. EW of Pa-β line is -2.2±0.2 Å , EW of Pa-δ line is -2.6±0.2 Å . CaII triplet (8542Å) has EW -4.6±0.4 Å. We estimated the spectral type of this source as K7 and T_{eff} as 3970 K. Based on the position on the HR diagram, this source is of age 7 Myr and mass 0.75 $M_\odot$.

- **2MASS J21003662+6803445:** There is no emission line present in the spectrum which indicates the accretion mechanism ongoing in this source. This source is detected by *Gaia* DR2 and is located as a distance 342^{+5}_{-5} pc.

But this source is showing proper motion in declination as -0.257±0.088 mas yr^{-1} which is inconsistent with the same for other YSO candidates. Kirk et al. (2009) identified this source as a YSO candidate based on the 5-Band method with a 24 micron detection. It is a Class III source with A$_V$ =1.3 magnitude. We did not find any signature of emission in hydrogen lines in the observed spectrum of this source. The T$_{eff}$ is estimated as 3600 K. It is of age 1 Myr and mass 0.35 M$_\odot$.

- **2MASS J21005808+6809382:** Based on 2.2 μm scan, Sellgren (1983) identified this source as a variable one. Astrometric measurements of this source are not given in *Gaia* DR2. Therefore, we considered the distance 335±11 pc as the distance to this source, similar to 2MASS J21030756+6808339. Also, there is no signature of accretion emission lines in the observed spectrum of this source. Kirk et al. (2009) identified this source as a YSO candidate based on the 5-Band method with a 24 micron detection, the IRAC, and the 2MASS/MIPS color-magnitude methods. It is a Class II source with A$_V$ =2.7 magnitude. We estimated T$_{eff}$ of this source is 4030 K and spectral type is K6. The mass and age are estimated as 0.8 M$_\odot$ and 10 Myr, respectively.

- **2MASS J21005550+6811273:** Based on near-IR photometry, Kirk et al. (2009) identified this source as a YSO candidate. It is located at a distance of 333$^{+12}_{-13}$ pc (Bailer-Jones et al., 2018). Kirk et al. (2009) identified this source as a YSO candidate based on the 5-Band method with a 24 micron detection, the IRAC, and the 2MASS/MIPS color-magnitude methods. It is a Class II source with A$_V$ =1.5 magnitude. We did not find any signature of emission in hydrogen lines in the observed spectrum of this source. Based on its position on the HR diagram, this source is of age 20 Myr, and mass 0.7 M$_\odot$. We estimated the T$_{eff}$ as 4000 K and spectral type as K6, of this source.

3.13 Summary and Conclusions

We acquired near-IR spectra of 10 sources distributed towards HD 200775 using 3-m IRTF. In all sources, we obtained Br-γ in filled-in emission except FU Cep, NGC 7023 RS 5, and 2MASS J21030756+6808339, which show emission in Br-γ. As a fraction of the sources were observed by Kun et al. (2009) spectroscopically in optical and emission in Hα were obtained in their spectra, we could expect the sources would show emission in Br-γ too as these sources are young. The positions

Table 3.12: Properties of sources observed in spectroscopic mode.

#	EW(Hα)* (Å)	EW(Br-γ) (Å)	2.21 μm (Å)	2.26 μm (Å)	Spectral Type	A_V (mag)	T_{eff} (K)	L_{bol} ($L_\odot$)	Age (Myr)	Mass ($M_\odot$)
1	-	-	3.2±0.2	2.3±0.1	K5	5.83	4100	1.00	1-2	0.7
2	-4.0	-	3.6±0.3	3.6±0.2	K7	2.14	3970	0.73	2	0.6
3	-64.5	-3.0±0.4	2.9±0.1	2.3±0.2	K5	1.47	4170	0.58	4	0.85
4	-28.8	-3.9±0.3	2.9±0.1	3.0±0.3	K7	3.20	3970	0.74	2	0.6
5	-63.9	-	3.7±0.4	3.2±0.2	K6	3.23	4000	0.62	2-3	0.7
6	-3.9	-	4.4±0.1	4.0±0.2	M0	2.91	3800	1.26	1	0.45
7	-	-3.6±0.2	3.9±0.1	3.7±0.2	K7	1.85	3970	0.30	7	0.75
8	-	-	5.5±0.2	4.2±0.2	M1	2.46	3600	0.76	1	0.35
9	-	-	3.6±0.1	3.0±0.2	K6	1.00	4030	0.28	10	0.8
10	-	-	3.3±0.2	2.0±0.2	K6	0.00	4000	0.14	20	0.7

* Obtained from Kun et al. (2009).

of the YSOs on evolutionary tracks on the HR diagram suggest these objects to be of low-mass and of age mostly 1−10 Myr.

The lack of emission in Br-γ in a majority of the observed sources indicate that they are not active accretors. Ages of these sources are higher than the estimated age of HD 200775 (∼ 0.5 Myr, part II), which suggests that star formation in the cloud complex might have started prior to the formation of HD 200775. The absence of Br-γ in emission in majority of the sources could be due to variability. But because the near-IR excess of these sources are also low, it is likely that these sources are more evolved low-mass stars of 1−10 Myr. Therefore, we believe that the star formation in L1174 might have got initiated by some external trigger as suggested by Kun et al. (2009), and continued till the formation of HD 200775. HD 200775 is currently destroying the cloud by creating cavities around it, causing the cloud material to disperse and possibly halting further star formation. In chapter 4, we find three additional co-moving Herbig Ae/Be stars, of which, two of them are found to be associated with cluster of low-mass sources that are kinematically associated, and are of around ∼10 Myr old. The event that created these relatively older population, might have been responsible for the formation of at least some of the older stellar members around HD 200775.

Part IV

Tracing the magnetic field morphology of LDN 1172/1174 cloud complex

3.14 Introduction

Star formation is often found to be associated with the densest regions of molecular clouds that are elongated and filamentary in shape. In fact, results obtained with the *Herschel* space observatory (Pilbratt et al., 2010) of nearby interstellar clouds (André et al., 2010), as well as in more distant and massive clouds (Molinari et al., 2010; Hill et al., 2011) reveal the ubiquity of complex networks of filaments. How molecular clouds form and then evolve into filaments, cores and finally collapse to form stars is still a puzzle. Turbulence, gravity and magnetic fields (e.g., Klessen et al., 2000; Ballesteros-Paredes et al., 2007; André et al., 2010; Molina et al., 2012; Kirk et al., 2015; Beattie & Federrath, 2020) are believed to collaborate or compete in the process of the formation of these observed structures. However, the relative importance of them in the whole process is still to be unraveled.

Several observations have presented evidence for longitudinal flow of material along the filaments (e.g., Kirk et al., 2013; Jiménez-Serra et al., 2014; Hajigholi et al., 2016; Rayner et al., 2017; Dutta et al., 2018; Chen et al., 2019) leading to the idea that the filaments are long-lived but out-of-equilibrium flow structures (Gómez & Vázquez-Semadeni, 2014; Gómez et al., 2018) that supply material to the central high-density hubs, the locations where the filaments converge forming an intricate and inhomogeneous network of filaments that in turn appear to accrete material from their surroundings (Schneider et al., 2010; Kirk et al., 2013; Peretto et al., 2014; Lu et al., 2018; Williams et al., 2018; Shimajiri et al., 2019; Treviño-Morales et al., 2019). Because these filaments are denser than their ambient medium, it is believed that some compression is essentially involved in their formation mechanism (Hennebelle, 2013). This led to the suggestion that filamentary structures are formed by gravitational and/or turbulent compressive motions (e.g., Padoan et al., 2001; Hartmann et al., 2001; Padoan & Nordlund, 2002; Ballesteros-Paredes et al., 2007; Arzoumanian et al., 2011). The magnetic fields are expected to play a vital part by acting as agents that help to channel cloud accumulation and fragmentation (e.g., Nagai et al., 1998; Fiege & Pudritz, 2000; Shetty & Ostriker, 2006; Van Loo et al., 2014; Seifried & Walch, 2015).

Polarization observations in optical (e.g., Vrba et al., 1976; Goodman et al., 1990; Bhatt & Jain, 1992; Alves et al., 2008; Franco et al., 2010; Neha et al., 2016; Neha et al., 2018), near-IR (e.g., Sato et al., 1988; Goodman et al., 1995; Sugitani et al., 2010; Tamura et al., 2011; Soam et al., 2015a; Eswaraiah et al., 2017) and sub-mm wavelengths (e.g., Matthews et al., 2009; Ward-Thompson et al., 2000; Qiu

---

[1]**The results presented in this part are under revision in A&A.**

et al., 2014; Planck Collaboration et al., 2016c; Soam et al., 2018) revealed the ubiquity of magnetic fields in the Galaxy. Studies that probed the relative orientation between the magnetic field and the elongated cloud structure suggest that they tend to be oriented either parallel or perpendicular to each other (Goodman et al., 1990; Goodman et al., 1992; Chapman et al., 2011; Li et al., 2014; Sugitani et al., 2011). The low-column density structures are preferably oriented parallel to the local mean magnetic field and the high-column density structures are statistically oriented perpendicular (Li et al., 2011; Li et al., 2013; Palmeirim et al., 2013; Heyer et al., 2016; Planck Collaboration et al., 2016c; Alina et al., 2019). These findings are consistent with the results obtained from the numerical simulations also (e.g., Stone et al., 1998; Nagai et al., 1998; Nakamura & Li, 2008; Hennebelle, 2013; Van Loo et al., 2014; Chen & Ostriker, 2014; Inutsuka et al., 2015; Wareing et al., 2016; Tritsis & Tassis, 2016).

In a flow driven molecular cloud formation scenario (e.g., Vázquez-Semadeni et al., 2011), the strength and the topology of the magnetic fields with respect to the flow direction may play a crucial role (Soler, 2019; Soler et al., 2013). Results from a study conducted by Gómez et al. (2018) to investigate the structure of magnetic field inside a self-gravitating filament formed in a turbulent environment suggest that the magnetic field geometry represents the flow pattern of the material inside and in the vicinity of the filaments. As cloud material tends to flow along the magnetic field lines forming sheets or filaments (Zamora-Avilés et al., 2017), the low density striations or low column density material tends to align parallel to the magnetic fields (Palmeirim et al., 2013; André & Kremer, 2014). Around the filaments, the gas gets accreted on to it, making the field lines to get oriented perpendicular to the filaments, which is often found in observations and simulations (Goodman et al., 1992; Chapman et al., 2011; Sugitani et al., 2011; Gómez & Vázquez-Semadeni, 2014; Gómez et al., 2018). But as the gas density increases, the flow pattern changes. The longitudinal flow of material towards the clumps drags the field lines along with it, making the field lines parallel to the filaments. Results from several studies have shown that the velocity and the B-fields are preferentially aligned (Matthaeus et al., 2008; Banerjee et al., 2009; Iffrig & Hennebelle, 2017) which is consistent with the correlations found between the B-field direction and the density gradient (Soler et al., 2013; Koch et al., 2013; Koch et al., 2014; Planck Collaboration et al., 2016c; Soler & Hennebelle, 2017). At the spine of the filaments, however, the field lines are expected to be perpendicular to connect the field lines from the opposite sides of the filament (Gómez et al., 2018).

LDN 1172/1174 (hereafter L1172/1174; Lynds, 1962) cloud complex was shown

by Myers (2009) as one of the typical examples of a hub-filament structure. The reflection nebula NGC 7023, illuminated by a Herbig Be (B2/3Ve) star HD 200775 (The et al., 1994; Manoj et al., 2006) forms the hub and a single filament of nearly 5 pc in length which runs towards the south-west with respect to the Galactic plane provide a "head-tail" appearance (Tachihara et al., 2002) to the whole cloud. Based on the *Gaia* DR2 parallax measurements of the young stellar objects (YSOs) associated with the cloud, Saha et al. (2020) estimated a distance of 335±11 pc to L1172/1174. Thus L1172/1174 forms a nearby structurally simple scenario of a single long filament terminating at a hub where a low- and intermediate-mass star formation is currently active (e.g., Weston, 1953; Kirk et al., 2009; Kun et al., 2009; Yuan et al., 2013; Rector & Schweiker, 2013) in L1174 which is located to the north-west of HD 200775 and in L1172 which is located on the filament. Based on polarization measurements of more than 200 stars projected on the cloud in R-band, we made magnetic field geometry of the outer regions of the cloud complex. Apart from knowing the magnetic field orientation in the cloud complex, it is also interesting to study if there is any effect of the HD 200775 on the ambient field orientation.

While the polarization measurements in optical wavelengths can trace the field geometry in the low-density inter-cloud media (ICM) and the periphery of molecular clouds, the polarized thermal emission due to the dust can trace the fields in the high-density parts of the cloud (e.g., Ward-Thompson et al., 2009; Li et al., 2009; Soam et al., 2019; Sharma et al., 2020). Thus by comparing the magnetic field geometry inferred from the optical and sub-mm wavelengths, the relationship between the magnetic field orientations inside the cloud and the ICM can be investigated. Using the dust polarization in emission at sub-mm wavelengths obtained with the *Planck* satellite, we made a low resolution magnetic field map of the low- and high-density regions of the cloud complex and compared them with those inferred from our R-band polarization measurements to understand the orientation of the field lines with respect to the column density distribution. The part is organized in the following manner. We describe the details of our observations and data reduction in §3.15. The polarization results are presented in §3.16 and we discuss our results in §3.17. Finally, we conclude our work with a summary given in §3.18.

3.15 Observation and data reduction

3.15.1 Optical polarization measurements in R-band

This section is already described in part I. The details of our optical polarimetric data reduction are provided in chapter 2. Table 3.13 provides the results of the observed polarimetric standard stars.

3.15.2 Planck polarization measurements in sub-mm

Planck observed the whole sky in 9 frequency bands (30-857 GHz) in total intensity, and up to 353 GHz in polarization (Planck Collaboration et al., 2014). The data were thus used to produce the first all-sky map of the polarized emission from dust at sub-mm wavelengths (Planck Collaboration et al., 2016a). We used the intensity and polarization data only at 353 GHz as this is the highest frequency channel with polarization capabilities and the one with the best signal-to-noise ratio (SNR) for dust polarization (Planck Collaboration et al., 2015). We used the whole sky map (bandpass leakage corrected) at 353 GHz provided by *Planck* Legacy Archive [1]. The polarization of the CMB has a negligible contribution to the sky polarization towards the molecular clouds at 353 GHz (Planck Collaboration et al., 2016b). So, CMB polarization was not taken into account in our analysis. The I, Q, and U maps analyzed here have been constructed using the gnomonic projection of the HEALPix[2] (Górski et al., 2005) all-sky maps. We have used *healpy* (Zonca et al., 2019) to extract and analyze data for calculation of P% and θ. *healpy* is a Python package to handle pixelated data on the sphere.

We estimated the Stokes I, Q, and U parameters from the smoothed *Planck* map of a 6° square area region obtained from the *Planck* 353 GHz image centered at HD 200775. Stokes I (total dust intensity) and Q, U (two components of the linearly polarized dust emission) parameters are related as Q = Icos(2ψ), U = Isin(2ψ). The total polarization P is related to the Q and U values as P = $\sqrt{Q^2 + U^2}$ and the fraction of the polarization fraction as P/I. The polarization angle, ψ, is related to Q and U values as $\psi = 0.5$ arctan(U, Q). The ψ is measured with respect to the Galactic coordinates with -90° < ψ < +90°, ψ = 0° towards Galactic north, increasing towards Galactic west (HEALPix convention). The angle of B$_{\rm POS}$ (χ) can be obtained by adding 90° to the polarization angle ($\chi = \psi + 90°$). The Stokes parameter maps are shown in accordance with the IAU convention ($\psi = 0°$

Table 3.13: Polarized standard stars observed in the R band (λ_{eff}=0.630 μm).

Date of observations	P$\pm\epsilon_P$ (%)	$\theta \pm \epsilon_\theta$ (°)
HD 236633 ([a]Standard values: 5.38 $\pm$ 0.02%, 93.°04 $\pm$ 0.°15)		
11 Oct, 2015	5.4$\pm$0.3	97$\pm$2
3 Nov, 2015	4.9$\pm$0.1	100$\pm$1
15 Nov, 2015	4.9$\pm$0.1	101$\pm$1
16 Nov, 2015	5.1$\pm$0.1	102$\pm$1
17 Nov, 2015	4.9$\pm$0.1	101$\pm$1
15 Dec, 2015	4.8$\pm$0.1	101$\pm$1
23 Oct, 2016	5.2$\pm$0.1	100$\pm$1
25 Oct, 2016	5.0$\pm$0.1	99$\pm$1
26 Oct, 2016	4.8$\pm$0.1	98$\pm$1
27 Oct, 2016	4.9$\pm$0.1	100$\pm$1
13 Oct, 2017	4.9$\pm$0.2	102$\pm$1
19 Oct, 2017	5.1$\pm$0.2	100$\pm$1
20 Oct, 2017	5.0$\pm$0.2	101$\pm$1
21 Oct, 2017	5.3$\pm$0.2	102$\pm$1
26 Oct, 2017	5.1$\pm$0.2	101$\pm$1
27 Oct, 2017	4.9$\pm$0.1	100$\pm$1
BD+59°389 ([a]Standard values: 6.43 $\pm$ 0.02 %, 98.°14 $\pm$ 0.°10)		
11 Oct, 2015	6.2$\pm$0.2	104$\pm$1
2 Nov, 2015	6.4$\pm$0.1	106$\pm$1
3 Nov, 2015	6.3$\pm$0.1	105$\pm$1
15 Nov, 2015	6.0$\pm$0.1	106$\pm$1
16 Nov, 2015	6.4$\pm$0.1	106$\pm$1
17 Nov, 2015	6.2$\pm$0.1	106$\pm$1
25 Oct, 2016	6.0$\pm$0.1	104$\pm$1
28 Oct, 2016	5.6$\pm$0.1	105$\pm$1
22 Nov, 2016	6.3$\pm$0.1	106$\pm$1
27 Nov, 2016	6.4$\pm$0.3	109$\pm$1
13 Oct, 2017	5.9$\pm$0.1	106$\pm$1
14 Oct, 2017	6.4$\pm$0.1	107$\pm$1
17 Oct, 2017	5.7$\pm$0.2	106$\pm$1
18 Oct, 2017	5.7$\pm$0.2	107$\pm$1
19 Oct, 2017	6.0$\pm$0.2	107$\pm$1
20 Oct, 2017	6.1$\pm$0.2	107$\pm$1
21 Oct, 2017	6.9$\pm$0.2	105$\pm$1
26 Oct, 2017	6.0$\pm$0.2	103$\pm$1
HD 19820 ([a]Standard values: 4.526 $\pm$ 0.025 %, 114.°46 $\pm$ 0.°16)		
15 Dec, 2015	4.6$\pm$0.1	123$\pm$1
22 Nov, 2016	4.3$\pm$0.1	126$\pm$1
26 Nov, 2016	4.2$\pm$0.1	124$\pm$1
HD 204827 ([a]Standard values: 4.893 $\pm$ 0.029 %, 59.°10 $\pm$ 0.°17)		
23 Oct, 2016	4.2$\pm$0.1	66$\pm$1
HD 25443 ([a]Standard values: 4.734 $\pm$ 0.045 %, 133.°65 $\pm$ 0.°28)		
26 Nov, 2016	4.7$\pm$0.2	143$\pm$1
27 Nov, 2016	4.8$\pm$0.2	143$\pm$1
HD 15445 ([a]Standard values: 3.683 $\pm$ 0.072 %, 88.°91 $\pm$ 0.°56)		
22 May, 2017	3.6$\pm$0.2	107$\pm$2
23 May, 2017	3.2$\pm$0.2	102$\pm$2

[a] Values in the R band from Schmidt et al. (1992).

towards the Galactic north, increasing towards the Galactic east) (Hamaker, J. P. & Bregman, J. D., 1996), using the relation U = -Ipsin(2ψ). At 353 GHz, the *Planck* data have an angular resolution of 4.8'. The polarization sensitivity was expected to be such that, at a resolution of 15', ISM structures with $A_V = 1$ mag would be detected with a relative uncertainty on the polarization fraction $\sim 40\%$ and an uncertainty on the polarization angle $\sim 30°$ (Pelkonen et al., 2009).

3.15.3 ^{12}CO (1-0) molecular line observations using TRAO

As a part of a comprehensive study of L1172/1174 to understand the gas dynamics (Sharma et al. 2020, under preparation), the whole cloud of L1172/L1174 was observed in ^{12}CO, C^{18}O, N$_2$H$^+$ (1-0) and CS (2-1) transitions using On-The-Fly (OTF) mapping technique using the 14 m diameter single-dish telescope of Taedeuk Radio Astronomy Observatory (TRAO) in Daejeon, South Korea between November 16-28, 2018. Here we present only the ^{12}CO lines results mainly to estimate magnetic field strengths in the cloud using the ^{12}CO line widths. The back-end system with fast fourier transform spectrometer has 4096$\times$2 channels at 15 kHz resolution ($\sim$0.05 km s^{-1} at 110 GHz). Spectral resolution of 0.05 km s^{-1} was used and typical rms noise in one channel was $\sim$0.35 K for ^{12}CO lines in T$_A^*$ scale. At 115 GHz the beam size (HPBW) of the telescope is about 47″ and the fraction of the beam pattern subtending main beam (beam efficiency) is 41$\pm$2% (Jeong et al., 2019). The system temperature was 550 K-600 K during the observations. The spectra were reduced using CLASS software of the IRAM GILDAS software package.

3.15.4 *Gaia* DR2

Gaia DR2 presents positions, parallaxes, and proper motions of more than a billion objects (Gaia Collaboration et al., 2018) with unprecedented precision. But if the relative uncertainties in parallax values were $\gtrsim 20\%$, the corresponding distances wouldn't follow the simple inversion of their parallaxes (Bailer-Jones, 2015). Recently, Bailer-Jones et al. (2018) provided a probabilistic estimate of the stellar distances from the parallax measurements in Gaia Collaboration et al. (2018), using an exponentially decreasing space density prior which is based on a galactic model. In our analysis, the stellar distances were obtained from Bailer-Jones et al. (2018), by giving a search around a circle of radius of 1″ around the source positions.

3.16 Results

3.16.1 Optical and sub-mm polarization

In Fig. 3.21 we show the results from our R-band polarization measurements (lines shown in yellow) of 249 stars. The lengths and orientations of the polarization vectors correspond to the degree of polarization (P_R) in per cent and the position angle (θ_R) in degree measured from the north to east, respectively. The polarization vectors are plotted over the $\sim 2°$ hydrogen column density map made using the images obtained with the *Herschel* satellite (André et al., 2010). The median value of the column density towards the 249 stars observed by us is found to be 9×10^{20} cm^{-2}. The outermost contour in Fig. 3.21 is drawn at this level, which corresponds to an extinction of ~ 1 magnitude converted using the relationship between the column density and the extinction derived by Bohlin et al. (1978). Also plotted in Fig. 3.21 are the *Planck* polarization vectors (lines shown in white) which are 90° rotated by their original orientations to indicate the magnetic field directions. Here again, the lengths and orientations of the polarization vectors correspond to the degree of polarization (P_p) and the position angle (θ_P) in degree measured from the north towards the east, respectively. Table 3.14 lists the R-band polarimetric results of the 249 stars.

For the purpose of analysis, R-band polarization vectors lying within a circular region of 0.4° (the extend over which we have R-band polarization across the cloud complex) radius around HD 200775 are considered as part of the head, and those lying outside of this region are considered as part of the tail region. The P_R and the θ_R for the sources lying towards the head and the tail regions are shown in Fig. 3.22 (a) using open circles in red and blue, respectively. The P_R are found to range from $\sim 0.6\%$ to $\sim 5.8\%$ towards the head and from $\sim 0.6\%$ to $\sim 4.1\%$ towards the tail region. The θ_R are in the range from $125° - 240°$ and from $145° - 223°$ towards the head and the tail regions, respectively. The median values of P_R and θ_R for the head region are 2.1% and 203°, and the median absolute deviations (MADs), more resilient to outliers in a data, of P_R and θ_R are found to be 0.7% and 15°, respectively. The median values of P_R and θ_R for the tail region are 2.0% and 196° with corresponding MADs of 0.5% and 6°, respectively. The histograms of θ_R for the head (red) and the tail (blue) regions are shown in Fig. 3.22 (b).

The *Planck* polarization measurements, P_P and θ_P for the head and the tail regions are also shown in Fig. 3.22 (a) using the filled circles in black with red and blue halo, respectively. Here, the *Planck* polarization vectors that fall within the
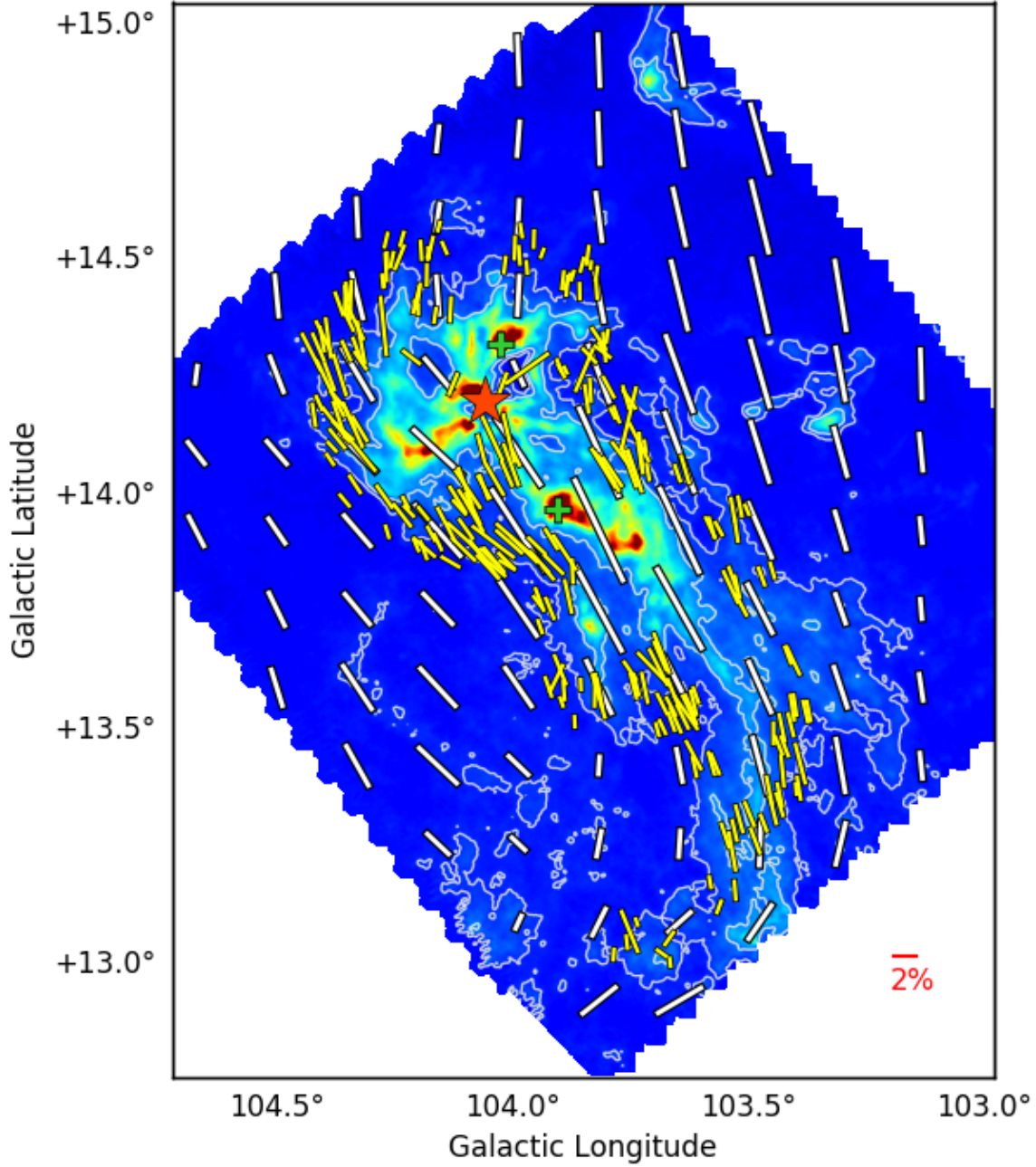
Figure 3.21: The R-band (yellow) and the *Planck* (white) polarization vectors (90°
rotated) overlaid on the *Herschel* dust column density map of L1172/1174 obtained
from André et al. (2010). The contour are drawn at 9×10^{20} cm^{-2} and 15×10^{20} cm^{-2}
levels to reveal the cloud structure. HD 200775 is marked with a red star symbol.
The green colored plus symbols imply the locations of L1172 (south) and L1174
(north). The lengths and the orientations of the vectors correspond to the degree
of polarization and the position angles measured with respect to the galactic north
increasing eastward, respectively. A polarization vector (red) corresponding to 2%
and oriented at 90° is shown for reference.
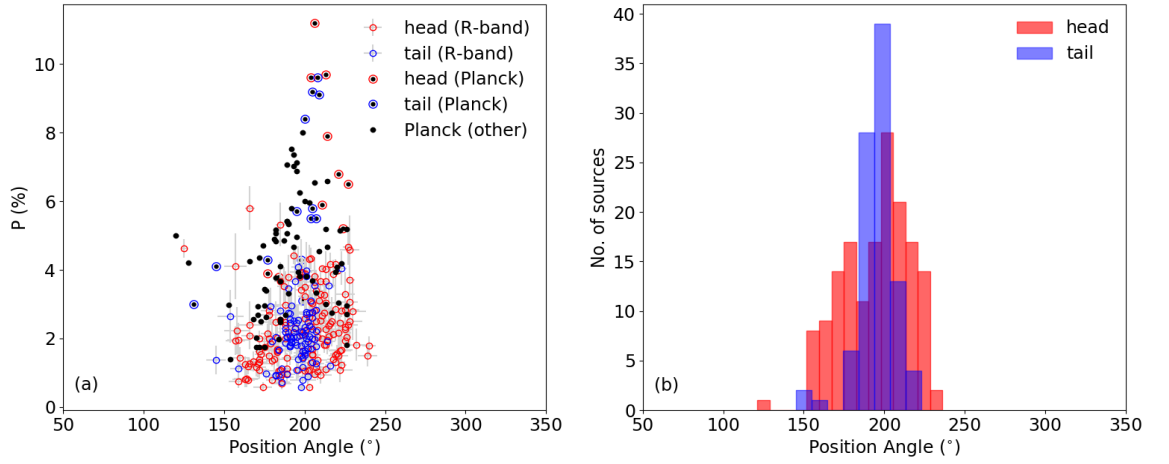
Figure 3.22: **(a):** P$_R$% vs. θ_R for the 249 sources observed by us in R-band and the *Planck*. The R-band polarization vectors from the head and the tail regions are shown using open circles in red and blue respectively. Similarly, for the *Planck*, the measurements from the head and the tail regions are shown using filled circles in black with red and blue halo, respectively. The *Planck* polarization measurements from the ICM are shown in filled circles in black. **(b):** Histograms of the θ_R belonging to the head and the tail regions of L1172/1174 obtained from our R-band polarization measurements.

9×10^{20} cm^{-2} contour are considered as associated with the cloud complex, and those lying outside (but within the *Herschel* field) are considered as polarization from the ICM. Of the measurements falling within the 9×10^{20} cm^{-2} contour, those lying within the circular region of 0.4° radius are considered as the part of the head region while those falling outside the circular region of 0.4° radius are considered as the part of the tail. The number of data points is lesser compared to the R-band polarization due to the coarse resolution of the *Planck* measurements. Though highly uncertain, in general, the P$_P$ measurements show a higher degree of polarization compared with the P$_R$, especially in locations that are projected on the high density parts of the cloud as seen in Fig. 3.21. The P$_P$ values are found to range from $\sim 2.4\%$ to $\sim 11.2\%$ towards the head and from $\sim 3.0\%$ to $\sim 9.6\%$ towards the tail region. The degree of polarization in the ICM is found to range from $\sim 1.4\%$ to $\sim 8.0\%$. The median values of P$_P$ are found to be 6.2% and 5.5% for the head and the tail regions, respectively with MAD of 2.3% and 1.4%, respectively. The θ_P values are found to range from 177° to 227° towards the head and from 131° to 209° towards the tail region. The median values of θ_P in the head and the tail regions are found to be 212° and 200° with MAD of 8° and 5°, respectively. The polarization position angle (θ_{ICM}) towards the ICM (region outside the 9×10^{20} cm^{-2} contour but within

the *Herschel* field) is found to range from 120° to 227° with a median and MAD values of 190° and 14° respectively.

3.16.2 ^{12}CO gas distribution in L1172/1174 complex

The ^{12}CO velocity for the entire cloud complex ranges from -2.8 km s^{-1} to 7.8 km s^{-1}. The average FWHM of the ^{12}CO is found to be $\sim$2.0 km s^{-1}. The cavity surrounding HD 200775 is conspicuous with high intensity peaks located along the rim of the cavity. The ^{12}CO is found to show gas structures, especially to the eastern and western directions of HD 200775 where the gas components in the velocity range of -2.5 km s^{-1} to 0 km s^{-1} and 5.0 km s^{-1} to 7.5 km s^{-1} respectively are located, supporting the earlier reporting of the presence of bipolar outflow lobes (Watt et al., 1986). The gas dynamics of the region surrounding HD 200775 will be presented in a subsequent article (Sharma et al. 2020, under preparation). In this work, we used the ^{12}CO line-widths to calculate the strength of the plane-of-the-sky component of the ambient magnetic field (B$_{POS}$).

3.17   Discussions

3.17.1   Magnetic field geometry of L1172/1174 complex

Interstellar dust grains produce both extinction of light from the background stars as well as emit thermal radiation. It is believed that the spinning grains tend to orient with their long axes perpendicular to the magnetic field lines (Davis & Greenstein, 1951; Lazarian, 2003). When the unpolarized starlight impinges on a series of aspherical dust grains, the electromagnetic wave is absorbed maximum along the long axis of grain. The transmitted radiation becomes partially plane polarized and lies along the B$_{POS}$ (Whittet, 2005). On the other hand, thermal emission from the dust grains is maximum along the longer axis, thus becomes polarized perpendicular to B$_{POS}$. Since dust grains are coupled with the magnetic field, measurements of dust polarization provide information on the structure and the strength of the magnetic field. The value of position angle depends on the orientation of the B$_{POS}$ and the efficiency of the dust grain alignment with the field. It also depends on the variation in the orientation of B$_{POS}$ along the line-of-sight (Lee & Draine, 1985). The polarization measurements in the optical bands trace the B$_{POS}$ only in the outskirts of the molecular clouds where the extinction (A$_V$) is relatively low (Guetter & Vrba, 1989; Harjunpää et al., 1999) while the polarization
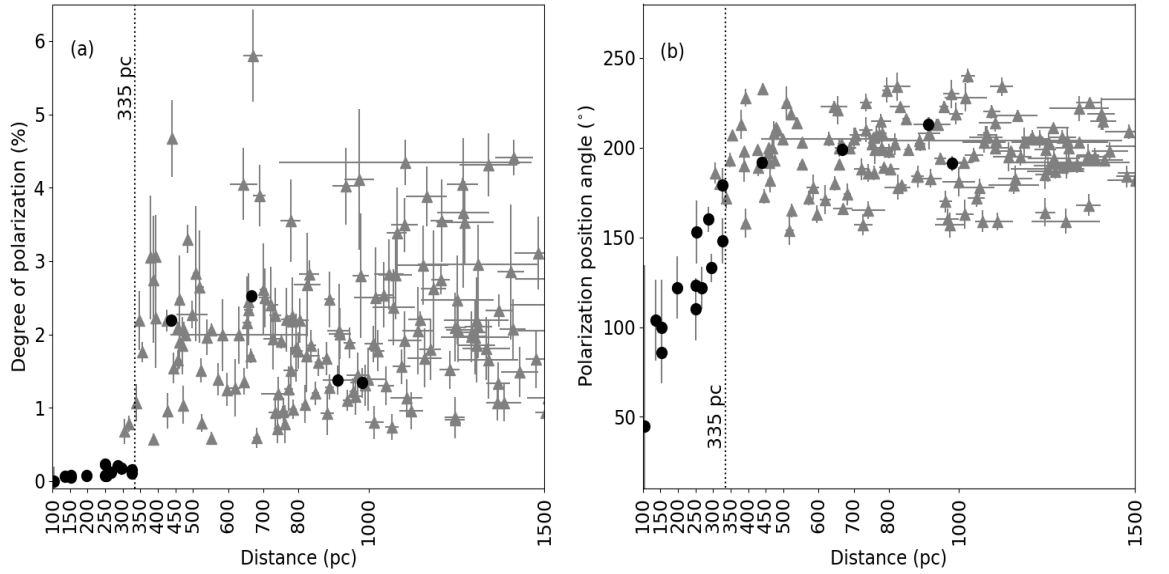
Figure 3.23: **(a)** Polarization (%) vs. distance plot for the stars projected towards the direction of L1172/1174 (filled triangles in grey). The filled circles in black are the sources for which the P% is obtained from the Heiles (2000) catalogue. **(b)** Polarization position angle vs. distance plot for the stars projected in the periphery of L1172/1174. The symbols are same as above.

measurements in sub-millimeter or millimeter can infer the B_{POS} inside the cloud where A_V is relatively high (e.g., Hildebrand et al., 1984; Goodman, 1995; Greaves et al., 1999).

The measured polarization in optical wavelengths is caused by the dust grains that are lying all along the light of sight (within the pencil beam) between the star and us. Though the dust grains present within the cloud are mostly responsible for the observed polarization, those that are present foreground to the cloud can also contribute. To infer the amount of polarization caused by the dust grains within the cloud (thus the magnetic field geometry), it is necessary to remove the foreground component. Generally, the stars located foreground to the cloud are used to estimate the foreground component of the polarization. The P_R vs. distance and θ_R vs. distance plots of the observed sources are shown in Fig. 3.23 (a) and (b), respectively using filled triangles in grey. Among the stars observed by us, only one star, located at 306 pc, is foreground to the cloud. Therefore, we searched in Heiles (2000) catalogue to get more foreground sources having polarization measurements. The search was made within a circular region of 6° radius about HD 200775. We obtained a total of 26 sources around HD 200775. These sources except for 4 sources may have intrinsic polarization (Coyne, 1976; Jain et al., 1990). Four sources, HD
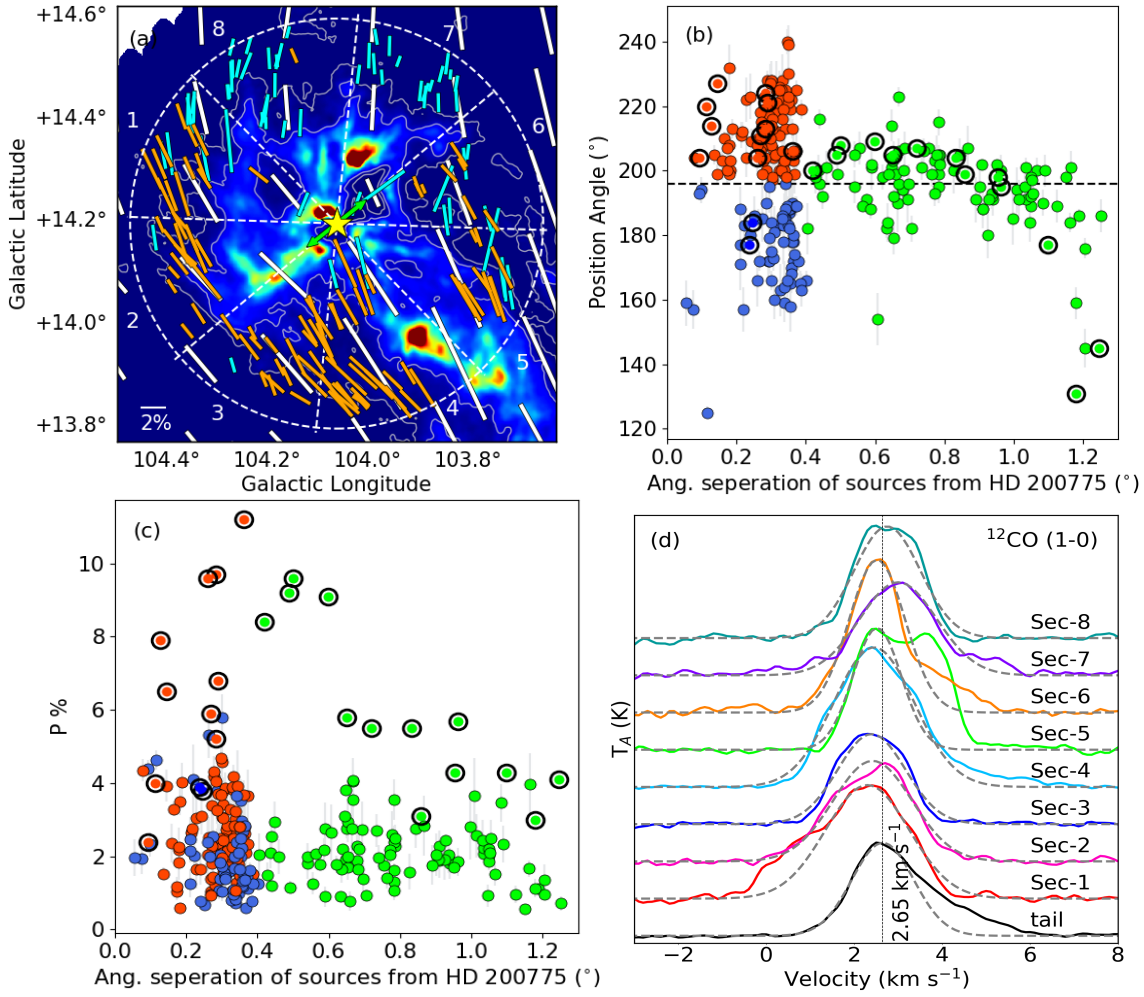
Figure 3.24: **(a)** The optical R-band and *Planck* polarimetric results overplotted on *Herschel* column density map. Location of HD 200775 (yellow star) is also shown. The green colored arrows imply the directions of outflow from HD 200775. The eight sectors are indicated using dashed white lines and also marked. Orange lines indicate the polarization measurements in R-band with $\theta_R > 196°$ and cyan lines represent the same with $\theta_R < 196°$. White lines represent *Planck* polarimetric results with $90°$ rotation. A polarization vector corresponding to 2% is shown for reference. **(b)** Variation of θ_R of the sources with respect to the angular separation from HD 200775. Upto $0.4°$ (sections 1-8) there are sources located towards the head region with two sets of distribution of position angles $\sim211°$ (red filled circles, shown in orange lines in **(a)**) and $\sim178°$ (blue filled circles, shown in cyan lines in **(a)**). The green filled circles are the sources distributed towards the tail region. The dashed horizontal line indicates the mean θ_R value ($\sim 196°$) of the same sources. Position angles obtained from *Planck* observations are shown using thick open black circles (shown in white lines in **(a)**). **(c)** Variation of $P_R\%$ of the sources with respect to the angular separation from HD 200775. The symbols represent the same as described in panel **(b)**. **(d)** The average ^{12}CO (J=1-0) line profile for the eight sectors made towards the head. The average ^{12}CO (J=1-0) line profile for the tail region is shown in black. The $V_{lsr} = 2.65$ km s^{-1} is identified using a dashed vertical line. The dashed curves are the Gaussian fitted lines used to obtain the ΔV.

200775, HD 193533, HD 208947, and HD 203467 were not considered in our analysis. HD 200775 is a Herbig Be star, HD 193533 is a variable source, HD 208947 is an Algol variable and HD 203467 is classified as a Be type star in the Simbad database. Of the remaining 22, we obtained the *Gaia* DR2 distance for 17 sources from the Bailer-Jones et al. (2018) catalogue.

The degree of polarization (P_H) in per cent and polarization position angles (θ_H) in degree of the 17 sources are shown using filled circles in black in both (a) and (b) of Fig. 3.23 respectively. As the foreground sources show a significantly low degree of polarization, we set no constraints on the P_H/σ_H values during their selection. Of the 17 sources, 13 sources are found to be located at distances less than 335 pc (distance to L1172/1174) and 4 sources are at distances greater than 335 pc. The mean values of P_H and θ_H for the 13 foreground sources are found to be 0.1% and 122°, respectively, and the corresponding mean values for the 4 background sources are found to be 1.9% and 199°, respectively. Both P_H and θ_H values of the 4 background sources are found to be consistent with the values of the sources observed by us towards L1172/1174. Using the mean values of P_H and θ_H obtained for the 13 stars, we calculated the mean Stokes parameters $Q_{fg}(= P\cos2\theta)$ and $U_{fg}(= P\sin2\theta)$ as -0.048 and -0.099, respectively. We subtracted these values from the Stokes parameters of the observed stars vectorially to calculate the foreground-corrected percentage of polarization (P_c) and the position angle (θ_C) values. No significant changes are noticed in the results after correcting for the foreground polarization. As a result, the R-band polarization vectors (in yellow) presented in Fig. 3.21 represent the B_{POS} geometry towards the periphery of L1172/1174 complex.

As evident from Fig. 3.21 and Fig. 3.22 (a), the orientations of B_{POS} obtained from the R-band (θ_R=203° for the head and θ_R=196° for the tail) and the *Planck* (θ_P=212° for the head and θ_P=200° for the tail) observations are found to be in good agreement all along the structure of the cloud complex. Such correlations between the magnetic field geometries inferred from the optical and the *Planck* polarization measurements are reported in a number of studies (e.g., Soler et al., 2016; Planck Collaboration et al., 2016c; Gu & Li, 2019). This implies that the magnetic fields inferred from the *Planck* polarization measurements and from the R-band polarization towards the high density parts and towards the outer envelope of L1172/1174, respectively, are well correlated with each other. Even the *Planck* polarization vectors from outside of the 9×10^{20} cm^{-2} contour which represent the B_{POS} in ICM (θ_{ICM}=190°) are correlated with both θ_R and θ_P implying that the cloud B_{POS} is threaded by the ICM B_{POS} surrounding the cloud.

In Fig. 3.24 (a) we show the projected B_{POS} geometry of the head region of

L1172/1174 inferred from our R-band and the *Planck* polarization results. The vectors are overlaid on the hydrogen column density map. In Fig. 3.24 (b) & (c) we show the θ_R and P_R values of the stars as a function of their angular separation from HD 200775 respectively. The primary goal here is to investigate whether the presence of HD 200775 has any effect on the magnetic field geometry around it. Two components of B_{POS} are apparent in Fig. 3.24 (b) for the sources lying towards the head region. These two components are identified using the filled circles in red and blue colors. The *Planck* measurements are identified with open circles in black. The results shown in filled circles in green are those from the tail region. The median value of the θ_R (=196°) in the tail region is shown using a dashed line in Fig. 3.24 (b). The change in the θ_R found beyond $\sim 1°$ towards the tail is due to the curved geometry of B_{POS} which is found to correlate well with the geometry of the cloud structure there. The median values of θ_R lying towards the head region and having $\theta_R \geqslant 196°$ and $< 196°$ are found to be 211° and 178° respectively with the MAD of 8° for both the distributions. The two components found towards the head are identified in Fig. 3.24 (a) using the vectors drawn in orange and cyan, respectively. The distribution of θ_R in Fig. 3.24 (b) actually reflects the distribution of the magnetic field vectors on the cloud as shown in Fig. 3.24 (a) with 178° component lying predominantly to the north-western parts of HD 200775 and the 211° component lying to the south-eastern parts.

To investigate the variation of the projected magnetic field orientations in more detail, we divided the head region into 8 equal sectors drawn within the circular area of 0.4° radius centered at HD 200775 as shown in Fig. 3.24 (a). The division of the region is made with respect to the symmetry axis of the outflow cavity believed to have been carved out by HD 200775 (Fuente et al., 1998b). The star formation process is ongoing mainly in this circular region. The median values of P_R (column 2), θ_R (column 3) and the MAD (column 4) of the θ_R for each sector are given in Table 3.15. The component showing the median value of 211° is dominant towards the sectors 2, 3, and 4, which lie to the south and south-east of HD 200775. The median value of P_R for this component is 2.4%. The component showing the median value of 178° is largely distributed towards the sectors 7 and 8, which lie to the north of HD 200775. The median value of P_R for this component is 1.6% which is relatively low ($\sim 2\sigma$). The sectors 1, 5, and 6 show the presence of both the components. The median values of the θ_R in these three regions are found to be $\sim 200°$ which is roughly the average of the two (178° and 211°) components. The deviation in the θ_R ($\Delta\theta_R$) is found to be the lowest towards the tail region and highest towards the sectors 5 and 6.

In Fig. 3.24 (d), we show the average ^{12}CO (J=1-0) line profiles for the eight sectors identified towards the head region. The ^{12}CO lines towards the line-of-sights of the stars for which we have R-band polarization measurements are used for getting the average profiles. The average ^{12}CO line profile for the tail region is also shown in Fig. 3.24 (d). The measurements having SNR $\geqslant$3 are used for generating the average profiles. The V_{lsr} =2.65 km s^{-1} of the cloud determined from the N$_2$H$^+$ line detected in the cores (Sharma et al. 2020, under preparation), is identified using a dashed black line. The V_{lsr} is computed as a mean of L1174 (2.5 km s^{-1}) and L1172 (2.8 km s^{-1}) regions. The ^{12}CO line towards the tail region is found to be peaking at the V_{lsr} velocity with a full width at half maximum (ΔV) value of 1.7 km s^{-1} obtained from a Gaussian fit to the profile. However, the profile shows a line profile skewed to the redder velocities, which is more likely to be due to the presence of high velocity (both blue- and red-shifted) gas.

The average ^{12}CO line profiles for the sectors 3, 4, and 7 are found to be consistent with a Gaussian shape, though the presence of high velocity components are seen towards most of the sectors similar to what we have observed towards the tail region. While the line peaks towards the sectors 1, 3, 4, and 5 are shifted towards the bluer velocities, the line towards the sector 7 shows a shift towards the redder velocity with respect to the V_{lsr}. The sectors 2 and 6 are found to peak at the V_{lsr} velocity. The line profiles at sectors 1 and 2 show additional components at bluer velocities, whereas a relatively narrow line width with high velocity wings to the redder velocities are seen for the profile in sector 6. Compared to other sectors, the sector 5 shows a distinct profile with an additional velocity component to the redder side of the line center having both the peaks with comparable intensity. Thus, for the sector 5, we fitted the observed line profile with the two Gaussian components and the line width (ΔV$\approx$1.3 km s^{-1}) corresponding to the component closest to the V_{lsr} is used to estimate the magnetic field strength.

It is observed that the high velocity gas is not widespread but localized. It is possible that the high velocity gas present towards, especially, the sectors 5 and 6 may be responsible for the disturbance of grain alignment and hence relatively higher $\Delta\theta_R$ seen in these two regions where two components of θ_R ($<$ 196° and $>$ 196°) are present. The symmetry axis of the cavity, believed to be carved out by the outflow from HD 200775 (Fuente et al., 1998b), is found to be in a direction almost perpendicular to the magnetic field direction. The cavity located to the north-west of HD 200775 is found to be more extended, suggesting that this part is relatively more affected by the star than the south-eastern cavity. The presence of high velocity gas in sector 6 supports these observations. In sector 5 also, the presence of additional

velocity component is considered to disturb the surrounding material, which results in a higher dispersion in θ_R. The additional velocity component is considered to originate from a loop structure close to L1172 (will be discussed in detail in Sharma et al. 2020, under preparation). The ΔV values estimated for the lines in all sectors are listed in Table 3.15. Unfortunately, we do not have ^{13}CO molecular line data towards this cloud complex using TRAO. Though the cloud is observed using $C^{18}O$ line, which traces the high density regions of L1172/1174, while the optical R-band polarimetric observations were acquired towards the periphery (low-density) region of the cloud. Therefore, we could be able to use ^{12}CO only in our analysis.

3.17.2 Magnetic field strength in L1172/1174

The strength of the plane of sky component of the magnetic field (B_{POS}) was estimated using the modified Chandrasekhar-Fermi (CF) relation (Chandrasekhar & Fermi, 1953; Ostriker et al., 2001),

$$B_{POS} = 9.3 \left[\frac{n_{H_2}}{cm^{-3}}\right]^{1/2} \left[\frac{\Delta V}{kms^{-1}}\right] \left[\frac{\Delta\theta}{1°}\right]^{-1} \mu G, \qquad (3.1)$$

where n_{H_2} represents the volume density of hydrogen gas in molecular clouds, ΔV is the full width at half maximum obtained from the velocity dispersion σV ($\sqrt{8ln2}$ σV), and $\Delta\theta$ is the dispersion in the position angles. The CF method is applicable for $\Delta\theta < 25°$. This method suggests that the B_{POS} can be computed by analyzing the small scale randomness in the magnetic field lines. The dispersion of line-of-sight velocity creates an irregular scatter in the position angles based on the assumptions that there is a mean field component in the area of analysis, that the turbulence which is considered to be responsible for the magnetic field perturbations is isotropic in nature, and that there is equipartition between the magnetic and turbulent kinetic energy (Heitsch et al., 2001b). The CF method to estimate B_{POS} is a statistical method that accompanies an error by a factor of ~ 2 for individual clouds.

The values of ΔV for the sectors 1-8 and for the tail, as identified in Fig. 3.24 (a), are obtained by fitting Gaussian profiles (single component) to the average ^{12}CO spectrum generated for the individual regions. The estimated values of ΔV are listed in the column 5 of Table 3.15. The angular extent of the head within the 9×10^{20} cm^{-2} contour is $\sim 0.6°$, which is ~ 3.5 pc considering its distance as ~ 335 pc (Saha et al., 2020). For the tail, based on the same contour level, the angular extent was found to be 0.3°, which translates to ~ 1.8 pc at 335 pc. Assuming a similar line of sight extent for the cloud and using the hydrogen column density values obtained

Table 3.14: Polarization results of 249 stars observed towards L1172/1174.

Star Id	α (J2000) (°)	δ (J2000) (°)	$P \pm \epsilon_P$ (%)	$\theta \pm \epsilon_\theta$ (°)	Star Id	α (J2000) (°)	δ (J2000) (°)	$P \pm \epsilon_P$ (%)	$\theta \pm \epsilon_\theta$ (°)
1	104.128116	14.231034	1.9±0.4	157±6	63	104.043729	14.115608	4.3±0.3	204±2
2	104.217190	14.287866	1.8±0.5	52±7	64	103.994239	14.075042	1.5±0.2	205±3
3	104.277089	14.354539	5.3±0.6	185±3	65	104.004217	14.059293	3.9±0.4	199±3
4	104.404037	14.248927	3.0±0.3	205±3	66	104.012635	14.040984	2.4±0.5	203±6
5	104.392257	14.247356	2.6±0.4	200±4	67	104.040345	14.029867	3.3±0.2	210±2
6	104.369866	14.251045	3.8±0.4	197±3	68	104.061791	14.012051	2.2±0.2	199±2
7	104.430929	14.299678	3.6±0.7	206±6	69	103.917862	13.901485	2.0±0.1	211±1
8	104.416347	14.309724	2.6±0.8	203±8	70	103.949191	13.887192	2.1±0.2	226±3
9	104.405975	14.334530	2.8±0.6	206±6	71	103.889634	13.873195	3.7±0.4	213±3
10	104.395140	14.329504	3.5±0.6	187±4	72	103.942720	13.852638	2.5±0.3	222±3
11	104.408042	14.326883	2.2±0.6	190±7	73	103.912882	13.847550	2.3±0.2	225±3
12	104.356073	14.301893	1.9±0.5	204±7	74	103.925239	13.830119	1.5±0.2	219±3
13	104.325527	14.320067	3.8±0.6	190±5	75	104.013781	13.855258	1.9±0.1	225±2
14	104.332801	14.304419	2.2±0.5	200±7	76	104.011561	13.846133	1.5±0.3	221±6
15	104.326000	14.281308	1.8±0.1	213±1	77	104.077033	13.878035	2.2±0.6	221±8
16	104.334197	14.356322	2.7±0.2	205±2	78	104.049324	13.862234	2.3±0.4	225±5
17	104.350080	14.363166	1.7±0.1	205±1	79	104.040420	13.856945	2.8±0.9	219±9
18	104.355040	14.404310	3.0±1.0	188±9	80	104.061949	13.859067	4.2±0.3	216±2
19	104.347367	14.418693	2.7±0.7	178±7	81	104.042081	13.844076	2.8±0.8	230±8
20	104.371715	14.402114	2.1±0.5	199±6	82	104.052854	13.842180	2.8±0.2	223±2
21	104.358815	14.413296	2.8±0.5	178±5	83	104.081708	13.949807	3.1±0.5	209±4
22	104.348908	14.424935	1.3±0.3	172±5	84	103.994364	13.897979	4.6±1.0	228±6
23	104.359251	13.983480	1.3±0.3	219±6	85	104.007753	13.895467	3.1±0.6	228±5
24	104.337399	14.017642	1.8±0.2	212±3	86	103.976066	13.879128	3.3±0.7	225±6
25	104.325274	14.085256	4.2±0.1	219±1	87	104.041785	13.895636	4.7±0.5	227±3
26	104.390020	14.071041	1.1±0.1	213±3	88	103.779461	14.166562	1.4±0.4	199±8
27	104.414166	14.191229	1.3±0.2	204±4	89	103.786605	14.168643	0.9±0.1	206±2
28	104.424996	14.165882	2.0±0.4	188±6	90	103.753376	14.158306	5.8±0.6	166±3
29	104.374637	14.199342	1.6±0.2	220±4	91	103.730889	14.107847	3.8±0.4	206±3
30	104.375014	14.189853	2.5±0.4	207±4	92	103.771324	14.083528	2.4±0.5	216±6
31	104.327117	14.135960	2.5±0.6	210±6	93	103.743481	14.053415	3.2±0.5	200±4
32	104.342139	14.143725	4.3±0.4	203±3	94	103.753142	14.055722	3.9±0.4	200±3
33	104.385528	14.097980	1.1±0.3	222±8	95	103.740288	14.046160	3.9±1.0	198±7
34	104.374790	14.115005	2.1±0.1	218±2	96	103.795808	14.041406	3.7±0.3	210±2
35	104.362494	14.132594	2.4±0.6	227±6	97	103.788275	14.044542	3.1±0.8	213±8
36	104.351013	14.165030	2.3±0.1	204±1	98	103.712075	14.044119	1.4±0.2	189±3
37	104.377829	14.145469	3.9±0.4	218±3	99	103.807211	14.052721	4.1±0.1	211±1
38	104.371279	14.155014	3.4±0.5	198±4	100	103.804980	14.054295	3.3±0.4	212±3
39	104.274425	13.991687	2.4±0.5	215±6	101	103.717844	14.098736	1.0±0.1	189±3
40	104.229025	13.979337	1.0±0.3	208±7	102	103.727308	14.084367	3.7±0.6	185±4
41	104.222302	13.960593	1.2±0.2	223±3	103	103.728869	14.078656	2.4±0.5	188±6
42	104.236310	13.952170	2.5±0.7	217±8	104	103.901924	14.271198	1.1±0.2	200±4
43	104.190936	13.956342	1.4±0.2	218±4	105	103.888410	14.261025	0.6±0.1	203±2
44	104.267690	13.917088	1.1±0.2	196±6	106	103.896591	14.258742	1.2±0.3	207±5
45	104.205921	13.888406	1.1±0.3	202±6	107	103.817426	14.327622	2.3±0.6	213±7
46	104.190082	13.877895	1.6±0.1	199±1	108	103.799506	14.333130	1.1±0.2	172±6
47	104.189132	13.884124	2.5±0.7	228±8	109	103.810584	14.308802	0.9±0.3	210±7
48	104.133295	13.852779	1.8±0.3	60±4	110	103.804584	14.310143	2.5±0.6	185±7
49	104.174435	13.912937	1.4±0.3	208±6	111	103.837299	14.291510	1.7±0.4	223±7
50	104.141667	13.932187	3.4±0.6	207±5	112	103.848589	14.261173	4.1±1.0	157±7
51	104.117886	13.985771	2.7±0.4	211±4	113	103.759157	14.202982	2.0±0.6	195±8
52	104.114463	13.968833	1.6±0.5	222±7	114	103.751810	14.198525	2.0±0.2	214±3
53	104.102274	14.013854	3.5±0.4	200±3	115	103.834634	14.218497	2.0±0.3	183±5
54	104.095605	14.007224	4.0±0.5	213±3	116	103.842941	14.199902	2.5±0.6	188±7
55	104.097804	13.977882	2.8±0.3	212±3	117	103.970348	14.264221	4.6±0.3	125±2
56	104.105705	13.906279	3.7±0.4	228±3	118	103.795807	14.224410	2.1±0.6	208±9
57	104.104955	13.879472	2.8±0.9	225±9	119	104.022255	14.231824	2.0±0.5	159±7
58	104.100318	13.922871	2.1±0.4	215±5	120	103.983313	14.557376	1.1±0.1	189±3
59	104.085362	13.965820	3.1±0.7	204±6	121	103.955544	14.539678	1.5±0.1	178±3
60	104.159795	13.895103	1.5±0.3	205±5	122	103.937410	14.509685	0.7±0.2	159±6
61	104.068255	14.095157	2.3±0.3	194±4	123	103.996604	14.520752	2.0±0.5	178±7
62	104.008566	14.116192	4.4±0.2	193±2	124	103.987328	14.504984	1.6±0.1	183±1

Table 3.14: *continued.*

Star Id	α (J2000) (°)	δ (J2000) (°)	P ± ε_P (%)	θ ± ε_θ (°)	Star Id	α (J2000) (°)	δ (J2000) (°)	P ± ε_P (%)	θ ± ε_θ (°)
125	103.970485	14.478970	1.0±0.3	184±7	188	103.427039	13.500412	2.4±0.1	191±1
126	104.017669	14.484564	1.4±0.2	172±4	189	103.445397	13.488413	1.9±0.6	180±7
127	103.894501	14.451970	1.5±0.2	173±4	190	103.420810	13.460331	1.9±0.4	200±5
128	103.884349	14.449414	1.4±0.3	160±6	191	103.433914	13.462983	1.7±0.1	202±1
129	103.822561	14.466048	1.2±0.3	170±6	192	103.569513	13.423153	1.9±0.1	202±1
130	103.884904	14.440311	1.7±0.3	175±4	193	103.577631	13.424342	2.0±0.6	195±6
131	103.858440	14.428986	1.4±0.4	181±8	194	103.615277	13.441983	2.8±0.8	207±7
132	103.822409	14.433230	1.7±0.4	183±7	195	103.613454	13.416918	1.8±0.5	191±7
133	103.841372	14.504933	1.6±0.2	172±3	196	103.662619	13.545521	1.8±0.1	207±2
134	103.852653	14.485000	1.2±0.2	165±5	197	103.681499	13.550944	2.0±0.3	206±4
135	103.833996	14.484050	0.6±0.1	174±6	198	103.638274	13.523002	2.3±0.2	205±2
136	103.872988	14.462072	0.8±0.2	163±8	199	103.653112	13.516389	2.4±0.5	203±5
137	104.271671	14.537384	1.3±0.2	166±3	200	103.662384	13.512556	1.6±0.2	199±3
138	104.242881	14.500877	2.2±0.7	158±8	201	103.680989	13.501700	1.3±0.1	205±2
139	104.184877	14.463091	1.8±0.2	179±3	202	103.691753	13.496346	1.1±0.3	195±5
140	104.180551	14.510612	0.9±0.3	185±8	203	103.610325	13.569492	1.4±0.3	199±4
141	104.196741	14.515530	1.6±0.5	183±7	204	103.615140	13.553508	2.2±0.4	193±4
142	104.133852	14.389952	2.1±0.3	177±4	205	103.657643	13.573459	2.7±0.4	201±4
143	104.201883	14.420479	2.0±0.2	172±3	206	103.622884	13.548024	2.1±0.4	203±5
144	104.206816	14.410361	2.4±0.7	166±8	207	103.625378	13.540711	2.6±0.6	205±6
145	104.166900	14.377326	1.3±0.4	171±8	208	103.620378	13.534314	2.5±0.4	202±4
146	104.210431	14.400087	0.7±0.2	186±6	209	103.631329	13.531912	3.5±0.6	215±4
147	104.203426	14.389243	0.8±0.1	180±4	210	103.750202	13.621534	1.9±0.4	214±5
148	104.277266	14.450763	1.0±0.2	186±4	211	103.718710	13.585106	2.7±0.8	191±7
149	104.278619	14.449882	1.1±0.1	185±2	212	103.737300	13.592209	1.9±0.2	194±3
150	104.146638	14.520769	1.1±0.3	203±8	213	103.743451	13.589382	2.3±0.6	194±6
151	104.159392	14.566307	0.8±0.1	165±4	214	103.690315	13.629575	3.6±0.6	206±4
152	104.237648	14.540158	1.2±0.2	163±5	215	103.699510	13.625001	4.0±0.5	223±3
153	104.259147	14.495868	1.3±0.3	168±6	216	103.682929	13.658846	3.8±0.2	201±1
154	104.270189	14.494670	1.4±0.2	180±4	217	103.683858	13.653563	1.7±0.3	204±5
155	104.272463	14.479830	2.5±0.6	182±7	218	103.685928	13.652803	2.7±0.3	203±2
156	104.177145	14.519745	2.1±0.4	166±5	219	103.898571	13.623524	2.8±0.7	201±7
157	103.735578	13.086863	0.6±0.1	198±2	220	103.824957	13.579997	2.9±0.5	179±5
158	103.751125	13.066935	4.0±0.8	201±5	221	103.814455	13.573526	2.8±0.9	190±9
159	103.757171	13.044135	1.1±0.1	186±2	222	103.855020	13.592059	0.9±0.1	182±3
160	103.784884	13.017830	1.0±0.2	176±3	223	103.817286	13.567570	4.1±0.6	196±4
161	103.666569	13.051837	1.4±0.4	145±6	224	103.907345	13.604975	2.6±0.8	154±8
162	103.664697	13.001426	0.7±0.2	186±5	225	103.890580	13.579406	1.7±0.4	184±6
163	103.527084	13.154722	1.7±0.2	184±3	226	103.924358	13.587156	1.8±0.2	198±4
164	103.579566	13.171484	1.0±0.2	189±5	227	103.895567	13.555001	0.8±0.3	199±8
165	103.561332	13.119313	1.1±0.3	159±5	228	103.867833	13.513033	0.9±0.2	182±4
166	103.388335	13.423807	3.7±1.0	194±7	229	103.530729	13.817294	2.2±0.2	199±2
167	103.425854	13.408299	2.8±0.9	185±8	230	103.522295	13.800443	2.0±0.2	192±2
168	103.391221	13.371439	2.0±0.1	189±1	231	103.536011	13.799642	3.1±0.2	204±1
169	103.396714	13.370003	0.9±0.3	184±6	232	103.513589	13.762300	2.2±0.4	207±5
170	103.432276	13.357525	2.1±0.1	191±1	233	103.446568	13.834850	1.4±0.4	196±6
171	103.453856	13.366588	2.6±0.6	191±6	234	103.469665	13.821971	1.6±0.1	200±2
172	103.496048	13.316274	2.2±0.3	201±3	235	103.561086	13.923598	1.3±0.3	207±5
173	103.466449	13.297720	1.5±0.3	200±4	236	103.576086	13.925862	1.8±0.4	195±5
174	103.517554	13.306443	2.4±0.5	195±5	237	103.578790	13.925869	2.0±0.4	205±4
175	103.484429	13.259809	2.3±0.5	200±5	238	103.500559	13.963767	0.9±0.3	202±6
176	103.528156	13.281864	1.9±0.2	192±3	239	103.515728	13.971093	1.8±0.2	191±2
177	103.547924	13.271056	2.2±0.1	198±1	240	103.531432	13.964377	2.1±0.1	189±1
178	103.532947	13.236985	3.5±0.5	190±4	241	103.524179	13.922084	2.2±0.3	188±3
179	103.432185	13.336416	2.1±0.1	197±1	242	103.632864	14.049986	2.5±0.4	196±4
180	103.446267	13.324590	2.5±0.5	193±5	243	103.648487	14.041594	1.5±0.3	198±5
181	103.413906	13.654661	1.6±0.5	200±7	244	103.873111	13.833073	2.1±0.6	182±8
182	103.403268	13.643440	2.8±0.5	205±5	245	103.941902	13.715247	1.2±0.2	199±3
183	103.369563	13.535764	1.8±0.4	191±5	246	103.882462	13.779338	3.0±0.5	192±4
184	103.399226	13.548511	1.9±0.5	188±6	247	103.943406	13.772898	2.1±0.4	200±5
185	103.376949	13.534869	1.9±0.4	192±4	248	103.920679	13.754134	2.0±0.5	201±5
186	103.405470	13.542955	2.3±0.4	188±4	249	103.946746	13.767981	1.2±0.2	216±3
187	103.407969	13.506287	2.1±0.1	193±1					

Table 3.15: P%, $\Delta\theta$, ΔV, n_{H_2} and B_{POS} in different sectors of L1172/1174 cloud complex.

Id[†]	$\overline{P_R}$[‡] (%)	θ_R^* (°)	$\Delta\theta_R$ (°)	ΔV (kms^{-1})	n_{H_2} (cm^{-3})	B_{POS} (μG)
(1)	(2)	(3)	(4)	(5)	(6)	(7)
1	2.7	199	7	2.2	93	29
2	2.2	213	7	2.1	91	27
3	2.4	212	7	1.8	90	23
4	2.6	219	8	2.2	101	26
5	3.2	200	11	1.3	121	12
6	2.0	200	13	1.5	70	9
7	1.4	173	8	2.1	67	20
8	1.3	177	9	1.8	93	18
tail	2.0	196	6	1.7	113	27

Column 1: [†] the identification numbers of 1-8 regions as shown in Fig. 3.24 (a); [‡] Mean value of P_R in each section; [*] Optical R-band measurements.

towards individual stars for which we made R-band polarization measurements, we calculated an average value for n_{H_2} for each sector and the tail region. The n_{H_2} thus obtained are given in column 6 of Table 3.15. The B_{POS} strength calculated for the head and the tail regions are given in column 7 of Table 3.15. The magnetic field strength is found to be weakest in sector 6, which is due to the combined effect of narrow ΔV and relatively high value of $\Delta\theta_R$. The average value of B_{POS} strength for the entire cloud is found to be $\sim$ 20 μG.

3.17.3 Large scale magnetic field and bulk motion

Overall, the B_{POS} geometry in L1172/1174 cloud complex inferred from both R-band and the *Planck* displays an "S" shape morphology with the field lines changing their orientation smoothly as we move from the head to the tail region with B_{POS} oriented almost parallel to the main filament of the cloud as traced by the 15×10^{20} cm^{-2} contour as seen in Fig. 3.21. In Fig. 3.25 (a) we show the magnetic field geometry of the region surrounding L1172/1174 and L1147/1158 (1.4° × 1.4°) cloud complexes. Based on the ^{13}CO (J=1-0) line study towards the Cassiopia and Cepheus regions, Yonekura et al. (1997) suggests that both the complexes share similar radial velocities (2.7−2.9 km s^{-1}) implying that the two regions are both spatially and kinematically connected. The distance of 340±3 pc to L1147/1158 (Sharma et al., 2020) suggests that both L1147/1158 and L1172/1174 are located roughly at a similar distance from us. At this distance, the spatial separation between the two
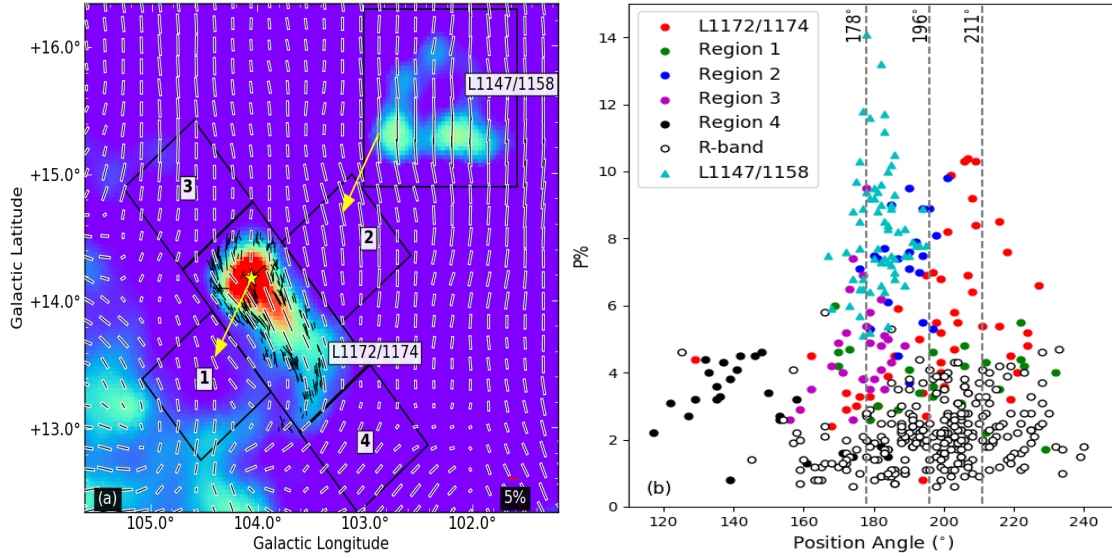
Figure 3.25: (**a**) The magnetic field map (lines in black with white border) of the region covering L1147/1158 and L1172/1174 inferred from the *Planck* polarization measurements. The magnetic field map of L1172/1174 produced using our R-band polarization measurements are also shown using black lines. The arrows show the mean proper motion vector directions of YSOs in L1172/1174 and L1147/1158, obtained from the *Gaia* DR2. (**b**) The boxes (1, 2, 3, 4, L1172/1174 and L1147/1158) are the regions from where we obtained *Planck* polarization measurements are plotted along with our R-band polarization measurements in L1172/1174.

complexes is ~ 9 pc.

In Fig. 3.25 (b) we plot P_P and θ_P from four regions (square boxes of size $0.8° \times 0.8°$) selected around L1172/1174 cloud complex as shown in Fig. 3.25 (a) to examine the large scale magnetic field orientation in the surrounding medium and how it is related to the cloud field lines. The P_P and θ_P from the region containing L1172/1174 are shown using filled circles in red. The P_R and θ_R obtained from our R-band polarization measurements are also shown using open circles in black. The broken lines identify the median values of the two position angle components identified from θ_R towards the head and the median value of the θ_R towards the tail as shown in Fig. 3.24 (b). Also shown are the *Planck* magnetic field orientation from a region containing L1147/1158 using filled triangles in cyan. The median and MAD values of θ_P towards L1148/1157 are 182° and 4° respectively. This is comparable to the 178° component of θ_R in north-west part of head region of L1172/1174. The θ_P distribution found towards the regions 1 (green), 2 (blue) and 3 (magenta filled circles) resembles the θ_P distribution found over the whole cloud complex L1172/1174. This is true for both the R-band and the *Planck* polarization results

suggesting that the cloud is permeated with the ICM magnetic field. The median values of θ_P for regions 1, 2, 3, and 4 are 197°, 190°, 178°, and 141° respectively. The θ_P in regions 1 and 2 are consistent with the median value of θ_R obtained for the tail region. The median value of 178° obtained for the region 3 is consistent with the 178° component obtained towards the sectors 7 & 8 in the head region suggesting that the magnetic field in the head inferred from the R-band polarization measurements is smoothly joining with the ICM field lines inferred from the *Planck* polarization measurements. The 141° component obtained for the region 4 resembles the change in the magnetic field geometry seen towards the tail part in R-band polarization measurements again suggesting a smooth merger between the cloud and ICM field lines. θ_R is found to be relatively scattered in region 1 and in its north-east part, the alignment of θ_R is similar to that of sectors 2 & 3. Globally, regions in north-west (L1147/1158, L1172/1174, 2 and 3) show $\theta_P \sim 180°$ whereas in the south-east part (including 1 and 4) θ_P is highly disturbed.

Based on the Histogram of Relative Orientations analysis (HRO; Soler et al., 2013) with decaying supersonic turbulence, it was shown that in the high-magnetization scenario, the magnetic field changes direction from being parallel to perpendicular with respect to the density structures. The relative orientation becomes random or parallel in the intermediate- or low-magnetization scenario suggesting that the strength of the magnetic field may also play a crucial role. The relative orientation is also found to change progressively with increasing column density, from mostly parallel or having no preferred orientation to mostly perpendicular (Planck Collaboration et al., 2016c). Applying HRO analysis, Soler (2019) presented the orientation of B_{POS} for the Cepheus flare region using the *Planck* polarization data (Fig. 3: Soler, 2019). It was noted that the elongated structure of the cloud complex and B_{POS} are almost parallel across all the column density values in L1172/1174 cloud complex while they are perpendicular in L1147/1158 cloud complex, which is clearly visible in Fig. 3.25 (a). There is also a marked difference between the magnetic field orientation to the north-western and south-eastern parts of L1172/1174. While the magnetic fields show an almost uni-directional pattern (mostly along 180°) in the north-western parts of L1172/1174 where L1147/1158 is also located, to the south-eastern parts, the magnetic field lines show more twists and turns.

Studies conducted to investigate the relative orientation between the filamentary structure and the magnetic field in a sample of molecular clouds associated with the Gould Belt report a bimodal distribution with the offsets being either parallel or perpendicular (Li et al., 2013; Gu & Li, 2019). Results from simulations (Seifried & Walch, 2015) and observational (Li et al., 2017) studies suggest that the bimodality

may have implications in cloud's evolution and subsequent star formation process. The molecular clouds with the long axes perpendicular to the magnetic field directions are shown to have more evenly distributed linear mass across the field lines (Law et al., 2019) and consistently show lower star formation rate (SFR)/mass for clouds (Li et al., 2017). The perpendicular alignment of magnetic field lines possesses a significantly higher flux compared to the parallel orientation and thus provides a stronger support to the molecular clouds against self-gravity (Li et al., 2017). A total of twelve molecular clouds with their SFR/mass and relative orientations of their long axes with magnetic field lines are listed by Li et al. (2017), based on optical and *Planck* measurements. Of these twelve clouds, six have projected magnetic field aligned perpendicular to the longer axes, while this alignment is parallel for other six clouds. Li et al. (2017) found a significant difference in SFR/cloud mass in these two sets of orientations. Our study makes further addition to the findings by Li et al. (2017).

We estimated the SFR in L1172/1174 complex using the total number of YSOs identified towards the cloud and by assuming a mean YSO mass of 0.5±0.1 $M_\odot$ and a period for star formation of 2±1 Myr (Heiderman et al., 2010; Evans et al., 2014; Li et al., 2017). A total of 74 YSOs have been identified so far towards L1172/1174 complex (Saha et al., 2020). Based on their positions on the color-magnitude diagram produced using the data from the *Gaia* DR2, Saha et al. (2020) found an age of ∼1-2 Myr for the YSOs, which is consistent with the median age of ∼1.6 Myr determined by Kun et al. (2009). Also, the majority of the sources identified so far in L1172/1174 complex are of low-mass M-types (0.7-0.1 $M_\odot$), which is found to be consistent with our assumptions. The SFR thus calculated is found to be 19±10 $M_\odot$ Myr^{-1}. The mass of the cloud was estimated by summing up all those pixels having the hydrogen column density threshold of 9×10^{20} cm^{-2} ($A_V \gtrsim$1.0 magnitude) and using it in the expression provided by Bresnahan et al. (2018). We estimated a cloud mass of 950±380 $M_\odot$. The error is estimated by propagating the uncertainties in the column density estimation (taken as 40%, Pokhrel et al., 2016) and in the distance. Recently, Di Francesco et al. (2020) estimated the mass of L1172/1174 as 1000 $M_\odot$ with A_V >1, which is consistent with the mass we obtained. Thus the SFR/mass estimated for L1172/1174 is 2.0±1.3 %Myr^{-1}, which is comparable with the mean value 1.98±0.92 %Myr^{-1} obtained by Li et al. (2017), for the clouds with parallel alignments (e.g., Ophiuchus, Corona Australis, Aquila, Perseus, etc.). Similarly, we estimated the SFR/mass of the neighbouring cloud complex L1147/1158, which has its long axis almost perpendicular to the projected magnetic field direction. Considering the same hydrogen column density threshold (9×10^{20} cm^{-2}) condition, the

mass of L1147/1158 is estimated to be 800±320 $M_\odot$, which is consistent with the mass 790 $M_\odot$, obtained by Di Francesco et al. (2020). A total of 14 YSO candidates (Kirk et al., 2009) including PV Cep are distributed within the defined threshold. The SFR is computed as 3.5±1.9 $M_\odot$ Myr^{-1}. Therefore, the estimated SFR/mass for L1147/1158 is 0.4 ± 0.3 %Myr^{-1}, which is significantly lower than the same obtained for L1172/1174. But it is consistent with the mean value for the clouds having magnetic field lines perpendicular to their long axes (0.620±0.37 % Myr^{-1}; Li et al., 2017). These results further support the claim by Li et al. (2017) that if the magnetic field lines are aligned parallel to the cloud's long axis (like in L1172/1174, Ophiuchus, Aquila, Perseus, etc.), the SFR is found to be higher than in the clouds where the magnetic field lines are aligned perpendicular to the cloud's long axis (like in L1147/1158, IC 5146, Pipe Nebula, Taurus, etc.).

Combining the proper motions (μ_l and μ_b) of the YSOs obtained from the *Gaia* DR2 and the radial velocities of L1147/1158 and L1172/1174 cloud complexes from molecular line observations, it was shown that both the cloud complexes are moving towards the Galactic plane (Sharma et al., 2020). In Fig. 3.25 (a), the arrows represent the directions of motion of the YSOs in the plane of the sky determined from the μ_l and μ_b. Assuming that the cloud and the YSOs share the same motion, these arrows represent the projected direction of the motion of the cloud. The relative offset between the directions of the projected motion and the B_{pos} for L1147/1158 and L1172/1174 is 30° and 47°, respectively, implying that both the clouds are moving obliquely with respect to the direction of ambient magnetic field. Using two- (Miniati et al., 1999) and three-dimensional (Gregori et al., 2000) simulations, the motion of a cloud through a magnetized medium was studied and suggested that the interaction depends on the angle between the initial cloud velocity and the background magnetic field. For large angles, the cloud motion can stretch the magnetic field efficiently, amplifying it significantly at the leading edge of the cloud. As we move from L1147/1158 to the region 2 and L1172/1174, the median position angle changes from 183° to 190° and 200°, respectively, which indicates some process that is linked to the formation of the cloud itself.

3.18 Summary and Conclusions

We present the results of our R-band polarization measurements of 249 sources projected on the cloud complex L1172/1174. Combining our results with those from the *Planck* polarization measurements of the region containing the complex,

we studied the magnetic field geometry of the cloud and its relationship with the ICM magnetic field. We summarize the results obtained from this work below:

- The magnetic field geometry inferred from our R-band polarization measurements and from the *Planck* are found to be in good agreement throughout the cloud. The magnetic field is found to be smooth (not chaotic) and oriented along the hub-filament structure of the cloud. The only changes noticed are towards the extreme ends of the head and the tail regions where the magnetic field lines are found to join smoothly with the ambient magnetic fields in the ICM.

- Overall, there is not much effect of the presence of HD 200775 on the magnetic field geometry of the surrounding region except towards north-western part of HD 200775 where field lines are showing relatively larger dispersion in the magnetic field vectors. The ^{12}CO line profile shows the presence of high-velocity clouds in this region, which may be responsible for disturbing the magnetic field geometry.

- The mean magnetic field strength for the entire cloud was found to be $\sim 20~\mu$G. Globally, the magnetic field geometry inferred from the *Planck* polarization is found to be oriented along a mean position angle of 180° towards the north-western side of L1172/1174 where the cloud complex L1147/1158 is located. At the location of the cloud, the magnetic field lines change to a mean position angle of 200° and then to the south-eastern side of L1172/1174, the magnetic field lines show more twists and turns.

- The higher SFR/mass of $2.0\pm1.3~\%\mathrm{Myr}^{-1}$ found for L1172/1174, compared to $0.4\pm0.3~\%\mathrm{Myr}^{-1}$ for L1147/1158, is consistent with the earlier results, which suggests that the molecular clouds with magnetic field lines oriented parallel to the cloud elongation are found to show relatively higher values of SFR compared to those with field lines perpendicular to the cloud elongation.

Chapter 4

Star formation around comoving HAeBe stars in the Cepheus Flare

4.1 Introduction

It is now widely accepted that a majority of star formation in the Galaxy does not occur in isolation but happens in groups or clusters (e.g., Elmegreen & Clemens, 1985; Evans, 1999; Carpenter, 2000; Lada & Lada, 2003). These aggregations are characterized by the number of members (N) contained in them and are often classified as groups if N < 100 and clusters if N > 100 (e.g., Adams & Myers, 2001). The richness of a stellar system depends on its most massive member, with the low-mass stars forming in small loose aggregates while the high-mass stars are usually found in dense clusters (Zinnecker & Yorke, 2007). There are growing evidence that even the Sun was formed in a group or cluster of stars, with a high-mass star that exploded as a supernova while our Sun was in its early stage of formation (e.g., Looney et al., 2006; Adams, 2010). The intermediate-mass stars falling in the mass interval $2 \lesssim M/M_\odot \lesssim 10$ are therefore of particular interest as they form a connection between well understood low-mass star formation and the enigmatic high-mass star formation. The pre-main sequence (PMS) stars that fall in the above mass range are known as Herbig Ae/Be stars (HAeBes; Herbig, 1960; Waters & Waelkens, 1998). Herbig (1960) first categorized sources as HAeBe stars, which are of spectral types B, A, and F showing emission lines, located in an obscured region and illuminates a bright nebula in its immediate vicinity. Though later observations revealed that these type of sources can be found in isolation and show IR excess due to the presence of circumstellar disks (Hu et al., 1989; Oudmaijer et al., 1992; The et al., 1994;

---

[1]The results presented in this chapter are under revision in A&A.

4. STAR FORMATION AROUND COMOVING HAEBE STARS IN THE CEPHEUS FLARE

Waters & Waelkens, 1998; van den Ancker et al., 2000; Meeus et al., 2001). Several astrometric and spectroscopic studies have been carried out on a large number of HAeBe stars recently by compiling them from the literature (Fairlamb et al., 2015; Vioque et al., 2018; Arun et al., 2019; Wichittanakom et al., 2020).

Several photometric studies of the fields containing HAeBe stars were performed in near- (Testi et al., 1997; Testi et al., 1998; Testi et al., 1999; Wang & Looney, 2007) and mid-IR (Habart et al., 2003) bands. These studies were based on the notion that the reduced extinction at these wavelength regimes would allow the detection of an accompanying population of low-mass embedded YSOs that might have possibly formed along with HAeBe stars in the same star formation event. The results suggested an apparent relationship between the spectral type of HAeBe stars and the richness of the embedded population around them. While the early-type Be stars are usually found within rich clusters, the late-type Be and Ae stars are never associated with any discernible group of YSOs (Testi et al., 1997; Testi et al., 1998; Testi et al., 1999).

The low-mass counterparts of HAeBe stars are T Tauri stars (TTS), the young stellar objects (YSOs) showing Balmer lines of hydrogen in emission (Appenzeller & Mundt, 1989), which is considered as a sign of active accretion of material from the surrounding circumstellar disk. Based on the equivalent width of $H\alpha$ emission line, the TTS are classified into classical T Tauri stars (CTTS) and weak-line T Tauri stars (WTTS). In WTTS, equivalent width of $H\alpha$ is weakly present ($\lesssim 10$ Å) or absent (naked T Tauri stars), which is considered to originate from the chromosphere (Barrado y Navascués & Martín, 2003). Based on an empirical sequence, YSOs can also be classified using the slope of their spectral energy distribution (SED) in the near-IR to sub-millimeter wavelengths. The low-mass YSOs that are deeply embedded are classified as "Class 0" objects, whereas those which are more evolved but still embedded in their envelope are "Class I" objects. Sources showing excess IR emission due to the presence of circumstellar material in a flattened geometry are "Class II" objects and sources having little or no IR excess emission are "Class III" objects (Lada, 1987; Andre et al., 1993; Greene et al., 1994). Though refinements to the above classification scheme were suggested in subsequent studies (e.g., Robitaille et al., 2007; Evans et al., 2009; McClure et al., 2010), it adequately presents an evolutionary sequence of YSOs. The Class II and Class III objects generally correspond to CTTS and WTTS, respectively. Thus, low-mass YSOs can be identified by carrying out photometry in near- and mid-IR bands and by $H\alpha$ surveys to detect emission line sources. Acquiring the physical properties among high-mass HAeBe stars and low-mass TTS is necessary for a full understanding of their formation and

evolution.

Of the HAeBe stars studied by Testi et al. (1998), HD 200775 was found to be peculiar as no surface density enhancement was detected in spite of it being a B2/3Ve spectral type star (The et al., 1994; Manoj et al., 2006). HD 200775 is responsible for illuminating a bright reflection nebula NGC 7023 located to the northern edge of an elongated molecular cloud LDN 1172/1174 (hereafter L1172/1174; Lynds, 1962), situated at a relatively high Galactic latitude ($l \sim 104.1°$, $b \sim +14.2°$) in the Cepheus Flare region at a distance of 335±11 pc (Saha et al., 2020). Kun et al. (2009) did a comprehensive study of star formation towards the Cepheus Flare region, where several signposts of low- to intermediate-mass star formation were analyzed. Another cloud complex, LDN 1147/1158 (hereafter L1147/1158), located about 2° to the north-west of L1172/1174 is also found to be located at a distance of 340 ± 3 pc (Sharma et al., 2020), consistent with that of L1172/1174. In addition to these, LDN 1177 (hereafter L1177), also known as CB 230 (Clemens & Barvainis, 1988), is located to the south-east of L1172/1174 at an angular distance of 1.5°. One of the stars, BD+67°1300, which illuminates the reflection nebula GN 21.15.8 (Magakian, 2003) and hence associated with L1177 (Kun et al., 2009) is found to be at a distance of 341^{+2}_{-3} pc (Bailer-Jones et al., 2018). The large-scale ^{13}CO (J=1-0) survey of the Cepheus and Cassiopia region made by Yonekura et al. (1997) show that these clouds share similar radial velocities ($2.7 - 2.9$ km s^{-1}) suggesting that all the three regions are both spatially and kinematically connected.

PV Cep, an A5 HAeBe star (Cohen et al., 1977), is situated to the north-eastern edge of L1147/1158 complex. Two emission line stars, HD 203024 and BD+68°1118, are found to be located at the north and towards the outer edge of the diffuse part of L1177. Both the stars, which are of B8.5V spectral type, are classified as Herbig Ae/Be candidates by Kun et al. (2000) and are considered to be part of the region. Later, Kun et al. (2009) estimated spectral type of BD+68°1118 to be A2. The distance and the proper motion values of BD+68°1118 ($d = 334^{+2}_{-3}$ pc, $\mu_{\alpha\star} = 7.778 \pm 0.042$ mas yr^{-1}, $\mu_{\delta} = -0.992 \pm 0.040$ mas yr^{-1}) and PV Cep ($d = 341^{+7}_{-7}$ pc, $\mu_{\alpha} = 8.228 \pm 0.126$ mas yr^{-1}, $\mu_{\delta} = -1.976 \pm 0.110$ mas yr^{-1}) obtained from the *Gaia* DR2 are found to be consistent with those of L1172/1174 (Saha et al., 2020). Thus, there are at least three early-type sources, namely, HD 200775, BD+68°1118, and PV Cep associated with the three star forming regions (no *Gaia* DR2 counterpart for HD 203024). These results imply that star formation is prevalent around L1172/1174 and extends over a wider area. The molecular cloud groups L1147/1158, L1172/1174, and L1177, the intermediate-mass stars PV Cep, HD 200775, BD+68°1118 and HD 203024, and the known YSOs found to-

wards the region are shown in Fig. 4.1 (LHS). Saha et al. (2020) identified 20 new comoving sources around HD 200775. Are there new comoving sources associated with BD+68°1118 and PV Cep also? A majority of new comoving sources found around HD 200775 are low-mass stars having considerably low near- and mid-IR excess emission. Spectroscopy of some sources shows Hα in emission but with smaller (∼10 Å) equivalent widths (Saha et al., 2020). Consequently, they escape detection in large-scale Hα and near- and mid-IR surveys. Therefore, it is possible that comoving sources could exist around the neighbouring HAeBe stars as well. In this study, we searched for this category of sources and made a preliminary study of them.

The investigation for additional comoving sources was made towards a circular region of radius 3.5° centered on HD 200775 containing the cloud groups L1147/1158, L1172/1174 and L1177 using the latest *Gaia* DR2. Based on optical and IR color-color and color-magnitude diagrams, we describe their characteristics. A complete census of young sources associated with a region is important since the knowledge of their spatial distribution is a key to understand the star formation history. The paper is organized in the following manner. We present the archival data used in this work in §4.2 and discuss our results in §4.3. Finally, we conclude this work with a summary given in §4.4.

4.2 Archival Data

Gaia DR2 (Gaia Collaboration et al., 2018) presents positions, parallaxes, and proper motions of more than a billion objects with unprecedented precision. But if the relative uncertainties in parallax values were $\gtrsim 20\%$, the corresponding distances wouldn't follow the simple inversion of their parallaxes (Bailer-Jones, 2015). Recently, Bailer-Jones et al. (2018) provided a probabilistic estimate of the stellar distances from the parallax measurements (provided by *Gaia* DR2), using an exponentially decreasing space density prior which is based on a galactic model. In our analysis, the stellar distances and proper motion values were obtained from Bailer-Jones et al. (2018) and from Gaia Collaboration et al. (2018), respectively, by giving a search around a circle of radius of $1''$ around the source positions.

To characterize the properties of the comoving sources identified in this work, we obtained their 2MASS (Skrutskie et al., 2006) and *WISE* (Wright et al., 2010) from Cutri et al. (2003) and Cutri & et al. (2012) catalogues, respectively. We also acquired PanSTARRS photometric data from Chambers et al. (2016). Only sources
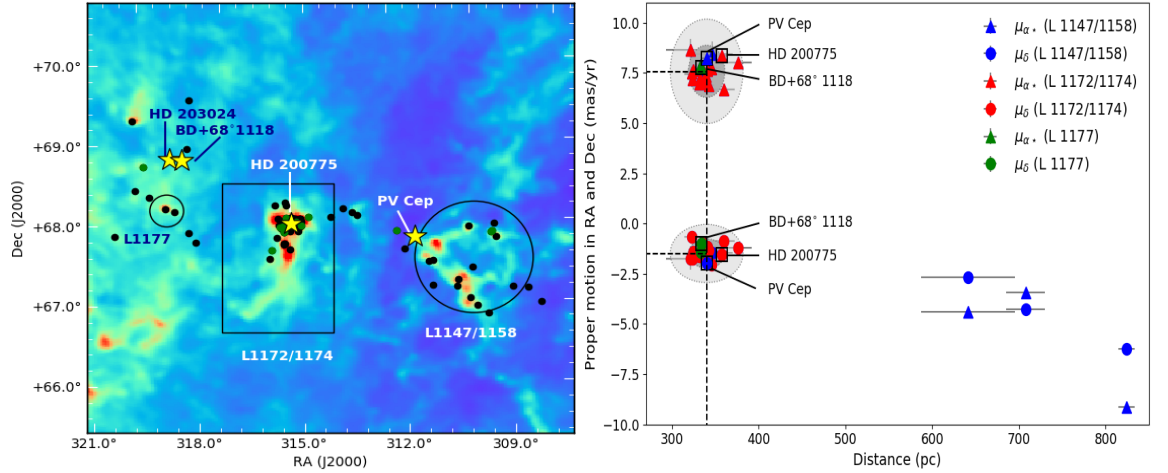
Figure 4.1: **(LHS)** The area studied in this work is shown in a $5° \times 5°$ *Planck* 857 GHz image. The regions include L1147/1158, L1172/1174 and L1177 cloud groups. The circles and rectangle show the extent of these groups. Positions of four intermediate-mass stars, HD 203024, BD+68°1118, HD 200775 and PV Cep, are indicated by star symbols in yellow. The black filled circles show the locations of YSOs obtained from the literature not detected in *Gaia* DR2. The green filled circles indicate the YSOs having reliable detection in *Gaia* DR2. **(RHS)** Proper motion values of the known YSO candidates as a function of their distances obtained from *Gaia* DR2. The triangles and circles in blue, red and green represent the distance-$\mu_{\alpha\star}$ and distance-μ_δ values of the sources located toward L1147/1158, L1172/1174 and L1177, respectively. The error ellipses corresponding to $3 \times$ MAD (darker shade) and $6 \times$ MAD (lighter shade) in proper motion and distance values are drawn. Locations of HD 200775, BD+68°1118 and PV Cep are also marked. The dashed lines show the median values of distance, $\mu_{\alpha\star}$ and μ_δ.

with photometric quality 'A' (SNR≥10) in all bands were considered.

4.3 Results and Discussion

4.3.1 Search for comoving sources around BD+68°1118, HD 200775 and PV Cep

Saha et al. (2020) identified 20 new comoving sources in the vicinity of HD 200775 based on the distance and proper motion values obtained from Bailer-Jones et al. (2018) and Gaia Collaboration et al. (2018), respectively. Following a similar methodology, we searched for comoving sources in the vicinity of BD+68°1118 and PV Cep. First, we collated all the known YSOs that are identified till date in the vicinity of L1147/1158, L1172/1174 and L1177 from literature. We found a

4. STAR FORMATION AROUND COMOVING HAEBE STARS IN THE CEPHEUS FLARE

total of 23, 58 and 13 YSO candidates (after accounting for the common sources among various studies) in the vicinity of L1147/1158, L1172/1174, and L1177 (Kun, 1998; Dunham et al., 2008; Kirk et al., 2009; Kun et al., 2009; Yuan et al., 2013), respectively. The list of the 58 sources found in the vicinity of L1172/1174 is provided in Table 3.3. We have listed the sources projected towards L1147/1158 and L1177 in Table 4.1. The distance and proper motion values for the YSO candidates were obtained from the Bailer-Jones et al. (2018) and Gaia Collaboration et al. (2018) catalogues, respectively. The sources were selected based on three criteria, (1) sources for which m/$\sigma_m \geqslant 3$ (where m stands for d, $\mu_{\alpha\star}$ and μ_δ values and the σ_m represents their respective errors); (2) sources that are at a distance $\leqslant 1$ kpc, and (3) sources having RUWE (Lindegren, 2018) $\leqslant 1.5$. A brief discussion about RUWE is provided in chapter 3.

Based on our selection criteria, we obtained *Gaia* DR2 counterparts for 24 sources (7 from L1147/1158 region, 15 from L1172/1174 region and 2 from L1177 region) well within a search radius of $1''$ radius (see Table 4.2). Of the 24, 18 sources have RUWE $\leqslant 1.4$ and 4 sources have 1.4<RUWE$\leqslant$1.5. To include the later sources also in our analysis, we adopted the limiting value of RUWE as 1.5 instead of the typical value of 1.4 as one of our criteria for selecting the sources. Though the RUWE value for HD 200775 is ~1.6, we included it also in our analysis. One source, *Gaia* DR2 2270941147188904704, associated with L1147/1158, does not have any estimated RUWE. The source has no G_{BP} and G_{RP} values given in the *Gaia* DR2 catalogue but has reliable proper motion and distance measurements (m/$\sigma_m \geqslant 3$) and hence included in our analysis. We obtained the median and MAD for these 24 YSO candidates. The median $d = 340\pm7$ pc, $\mu_{\alpha\star} = 7.580\pm0.434$ mas yr^{-1} and $\mu_\delta = $ -1.495$\pm$0.242 mas yr^{-1}. The *Gaia* DR2 results for the YSO candidates from L1147/1158 (blue), L1172/1174 (red) and L1177 (green) are shown in Fig. 4.1 (RHS). The triangles and circles represent the distance-$\mu_{\alpha\star}$ and the distance-μ_δ values, respectively. 21 sources are found to form a tight group, while 3 sources belonging to the L1147/1158 region seem to be clear outliers. The ellipses with darker and lighter shades are defined by 3 $\times$ and 6 $\times$ MAD values of proper motion and distance, and the dotted lines represent corresponding median values. Considering that all the sources that form the tighter group fall within 6 $\times$ MAD values, we used this as the criterion to select additional comoving sources from the regions.

In order to identify the comoving sources around BD+68°1118 and PV Cep, we first obtained the proper motions and distances of all the sources that fall within a circular region of radius 3.5° centered on HD 200775. The choice of the search region

Table 4.1: YSOs & candidates associated with the clouds.

No.	Source Name	RA (°)	Dec (°)	Detection by *Gaia* DR2
(1)	(2)	(3)	(4)	(5)
	sources associated with L1147/1158			
1	2MASS J203109996700272	307.791647	67.007567	✓
2	2MASS J203232776712207	308.136621	67.205802	✓*
3	2MASS J203418996714289	308.579205	67.241368	✓
4	IRAS 203536742	308.943021	67.883888	-
5	2MASS J203547946802564	308.949804	68.049007	✓
6	2MASS J203611656757093	309.048586	67.952615	✓
7	IRAS 203596745	309.082766	67.942137	✓
8	2MASS J203740296656231	309.417882	66.939775	✓*
9	2MASS J203852386702466	309.718280	67.046303	-
10	2MASS J203904646731116	309.769411	67.519903	✓*
11	IRAS 203866751	309.775800	68.037500	-
12	2MASS J203942986708302	309.929009	67.141717	-
13	2MASS J204056646723047	310.236040	67.384670	-
14	[DCE 2008] 033	310.274790	67.305810	-
15	[DCE 2008] 034	310.981290	67.647310	-
16	V* FI Cep	311.040550	67.340000	✓*
17	[DCE 2008] 035	311.113210	67.643310	-
18	PV Cep	311.474807	67.960744	✓
19	2MASS J204721826748506	311.840900	67.814059	-
20	2MASS J204810266803018	312.042763	68.050522	✓
21	[K98c]Em* 16	313.272730	68.261115	-
22	2MASS J205347636818038	313.448457	68.301083	-
23	2MASS J205453026820375	313.720958	68.343765	✓
	sources associated with L1177			
1	IRAS Z21128+6741A	318.388758	67.899749	-
2	[K98c] Em* 52	318.618260	68.012434	-
3	IRAS 21147+6851	318.853989	69.060171	-
4	[K98c] Em* 53	318.899806	69.679917	✓
5	HD 203024	319.012706	68.914472	-
6	BD+67°1300	319.109702	68.260155	✓
7	IRAS 21169+6804	319.410920	68.292780	-
8	BD+68°1118	319.413251	68.919365	✓
9	[K98c] Em* 55	319.966593	68.426709	✓*
10	[K98c] Em* 58	320.241055	68.805108	✓
11	[K98c] Em* 59	320.447883	68.495148	-
12	2MASS J21225426+6921344	320.726108	69.359572	✓*
13	IRAS 21229+6741	320.951411	67.905562	-

sources associated with L1172/1174 are listed in Table 3.3.

was made based on the fact that all the 94 YSO candidates that are identified in the vicinity of L1147/1158, L1172/1174 and L1177 fall within this circular region. The advantage of selecting a wider region to search for comoving sources is that this will allow us to ascertain whether the comoving sources are distributed uniformly over

4. STAR FORMATION AROUND COMOVING HAEBE STARS IN THE CEPHEUS FLARE

the entire region or are clustered around the regions of current star formation. While a uniform distribution of comoving sources could imply that they are just a chance projection of field stars, a clustered distribution nearer to any of the existing star forming regions would imply that they are likely to be members of the respective star forming regions. We found a total of 62,637 sources within the circular area of radius 3.5°. Here again, to select the sources, we used the same three criteria that we used for selecting the *Gaia* DR2 counterparts for the known YSO candidates ($m/\sigma_m \geqslant 3$, distance $\leqslant 1$ kpc, RUWE$\leqslant 1.5$). Of the 62,637 sources, 74 are found within the ellipses defined by the $6 \times$ MAD values of proper motions and distance and drawn at the median values obtained for the known YSO candidates.

The proper motion and distance values of the 74 comoving sources are shown in Fig. 4.2 (LHS) and the results are presented in Table 4.3. The distance-$\mu_{\alpha\star}$ and distance-μ_δ values of the comoving sources are shown using open triangles and circles in blue, respectively, and the corresponding values of the known YSO candidates are shown using filled triangles and circles in red, respectively. The ellipses drawn in grey in Fig. 4.2 (LHS) represent the constraint of $6 \times$ MAD drawn at the median values of d, $\mu_{\alpha\star}$ and μ_δ of the known YSO candidates. Here again, the d, $\mu_{\alpha\star}$ and μ_δ values of HD 200775, BD+68°1118 and PV Cep are marked. As in the case of the known YSO candidates, a similar clustering of a number of sources are apparent. The $\mu_{\alpha\star}$-μ_δ values of both the comoving and the YSO candidates are shown in Fig. 4.2 (RHS) using open circles in blue and filled circles in red, respectively. A clustering of sources is clearly noticeable when compared with the sources that fall outside the ellipses in Fig. 4.2 (RHS). Some of the sources that fall inside the ellipse in Fig. 4.2 (RHS), but not selected are those that do not satisfy the distance criterion, they fall just outside the ellipses drawn in this figure.

The distribution of the known YSO candidates (circles in red) and the 74 comoving sources (circles in yellow) are shown on the color-composite image made using *Planck* 353 (red), 545 (green), and 857 (blue) GHz images in Fig. 4.3. The arrows in red and yellow show the proper motion directions of the known YSO candidates and newly identified comoving sources, respectively. HD 200775, BD+68°1118, and PV Cep are identified and labeled. The distribution of the comoving sources is not uniform over the entire search area but concentrated mainly towards HD 200775, BD+68°1118, and HD 203024.
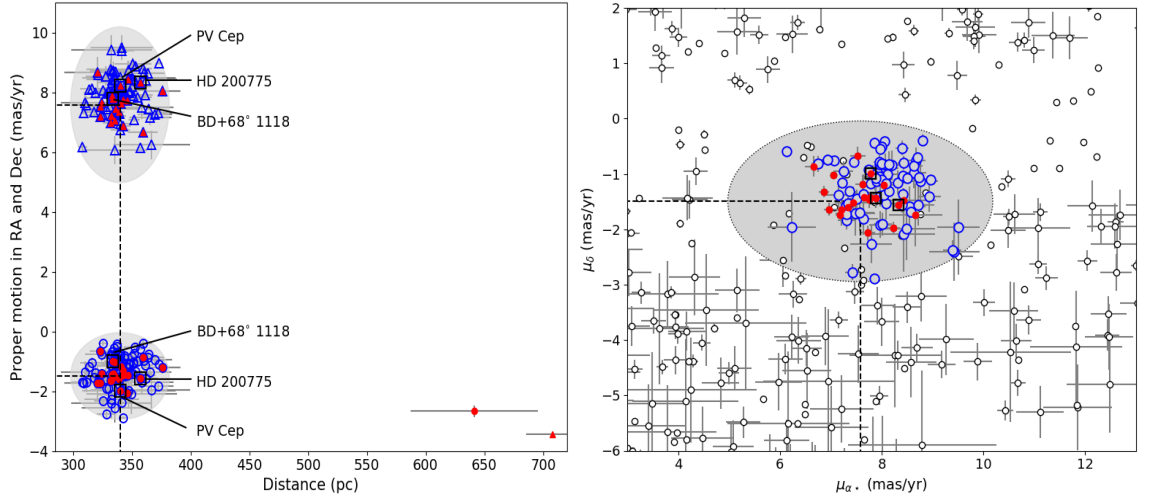
Figure 4.2: **(LHS)** Proper motion vs. distance plot for the known YSO candidates and the newly identified comoving sources. The filled triangles and circles in red represent the distance-$\mu_{\alpha\star}$ and distance-μ_δ values of the known YSO candidates in L1147/1158, L1172/1174, and L1177. The open blue triangles and circles are the distance-$\mu_{\alpha\star}$ and distance-μ_δ values of the comoving sources, respectively. Locations of HD 200775, BD+68°1118, and PV Cep are identified by square boxes. The grey ellipses represent the boundaries of the proper motion values and the distance ranges used to identify the new comoving sources. The dashed lines show the median values of distance, $\mu_{\alpha\star}$ and μ_δ. **(RHS)** μ_δ vs. $\mu_{\alpha\star}$ plot for the known YSO candidates and for the comoving sources. Red filled circles represent proper motion values of known YSO candidates in L1147/1158, L1172/1174, and L1177. PV Cep, HD 200775, and BD+68°1118 are marked in black open squares. The open circles in blue represent the same for the comoving sources. The grey ellipse shows the boundary of the proper motion values considered to select the comoving sources. The open circles in black represent sources not satisfying the 6 × MAD conditions in the distance and proper motion values. The dashed lines show the median values of $\mu_{\alpha\star}$ and μ_δ.

4.3.2 Properties of the comoving sources

4.3.2.1 *Gaia* DR2 color-magnitude diagram

In Fig. 4.4 we show the M_G vs. $(G\text{-}G_{\mathrm{RP}})$ color-magnitude diagram (CMD) for the known YSO candidates and the newly identified comoving sources found from this study. The G and G_{RP} magnitudes for the 21 YSO candidates and the 74 comoving sources are obtained from the *Gaia* DR2 database. The PMS isochrones corresponding to 0.1, 0.5, 1, 3, 10, and 60 Myr are also shown. We used two grids of models, the CIFIST 2011-2015 models for low-mass stars (thick curves in black, Baraffe et al., 2015), and the PADOVA tracks Parsec 3.3 for the higher-mass stars (dashed curves in black, Marigo et al., 2017). We converted the G magnitudes
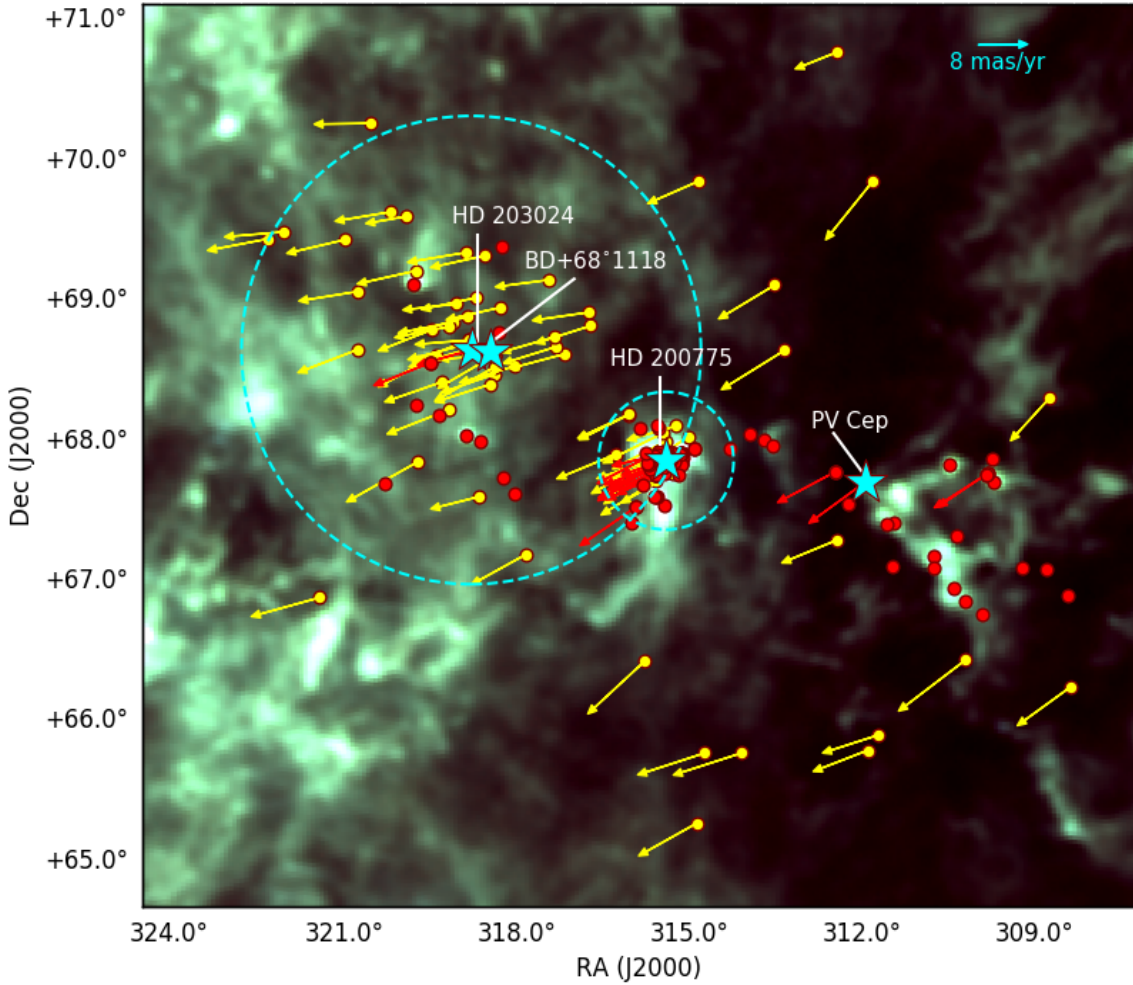
Figure 4.3: Proper motion plot for the YSO candidates (red arrows) and comoving sources (yellow arrows) overplotted on the color-composite image of *Planck* 353 (red), 545 (green) and 857 (blue) GHz images. The YSOs and candidates without detection in *Gaia* DR2 are presented in red filled in circles. HD 200775, HD 203024, BD+68°1118 and PV Cep are indicated by star symbols in cyan. A vector of proper motion 8 mas yr^{-1} is shown as reference.

into absolute magnitudes using the expression $M_G = G + 5 - 5 \log(d)$, where d is the distance taken from Bailer-Jones et al. (2018). Out of the 21 YSO candidates having reliable *Gaia* DR2 data (Table 4.2), extinction values for only 12 of them are available in Kun et al. (2009). As almost half of the sources show lack of extinction values, we made M_G vs. (G-G_{RP}) CMD without extinction correction. The extinction values provided by the *Gaia* DR2 catalogue are not used in our analysis because these values do not show the accuracy at the level of single star (Andrae et al., 2018). Based on a naked stellar model neglecting the contribution from the circumstellar dust, the *Gaia* DR2 provides the effective temperatures and

156

extinction values.

In Fig. 4.4, HD 200775, BD+68°1118 and PV Cep are identified using star symbols in red, cyan and blue colors, respectively. Based on its location, we infer an age of ∼10 Myr for BD+68°1118, which is consistent with the 7 Myr age estimated by Kun et al. (2009). HD 200775 is found to be of ∼0.5 Myr age, which is in agreement with the age estimates available in the literature (Alecian et al., 2008; Arun et al., 2019; Vioque et al., 2018). The position of PV Cep in Fig. 4.4 seems to imply that the star is in its very early stage of evolution (0.1 Myr; Fuente et al., 1998a). As the extinction vector is in general parallel to the isochrones for the sources having $M_G \lesssim 8$ magnitude, the effect of extinction will not affect their age estimation. However, for the sources having $M_G \gtrsim 8$ magnitude, there can be a significant effect of extinction on their age estimate. The green, red, and blue plus symbols indicate the locations of HAeBe stars (The et al., 1994), CTTS and WTTS (Wahhaj et al., 2010).

Assuming that the YSOs and the comoving sources are all formed initially very close to BD+68°1118, HD 200775, or PV Cep as an association or a group, we estimated the extent to which the sources could drift away due to their random velocity dispersion. Using a typical velocity dispersion of ∼1 kms^{-1} (e.g., Gomez et al., 1993; Foster et al., 2015), the age of the intermediate-mass star and a distance of 340 pc, the estimated values are found to be ∼1.7° (∼10 pc), 0.5° (∼3 pc) and 0.02° (∼0.1 pc) for BD+68°1118, HD 200775 and PV Cep, respectively (indicated by dashed circles in cyan in Fig. 4.3 for each star). Though the location of HD 200775 in Fig. 4.4 suggests it to be of ∼0.5 Myr, the positions of the other known YSO candidates associated with the region (identified in Fig. 4.4 using red filled circles with a black halo) suggests a range in the age from ∼1-3 Myr (also see Saha et al., 2020). This is consistent with the median age of the YSO candidates (∼1.6 Myr) obtained by Kun et al. (2009). Thus, in the case of HD 200775, we used an age of 3 Myr in our calculation.

A total of 39 comoving sources are found within the circular region of radius 1.7° centered on BD+68°1118 and 17 comoving sources within the circular region of radius 0.5° about HD 200775. Even though a number of sources close to HD 200775 also fall within the 1.7° circle drawn at BD+68°1118, we assigned them to the HD 200775 group because of their proximity to the star. No comoving sources are found close to PV Cep. The comoving sources associated with BD+68°1118 and HD 200775 are identified in Fig. 4.4 using filled circles in cyan and red, respectively. The 18 sources that are not identified with any of these three regions are shown using filled circles in black. The comoving sources belonging to HD 200775 show a
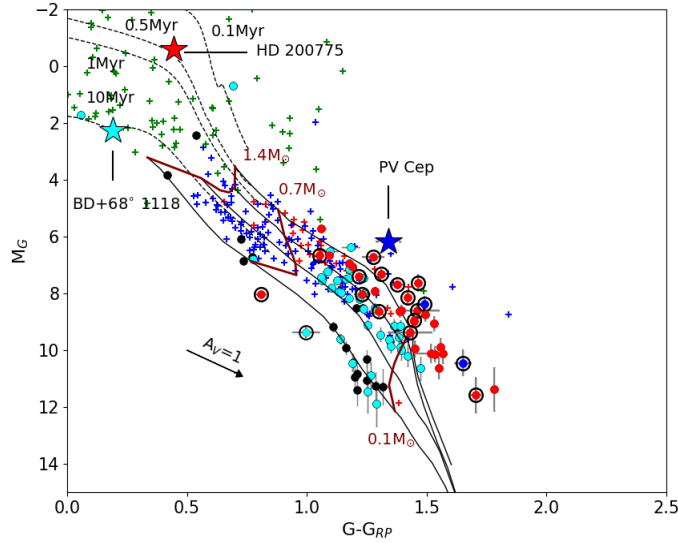
Figure 4.4: The M_G vs. $(G\text{-}G_{\mathrm{RP}})$ colour-magnitude plot of the YSO candidates and the comoving sources. The dashed lines indicate the isochrones from PARSEC models (Marigo et al., 2017) for 0.1, 0.5, 1 and 10 Myr. The solid curves represent the same from CIFIST models (Baraffe et al., 2015) for 1, 3, 10 and 60 Myr. Blue, red and cyan filled circles with and without black open circles are the YSO candidates having reliable *Gaia* DR2 data and comoving sources towards L1147/1158, L1172/1174 and L1177, respectively. The comoving sources not associated with any of the cloud complexes are presented using black filled circles. The green, red and blue plus symbols indicate the HAeBe stars, CTTS and WTTS. The arrow represents extinction of 1.0 magnitude.

well defined sequence roughly following the $1-3$ Myr isochrones similar to the distribution of the known YSO candidates (red circles with a black halo). Spectroscopy of four sources belonging to HD 200775 region shows Hα in emission (Saha et al., 2020), which is considered to be an indicator of their youth as the line is formed mainly due to the accretion process and stellar magnetic activity (Edwards et al., 1994; Muzerolle et al., 1998). It is evident that the comoving sources surrounding BD+68°1118 are showing an age of $\sim$10 Myr which is consistent with the age of BD+68°1118 itself.

4.3.2.2   The (g-r) vs. (r-i) color-color diagram

In Fig. 4.5 we present $(g-r)$ vs. $(r-i)$ color-color (CC) diagram for the sources studied here based on the data obtained from the Pan-STARRs (Chambers et al., 2016) by giving a search radius of $1''$ for individual sources. Symbols in cyan, red and blue filled circles represent the sources belonging to BD+68°1118, HD 200775,

and PV Cep, respectively. Of these, the known YSO candidates are identified using a black halo. The comoving sources falling outside of these three regions are shown using filled circles in black. The grey dots represent the loci of main sequence stars of spectral types ranging from A0 to M7 obtained from the Simbad database and from a region around the star 10 Lac, which shows negligible foreground extinction, based on our previous studies. Of the 94 YSO candidates found in the region, we obtained g, r, and i data for 30 sources, of which 12 are in common with those having *Gaia* DR2 data. Out of 74 comoving sources found in the region, we obtained g, r, and i data for 65 sources. The arrow in Fig. 4.5 represents the reddening vector corresponding to A_V of 1 magnitude.

Reddened and unreddened M-dwarfs occupy a distinct locus in the $(g - r)$ vs. $(r - i)$ CC diagram compared to the rest of the early main-sequence stars and the giants, allowing us to distinguish them clearly. From Fig. 4.5 it is apparent that a majority of the sources identified as known YSO candidates and comoving sources are M-dwarfs. Of these, the comoving sources around BD+68°1118 and those not belonging to any of the three regions follow unreddded M-dwarf loci suggesting a negligible foreground extinction. Some of the YSOs may have a contribution from circumstellar material apart from the foreground extinction. Sources belonging to HD 200775 and PV Cep region are the ones showing relatively higher extinction. The position of PV Cep in Fig. 4.5 suggests it to be a late spectral type source. PV Cep is recognized as a PMS eruptive star, highly variable, still in accreting phase which is also known to show an absorption spectrum similar to a spectral type of G8-K0 star (Magakian & Movsesian, 2001). Though the spectral type of this star is highly uncertain (Cohen et al., 1981; The et al., 1994; Fuente et al., 1998a; Ábrahám et al., 2000; Magakian & Movsesian, 2001), the presence of H_2O MASER emission, presence of a relatively massive circumstellar disk, spectrum showing UV pumped lines in emission and a high jet velocity are shown as the evidence to support the conjecture of PV Cep being an embedded and young Herbig Ae star (Caratti o Garatti et al., 2013). The A_V towards PV Cep is found to be ranging from ∼5-15 magnitude (Caratti o Garatti et al., 2013; Dunham et al., 2013). It is possible that the current position of PV Cep in Fig. 4.5 is due to the foreground as well as circumstellar extinction suffered by the star.

4.3.2.3   Near-IR and mid-IR properties

The near- and mid-IR properties of the newly found comoving sources are investigated by obtaining their 2MASS, and *WISE* magnitudes from Cutri et al. (2003) and
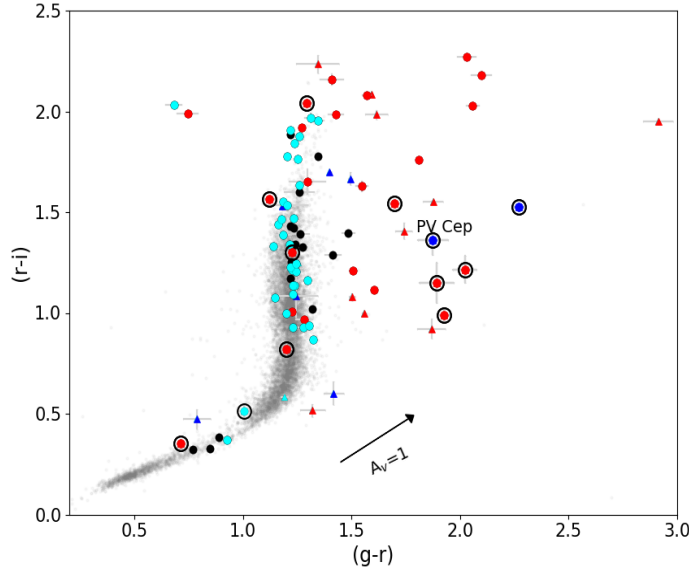
Figure 4.5: The (r-i) vs. (g-r) CC diagram for the known YSO candidates and newly identified comoving sources. Filled circles in cyan, red and blue: comoving sources identified towards BD+68°1118, HD 200775 and PV Cep; Filled open circles in cyan, red and blue with black open circles: known YSO candidates identified towards BD+68°1118, HD 200775 and PV Cep. Filled triangles in cyan, red and blue: YSO candidates not detected/without reliable *Gaia* DR2 data identified towards BD+68°1118, HD 200775 and PV Cep. The comoving sources not associated with any of the three regions are presented using black filled circles. The arrow represents the reddening vector corresponding to A_V of 1 magnitude.

Cutri & et al. (2012) catalogues, respectively. The region surrounding BD+68°1118 was not observed by the *Spitzer* satellite. Out of 74 comoving sources, we found 2MASS counterpart for 65 of them within a search radius of $1''$. Of the 21 known YSO candidates having reliable *Gaia* DR2 data, we found 2MASS data for 18 of them. The known YSO candidates having reliable *Gaia* DR2 data and the comoving sources are shown in the (J-H) vs. (H-K_S) CC diagram in Fig. 4.6 (a). Filled circles in cyan and red represent the comoving sources identified towards BD+68°1118 and HD 200775 respectively. The filled circles in cyan, red and blue with a black halo represent the positions of the known YSO candidates towards BD+68°1118, HD 200775, and PV Cep, respectively. The comoving sources not associated with any of the three regions are presented using filled circles in black. Details of these sources are listed in Table 4.5. The remaining YSO candidates lacking reliable data or detection by the *Gaia* DR2 towards BD+68°1118, HD 200775, and PV Cep are shown using cyan, red and blue filled triangles in Fig. 4.6, respectively.

In Fig. 4.6 (a), while a majority of the known YSO candidates shows a relatively
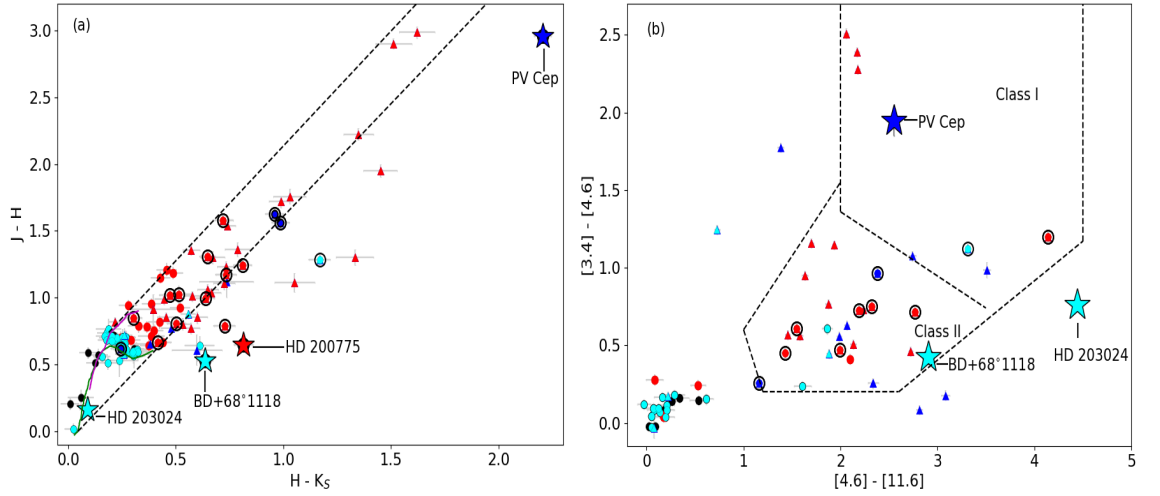
Figure 4.6: **(a)** The (*J-H*) vs. (*H-K_S*) CC diagram for the known YSO candidates and newly identified comoving sources. The blue, red and cyan filled circles with and without black open circles are the YSO candidates having reliable *Gaia* DR2 data and comoving sources towards PV Cep, HD 200775, and BD+68°1118, respectively. The blue, red and cyan filled triangles present the YSO candidates not detected/without reliable *Gaia* DR2 data towards PV Cep, HD 200775, and BD+68°1118, respectively. The comoving sources not associated with any cloud complex are presented using black filled circles. The solid curves in green and magenta represent the loci of the unreddened main sequence stars and the giants, respectively. **(b)** The *WISE* CC diagram for the known YSO candidates and newly identified comoving sources. The symbols represent the same as shown in **(a)**. The dashed lines separate the regions occupied by the Class I and Class II sources (Koenig & Leisawitz, 2014).

high amount of extinction and near-IR excess, the newly identified comoving sources exhibit relatively less extinction and also show a small or negligible amount of near-IR excess emission. PV Cep shows extremely high near-IR excess and extinction, which is consistent with its very young age ($\lesssim$ 1 Myr). Based on the *J*, *H* and *K* magnitudes obtained by Lorenzetti et al. (2015) for PV Cep in 2012 (JD2456101.5), the source is found to be brighter in *J* but got fainter in *H* and *K* significantly when compared to the respective values obtained by the 2MASS in 1999 (JD2451449.6). The $J - H$ (=1.57) and $H - K$ (=1.93) colors of PV Cep during JD2456101.5 are significantly different from the values obtained by the 2MASS showing a highly variable extinction and IR excess emission. The sources, HD 200775 and BD+68°1118, occupy the region normally occupied by HAeBe stars. It is intriguing to note that in spite of being a ~10 Myr star, BD+68°1118 still shows significant near-IR excess. The comoving sources around BD+68°1118, on the other hand, show very less or no

4. STAR FORMATION AROUND COMOVING HAEBE STARS IN THE CEPHEUS FLARE
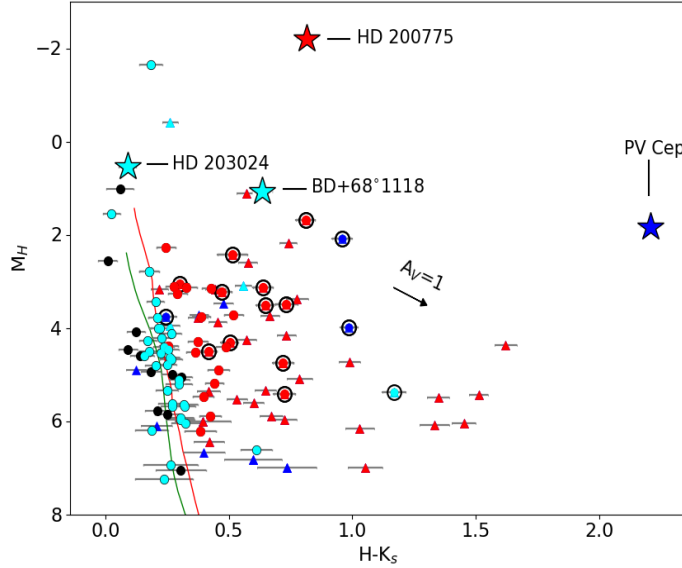
Figure 4.7: M_H vs. H-K_S CMD for the known YSO candidates and newly identified comoving sources. The blue, red and cyan filled triangles present the YSO candidates not detected/without reliable *Gaia* DR2 data towards PV Cep, HD 200775 and BD+68°1118, respectively. The blue, red and cyan filled circles with and without black open circles are the YSO candidates having reliable *Gaia* DR2 data and comoving sources towards L1147/1158, L1172/1174 and L1177, respectively. PV Cep, HD 200775, HD 203024 and BD+68°1118 are indicated by star symbols and marked. The comoving sources not associated with any of the cloud complexes are shown using black filled circles. The arrow represents extinction of 1.0 magnitude.

extinction and near-IR excess emission. A significant number of comoving sources around HD 200775 shows evidence of some amount of extinction and near-IR excess emission. A majority of the comoving sources found in the vicinity of BD+68°1118 are located along the loci occupied by the M-dwarfs, which is consistent with the deductions in Fig. 4.5.

The *WISE* magnitudes of the sources are obtained from the catalogue provided by Cutri & et al. (2012), with a search radius of 3″. We selected only the *W1*, *W2* and *W3* bands as for a majority of them, the magnitudes given in the *W4* band are only an upper limit. We verified the detection of the sources in each of the bands by inspecting them visually in the *WISE* images as we noticed that for a significant number of sources, though the magnitudes in *W3* and *W4* μm bands are provided in the *WISE* catalogue, no detection was found in the corresponding images. The results are shown in Fig. 4.6 (b) in the [3.4]−[4.6] vs. [4.6]−[11.6] CC diagram. Koenig & Leisawitz (2014) used the dashed lines to separate the regions occupied by the YSOs classified as Class I and Class II sources. Of the 74 comoving sources,

we found a counterpart for 29 in the *WISE* database. Out of 21 YSO candidates with reliable *Gaia* DR2 data, we obtained *WISE* magnitudes for 12 sources. Symbols have the same meaning as in Fig. 4.6 (a). Of the remaining known YSO candidates devoid of reliable data or no *Gaia* DR2 detection, we obtained *WISE* magnitudes for 24 sources. The distribution of the known YSO candidates and the comoving sources are more distinguishable in Fig. 4.6 (b). Evidently, the known YSO candidates fall in a region generally populated by Class I and Class II objects. A majority of the newly identified comoving sources fall in a region generally occupied by the Class III sources consistent with our deductions in Fig 4.5 and Fig. 4.6 (a).

In Fig. 4.7 we present M_H vs. (H-K_S) CMD for the previously known YSO candidates and the newly found comoving sources. The symbols are same as in Fig. 4.6. The PMS isochrones of 1 and 10 Myr are taken from the CIFIST models and are shown as red and green curves, respectively. A reddening vector of $A_V = 1$ magnitude is also shown. Evidently, the sources located in the vicinity of HD 200775 show higher values of (H-K_S) colors compared to that of the sources identified towards the association of BD+68°1118. The higher (H-K_S) colors of the sources towards HD200775 could be due to the contribution of a substantial amount of circumstellar and interstellar material present along the line of sight, which is consistent with their relatively younger ages.

4.3.2.4 Spatial distribution of sources surrounding HD 200775 and BD+68°1118

HD 203024, which is located at an angular distance of ∼8.5′ (0.9 pc) west of BD+68°1118, is identified as a spectroscopic binary (Alecian et al., 2013a). The effective temperatures and masses of the components are found to be 9250 K, 6500 K, and 2.8 $M_\odot$ and 1.6 $M_\odot$, respectively. The ages of the components are estimated as 9.3 Myr and 2.7 Myr, respectively (Alecian et al., 2013a). The binary nature of HD 203024 could be the reason why the parallax and proper motion solutions are not listed in *Gaia* DR2 catalogue. Miroshnichenko et al. (1997) and Kun et al. (2000) detected Hα in emission. The assigned spectral type of the star ranges from B8.5V to A5V (Miroshnichenko et al., 1997; Mora et al., 2001; Alecian et al., 2013a). The star was classified as an HAeBe candidate by Kun et al. (2000), and the presence of a debris-disk (Riviere-Marichalar et al., 2016) surrounding the star suggests that it is at an advanced stage of evolution. The proper motion values derived by Fedorov et al. (2011) for HD 203024 are found to be $\mu_{\alpha\star} = 9.89$ mas yr^{-1} and μ_δ = -2.10 mas yr^{-1}, which are in good agreement with those of BD+68°1118, HD 200775 and

4. STAR FORMATION AROUND COMOVING HAEBE STARS IN THE CEPHEUS FLARE

PV Cep. Thus, they together form an isolated intermediate-mass stellar association connected both physically and kinematically but distributed over a wide area in the sky and show ~1-10 Myr age spread.

Although BD+68°1118, HD 200775 and PV Cep, are at similar distances and share similar proper motions, they show stark differences. BD+68°1118 region lacks molecular cloud material within the radial velocity range of 2.7-2.9 km s^{-1} associated with it except L1177 in contrast to the region surrounding HD 200775 and PV Cep (Yonekura et al., 1997). The known YSO candidates and the newly identified comoving sources surrounding BD+68°1118 are distributed over a larger area in the sky in comparison with those surrounding HD 200775, as shown in Fig. 4.8. In this figure, along the vertical axis, we show histograms of the two associations (YSO candidates + comoving sources) towards HD 200775 and BD+68°1118 in white and grey colors, respectively. While all the sources surrounding HD 200775 (described in Saha et al., 2020) are distributed within a spatial distance of ~3 pc from it (a noticeably sharp fall of the number of sources at ~ 1 pc), those surrounding BD+68°1118 are distributed over a distance upto ~10 pc. The sources around BD+68°1118 lack near- and mid-IR excess emission while a significant number of sources around HD 200775 show excess emission. This is consistent with the findings that the sources around BD+68°1118 are relatively more evolved, showing an age of ~3-10 Myr while those around HD 200775 are comparatively younger (~1−3 Myr).

We also present a 3-D distribution of these associations in the rectangular Galactic (x, y, z) coordinate system, as shown in Fig. 4.9. In this system, the Sun is at the center, the (Ox) axis is directed towards the Galactic center from the Sun, the (Oy) axis is orthogonal to the (Ox) axis and is directed towards the Galactic rotation, lastly, the (Oz) axis is perpendicular to the Galactic plane and is oriented towards the Galactic North Pole. BD+68°1118, HD 200775, and PV Cep are indicated by star symbols in green, red, and blue, respectively. Their projections on the X, Y, and Z planes are shown using star symbols in orange (X positive towards the Galactic center, Y positive towards the Galactic east, and Z positive towards the Galactic north). The YSO candidates and comoving sources associated with BD+68°1118, HD 200775, and PV Cep are indicated using green, red, and blue filled circles, respectively. Their respective projections on all the three planes are shown using plus, triangle, and square symbols in grey, respectively.
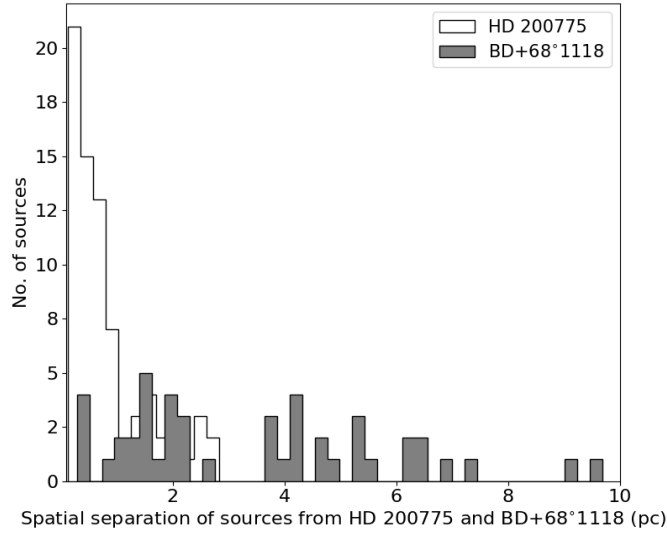
Figure 4.8: Histograms of the spatial distribution of the known YSO candidates and the newly identified comoving sources with respect to HD 200775 (white) and BD+68°1118 (grey).

4.3.2.5 Kinematic properties of the sources with respect to HD200775 & BD+68°1118

The proper motion of a group of young stars in a well defined reference frame shows its motion projected in the plane-of-sky as a whole. However, the proper motion values of each member of the group subtracted from the mean proper motion of the whole group determines their projected internal motion (Jones, 1997). As a natural consequence of star formation, due to the impulsive expulsion of the residual gas in the natal cloud, the young stars may move away from their origins of birth (e.g., Pfalzner & Kaczmarek, 2013). In order to analyze the internal motion of the sources in the sky plane, surrounding BD+68°1118 and HD 200775, we studied their motion relative to the system center.

Fig. 4.10 (a) and (b) represent the relative proper motion (yellow vectors) of the sources distributed around BD+68°1118 and HD 200775, respectively, in the Galactic coordinates. Locations of HD 203024, BD+68°1118, and HD 200775 are marked with red star symbols. The members of the association of BD+68°1118 move outward in all directions while a majority of the sources surrounding HD 200775 tend to move in the north-west and south-east directions, which is also the direction of outflow of HD 200775 (Fuente et al., 1998b), which is currently inactive. The velocity components v_l and v_b along the Galactic longitude and latitude were computed using $v_l = 4.74 d\mu_l$ and $v_b = 4.74 d\mu_b$, respectively. The factor $4.74 \times d$

4. STAR FORMATION AROUND COMOVING HAEBE STARS IN THE CEPHEUS FLARE
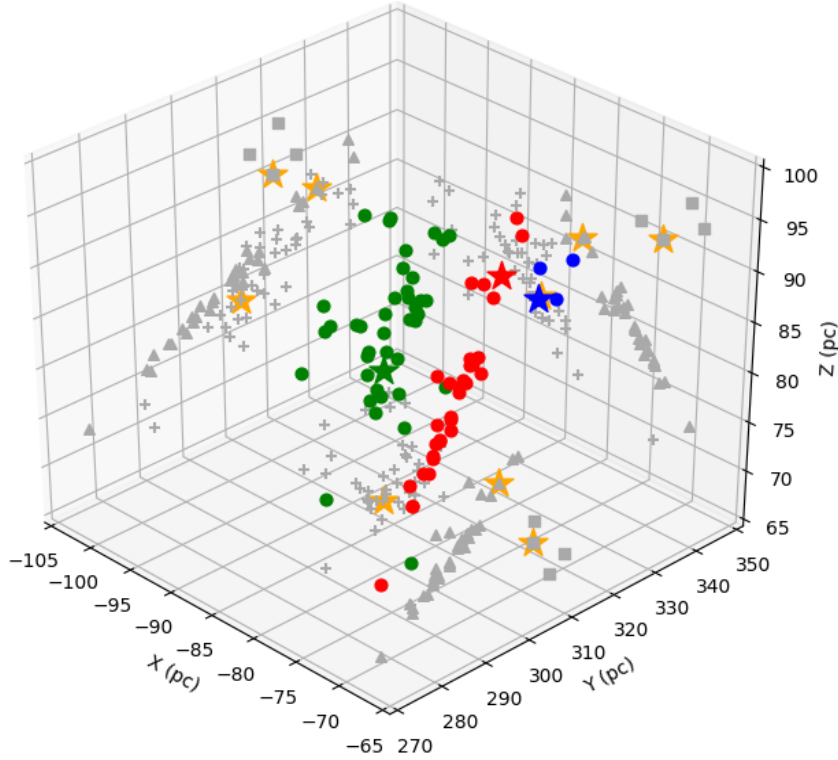
Figure 4.9: The 3D distribution of the known YSO candidates and the comoving sources having *Gaia* DR2 distances. BD+68°1118, HD 200775, and PV Cep are indicated by star symbols in green red and blue, respectively. Their projections on the X, Y, and Z planes are shown using star symbols in orange (X positive towards the Galactic center, Y positive towards the Galactic east, and Z positive towards the Galactic north). The YSO candidates and comoving sources associated with L1177, L1172/1174, and L1147/1158 are indicated using green, red, and blue filled circles, respectively. Their respective projections on all three planes are shown using plus, triangle, and square symbols in grey, respectively.

(kpc) transforms the unit of proper motion from mas yr^{-1} into km s^{-1}. The possible compression/expansion of the associations of BD+68°1118 and HD 200775 were calculated using *Gaia* DR2 proper motions of the surrounding YSO candidates and comoving sources. The parameters of compression/expansion following the methods provided by Mel'nik & Dambis (2017).

$$v_l = v_{l0} + p_l \, dsin(l - l_0) \tag{4.1}$$

$$v_b = v_{b0} + p_b \, dsin(b - b_0) \tag{4.2}$$

where v_{l0} and v_{b0} are the average velocities of the sources in the l and b directions, respectively. l_0 and b_0 are the coordinates of the center of the association. p_l or
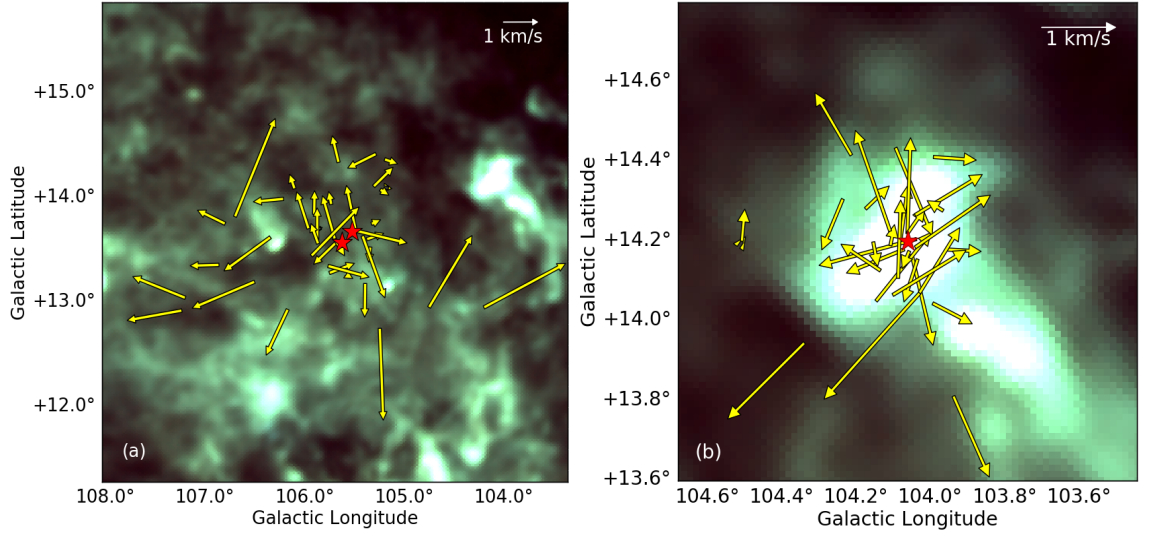
Figure 4.10: **(a)** Proper motion vectors of YSO candidates and comoving sources relative to the proper motion of BD+68°1118 are shown using yellow arrows overplotted on the color-composite image of *Planck* 353 (red), 545 (green) and 857 (blue) GHz images. Positions of BD+68°1118 and HD 203024 are presented using red star symbols. **(b)** Same as **(a)**, but for the system of HD 200775 (marked as red star).

p_b are the parameters which indicate the expansion/compression along the l and b direction (positive and negative values signify expansion and compression of the system, respectively), d is the distance to the association. Using equations (4.3) and (4.4) we estimated mean $p_l = 175 \pm 21$ and $p_b = 80 \pm 40$ km s^{-1} kpc^{-1} for the groups of BD+68°1118 and $p_l = 270 \pm 170$ and $p_b = 360 \pm 160$ km s^{-1} kpc^{-1} for HD 200775, respectively. These values signify that both the systems are expanding. The errors are estimated by propagating uncertainties in the parameters. The observed velocity of expansion in l and b directions are determined using the following equations provided by Mel'nik & Dambis (2017).

$$u_l = p_l a \tag{4.3}$$

$$u_b = p_b a \tag{4.4}$$

where a is the radius of the association in kpc. We estimated a as the radius containing 99.7 per cent of the associated members. Therefore, the computed radii a for the associations of BD+68°1118 and HD 200775 are ∼8 and ∼2 pc, respectively. The estimated u_l and u_b for the association of BD+68°1118 are 1.4±0.2 and 0.7±0.3 km s^{-1} and the same for HD 200775 are 0.5±0.3 and 0.7±0.3 km s^{-1}, respectively. We also estimated the tangential velocities (v_t) of the systems of BD+68°1118 as

4. STAR FORMATION AROUND COMOVING HAEBE STARS IN THE CEPHEUS FLARE
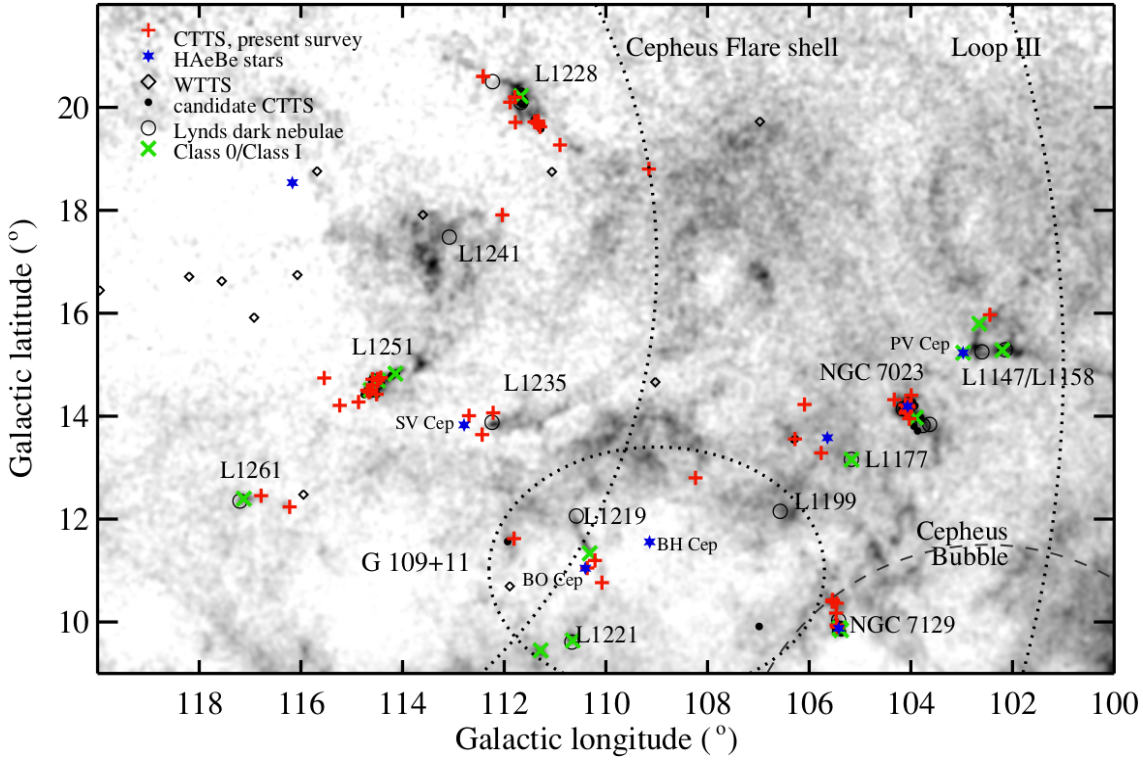
Figure 4.11: Distribution of various clouds and YSOs in the Cepheus Flare region. Figure credit: Kun et al. (2009).

1.5 ± 0.2 and for HD 200775 as 0.9 ± 0.3 km s^{-1} following $v_t = \sqrt{u_l^2 + u_b^2}$.

L1147/L1158, L1172/1174, and L1177 are located outside of the Cepheus Flare Shell (CFS), but near the periphery of Loop III (Kun, 2007). In Fig. 4.11, we present the distributions of these three clouds from Kun et al. (2009). Details of this figure are already described by Kun et al. (2009), hence not discussed here. Located at ~300 pc, these huge, nearly concentric shells are considered to be effects of multiple supernova explosions, indicating the presence of OB stars a few million years ago (Olano et al., 2006; Kun, 2007). The spatial distribution of YSO candidates in the star forming centeres towards the CFS are located close to the edges of the molecular clouds, indicating star formation was possibly induced by expansion of the shell (Kun, 1998, 2007). In our study, we found the age of YSOs to be ~10 Myr towards L1177 (stellar association of BD+68°1118), located innermost to the CFS/loop III, then the sources of age ~1-3 Myr are distributed in L1172/1174 (stellar association of HD 200775), which is located at the middle and the youngest source PV Cep (~0.1 Myr) embedded in L1147/1158, is lying at the outer edge of the CFS/loop III. Therefore, the spatial distribution of the stellar age revealed in our work further confirms the triggered star formation happening in the CFS.

4.4   Summary and Conclusions

We studied the kinematics of the entire region containing four intermediate-mass young sources, namely, BD+68°1118, HD 203024, HD 200775, and PV Cep. Using the *Gaia* DR2 distance and proper motion measurements of sources, we identified new comoving sources surrounding BD+68°1118 and HD 203024. Combining the new comoving sources identified towards HD 200775 (Saha et al., 2020) with the new comoving sources identified in this work, we made an attempt to understand the star formation history of the region as a whole. Our main results are summarized below.

- Our search for comoving sources using the *Gaia* DR2 distance and proper motion values within a circular region of 3.5° radius, containing BD+68°1118, HD 200775, PV Cep and the known low-mass YSO candidates resulted in the identification of 74 sources. Of these, 39 are found to be distributed around BD+68°1118, 17 are around HD 200775, and rest are distributed over a wider region. No comoving sources are found around the much younger PV Cep.

- Based on the *Gaia* DR2 G versus $(G - G_{RP})$ color-magnitude and near- and mid-IR color-color and color-magnitude diagrams, the comoving sources identified around BD+68°1118 are found to be older ($\sim$10 Myr) than those found around HD 200775 ($\sim$1-3 Myr). Mostly the comoving sources are M dwarfs showing no or negligible near- and mid-IR excess emission.

- The positive values of the coefficients p_l and p_b for the stellar associations surrounding BD+68°1118 and HD 200775 indicate that both the systems are in expanding phase with similar tangential velocities.

- The decrease in age of the sources ($\sim$10, 3 and 0.1 Myr for the sources located towards L1177, L1172/1174 and L1147/1158, respectively) with increasing distance from the center of the CFS agrees with the previous studies supporting the concept of triggered star formation happening by the external impacts.

Table 4.2: Properties of the known YSO candidates identified towards L1147/1158, L1172/1174 and L1177 from *Gaia* DR2.

#	RA(2015.5) (°)	Dec(2015.5) (°)	Source ID	Distance (pc)	$\mu_{\alpha\star}$ ($\Delta\mu_{\alpha\star}$) (mas/yr)	μ_δ ($\Delta\mu_\delta$) (mas/yr)	G (eG) (mag)	RUWE	PanSTARRs	2MASS	WISE
(1)	(2)	(3)	(4)	(5)	(6)	(7)	(8)	(9)	(10)	(11)	(12)
				sources associated with L1172/1174							
1	314.845315	68.245467	2270256357606156160	339^{+5}_{-5}	7.333±0.087	−1.599±0.079	14.3789±0.0150	1.1	✓	✓	✓
2	315.084447	68.140772	2270240208529136128	341^{+10}_{-10}	7.630±0.147	−1.182±0.158	17.0301±0.0309	1.1	✓	✓	✓
3	315.231481	68.190885	2270240723925216640	333^{+12}_{-13}	7.205±0.184	−1.649±0.280	16.5545±0.0020	1.3	✓	✓	-
4	315.359984	68.177338	2270245637367812352	325^{+7}_{-13}	7.652±0.104	−1.416±0.121	14.8691±0.0049	1.2	-	✓	✓
5	315.362884	68.177214	2270245637367812608	360^{+13}_{-13}	6.667±0.174	−0.865±0.189	16.3712±0.0266	1.5	-	✓	-
6	315.400352	68.139576	2270245259410695808	332^{+6}_{-6}	6.971±0.106	−1.638±0.117	15.6235±0.0130	1.4	-	-	-
7	315.403923	68.163263	2270245431209611776	357^{+6}_{-5}	8.336±0.079	−1.566±0.083	7.1592±0.0010	1.6	-	✓	-
8	315.427117	68.215960	2270246148467658624	323^{+9}_{-8}	7.530±0.148	−0.668±0.164	15.6942±0.0033	1.5	✓	✓	-
9	315.444875	68.145894	2270057689598399360	335^{+5}_{-4}	7.770±0.071	−1.428±0.078	15.0363±0.0057	1.1	✓	✓	-
10	315.558650	68.233141	2270247492790812928	321^{+26}_{-31}	8.666±0.528	−1.736±0.568	19.1129±0.0059	1.1	-	✓	✓
11	315.617758	68.058287	2270056246489398528	343^{+6}_{-6}	6.868±0.098	−1.319±0.107	15.3618±0.0053	1.1	✓	-	-
11b	315.618244	68.057669	2270056246489398400	376^{+16}_{-15}	8.041±0.193	−1.202±0.215	15.5062±0.0010	1.5	-	-	✓
12	315.637634	68.124746	2270056968043900928	336^{+3}_{-2}	7.054±0.044	−1.017±0.078	14.2794±0.0078	1.0	✓	✓	-
13	315.747855	68.108939	2270053875667453056	323^{+5}_{-4}	7.174±0.079	−1.738±0.075	15.5766±0.0061	1.5	✓	✓	✓
14	315.997585	67.824847	2270035287049455616	346^{+8}_{-9}	7.722±0.152	−2.061±0.133	16.3326±0.0041	1.4	✓	✓	✓
				sources associated with L1177							
1	319.413344	68.919361	2270536045876468096	334^{+2}_{-3}	7.778±0.042	−0.992±0.040	9.8782±0.0004	1.0	-	✓	✓
2	320.241149	68.805102	2222486906706076544	333^{+9}_{-8}	7.888±0.141	−1.440±0.175	16.9815±0.0164	1.2	✓	✓	✓
				sources associated with L1147/1158							
1*	307.791609	67.007548	2246449594402553088	708^{+23}_{-22}	−3.443±0.087	−4.257±0.084	16.4659±0.0008	1.0	✓	✓	-
2*	308.579103	67.241341	2246818824150192768	824^{+10}_{-9}	−9.152±0.029	−6.229±0.031	14.2628±0.0003	1.1	✓	✓	✓
3*	308.949753	68.048996	2247157198854324224	641^{+59}_{-49}	−4.395±0.225	−2.670±0.190	17.7134±0.0017	1.1	✓	✓	✓
4	309.048672	67.952608	2246967838039390848	336^{+23}_{-20}	7.436±0.351	−1.514±0.284	18.0815±0.0108	1.0	-	✓	✓
5	309.082855	67.942131	2246967876695385728	343^{+14}_{-13}	7.753±0.189	−1.469±0.143	16.0569±0.0040	1.2	✓	✓	-
6	311.474902	67.960735	2246924068029363840	341^{+7}_{-7}	8.228±0.126	−1.976±0.110	13.8423±0.0163	1.3	✓	✓	✓
7	312.042682	68.050417	2270941147188904704	347^{+25}_{-22}	8.426±0.637	−1.476±0.221	15.9581±0.0019	-	-	✓	✓

Columns 2 & 3: 2015.5 epoch Right Ascension & Declination of sources given by *Gaia* DR2.
Column 4: Source id taken from *Gaia* DR2.
Column 5: Distance taken from the Bailer-Jones et al. (2018) catalogue.
Columns 6 & 7: Proper motion in Right Ascension & Declination of sources given by *Gaia* DR2.
Column 8: G magnitude of sources given by *Gaia* DR2.
Column 9: Renormalised Unit Weight Error (RUWE) of sources obtained from *Gaia* DR2.
Stars #4 & #5 appear as double sources. Resolved by *Gaia*, 2MASS and *Spitzer*. In *WISE*, they are detected as single source. *WISE* is assigned to the brightest source in K_s band.
Stars #11 & #11b appear as double sources. Resolved only by *Gaia*. 2MASS classified it as an extended source.
* Sources considered as outliers in our analysis.

Table 4.3: Astrometric and photometric properties of the comoving sources identified towards L1147/1158, L1172/1174 and L1177 from *Gaia* DR2.

#	RA(2015.5) (°)	Dec(2015.5) (°)	Source ID	Distance (pc)	$\mu_{\alpha\star}$ ($\Delta\mu_{\alpha\star}$) (mas/yr)	μ_{δ} ($\Delta\mu_{\delta}$) (mas/yr)	G (eG) (mag)	RUWE	PanSTARRs	2MASS	WISE
(1)	(2)	(3)	(4)	(5)	(6)	(7)	(8)	(9)	(10)	(11)	(12)
				sources associated with L1172/1174							
hd_c1	314.963955	68.336928	2270263092114875520	373^{+13}_{-13}	7.315 ±0.177	-1.844 ±0.166	16.8250 ±0.0022	1.0	✓	✓	✓
hd_c2	315.201051	68.415148	2270265016260228608	352^{+5}_{-5}	7.073 ±0.074	-0.752 ±0.079	14.7996 ±0.0009	1.1	✓	✓	✓
hd_c3	315.271845	68.072754	2270238795483033728	340^{+3}_{-3}	7.294 ±0.048	-1.576 ±0.056	13.3625 ±0.0058	1.2	-	✓	-
hd_c4	315.350786	68.150243	2270245289474206848	351^{+17}_{-16}	8.195 ±0.233	-0.846 ±0.271	17.6219 ±0.0026	1.3	✓	✓	-
hd_c5	315.420625	68.301379	2270248798463735808	331^{+9}_{-8}	7.510 ±0.142	-1.452 ±0.170	16.2431 ±0.0011	1.2	✓	✓	-
hd_c6	315.422157	68.182326	2270245465569124608	337^{+6}_{-6}	7.222±0.096	-1.154±0.105	15.5642±0.0020	1.3	✓	✓	-
hd_c7	315.450292	68.115938	2270057517799708032	338^{+13}_{-13}	8.084 ±0.206	-1.537 ±0.280	17.7758 ±0.0019	1.0	✓	✓	✓
hd_c8	315.452017	68.135740	2270057685302330240	350^{+43}_{-34}	8.426 ±0.623	-2.081 ±0.684	19.0878 ±0.0043	1.3	-	✓	-
hd_c9	315.458232	68.158415	2270057723958137600	333^{+12}_{-12}	8.312±0.202	-1.153±0.219	16.6736±0.0013	1.5	✓	✓	✓
hd_c10	315.470563	68.362746	2270252367579936768	328^{+18}_{-17}	8.544 ±0.324	-1.593 ±0.369	18.2045 ±0.0021	1.1	✓	✓	✓
hd_c11	315.501565	68.192440	2270245809166510080	319^{+11}_{-10}	7.975 ±0.177	-1.400 ±0.193	16.2597 ±0.0013	1.3	✓	✓	✓
hd_c12	315.612647	68.015216	2270053081097108480	339^{+17}_{-14}	7.643 ±0.282	-1.804 ±0.294	17.7825 ±0.0020	1.0	✓	✓	-
hd_c13	315.675742	68.172632	2270058651671079808	334^{+15}_{-13}	7.885 ±0.231	-1.042 ±0.250	17.5657 ±0.0052	1.3	✓	✓	✓
hd_c14	315.853497	68.132781	2270055421855682688	318^{+8}_{-8}	7.334 ±0.146	-1.539 ±0.137	16.1028 ±0.0015	1.2	✓	✓	✓
hd_c15	316.150453	68.498418	2270280409423293952	336^{+5}_{-5}	7.372 ±0.078	-1.308 ±0.068	14.5711 ±0.0044	1.4	✓	✓	✓
hd_c16	316.151474	68.496975	2270280405127009024	366^{+19}_{-17}	7.148 ±0.242	-1.375 ±0.237	17.9247 ±0.0174	1.0	✓	-	-
hd_c17	316.394054	68.209051	2270068512916332672	336^{+3}_{-3}	8.417 ±0.054	-1.372 ±0.053	14.2905 ±0.0025	1.2	✓	✓	✓
				sources associated with L1177							
bd_c1	316.970365	69.135322	2270674545683908224	340^{+13}_{-13}	8.110 ±0.195	-1.011 ±0.204	18.1137 ±0.0016	0.9	✓	✓	-
bd_c2	317.016704	69.232990	2270699666950862336	353^{+9}_{-9}	8.401±0.127	-0.533±0.132	16.2560±0.0010	1.4	✓	✓	✓
bd_c3	317.485774	68.926013	2270478145419384832	344^{+20}_{-18}	8.068 ±0.264	-0.894 ±0.264	17.8806 ±0.0015	1.1	-	✓	-
bd_c4	317.660746	68.976917	2270501823576986752	355^{+13}_{-11}	7.821 ±0.155	-1.007 ±0.164	17.2027 ±0.0013	1.1	✓	✓	✓
bd_c5	317.719747	69.045445	2270505396989771904	339^{+4}_{-3}	7.741 ±0.053	-0.928 ±0.058	15.2079 ±0.0009	1.1	✓	✓	✓
bd_c6	317.880961	69.457870	2270709356397123328	337^{+5}_{-5}	8.003 ±0.070	-0.504 ±0.081	15.5943 ±0.0013	1.1	✓	✓	-
bd_c7	318.109692	67.460453	2221932649766967296	309^{+2}_{-2}	7.317 ±0.060	-1.724 ±0.050	8.1432 ±0.0003	0.9	-	✓	✓
bd_c8	318.504950	68.822118	2270438498579303808	343^{+6}_{-6}	7.950 ±0.078	-1.046 ±0.082	15.1636 ±0.0008	1.3	✓	✓	✓
bd_c9	318.867019	69.240512	2270593529718918016	344^{+4}_{-4}	7.955 ±0.057	-0.822 ±0.066	15.2133 ±0.0041	1.1	✓	✓	✓
bd_c10	318.894184	68.757180	2270439254493609088	345^{+4}_{-4}	7.781 ±0.058	-1.172 ±0.060	14.9226 ±0.0065	1.1	✓	-	✓
bd_c11	318.903254	68.809839	2270440491444181504	348^{+44}_{-36}	8.482 ±0.561	-1.994 ±0.559	19.5934 ±0.0049	0.9	✓	✓	-
bd_c12	318.926286	68.893498	2270445439246710400	326^{+4}_{-4}	8.058 ±0.079	-0.406 ±0.081	15.0225 ±0.0034	1.3	✓	✓	✓
bd_c13	318.926976	68.893279	2270445439244424576	329^{+11}_{-10}	7.966 ±0.213	-1.919 ±0.243	16.5337 ±0.0039	-	✓	✓	✓
bd_c14	318.977864	68.681023	2270427056786514432	361^{+7}_{-6}	7.897 ±0.089	-1.130 ±0.087	15.9845 ±0.0027	1.1	-	✓	✓
bd_c15	319.066179	67.862292	2222324502955259392	340^{+9}_{-8}	6.749 ±0.127	-0.817 ±0.141	17.2564 ±0.0011	1.0	✓	✓	✓
bd_c16	319.251660	69.609775	2270618131291563392	333^{+11}_{-11}	8.150 ±0.179	-0.832 ±0.244	17.4985 ±0.0015	1.0	✓	✓	✓
bd_c17	319.386343	69.300456	2270597481088870784	333^{+4}_{-4}	8.038 ±0.075	-0.827 ±0.080	15.0735 ±0.0017	1.1	✓	-	-
bd_c18	319.481172	68.990355	2270537970021813248	349^{+3}_{-3}	7.853 ±0.040	-0.439 ±0.032	14.1669 ±0.0030	1.1	-	✓	✓
bd_c19	319.482031	68.989987	2270537970021813376	349^{+2}_{-2}	8.044 ±0.035	-1.384 ±0.030	14.0933 ±0.0029	1.2	-	✓	-
bd_c20	319.525646	68.958045	2270525944113390848	352^{+6}_{-7}	8.417 ±0.087	-1.028 ±0.086	15.7204 ±0.0011	1.1	✓	✓	✓

Table 4.3 continued.

#	RA(2015.5) (°)	Dec(2015.5) (°)	Source ID	Distance (pc)	$\mu_{\alpha\star}$ ($\Delta\mu_{\alpha\star}$) (mas/yr)	μ_δ ($\Delta\mu_\delta$) (mas/yr)	G (eG) (mag)	RUWE	PanSTARRs	2MASS	WISE
(1)	(2)	(3)	(4)	(5)	(6)	(7)	(8)	(9)	(10)	(11)	(12)
			sources associated with L1177								
bd_c21	319.529989	69.162791	2270548758979644672	351^{+12}_{-11}	7.890 ±0.158	-1.078 ±0.161	16.8664 ±0.0014	1.1	✓	✓	-
bd_c22	319.548402	68.916756	2270524157407004032	348^{+6}_{-6}	7.999 ±0.087	-1.108 ±0.079	15.8677 ±0.0011	1.1	✓	✓	-
bd_c23	319.666806	69.622424	2270629500068006400	336^{+12}_{-12}	8.679 ±0.178	-0.752 ±0.226	17.5128 ±0.0014	1.0	✓	✓	-
bd_c24	319.772666	68.479597	2222380318501436800	335^{+21}_{-11}	8.712 ±0.323	-1.557 ±0.376	18.2628 ±0.0074	1.1	-	✓	✓
bd_c25	319.778646	69.246885	2270550889283700224	335^{+4}_{-3}	7.972 ±0.062	-0.552 ±0.058	9.3328 ±0.0004	1.1	✓	✓	✓
bd_c26	319.833473	69.110315	2270544837671634560	332^{+8}_{-8}	7.954 ±0.114	-0.784 ±0.119	16.7284 ±0.0013	1.0	✓	✓	-
bd_c27	319.890995	69.078856	2270533022219508352	340^{+5}_{-4}	8.000 ±0.061	-0.817 ±0.061	15.6177 ±0.0019	1.0	✓	✓	✓
bd_c28	319.955372	68.675289	2222478797807817600	339^{+4}_{-3}	8.150 ±0.050	-1.304 ±0.051	15.0690 ±0.0008	1.0	✓	✓	✓
bd_c29	320.131710	68.861316	2222488212376118912	330^{+12}_{-11}	8.020 ±0.179	-1.905 ±0.212	17.2170 ±0.0011	1.1	✓	✓	-
bd_c30	320.251722	69.046986	2270530200423580416	310^{+29}_{-19}	7.637 ±0.294	-1.360 ±0.350	18.3472 ±0.0020	1.1	✓	✓	✓
bd_c31	320.344413	68.078359	2222308339145993728	333^{+38}_{-31}	9.425 ±0.494	-2.403 ±0.528	19.0752 ±0.0031	1.0	-	-	-
bd_c32	320.684040	69.461889	2270579614025029376	360^{+19}_{-17}	8.633 ±0.245	-0.981 ±0.269	17.7769 ±0.0038	1.1	✓	✓	✓
bd_c33	320.982123	69.848891	2270898963252942720	357^{+2}_{-2}	6.139 ±0.030	-0.584 ±0.032	14.5512 ±0.0006	1.1	✓	✓	-
bd_c34	321.319431	69.870931	2270908927757724416	336^{+7}_{-7}	8.424 ±0.114	-0.801 ±0.123	16.1774 ±0.0029	1.2	✓	✓	✓
bd_c35	321.726628	68.853701	2222452856205683968	362^{+10}_{-10}	8.404 ±0.153	-1.560 ±0.140	16.9416 ±0.0020	1.0	✓	✓	✓
bd_c36	321.853223	69.272097	2224021893658285952	364^{+14}_{-14}	8.627 ±0.177	-0.859 ±0.205	17.3336 ±0.0013	1.1	✓	✓	-
bd_c37	322.245905	69.633510	2224035946791401216	340^{+5}_{-4}	8.498 ±0.076	-1.076 ±0.076	15.4698 ±0.0022	1.1	✓	✓	✓
bd_c38	323.560526	69.634333	2224048178858580736	333^{+5}_{-5}	8.709 ±0.087	-0.699 ±0.089	14.7469 ±0.0027	1.3	✓	✓	✓
bd_c39	323.869465	69.568596	2223997326445821696	347^{+8}_{-7}	8.730 ±0.095	-1.067 ±0.087	16.2078 ±0.0013	1.1	✓	✓	-
			sources not associated with any cloud								
c1	307.672240	68.438749	2247137609506697728	367^{+35}_{-30}	6.234 ±0.475	-1.960 ±0.632	19.1158 ±0.0036	0.9	✓	-	-
c2	307.929469	66.343862	2246345346956211200	311^{+14}_{-12}	7.575 ±0.280	-1.698 ±0.331	18.3046 ±0.0025	1.0	✓	-	-
c3	309.820816	66.616681	2245991235492832512	341^{+12}_{-10}	9.387 ±0.181	-2.371 ±0.178	17.5811 ±0.0016	0.9	✓	✓	✓
c4	310.902769	70.134329	2271441184463842560	343^{+2}_{-2}	7.855 ±0.035	-2.885 ±0.035	10.1049 ±0.0002	1.0	-	✓	✓
c5	311.509466	71.085859	2274882930735828736	340^{+9}_{-8}	6.938 ±0.115	-0.747 ±0.106	16.8358 ±0.0010	1.0	✓	✓	✓
c6	311.520948	66.124230	2245924401612064	365^{+3}_{-2}	7.450 ±0.034	-0.779 ±0.031	13.8946 ±0.0020	1.1	✓	✓	-
c7	311.733175	66.018168	2245735113706518528	370^{+15}_{-14}	7.248 ±0.197	-0.956 ±0.190	17.5133 ±0.0016	1.1	✓	✓	-
c8	312.080716	67.554984	2246149767027696896	339^{+14}_{-14}	7.872 ±0.247	-1.072±0.220	17.9527 ±0.0017	1.0	✓	✓	-
c9	312.957679	68.947681	2271099648664907392	341^{+29}_{-24}	9.503 ±0.418	-1.957 ±0.493	19.0595 ±0.0030	0.9	✓	-	✓
c10	313.117760	69.422860	2271163523418749568	321^{+3}_{-3}	8.575 ±0.045	-1.681 ±0.051	11.3718 ±0.0003	0.9	✓	✓	-
c11	314.025942	66.036337	2245760269331745664	373^{+3}_{-3}	8.967 ±0.041	-1.109 ±0.038	14.5641 ±0.0004	0.8	✓	✓	✓
c12	314.679887	70.192278	2271586045120993792	314^{+2}_{-2}	8.082 ±0.034	-1.173 ±0.032	14.3251 ±0.0004	0.9	✓	✓	-
c13	314.700118	66.040266	2197740915755258816	332^{+20}_{-20}	8.761 ±0.343	-1.131 ±0.342	18.5524 ±0.0019	1.1	✓	✓	✓
c14	314.848513	65.534143	2197648354919811456	358^{+25}_{-25}	7.482 ±0.389	-1.710 ±0.398	18.8231 ±0.0028	1.1	✓	-	-
c15	315.812443	66.704797	2221785933684340736	329^{+8}_{-8}	7.431 ±0.155	-2.773 ±0.147	16.7894 ±0.0015	1.0	✓	-	-
c16	316.373414	64.796710	2197367528481936128	333^{+25}_{-22}	7.795 ±0.413	-2.264 ±0.344	18.8689 ±0.0028	1.0	✓	-	-
c17	321.967321	70.492754	2272185072800774784	360^{+8}_{-8}	8.798 ±0.098	-0.391 ±0.105	16.2997 ±0.0027	1.1	✓	✓	✓
c18	321.977437	67.034826	2221257304812229376	351^{+17}_{-15}	8.938 ±0.228	-1.404 ±0.281	18.1570 ±0.0016	1.0	✓	✓	-

Table 4.4: PanSTARRS, 2MASS and *WISE* magnitudes for the known YSO candidates with photometric quality 'A' in all bands.

#	RA	Dec	J±eJ	H±eH	K±eK	g±eg	r±er	i±ei	W1±eW1	W2±eW2	W3±eW3
					YSO candidates towards L1172/1174						
1	314.845315	68.245467	10.588±0.026	9.342±0.032	8.532±0.021	16.7174±0.0479	14.8261±0.0614	13.6770±0.0765	7.610±0.024	6.870±0.020	4.687±0.014
2	315.084447	68.140772	12.472±0.024	11.165±0.027	10.518±0.021	19.5930±0.0491	17.5710±0.0224	16.3556±0.0640	9.894±0.023	9.133±0.020	6.754±0.019
3	315.231481	68.190885	12.831±0.024	12.166±0.029	11.749±0.020	19.3048±0.0270	18.0107±0.0088	15.9712±0.0034	-	-	-
4[†]	315.359984	68.177338	11.107±0.042	10.084±0.046	9.571±0.039	9.192±0.059	8.250±0.053	7.874±0.053	8.314±0.019	7.595±0.017	5.128±0.013
5[†]	315.362884	68.177214	12.323±0.031	11.150±0.036	10.417±0.025	-	-	-	-	-	-
6	315.400352	68.139576	-	-	-	10.166±0.054	9.404±0.053	7.663±0.087	-	-	-
7	315.403923	68.163263	6.111±0.030	5.465±0.031	4.651±0.017	-	-	-	-	-	-
8	315.427117	68.215960	11.911±0.031	10.892±0.033	10.421±0.023	18.1666±0.0245	16.4682±0.0112	14.9231±0.0063	-	-	-
9	315.444875	68.145894	11.792±0.024	10.798±0.033	10.159±0.022	16.7669±0.0039	15.5405±0.0331	14.2396±0.0080	-	-	-
10	315.558650	68.233141	13.982±0.032	12.405±0.033	11.686±0.024	10.870±0.052	10.513±0.058	10.179±0.055	-	-	-
11[*]	315.617758	68.058287	-	-	-	17.5733±0.0097	15.6471±0.0279	14.6588±0.0077	9.097±0.022	8.662±0.020	6.623±0.016
11b[*]	315.618244	68.057669	-	-	-	-	-	-	-	-	-
12	315.637634	68.124746	11.559±0.027	10.713±0.029	10.411±0.021	15.6739±0.0142	14.4761±0.0255	13.6574±0.0208	9.869±0.022	9.433±0.020	7.629±0.023
13	315.747855	68.108939	13.871±0.035	13.083±0.033	12.357±0.028	16.3522±0.0044	15.6391±0.0097	15.2863±0.0051	11.230±0.023	10.020±0.020	5.950±0.015
14	315.997585	67.824847	12.789±0.029	11.981±0.031	11.478±0.019	18.3370±0.0262	17.2170±0.0069	15.6506±0.0011	10.901±0.023	10.317±0.020	8.683±0.019
					YSO candidates towards L1177						
1	319.413344	68.919361	9.269±0.022	8.741±0.029	8.105±0.023	-	-	-	7.094±0.033	6.669±0.020	3.711±0.015
2	320.241149	68.805102	14.318±0.034	13.035±0.035	11.866±0.030	17.9839±0.0136	16.9800±0.0270	16.4663±0.0226	10.633±0.023	9.436±0.020	6.036±0.014
					YSO candidates towards L1147/1158						
1	307.791609	67.007548	14.269±0.029	13.753±0.042	13.546±0.047	17.6575±0.0109	16.4593±0.0019	15.9282±0.0032	-	-	-
2	308.579103	67.241341	12.907±0.024	12.570±0.036	12.445±0.022	14.8000±0.0071	14.2481±0.0026	14.0044±0.0014	12.261±0.023	12.141±0.021	11.128±0.059
3	308.949753	68.048996	-	-	-	19.5060±0.0301	18.0172±0.0049	17.0123±0.0025	13.832±0.029	13.580±0.031	11.434±0.135
4	309.048672	67.952608	13.212±0.028	11.653±0.029	10.667±0.021	-	-	-	9.785±0.023	8.833±0.020	6.446±0.015
5	309.082855	67.942131	11.364±0.026	9.739±0.032	8.781±0.021	19.1880±0.0206	16.9180±0.0062	15.3903±0.0064	5.264±0.068	3.315±0.069	0.765±0.009
6	311.474902	67.960735	12.453±0.026	9.497±0.028	7.291±0.020	18.5799±0.0241	16.7057±0.0641	15.3435±0.036	-	-	-
7	312.042682	68.050417	12.030±0.026	11.411±0.035	11.167±0.023	-	-	-	10.826±0.022	10.561±0.021	9.480±0.032

[†] Stars #4 and #5 are resolved as two sources in 2MASS, *Spitzer* and *Gaia*, but *WISE* detected them as a single source. We assigned the *WISE* to the brightest of them in K_s.

[*] Stars #11 & #11b appear as double sources of ~2'' in *Gaia*. 2MASS classified it as an extended source. Visual inspection also show them as two sources. But detected as single source by 2MASS and *WISE*.

Table 4.5: PanSTARRS, 2MASS and *WISE* magnitudes for the newly identified comoving sources with photometric quality 'A' in all bands.

#	RA	Dec	J±eJ	H±eH	K±eK	g±eg	r±er	i±ei	W1±eW1	W2±eW2	W3±eW3
					Comoving sources towards L1172/1174						
hd_c1	314.963955	68.336928	12.954±0.026	12.173±0.030	11.808±0.025	19.802±0.019	18.233±0.012	16.152±0.007	11.657±0.023	11.389±0.021	11.493±0.103
hd_c2	315.201051	68.415148	11.715±0.026	10.773±0.030	10.495±0.019	16.815±0.006	15.212±0.006	14.096±0.009	10.377±0.023	10.339±0.020	10.166±0.034
hd_c3	315.271845	68.072754	10.630±0.024	9.928±0.032	9.683±0.022	-	-	-	-	-	-
hd_c4	315.350786	68.150243	13.516±0.024	12.851±0.029	12.411±0.022	19.921±0.054	18.624±0.066	16.973±0.008	-	-	-
hd_c5	315.420625	68.301379	12.662±0.027	12.051±0.033	11.796±0.021	18.718±0.010	17.449±0.004	15.530±0.006	-	-	-
hd_c6	315.422157	68.182326	12.300±0.029	11.373±0.033	10.854±0.022	17.545±0.011	16.037±0.015	14.826±0.005	-	-	-
hd_c7	315.450292	68.115938	13.893±0.027	13.136±0.033	12.739±0.025	19.767±0.047	19.022±0.021	17.033±0.007	-	-	-
hd_c8	315.452017	68.135740	14.588±0.035	13.876±0.048	13.491 ±0.042	-	-	-	-	-	-
hd_c9	315.458232	68.158415	12.589±0.024	11.948±0.032	11.573±0.023	19.611±0.048	18.201±0.030	16.045±0.008	-	-	-
hd_c10	315.470563	68.362746	13.771±0.029	12.561±0.035	12.104±0.026	21.856±0.045	19.759±0.019	17.579±0.005	11.918±0.022	11.689±0.020	11.313±0.085
hd_c11	315.501565	68.192440	11.968±0.027	10.816±0.032	10.387 ±0.019	19.655±0.031	17.598±0.009	15.569±0.007	-	-	-
hd_c12	315.612647	68.015216	13.258±0.030	12.073±0.032	11.585±0.024	21.458±0.042	19.428±0.017	17.157±0.002	-	-	-
hd_c13	315.675742	68.172632	14.368±0.035	13.549±0.037	13.125±0.024	20.283±0.036	18.854±0.011	16.868±0.012	-	-	-
hd_c14	315.853497	68.132781	12.364±0.029	11.410±0.030	11.024±0.021	18.954±0.014	17.144±0.005	15.386±0.010	-	-	-
hd_c15	316.150453	68.498418	11.570±0.030	10.782±0.037	10.454±0.023	16.199±0.040	14.918±0.012	13.952±0.010	9.772±0.023	9.357±0.020	7.246±0.016
hd_c16	316.151474	68.496975	-	-	-	20.460±0.014	18.913±0.024	17.284±0.014	-	-	-
hd_c17	316.394054	68.209051	11.600±0.027	10.918±0.031	10.626±0.021	15.841±0.009	14.614±0.005	13.608±0.002	10.543±0.022	10.505±0.020	10.571±0.059
					Comoving sources towards L1177						
bd_c1	316.970365	69.135322	15.426±0.053	14.897±0.069	14.660±0.096	19.849±0.019	18.552±0.008	17.388±0.006	-	-	-
bd_c2	317.016704	69.232990	13.097±0.024	12.442±0.028	12.190±0.023	18.236±0.007	17.051±0.004	15.499±0.002	12.073±0.022	11.900±0.021	10.871±0.044
bd_c3	317.485774	68.926013	14.227±0.033	13.627±0.037	13.323±0.043	20.476±0.028	19.130±0.007	17.176±0.003	-	-	-
bd_c4	317.660746	68.976917	13.963±0.029	13.352±0.032	13.032±0.028	19.348±0.006	18.088±0.004	16.453±0.008	-	-	-
bd_c5	317.719747	69.045445	12.648±0.027	11.932±0.030	11.761±0.018	16.767±0.008	15.443±0.012	14.577±0.011	11.621±0.023	11.571±0.021	10.966±0.046
bd_c6	317.880961	69.457870	12.903±0.027	12.164±0.032	11.986±0.023	17.264±0.005	16.035±0.009	14.943±0.004	-	-	-
bd_c7	318.109692	67.460453	6.527±0.023	6.016±0.044	5.833±0.018	-	-	-	5.799±0.054	5.789±0.025	5.781±0.015
bd_c8	318.504950	68.822118	12.351±0.024	11.674±0.029	11.459±0.023	16.903±0.006	15.676±0.003	14.463±0.002	11.319±0.023	11.209±0.021	10.874±0.045
bd_c9	318.867019	69.240512	12.487±0.026	11.781±0.032	11.513±0.024	16.732±0.008	15.532±0.007	14.532±0.003	11.380±0.023	11.310±0.020	11.088±0.052
bd_c10	318.894184	68.757180	12.348±0.025	11.659±0.030	11.439±0.023	16.408±0.031	15.130±0.010	14.202±0.007	11.243±0.023	11.180±0.021	10.821±0.044
bd_c11	318.903254	68.809839	-	-	-	21.557±0.096	20.353±0.013	18.816±0.009	-	-	-
bd_c12	318.926286	68.893498	12.124±0.025	11.429±0.028	11.218±0.026	16.494±0.006	15.188±0.013	14.251±0.023	11.098±0.022	11.014±0.020	11.261±0.063
bd_c13	318.926976	68.893279	-	-	-	-	-	-	-	-	-
bd_c14	318.977864	68.681023	12.962±0.026	12.302±0.030	12.042±0.026	17.747±0.015	16.606±0.012	15.274±0.014	11.918±0.022	11.770±0.021	10.889±0.046
bd_c15	319.066179	67.862292	14.626± 0.035	13.859± 0.045	13.671± 0.050	18.926± 0.018	17.688± 0.007	16.552± 0.008	-	-	-
bd_c16	319.251660	69.609775	14.148±0.034	13.582±0.040	13.278±0.037	19.783±0.012	18.532±0.008	16.768±0.007	-	-	-
bd_c17	319.386343	69.300456	-	-	-	16.812±0.005	15.593±0.011	14.364±0.009	10.973±0.023	10.858±0.020	10.926±0.052
bd_c18	319.481172	68.990355	11.143±0.022	10.457±0.030	10.280±0.026	-	-	-	10.122±0.023	10.086±0.020	10.171±0.042
bd_c19	319.482031	68.989987	11.143±0.022	10.457±0.030	10.280±0.026	-	-	-	-	-	-

Table 4.5 continued.

#	RA	Dec	J±eJ	H±eH	K±eK	g±eg	r±er	i±ei	W1±eW1	W2±eW2	W3±eW3
						Comoving sources towards L1177					
bd.c20	319.525646	68.958045	12.724±0.024	12.064±0.031	11.828±0.029	17.583±0.009	16.423±0.004	14.985±0.003	11.671±0.023	11.515±0.021	11.588±0.100
bd.c21	319.529989	69.162791	13.444±0.028	12.861±0.040	12.563±0.034	19.206±0.007	17.969±0.002	16.128±0.005	-	-	-
bd.c22	319.548402	68.916756	12.987±0.027	12.328±0.032	12.062±0.031	17.668±0.016	16.425±0.025	15.220±0.005	-	-	-
bd.c23	319.666806	69.622424	13.927±0.026	13.344±0.032	13.073±0.034	19.932±0.011	18.674±0.010	16.798±0.009	-	-	-
bd.c24	319.772666	68.479597	14.914±0.044	14.272±0.050	13.661±0.038	20.261±0.036	19.579±0.014	17.548±0.009	12.916±0.023	12.322±0.022	10.126±0.030
bd.c25	319.778646	69.246885	9.229±0.029	9.210±0.028	9.185±0.022	-	-	-	9.143±0.023	9.179±0.020	9.126±0.020
bd.c26	319.833473	69.110315	13.628±0.027	13.007±0.033	12.758±0.030	18.685±0.008	17.453±0.004	15.985±0.003	-	-	-
bd.c27	319.890995	69.078856	12.884±0.029	12.202±0.031	11.977±0.029	17.305±0.011	16.075±0.006	14.938±0.005	11.870±0.023	11.751±0.022	12.423±0.338
bd.c28	319.955372	68.675289	12.576±0.024	11.875±0.024	11.649±0.028	16.551±0.006	15.321±0.010	14.390±0.005	11.541±0.022	11.502±0.020	10.594±0.039
bd.c29	320.131710	68.861316	13.909±0.029	13.300±0.037	12.981±0.039	19.439±0.015	18.235±0.007	16.457±0.003	-	-	-
bd.c30	320.251722	69.046986	15.251±0.053	14.595±0.071	14.332±0.085	20.252±0.022	19.074±0.013	17.610±0.006	-	-	-
bd.c31	320.344413	68.078359	-	-	-	20.879±0.033	19.693±0.023	18.305±0.007	13.112±0.023	12.865±0.023	11.048±0.052
bd.c32	320.684040	69.461889	14.302±0.031	13.704±0.036	13.379±0.046	15.454±0.002	14.527±0.006	14.156±0.004	-	-	-
bd.c33	320.982123	69.848891	12.809±0.021	12.248±0.030	12.091±0.028	17.958±0.012	16.742±0.004	15.401±0.008	-	-	-
bd.c34	321.319431	69.870931	13.143±0.024	12.465±0.032	12.262±0.030	-	-	-	-	-	-
bd.c35	321.726628	68.853701	13.369±0.025	12.774±0.033	12.475±0.028	19.537±0.025	18.224±0.021	16.254±0.016	-	-	-
bd.c36	321.853223	69.272097	13.903±0.032	13.289±0.039	13.020±0.038	19.710±0.012	18.490±0.008	16.584±0.003	-	-	-
bd.c37	322.245905	69.633510	12.834±0.025	12.124±0.031	11.870±0.028	17.030±0.018	15.881±0.007	14.807±0.009	11.830±0.023	11.755±0.021	11.539±0.088
bd.c38	323.560526	69.634333	11.820±0.023	11.104±0.027	10.901±0.022	16.524±0.009	15.280±0.010	14.036±0.005	10.788±0.023	10.654±0.020	10.645±0.066
bd.c39	323.869465	69.568596	13.298±0.027	12.597±0.029	12.412±0.029	18.052±0.012	16.811±0.003	15.471±0.006	-	-	-
						Comoving sources not associated with any cloud					
c1	307.672240	68.438749	-	-	-	21.206±0.070	19.947±0.015	18.347±0.006	-	-	-
c2	307.929469	66.343862	-	-	-	20.117±0.017	18.889±0.013	17.555±0.005	-	-	-
c3	309.820816	66.616681	-	-	-	19.257±0.012	18.039±0.004	16.866±0.002	-	-	-
c4	310.902769	70.134329	8.926±0.027	8.675±0.051	8.616±0.020	-	-	-	8.522±0.023	8.559±0.020	8.516±0.017
c5	311.509466	71.085859	14.908±0.042	14.270±0.056	13.999±0.063	18.486±0.014	17.166±0.004	16.145±0.004	-	-	-
c6	311.520948	66.124230	14.229±0.032	13.524±0.036	13.272±0.039	14.658±0.004	13.888±0.007	13.563±0.013	13.090±0.023	13.017±0.023	11.326±0.057
c7	311.733175	66.018168	12.247±0.026	11.735±0.029	11.611±0.024	19.873±0.014	18.527±0.007	16.751±0.006	-	-	-
c8	312.080716	67.554984	14.147±0.032	13.429±0.036	13.217±0.037	19.849±0.022	18.630±0.004	17.201±0.003	-	-	-
c9	312.957679	68.947681	14.820±0.036	14.332±0.055	14.027±0.064	21.013±0.038	19.599±0.013	18.312±0.008	-	-	-
c10	313.117760	69.422860	-	-	-	12.272±0.008	11.883±0.030	14.052±0.001	-	-	-
c11	314.025942	66.036337	10.423±0.024	10.217±0.032	10.208±0.022	15.426±0.002	14.536±0.002	14.154±0.002	10.131±0.023	10.152±0.020	10.172±0.038
c12	314.679887	70.192278	12.831±0.026	12.260±0.032	12.120±0.024	15.123±0.002	14.275±0.002	13.947±0.003	11.922±0.023	11.990±0.021	11.969±0.106
c13	314.700118	66.040266	12.708±0.024	12.120±0.030	12.029±0.024	20.411±0.025	19.138±0.012	17.813±0.006	-	-	-
c14	315.812443	66.704797	-	-	-	19.175±0.019	17.955±0.004	16.070±0.005	-	-	-
c15	314.848513	65.534143	13.322±0.028	12.706±0.035	12.400±0.026	20.917±0.028	19.433±0.017	18.037±0.007	12.216±0.023	11.971±0.021	11.435±0.073
c16	316.373414	64.796710	-	-	-	20.745±0.046	19.482±0.010	18.088±0.006	-	-	-
c17	321.967321	70.492754	13.360±0.027	12.659±0.032	12.388±0.030	18.228±0.008	16.994±0.024	15.573±0.006	12.251±0.023	12.104±0.021	11.386±0.073
c18	321.977437	67.034826	15.291±0.055	14.712±0.063	14.407±0.080	19.890±0.012	18.669±0.005	17.417±0.004	-	-	-

Chapter 5

Characterization of young intermediate-mass stars associated with the Perseus OB2

5.1 Introduction

As mentioned in chapter 3, the cloud complex L1172/1174 is located at a height of 14° above the galactic mid-plane($\sim$ 80 pc, considering distance 335 pc to L1172/1174). This is higher in comparison to the scale-heights of the molecular gas (e.g. Heyer & Dame, 2015) and OB stars in the local galactic disk (Reed, 2000). Bhatt (2000) suggested a prominent shell-like distribution of high-latitude clouds, which is centered around the Cas-Tau/Per OB3 association. Fig. 5.1 shows the shell of high-latitude clouds (black filled circles) surrounding the Cas-Tau OB/Per OB3 association. The shell-like structure appears as an elliptical cavity centered on l =143°, $b = -5$° (the dashed grey ellipse shown in Fig. 5.1 having a red filled circle indicating its central position). The projected major and minor axes of this ellipse are 90° and 68°, with the major axis inclined with the Galactic plane by an angle $\sim$118°. Bhatt (2000) proposed that the elliptical cavity is an outcome of the supernova explosions and stellar winds from the massive OB stars of the Cas-Tau/Per OB3 association $\sim$35 Myr ago. The location of L1172/1174 (l =104.1°, b =+14.2°) is shown with a thick red colored plus symbol. The Perseus region (along with substructures IC 348 and NGC 1333) is located almost diagonally opposite to L1172/1174. There are several young intermediate-mass (IM) stars located towards Perseus OB2 association (l =159.2°, $b = -17.1$°). The location of Perseus OB2 is also shown using a red plus symbol in Fig. 5.1. The blue arrows indicate the directions of L1172/1174 and

5. CHARACTERIZATION OF YOUNG INTERMEDIATE-MASS STARS ASSOCIATED WITH THE PERSEUS OB2
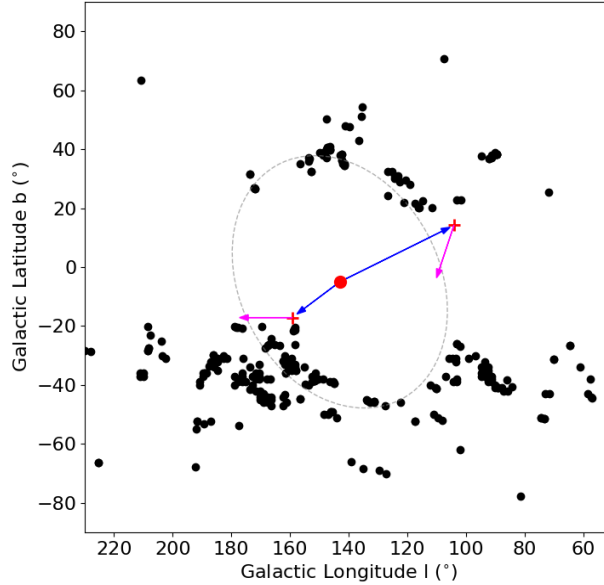
Figure 5.1: The shell of high-latitude clouds (black filled circles) surrounding the Cas-Tau OB/Per OB3 association is shown. The dashed grey ellipse is schematically fitted to the shell-like structure. The red filled circle indicates the center of the ellipse. The red plus symbols show the positions of L1172/1174 and Perseus OB2 association. The blue arrows show the directions of these regions from the center of the ellipse.

Perseus OB2 association from the center of the ellipse. The directions of projected motions of these two regions are shown using magenta colored arrows.

IM stars are linked with the reasonably well understood formation of low-mass stars and with the rarer, more deeply embedded high-mass stars. Extensive near-IR, mid-IR, sub-millimeter, and millimeter observations of low-mass star disks (with stellar spectral types later than ∼K5) have revealed that, by the age of 5−7 Myr, ∼90% of these stars lose their optically thick inner disks (Strom et al., 1989; Haisch et al., 2001; Hillenbrand et al., 2008). Investigations in the more massive Herbig Ae/Be (HAeBe) stars ($M_\star = 2-8$ $M_\odot$) indicate that their circumstellar disks might dissipate by a shorter timescale ∼3 Myr (Hernández et al., 2005; Carpenter et al., 2006; Manoj et al., 2006). However, such surveys have been limited to small samples of IM stars distributed in several nearby star-forming regions. Although HAeBes are defined to have a mass range ∼2−8 $M_\odot$ and with spectral types of B, A (and also F in few cases; Herbig, 1960), the presence of circumstellar disks around stars of spectral type earlier than B5 is not very well confirmed as these massive stars have highly rapid disk lifetime (Fuente et al., 2002; Zinnecker & Yorke, 2007). In addition, the number of massive stars (> 6 $M_\odot$) is relatively smaller because of
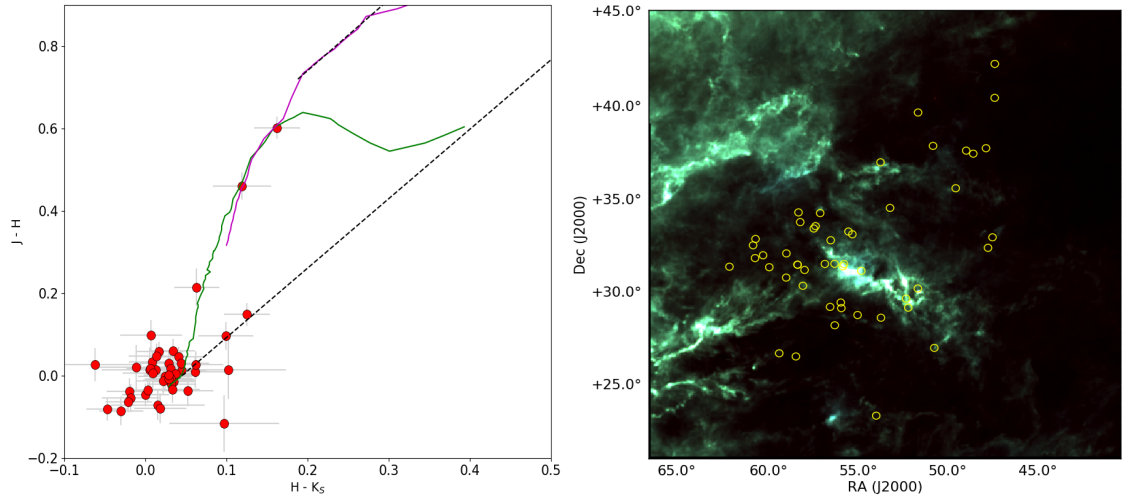
Figure 5.2: **(LHS)** JHK_s color-color diagram of the IM sources (shown in red filled circles) distributed in the Perseus OB2 association). The dashed curves in green and magenta represent colors of main-sequence and giants respectively. The dashed lines in black show the reddening vectors. **(RHS)** Spatial distribution of the same sources (shown in yellow circles) overplotted in the color- composite image made by *Planck* 353 (red), 545 (green) and 857 (blue) GHz images.

the initial mass function (IMF), which varies stochastically from cluster to cluster. Several studies of non-emission line sources have been found in literature (e.g. The et al., 1994; Manoj et al., 2002). Typical properties of young stars are less clearly visible in them. They are considered to be transition objects between the PMS and MS stages, as the authors suggest.

OB associations are stellar groups having significant populations of IM stars with stellar mass density <0.1 $M_\odot pc^{-3}$ (Brown et al., 1998). Based on the HR diagram, their estimated ages indicate that they are young (e.g., Blaauw, 1964). For this reason, OB associations are considered to be excellent laboratories for studying YSOs covering a complete range of mass (Preibisch et al., 2002). Perseus OB2 consists of a range of star forming environments, it harbors both IM and massive stars, while low- to IM stars are being formed presently in the Perseus molecular cloud (Enoch et al., 2009; Arce et al., 2010; Sadavoy et al., 2014; Azimlu et al., 2015). Therefore, identification of the members of Perseus OB2 association and estimation of their characteristics, such as spectral type, temperature, age, and mass, would provide crucial information related to the processes involved in star formation history in Perseus OB2.

Steenbrugge et al. (2003) reported radial velocities of 29 early type members of Perseus OB2 association based on optical spectroscopy. Later, based on near-

Table 5.1: Log of observations:

Year	Month (Date)
2017	October (27, 28, 29)
	December (21)
2018	January (7, 8)

and mid-IR photometry and optical low resolution spectroscopy, Yasui et al. (2014) identified 31 IM stars towards the same region. There are 10 sources in common, so, 50 early type members reside in the Perseus OB2 association. We made an attempt of characterization of 12 of this (brighter than Vmag$\sim$ 9) IM members of Perseus OB2 association by high resolution spectroscopic study. We estimated spectral type, age, mass, etc. of these sources by combining our observed data with the archival data obtained from the Gaia DR2 catalog (Gaia Collaboration et al., 2018). Fig. 5.2 (LHS) presents 2MASS 2MASS $J-H$ versus $H-K_s$ color-color diagram of these 50 young IM stars. This figure clearly shows that these sources have a lack of near-IR excess following the absence of circumstellar disks. The dashed curves in green and magenta represent the colors of main-sequence and giants, respectively. The dashed lines in black show the reddening vectors. The spatial distribution of these sources is also shown using yellow circles in Fig. 5.2 (RHS). The sources are overplotted in the color- composite image made by *Planck* 353 (red), 545 (green) and 857 (blue) GHz images. We present the details of the observations and data reduction in section 5.2. In section 5.3, we discuss the results obtained for the observed sources. Finally we present our conclusion in section 5.4.

5.2 Observation and Data Reduction

High resolution (R=60,000) spectroscopic data of the young IM stars were obtained using HESP attached with 2-m HCT, IIA, India. The log of observations is shown in Table 5.1. We used the standard packages of IRAF and data reduction pipeline by Arun, which is described in chapter 2 in detail. We obtained the distance and the proper motion values of these sources from Bailer-Jones et al. (2018) and Gaia Collaboration et al. (2018), respectively, by giving a search radius of 1″. We excluded the sources which are lying nearer or further to the cloud and having RUWE> 1.4 (Lindegren, 2018) as a value of RUWE $\leq$ 1.4 indicates a good astrometric solution of any source. Table 5.2 presents the basic kinematic parameters and RUWE of the observed sources obtained from the *Gaia* DR2. We listed the estimated spectral properties in Table 5.3.

5.3 Results and discussions:

Out of 50 IM stars, 44 sources are detected in *Gaia* DR2 with m/Δm$\geq$3 and RUWE$\leq$1.4. We will first discuss the kinematic properties of these sources based on *Gaia* DR2 in section 5.3.1, and then discuss the spectroscopic results of the observed sources in section 5.3.2.

5.3.1 Kinematic properties of the Perseus OB2 association:

The distance to the Perseus OB2 association has been estimated by various authors using different methods till date. Herbig & Jones (1983) adopted the distance to NGC 1333 as 350 pc, which is located in the western end of the cloud, based on several earlier measurements around Perseus OB2 and IC 348. Based on interstellar extinction, Cernis (1990) and Cernis (1993) found a gradient in the distance across the cloud, with 220 pc to the western part of the cloud and 260−340 pc to the eastern zone. Herbig (1998) adopted a distance to IC 348 as 316 pc, which is situated at the eastern end of the Perseus cloud complex based on extinction measurements. Based on *Hipparcos* parallax measurements of the early type and late type members of Perseus OB2, de Zeeuw et al. (1999) estimated its distance at 318±27 and 282±21 pc, respectively. Using *Hipparcos* parallax measurements and the method of M$_V$ vs. B-V CMD of the stars in Perseus OB2, Hernández et al. (2005) estimated the distance to this region as 313±13 pc and 300±15 pc, respectively. A distance of 300 pc was adopted by Bally et al. (2008) for the entire Perseus cloud based on various previous measurements. Based on the very long baseline interferometry (VLBI) studies of H$_2$O masers, Hirota et al. (2008) estimated the distance 235±18 pc for NGC 1333 and Hirota et al. (2011) estimated the same as 232±18 pc to L1448 which are located to the western end of Perseus. Enoch et al. (2006) and Young et al. (2015) adopted a value of 250±50 pc as the distance to Perseus OB2. Based on PanSTARRS-1 photometry, Schlafly et al. (2014) found that the western part of the cloud is at a distance 260±26 pc, while the eastern part is at 315±32 pc. Recently, using *Gaia* DR2 data, Ortiz-León et al. (2018) estimated a distance of 320 ± 26 pc to IC 348 and 293 ± 22 pc to NGC 1333. These measurements provide evidence that a gradient in distance is present across the cloud complex, with values ranging from 212−293 pc in the western region (Cernis, 1990; Lombardi et al., 2010; Hirota et al., 2008; Schlafly et al., 2014; Ortiz-León et al., 2018) and 260 − 320 pc in the eastern region (Cernis, 1993; Lombardi et al., 2010; Schlafly et al., 2014; Ortiz-León et al., 2018).

5. CHARACTERIZATION OF YOUNG INTERMEDIATE-MASS STARS ASSOCIATED WITH THE PERSEUS OB2
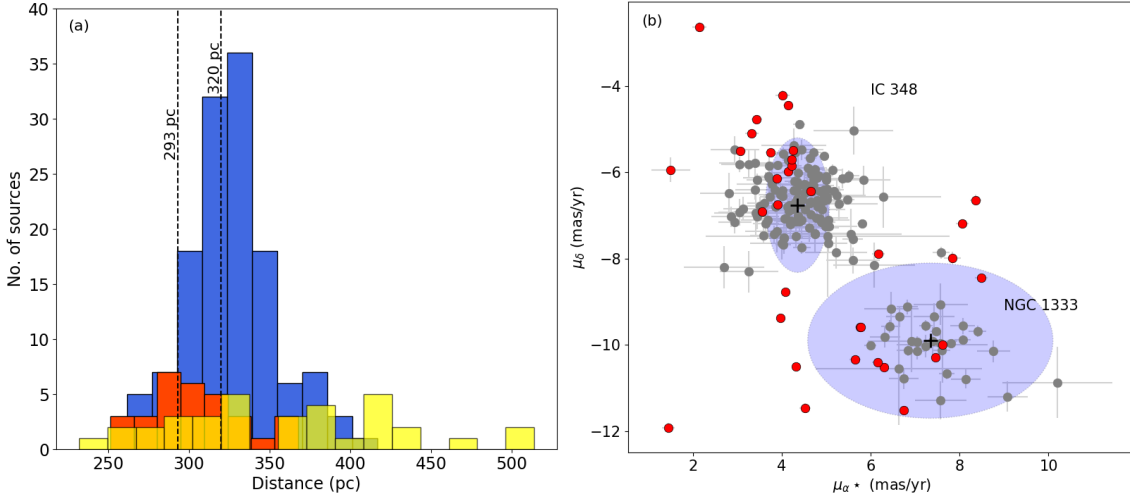
Figure 5.3: **(a)** Histograms of distances of low-mass sources located towards IC 348 (blue), NGC 1333 (red) and IM sources towards Perseus OB2 region (yellow) with binsize ∼14 pc. The distances to IC 348 (∼320 pc) and NGC 1333 (∼293 pc) are shown using vertical dashed lines. **(b)** The proper motion plot of the low-mass and IM sources, indicated by gray and red filled circles, respectively. The thick black '+' signs indicate the average $\mu_{\alpha\star}$ and μ_δ of IC 348 and NGC 1333. The light grey ellipses show the boundaries defined by 3 times dispersion values of $\mu_{\alpha\star}$ and μ_δ for IC 348 and NGC 1333.

In Fig. 5.3 (a) we have shown the histograms of distances of sources located towards IC 348 (blue), NGC 1333 (red) and Perseus OB2 region (yellow) with binsize ∼14 pc. The distances to IC 348 (∼320 pc) and NGC 1333 (∼293 pc) estimated by Ortiz-León et al. (2018), are shown using vertical dashed lines. From Fig. 5.3 (a) it is clear that a fraction of IM sources is lying at a distance similar to IC 348 and NGC 1333, though they are relatively more scattered in comparison to the low-mass sources in IC 348 and NGC 1333. We present the distribution of the same sources in the proper motion plane ($\mu_{\alpha\star}$ versus μ_δ) in Fig. 5.3 (b). The low-mass sources distributed towards IC 348 and NGC 1333 are shown using grey filled circles, while the young IM stars are indicated using red filled circles. The estimated average $\mu_{\alpha\star}$ and μ_δ) for IC 348 and NGC 1333 are 4.35±0.03, −6.76±0.01 mas yr^{-1} and 7.34±0.05, −9.90±0.03 mas yr^{-1}, respectively (Ortiz-León et al., 2018). The light grey ellipses show the boundaries defined by 3 times dispersion values of $\mu_{\alpha\star}$ and μ_δ for IC 348 (0.24±0.03 and 0.52±0.01 mas yr^{-1}, respectively) and NGC 1333 (0.92±0.05 and 0.60±0.03 mas yr^{-1}, respectively), obtained by Ortiz-León et al. (2018). The average $\mu_{\alpha\star}$ and μ_δ values of IC 348 and NGC 1333 are indicated by thick black '+' symbols. A part of the young IM stars share proper motions similar to the young low-mass sources towards IC 348 and NGC 1333, but a significant
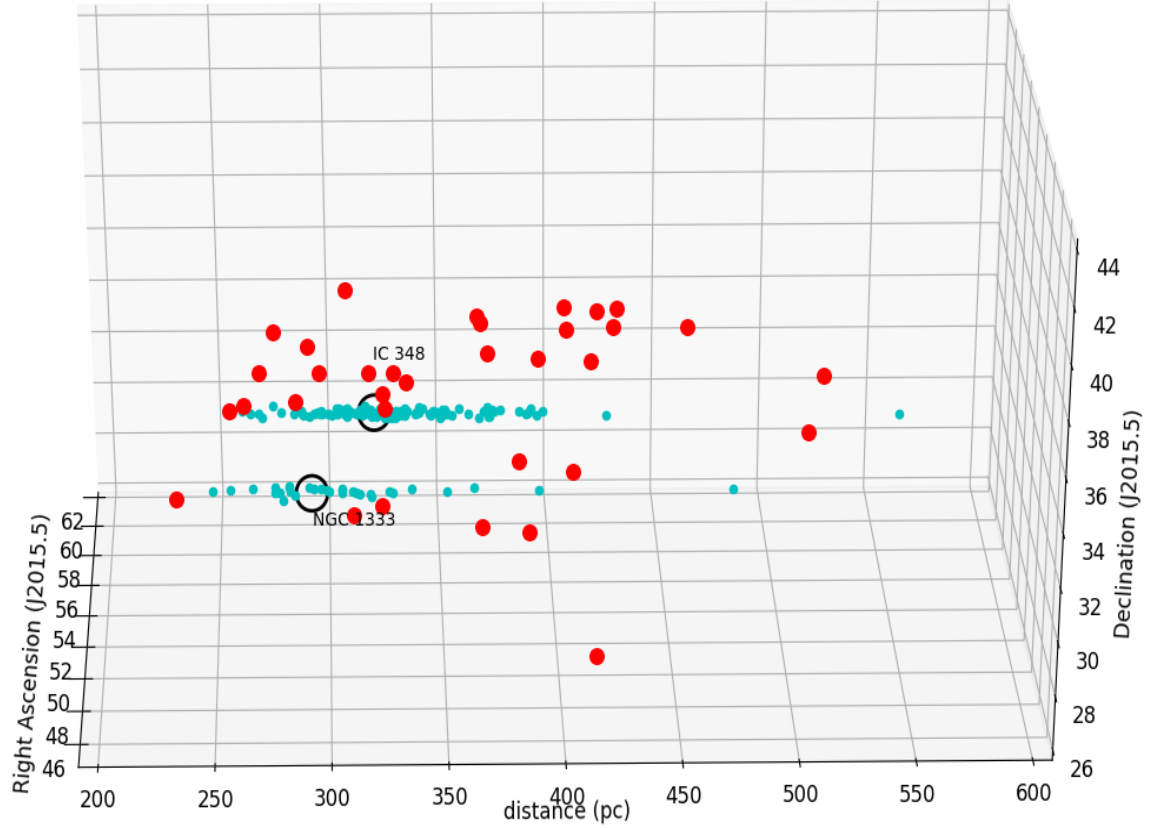
Figure 5.4: 3D distribution of low-mass YSOs and young IM stars. The cyan filled circles are the low-mass sources, while the red filled circles are the IM sources. The black open circles indicate the centers of IC 348 and NGC 1333.

fraction of the IM stars are having proper motions randomly distributed. Therefore, the IM sources are highly scattered in terms of distance and proper motion. In Fig. 5.4, we show the distribution of young low-mass and IM sources in 3D. The cyan filled circles are the low-mass sources from Ortiz-León et al. (2018). The red filled circles are the IM sources. We have marked the centers of IC 348 and NGC 1333 as black open circles. The IM sources are distributed further away from the low-mass sources and widely scattered.

In Fig. 5.5 (a), we have shown the proper motion vs. distance of the young IM stars. Red filled triangles represent $d - \mu_{\alpha\star}$ and blue filled circles represent $d - \mu_{\delta}$ values of the sources. The dashed lines indicate the median values of distance ($d = 365$ pc) and proper motion ($\mu_{\alpha\star} = 7.922$ km s^{-1} or 4.238 mas yr^{-1}, $\mu_{\delta} = -12.457$ km s^{-1} or -7.541 mas yr^{-1}). The MAD of d, $\mu_{\alpha\star}$ and μ_{δ} are 60 pc, 1.825 and 2.445 km s^{-1}, respectively. In mas yr^{-1} unit, MAD of $\mu_{\alpha\star}$ and μ_{δ} are 1.588 and 2.451 mas yr^{-1}, respectively. The red and blue points are 34 sources lying within the boundaries
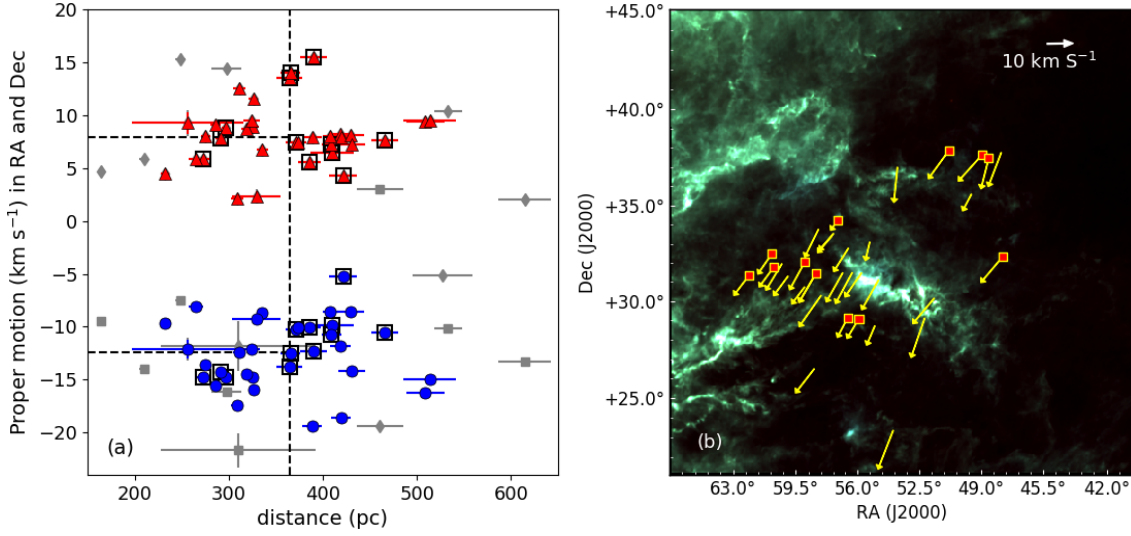
Figure 5.5: **(a)** Distance vs. proper motion plot of the young IM stars. Red filled triangles represent proper motion in RA and blue filled circles represent proper motion in Dec. The dashed lines indicate the median values of distance and proper motion. The red and blue points are sources lying within the boundaries defined by $3\times$MAD in d, $\mu_{\alpha\star}$ and μ_{δ} with respect to their median values. The sources outside of the $3\times$MAD boundaries are presented as grey diamonds and squares for $d - \mu_{\alpha\star}$ and $d - \mu_{\delta}$ values, respectively. The sources observed by us are marked in black open squares. **(b)** Spatial distribution of the sources with proper motion vectors (lying within $3\times$MAD boundaries, shown using yellow arrows) overplotted in the color-composite image made by *Planck* 353 (red), 545 (green) and 857 (blue) GHz images. The sources observed by us are marked in red squares with yellow borders.

defined by $3\times$MAD in d, $\mu_{\alpha\star}$ and μ_{δ} with respect to their median values. The sources outside of the $3\times$MAD boundaries are presented as grey diamonds and squares for $d - \mu_{\alpha\star}$ and $d - \mu_{\delta}$ values, respectively. The sources observed in spectroscopic mode are marked in black open square symbols. Table 5.2 lists the astrometric measurements of these observed sources obtained from *Gaia* DR2. Columns 1, 2, and 3 present names of the sources and their positions in RA and Dec. Column 3 provides the V magnitudes of these sources. d, $\mu_{\alpha\star}$ and μ_{δ} values are presented in columns 5, 6, and 7. Columns 8 and 9 show their G magnitudes and RUWE values. In Fig. 5.5 (b), we have shown the directions of proper motion of these sources using yellow vectors. The 12 IM stars observed by us are marked in red squares with yellow borders.

Table 5.2: Kinematic properties of the observed sources obtained from *Gaia* DR2:

Name	RA	Dec	d	$\mu_{\alpha\star} \pm \Delta\mu_{\alpha\star}$	$\mu_{\delta} \pm \Delta\mu_{\delta}$	$G \pm \Delta G$	RUWE
	(°)	(°)	(pc)	(mas yr^{-1})	(mas yr^{-1})	(mag)	
(1)	(2)	(3)	(4)	(5)	(6)	(7)	(8)
HD 25799	61.662699	32.385039	466^{+14}_{-14}	3.432±0.118	-4.776±0.072	7.0030±0.0006	1.2
HD 23597	56.856972	29.875757	386^{+12}_{-12}	3.064±0.122	-5.498±0.084	8.1841±0.0005	1.0
HD 24012	57.713744	35.099760	422^{+15}_{-15}	2.150±0.160	-2.629±0.109	7.7845±0.0006	1.2
HD 23244	56.169574	29.822448	410^{+24}_{-21}	3.324±0.147	-5.094±0.100	8.3331±0.0007	1.1
HD 24600	58.994494	32.163304	296^{+4}_{-3}	6.291±0.088	-10.525±0.049	8.5928±0.0003	1.0
HD 26499	63.188232	31.794713	371^{+12}_{-11}	4.216±0.226	-5.852±0.133	9.0125±0.0003	1.2
HD 281537	61.852126	33.087942	409^{+11}_{-10}	3.746±0.115	-5.544±0.068	9.1167±0.0003	1.1
HD 20653	50.223055	38.885284	365^{+14}_{-13}	7.835±0.191	-7.980±0.138	8.6382±0.0009	1.3
HD 19359	46.962594	33.054977	366^{+10}_{-10}	8.060±0.139	-7.191±0.108	8.9070±0.0005	1.3
HD 24913	59.731196	32.756430	291^{+5}_{-5}	5.650±0.130	-10.333±0.065	8.3693±0.0003	1.0
HD 19749	47.990247	38.538138	390^{+15}_{-14}	8.361±0.133	-6.641±0.120	9.1069±0.0005	1.2
HD 19567	47.526284	38.345476	272^{+8}_{-6}	4.525±0.122	-11.464±0.106	7.5851±0.0006	0.9

5.3.2 Spectroscopic Properties of the observed sources:

The spectra of 12 sources have been presented in Fig. 5.6. An enlarged image of the same sources containing the Hα, Hβ, and Hγ, and Hδ lines are shown in Fig. 5.7. The spectroscopic results of the observed IM stars are presented in Table 5.3. We have used Bertone's synthetic spectra (Bertone et al., 2008) which are of spectral resolution R= 10,000 to determine the spectral types of the observed sources. We have compared the features of spectral lines of the observed and template spectra. Before comparing, we normalized the spectra of our observed sources and took them to a common resolution with the template spectra. Then we made chi-square fitting of our observed spectra and template spectra and obtained their spectral types. Then we computed E(B-V) of these sources using observed (B-V) from NOMAD (Zacharias et al., 2004) and intrinsic (B-V) provided by Kenyon & Hartmann (1995). Then we computed A$_V$ by using the well known equation A$_V$=3.1 E(B-V) (Savage & Mathis, 1979; Seaton, 1979; Cardelli et al., 1989).

Based on photometric studies, Gimenez & Clausen (1994) estimated an age 10−15 Myr for Per OB2. Brown et al. (1999) suggested an age between 4 and 8 Myr, using ages reported by several authors. There is a concentration of young stars embedded in Per OB2, with age 5−20 Myr (Strom et al., 1974), 5−7 Myr (Lada & Lada, 1995), 3−7 Myr (Trullols & Jordi, 1997), and 1.3−3.0 Myr (Herbig, 1998). de Zeeuw et al. (1999) estimated an age ∼ 6 Myr of Per OB2, while stars of different generations are also present with age < 15 Myr (e.g., Bally et al., 2008, and references therein).

We have made *Gaia* CMD of the IM stars using MESA isochrones (Choi et al., 2016; Dotter, 2016) and have shown it in Fig. 5.8. This figure indicates that a

5. CHARACTERIZATION OF YOUNG INTERMEDIATE-MASS STARS ASSOCIATED WITH THE PERSEUS OB2
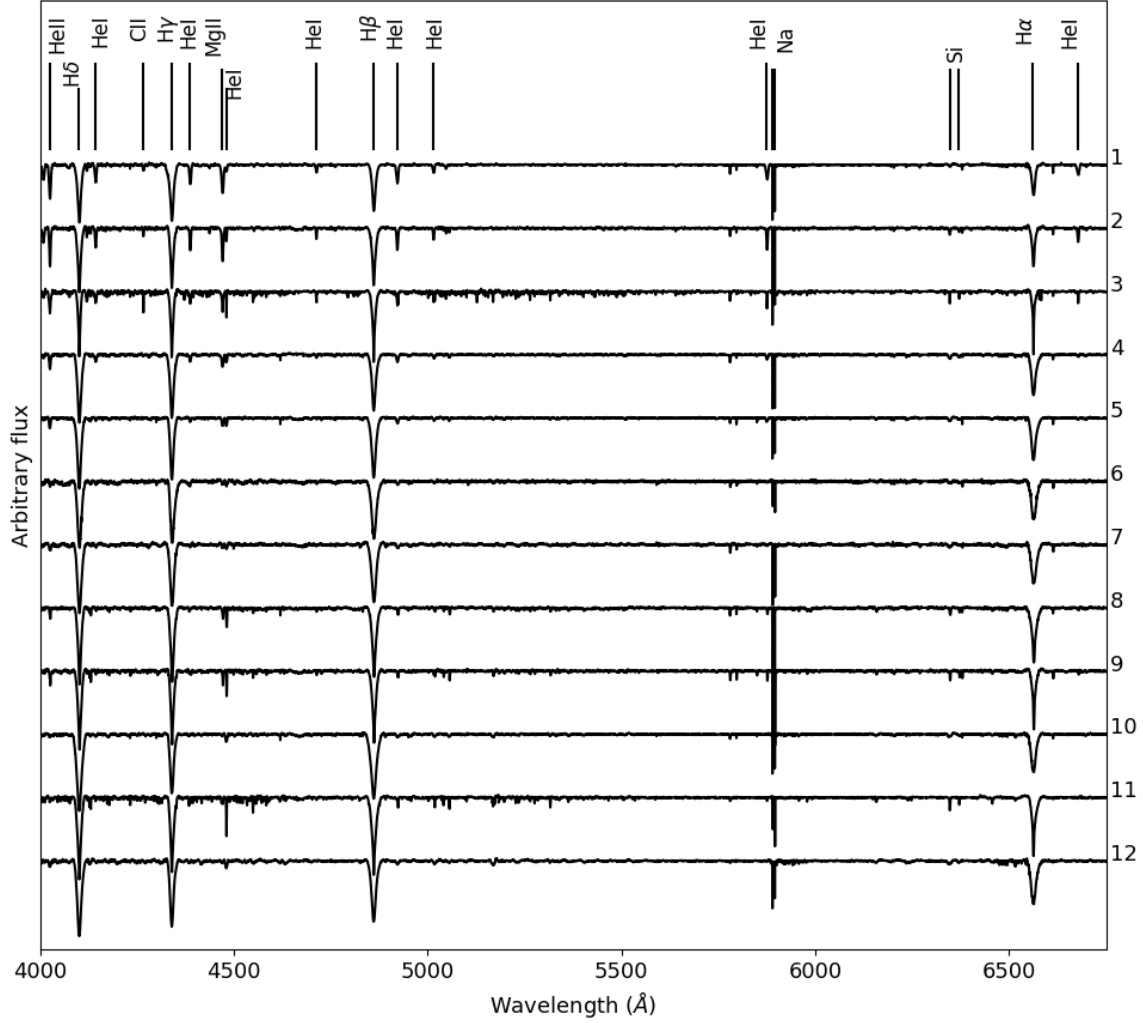
Figure 5.6: Spectra of the observed sources. The object numbers are mentioned in the right end.

Table 5.3: Spectral properties of the observed sources:

#	Name	Sp. Type	T_{eff} (K)	A_V (mag)	L_{bol} ($L_\odot$)	Mass ($M_\odot$)	Age (Myr)	EW(Hα) (Å)	EW(Hβ) (Å)	EW(Hγ) (Å)	EW(Hδ) (Å)
(1)	(2)	(3)	(4)	(5)	(6)	(7)	(8)	(9)	(10)	(11)	(12)
1	HD 25799	B0	30000	0.99	9156.60	6.2	0.3	2.7±0.4	3.9±0.3	3.9±0.4	4.8±0.7
2	HD 23597	B5	15400	0.54	368.75	3.2	1.7	2.5±0.3	4.6±0.2	3.9±0.3	4.6±0.8
3	HD 24012	B5	15400	0.45	580.90	3.7	1.2	2.1±0.9	3.9±0.8	3.7±0.8	3.1±0.9
4	HD 23244	B7	13000	0.47	226.88	3.1	2.0	3.8±0.8	5.4±0.7	4.7±0.6	5.9±0.7
5	HD 24600	B8	11900	0.85	101.35	2.7	4.0	4.5±0.4	6.1±0.8	4.5±0.6	6.5±0.8
6	HD 26499	B8	11900	0.71	92.86	2.6	3.0	3.8±0.3	6.8±0.8	5.5±0.6	6.4±0.7
7	HD 281537	B8	11900	0.53	88.10	2.5	3.3	3.7±0.7	6.5±0.9	4.8±0.8	6.8±0.8
8	HD 20653	B7	13000	0.75	175.15	2.9	2.2	4.2±0.4	6.2±0.7	5.1±0.4	5.9±0.7
9	HD 19359	B7	13000	0.63	116.21	2.6	3.0	3.0±0.1	5.4±0.3	5.0±0.3	5.8±0.5
10	HD 24913	B9	10500	0.79	80.85	2.8	2.3	3.8±0.4	8.6±0.4	4.3±0.2	9.1±0.6
11	HD 19749	B8	11900	0.50	81.02	2.4	4.0	3.9±0.9	6.7±0.8	4.8±0.9	6.4±0.9
12	HD 19567	B9	10500	0.38	100.23	2.9	2.4	4.6±0.3	6.7±0.4	5.7±0.6	7.6±0.6
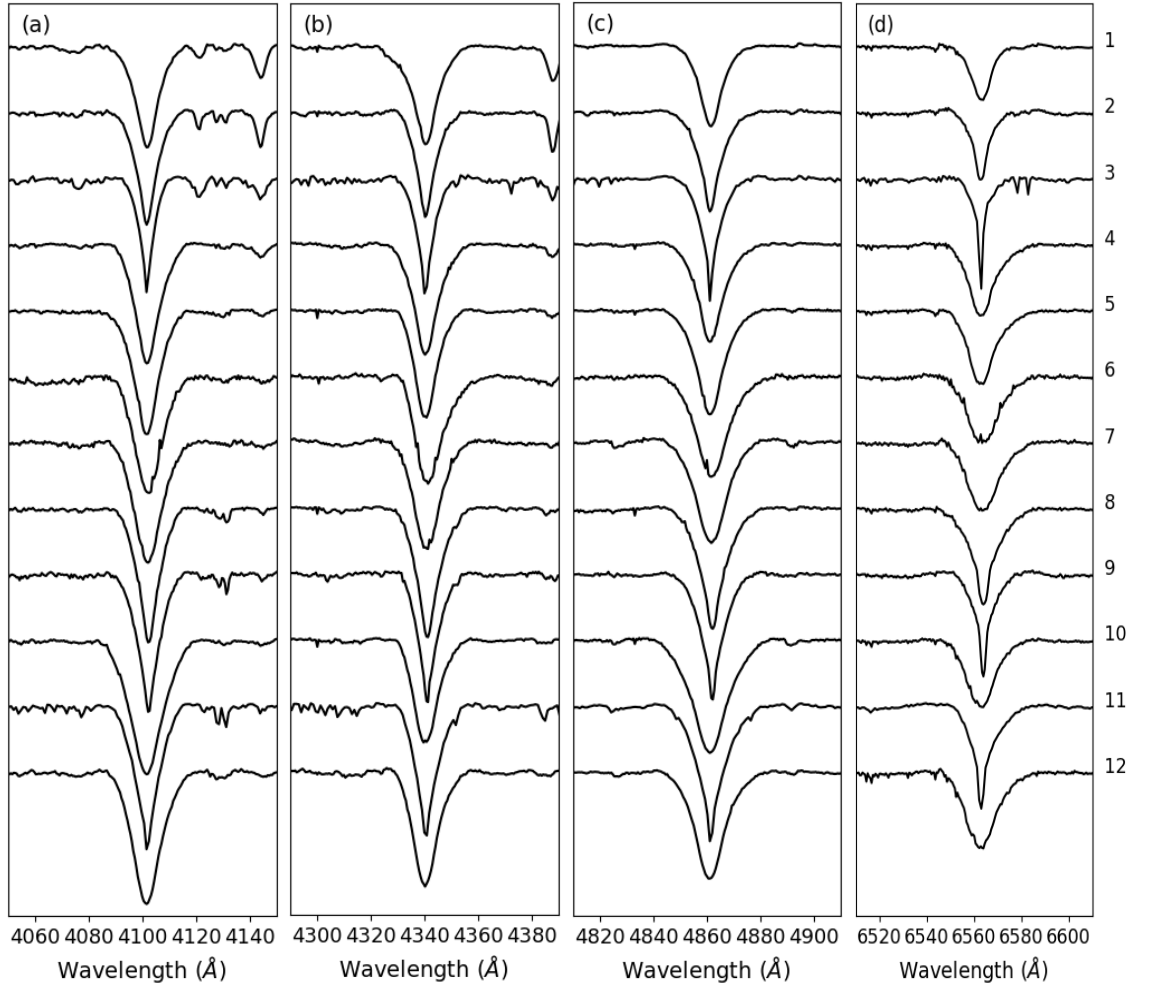
Figure 5.7: Hδ **(a)**, Hγ **(b)**, Hβ **(c)** and Hα **(d)** profiles of the observed sources. The object numbers are mentioned in the right end.

majority of the sources having age $2-4$ Myr. In this age range, typical error is found to be 0.4 Myr. We obtained typical error in mass as 0.4 M$_\odot$ in the same set of sources. We have listed the age, mass, luminosity of the sources in Table 5.3. Yasui et al. (2014) estimated the lifetime of the innermost dust disk (K disk) and mid-IR disk to be ~ 3 and ~ 6.5 Myr for IM stars. As the observed sources are having age $\sim 2-4$ Myr, the accretion process could possibly get ceased.

From the 2MASS CC diagram (Fig. 5.2 (a)), it is well evident that these IM stars show an almost complete absence of near-IR excess, which further reveals the absence of accretion disks. Our spectroscopic results are also showing similar evidence by the absence of emission in Balmer lines and He I lines, which is a signature of accretion mechanism, indicating that these stars are beyond their accretion phase.

Yasui et al. (2014) provided a detailed discussion on the observed shorter timescales

187

5. CHARACTERIZATION OF YOUNG INTERMEDIATE-MASS STARS ASSOCIATED WITH THE PERSEUS OB2
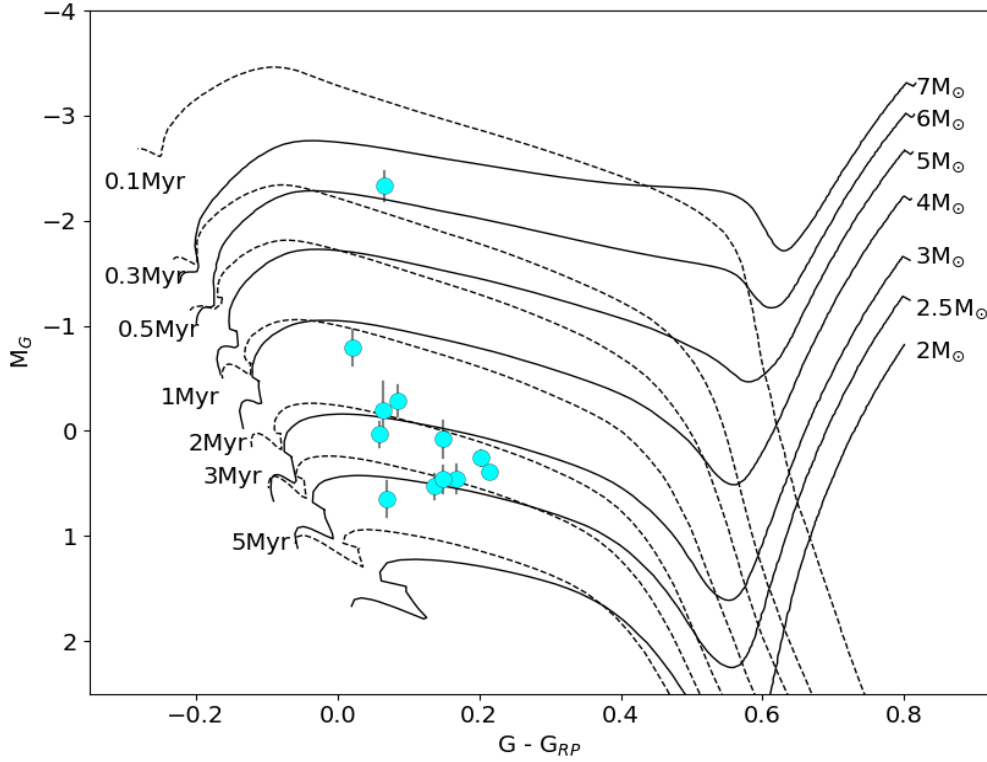
Figure 5.8: *Gaia* CMD of the IM stars (cyan filled circles) using MESA isochrones.

of the disk evolution of the IM stars. Although disk evolution is related to several processes, two basic categories were mainly focused by Yasui et al. (2014): (1) the disk dispersal processes, such as accretion of circumstellar mass and dissipation of disk by photoevaporation, and (2) settling of the dust grains to the disk mid-plane and subsequent dust growth, which could be linked to formation of planets. Yasui et al. (2014) suggested that the second process is more plausible for the rapid disappearance of the K disks.

The first process, i.e., the disk dispersal process, is a combination of two mechanisms: accretion of circumstellar material onto the central star and dissipation into the ISM (Hollenbach et al., 2000). This mechanism is considered to be one of the major processes of overall disk dispersal (Williams & Cieza, 2011), as it can describe the almost simultaneous dissipation of the whole disk. The faster mass accretion for higher mass stars could be a possible mechanism for the short lifetime of the K-disk of the IM stars. Based on observations of UV Balmer excess, Mendigutía et al. (2011) suggested that mass accretion rate strongly depends on the mass. Results of Yasui et al. (2014) suggested that the gas accretion disk survives for a longer lifetime than the same for the K disk, almost similar to the MIR disk. So, faster accretion and the resultant lack of circumstellar matter are not expected to be the

reason for the faster destruction of the K disk.

Photoevaporation is another powerful candidate for the dissipation mechanism, which might cause the short lifetime of K-disk. This mechanism is known to be effective for regions beyond the gravitational radius, r_g, where the gravitational potential balances the thermal energy. For IM and low-mass stars, typical values of r_g are $\sim$25 and $\sim$5 AU, respectively. The corresponding radii of K-disks (r_K) are $\sim$0.3 and $\sim$0.1 AU for IM and low-mass stars, respectively. Similarly, the corresponding radii of MIR-disks (r_{MIR}) are $\sim$5 and $\sim$1 AU, respectively. Though these radii depend on the stellar mass, usually, $r_K <r_{MIR} <r_g$. It should not change for both low-mass and IM stars. Therefore, photoevaporation is not probably the cause of the faster dissipation of K-disks for IM stars (Yasui et al., 2014).

The rapid dissipation of the innermost area of dust disk compared to other parts of the disk is considered to be due to the dust settling on to disk mid-plane (Kenyon & Hartmann, 1987; Dullemond & Dominik, 2005) and/or dust growth (Dullemond & Dominik, 2004). Analytically the dust settling time can be expressed to be proportional to $r^{3/2}M_\star^{-1/2}$ (Nakagawa et al., 1981). As the dust settling/growth takes place more effectively in the inner disk, the K-disk lifetime is expected to be shorter than that of the MIR disk for the IM stars. On the other hand, for the low-mass stars, there is no significant difference in the lifetimes of the K, MIR, and the sub-mm disks. However, several ranges in the disk lifetime have been noted (Luhman et al., 2010; Currie & Sicilia-Aguilar, 2011). Considering the dependence of disk lifetime (t_{life}) on the stellar mass $M_\star$, it can be expected that for the IM stars would have much shorter t_{life} ($\sim$3 Myr) for K-disk than that of the low-mass stars ($\sim$9$-$10 Myr). But if we consider the dependence of r also, IM stars are expected to have a longer time scale of dust settling than that of low-mass stars, which is opposite compared to the timescales estimated by observations. It could suggest that turbulence in the innermost disk of the IM stars is much weaker than that for the low-mass stars, which is why the dust growth/settling occurs rapidly (Yasui et al., 2014).

5.3.2.1   Search for Diffuse Interstellar Bands:

We additionally searched for the presence of diffuse interstellar bands (DIBs) in the spectra of the observed stars. The DIBs are basically absorption features, which can be seen in the stellar spectra having significant column densities of ISM. Heger (1922) first reported about two diffuse absorption features found at 5780 Å and 5797 Å. Later, 127 DIBs have been identified in the spectral region between 0.4$-$1.3
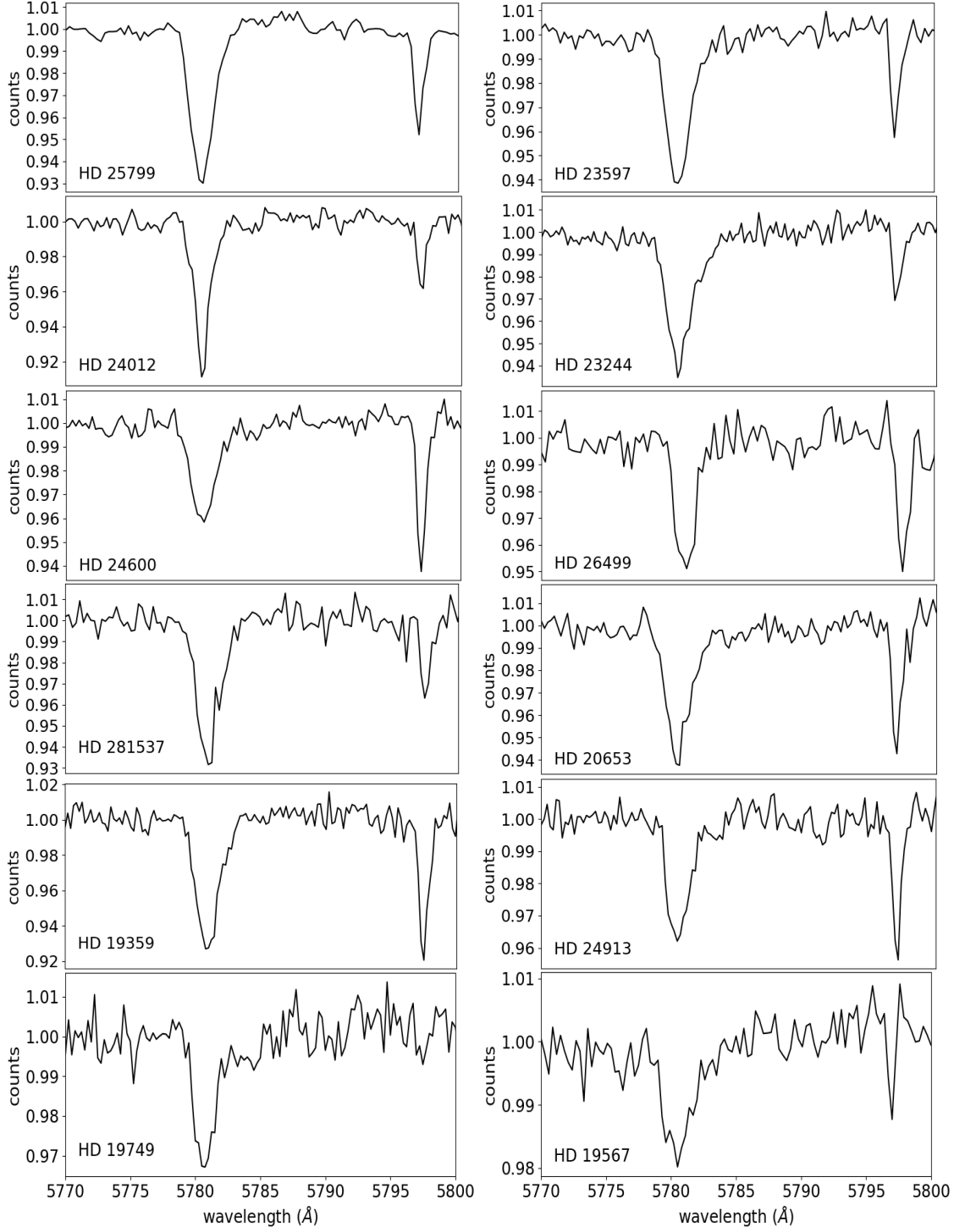
Figure 5.9: Plots of the DIBs (5780 and 5797 Å) of the observed sources.
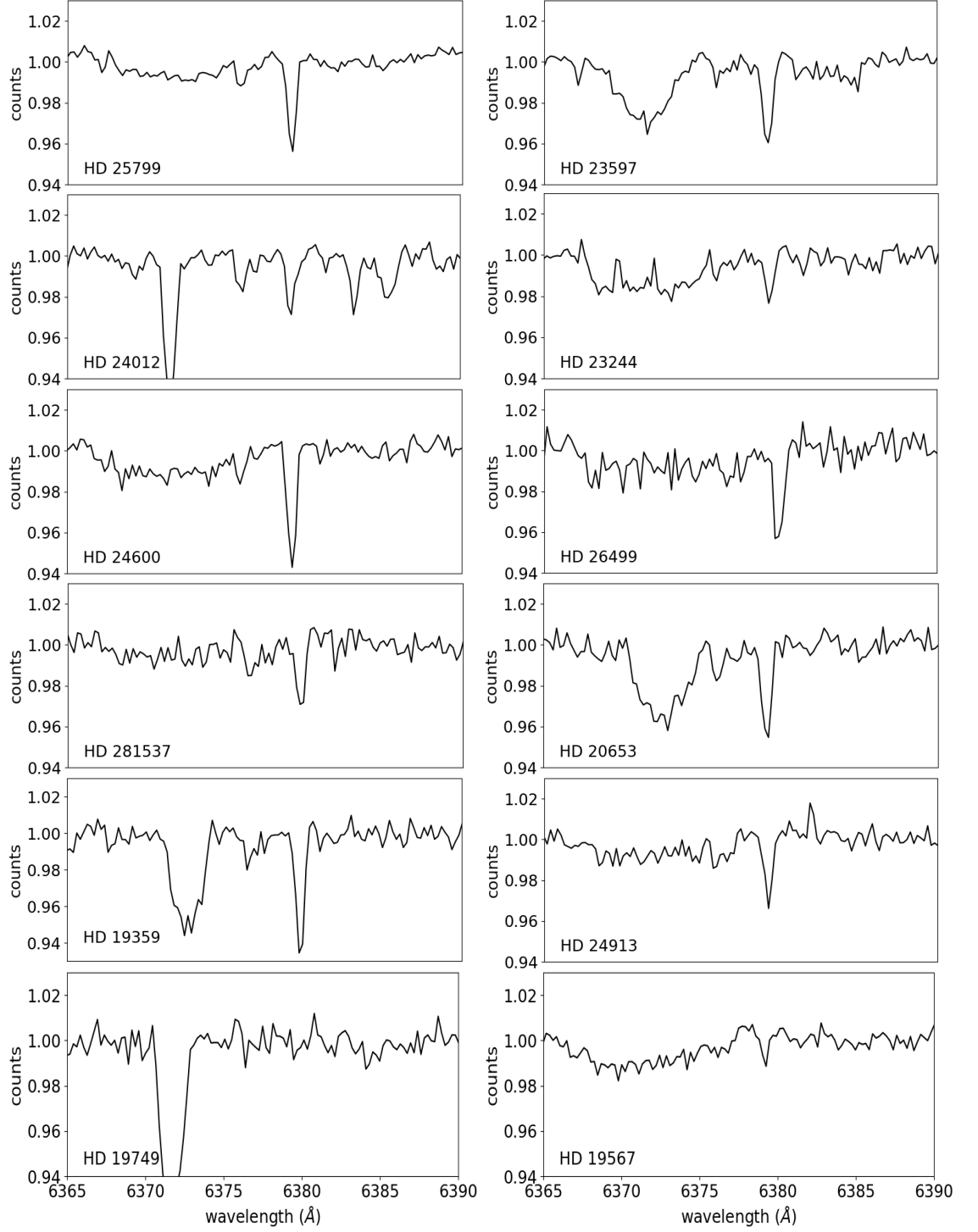
Figure 5.10: Plots of the DIB (6379 Å) of the observed sources.
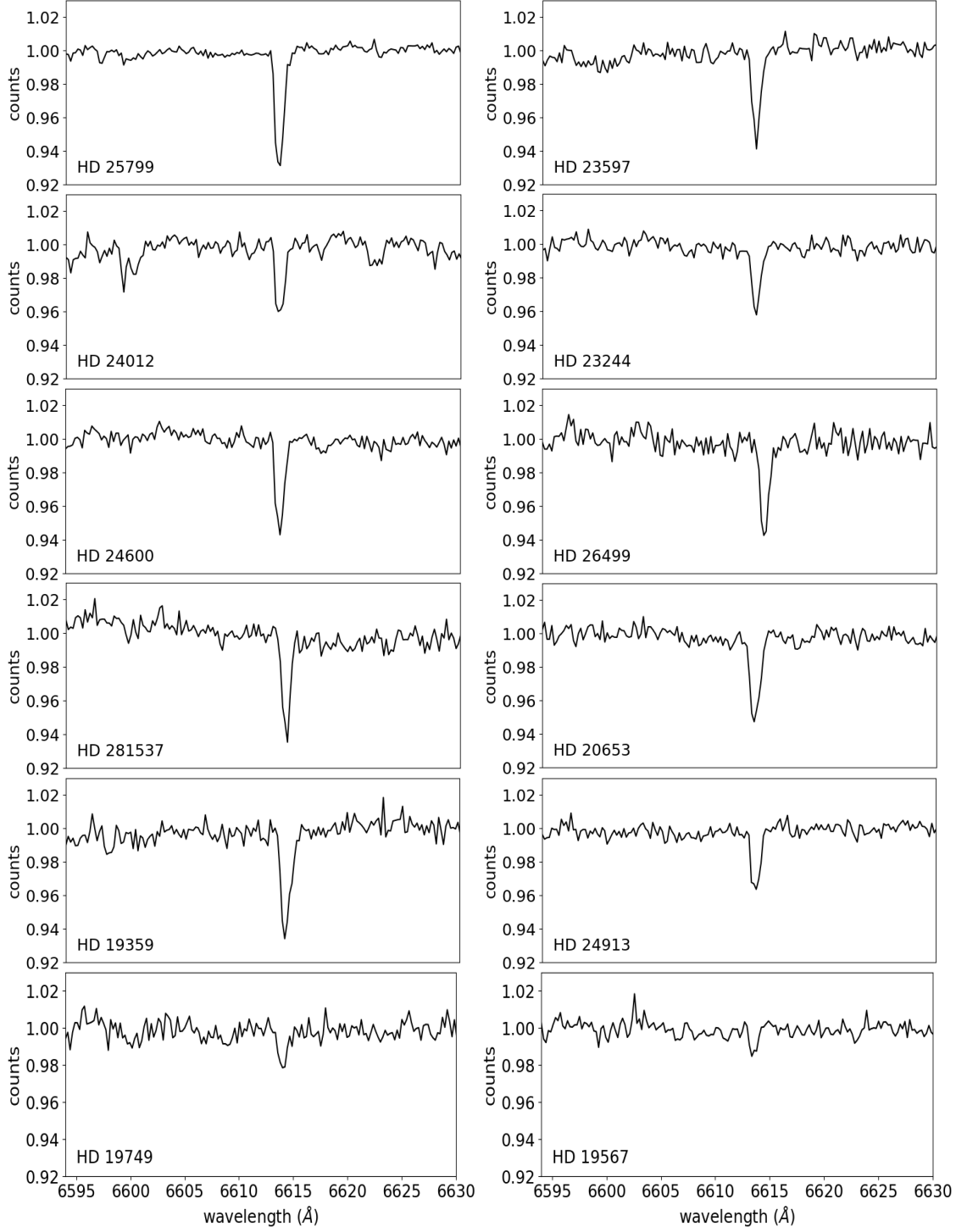
Figure 5.11: Plots of the DIB (6613 Å) of the observed sources.
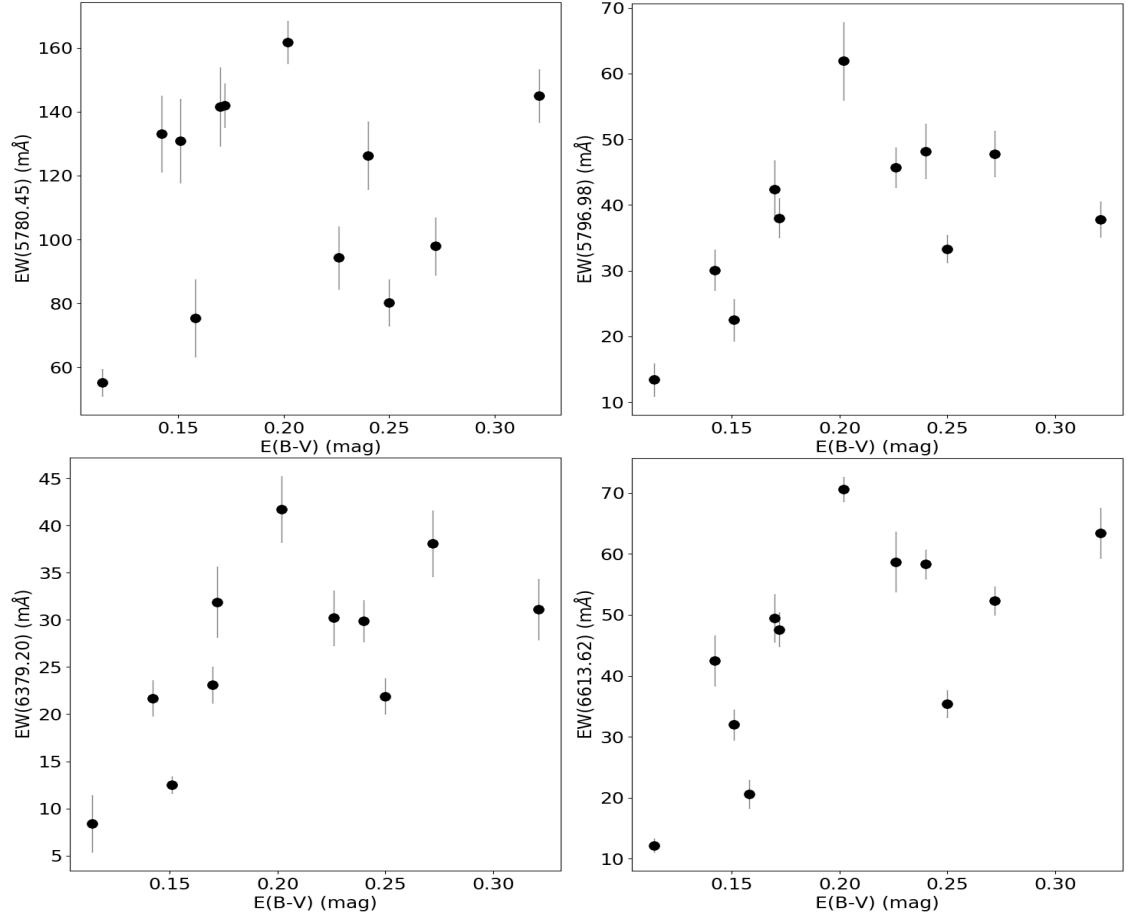
Figure 5.12: Plots of EWs of the DIBs versus color excess of the observed sources.

Table 5.4: Equivalent widths of diffuse interstellar bands in the observed IM stars:

Name	5780.45 (mÅ)	5796.98 (mÅ)	6379.20 (mÅ)	6613.62 (mÅ)
HD 25799	145±8.2	37.8±2.7	31.1±3.2	63.4±4.1
HD 23597	142±6.8	38.0±3.0	31.9±3.7	47.6±2.8
HD 24012	133.2±11.9	30.1±3.1	21.7±1.9	42.5±4.1
HD 23244	130.9±13.2	22.5±3.2	12.5±0.9	32.0±2.5
HD 24600	97.9±8.9	47.8±3.5	38.1±3.5	52.3±2.3
HD 26499	94.3±9.8	45.7±3.0	30.2±2.9	58.7±4.9
HD 281537	141.5±12.3	42.4±4.4	23.1±1.9	49.5±3.9
HD 20653	126.3±10.6	48.2±4.2	29.9±2.2	58.3±2.4
HD 19359	161.8±6.6	61.9±5.9	41.7±3.5	70.6±2.0
HD 24913	80.2±7.3	33.3±2.1	21.9±1.9	35.4±2.2
HD 19749	75.4±12.2	-	-	20.6±2.3
HD 19567	55.2±4.2	13.4±2.5	8.4±3.0	12.2±1.1

μm (Herbig, 1995). As for strengths of the DIBs increase almost proportional to color excess, earlier it was suspected that they are produced by the interstellar grains (Merrill & Wilson, 1938). But later evidence favors some species of neutral or ionized polyatomic molecules (Crawford et al., 1985; Kroto, 1988; Leger et al., 1988; Snow & McCall, 2006; Cox, 2011). Till date, more than 400 DIBs are listed in optical (e.g., Hobbs et al., 2009) and nearly 30 DIBs have been identified in the near-IR wavelengths (e.g., Elyajouri et al., 2017).

We detected four DIBs, of wavelengths 5780.45, 5796.98, 6379.20 and 6613.62 Å in the spectra of 12 sources. In Fig. 5.9, we have shown the DIBs located at 5780.45 and 5796.98 Å. The DIB of 6379.20 Å of all sources are shown in Fig. 5.10. In this figure, one component of Si II doublet (6347, 6371) is also prominent at 6371 Å. In Fig. 5.11, we present the DIB of 6613.62 Å of all sources. An increase in color excess, and thus extinction would imply the presence of higher column of dust graines along the line of sight. If the carriers of the DIBs are related to the dust, then we would expect a correlation with the extinction (e.g., Merrill, 1936; Snow et al., 1977). This is clearly visible in Fig. 5.12. In this figure, we present the EWs of the DIBs versus color excess of the observed sources using black filled circles. We found a clear trend of increase in the EWs of all four DIBs with the color excess of the observed sources in these plots.

5.3.2.2   Na doublet lines in HD 20653 and HD 19359:

In general, as most of the stars contain Na, their Na absorption lines would be the combination of stellar and interstellar Na, when the starlight passes through the insterstellar clouds. Now, the interstellar Na lines are usually much weaker and can appear as an additional component of the relatively broader stellar Na absorption lines. Both the interstellar Na lines (5890 Å (D1) and 5896 Å (D2)) will have similar Doppler shift, because of the relative velocity between the cloud and the star. With the help of high resolution (60,000 in our observations) spectra, we can study the structures of the Na D1 and D2 lines and search for the additional interstellar components as well.

Out of the 12 sources observed by us, 2 of them, HD 20653 and HD 19359, show multiple components in the Na D1, D2 absorption lines. In Fig. 5.13 LHS and RHS, the spectra of Na doublet are shown for HD 20653 and HD 19359, respectively. In the case of HD 20653, we can see one additional component at the redshifted part of the D1 and D2 lines. For HD 19359, there are two additional interstellar components present at the redshifted parts of the D1 and D2 lines, possibly due to multiple cloud
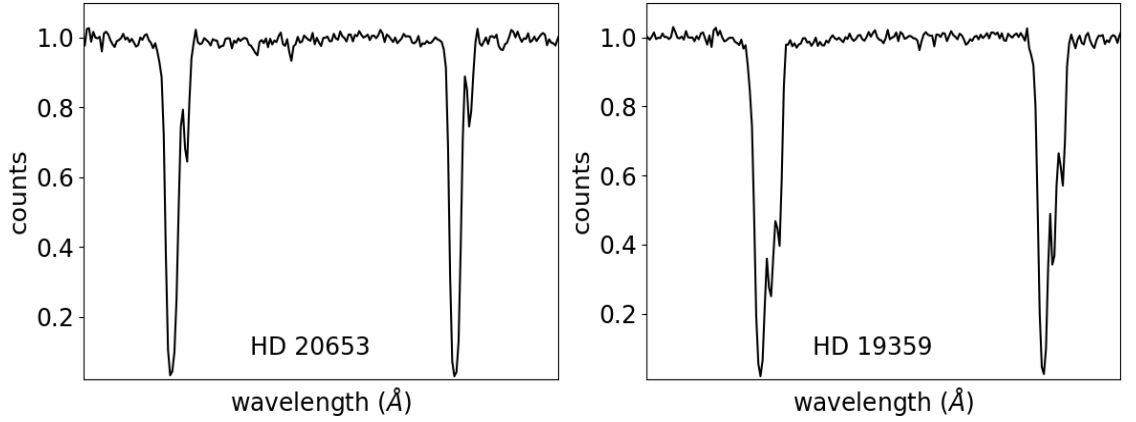
Figure 5.13: Na doublet in the spectrum of HD 20653 (**LHS**) and (**RHS**).

layers. We estimated the relative velocity of the star HD 20653 and the cloud as $\sim$17 km s^{-1}. For HD HD 19359, where we obtained two interstellar components, the relative velocities are, $\sim$11 and $\sim$20 km s^{-1}, for the first and second redshifted components, respectively. Unfortunately, we did not observe any radial velocity standard star during our observations, due to which, the radial velocities of the sources could not be estimated from our observations. For other 12 IM sources, we did not find any noticeable additional components of interstellar Na lines, which could be because of absence of cloud layers along the line-of-sight of the star or the relative velocity between the star and the cloud is relatively smaller.

5.4 Summary and Conclusions

We obtained high resolution spectroscopic observations of 12 IM stars associated with the Perseus OB2 association. Also, based on *Gaia* DR2 measurements of distances and proper motions of the IM stars, we studied their kinematics. The main results of our study are summarized below:

- The 2MASS CC diagram shows that these sources have no or a little near-IR excess, signifying they don't possess any circumstellar disks.

- The IM sources, located towards Perseus OB2 association, are found to be highly scattered in the distance and proper motion planes.

- We obtained high resolution spectra of 12 young relatively brighter (V≤9) IM stars. Emission in Balmer lines, which signifies the presence of circumstellar disks of the sources, is absent in all the observed spectra.

5. CHARACTERIZATION OF YOUNG INTERMEDIATE-MASS STARS ASSOCIATED WITH THE PERSEUS OB2

- Based on the MESA *Gaia* isochrones and evolutionary tracks, we estimated the masses and ages of these young IM stars. A majority of these sources are lying within $2-4$ Myr age. This is comparable with the typical disk dispersal timescale of $3-7$ Myr, which is why these IM sources could possibly have shredded their circumstellar disks.

- Mass of these sources ranges from $2-6$ $M_\odot$ while luminosity ranges from $80-1000$ $L_\odot$.

- We obtained EWs of four DIBs in the observed spectra and found a trend of increase of EW with the color excess of the sources. It indicates that the increase in color excess and thus extinction would also increase the number of dust grains, which in turn enlarge the EWs of the DIBs.

- We also obtained pairs of interstellar Na-lines in the spectra of HD 20653 and HD 19359. Presence of additional interstellar Na lines in them indicates the higher relative velocities between the stars and the interstellar cloud layers.

Chapter 6

Spectro-polarimetry of Herbig Ae/Be stars using SALT

6.1 Introduction

One of the most fascinating problems in astrophysics is to understand the processes involved in the formation of stars and planets. Although we made good progress in understanding the formation sequences of low-mass pre-main sequence (PMS) stars (or T Tauri stars, TTs), our knowledge on the formation of their higher mass ($2\,M_\odot$) counterparts is still incomplete. The intermediate mass (2-$10\,M_\odot$) analog of TTs are known as Herbig Ae/Be stars (HAeBes). The sources massive than $10\,M_\odot$ spend their whole PMS time in obscuration. Therefore study of HAeBes are important as they form an interface between the well studied TTs and still enigmatic high-mass PMS stars.

The HAeBes are, in general, emission-line sources of spectral types A or B and in most cases are associated with regions of dark clouds and bright nebulosities (e.g., Herbig, 1960). Based on their positions in the Hertzsprung-Russell diagram, HAeBes are young and still evolving towards the main sequence. While observations in millimeter-wave emission suggest the presence of circumstellar material, dusty disk model can in principle explain the IR excess emission observed in many of the HAeBes (e.g., van den Ancker et al., 1997b; Natta et al., 2000; Natta et al., 2001). The emission lines seen in HAeBes exhibit variety of line profiles. While the P-Cygni profiles are thought to be formed in stellar winds, more symmetric lines are considered to emerge from hot, extended chromoshpere. But it was the detection of inverse P-Cygni profile which led to the idea that the magnetospheric accretion (MA) model, applied to TTs (Muzerolle et al., 2001), may be applicable to HAeBes

6. SPECTRO-POLARIMETRY OF HERBIG AE/BE STARS USING SALT
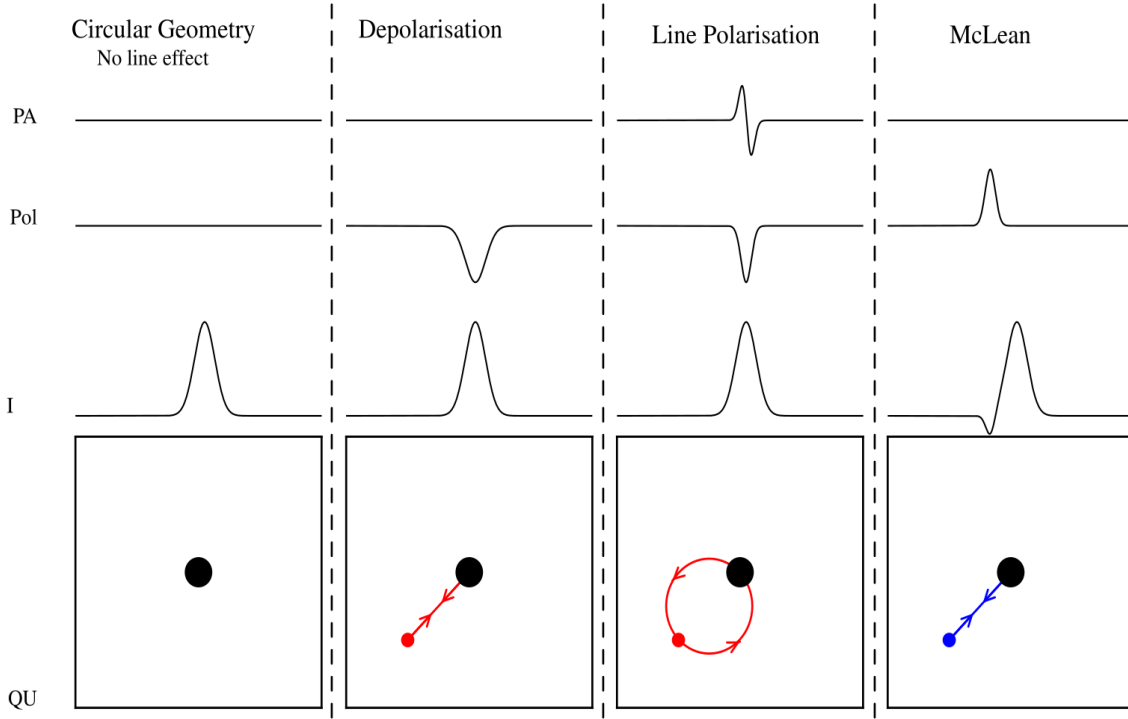
Figure 6.1: A schematic diagram showing possible results of spectropolarimetry across the Hα line in triplots and (Q, U) diagrams (top and bottom, respectively). In the triplot, the position angle (PA) is presented in the upper panel, while the polarization (%) and the Stokes intensity (I) are shown in the middle and bottom panel, respectively. The first column presents a circular geometry of the stellar system on the sky plane, so no line effect can be detected in this case. The other three columns present the expectations where the geometry of the system is non-circular and thus a line effect can be seen. The second column presents a depolarization across Hα line which has similar width of Stokes I. In this case the (Q, U) diagram seems a linear excursion from the continuum towards the central Hα line. In all the (Q, U) diagrams the arrows signify that the polarization directs in and out of the line effect from blue to red wavelengths. In the third column an intrinsic line polarization is shown, where the Hα line from the narrow, compact accreting region is scattered in a rotating circumstellar disk. Here the polarization across the Hα line is narrower compared to the width of Stokes I. Due to the presence of a rotating circumstellar disk, a flip can be seen in PA. This flip can also be seen as a loop in the (Q, U) diagram. Finally the fourth column presents a different pattern of polarization with an absorption component of Hα line, which is commonly known as the 'McLean effect'. Figure credit: Ababakr et al. (2017).

also (Muzerolle et al., 2004).

In MA model, the strong surface magnetic fields ($\sim 1-3$ kG) of TTs (e.g., Guenther et al., 1999) are believed to truncate the accretion flow of circumstellar material, at a distance of a few stellar radii from the central star for a typical mass accretion

rates of $10^{-7} - 10^{-9}$ M yr^{-1} in the circumstellar disks (e.g., Basri & Bertout, 1989; Gullbring et al., 1998). The circumstellar disk material is then transferred from the inner disk zone to the star through accretion columns confined by the magnetic field lines. The free falling matter plunges onto the stellar surface creating accretion shocks near the magnetic poles. The stellar envelope in HAeBes is, however, expected to be fully radiative making the generation of magnetic fields of sufficient strength required to support MA difficult. Recent measurements of magnetic fields in HAeBes have, indeed, established that only a few percent of them have significant field detection (e.g., Alecian et al., 2013a) and the derived upper limits on the magnetic field strength are not sufficient to sustain MA in them.

Nevertheless, the presence of circumstellar disks around numerous HAeBes is now confirmed (e.g., Grady et al., 2000; Matter et al., 2014) and a significant number of them are actively accreting circumstellar material through their disks (Donehew & Brittain, 2011; Mendigutía et al., 2011, 2012). Using the profile of HeI 10830 Å line, believed to trace the kinematics and structure of outflow and accretion in young stars (e.g., Takami et al., 2002), Cauley & Johns-Krull (2014, 2015) showed that the MA columns spanning to several stellar radii above the stellar surface is not very common for HAes and late-type HBes, instead, found evidence for a more compact accretion geometry closer to the star. They further added that the accretion mechanism in early HBes may be a different one altogether. Thus the region of few stellar radii from the surface of the star holds key to understand the accretion mechanisms in HAeBes.

The technique of linear Stokes QU spectropolarimetry, first used to study classical Be stars (e.g., Poeckert & Marlborough, 1976), is an effective way to probe the geometry of ionized inner circumstellar matter around HAeBes on scales of the order of stellar radii. Recently, based on a study, Ababakr et al. (2017) (hereafter Ab17) found that 75% of HAeBes showed line effects (intrinsic line polarization, depolarization, McLean effect or complex flip across the line) in Hα and 25% not. While intrinsic polarization across a line is explained by the scattering of photons from the compact emission regions, such as magnetospheric columns, the depolarization and the McLean effects are believed to happen when photons across the line is less polarized compared to the continuum due to the presence of a smaller circumstellar disk which reflects the emission photons to our line of sight (e.g., Vink et al., 2002; Vink et al., 2003; Vink et al., 2005b; Vink, 2015). In the McLean line effect, polarization is detected across an absorption component which accompanies an emission component when unscattered stellar light is absorbed. This profile is similar to a typical (inverse) P Cygni, indicating an infall or outflow respectively.

6. SPECTRO-POLARIMETRY OF HERBIG AE/BE STARS USING SALT

The absorbed stellar photons then re-emits isotropically and a fraction of this emission can be scattered into the line of sight. Now, if the geometry of the scattering agents is non-circular in the sky plane, then an enhanced polarization would be detected across the absorption component compared with the continuum. In Fig. 6.1, we have shown different possible polarization patterns.

Among HAeBes, line effects are seen more in HAes (85%) than HBes (66%). Of those that show line effects, majority of the HBes show depolarization or McLean effect while majority of the HAes show intrinsic polarization (Ab17). This difference in the type of line effects seen in HAes and HBes could be an indication of a possible change in the accretion mechanism probably from MA to a disk accretion. But certainly requires improvement in the statistics to confirm the above findings.

The best lines to probe the innermost (few stellar radii from the surface) region of HAeBes is Hα as noted by Ab17. But the difference in the line effects seen between HAes and HBes can also be due to the high level of Hα emission present in HBes diluting the polarized Hα emission emerging from the compact inner region (Vink et al., 2002). Hβ, being a higher excitation emission line, the dilution should be minimal and could show intrinsic polarization across the line in both HAes and HBes. Observations of a few sources do indicate that the line effects seen in Hα and Hβ are consistent and that the difference in the accretion mechanism in HAes and HBes may be real (Mottram et al., 2007).

Hβ, is expected to originate in the similar locations as the Hα line which creates the line polarization in the HAe stars. So, although if the optical depth and extension of Hα emission in HBes stars mask the evidence for a compact source, then observations of the higher Balmer lines, e.g. Hβ should reveal the rotations in the position angles (PAs) and QU loops in the HBe stars. If these rotations do not appear in this line in the HBe stars, while they are observed at Hα among the HAe stars, this would signify that the surrounding environments of HBe stars are different from HAe stars. Thus in this work we present spectropolarimetric results of 6 HAeBes using RSS in spectropolarimetric mode in both Hα and Hβ lines. The sources have been taken from Fairlamb et al. (2017) and Ab17. With the intention to improve the existing statistics, we selected HAeBe sources located to the southern hemisphere which are least studied so far.

Table 6.1: Log of observations.

Star	Year	Month (Date)	V (mag)	Sp. Type*	Exposure Time (s)	SNR (Hα)	SNR (Hβ)
HD 163296	2018	May (22)	6.85	A1V	993	600	480
HD 169142	2018	July (4)	8.16	A8V	1233	450	280
HD 141926	2018	June (22)	9.13	B2III	1340	430	360
HD 135344 B	2018	July (26)	8.71	F8V	1371	380	110
HD 68695	2018	October (24)	9.87	A3V	2134	500	440
HD 130437	2018	May (26)	10.04	B1V	2190	530	330

* Spectral types are obtained from literature, mentioned in the text.

6.2 Observations and Data Reduction

The RSS spectropolarimeter available with the SALT telescope was used for the study. Spectropolarimetry is a photon hungry observation. Hence, based on the brightness of the sources, we selected 14 sources that represent spectral types ranging from B- to early F-types for our observations. Unfortunately, due to poor weather conditions and technical faults we could observe only 6 out of the 14 sources. The log of the observations is provided in Table 6.1. Also, V band magnitude, spectral type, total exposure time given during observations and the SNR obtained for Hα and Hβ spectra, are given in Table 6.1, respectively. The details of data reduction steps and estimation of polarization values and PAs have been elaborated in chapter 2. We selected long slit spectroscopic mode of RSS and included polarimetry by selecting "Linear" option (waveplate pattern 0, 22.5, 45, and 67.5). Instrumental polarization is found to be ∼0.2%. For spectropolarimetry across Hα and Hβ lines, we selected a slit width of 1.5″. For Hβ line, we selected pg3000 grating, camera station at 94° and grating angle at 47°. The set-up gave central wavelength of 4872.2 Å with a spectral resolution of 4020. Calculated the exposure time at specified wavelength of 4861 Å. For Hα line, we selected pg2300 grating, camera station at 98.5° and grating angle at 49.25°. This set-up gave central wavelength of 6576.8 Å with a spectral resolution of 4350.

6.3 Results and Discussions

Presence of circumstellar disks makes the HAeBe stars to be associated with IR excess. In Fig. 6.2 we present the 2MASS $J - H$ vs. $H - K_S$ color-color diagram of our observed sources (cyan filled circles with magenta colored boxes) along with other HAeBe stars (black filled circles) catalogued in literature (e.g. Testi et al.,

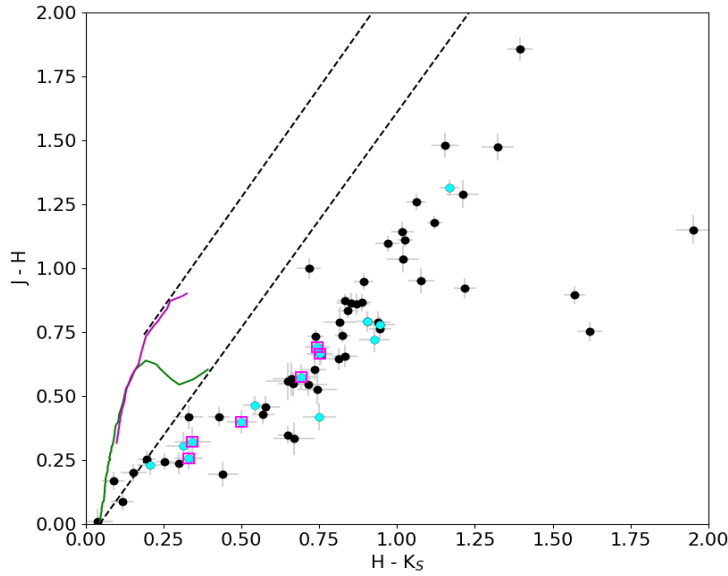Figure 6.2: The $(J\text{-}H)$ vs. $(H\text{-}K_S)$ color-color diagram for the observed HAeBes (cyan filled circles with magnenta colored boxes) and other HAeBes mentioned in the literature (black filled circles). The HAeBes which were listed for our observations, but could not be observed due to several issues, are shown using cyan filled circles. The solid curves in green and magenta represent the locii of the unreddened main sequence stars and the giants, respectively.

1997; Ababakr et al., 2017; Fairlamb et al., 2017). The cyan filled circles without magnenta colored boxes are the targets listed by us for observation, but could not be observed due to weather issues and technical faults. Clearly, the IR excess is noticeable for these category of sources, because of the presence of circumstellar disks. Our target sources have less extinction, because of which they are optically brighter.

Among Hα and Hβ, the line emission is expected to be stronger for lower order recombination lines. Hβ line in emission is also present in the observed spectra, but in some cases, it barely fills the underlying the photospheric absorption line. Nevertheless, the Hβ line shows line effect similar to Hα, although its transition probability is much smaller (Mottram et al., 2007).

We rebinned the data to minimize the error in polarization and thus, increase the SNR. Typically, the error in polarization is $\lesssim 0.1\%$ for the observed HAeBes. The continuum polarization (P$_{cont}$) across the Hα and Hβ lines are quite similar, while we found a difference in the continuum PA (θ_{cont}) across these lines. The QU behaviour is also very similar in these two lines. Based on the similar line effects in most sources in the Hα and Hβ polarization spectra and also in the QU behaviour, we can conclude that the accretion mechanisms responsible for the polarization in

Table 6.2: Spectropolarimetric properties of the observed sources.

Star	EW (Å)		P_{cont} (%)		θ_{cont} (Å)		Line effect		QU behaviour	
	Hβ	Hα	Hβ	Hα	Hβ	Hα	Hβ	Hα	Hβ	Hα
(1)	(2)	(3)	(4)	(5)	(6)	(7)	(8)	(9)	(10)	(11)
HD 163296	13.10	-18.62	0.7±0.1	0.6±0.1	21±3	50±5	yes	yes	loop	loop
HD 169142	7.68	-3.39	0.2±0.1	0.2±0.1	103±11	97±10	no	yes	C	C
HD 141926	-3.46	-23.96	1.7±0.1	1.5±0.1	68±2	76±2	yes	yes	loop	loop
HD 135344 B	-	-8.45	0.3±0.1	0.3±0.1	179±8	107±9	no	no	C	C
HD 68695	15.56	-4.73	0.3±0.1	0.3±0.1	138±14	124±12	yes	no	C	C
HD 130437	-4.00	-44.99	5.6±0.1	5.7±0.2	58±1	56±1	yes	yes	C	C

C: complex

- and + signs in EW indicates emission and absorption.

Hα are also acting similarly in Hβ. We present spectropolarimetric results of these sources in Table 6.2. The EWs of Hα and Hβ lines are provided in columns (2) and (3). Typically, the error in EW is found to be $\lesssim$10%. We used IRAF package to estimate the EWs. Columns (4) to (7) list the measured P_{cont} % and θ_{cont} across the Hα and Hβ lines, respectively. We present the line effect and QU behaviour in columns (8) to (11) for Hα and Hβ lines, respectively. In Figs. 6.3-6.8 (a) and (b) we present the spectropolarimetric results across both Hβ and Hα lines, respectively. The Stokes intensity (I) is shown in the first row, linear polarization (%) in the second and the PA is shown in the third row. In last row, we present the QU behaviour across the same lines.

1. **HD 163296:** It is located at a distance ∼101 pc (Bailer-Jones et al., 2018). Mora et al. (2001) estimated the spectral type of HD 163296 as A1V. Based on X-shooter spectroscopic study, Fairlamb et al. (2015) estimated a temperature of 9250±250 K for this source. The extinction A_V of HD 163296 was computed as 0.0 and distance as 101^{+4}_{-3} pc which agrees very well with the distance estimated by *Gaia* DR2. The p% estimated by us in Hα and Hβ lines are 0.6% and 0.7%, respectively. The estimated PA are 50° and 23° in Hα and Hβ, respectively. Based on Hα linear spectropolarimetry of HD 163296, Ababakr et al. (2017) found p% and PA of this source to be 0.2% and 49°. In previous observations, Ababakr et al. (2016) found p% and PA of HD 163296 to be 0.7% and 2°. We deliberately included this source in our sample to investigate whether the polarization show any variability. In Fig. 6.3, we present the spectropolarimetric results of HD 163296 across both Hα and Hβ lines, respectively. The Hα line shows emission while Hβ shows emission within absorption. The EW of absorption is 13.10 Å, while the emission component has

the EW 1.45 Å. The line effect in Hβ line in the p% plot follows the emission component of the total intensity plot. The QU plots of both lines behave as loops indicating the accretion mechanism taking place in this source.

2. **HD 169142:** Bailer-Jones et al. (2018) estimated distance to HD 169142 as 113^{0}_{-1} pc. Similar to HD 163296, HD 169142 (A8V; Grady et al., 2007) also shows Hα in emission and Hβ in absorption (see Fig. 6.4). A change in polarization across the Hα line is visible, while Hβ line does not show any noticeable change in polarization. QU behaviour shows a complex distribution for both Hα and Hβ lines. We estimated p% of HD 169142 as 0.2% for both Hα and Hβ lines, while the measured PA are 97 and 103°, for Hα and Hβ, respectively.

3. **HD 141926:** Vieira et al. (2003) estimated the spectral type of HD 141926 as B2III. Fairlamb et al. (2015) estimated temperature of this source 28000±1500 K. The extinction was computed as ∼2.40 and the distance to this source was estimated as 1254^{+143}_{-175} pc. Bailer-Jones et al. (2018) estimated the distance to this source as 1345^{+88}_{-77} pc. We can see emission in both Hα and Hβ lines for this source (Fig. 6.5). We could see a clear change in both p% and PA across the Hα and Hβ lines. A loop in QU plane of Hα line is noticeable, while it is not clearly visible in the same for Hβ line. It is surprising that the spectral type of HD 141926 is B2, though the QU behaviour shows a loop structure, which is expected for an A type or at most B9 type star. From literature, we have found that HD 169142 is a X-ray binary (Liu et al., 2000; Malkov et al., 2015). We could not obtain any information of the binary component (1H1555−552) from literature. But a possibility is there that a magnetically active component could be responsible for the line polarization and hence the loop in the QU behaviour. Based on our spectropolarimetric observations, we estimated p% and PA of HD 169142 to be 1.5% and 1.7% and 76° and 68°, for Hα and Hβ, respectively.

4. **HD 135344 B:** The spectral type of HD 135344 B is F8V (Coulson & Walther, 1995). Bailer-Jones et al. (2018) estimated the distance to this source as 135^{+2}_{-1} pc. We present spectropolarimetric results of HD 135344 B in Fig. 6.6. Hα shows emission while Hβ shows absorption, though we could not measure the EW of Hβ because of its very low SNR. Line effect can not be clearly seen across the Hα and Hβ lines. Also, the QU behaviour shows a complex distribution in Hα as well as Hβ. The estimated p% is found to be 0.3% across

both Hα and Hβ lines. PA values for Hα and Hβ lines are measured as 107° and 179°, respectively.

5. **HD 68695:** Gray et al. (2017) estimated spectral type of this source as A3V. Fairlamb et al. (2015) estimated temperature of this source 9250±250 K. The extinction was computed as ∼0.0 and the distance to this source was estimated as 344^{+106}_{-103} pc. Bailer-Jones et al. (2018) estimated the distance to HD 68695 as 391^{+6}_{-5} pc. In Fig. 6.7, line effect of this source can be seen in Hβ while there is no visible change in p% in Hα. We estimated the p% of this source to be 0.3% for both Hα and Hβ lines. The estimated PA are 124° and 138°, for Hαand Hβ lines, respectively. The Hα line shows emission while Hβ shows a small emission within absorption. In the QU plane, we did not find any noticeable structure for both the lines.

6. **HD 130437:** Levenhagen & Leister (2006) estimated the spectral type of HD 130437 as B1V. Bailer-Jones et al. (2018) estimated the distance to HD 130437 as 1662^{+107}_{-95} pc. Based on our observations, we estimated p% of HD 130437 are 5.7% and 5.6% for Hα and Hβ lines, respectively. The estimated PA of this source are 56° and 58°, for Hα and Hβ lines, respectively. In the QU plane, we did not find any noticeable structure for both the lines. We can see emission in both Hα and Hβ lines for this source (Fig. 6.8). There are noticeable broad depolarization present in both the Hα and Hβ emission lines, which further confirms the disk accretion in the HBe stars.

We have found complex QU behaviour in a majority of our observed HAeBes. This pattern depends on the bulk motions and specific geometry of the scattering agents surrounding the origin of Hα and Hβ emission. A loop in the QU plot usually indicates that the scatterers are distributed within a rotating geometry, but if the scattering happens in an expanding medium, the QU pattern will be more 'linear'. In case of an expanding and a rotating medium, the QU behaviour is expected to be more complex (Vink et al., 2002).

Though we have a limited sample size, we could contribute in the improvement of the statistics of studying the accretion mechanism in HAeBes. In Fig. 6.9, we present the histogram of HAeBes (as well as low-mass TTSs) of different spectral types with respect to the type of Hα line effect in them, from Ab17. This figure suggests that in the low-mass TTSs and late type HAes, the dominant effect is the intrinsic line polarization (dark blue), whereas in case of early HBes, depolarization (dark red) is mostly prominent. Also, there is evidence of McLean line effect (yellow)

in some of the targets. In addition to these, 6 sources show complex (dark green) behaviour in terms of line effects. In this figure, the line effect clearly appears to change from line polarization to depolarization from late-type to early-type sources, especially from B7 spectral type. Interestingly, majority of the sources showing complex behavior are lying between the early and late type HAeBe stars suggesting that a combination of disk and magnetospheric accretion may be present in them.

Along with these sources listed by Ab17, our observed sources are also added in Fig. 6.9. The light green color suggests sources showing complex behaviour (HD 135344 B, HD 169142, HD 68695). The light red color indicates the line polarization in HD 141926 (B2III). HD 130437 (B1V) shows depolarization which is shown using light blue color. We did not show HD 163296 (A1V) as this source is already included in this figure, by Ab17, which shows line polarization. Bases on our study, we added one source each to the spectral types of B1, B2, A3, A8, and F8 spectral type. There is a need to increase the statistics in the range of B8$-$B0 to further confirm the ongoing disk accretion in the HBe stars.

6.4   Summary and Conclusions

We observed six HAeBe stars in spectropolarimetric mode to understand their accretion mechanism using RSS attached with 10-m SALT. The change in polarization across the Hα and Hβ lines in the observed targets are studied here.

In the observed spectra of HD 163296 (A1V), we obtained evidence of line polarization in this source, suggesting its magnetospheric accretion. A change in polarization across the Hα line is visible in HD 169142 (A8V), while Hβ line does not show any noticeable change in polarization. In case of HD 141926 (B2III), we obtained a clear change in p% and PA across both the emission lines. In the spectropolarimetric results of HD 135344 B (F8V), line effect could not be seen in both Hα and Hβ lines. HD 68695 (A3V) shows line effect across Hβ while there is no visible change in p% in Hα. There are noticeable broad depolarization present in both the Hα and Hβ emission lines in HD 130437 (B1V), which further confirms the disk accretion in the HBe stars.

Our study of 6 HAeBes has contributed upto $\sim$9% improvement of the statistics of HAeBes (56 sources studied by Ab17), which is significantly low. We need more samples of spectral types earlier than B0 to improve the statistics for the confirmation of disk accretion in the HBe stars. Using 10-m SALT, we can enlarge the number of samples, especially which are located in the southern hemisphere.
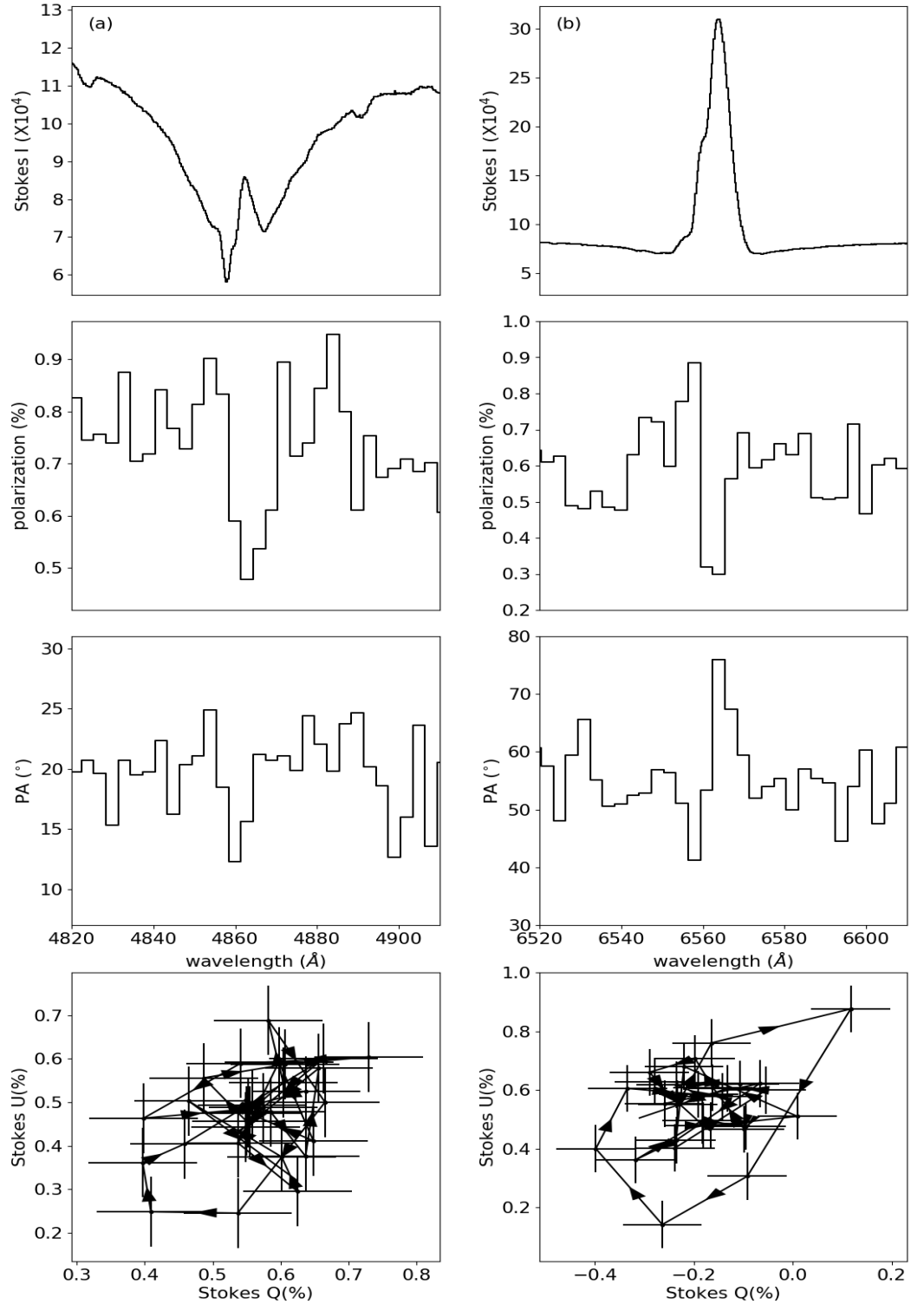
Figure 6.3: **(a)** Line effect in the Hβ spectropolarimetry of HD 163296 as a combination of triplot. In the triplot polarization spectra, the Stokes intensity (I) is shown in the top panel, linear polarization (%) in the centre and the PA is shown in the bottom panel. **(b)** Line effect in the Hα spectropolarimetry of the same source. The triplot represent the same as **(a)**.

Figure 6.4: Line effect in the Hβ **(a)** and Hα **(b)** spectropolarimetry of HD 169142. The triplot represent the same as 6.3.

Figure 6.5: Line effect in the Hβ **(a)** and Hα **(b)** spectropolarimetry of HD 141926. The triplot represent the same as 6.3.
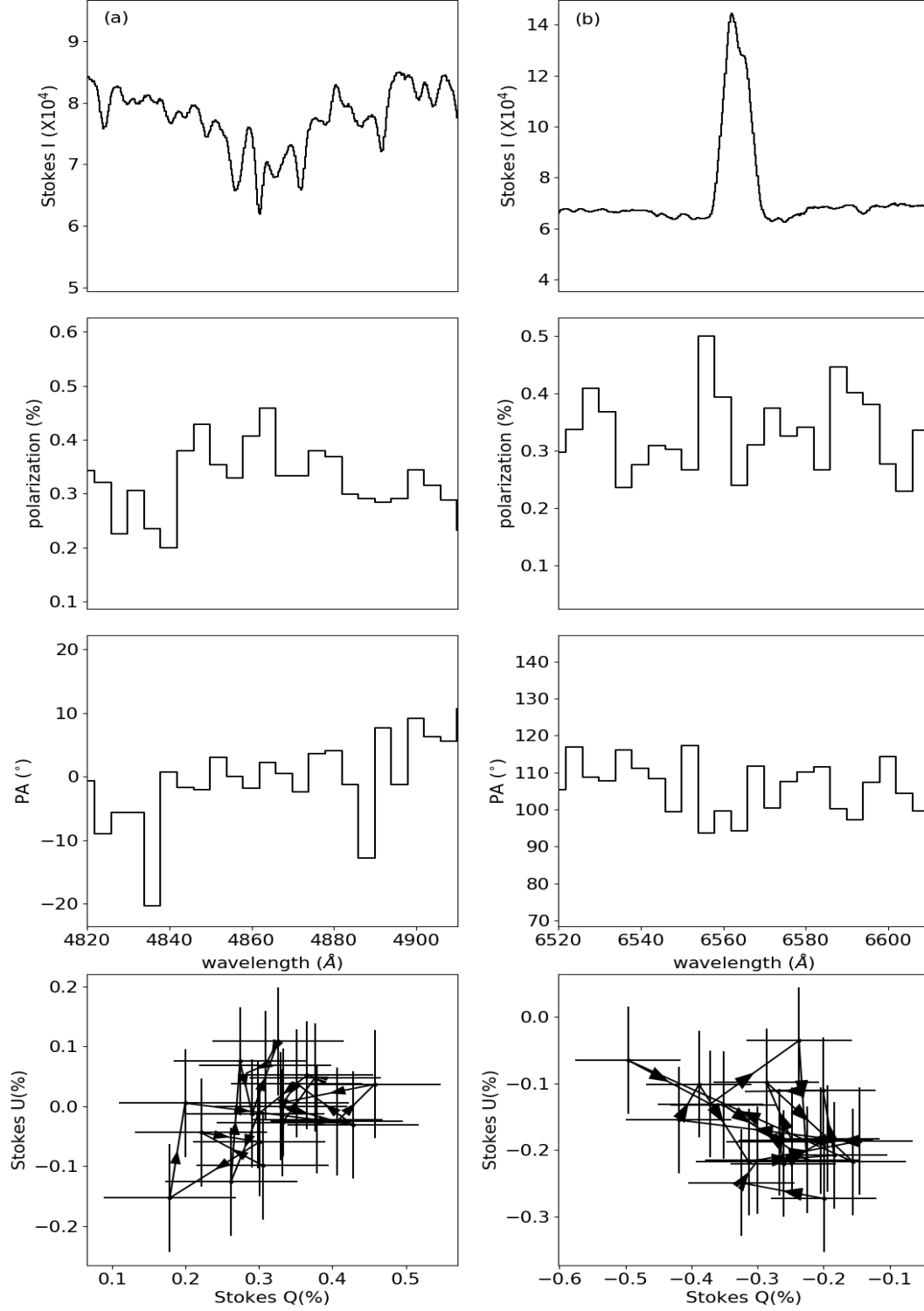
Figure 6.6: Line effect in the Hβ **(a)** and Hα **(b)** spectropolarimetry of HD 135344B. The triplot represent the same as 6.3.
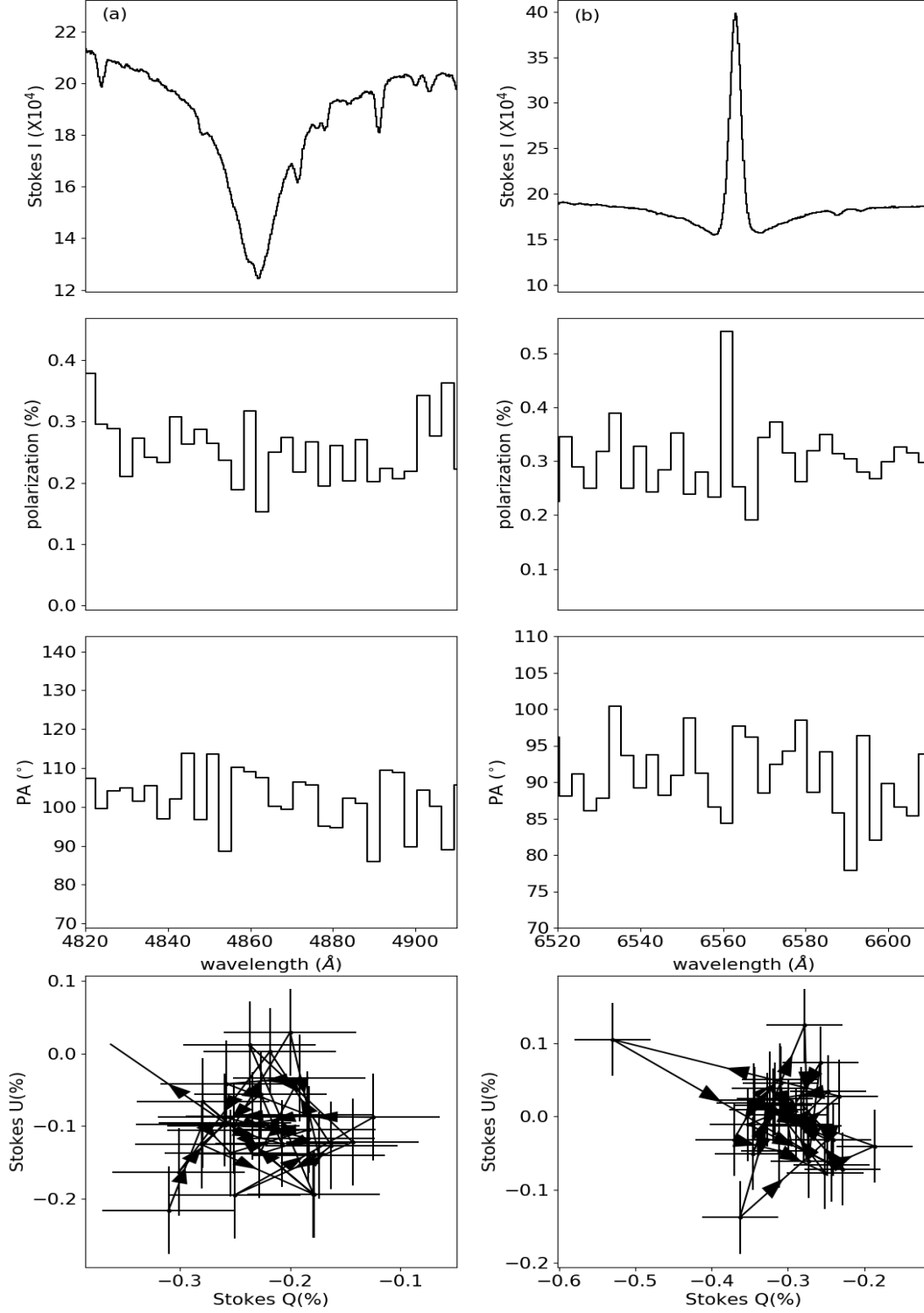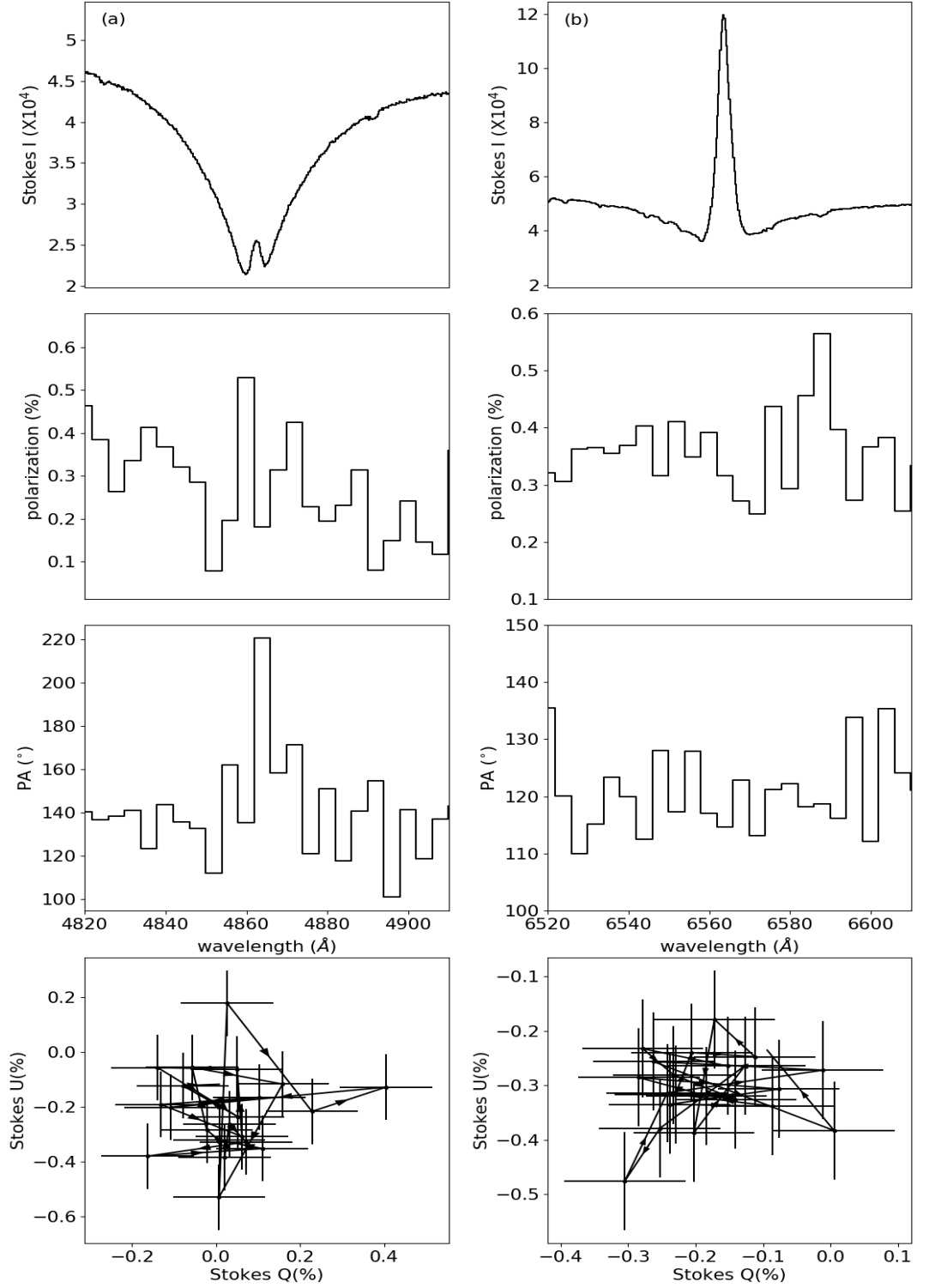
Figure 6.7: Line effect in the Hβ **(a)** and Hα **(b)** spectropolarimetry of HD 68695. The triplot represent the same as 6.3.
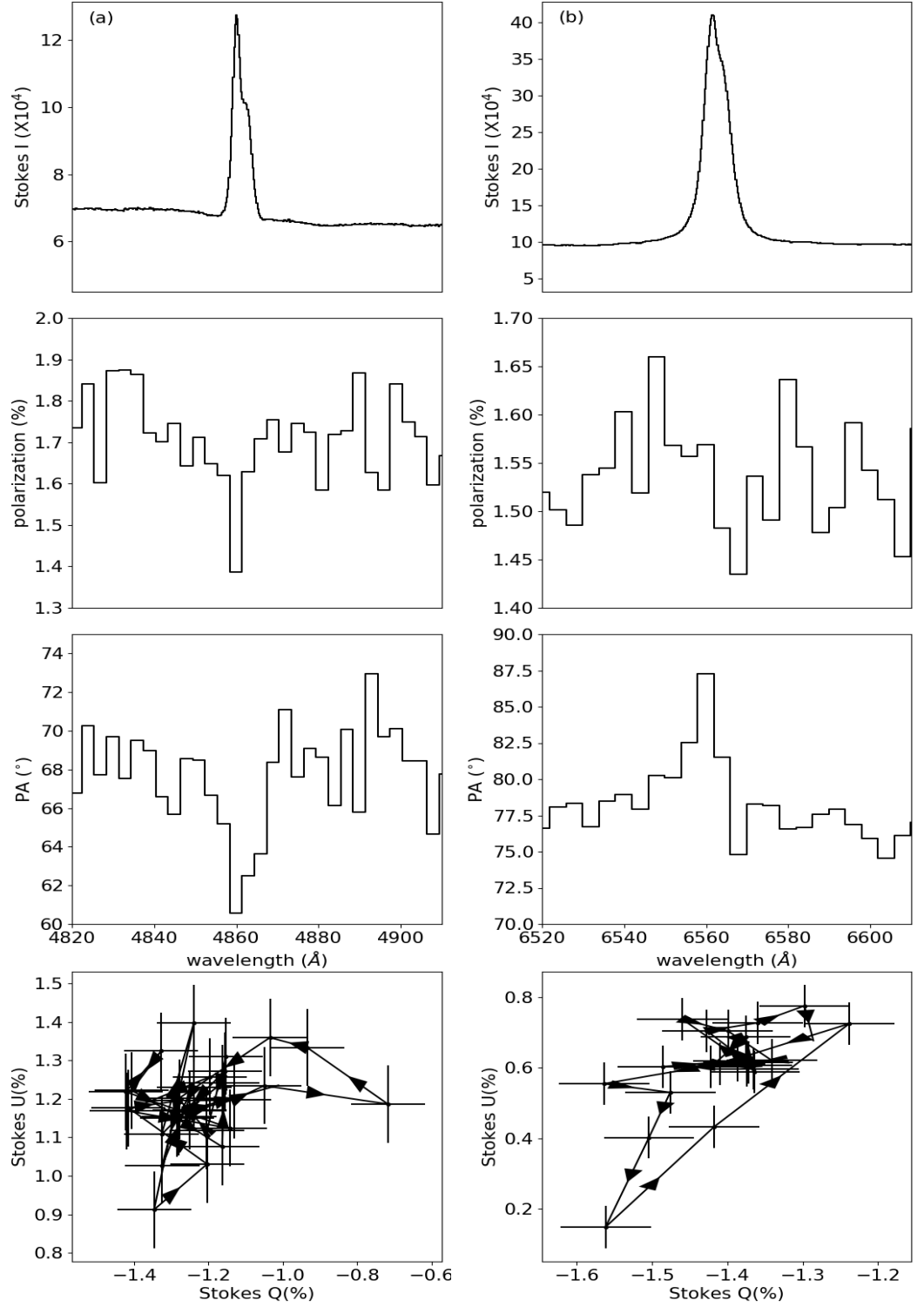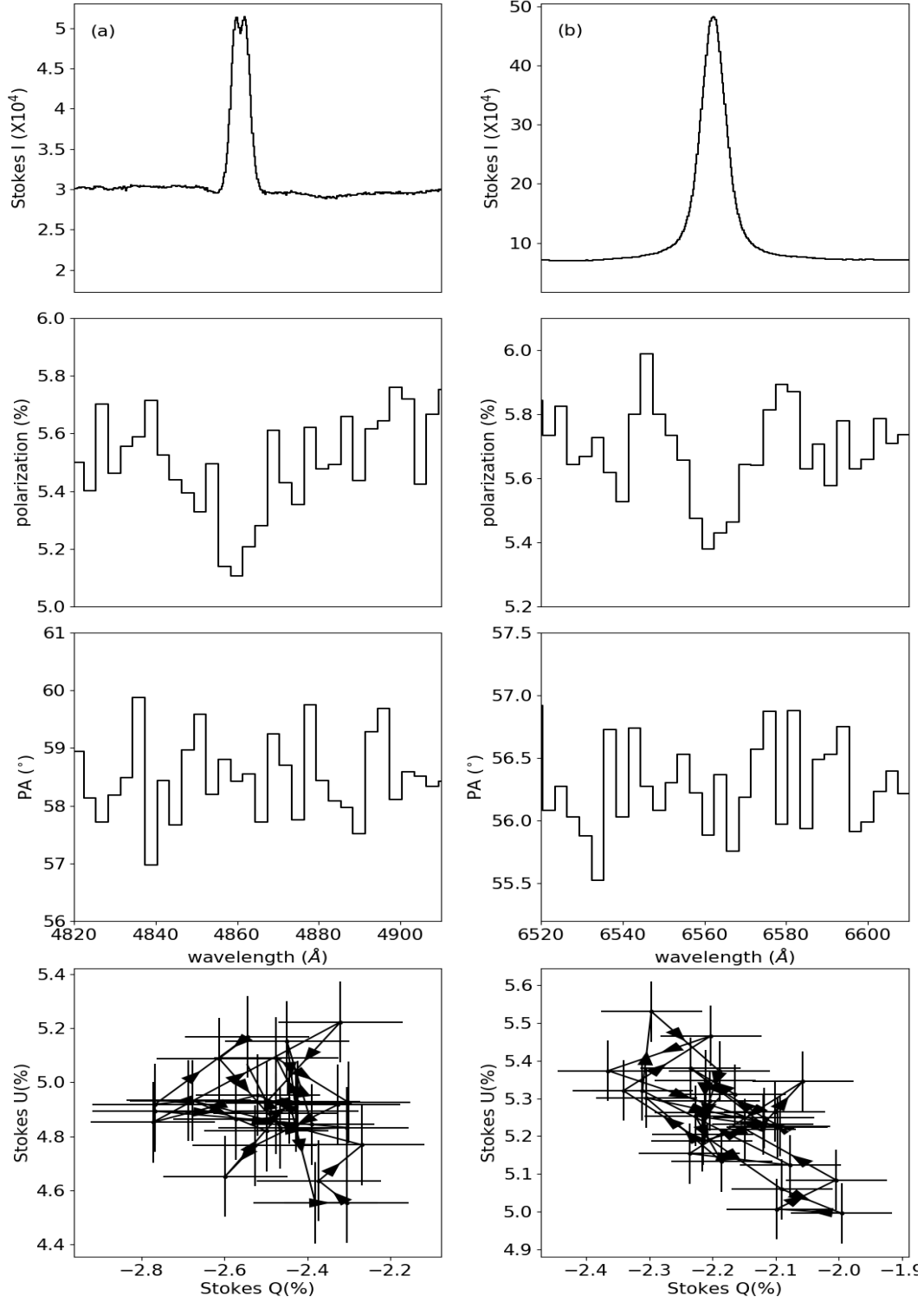
Figure 6.8: Line effect in the Hβ **(a)** and Hα **(b)** spectropolarimetry of HD 130437. The triplot represent the same as 6.3.
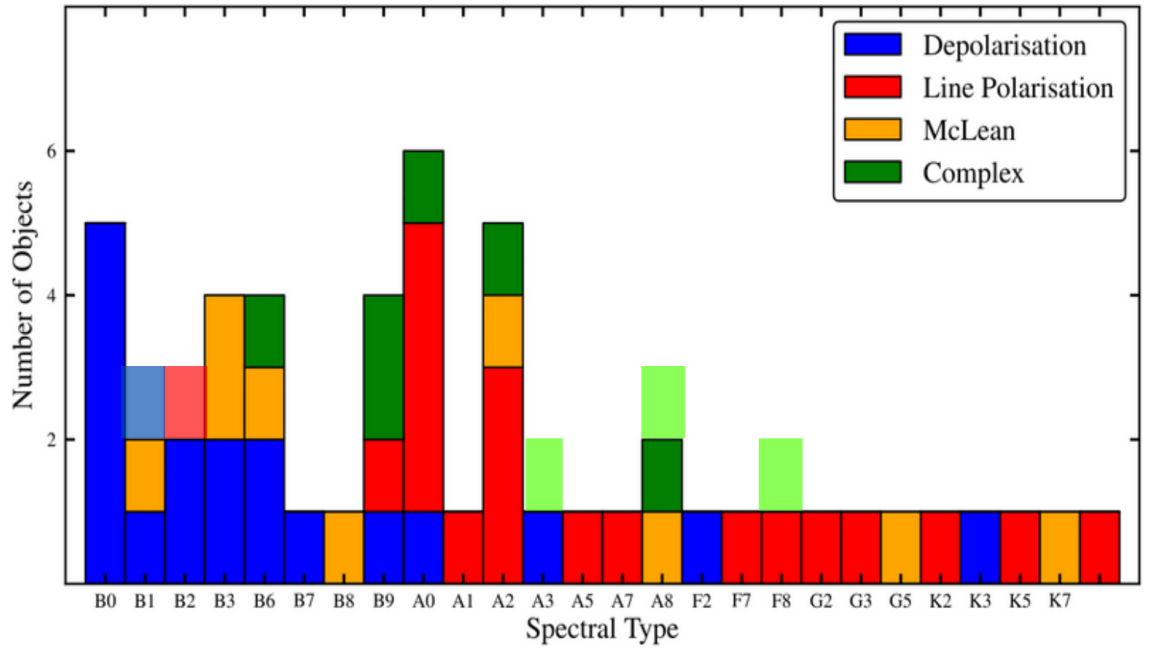
Figure 6.9: Figure adopted from Ab17 representing the type of the line effects observed across Hα line with respect to the spectral types of the massive HAeBes and low-mass TTSs. We added our contribution in lighter colors. The light red color shows the line polarization in HD 141926 (B2III). HD 130437 (B1V) shows depolarization which is indicated using light blue color. We did not present HD 163296 (A1V) as this source is already included in this figure, by Ab17, which shows line polarization. Other sources showing complex behaviour are shown in light green colors.

Chapter 7

Investigation of Rocket Effect in Bright rimmed clouds using *Gaia* DR2

7.1 Introduction

The effect of stellar feedback on star formation rates, efficiency, and the initial mass function is one of the main focuses of the study of star formation and galaxy evolution. The stellar feedback is considered as positive when it triggers collapse in otherwise stable molecular condensations and as negative when it hinders star formation by dispersing material which otherwise would have formed stars. Massive OB stars emit a copious amount of ionizing radiation, which quickly ionizes and heats the surrounding medium. The ionizing heating of the star-facing side of pre-existing density structures drives high-pressure waves into them, leading to their compression and subsequent star formation. This mechanism of radiation-triggered star formation is called radiation-driven implosion (RDI; Bertoldi, 1989; Bertoldi & McKee, 1990; Lefloch & Lazareff, 1994; Miao et al., 2009; Haworth et al., 2012). The consequent clouds are called bright-rimmed clouds (BRCs; Sugitani et al., 1991; Sugitani & Ogura, 1994), which are usually found to be located at the edges of HII regions, having a bright rim facing the ionizing source/s and often followed by an extended structure in the opposite side.

In the RDI mode, the evolution of a dense (optically thick) clump being photo-ionized proceeds in two phases - the collapse and transient phase (Bertoldi, 1989; Lefloch & Lazareff, 1994) and the cometary phase (Bertoldi & McKee, 1990; Lefloch & Lazareff, 1994). The collapse phase, which lasts for $\sim 10^5$ yr, begins when an

ionization front preceded by a shock wave propagates through the cloud, causing it to compress on its axis and heating. At the ionization front, the material gets ionized and escapes towards the ionizing source, causing a photo-evaporation flow. The escaping material has an equal and opposite reaction on the cloud, causing it to accelerate away from the ionizing star, similar to a jet emitted from a rocket. This phenomenon, called the "Rocket Effect", was proposed by Oort (1954). In the cometary phase, the cloud enters into a quasi-equilibrium state, continues to accelerate away from the ionizing source and may eventually get photo-evaporated completely. Typically, a B2 star can push a cloud of mass 100 $M_\odot$ with a speed of ~ 19 km s^{-1}, which eventually goes down to a final speed of $3 - 4$ km s^{-1} (Kahn, 1954). The time ($t_\star$) at which the star formation starts and the fraction of the cloud material that gets converted into stars critically depend on the amount of incident ionizing flux (Bisbas et al., 2011). For a typical values of the incident ionizing flux, 10^9 cm^{-2}s^{-1} (Morgan et al., 2004; Thompson et al., 2004), the $t_\star$ is $\sim 10^5$ yr. Therefore, if the star formation is triggered in BRCs, the YSOs that are formed inside the accelerating cloud should share a similar motion and hence would also move approximately radially away from the ionizing star or stars which is or are responsible for the triggering (Dale et al., 2015).

Based on their association with *IRAS* (Infrared Astronomical Satellite) sources, a total of 89 BRCs (44 in the northern hemisphere and 45 in the southern hemisphere) were cataloged by Sugitani et al. (1991) and Sugitani & Ogura (1994). Signposts of recent and ongoing star formation, e.g., Hα emitting stars, Herbig-Haro objects, *IRAS* point sources, molecular outflows, etc. have been noted in BRCs (e.g. Table 1 of Elmegreen, 1998). BRCs are, thus, potential sites of radiation-triggered star formation (e.g., Elmegreen, 2011). Subsequent studies of BRCs revealed the presence of small aggregates or clusters of young stellar objects (YSOs), with the older sources lying closer to the ionizing source and the younger ones lying closer to the *IRAS* source located inside the BRCs. This led to the hypothesis of "small-scale sequential star formation" (SSSSF; Sugitani et al., 1995; Matsuyanagi et al., 2006; Getman et al., 2007; Ikeda et al., 2008; Chauhan et al., 2009; Getman et al., 2009; Choudhury et al., 2010).

In this chapter, we present results of our R-band polarimetric measurements of 12 YSOs identified in the direction of BRC 18 to infer their projected disk orientations. We intend to investigate the impact of the cloud's magnetic field as well as the impact of energetic radiation from the ionizing source, λ-Ori, on the orientation of the circumstellar disks around the YSOs associated with the cloud. We selected BRC 18 because it is one of the closest BRCs to the Sun (~ 400 pc, using latest *Gaia*

DR2; Kounkel et al., 2018) and because of the knowledge of the cloud's magnetic field inferred from the R-band polarization measurements of the stars projected background of it (Neha et al. under preparation).

Magnetic fields are believed to play a significant role in the evolution of molecular clouds as well as in regulating the star formation in them (e.g., Crutcher, 1999; Chen & Ostriker, 2014; Hennebelle & Inutsuka, 2019). Stars are born as a consequence of the gravitational contraction of molecular cores. During this process, gravity affects neutral species of the cloud, while ions are attached with the magnetic field. In a system of the cloud with straight magnetic field lines, Galli & Shu (1993) showed that major axes of the pseudo-disks are oriented perpendicular to the magnetic field lines, which is expected if the gravitational collapse happens preferentially along the field lines. Therefore, the orientations of YSOs with circumstellar disks can provide information on the impact of the magnetic field during the gravitational collapse. The circumstellar disks are expected to be aligned with their symmetry axes almost parallel to the cloud's magnetic field. Now, if the collapse is not significantly affected by the magnetic field, the orientation of the circumstellar disks could be random.

The presence of circumstellar material around YSOs associated with the BRCs has been established by the observations of strong IR excess (e.g. Ikeda et al., 2008; Rebull et al., 2013; Panwar et al., 2014; Sharma et al., 2016) and emission line features (e.g. Ogura et al., 2002; Ikeda et al., 2008; Hosoya et al., 2020). The dust grains and electrons present in these flattened disks scatter the light off from the central source and hence, are mainly responsible for the observed polarization (Strom, 1977; Elsasser & Staude, 1978; Bastien & Landstreet, 1979; Bastien, 1982; Bastien, 1985; Sato, 1988). The degree of polarization depends on the amount of dust grains, also on the degree of flatness of the disk and its alignment with respect to the line-of-sight. For an optically thin disk, if linear polarization is made by single scattering, the position angle of the polarized light is oriented perpendicular to the disk, while in case of an optically thick disk, where the polarization is processed by the scattering dust grains oriented perpendicular to the disk, the position angle is aligned parallel to the disk plane (e.g. Brown & McLean, 1977; Elsasser & Staude, 1978). Therefore, polarimetry can be used as a tool to obtain the geometrical structure of the circumstellar material around the YSOs (Ménard, 2005).

The distances and the proper motion values provided by the *Gaia* DR2 are utilized to establish the association of the YSOs with BRC 18. We found that the majority of the YSOs, both having polarimetric observations made by us and otherwise, show similar proper motion values suggesting that they are all moving together as a group. If the YSOs are all formed as a result of triggering, and their

motions are affected by the cloud's "Rocket Effect", then they should be moving away from the λ Ori. The subtraction of the global motion of the λ Ori HII region from the proper motions of the YSOs vectorially gave us the true internal motions of these YSOs in the sky plane. We found that the median direction of motion is indeed away from the direction of the λ Ori as expected. Inspired by this finding, we searched for YSOs associated with the rest of the BRCs having the *Gaia* DR2 data to investigate their motion and the "Rocket Effect".

Of the 89 BRCs, YSO candidates have been identified towards 54 of them using various methods till date. Ogura et al. (2002) detected Hα emission stars in 28 BRCs using slitless grism spectroscopy and Ikeda et al. (2008) updated the sources using the same technique. Recently, Hosoya et al. (2020) identified Hα emitting sources in 14 BRCs based on slitless optical spectroscopy. Hayashi et al. (2012) made wide-field near-IR imaging observations towards 32 BRCs. Koenig et al. (2015) conducted optical spectroscopic observations of a number of YSO candidates identified based on the *WISE* data in σ Ori and λ Ori region which harbor 2 BRCs. Sharma et al. (2016) identified YSOs in 8 BRCs located in the southern hemisphere based on near-IR observations and *Spitzer* archival data. Using BVI_c and near-IR photometry Chauhan et al. (2009) studied triggered star formation in 6 BRCs. Based on *Spitzer* IRAC and MIPS archival data and follow up optical photometric and spectroscopic observations, Choudhury et al. (2010) identified and characterized young sources in BRC 38. Rebull et al. (2013) identified a number of new candidate YSOs in BRC 27 and 34. On the bases of optical observations and archival near-IR and mid-IR data, Panwar et al. (2014) detected YSOs in 3 BRCs. Sicilia-Aguilar et al. (2006a,b) made optical imaging and spectroscopy in the Cepheus OB2 region to identify cluster members in Trumpler 37 (BRC 36) and NGC 7160 and characterized their nature as young sources. A rigorous study of identification of YSOs has been done towards BRC 36 so far (e.g. Reach et al., 2004; Sicilia-Aguilar et al., 2005; Sicilia-Aguilar et al., 2006a; Sicilia-Aguilar et al., 2006b; Morales-Calderón et al., 2009; Reach et al., 2009; Sicilia-Aguilar et al., 2010; Barentsen et al., 2011; Getman et al., 2012; Hayashi et al., 2012; Sicilia-Aguilar et al., 2013). Recently, Kounkel et al. (2018) used spectroscopic and astrometric data from APOGEE-2 and *Gaia* DR2 to identify structures towards λ-Ori where BRC 17 and 18 are located.

In this chapter, we begin by presenting the results from our R-band polarimetric analysis of the YSOs associated with the BRC 18 and discuss their projected disk orientations and the impact of the cloud's magnetic field and RDI on their orientations. We then present the results of the motion of the YSOs associated with BRC 18 and subsequently of the YSOs associated with other BRCs to investigate the

Table 7.1: Log of observations.

Year	Month (Date)
2016	October 26, 28
	November 22, 23, 24, 25, 26, 27

"Rocket Effect". We organize the chapter in the following manner. Description of the observational and archival data we used are provided in section 7.2, preliminary results and relevant discussions are presented in sections 7.3 and 7.4, respectively. Finally, we conclude the work with a summary of the results in section 7.5.

7.2 Observational and Archival Data and Analysis

7.2.1 R-band polarimetric data

We acquired optical R-band ($\lambda_{eff} = 0.760$ μm) polarimetric data of 12 YSOs using ARIES Imaging POLarimeter (AIMPOL; Rautela et al., 2004) attached with 1.04 m Sampurnanand Telescope, ARIES, Nainital, India. The log of the observations is presented in Table 7.1. The details of our optical polarimetric data reduction are provided in chapter 2. In order to estimate the reference direction of the HWP during the observing runs, we observed four polarized standard stars (HD 236633, HD 19820, BD+59°389 and HD 25443) from the list provided by Schmidt et al. (1992). Table 7.2 provides the results of the observed polarimetric standard stars.

7.2.2 Archival Data

Based on various methods, for example, 2MASS, *Spitzer*, *WISE* archival data and results from near- and mid-IR photometric observations (e.g. Hayashi et al., 2012; Panwar et al., 2014; Sharma et al., 2016), slitless spectroscopy (Ogura et al., 2002; Ikeda et al., 2008; Hosoya et al., 2020), optical BVI$_c$ photometry (e.g. Chauhan et al., 2009), optical spectroscopy (e.g. Choudhury et al., 2010; Kounkel et al., 2018), X-ray imaging (Getman et al., 2012), astrometry from recently released *Gaia* DR2 (Kounkel et al., 2018), presence of the YSOs and candidates in the BRCs have been reported. We collected information of all sources available in the literature for our study.

We obtained distances (d) of the YSOs and candidates associated with BRCs from the catalog given by Bailer-Jones et al. (2018) and the proper motion mea-

Table 7.2: Results of polarized standard stars observed in the R band (λ_{eff}=0.630 μm).

Date of observations	P$\pm\epsilon_P$ (%)	$\theta \pm \epsilon_\theta$ (°)
HD 236633 ([a]Standard values: 5.38 ± 0.02%, 93.°04 ± 0.°15)		
26 Oct, 2016	4.8±0.1	98±1
BD+59°389 ([a]Standard values: 6.43 ± 0.02 %, 98.°14 ± 0.°10)		
28 Oct, 2016	5.6±0.1	105±1
22 Nov, 2016	6.3±0.1	106±1
24 Nov, 2016	6.2±0.2	106±1
27 Nov, 2016	6.4±0.3	109±1
HD 19820 ([a]Standard values: 4.526 ± 0.025 %, 114.°46 ± 0.°16)		
22 Nov, 2016	4.3±0.1	126±1
26 Nov, 2016	4.2±0.1	124±1
HD 25443 ([a]Standard values: 4.734 ± 0.045 %, 133.°65 ± 0.°28)		
23 Nov, 2016	4.6±0.1	144±1
24 Nov, 2016	4.8±0.2	138±1
26 Nov, 2016	4.7±0.2	143±1
27 Nov, 2016	4.8±0.2	143±1

[a] Values in the R band from Schmidt et al. (1992).

surements in right ascension ($\mu_{\alpha\star}$) and declination (μ_δ) from *Gaia* DR2 (Gaia Collaboration et al., 2018) by making a search around each source within a search radius of $1''$. Sources having their ratio, m/Δm (here m represents the d, $\mu_{\alpha\star}$ and μ_δ values and the Δm represents their respective errors) $\geqslant 3$ are considered for this study. We excluded sources for which RUWE (Renormalized Unit Weight Error) >1.4 (Lindegren, 2018).

To investigate the near-IR excess of the observed YSOs towards BRC 18, we obtained their PanSTARRS g (Chambers et al., 2016) and *WISE W*1 magnitudes (Wright et al., 2010) from (Chambers et al., 2016) and Cutri & et al. (2014) catalogs, by giving a search radius of $1''$ and $3''$, respectively. We also used 2MASS (Skrutskie et al., 2006) colors of the sources in the BRCs from Cutri et al. (2003).

7.3 Results

The polarimetric results are presented in Table 7.3. The right ascension and declination of the sources observed by us are given in columns 2 and 3. The degree of polarization (P%) and polarization position angle (θ in degree) of the YSOs measured in R-band are given in columns 4 and 5 with their corresponding measurement uncertainties. The P% values range from 0.4 to 4.1. The distances of 12 sources obtained from the Bailer-Jones et al. (2018) catalog are listed in column 6 of Table

Table 7.3: Results of polarization measurements and astrometric properties of the observed YSOs towards and BRC 18 in R-band.

Id	RA (°)	Dec (°)	P$\pm\Delta$P	$\theta \pm \Delta\theta$	$d \pm \Delta d$	$\mu_{\alpha\star} \pm \Delta\mu_{\alpha\star}$	$\mu_\delta \pm \Delta\mu_\delta$	$G \pm \Delta G$
	(2015.5)	(2015.5)	(%)	(°)	(pc)	(mas yr^{-1})	(mas yr^{-1})	(mag)
(1)	(2)	(3)	(4)	(5)	(6)	(7)	(8)	(9)
1	85.837176	9.101956	0.4±0.2	175±8	392^8_{-7}	2.369±0.080	-2.588±0.067	12.5723±0.0147
2	86.008673	9.260364	2.3±0.3	95±4	387^{10}_{-10}	2.360±0.111	-2.518±0.088	15.0576±0.0025
3	86.030252	9.110574	0.6±0.2	175±7	393^6_{-6}	1.864±0.086	-2.695±0.061	13.6469±0.0042
4	86.037486	9.154068	1.3±0.4	175±11	397^5_{-5}	2.029±0.067	-2.137±0.052	13.5909±0.0505
5	86.044381	9.212530	0.7±0.2	181±9	402^4_{-4}	2.499±0.045	-2.432±0.038	13.8156±0.0014
6	86.080096	9.209679	0.8±0.2	174±9	381^5_{-6}	2.743±0.064	-1.958±0.054	13.9851±0.0026
7	86.080667	9.089784	0.8±0.4	146±11	382^{10}_{-9}	2.713±0.127	-2.664±0.101	15.4755±0.0013
8	86.091193	9.147916	1.6±0.3	67±5	415^8_{-8}	2.103±0.069	-2.435±0.057	14.4761±0.0028
9	86.096725	9.201062	4.1±0.1	18±5	405^6_{-6}	2.854±0.065	-2.426±0.056	11.7496±0.0020
10	86.108237	9.116840	0.7±0.2	178±9	403^4_{-4}	2.472±0.043	-2.609±0.036	13.5392±0.0113
11	86.220056	9.218111	2.4±0.2	83±5	399^5_{-4}	1.838±0.048	-2.283±0.045	14.0838±0.0050
12	86.267100	9.081243	1.1±0.3	128±6	399^9_{-8}	2.357±0.099	-3.027±0.088	15.2518±0.0049

7.3. The ($\mu_{\alpha\star}$) and (μ_δ) values obtained from (Gaia Collaboration et al., 2018) are listed in columns 7 and 8 respectively, along with their magnitudes in G-band in column 9.

7.4 Discussions

7.4.1 The YSOs associated with BRC 18

7.4.1.1 Polarization of the YSOs

The λ Ori is believed to be responsible for the bright-rim seen towards BRC 18 (Sugitani et al., 1991). If the YSOs associated with the BRC 18 are all formed as a results of trigger due to the RDI caused by the λ Ori, then they are expected to have an age of approximately ∼3.5 Myr considering an angular separation of ∼2.4° between λ Ori and BRC 18. We adopted a distance and an age of ∼400 pc and ∼ 5 Myr respectively for the λ Ori cluster (Kounkel et al., 2018) and a typical isothermal sound speed in HII region of 11.4 km s^{-1} (Bertoldi, 1989; Bertoldi & McKee, 1990) in the calculation. This age is consistent with the average age of the YSOs distributed in the direction of BRC 18 estimated by Kounkel et al. (2018) within the uncertainty. Then, assuming a typical velocity dispersion of ∼ 1 km s^{-1} for the YSOs (Luhman et al., 2009; Wilking et al., 2015), the maximum extent

7. INVESTIGATION OF ROCKET EFFECT IN BRIGHT RIMMED CLOUDS USING *GAIA* DR2
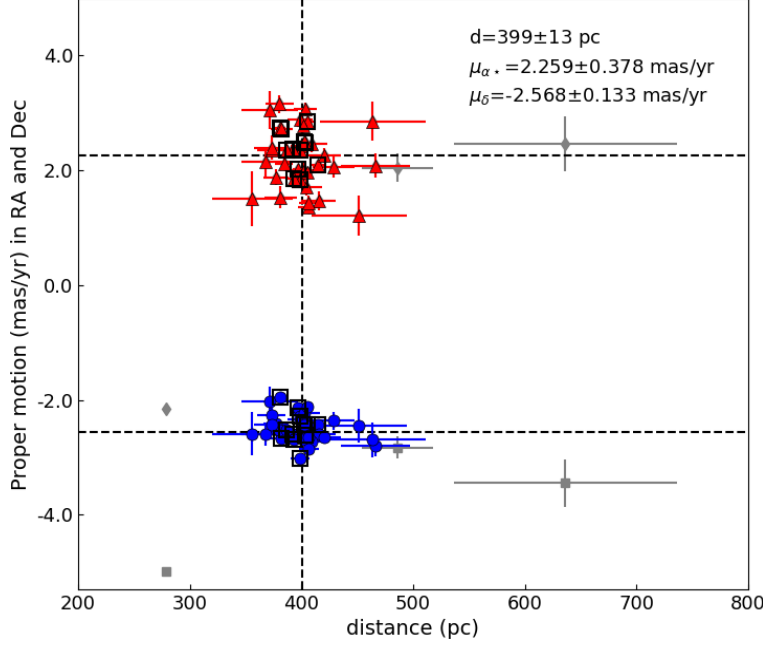

Figure 7.1: Proper motion values of the known YSO candidates associated with BRC 18 are plotted as a function of their distances obtained from *Gaia* DR2 which are lying within $5 \times$ MAD in proper motion and distance values. The red triangles and blue circles represent the d-$\mu_{\alpha\star}$ and d-μ_δ values respectively. The gray squares and diamonds represent the d-$\mu_{\alpha\star}$ and d-μ_δ values of the outliers. The dashed lines show the median values of d, $\mu_{\alpha\star}$ and μ_δ of the YSO candidates.

to which the YSOs could move from their place of birth is approximately $0.5°$. Therefore, all the sources located within a circular area of radius $0.5°$ about the *IRAS* source is considered as a part of the BRC 18 cloud.

We found a total of 76 YSOs within a circular region of radius $0.5°$ about the *IRAS* source in BRC 18. Of the 76, we obtained the *Gaia* data for 39 sources after applying all the selection criteria. In Fig. 7.1 we show the $\mu_{\alpha\star}$ and μ_δ of the sources as a function of their distances (d) using the red triangles and blue circles, respectively. The spatial distribution of the 76 known YSO candidates associated with BRC 18 is shown using yellow filled circles in Fig. 7.6 (a). We used the median absolute deviation (MAD) to estimate the statistical dispersion in our data-sets. The median values of d, $\mu_{\alpha\star}$ and μ_δ are 401 pc, 2.205 and -2.581 mas yr^{-1}, respectively, with corresponding MAD values as 14 pc, 0.309 and 0.151 mas yr^{-1}, respectively. We selected the sources lying within $5\times$MAD with respect to the median values of the distance and the proper motions as sources that are associated with BRC 18. Choice of $5\times$MAD was made based on the fact that most of the sources are lying within this limit. A total of 37 sources satisfy this condition and the remaining

three are considered as outliers (shown in Fig. 7.1 as gray squares and diamonds representing the d-$\mu_{\alpha\star}$ and d-μ_{δ} values, respectively). We recomputed the median and the MAD values for the 37 sources after eliminating the outliers to get the final astrometric results for the YSOs in BRC 18. The new median values for d, $\mu_{\alpha\star}$ and μ_{δ} are 399 pc, 2.259 and -2.568 mas yr^{-1}, respectively. The calculated MAD values are 13 pc, 0.378 mas yr^{-1} and 0.133 mas yr^{-1}, respectively. The proper motion vectors of the 37 YSO candidates obtained from *Gaia* DR2 are shown as yellow arrows in Fig. 7.6 (b).

We obtained R-band polarization measurements for 12 out of 37 sources. These 12 sources are identified using open black boxes in Fig. 7.1. The measured polarization values have contributions from the dust grains located within the pencil beam along the line-of-sight of the stars, which could be the foreground, located in the cloud, and in the circumstellar material. As the cloud is located at $\sim$400 pc away from the Sun, it is important to remove the contribution of the foreground material from the measured polarization values. For this, six foreground stars (HD 38527, HD 39007, HD 37408, HD 37355, HD 38096, and HD 37522), located within a circle of radius 2° centered on IRAS 05417+0907 were selected. The distances of these sources obtained from the Bailer-Jones et al. (2018) catalog range from $\sim 94 - 317$ pc. In Fig. 7.2, the P (%) vs distance (pc) and the θ (°) vs distance (pc) plots for the six foreground sources are shown using open circles. The mean values of the P% and θ for these sources are 0.2% and 117° respectively, with corresponding standard deviations as 0.1% and 6° respectively. The foreground contribution to the measured polarization was subtracted vectorially. No significant change was noticed as expected since the foreground polarization is found to be very low.

In Fig. 7.2 (a) and (b) we show the P% and θ plots for the 12 sources with respect to their distances obtained from Bailer-Jones et al. (2018). Red filled circles represent polarimetric results for the YSOs. Polarization measurements of a large number of sources lying towards the direction of BRC 18 are obtained by Neha et al. (under preparation). The foreground corrected values of these sources are shown in Fig. 7.2 (a) and (b) using filled circles in black. As it is evident that a majority of these sources is lying behind the cloud and hence represents the orientation of the cloud's magnetic field. Two sources, lying at 260 pc and 320 pc, show very low P% values, consistent with the values obtained from the six foreground sources. The dotted line represents the mean distance of 399 pc, and the pink patch represents the five times of the MAD value. As a group, the YSOs show a relatively higher degree of polarization with a mean value of 1.4%. The dispersion in P% is 1.0%. The mean value of θ for the sources observed by Neha et al. is 171°, and the corre-

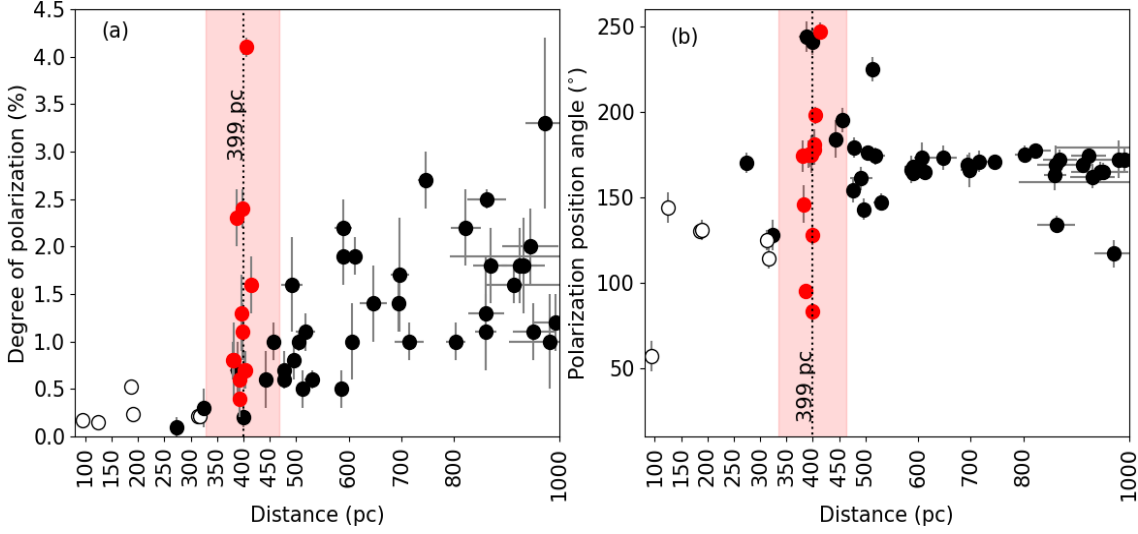# 7. INVESTIGATION OF ROCKET EFFECT IN BRIGHT RIMMED CLOUDS USING *GAIA* DR2

Figure 7.2: **(a)** Plot of degree of polarization vs. distance of the sources projected towards BRC 18 is shown using black filled circles. The observed YSOs having m/Δm $\gtrsim$3 and RUWE $\lesssim$1.4 are shown using red filled circles. The six foreground sources are presented using open black circles. The distance of 399 pc (distance of BRC 18) is shown using dotted vertical line. The pink patch represents the cloud extent which is 5×MAD from 399 pc. **(b)** Polarization position angle vs. distance plot for the same sources. Symbols represent the same as in **(a)**.

sponding dispersion is 8°, which is small compared to the dispersion in θ estimated for the YSOs (62°). This suggests that the cloud has a well ordered magnetic field morphology, and YSOs are showing much diverse values of position angles.

In Fig. 7.3 we show the P% as a function of the $(g - W1)$ colors. The g magnitudes for the sources are obtained from the PanSTARRS ($\lambda_{eff} \sim 4810$Å; Chambers et al., 2016) and $W1$ is obtained from ($\lambda_{eff} \sim 3.6$ μm; Wright et al., 2010). The circles in black indicate the sources observed by Neha et al. under preparation, which are likely to be the normal field stars, while the circles in red are the 10 of the 12 YSOs for which we have polarization measurements and $g - W1$ colors. In a study conducted to investigate correlations between polarization and other observable properties, Bastien (1982) found correlations between polarization and average IR color indices, especially, $V - L$. The observed correlation was attributed to the absorption of stellar radiation by the dust and re-emission in infrared wavelengths. We took the polarization measurements of a number of T Tauri (TT) stars from Bastien (1982) made at 7543 Å and plotted as a function of their $g - W1$ colors. Of the 50 TT stars studied by them, for 24, we obtained $g - W1$ colors, which are shown using filled circles in cyan in Fig. 7.3. We also added polarimetric measurement of one TT star (V773 Tau) from (Vink et al., 2005a), observed in R band (6500
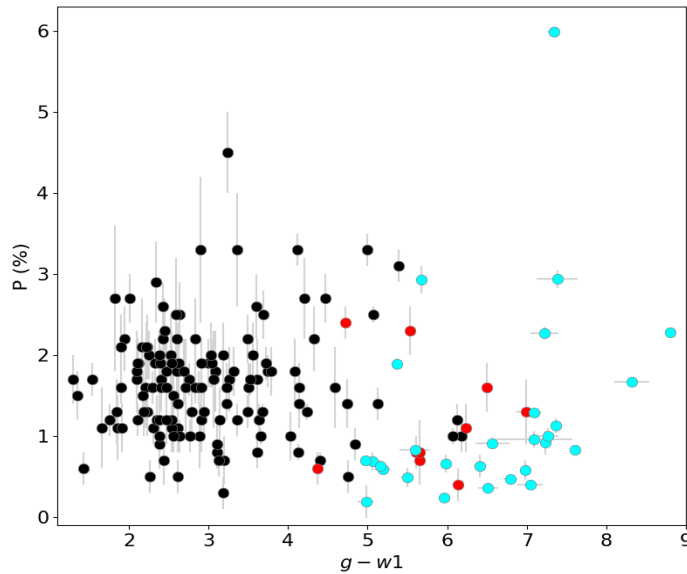
224

Figure 7.3: Plot of the degrees of polarization (P%) vs. PanSTARRS g - *WISE* $W1$ colors of the sources. The black points indicate the sources projected background of BRC 18, while the red points are the YSOs associated with the cloud. The cyan points are the T tauri stars obtained from Bastien (1982); Vink et al. (2005a).

Å). The 10 YSOs observed by us are also falling in the region occupied by these TT stars. It is to be noted that the polarization and color measurements are not simultaneous, and young sources are known for their variability in both the P% and magnitudes (e.g., Joshi et al., 1987; Manset et al., 2009; Lorenzetti et al., 2011). While the normal field stars (circles in black) are showing very less $g - W1$ colors, the YSOs and TT stars are showing a decreasing trend in P% with the increase in the $g - W1$ color. Some TT stars show higher P% and $g - W1$ color, for example, V536 aql.

The distribution of degree of polarization (P%) and polarization position angle (PA) of YSOs and other background sources (observed by Neha et al. in preparation) are shown in Fig. 7.4 (LHS) using red filled circles and gray open circles, respectively. In Fig. 7.4 (RHS) we present the polarization vectors of the YSOs in cyan vectors overplotted on the *WISE* color composite diagram using 3.6 (blue), 4.5 (green) and 12 (red) μm images. The yellow and cyan lines represent the polarization vectors of the background sources (obtained from Neha et al. under preparation) and YSOs, respectively. The white dashed line represents the Galactic plane. A vector with 1% polarization is shown for reference. Neha et al. under preparation estimated the mean P% and PA of the projected stars towards BRC 18 as $1.7 \pm 0.3\%$ and $171 \pm 8°$, respectively. From Fig. 7.2 and 7.4, it is clear that the polarimetric results YSOs

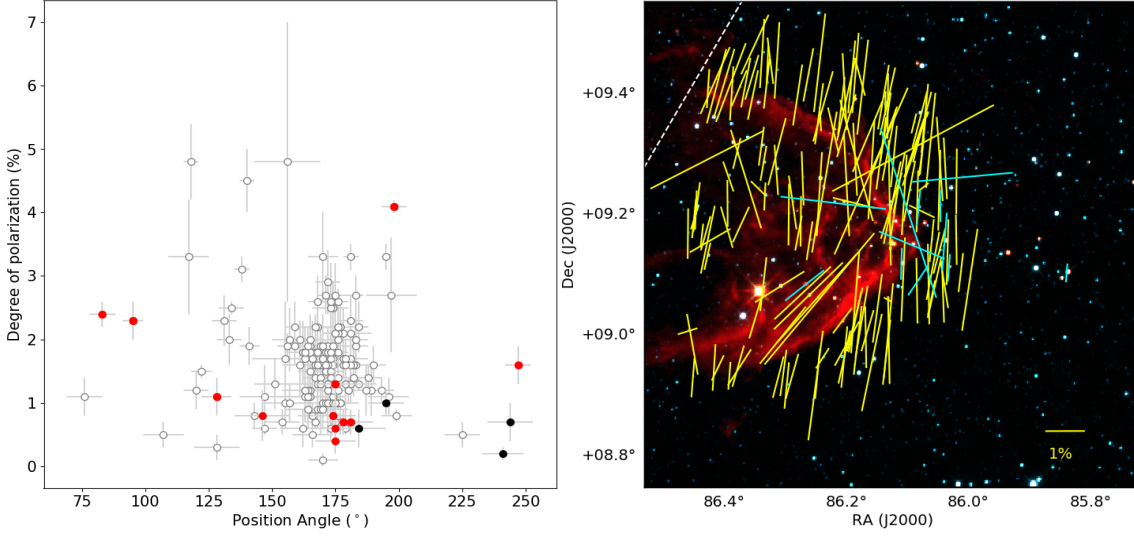# 7. INVESTIGATION OF ROCKET EFFECT IN BRIGHT RIMMED CLOUDS USING *GAIA* DR2

Figure 7.4: **(LHS)** Plot of degree of polarization vs. position angle of the sources projected towards BRC 18. The known YSOs are indicated by red filled circles. Other observed sources projected background towards BRC 18 are shown using grey open circles. The observed sources lying within $5 \times$ MAD from the median distance of BRC 18, but not identified as YSOs, are indicated using black filled circles. **(RHS)** Polarimetric results of the same sources are overplotted on the *WISE* color composite diagram using 3.6 (blue), 4.5 (green) and 12 (red) μm images. The cyan lines represent the polarization vectors of the observed YSOs. The yellow lines represent the polarization vectors of the background sources (Neha et al under preparation). The white dashed line represents the Galactic plane.

are relatively more scattered than those of the other stars projects towards BRC 18, which further confirms the presence of circumstellar disks around these YSOs.

The sudden rise in P% also determines the distance of BRC 18 at $\sim$ 399 pc. When the unpolarized starlight travels through regions containing any molecular cloud, the light gets polarized due to the selective absorption by the dust grains present in that cloud. Normally, there is a stable increase in P% with the increasing column of dust grains along the line-of-sight of the starlight. But when it encounters any molecular cloud, a sudden rise in the values of P% can be noticed. The stars that are foreground to any molecular cloud are expected to show lower P%, compared to the P% shown by the stars that are located behind the same cloud. The distance at which P% rises immediately, is considered as the distance of the cloud (e.g. Straizys et al., 1992; Whittet et al., 1997; Knude & Hog, 1998; Alves & Franco, 2007).
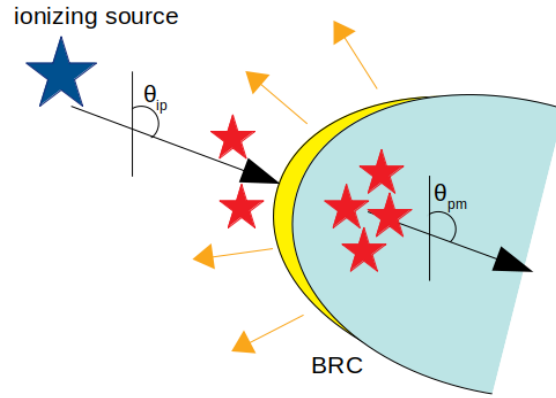
Figure 7.5: Cartoon diagram of a system consisting of a BRC and one ionizing source (not to scale). The massive ionizing source is indicated by a blue star symbol, while the YSOs projected towards the BRC are shown using red star symbols. The thick yellow border indicates the bright rim of the cloud. The angle of ionizing photons with respect to the north is indicated by θ_{ip} and the angle of the proper motion of YSOs with respect to the same is presented by θ_{pm}. The yellow colored arrows indicate the direction of photo-evaporating cloud material, as a reaction of which the BRC accelerates away from the ionizing source.
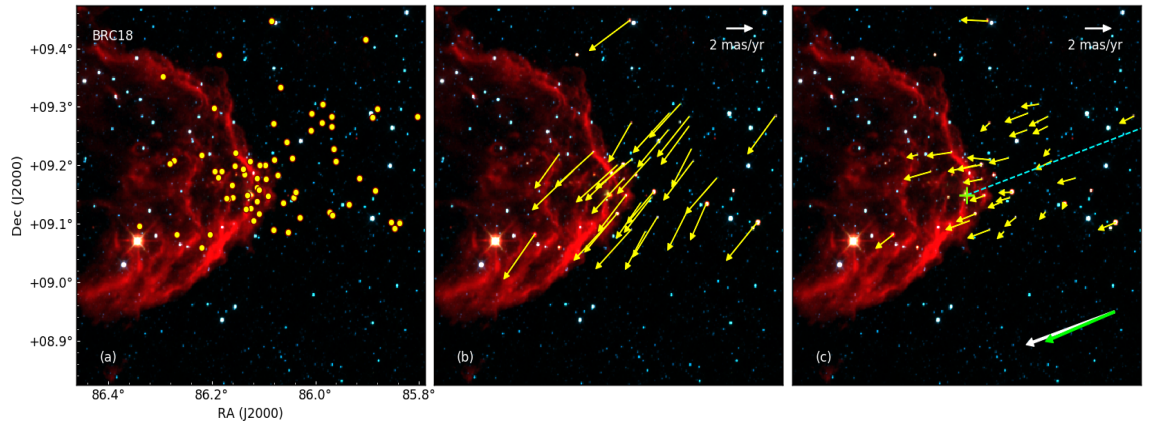

Figure 7.6: Proper motion properties of the YSOs and candidates in BRC 18 on the *WISE* color composite diagram using 3.6 (blue), 4.5 (green) and 12 (red) μm images. **(a)** The spatial distribution of the 76 known YSO candidates associated with BRC 18 is shown using yellow circles. **(b)** The yellow arrows represent the observed proper motion vectors of the YSO candidates obtained from *Gaia* DR2. **(c)** The yellow arrows represent the relative proper motion vectors of the YSO candidates with respect to the ionizing source. The cyan dashed line represents the direction of the ionizing radiation with respect to the *IRAS* source (green '+' symbol) embedded in BRC 18. The median value of the relative proper motions of the YSO candidates and the direction of ionizing photons are indicated using green and white vectors in the lower right corner.

7.4.2   R-band polarimatry of YSOs in BRC 18

It is evident from Fig. 7.4 (RHS), that the projected magnetic field of BRC 18 is oriented roughly in the north-south direction with a significant bending towards FU Ori. Now, the polarization vectors (shown using red filled circles in Fig. 7.4 (LHS) and cyan vectors in 7.4 (RHS) of the observed YSOs trace the rotation axis, i.e. perpendicular to the circumstellar disks. From Fig. 7.4 (LHS) and (RHS) it is clear that the orientations of YSOs are relatively more scattered, which agree well with the results obtained by Ménard & Duchêne (2004) in Taurus. They studied the polarization of the YSOs in Taurus and found that they are aligned in an irregular way. One possibility is that the YSOs in Taurus region are formed with random orientations, leading to the subsequent disk formation also in an arbitrary way (Ménard & Duchêne, 2004). Additionally, the irregularity can be originated from the projection effect also. The third reason could be that the magnetic field strongly drives the gravitational collapse, turning all systems to be oriented parallel to the field lines, and some of these systems become misaligned later by some unidentified processes, for example, close dynamical encounters.

In the case of BRC 18, the energetic ionizing photons could be expected to be responsible for the random orientations of the circumstellar disks of YSOs. But then, the cloud's magnetic field lines also should be affected by the same. Henney et al. (2009) presented the first three-dimensional magnetohydrodynamical (MHD) simulations of magnetized globules. They showed that these globules would evolve into a flattened sheet like structures if they have a strong magnetic field, aligned perpendicular to the direction of ionization. Mackey & Lim (2011) showed that initially perpendicular weak and medium magnetic field lines are eventually aligned with the elongated structures of the evolved clouds. The magnetic field strength towards BRC 18 is estimated by Neha et al. in preparation as $\sim 80~\mu$G, which is of a medium strength, oriented almost perpendicular to the direction of ionization. The moderate strength of the magnetic field does not significantly influence the interaction of the cloud and ionization front, and the ionized photo-evaporation flow can escape out (Arthur et al., 2011). But it can affect in small scales, i.e. stellar sizes, which could be responsible for the randomization of the circumstellar disks of the YSOs.

7.4.2.1   Relative projected motion of the YSOs in BRC 18

Proper motion of an HII region in a well defined reference frame can be used to estimate its motion as a whole in the plane-of-sky. However, the proper motion

values of individual stars subtracted from the mean proper motion of the HII region determines their projected internal motion (Jones, 1997). We can consider the proper motion of the ionizing source as the proxy of the proper motion of its HII region. In Fig. 7.5, we have shown a cartoon diagram of a system containing a BRC and one ionizing source. The massive ionizing source is shown using a blue star symbol, while the YSOs projected towards the BRC are indicated by red star symbols. The yellow colored arrows indicate the direction of photo-evaporation of the cloud material. θ_{ip} and θ_{pm} represent the angle of ionizing photons and the angle of the proper motion of YSOs with respect to the north, respectively.

In order to obtain the internal motion of the YSOs in BRC 18, which is located at the eastern edge of the λ Ori HII region, we first note the astrometric parameters of the earliest type ionizing source λ Orionis. The *Gaia* DR2 distance of this star is found to be more closer than expected, with $d = 279^{56}_{-40}$ pc, $\mu_{\alpha\star} = 0.032\pm0.955$ mas yr^{-1} and μ_{δ} = -0.990$\pm$0.871 mas yr^{-1}. The astrometric excess noise (ϵi), which measures the disagreement between the observations of a source and the best-fitting standard astrometric model is found to be 1.792 milli-arcsec. The significance of ϵi depends on D, which is 855 for λ Ori, indicating that ϵi is significant for this star and a disagreement between the standard astrometric model and observations. However, RUWE for λ Ori is low (0.9). There could be a presence of unresolved binaries, which is responsible for such deviations (Gaia Collaboration et al., 2018). Therefore it is possible that the present *Gaia* DR2 parallax measurement of λ Ori may be uncertain. We, therefore, consider the median value of proper motions and distances of the spectroscopically confirmed members of the cluster Collinder 69 (Bayo et al., 2012) which are responsible for the ionization of the λ Ori HII region. The median d is 399$\pm$13 pc, $\mu_{\alpha\star} = 1.111\pm0.350$ mas yr^{-1} and μ_{δ} = -2.166$\pm$0.221 mas yr^{-1}. We have used these values in our analysis instead of single value of the same for λ Orionis.

These computed proper motion values were subtracted from the observed proper motion values of the YSOs to obtain their internal motions. In Fig. 7.6 (c) the yellow arrows represent the relative proper motion vectors of the YSO candidates. The cyan dashed line represents the direction of the ionizing radiation with respect to the *IRAS* source (green '+' symbol) embedded in BRC 18. The median value of the relative proper motions of the YSO candidates and the direction of ionizing photons are indicated using green and white vectors in the lower right corner. Being formed inside the cloud, the YSOs share similar kinematics as the former. If we consider the median angle made by proper motion of the YSOs as θ_{pm} with respect to the celestial N-S axis, and the angle made by ionizing photons as θ_{ip} with respect to the
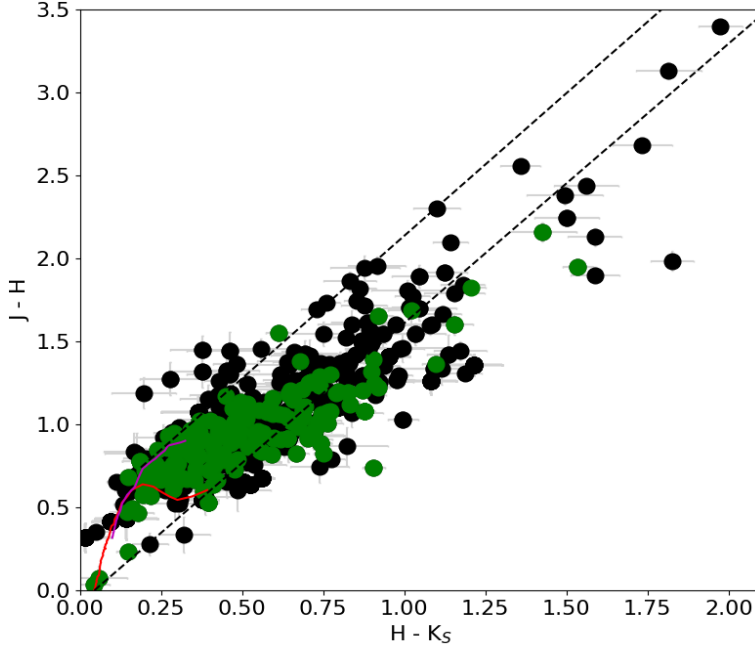
Figure 7.7: 2MASS $J-H$ vs. $H-K_s$ color-color diagram of the YSOs and candidates in the BRCs. Black filled circles indicate YSOs with non-reliable or without *Gaia* DR2 detection. Green filled circles indicate YSOs with reliable *Gaia* DR2 detection. The solid curves in red and magenta represent the loci of the unreddened main sequence stars and the giants, respectively. The black dashed lines indicate the extinction vectors.

same, then in ideal "Rocket Effect" phenomenon, $\mid \theta_{ip} - \theta_{pm} \mid$ would be $\simeq 0°$. The θ_{ip} has been computed as the angle of the line joining the ionizing sources and the *IRAS* point sources located in the BRCs with respect to celestial N-S axis (see Fig. 7.5). In BRC 18 we found $\mid \theta_{ip} - \theta_{pm} \mid = 2°$, which is pretty close to 0°. Inspired by this result, we repeat the same analysis for other BRCs having a significant number of YSOs with reliable data in *Gaia* DR2.

7.4.3 Relative projected motion of YSOs in other BRCs

As mentioned earlier, out of 89 BRCs, we have information of YSOs in 54 of them. Among 54 BRCs, we selected 21 of them, which are associated with at least 4 YSOs and candidates having m/Δm$\gtrsim$ 3 and RUWE$\lesssim$ 1.4. Of the 21 BRCs, we excluded BRCs 7, 30, 79 as the YSOs located towards are found to have extremely high dispersion in d, $\mu_{\alpha\star}$ and μ_{δ}. BRCs 64 is excluded in this work as we have found a high inconsistency in the distances estimated by the YSOs and the ionizing sources. For BRC 64, 12 YSOs have been detected in *Gaia* DR2, which show a

median distance of 2238±275 pc, while the ionizing source, LSS2231, is located at a distance 4517^{1347}_{-890} pc (RUWE=0.97). BRC 76 also shows a huge discrepancy in the distances of the ionizing source and the associated YSOs. The ionizing source, HD 144918 is located at 2732^{613}_{-431} pc (RUWE=1.3), while the median distance of 5 YSOs, which are well detected in *Gaia* DR2, is 1531±183 pc. As there is lack of information of cluster members in literature for the HII regions BBW 347 and RCW 105 where BRCs 64 and 76 are located, we could not get any alternative way to estimate the correct distances of the ionizing sources, as we could be able to obtain for λ Ori. Therefore, BRCs 64 and 76 were excluded in our further analysis.

Thus, our study focuses on 16 BRCs (including BRC 18), which consist of a considerable number of YSOs and candidates with reliable measurements in *Gaia* DR2. Mostly the YSOs are embedded deep in the natal cloud, so the optical emission from many of them are highly obscured by the circumstellar dust resulting less or no detection in *Gaia* DR2. In Fig. 7.7, we show the distribution of the YSOs in 16 BRCS in the 2MASS JHK color-color diagram. Black filled circles indicate YSOs with non-reliable or without *Gaia* DR2 data. Green filled circles indicate YSOs with reliable *Gaia* DR2 data. The solid curves in red and magenta represent the loci of the unreddened main sequence stars and the giants, respectively. The black dashed lines indicate the extinction vectors. It is evident from this figure that *Gaia* DR2 detected sources with less extinction and less near-IR excess. In Table 7.4 we provide kinematics results of YSOs in individual BRCs. BRC ids are shown in column (1). Median d, $\mu_{\alpha\star}$ and μ_δ of the YSOs in individual BRCS are presented in columns (2), (3) and (4), respectively. The HII regions where the BRCs belong to and the massive sources responsible for the ionization are listed in column (5) and (6), respectively. d, $\mu_{\alpha\star}$ and μ_δ of all the ionizing sources are denoted as d_s, $\mu_{\alpha\star s}$ and μ_{δ_s} and presented in columns (7), (8) and (9).

The strategies followed to obtain the internal motion of the YSOs in each BRCs are discussed in 7.4.3.1. In figure 7.8 (a) we present the distribution of θ_{ip} vs. θ_{pm} of 16 BRCs with red filled circles. The dashed black line signifies the angle with slope=1. The solid blue line shows the best-fitted line. Table 7.5 lists the reference and relative proper motions in RA and Dec and θ_{ip} and θ_{pm} for each BRC. Error in θ_{pm} is estimated using the error propagation method. The error in θ_{ip} is negligible (because the positional error is of the order of mas). In order to obtain the correlation between θ_{ip} vs. θ_{pm}, we computed the Pearson's correlation coefficient. The value is found to be 0.961 with pnull 3.072e-09. The Spearman's correlation coefficient is estimated as 0.940, with pnull as 6.115e-08. Along with these, we also performed KolmogorovSmirnov (K−S) test on these angles. The computed statistic

is 0.125, and the pvalue is 0.999. Figure 7.8 (b) shows histogram of the difference between θ_{ip} and θ_{pm} ($\mid \theta_{ip} - \theta_{pm} \mid$) with binsize $\sim 5°$. Out of 16, 11 BRCs, which have $\mid \theta_{ip} - \theta_{pm} \mid \leq 20°$, which indicates that $\sim 69\%$ of them strongly show the "Rocket Effect" happening in them. However, in our analysis of BRCs, a majority of them has a lack of YSOs identified in *Gaia* DR2 with good quality, which results in less number of samples. Statistically, it can be improved with the upcoming *Gaia* DR3.

7.4.3.1   Comments on individual BRCs:

BRC 5: There are three early type sources considered to be responsible for ionization of BRC 5, namely, BD +60 502 (O5V), BD +60 504 (O4V), and BD +60 507 (O5V) (Ishida, 1970; Morgan et al., 2004). RUWE for BD +60 502, BD +60 504, and BD +60 507 are 2.2, 0.9 and 0.9, respectively. Proper motion of BD +60 502 was not considered as the reference as its RUWE >1.4. We used BD +60 504 in our analysis as it is closer to BRC 5 and earlier than BD +60 507.

BRC 17: As this cloud is located at the northern edge of HII region λ Ori where BRC 18 is also located, we considered the same ionizing source λ Orionis, whose age is $\sim$5 Myr (Kounkel et al., 2018). The angular distance of the *IRAS* source in BRC 17 and λ Orionis is $\sim 2.4°$. We considered the distance of λ Ori HII region $\sim$400 pc (Kounkel et al., 2018). We computed the angular distance traversed by YSOs $\sim 0.5°$, following the same methodology we used for BRC 18. Therefore, we considered those YSOs in BRC 17, which are distributed within a circle of $0.5°$ radius centered on the position of the embedded *IRAS* source (IRAS 05286+1203).

BRC 25: The massive source considered to ionize BRC 25 is HD 47839 is located at 3216^{2132}_{-1341} pc (Bailer-Jones et al., 2018), which is too far away from the median distance 720 ± 29 pc, obtained from the YSOs located towards BRC 25. A higher RUWE (= 1.9) of HD 47839 makes its astrometric measurements unreliable. Therefore, we obtained the reference proper motion values of NGC 2264 from Buckner et al. (2020) where $\mu_{\alpha\star}$=-1.817$\pm$0.005 and μ_{δ}=-3.919$\pm$0.004 mas yr^{-1}.

BRC 27: In our search for the sources of the shock front in the BRCs, there is an uncertainty in the case of BRC 27, it is probably HD 53456 (B0V), located at the south-east, indicated by the direction of the bright rim (Rebull et al., 2013). Morgan et al. (2004) also considered the same star as the main ionizing source for BRC 27. The distance (d) of HD 53456 is 1089^{66}_{-59} pc with $\mu_{\alpha\star}$ = -4.657$\pm$0.087 mas yr^{-1} and μ_{δ} = 1.358$\pm$0.078 mas yr^{-1}. However, in figure 1 of Morgan et al. (2004), they showed the directions of HD 53456 as well as HD 54662 (O6.5V), the

later is earlier than HD 53456, and it is located at 1142 pc, similar to the distance of BRC 27 (∼1150 pc), estimated from the median distance of the associated YSOs and candidates. This source is having $\mu_{\alpha\star}$ = -2.055±0.142 mas yr^{-1} and μ_δ = 2.645±0.169 mas yr^{-1}. Though the angular distance between the *IRAS* source (IRAS 07016-1118) embedded in BRC 27 and HD 54662 is 1.68°, which is far away from the same between IRAS 07016-1118 and HD 53456 (0.21°), the impact of HD 54662 on BRC 27 is not negligible. Most importantly, the angle of movement of the YSOs and candidates in BRC 27 with respect to the celestial N-S axis is found to be closer to the angle made by HD 54662 and IRAS 07016-1118 with respect to the same.

BRC 36-39: The HII region 1396 consists of multiple BRCs, namely 36, 37, 38, and 39, and a few other BRCs also. The central ionizing source HD 206267 has RUWE=2.8. Therefore, it's proper motion values can not be used as the reference. We used proper motion values of the cluster members of IC 1396 from Sicilia-Aguilar et al. (2019), which are -2.500±1.500 and -4.600±1.300 mas yr^{-1}. Based on the median distance of the YSOs and candidates in the BRCs, BRC 36 seems to be the closest cloud in IC 1396, as its distance is 926 ± 46 pc, while BRCs 37 and 39 are located at relatively longer distances (981 ± 58 and 974 ± 75 pc, respectively). BRC 38, which is found to be located at the furthest distance having $d = 1014 \pm 121$ pc. However, considering their MAD values, all these BRCs are located at a similar distance.

BRC 55: In the HII region RCW 27, the massive source responsible for ionizing BRC 55 is HD 73882, having RUWE = 13.2, which makes its astrometric measurements unreliable. Therefore, we obtained members of RCW 27 provided by Prisinzano et al. (2018). We estimated the median $\mu_{\alpha\star} = -5.459$ and $\mu_\delta = 3.516$ mas yr^{-1} of the cluster members with corresponding MAD as 0.373 and 0.394 mas yr^{-1}. In order to find the relative proper motions of the YSOs in BRC 55, we used these values as the reference.

BRC 68: There are three early type sources considered to be responsible for ionization of BRC68, namely, HD 101131, HD 101205, and HD 101436 (Yamaguchi et al., 1999; Thompson et al., 2004). RUWE for HD 101131, HD 101205, and HD 101436 are 1.5, 0.9, and 2.0, respectively. Therefore, we used proper motion values of HD 101205 as the reference, to compute the internal motions of the YSOs located towards BRC 68.

BRC 82: There are three early type sources considered to be responsible for ionization of BRC68, namely, HD 152233 (O6 III), HD 326286 (B0), and HD 152245 (B0Ib) (Yamaguchi et al., 1999; Thompson et al., 2004). The earliest type ionizing

source is HD 152233 is also a member of cluster NGC 6231. There is a high possibility of influence of other massive members. Therefore, we obtained median proper motion of the cluster members ($\mu_{\alpha\star} = -0.562$ mas yr^{-1}, $\mu_\delta = -2.076$ mas yr^{-1}) from Kuhn et al. (2017) and calculated the relative proper motion of the YSOs in BRC 82 with respect to those median values.

Other BRCs, namely, BRC 2, 31, 54, and 89 are associated with HII regions having reliable counterparts of the ionizing sources in the *Gaia* DR2 catalog.

Table 7.4: Kinematic properties of the YSOs and candidates in the BRCs.

BRC ID	$d(\pm\Delta d)$ (pc)	$\mu_{\alpha\star}(\pm\Delta\mu_{\alpha\star})$ (mas/yr)	$\mu_\delta(\pm\Delta\mu_\delta)$ (mas/yr)	HII region	Ionizing Star	$d(\pm\Delta d)_s$ (pc)	$\mu_{\alpha\star}(\pm\Delta\mu_{\alpha\star})_s$ (mas/yr)	$\mu_\delta(\pm\Delta\mu_\delta)_s$ (mas/yr)	search radius (°)	N
(1)	(2)	(3)	(4)	(5)	(6)	(7)	(8)	(9)	(10)	(11)
BRC 2	1042±45	-1.272±0.120	-1.217±0.156	Sh-171	BD+66°1673[a]	958^{30}_{-27}	-1.570±0.043	-1.774±0.045	0.07	3
BRC 5	2334±89	-1.088±0.290	-0.723±0.029	IC 1805	BD+60°504[a]	2341^{213}_{-182}	-0.612±0.040	-0.847±0.063	0.16	4
BRC 17	392±11	1.232±0.455	-1.218±0.596	Sh2-264	λ Ori[b]	279^{56}_{-40}	0.032±0.955	-0.990±0.871	0.50	25
BRC 18	399±13	2.259±0.378	-2.568±0.133	Sh2-264	λ Ori[b]	279^{56}_{-40}	0.032±0.955	-0.990±0.871	0.50	24
BRC 25	720±29	-1.656±0.075	-3.570±0.141	NGC 2264	HD 47839[c]	3216^{2132}_{-1341}	-4.385±0.992	-6.575±0.846	0.39	116
BRC 27	1150±92	-4.500±0.192	1.690±0.113	Sh2-296	HD54662[d]	1142^{120}_{-99}	-2.055±0.142	2.645±0.169	0.14	90
BRC 31	882±47	-1.220±0.073	-4.163±0.134	S 117	HD 199579[e]	918^{54}_{-48}	0.306±0.097	-2.109±0.104	0.16	13
BRC 36	926±46	-2.734±0.203	-4.657±0.245	Sh2-131	HD 206267[f]	1191^{751}_{-337}	-2.956±0.491	-5.764±0.446	0.24	116
BRC 37	981±58	-1.782±0.139	-6.559±0.168	Sh2-131	HD 206267[f]	1191^{751}_{-337}	-2.956±0.491	-5.764±0.446	0.16	3
BRC 38	1014±121	-1.872±0.225	-3.228±0.308	Sh2-131	HD 206267[f]	1191^{751}_{-337}	-2.956±0.491	-5.764±0.446	0.13	35
BRC 39	974±75	-1.051±0.223	-3.770±0.607	Sh2-131	HD 206267[f]	1191^{751}_{-337}	-2.956±0.491	-5.764±0.446	0.15	25
BRC 54	936±75	-5.903±0.193	3.184±0.160	NGC 2626	vBH17a[g]	901^{20}_{-19}	-5.707±0.044	3.980±0.045	0.14	67
BRC 55	918±65	-5.107±0.156	3.153±0.104	RCW 27	HD 73882[f]	358^{79}_{-55}	-11.811±0.946	-1.766±0.743	0.10	12
BRC 68	2655±199	-6.033±0.718	0.579±0.569	RCW 62	HD 101205[g]	2765^{1764}_{-843}	-4.168±0.294	0.311±0.143	0.09	372
BRC 82	1435±191	-1.889±0.228	-1.557±0.311	RCW 113/116	HD 152233[g]	1714^{161}_{-135}	-1.733±0.093	-2.794±0.067	0.14	81
BRC 89	1220±136	1.925±0.098	-1.782±0.129	S 29	HD 165921[g]	1072^{71}_{-62}	2.470±0.114	-1.130±0.095	0.06	9

BRCs are identified as SFO (Sugitani, Fukui, Ogura) in Simbad.
[a] Crampton & Fisher (1974); [b] Reynolds & Ogden (1979); [c] ?; [d] Clariá (1974); [e] Bally & Scoville (1980); [f] Matthews (1979); [g] Yamaguchi et al. (1999). N = Number of comoving souces in search radius.
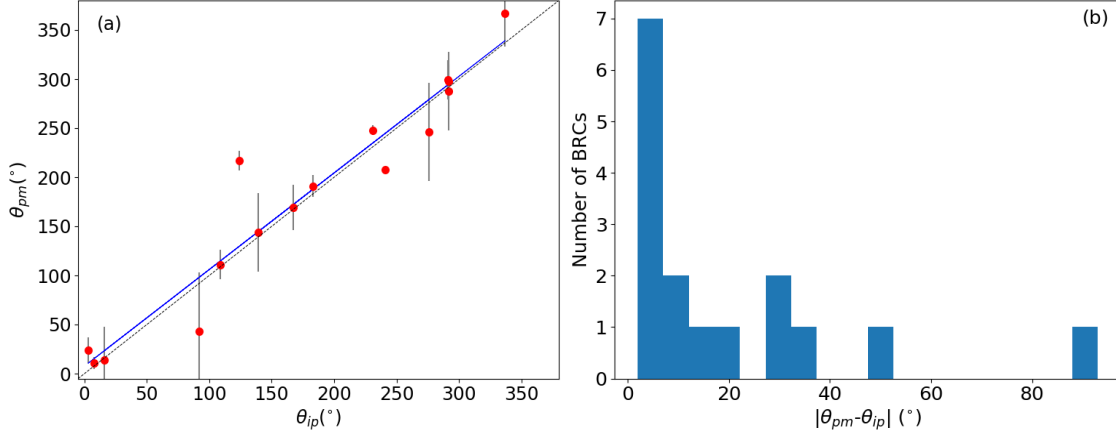
Figure 7.8: **(a)** Plot of θ_{ip} vs. θ_{pm} is shown using red filled circles. The dashed black line signifies the angle with slope=1. The solid blue line shows the best-fitted line. **(b)** Histogram of the difference between θ_{ip} and θ_{pm} with binsize $\sim 5°$.

7.4.4 Search for additional comoving sources towards BRCs

Similar to the work done towards L1172/1174 to search extra sources comoving with the known YSOs and candidates (see chapter 3 part II), we looked for additional sources sharing similar kinematics as the YSOs in BRCs. These sources could possibly be young stars not identified in earlier studies. As we don't have enough information (especially age) of the massive source/s responsible for ionizing the BRCs, we defined a circle of radius similar to the distance of the furthest YSO from the central *IRAS* source in each BRC. For the BRCs located in λ Ori and IC 1396, the search radius is obtained by the calculation mentioned in section 7.4.1 as the ages of the central ionizing sources are well determined. All the comoving sources have m/Δm$\gtrsim$ 3 and RUWE$\leq$ 1.4 and are lying within 5 $\times$ MAD ellipses with respect to the median values of d, $\mu_{\alpha\star}$ and μ_{δ} of the known YSOs. In Table 7.4, columns 10 and 11 provide the search radius and the number of comoving sources distributed within the defined radius in each BRC, respectively. Though this analysis comes with a caveat that there could be other comoving sources outside of the defined circle, which are getting missed here. In Fig. 7.14 (a), we show the YSO candidates and comoving sources using yellow and cyan filled circles, respectively, associated with BRCs, overplotted on the *WISE* color composite diagram using 3.6 (blue), 4.5 (green) and 12 (red) μm images. We present the proper motion values of the YSO candidates and comoving sources as a function of their distances obtained from *Gaia* DR2 in Fig. 7.14 (b). The red triangles and blue circles represent the d-$\mu_{\alpha\star}$ and d-μ_{δ} values respectively. The gray squares and diamonds indicate the d-$\mu_{\alpha\star}$ and d-μ_{δ} values lying outside of the 5 $\times$ MAD boundaries with respect to the median values
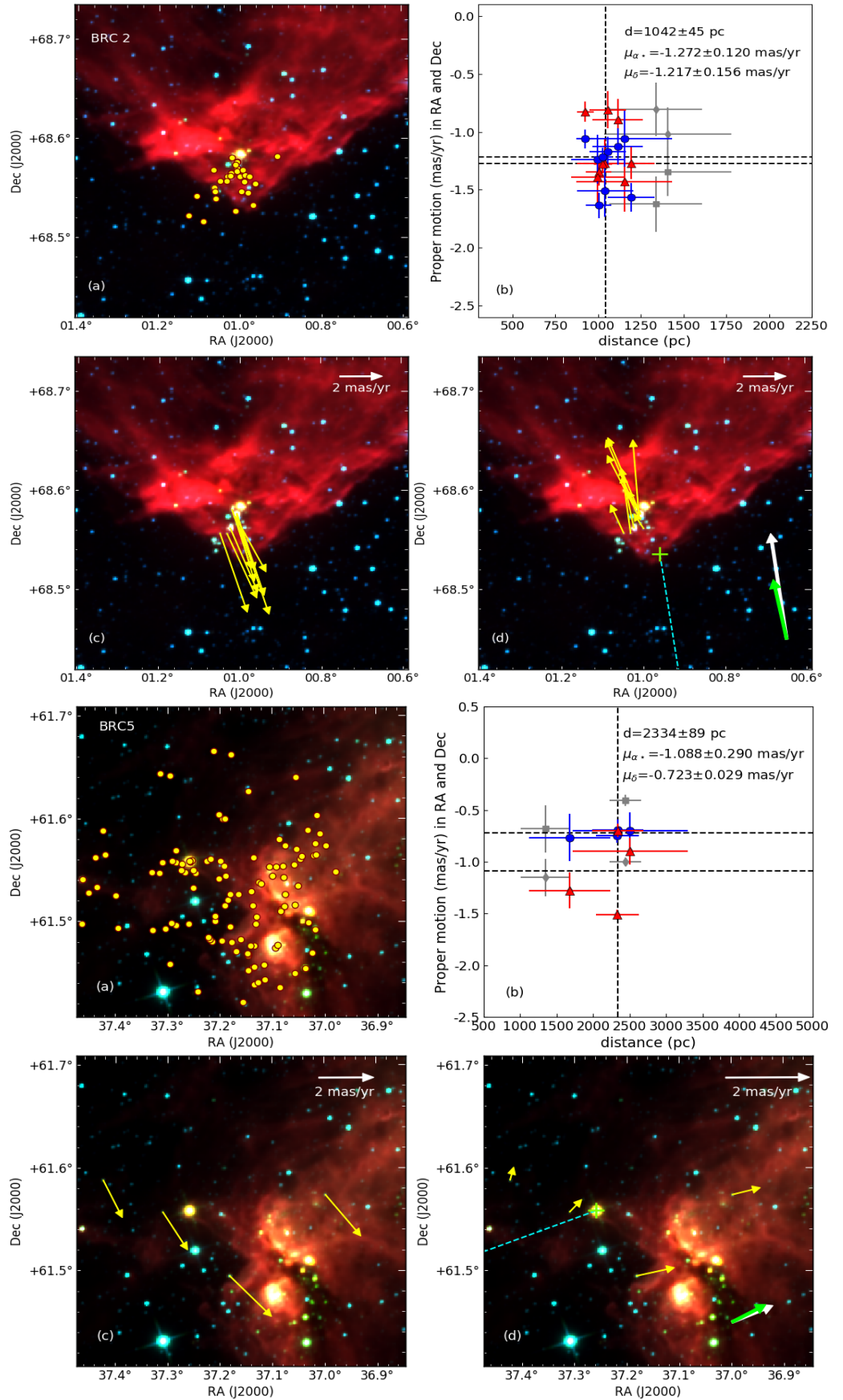
Figure 7.9: Same as Fig. 7.6 but for BRC 2 and 5.

Figure 7.9: Same as Fig. 7.6 but for BRC 17 and 25.

Figure 7.9: Same as Fig. 7.6 but for BRC 27 and 31.

Figure 7.9: Same as Fig. 7.6 but for BRC 36 and 37.

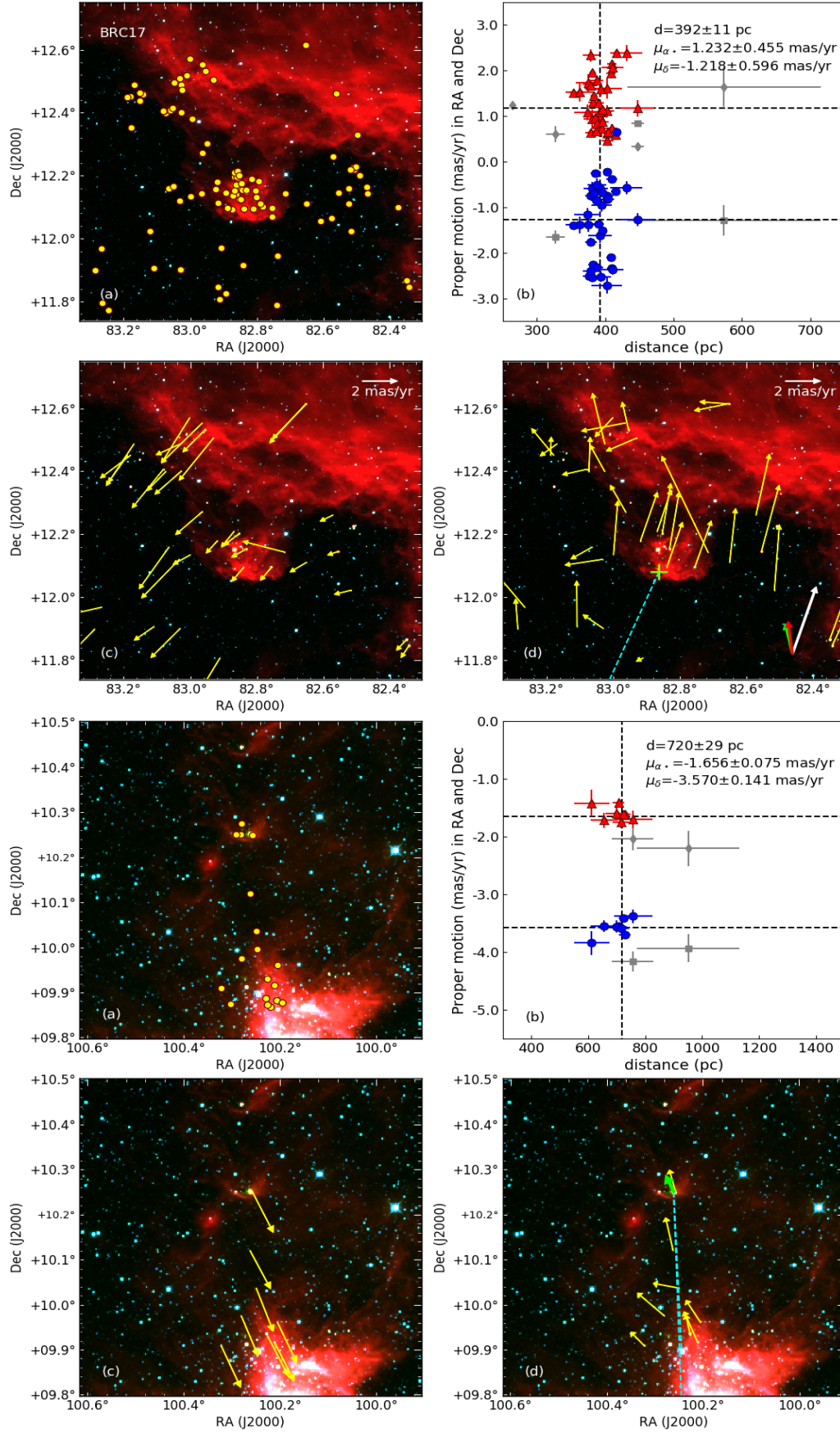Figure 7.10: Same as Fig. 7.6 but for BRC 38 and 39.
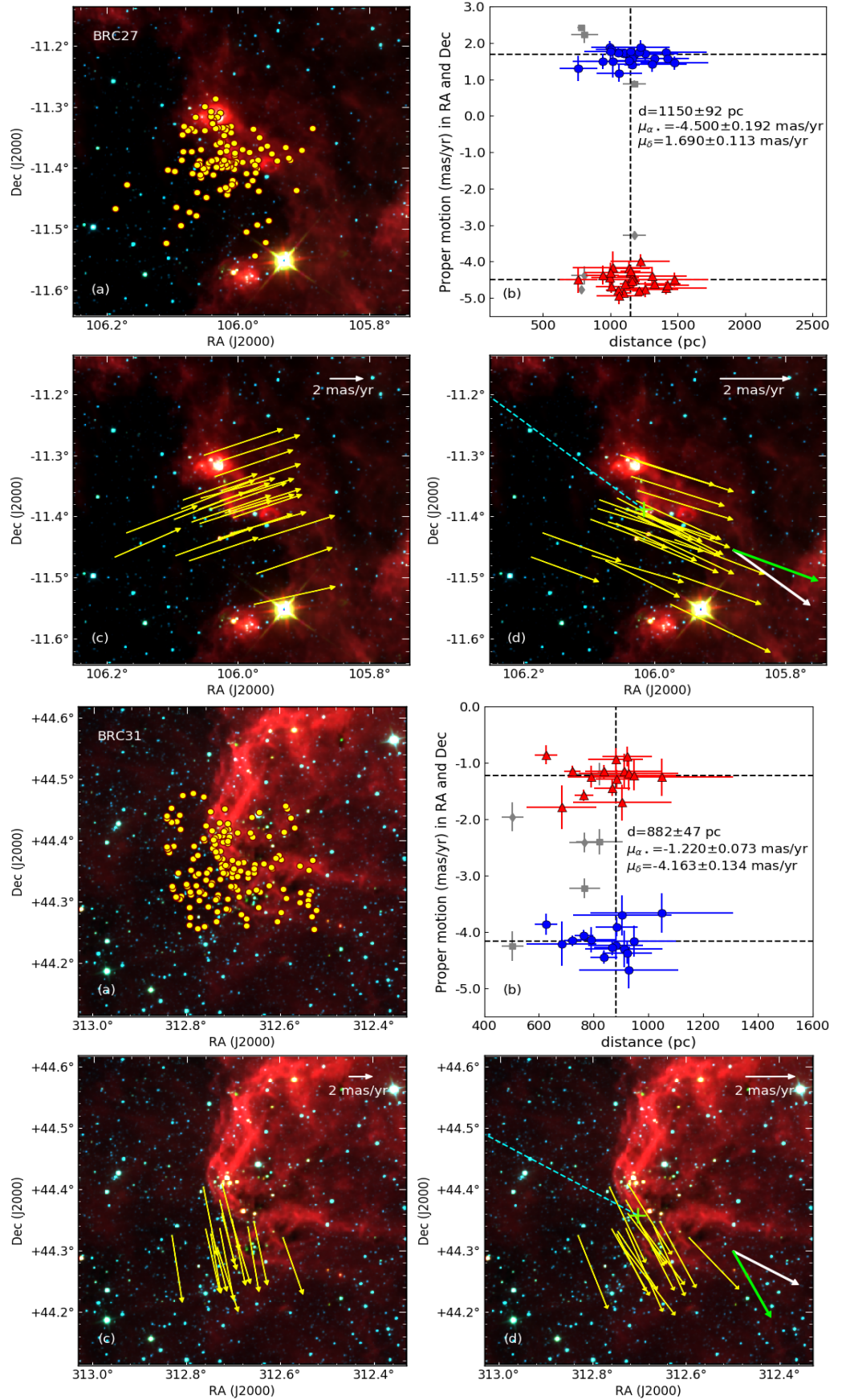
Figure 7.11: Same as Fig. 7.6 but for BRC 54 and 55.

Figure 7.12: Same as Fig. 7.6 but for BRC 68 and 82.

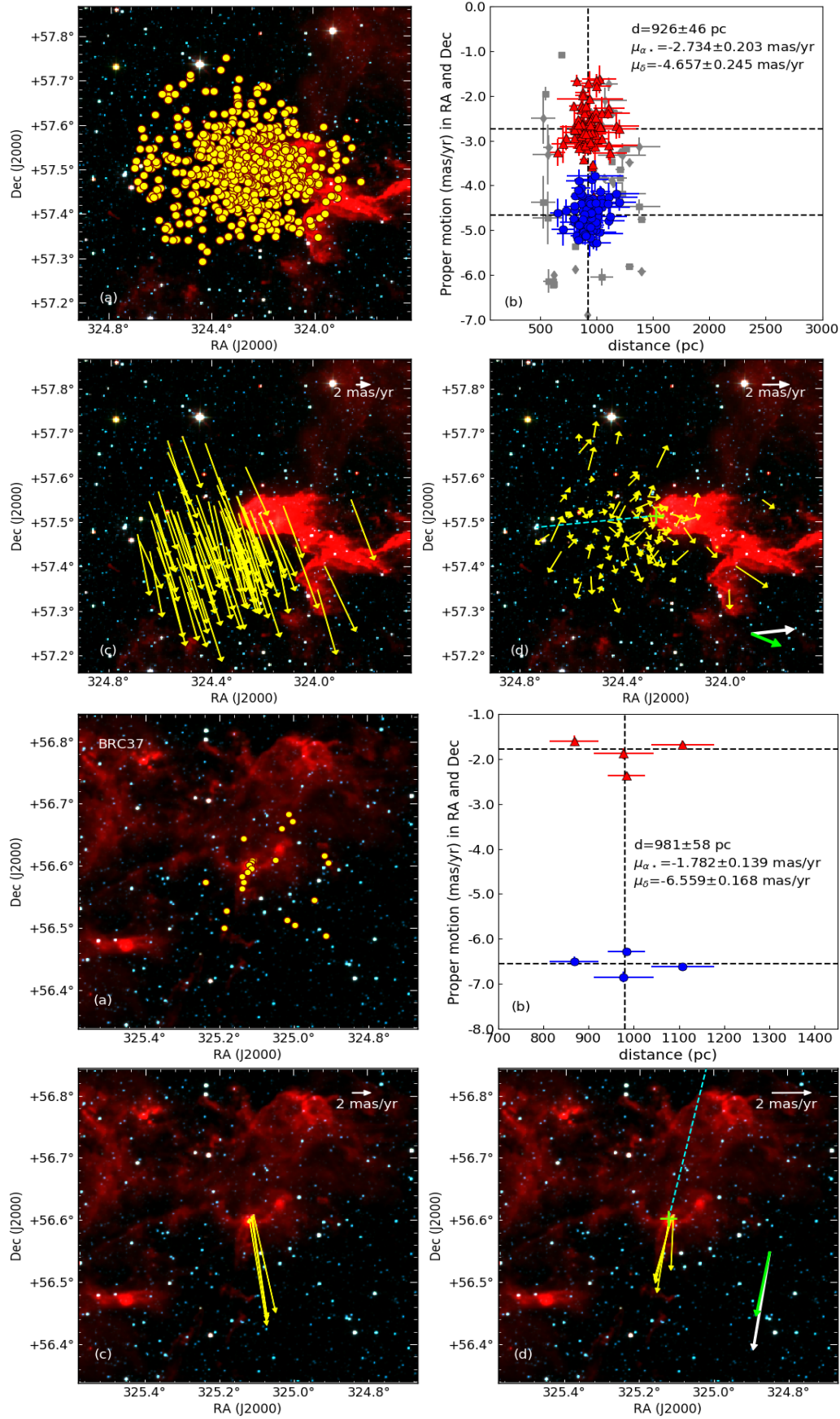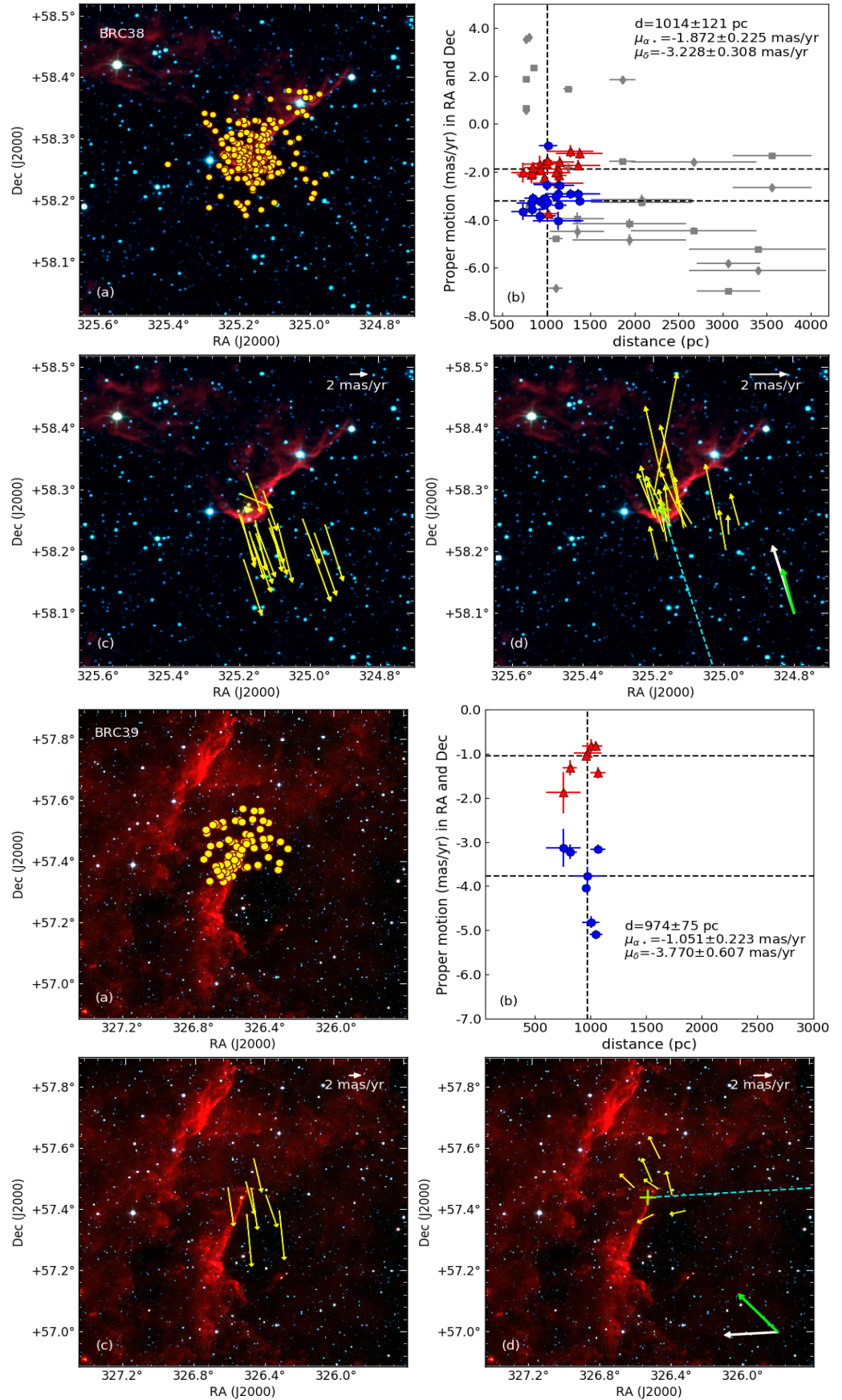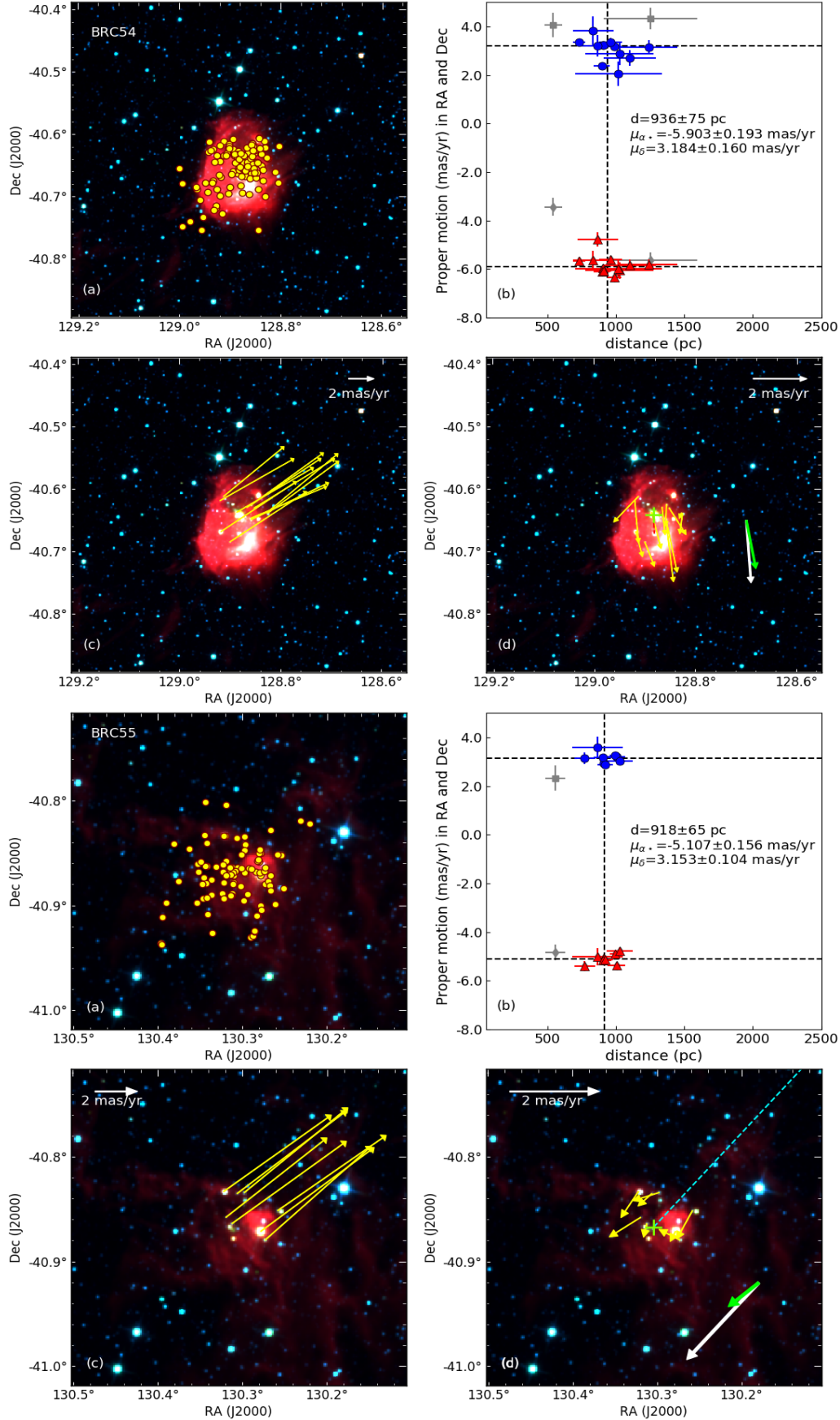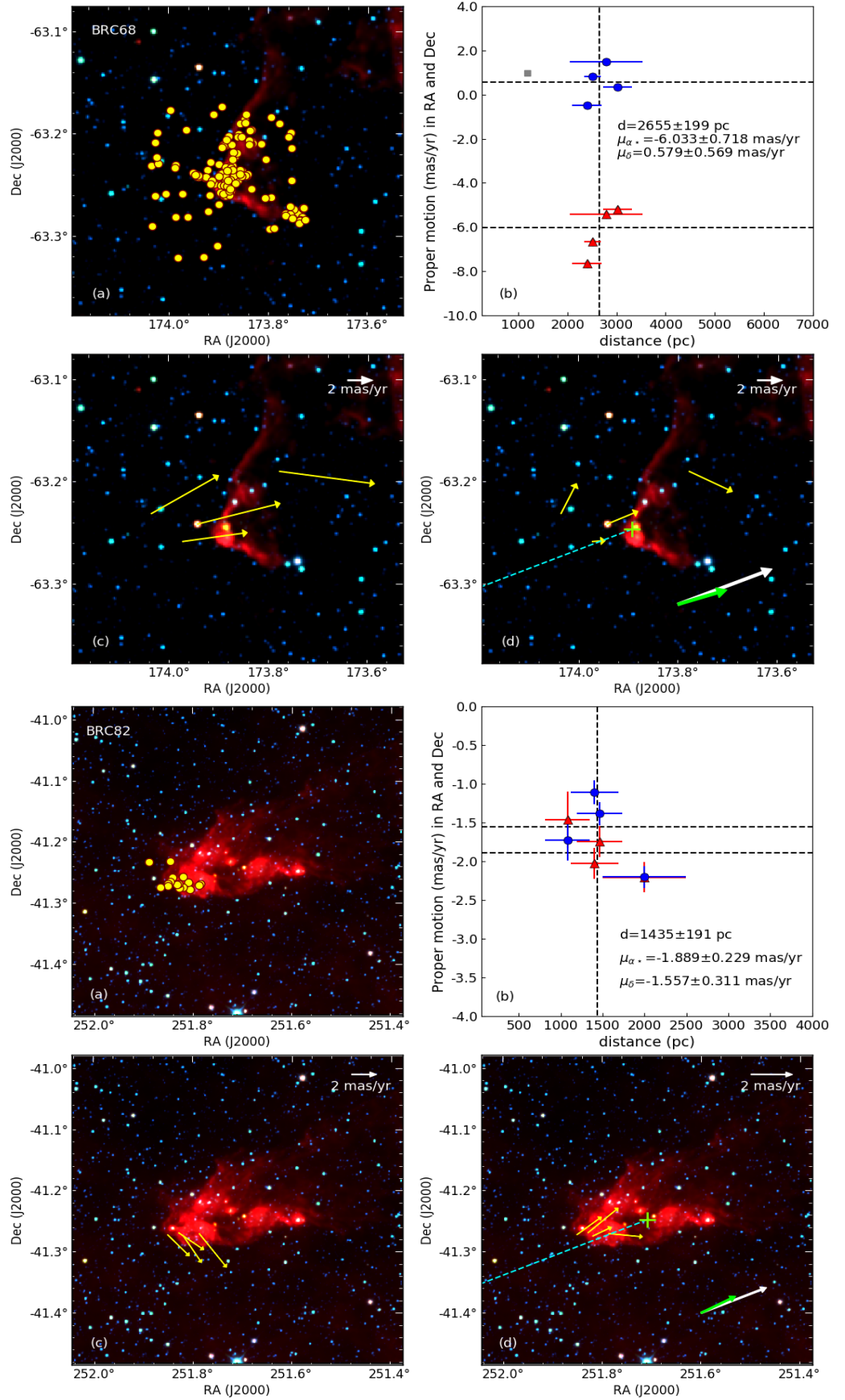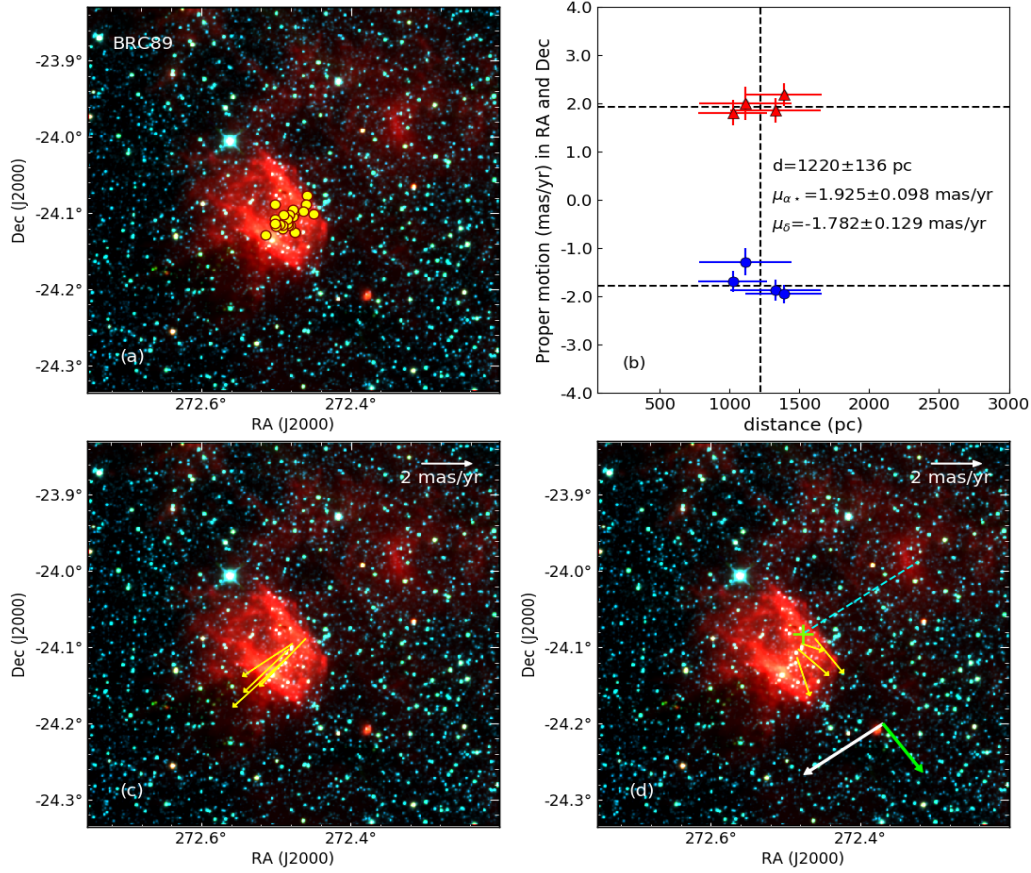# 7. INVESTIGATION OF ROCKET EFFECT IN BRIGHT RIMMED CLOUDS USING *GAIA* DR2

Figure 7.13: Same as Fig. 7.6 but for BRC 89.

Table 7.5: Reference proper motions, relative proper motions of YSO candidates, θ_{ip} and θ_{pm} in the BRCs.

BRC No.	$(\mu_{\alpha\star} \pm \Delta\mu_{\alpha\star})_0$	$(\mu_\delta \pm \Delta\mu_\delta)_0$	$(\mu_{\alpha\star} \pm \Delta\mu_{\alpha\star})_r$	$(\mu_\delta \pm \Delta\mu_\delta)_r$	θ_{ip}	θ_{pm}
BRC 2	-1.570±0.043	-1.774±0.045	0.298±0.127	0.557±0.162	8	11±6
BRC 5	-0.612±0.040	-0.847±0.063	-0.476±0.293	0.124±0.069	291	299±20
BRC 17	1.111±0.350	-2.166±0.221	0.121±0.574	0.948±0.636	337	7±34
BRC 18	1.111±0.350	-2.166±0.221	1.094±0.483	-0.405±0.257	109	111±15
BRC 25	-1.817±0.005	-3.919±0.004	0.161±0.075	0.349±0.141	3	24±13
BRC 27	-2.055±0.142	2.645±0.169	-2.445±0.239	-0.955±0.203	231	248±5
BRC 31	0.306±0.097	-2.109±0.104	-1.526±0.121	-2.054±0.170	241	208±3
BRC 36	-2.500±1.500	-4.600±1.300	-0.234±1.514	-0.057±1.323	276	246±50
BRC 37	-2.500±1.500	-4.600±1.300	0.718±1.506	-1.959±1.311	167	169±23
BRC 38	-2.500±1.500	-4.600±1.300	0.628±1.517	1.372±1.336	16	14±34
BRC 39	-2.500±1.500	-4.600±1.300	1.449±1.516	0.830±1.435	92	43±60
BRC 54	-5.707±0.044	3.980±0.045	-0.196±0.198	-0.796±0.166	183	191±11
BRC 55	-5.459±0.373	3.516±0.394	0.352±0.404	-0.363±0.407	139	144±40
BRC 68	-4.168±0.294	0.311±0.143	-1.865±0.776	0.268±0.587	292	288±40
BRC 82	-0.562±0.122	-2.076±0.176	-1.327±0.259	0.519±0.357	292	298±17
BRC 89	2.470±0.114	-1.130±0.095	-0.545±0.150	-0.652±0.160	124	217±10

of d, $\mu_{\alpha\star}$ and μ_δ. The YSO candidates are marked with black open square boxes. In Fig. 7.14 (c), the observed proper motion vectors of the YSO candidates and the comoving sources, obtained from *Gaia* DR2, are shown using yellow and cyan vectors, respectively. Fig. 7.14 (d) presents the relative proper motion vectors of the YSO candidates (yellow vectors) and the comoving sources (cyan vectors) with respect to the central ionizing source BD+66°1673. The direction of the ionizing radiation with respect to the *IRAS* sources embedded in BRCs is shown using a cyan dashed line.

At this point, we note that in the R-band polarimetric analysis of YSOs in BRC 18, there are 4 sources (see Fig. 7.2 and 7.4) located within a similar distance range as YSOs. But in literature, these sources were not identified as YSOs. After the kinematic studies of sources within BRC 18, we found that 1 out of these 4 sources is comoving with the YSOs. This finding supports the probability of young age of the comoving sources.

In our findings of comoving sources, the BRCs which are located at a relatively longer distance, especially BRCs 64, 68 and 82, the number of comoving sources is much larger comparing the same for the other BRCs located nearer. This is because the larger dispersion in the distance leads to picking more number of sources moving in a similar way as the YSOs associated with the BRCs. Thus, there could be a possibility of the selection of field stars instead of additional young sources. A detailed spectroscopic study of these sources can help to extract the real young sources.

In Fig. 7.14 (e) we show the *Gaia* CMD (not corrected for extinction) to investigate if they share similar age as the YSOs and candidates. In order to obtain a crude estimate of the nature of the comoving sources, we made *Gaia* M_G vs. (G-G_{RP}) CMD of them (filled circles in black) and YSO candidates (filled circles in cyan). From these figures, it is clear that the comoving sources have almost similar ages as the YSO candidates. The PMS isochrones corresponding to 1, 3, and 10 Myr are also shown. We used the CIFIST 2011_2015 models (thick curves in black, Baraffe et al., 2015) for low-mass stars, and the PADOVA tracks Parsec 3.3 for the high-mass stars (dashed curves in black, Marigo et al., 2017). A reddening vector corresponding to $A_V = 1$ magnitude is also shown. The reddening vector is computed based on Bossini et al. (2019).

We show 2MASS $J - H$ vs. $H - K_s$ color-color diagram of YSOs and candidates and comoving sources in figure 7.14 (f), using cyan and black filled circles, respectively. The solid curves in green and magenta represent the loci of the unreddened main sequence stars and the giants, respectively. The black dashed lines indicate

the extinction vectors. This plot clearly shows that the later suffer from less extinction and less near-IR excess, although a fraction of them are found to have similar excess as the known YSOs and candidates. This further confirms that the comoving sources are potential YSOs evolving along with the known YSOs and candidates not identified in earlier studies. However, we need more detailed studies to confirm the young nature of the comoving sources.

7.5   Summary and Conclusions

We present R-band polarimetric results of 12 YSOs projected towards BRC 18 to study their circumstellar disk orientations. Star formation in BRC 18 is considered to be affected by the impact of the ionizing sources, which is called RDI. As a consequence of the RDI effect, the collapse of the BRCs leads to triggered star formation, leaving behind a chain of YSOs, as reminiscent of the elongated cloud. Furthermore, the cloud accelerates away from the direction of the ionizing sources due to the photo-evaporation of cloud material towards the ionized medium which is known as "Rocket Effect". The fact that the projected motion of the YSOs mirrors the motion of the parental cloud in the plane-of-sky, is investigated here in 16 BRCs using the astrometric information of the YSOs from *Gaia* DR2. The main conclusions of this work are summarized below:

- We obtained the disk orientations of 12 YSOs in BRC 18 to be randomly oriented, suggesting that the projected magnetic field of BRC 18 has more impact at large scale, and its impact decreases at a smaller scale (scale of individual YSOs). Another possibility is that the YSOs could have changed their disk orientations since birth.

- We computed the Pearson's correlation coefficient of θ_{ip} and θ_{pm} for 16 BRCs. The value is found to be 0.961 with pnull 3.072e-09. The Spearman's correlation coefficient is found to be 0.940, with pnull as 6.115e-08. The statistic of K$-$S test is 0.125 and the pvalue is 0.999. Almost 69% of the BRCs have $\mid \theta_{ip} - \theta_{pm} \mid \leq 20°$ confirming the evidence of "Rocket Effect".

- We searched for additional comoving sources located towards these 16 BRCs. We obtained a considerable number of sources moving with similar fashion as the other YSOs do. Most of them show a distribution similar to the YSOs in the *Gaia* CMDs. Based on 2MASS $J - H$ vs. $H - K_s$ color-color diagrams,
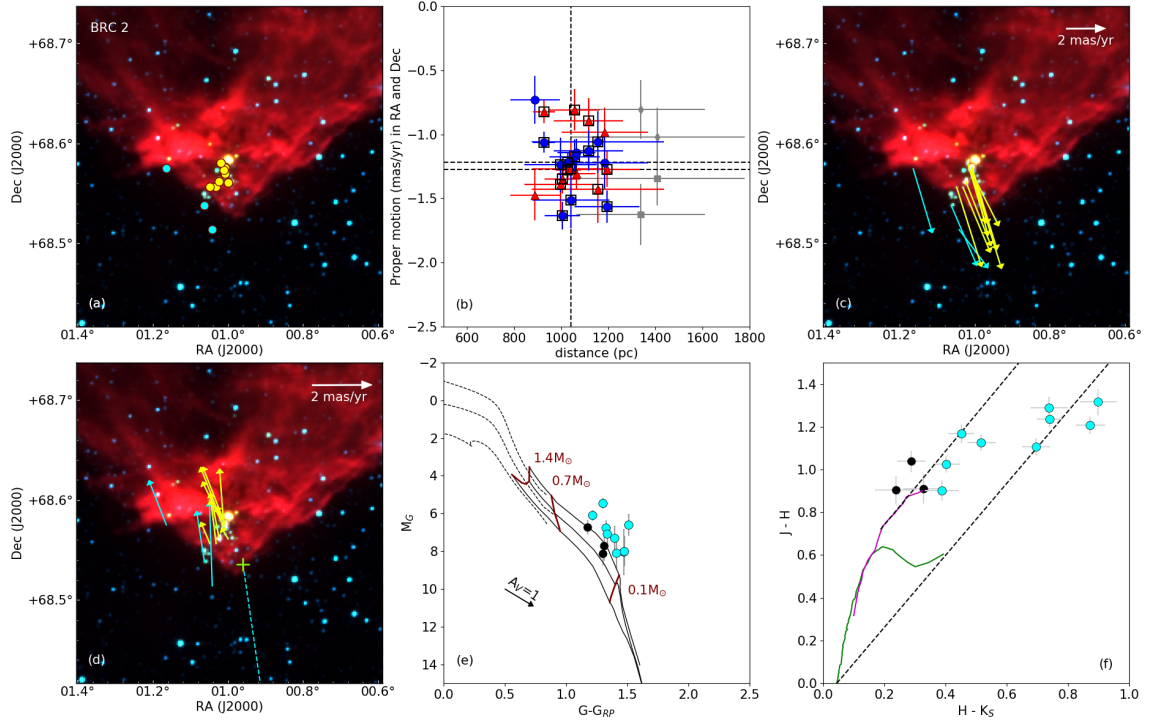
Figure 7.14: **(a)** The known YSO candidates (yellow filled circles) and comoving sources (cyan filled circles) associated with BRC 2 overplotted on the *WISE* color composite diagram using 3.6 (blue), 4.5 (green) and 12 (red) μm images. **(b)** Proper motion values of the known YSO candidates and comoving sources are plotted as a function of their distances obtained from *Gaia* DR2. The red triangles and blue circles represent the d-$\mu_{\alpha\star}$ and d-μ_{δ} values respectively. The gray squares and diamonds represent the d-$\mu_{\alpha\star}$ and d-μ_{δ} values lying outside of the boundaries defined by $5 \times$ MAD ellipses with respect to the median values of d, $\mu_{\alpha\star}$ and μ_{δ}. The YSO candidates are marked with black open square boxes. The dashed lines show the median values of d, $\mu_{\alpha\star}$ and μ_{δ} of the YSO candidates. **(c)** The observed proper motion vectors of the known YSO candidates (yellow vectors) and the comoving sources (cyan vectors) obtained from *Gaia* DR2. **(d)** The relative proper motion vectors of the known YSO candidates (yellow vectors) and the comoving sources (cyan vectors) with respect to the central ionizing source. The cyan dashed line represents the direction of the ionizing radiation with respect to the *IRAS* source embedded in BRC 2. **(e)** *Gaia* M_G vs. (G-G_{RP}) CMD of the YSO candidates (cyan filled circles) and comoving sources (black filled circles). The dashed lines indicate the isochrones from PARSEC models and solid curves represent the same from CIFIST models. The PMS isochrones corresponding to 1, 3, and 10 Myr are shown. A reddening vector corresponding to $A_V = 1$ magnitude is also shown. **(f)** 2MASS $J - H$ vs. $H - K_s$ color-color diagram of YSOs and candidates (cyan filled circles) and comoving sources (black filled circles). The solid curves in green and magenta represent the loci of the unreddened main sequence stars and the giants, respectively. The black dashed lines indicate the extinction vectors.

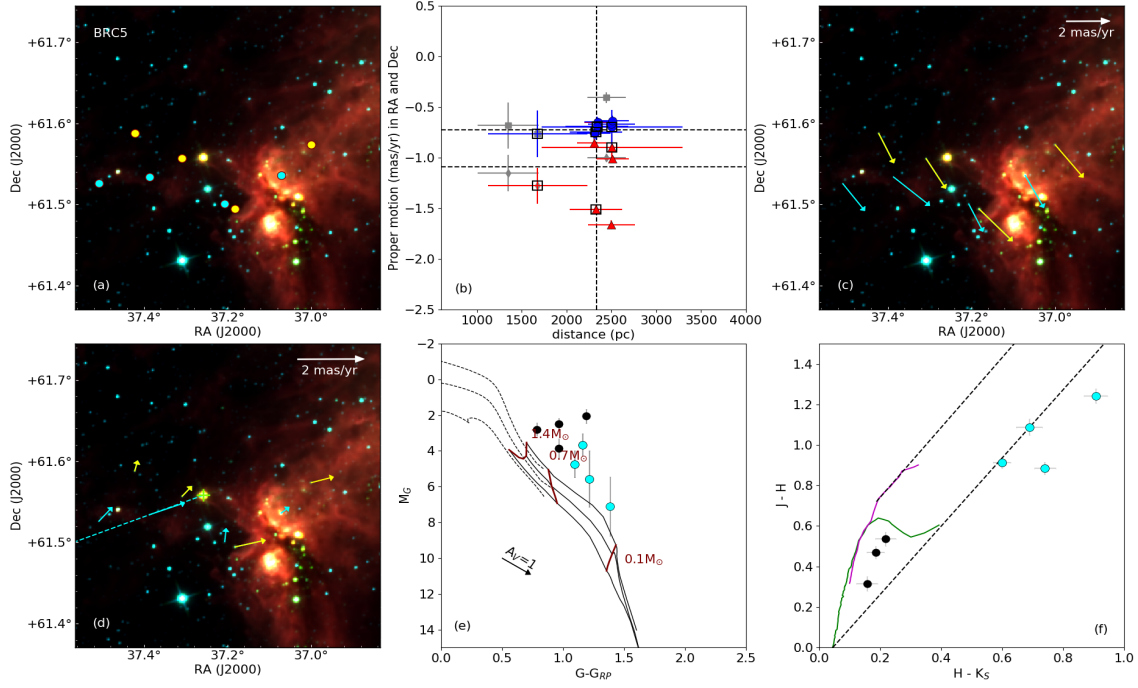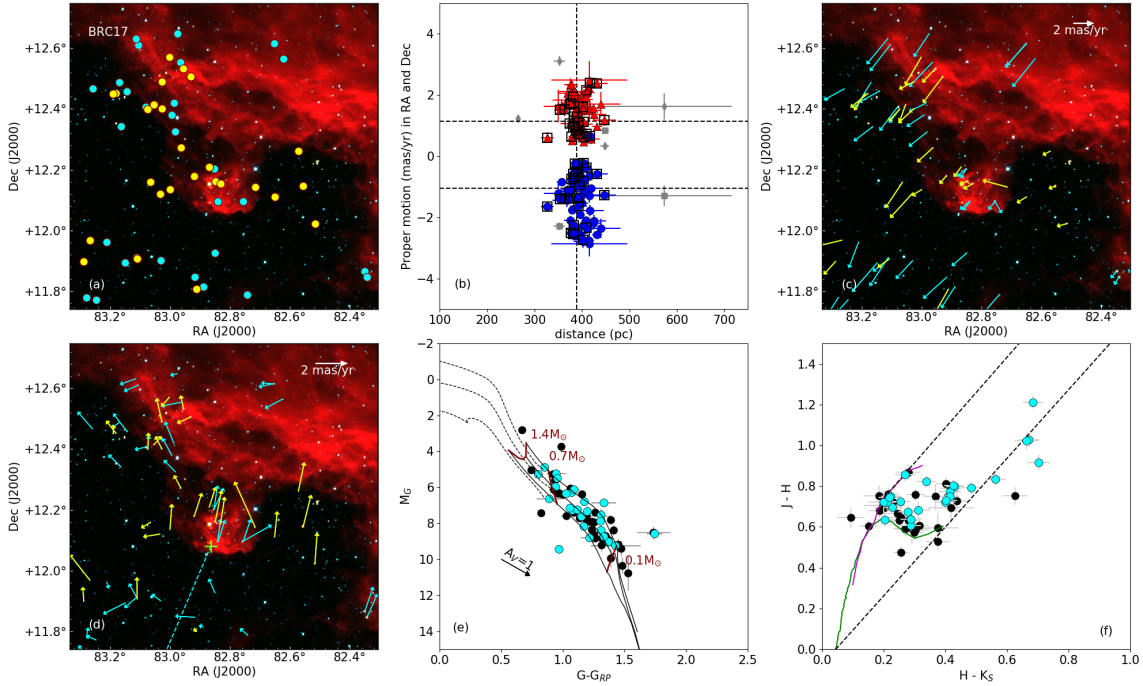Figure 7.14: Similar as BRC 2 but for BRC 5.

Figure 7.14: Similar as BRC 2 but for BRC 17.
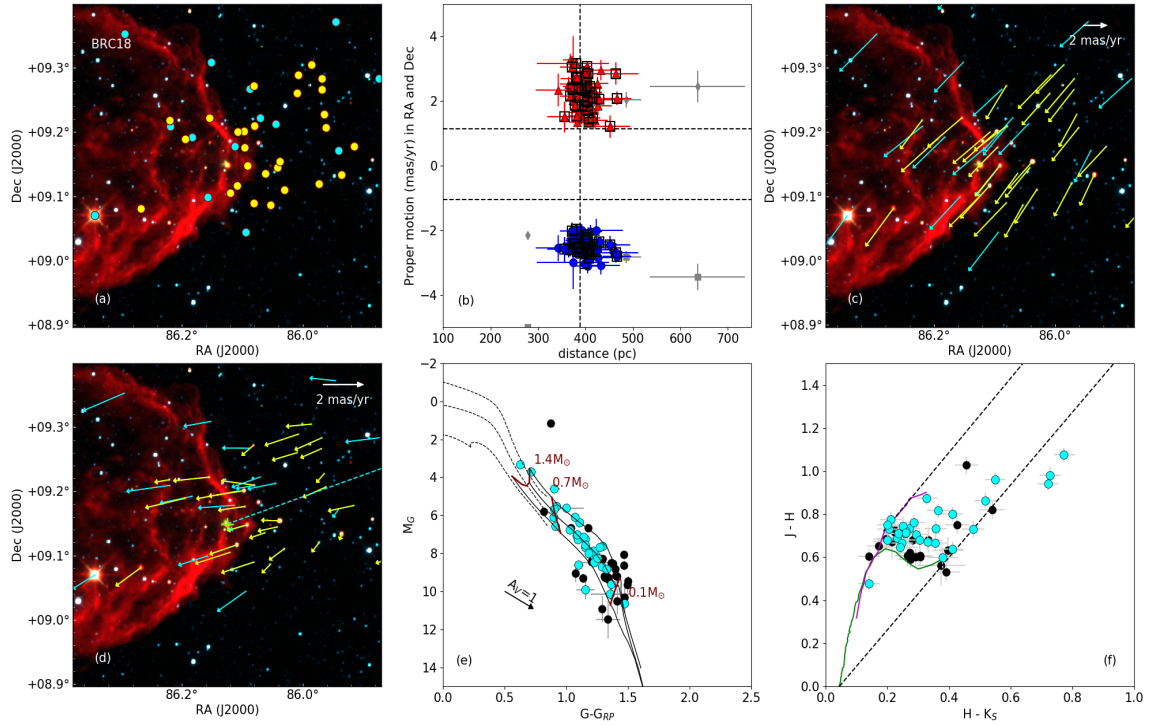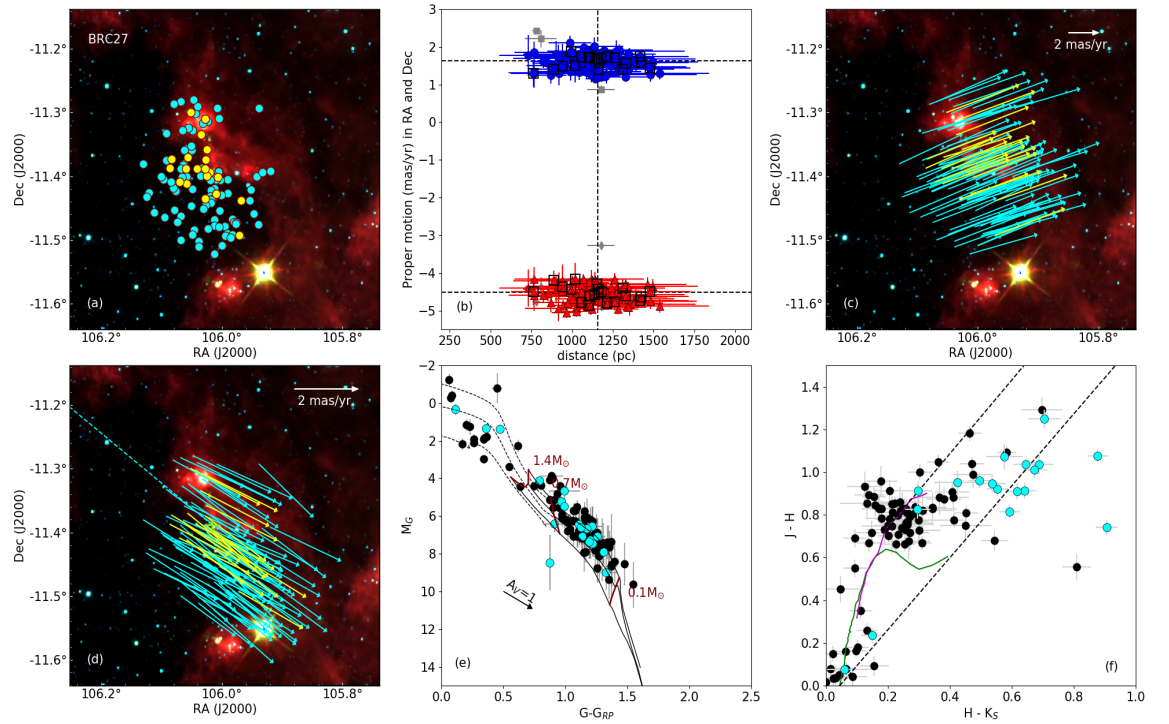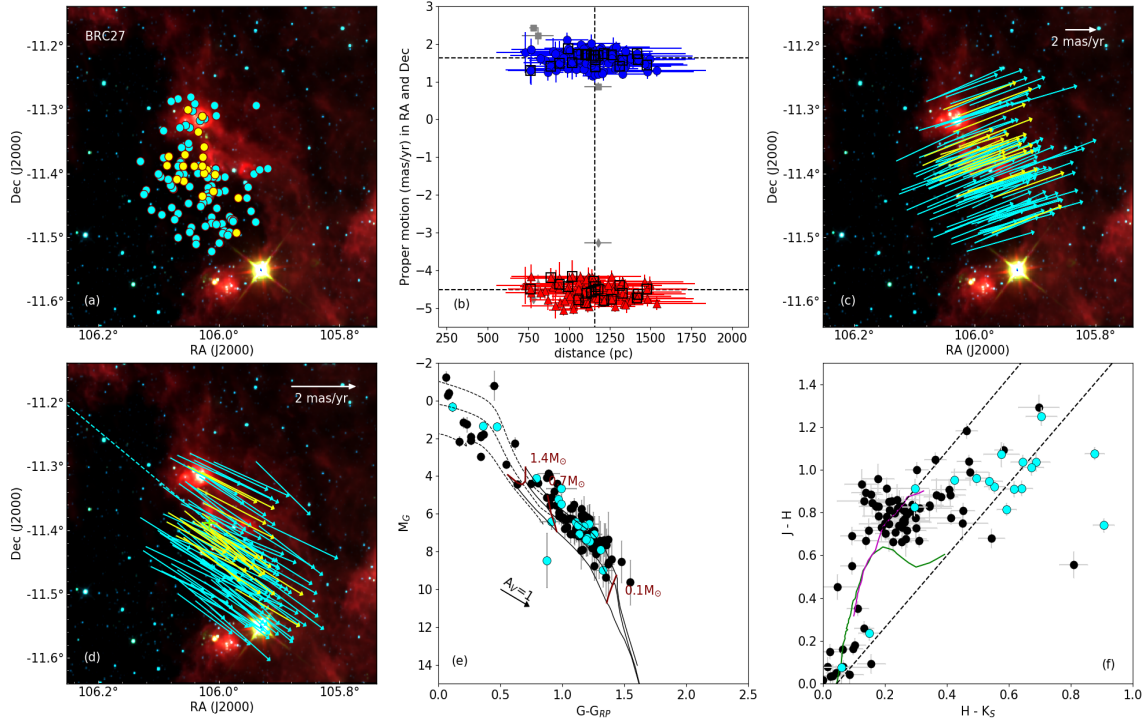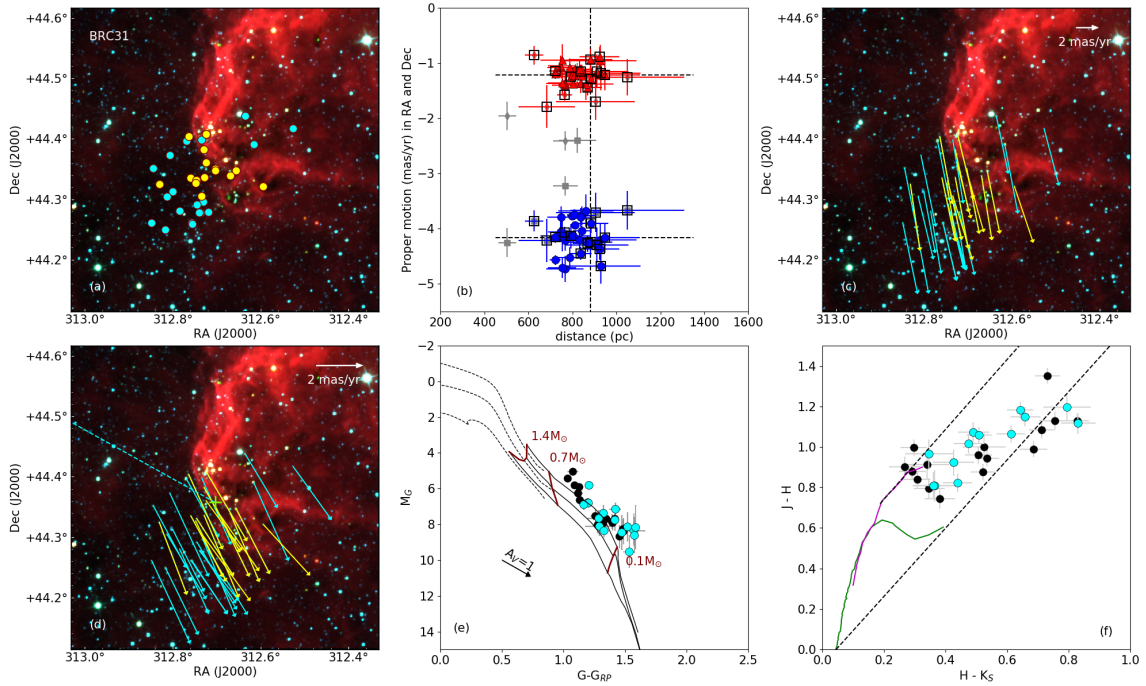
Figure 7.14: Similar as BRC 2 but for BRC 18.

Figure 7.14: Similar as BRC 2 but for BRC 27.

249

Figure 7.14: Similar as BRC 2 but for BRC 27.

Figure 7.14: Similar as BRC 2 but for BRC 31.
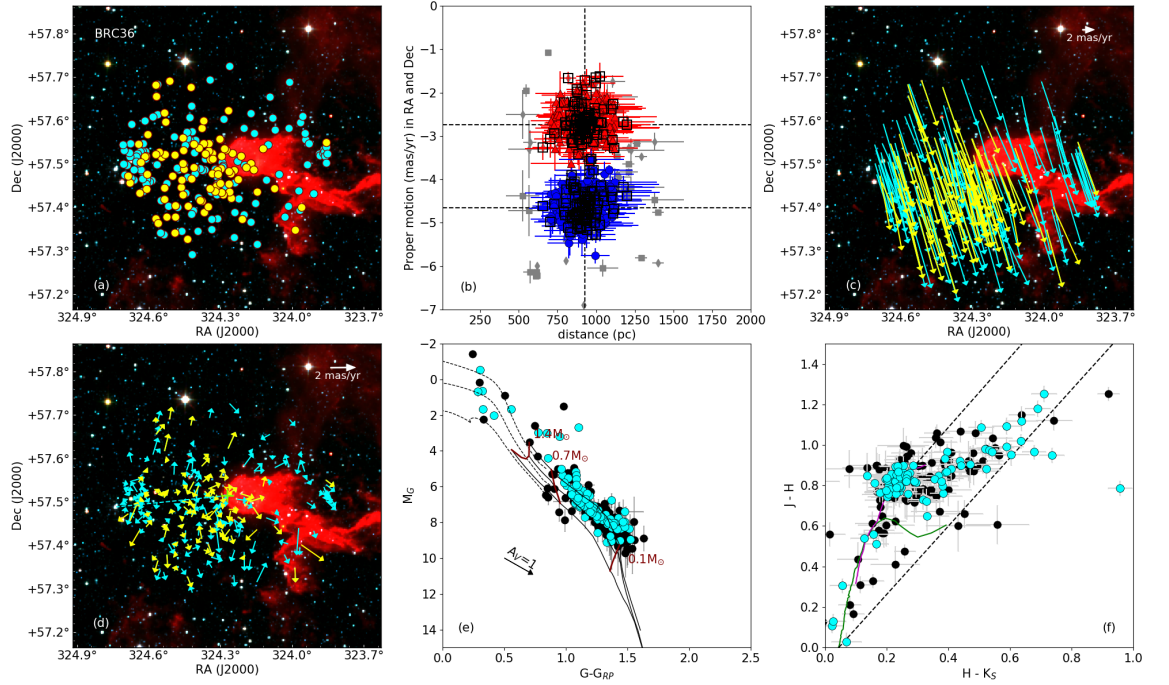
Figure 7.14: Similar as BRC 2 but for BRC 36.

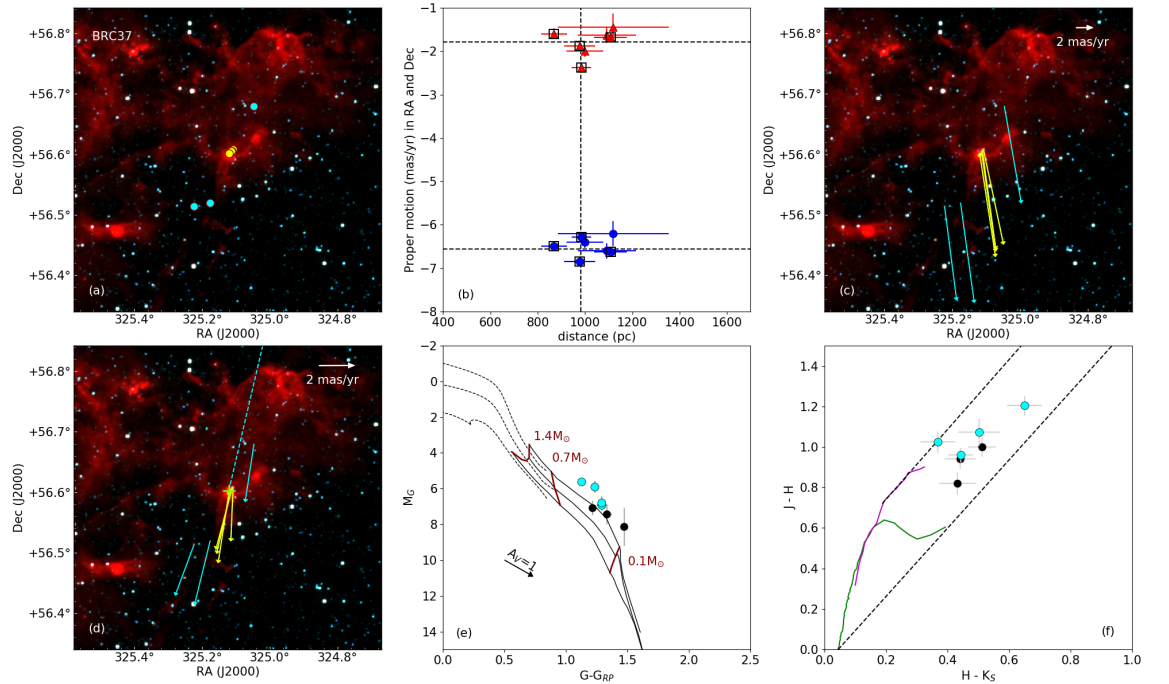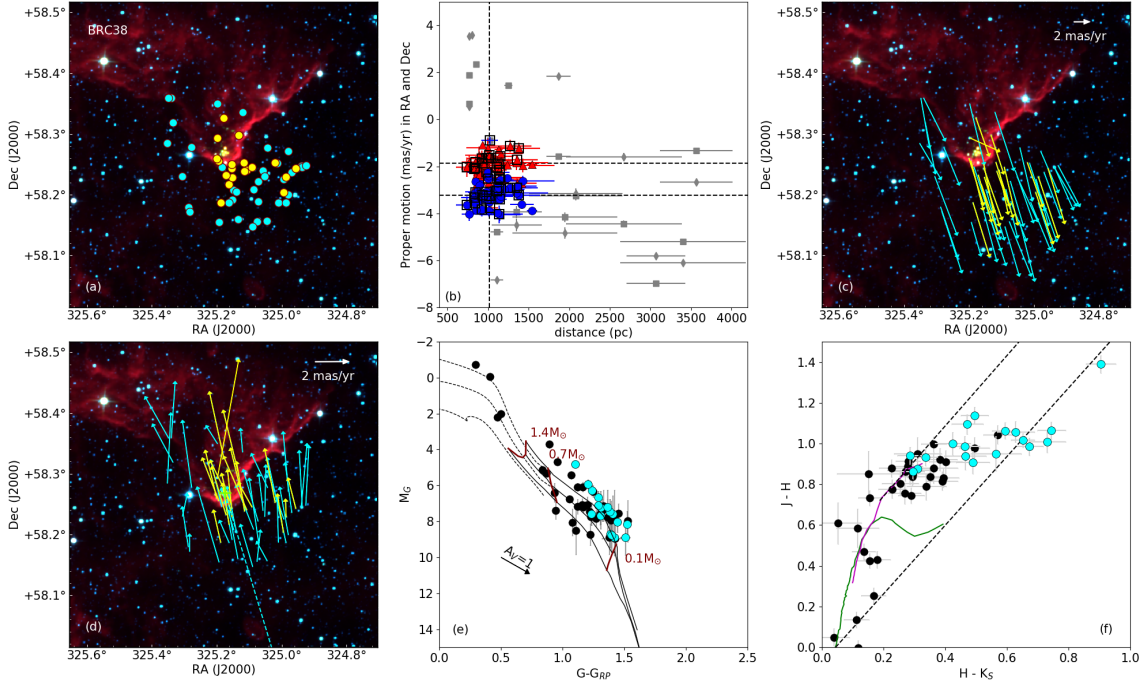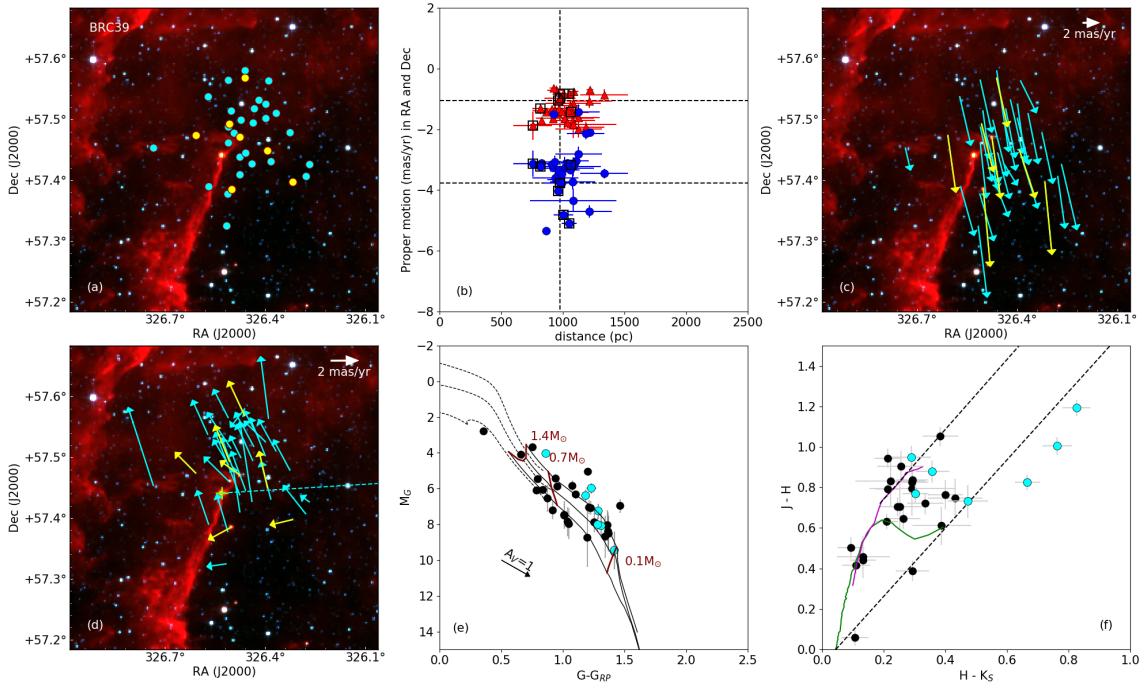Figure 7.14: Similar as BRC 2 but for BRC 37.

Figure 7.14: Similar as BRC 2 but for BRC 38.

Figure 7.14: Similar as BRC 2 but for BRC 39.
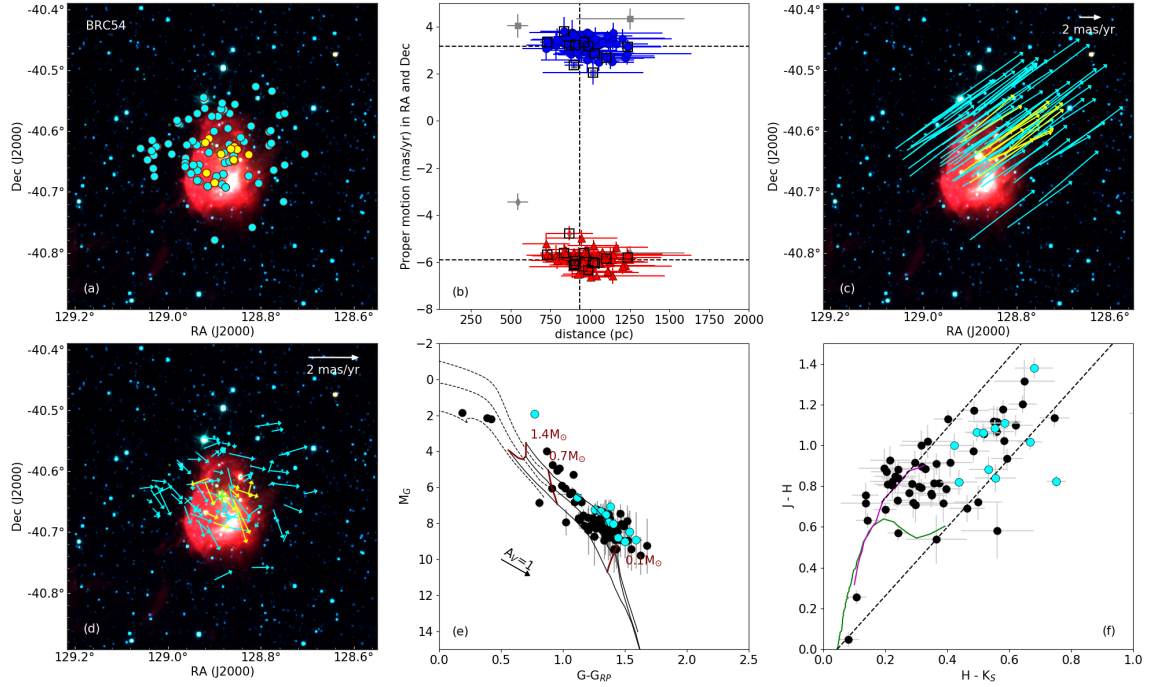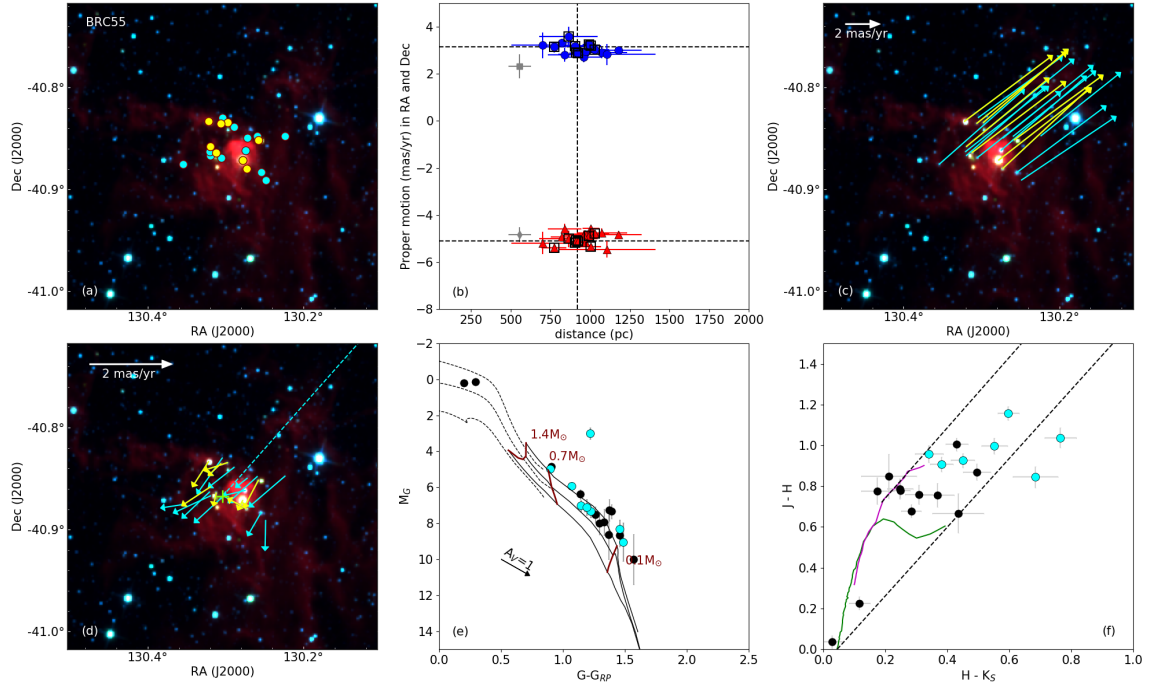
Figure 7.14: Similar as BRC 2 but for BRC 54.

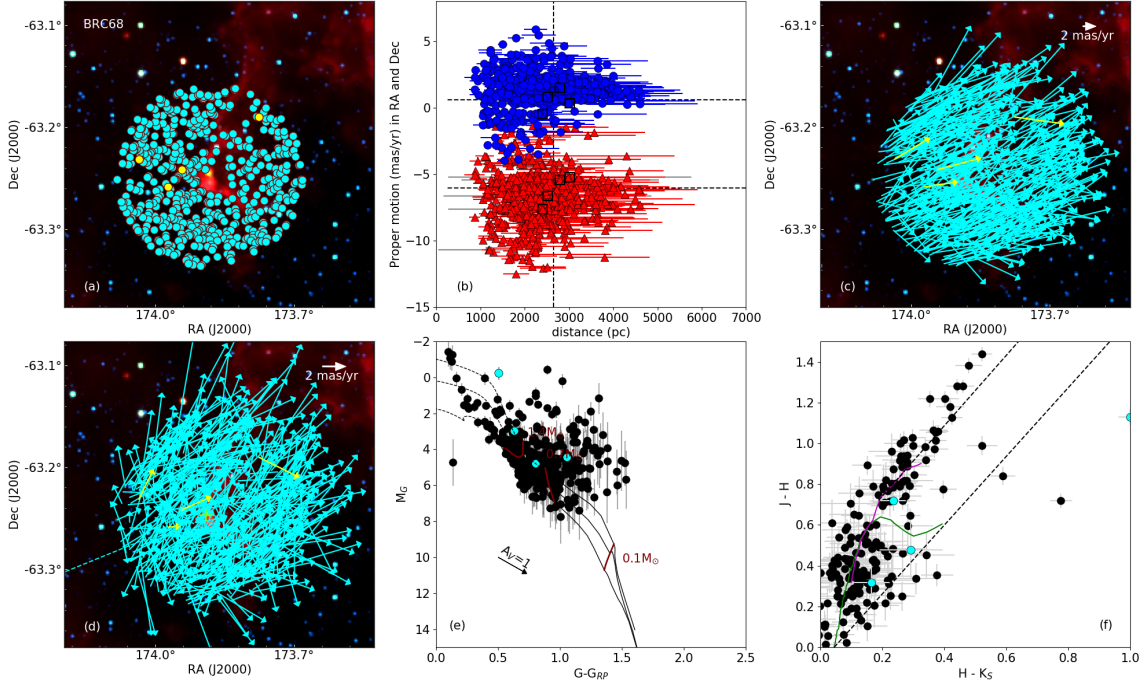Figure 7.14: Similar as BRC 2 but for BRC 55.
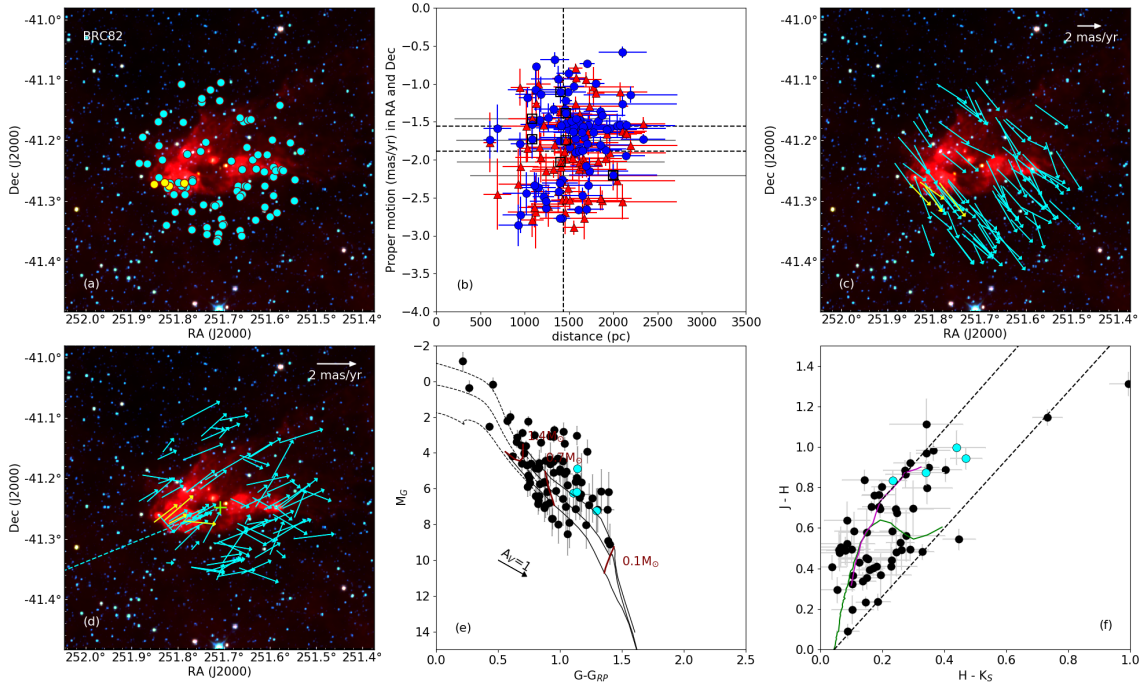
Figure 7.14: Similar as BRC 2 but for BRC 68.

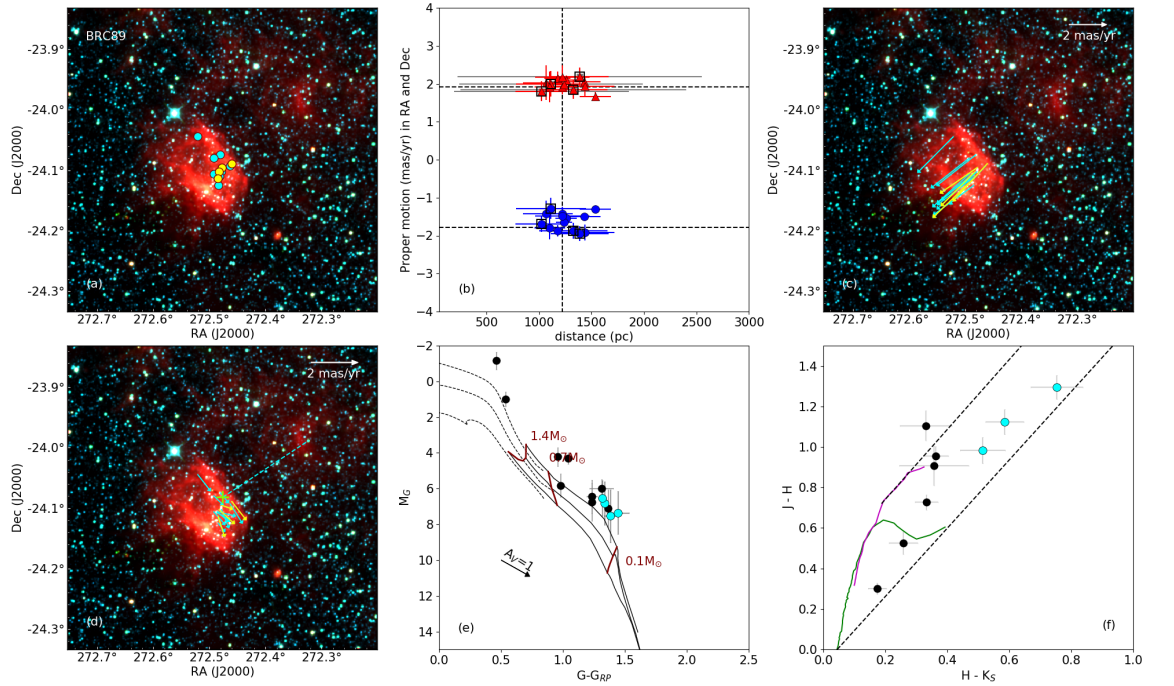Figure 7.14: Similar as BRC 2 but for BRC 82.

Figure 7.14: Similar as BRC 2 but for BRC 89.

we found less extinction and little or no near-IR excess in these newly found comoving sources.

As the operating wavelength of *Gaia* is optical, the number of YSOs detected is less due to the presence of dense gas and dust surrounding them. More deep observations with good quality data would help us to increase the statistics and a better understanding.

Chapter 8

Summary, Conclusion and Future Prospects

8.1 Summary and conclusions

The aim of this thesis is the identification and characterization of young stars using various techniques, e.g., optical and near-IR photometry, spectroscopy, and optical spectropolarimtery and astrometry. The main scientific goals of this thesis were,

(1) to understand the kinematics of the YSOs in the molecular clouds.

(2) to understand the accretion mechanism of the YSOs.

(3) to understand the effect of magnetic field on star formation and cloud evolution.

For these purposes, archival astrometric data (*Gaia* DR2) of the YSOs have been used to study their kinematics. Optical and near-IR spectroscopic observations have

Table 8.1: Skills and expertises learnt during the thesis tenure.

Software	Application
Python	Used to analyse the observed data.
IRAF and Pyraf	Polarimetric, photometric, spectroscopic and spectropolarimetric data reduction.
Observation experience	
Band	**Observation**
Optical	Polarimetric, spectroscopic and spectropolarimetric observations using 1.04-m ST, 2-m HCT and 10-m SALT.
Near-IR	Spectroscopic observations using 3-m IRTF.

257

been performed to study the properties of YSOs embedded in the clouds. Also, we have used optical polarimetric observations to map the magnetic field morphology of the molecular clouds. The skills, that I have learnt during the thesis tenure, are listed in Table 8.1. The summarized results of the various projects carried out during this thesis have been written in detail in the following subsections.

8.1.1 Kinematic and photometric study of YSOs and co-moving sources in molecular clouds

In chapter 3, we worked on the investigation and characterization of young stars towards the cloud complex L1172/1174, located in the Cepheus Flare. Similar to a comet-like shape, the head part of the cloud, L1174, is illuminated by a Herbig Be star HD 200775, followed by an elongated structure L1172. The distance to this cloud is not well determined in the previous literature. Therefore, based on the latest *Gaia* DR2, we aimed to estimate the distance to this cloud complex. There are 58 YSOs located towards L1172/1174 identified in previous studies. The *Gaia* DR2 detects 20 of these YSOs, and based on their distances, we compute the distance to this cloud as 335±11 pc. We further confirm the estimated distance to this cloud complex, based on the polarization measurements of 249 stars projected background to the cloud. In the polarization vs. distance (obtained from *Gaia* DR2) plot of these 249 stars, we found a hike in polarization at ∼ 335 pc, further confirming its distance.

Now, based on the median absolute deviation (MAD) of the distances and proper motion values of the YSOs, we found 20 additional sources, which lie within 5× MAD with respect to the median values of distance and proper motion. These comoving sources could possibly be YSOs missed in the earlier studies. We made optical spectroscopic observations of four of the comoving sources and found Hα in emission in three of them. The other source shows Hα in filled-in emission. 10 YSOs and 4 comoving sources show X-ray in emission. These sources are having little or no near-IR excess. We classify them based on their spectral index. In the *Gaia* DR2 color-magnitude diagram we found that these comoving sources are of ∼ 1 − 3 Myr in age. We made a census of YSOs towards HD 20075, which is a Herbig Be star responsible to ionize L1174.

We extend this work to a wider scale in chapter 4, where the presence of three more HAeBe candidates in the Cepheus Flare within 1.5° radius centered on HD 200775 suggests that star formation is prevalent in the clouds L1147/1158, L1172/1174 and L1177. A number of YSOs are found to be distributed towards

these cloud complexes along with the HAeBe stars. Various star formation studies clearly indicate ongoing low-mass star formation inside the clouds of this region. Sources associated with less near-IR excess and less Hα emission lead to a possibility that more low-mass YSOs are present in this region, which were not identified in previous studies. We conducted a search for such additional young sources kinematically associated with the previously known YSOs and characterized their properties. Based on the *Gaia* DR2 distances and proper motions, we found that the HAeBe candidates, BD+68° 1118, HD 200775, and PV Cep, are all spatially and kinematically associated. Based on the *Gaia* DR2 distances of the HAeBe candidates and surrounding low-mass YSOs, we estimated a distance of 340±7 pc to the whole association containing BD+68° 1118, HD 200775, and PV Cep. Based on the distance and proper motions of all the known YSOs, a total of 74 additional comoving sources are found in this region, of which 39 form a loose association surrounding BD+68° 1118. These sources are characterized using optical and near-IR color-color and color-magnitude diagrams. These sources are predominantly M-type sources of ~ 10 Myr age with no or very little near-IR excess emission. Distribution of comoving sources around BD+68° 1118 is much scattered than those found around HD 200775. The positive expansion coefficients obtained by projected internal motions of the sources surrounding BD+68° 1118 and HD 200775 show that the comoving sources are in a state of expansion with respect to the respective HAeBe stars. A spatio-temporal gradient of these sources towards the center of the Cepheus Flare Shell supports the concept of triggered star formation due to external impacts.

8.1.2 Importance of magnetic field in molecular clouds

In chapter 3 part III, we mapped the magnetic field geometry towards a cometary cloud complex, L1172/1174, based on our R-band polarization measurements of sources projected background to the cloud. Based on the distances obtained from the *Gaia* DR2 of the YSOs located towards L1174, we estimated a distance 335 ± 11 pc towards this cloud. Also, in the distance versus degree of polarization plot of the sources projected background to L1172/1174, there is a clear hike in polarization at ~ 335 pc, which further confirms the distance to this cloud. In order to remove the polarization caused by the foreground material present along line-of-sight, we searched in Heiles (2000) catalogue to get foreground sources having polarization measurements. The search was made within a circular region of 6° radius about HD 200775. We obtained distances of total 17 sources from the Bailer-Jones et al. (2018) catalogue. We did not notice any significant change in the results after correcting

for the foreground polarization. The magnetic field is found to be smooth and oriented along the hub-filament structure of the cloud. The magnetic field geometry inferred from the *Planck* observations is found to be in good agreement with our R-band polarization measurements throughout the cloud. The mean magnetic field strength for the entire cloud was found to be 20 μG. We also estimated the magnetic field geometry towards the cloud complex L1147/1158, which is located towards the north-western side of L1172/1174 using the *Planck* polarization measurements. The magnetic field lines towards L1147/1158 are found to be oriented along a mean position angle of 180°. The higher star formation rate per cloud mass of 2.0±1.3 %Myr^{-1} found for L1172/1174, compared to 0.4±0.3 %Myr^{-1} for L1147/1158, is consistent with the earlier results (Li et al., 2017), which suggests that the molecular clouds with parallel magnetic field lines with respect to the cloud elongation are found to show relatively higher values of star formation rate compared to those with field lines perpendicular to the cloud elongation.

8.1.3 Spectroscopic studies of young stars

In chapter 3, we carried out the optical and near-IR spectroscopic observations of the comoving sources and YSOs towards L1172/1174. Out of four of the comoving sources and we found Hα in emission in three sources. The other source shows Hα in filled-in emission. We estimated the spectral types of these sources by comparing the features in the spectrum of our sources with those in the templates of main sequence stars from the stellar library provided by Jacoby et al. (1984). Two comoving stars (#c8 and #c18) are found to be of M1 spectral type while #c14 is found to be of M3 spectral type. All the three are found to be X-ray emitters too. We detected Hα in emission in all three of them. The EW(Hα) of #c8 and #c18 are found to be -15.03 ± 1.52 Å and -13.01 ± 1.30 Å, respectively. According to Barrado y Navascués & Martín (2003), these two sources can be classified as CTTS. Variability of Hα emission in these sources could be a plausible reason why they were not detected in any of the earlier star formation surveys. The EW(Hα) of #c14 is found to be -4.06 ± 0.41 Å which could possibly be a WTTS (Barrado y Navascués & Martín, 2003). The fourth star, #c9, is having Hα in filled-in emission. This star is found to be of a K2 spectral type. To reveal its Hα emission, we have subtracted the spectrum of a main sequence K2 spectrum from that of the source #c9. The EW(Hα) obtained from the resultant spectrum is found to be -0.69 ± 0.08 Å.

We also carried out near-IR spectroscopic study of 10 YSOs located in the vicinity of HD 200775. Mostly, these sources do not show Brγ in emission. Rather,

these sources show Brγ in filled-in emission, which signifies that they are not active accretors. Also these sources are of age higher than HD 200775, indicating that star formation started in this cloud prior to HD 200775. We also suspect that variability in the accretion tracer lines (Hα, Brγ etc.) could be a possible reason for not getting Brγ line in emission.

8.1.4 Characterization of young intermediat-mass stars associated with the Perseus OB2

We carried out optical spectroscopic observations of 12 young IM stars located in the Perseus region with high resolution mode (R=60,000), to estimate their spectral types with better accuracy. These sources do not have near-IR excess and emission in Balmer lines. Although most of them are of ages within 2−4 Myr, they do not show any evidence of circumstellar disks. The typical disk dispersal timescale (3−7 Myr; Yasui et al., 2014) is comparable with their ages due to which it is suspected that these sources have already shredded their surrounding disks. We present temperature, extinction, mass, age, and other properties of the observed sources. We also explained their kinematic properties using the latest *Gaia* DR2 and have found these sources are widely scattered across the region. We estimated median values of d =365 pc, $\mu_{\alpha\star}$ =4.238 mas yr^{-1} and μ_{δ} =-7.541 mas yr^{-1}). The corresponding MAD of d, $\mu_{\alpha\star}$ and μ_{δ} are 60 pc, 1.588 and 2.451 mas yr^{-1}, respectively. Some of these sources are kinematically associated with the low-mass YSOs also, though a significant fraction of them are widely scattered. Relative proper motions of the IM stars show random orientations as the low-mass YSOs. Additionally, we searched for the presence of DIBs in the spectra of the observed stars. We found 4 DIBs of wavelengths 5780.45, 5796.98, 6379.20, and 6613.62 Åin the observed spectra. A trend of increasing EWs of DIBs with color excess can be noticed. In two IM stars, we obtained pairs of interstellar Na-lines, along with the stellar Na-lines. It indicates the higher relative velocities between the stars and the interstellar cloud layers.

8.1.5 Accretion mechanism in Herbig AeBe stars

Low-mass stars are formed through magnetospheric accretion, whereas high-mass stars are thought to form via disk accretion. Linear spectropolarimetry is an excellent technique to probe the circumstellar disks around stars on scales of the order of a few stellar radii, i.e., their accretion regions. We acquired spectropolarimetric data

of six Herbig AeBe (HAeBe) stars (namely, HD 163296, HD 169142, HD 141926, HD 68695, HD 135344 B, and HD 130437), using RSS attached with 10-m SALT. The variation in polarization across the Hα and Hβ lines are studied here.

The spectropolarimetric results of HD 163296 (A1V) indicate line polarization across both Hα and Hβ lines. The QU plots of both lines behave as loops indicating the accretion mechanism taking place in this source. For HD 169142 (A8V), there is a visible change in polarization across the Hα line, while the Hβ line does not show any noticeable change in polarization. QU behaviour shows a smear distribution for both Hα and Hβ lines. A loop in the QU plane of the Hα line is noticeable for HD 141926 (B2III), while it is not clearly visible in the same for the Hβ line. In the spectropolarimetric results of HD 135344 B (F8V), no line effect can be seen across both Hα and Hβ. HD 68695 (A3V) shows line effect across Hβ while there is no visible change in P% in Hα. In the QU plane, we did not find any noticeable pattern for both the lines. For HD 130437 (B1V), there is a noticeable broad depolarization present in both the Hα and Hβ emission lines, which further confirm the disk accretion. The QU pattern appears to be complex across both lines. We added our results to the previous spectropolarimetric studies of 56 HAeBe stars (Ababakr et al., 2017), thus increasing the statistics by $\sim$9%.

8.1.6 Study of "Rocket Effect" in the BRCs

BRCs are the ideal candidates to study the RDI mode of star formation as they are potential sites of triggered star formation. Several YSOs have been identified towards a number of BRCs that are likely to have been formed as a result of the compression caused due to the RDI process. We conduct a study to investigate any preferred orientations of the disks around YSOs associated with BRC 18 with respect to the ambient magnetic field and the direction of the energetic photons from the ionizing star. We also find the possible direction of acceleration of BRC 18 away from the ionizing source as a result of recoil experience due to the evaporation of the gas towards the ionized medium from the surface facing it. We made R-band polarimetric observations of 12 YSOs identified in the vicinity of BRC 18 to infer the orientations of the disks around them. Using the distance and the proper motion measurements obtained from the *Gaia* DR2 of the sources identified as YSOs in the vicinity of the BRCs, we determined the projected motion of the YSOs and hence the BRCs on the sky plane by assuming that both are kinematically coupled. We found that the disk orientations of the YSOs are oriented randomly with respect to the projected magnetic field towards BRC 18. The relative proper motions of

the YSOs associated with the BRC 18 are found to show a trend of them moving away from the direction of ionizing sources. Using BRC 18 as a prototype, we made our analysis for 15 other BRCs, which showed a similar trend. We computed the offset between the angle of direction of ionization and relative proper motion of YSOs and found it to lie close to being parallel to each other. The Pearsons correlation coefficient of these two angles is found to be 0.961 with pnull 3.072e-09. The Spearman's correlation coefficient is estimated as 0.940, with pnull as 6.115e-08. Along with these, we also performed K−S test on these angles. The computed statistic is 0.125 and the pvalue is 0.999. All these results indicate that the YSOs and hence the BRCs are most likely accelerating away from the ionizing source due to the "Rocket Effect". In addition to these, we also found several sources lying in the vicinity of several BRCs that are kinematically associated with the previously known YSOs and, therefore, could be YSO candidates unidentified in earlier studies.

8.2 Future perspectives

The universe is fascinating yet stranger than our limit of imagination. Exploring the mysteries of the universe is an endless job. The innumerable problems make us floating in a vast ocean of unanswered questions. Therefore, we need to put significant effort into finding the answers. Although several projects have been completed in my PhD journey, these helped me in finding some new ideas which I am planning to carry out in the future. Most of the projects are linked to my thesis work. This section briefly describes the following projects which will be carried out in the immediate future. Since my thesis work is based on the identification and characterization of YSOs, the following projects are also oriented towards the same.

8.2.1 Kinematic study of YSOs and comoving sources with *Gaia* DR3

In chapter 7 we studied the "Rocket Effect" happening in the BRCS, based on the proper motions of the associated YSOs obtained from the *Gaia* DR2 catalog. As *Gaia* operates in the optical regime, the number of YSOs detected in the *Gaia* archive is significantly less as these young sources are often found to be surrounded by gas and dust. We could obtain projected motion only for 16 BRCs. The upcoming *Gaia* EDR3 and DR3 would help us to obtain more sources with astrometric parameters having better accuracy. With the new data, we would be able to include more BRCs with a considerable number of YSOs and to increase the statistics

supporting the "Rocket Effect".

In addition to this project, we will conduct a study to find the additional sources kinematically coupled with the known YSOs associated with cloud complexes LDN 1251, 1235, and 1228. These clouds are having elongated structures, located towards higher latitude in the Cepheus Flare, with the YSOs predominantly in the head regions. This project will be similar to the work done chapter 3. Based on the optical and near-IR color-color and color-magnitude diagrams of the YSOs and comoving sources, we would characterize them.

8.2.2 Spectroscopic study of young sources

In chapter 7 describing "Rocket Effect", we found additional sources in the 16 BRCs, located at similar distances and having similar proper motions as previously known YSOs, which are possible young sources. Due to less near-IR excess and less Hα emission, these sources could be missed in the identification of YSOs in the previous star formation studies towards the BRCs. We plan to carry out optical spectroscopic observations towards these new additional comoving sources, using 2-m HCT, IIA, and 3.6-m DOT, ARIES, India. Based on spectroscopic data, we can estimate the physical parameters of these sources, for example, temperature, age, extinction, mass, etc. Also, based on the EW of Hα emission, we can classify them.

8.2.3 Spectropolarimetric study of Herbig AeBes

We carried out optical spectropolarimetric observations of six HAeBes to study their accretion mechanisms and increase the number of samples of early type stars. As, till date, there is comparatively less number of samples showing disk accretion mechanisms, we need more sources to improve the statistics and further confirm this argument. Therefore, a larger number of early type sources from the southern sky are planned to observe in spectropolarimetric mode using RSS in 10-m SALT.

8.2.4 near-IR photometric study of YSOs in the λ Ori HII region

A dark ring surrounding the HII region Sh2-264 (Sharpless, 1959) was first recognized by Wade (1958). Dense portions of the ring were catalogued as dark clouds Barnard (B) 30, B 35, and B 223 by Barnard (1927). CO emission was observed towards some of the dark clouds along the border of the HII region, e.g., B 35 (Lada & Black, 1976). In a large scale CO survey of the region, a ring of molecular gas was

identified (Maddalena et al., 1986). Based on optical photometry and multi-band spectroscopy for lithium absorption to identify PMS stars, Dolan & Mathieu (2001) identified 266 PMS stars towards λ Orionis. They found that the low-mass star formation started throughout the region together with the birth of the massive stars. Within the last $1-2$ Myr, star formation ceased in the center of the OB association, but is still active in the dark clouds $\sim$ 20 pc away from the center concentrated in the ring structure. Three bipolar outflow driving protostars, cataloged as IRAS 05417+0907, IRAS 05496+0812, and IRAS 05295+1247 have been detected in B 35, L1598, and B 30 respectively (Chini et al., 1997; Reipurth et al., 1997). There are two more YSOs associated with outflow, IRAS 05155+0707 and HH 114 MMS, which are detected in B 223 (Reipurth et al., 1997).

We have initiated a program to map the B_{POS} geometry of the outflow regions in λ Ori ring to know the impact of magnetic field orientation and strength on star formation. Our further plan is to carry out broad-band imaging in J, H, and K filters in 3.6-m Devasthal Optical Telescope (DOT) to obtain photometric flux of the central $IRAS$ sources in B 30, B 35, and B 223 since we have only upper limits/poor quality data in the J band from 2MASS observations. In order to identify the outflow source, we also would like to carry out narrow-band imaging using Brγ, K-continuum and L-band filters. This study will allow us to construct the SED with good photometric data, and we can get the evolutionary stages and stellar properties (mass, temperature, radius, etc.) of these YSOs. Also, we would be able to understand the morphology of the outflows in the context of the magnetic field geometry traced by our polarimetric observations.

References

Ababakr K. M., Oudmaijer R. D., Vink J. S., 2016, MNRAS, 461, 3, 3089 12, 203

Ababakr K. M., Oudmaijer R. D., Vink J. S., 2017, MNRAS, 472, 1, 854 lx, 12, 198, 199, 202, 203, 262

Ábrahám P., Leinert C., Burkert A., Henning T., Lemke D., 2000, A&A, 354, 965 159

Adams F. C., 2010, ARA&A, 48, 47 147

Adams F. C., Myers P. C., 2001, ApJ, 553, 2, 744 147

Aikawa Y., Ohashi N., Herbst E., 2003, ApJ, 593, 906 4

Alecian E., Catala C., Wade G. A., et al., 2008, MNRAS, 385, 391 58, 94, 157

Alecian E., Catala C., Wade G. A., et al., 2009, in EAS Publications Series, edited by C. Neiner, J. P. Zahn, vol. 39 of EAS Publications Series, 121–132 11

Alecian E., Wade G. A., Catala C., et al., 2013a, MNRAS, 429, 2, 1001 11, 12, 163, 199

Alecian E., Wade G. A., Catala C., et al., 2013b, MNRAS, 429, 2, 1027 12

Alina D., Ristorcelli I., Montier L., et al., 2019, MNRAS, 485, 2, 2825 124

Alves F. O., Franco G. A. P., 2007, A&A, 470, 597 65, 72, 226

Alves F. O., Franco G. A. P., Girart J. M., 2008, A&A, 486, L13 123

Anantha C., Roy J., Mahesh P. K., et al., 2013, in Astronomical Society of India Conference Series, vol. 9, 136 30

Anderson C. M., Weitenbeck A. J., Code A. D., et al., 1996, AJ, 112, 2726 17

REFERENCES

Andrae R., Fouesneau M., Creevey O., et al., 2018, A&A, 616, A8 93, 156

André P., 2011, Spectral Classification of Embedded Stars, 1549–1553, Springer Berlin Heidelberg, Berlin, Heidelberg xlv, 9

André P., Men'shchikov A., Bontemps S., et al., 2010, A&A, 518, L102 lii, 123, 129, 130

Andre P., Ward-Thompson D., Barsony M., 1993, ApJ, 406, 122 79, 148

André R., Kremer G. M., 2014, arXiv e-prints, arXiv:1411.6096 124

Appenzeller I., Mundt R., 1989, A&A Rev., 1, 291 79, 148

Arce H. G., Borkin M. A., Goodman A. A., Pineda J. E., Halle M. W., 2010, ApJ, 715, 2, 1170 179

Armandroff T. E., Herbst W., 1981, AJ, 86, 1923 65

Arthur S. J., Henney W. J., Mellema G., de Colle F., Vázquez-Semadeni E., 2011, MNRAS, 414, 1747 228

Arun R., Mathew B., Manoj P., et al., 2019, AJ, 157, 4, 159 94, 148, 157

Arzoumanian D., André P., Didelon P., et al., 2011, A&A, 529, L6 123

Azimlu M., Martínez-Galarza J. R., Muench A. A., 2015, AJ, 150, 3, 95 179

Bailer-Jones C. A. L., 2015, PASP, 127, 994 67, 128, 150

Bailer-Jones C. A. L., Rybizki J., Fouesneau M., Mantelet G., Andrae R., 2018, AJ, 156, 58 67, 69, 70, 72, 73, 81, 93, 104, 114, 115, 117, 118, 128, 135, 149, 150, 151, 152, 156, 170, 180, 203, 204, 205, 219, 220, 223, 232, 259

Ballesteros-Paredes J., Klessen R. S., Mac Low M. M., Vazquez-Semadeni E., 2007, in Protostars and Planets V, edited by B. Reipurth, D. Jewitt, K. Keil, 63 123

Bally J., Moeckel N., Throop H., 2005, in Chondrites and the Protoplanetary Disk, edited by A. N. Krot, E. R. D. Scott, B. Reipurth, vol. 341 of Astronomical Society of the Pacific Conference Series, 81 14

Bally J., Scoville N. Z., 1980, ApJ, 239, 121 235

Bally J., Walawender J., Johnstone D., Kirk H., Goodman A., 2008, The Perseus Cloud, vol. 4, 308 181, 185

Banerjee R., Vázquez-Semadeni E., Hennebelle P., Klessen R. S., 2009, MNRAS, 398, 1082 124

Baraffe I., Homeier D., Allard F., Chabrier G., 2015, A&A, 577, A42 l, lvi, 94, 95, 155, 158, 245

Barcons X., Carrera F. J., Ceballos M. T., et al., 2007, A&A, 476, 1191 86

Barentsen G., Vink J. S., Drew J. E., et al., 2011, MNRAS, 415, 103 218

Barnard E. E., 1927, Catalogue of 349 dark objects in the sky 264

Barrado y Navascués D., Martín E. L., 2003, AJ, 126, 6, 2997 79, 88, 148, 260

Basri G., Bertout C., 1989, ApJ, 341, 340 199

Basri G., Marcy G. W., 1995, AJ, 109, 762 79

Bastien P., 1982, A&AS, 48, 153 lxii, 217, 224, 225

Bastien P., 1985, ApJS, 59, 277 217

Bastien P., Landstreet J. D., 1979, ApJ, 229, L137 217

Basu S., Mouschovias T. C., 1994, ApJ, 432, 720 3

Bayo A., Barrado D., Huélamo N., et al., 2012, Astronomy and Astrophysics, 547, A80 229

Beattie J. R., Federrath C., 2020, MNRAS, 492, 1, 668 123

Beck R., Brandenburg A., Moss D., Shukurov A., Sokoloff D., 1996, ARA&A, 34, 155 16

Belloche A., Hennebelle P., André P., 2006, A&A, 453, 145 7

Benisty M., Perraut K., Mourard D., et al., 2013, A&A, 555, A113 64, 65, 98

Berkhuijsen E. M., 1973, A&A, 24, 143 57

Bertoldi F., 1989, ApJ, 346, 735 5, 6, 7, 215, 221

Bertoldi F., McKee C. F., 1990, ApJ, 354, 529 7, 215, 221

Bertone E., Buzzoni A., Chávez M., Rodríguez-Merino L. H., 2008, A&A, 485, 3, 823 185

REFERENCES

Bhatt H. C., 2000, A&A, 362, 715 177

Bhatt H. C., Jain S. K., 1992, MNRAS, 257, 57 123

Bisbas T. G., Wünsch R., Whitworth A. P., Hubber D. A., Walch S., 2011, ApJ, 736, 142 216

Blaauw A., 1964, ARA&A, 2, 213 179

Bohlin R. C., Savage B. D., Drake J. F., 1978, ApJ, 224, 132 129

Bok B. J., Bok F., 1941, The Milky way 63

Bonnell I. A., Bate M. R., Clarke C. J., Pringle J. E., 1997, MNRAS, 285, 201 13, 14

Bonnell I. A., Bate M. R., Clarke C. J., Pringle J. E., 2001, MNRAS, 323, 4, 785 14

Bonnell I. A., Bate M. R., Zinnecker H., 1998, MNRAS, 298, 1, 93 13, 100

Bonnell I. A., Vine S. G., Bate M. R., 2004, MNRAS, 349, 2, 735 13

Bossini D., Vallenari A., Bragaglia A., et al., 2019, A&A, 623, A108 94, 245

Brandenburg A., Subramanian K., 2005, Phys. Rep., 417, 1 16

Bresnahan D., Ward-Thompson D., Kirk J. M., et al., 2018, A&A, 615, A125 144

Brown A. G. A., Blaauw A., Hoogerwerf R., de Bruijne J. H. J., de Zeeuw P. T., 1999, in NATO Advanced Science Institutes (ASI) Series C, edited by C. J. Lada, N. D. Kylafis, vol. 540 of NATO Advanced Science Institutes (ASI) Series C, 411 185

Brown A. G. A., Walter F. M., Blaauw A., 1998, arXiv e-prints, astro–ph/9802054 179

Brown J. C., McLean I. S., 1977, A&A, 57, 141 217

Buckner A. S. M., Khorrami Z., González M., et al., 2020, A&A, 636, A80 232

Calvet N., Basri G., Imhoff C. L., Giampapa M. S., 1985, ApJ, 293, 575 84

Calvet N., Gullbring E., 1998, ApJ, 509, 802 84

Caratti o Garatti A., Garcia Lopez R., Weigelt G., et al., 2013, A&A, 554, A66 159

270

Cardelli J. A., Clayton G. C., Mathis J. S., 1989, ApJ, 345, 245 185

Carpenter J. M., 2000, AJ, 120, 6, 3139 147

Carpenter J. M., Mamajek E. E., Hillenbrand L. A., Meyer M. R., 2006, ApJ, 651, 1, L49 24, 178

Cauley P. W., Johns-Krull C. M., 2014, ApJ, 797, 2, 112 199

Cauley P. W., Johns-Krull C. M., 2015, ApJ, 810, 1, 5 199

Cernis K., 1990, Ap&SS, 166, 2, 315 181

Cernis K., 1993, Baltic Astronomy, 2, 214 181

Chambers K. C., Magnier E. A., Metcalfe N., et al., 2016, ArXiv e-prints 150, 158, 220, 224

Chandrasekhar S., Fermi E., 1953, ApJ, 118, 113 17, 138

Chapman N. L., Goldsmith P. F., Pineda J. L., Clemens D. P., Li D., Krčo M., 2011, ApJ, 741, 21 124

Chauhan N., Pandey A. K., Ogura K., et al., 2009, MNRAS, 396, 964 216, 218, 219

Chen C.-Y., Ostriker E. C., 2014, ApJ, 785, 1, 69 124, 217

Chen H.-R. V., Zhang Q., Wright M. C. H., et al., 2019, ApJ, 875, 1, 24 123

Chini R., Reipurth B., Sievers A., et al., 1997, A&A, 325, 542 265

Choi J., Dotter A., Conroy C., Cantiello M., Paxton B., Johnson B. D., 2016, ApJ, 823, 102 185

Choudhury R., Mookerjea B., Bhatt H. C., 2010, ApJ, 717, 1067 xlix, 90, 91, 216, 218, 219

Ciolek G. E., Basu S., 2000, ApJ, 529, 925 3

Clariá J. J., 1974, A&A, 37, 229 235

Clarke C. J., Bonnell I. A., Hillenbrand L. A., 2000, in Protostars and Planets IV, edited by V. Mannings, A. P. Boss, S. S. Russell, 151 13

Clarke D., McLean I. S., 1974, MNRAS, 167, 27P 12

REFERENCES

Clemens D. P., Barvainis R., 1988, ApJS, 68, 257 149

Clemens D. P., Pinnick A. F., Pavel M. D., Taylor B. W., 2012, ApJS, 200, 2, 19 17

Clemens D. P., Yun J. L., Heyer M. H., 1991, ApJS, 75, 877 63

Cohen M., Kuhi L. V., Harlan E. A., 1977, ApJ, 215, L127 149

Cohen M., Kuhi L. V., Harlan E. A., Spinrad H., 1981, ApJ, 245, 920 159

Coulson I. M., Walther D. M., 1995, MNRAS, 274, 4, 977 204

Cox N. L. J., 2011, in EAS Publications Series, edited by C. Joblin, A. G. G. M. Tielens, vol. 46 of EAS Publications Series, 349–354 194

Coyne G. V., 1976, in Be and Shell Stars, edited by A. Slettebak, vol. 70 of IAU Symposium, 233 133

Crampton D., Fisher W. A., 1974, Publications of the Dominion Astrophysical Observatory Victoria, 14, 283 235

Crawford M. K., Tielens A. G. G. M., Allamandola L. J., 1985, ApJ, 293, L45 194

Crutcher R., 2005, in The Magnetized Plasma in Galaxy Evolution, edited by K. T. Chyzy, K. Otmianowska-Mazur, M. Soida, R.-J. Dettmar, 103–110 17

Crutcher R. M., 1999, ApJ, 520, 706 217

Crutcher R. M., 2012, ARA&A, 50, 29 18, 72

Crutcher R. M., Troland T. H., 2007, in Triggered Star Formation in a Turbulent ISM, edited by B. G. Elmegreen, J. Palous, vol. 237 of IAU Symposium, 141–147 13

Cudlip W., Furniss I., King K. J., Jennings R. E., 1982, MNRAS, 200, 1169 17

Currie T., Sicilia-Aguilar A., 2011, ApJ, 732, 1, 24 189

Cushing M. C., Vacca W. D., Rayner J. T., 2004, PASP, 116, 362 45

Cutri R. M., et al., 2012, VizieR Online Data Catalog, II/311 150, 160, 162

Cutri R. M., et al., 2014, VizieR Online Data Catalog, 2328 90, 220

Cutri R. M., Skrutskie M. F., van Dyk S., et al., 2003, VizieR Online Data Catalog, 2246, 0 54, 88, 150, 159, 220

Dale J. E., Haworth T. J., Bressert E., 2015, MNRAS, 450, 2, 1199 216

Davies J. K., Evans A., Bode M. F., Whittet D. C. B., 1990, MNRAS, 247, 517 10

Davis Jr. L., Greenstein J. L., 1951, ApJ, 114, 206 17, 72, 132

de Wit W. J., Testi L., Palla F., Vanzi L., Zinnecker H., 2004, A&A, 425, 937 13

de Zeeuw P. T., Hoogerwerf R., de Bruijne J. H. J., Brown A. G. A., Blaauw A., 1999, AJ, 117, 354 181, 185

Deharveng L., Zavagno A., Salas L., Porras A., Caplan J., Cruz-González I., 2003, A&A, 399, 1135 5

Di Francesco J., Keown J., Fallscheer C., et al., 2020, arXiv e-prints, arXiv:2010.09894 144, 145

Dolan C. J., Mathieu R. D., 2001, AJ, 121, 2124 265

Donehew B., Brittain S., 2011, AJ, 141, 2, 46 199

Dotson J. L., Davidson J., Dowell C. D., Schleuning D. A., Hildebrand R. H., 2000, ApJS, 128, 335 17

Dotter A., 2016, ApJS, 222, 8 185

Dullemond C. P., Dominik C., 2004, A&A, 417, 159 189

Dullemond C. P., Dominik C., 2005, A&A, 434, 3, 971 189

Dunham M. M., Arce H. G., Allen L. E., et al., 2013, AJ, 145, 4, 94 159

Dunham M. M., Crapsi A., Evans II N. J., et al., 2008, ApJS, 179, 249 152

Dutta S., Mondal S., Samal M. R., Jose J., 2018, ApJ, 864, 2, 154 123

Dzib S. A., Loinard L., Ortiz-León G. N., Rodríguez L. F., Galli P. A. B., 2018, ApJ, 867, 151 65, 67, 80

Edwards S., Hartigan P., Ghandour L., Andrulis C., 1994, AJ, 108, 1056 158

REFERENCES

Elmegreen B. G., 1998, in Origins, edited by C. E. Woodward, J. M. Shull, H. A. Thronson, Jr., vol. 148 of Astronomical Society of the Pacific Conference Series, 150 216

Elmegreen B. G., 1999, ApJ, 515, 1, 323 100

Elmegreen B. G., 2011, in EAS Publications Series, edited by C. Charbonnel, T. Montmerle, vol. 51 of EAS Publications Series, 45–58 216

Elmegreen B. G., Clemens C., 1985, ApJ, 294, 523 147

Elmegreen B. G., Lada C. J., 1977, ApJ, 214, 725 4, 5

Elmegreen D. M., Elmegreen B. G., 1978, ApJ, 220, 510 58

Elsasser H., Staude H. J., 1978, A&A, 70, L3 217

Elyajouri M., Lallement R., Monreal-Ibero A., Capitanio L., Cox N. L. J., 2017, A&A, 600, A129 194

Enoch M. L., Evans Neal J. I., Sargent A. I., Glenn J., 2009, ApJ, 692, 2, 973 179

Enoch M. L., Young K. E., Glenn J., et al., 2006, ApJ, 638, 1, 293 181

Eswaraiah C., Lai S.-P., Chen W.-P., et al., 2017, ApJ, 850, 2, 195 123

Evans Neal J. I., 1999, ARA&A, 37, 311 147

Evans Neal J. I., Dunham M. M., Jørgensen J. K., et al., 2009, ApJS, 181, 2, 321 79, 148

Evans Neal J. I., Heiderman A., Vutisalchavakul N., 2014, ApJ, 782, 2, 114 144

Faherty J. K., Bochanski J. J., Gagné J., et al., 2018, ApJ, 863, 91 80

Fairlamb J. R., Oudmaijer R. D., Mendigutía I., Ilee J. D., van den Ancker M. E., 2015, MNRAS, 453, 1, 976 148, 203, 204, 205

Fairlamb J. R., Oudmaijer R. D., Mendigutia I., Ilee J. D., van den Ancker M. E., 2017, MNRAS, 464, 4, 4721 200, 202

Fang M., van Boekel R., Wang W., Carmona A., Sicilia-Aguilar A., Henning T., 2009, A&A, 504, 461 xlix, 90, 91

Fedorov P. N., Akhmetov V. S., Bobylev V. V., 2011, MNRAS, 416, 1, 403 163

Fiege J. D., Pudritz R. E., 2000, MNRAS, 311, 1, 105 123

Foster J. B., Cottaar M., Covey K. R., et al., 2015, ApJ, 799, 2, 136 157

Franco G. A. P., 2002, MNRAS, 331, 2, 474 63

Franco G. A. P., Alves F. O., Girart J. M., 2010, ApJ, 723, 146 123

Fuente A., Martin-Pintado J., Bachiller R., Neri R., Palla F., 1998a, A&A, 334, 253 11, 101, 157, 159

Fuente A., Martın-Pintado J., Bachiller R., Rodrıguez-Franco A., Palla F., 2002, A&A, 387, 977 178

Fuente A., Martin-Pintado J., Neri R., Rogers C., Moriarty-Schieven G., 1996, A&A, 310, 286 101, 102

Fuente A., Martin-Pintado J., Rodriguez-Franco A., Moriarty-Schieven G. D., 1998b, A&A, 339, 575 58, 136, 137, 165

Fuente A., Neri R., Martín-Pintado J., Bachiller R., Rodríguez-Franco A., Palla F., 2001, A&A, 366, 873 100

Gaia Collaboration, Brown A. G. A., Vallenari A., et al., 2018, A&A, 616, A1 66, 67, 69, 81, 99, 128, 150, 151, 152, 180, 220, 221, 229

Galli D., Shu F. H., 1993, ApJ, 417, 243 217

Getman K. V., Broos P. S., Feigelson E. D., et al., 2011, ApJS, 194, 3 85

Getman K. V., Feigelson E. D., Garmire G., Broos P., Wang J., 2007, ApJ, 654, 316 216

Getman K. V., Feigelson E. D., Luhman K. L., Sicilia-Aguilar A., Wang J., Garmire G. P., 2009, ApJ, 699, 1454 216

Getman K. V., Feigelson E. D., Sicilia-Aguilar A., Broos P. S., Kuhn M. A., Garmire G. P., 2012, MNRAS, 426, 2917 218, 219

Giampapa M. S., Calvet N., Imhoff C. L., Kuhi L. V., 1981, ApJ, 251, 113 84

Gimenez A., Clausen J. V., 1994, A&A, 291, 795 185

Gómez G. C., Vázquez-Semadeni E., 2014, ApJ, 791, 2, 124 123, 124

REFERENCES

Gómez G. C., Vázquez-Semadeni E., Zamora-Avilés M., 2018, MNRAS, 480, 3, 2939 123, 124

Gomez M., Hartmann L., Kenyon S. J., Hewett R., 1993, AJ, 105, 1927 157

Gomez M., Jones B. F., Hartmann L., et al., 1992, AJ, 104, 762 94

Gomez de Castro A. I., Lamzin S. A., 1999, MNRAS, 304, L41 84

Goodman A. A., 1995, in From Gas to Stars to Dust, edited by M. R. Haas, J. A. Davidson, E. F. Erickson, vol. 73 of Astronomical Society of the Pacific Conference Series 133

Goodman A. A., Barranco J. A., Wilner D. J., Heyer M. H., 1998, ApJ, 504, 223 4

Goodman A. A., Bastien P., Myers P. C., Menard F., 1990, ApJ, 359, 363 123, 124

Goodman A. A., Jones T. J., Lada E. A., Myers P. C., 1992, ApJ, 399, 108 124

Goodman A. A., Jones T. J., Lada E. A., Myers P. C., 1995, ApJ, 448, 748 123

Górski K. M., Hivon E., Banday A. J., et al., 2005, ApJ, 622, 2, 759 126

Grady C. A., Devine D., Woodgate B., et al., 2000, ApJ, 544, 2, 895 199

Grady C. A., Schneider G., Hamaguchi K., et al., 2007, ApJ, 665, 2, 1391 204

Gray R. O., Riggs Q. S., Koen C., et al., 2017, AJ, 154, 1, 31 205

Greaves J. S., Holland W. S., Minchin N. R., Murray A. G., Stevens J. A., 1999, A&A, 344, 668 133

Greene T. P., Wilking B. A., Andre P., Young E. T., Lada C. J., 1994, ApJ, 434, 614 8, 9, 79, 93, 148

Gregori G., Miniati F., Ryu D., Jones T. W., 2000, ApJ, 543, 2, 775 145

Grenier I. A., Lebrun F., Arnaud M., Dame T. M., Thaddeus P., 1989, ApJ, 347, 231 64

Gu Q., Li H.-b., 2019, ApJ, 871, 1, L15 135, 143

Güdel M., Skinner S. L., Briggs K. R., Audard M., Arzner K., Telleschi A., 2005, ApJ, 626, L53 84

Guenther D. B., Kallinger T., Zwintz K., Weiss W. W., Tanner J., 2007, ApJ, 671, 581 84

Guenther E. W., Lehmann H., Emerson J. P., Staude J., 1999, A&A, 341, 768 198

Guetter H. H., Vrba F. J., 1989, AJ, 98, 611 132

Gulbis A. A. S., Bus S. J., Elliot J. L., et al., 2011, PASP, 123, 902, 461 30

Gullbring E., Calvet N., Muzerolle J., Hartmann L., 2000, ApJ, 544, 927 84

Gullbring E., Hartmann L., Briceño C., Calvet N., 1998, ApJ, 492, 323 199

Habart E., Testi L., Natta A., Vanzi L., 2003, A&A, 400, 575 148

Haisch Karl E. J., Lada E. A., Lada C. J., 2001, ApJ, 553, 2, L153 178

Hajigholi M., Persson C. M., Wirström E. S., et al., 2016, A&A, 585, A158 123

Hall J. S., 1949a, Science, 109, 166 16

Hall J. S., 1949b, Science, 109, 166 17

Hamaker, J. P., Bregman, J. D., 1996, Astron. Astrophys. Suppl. Ser., 117, 1, 161 128

Harjunpää P., Kaas A. A., Carlqvist P., Gahm G. F., 1999, A&A, 349, 912 132

Hartmann L., Ballesteros-Paredes J., Bergin E. A., 2001, ApJ, 562, 852 123

Hartmann L., Herczeg G., Calvet N., 2016, ARA&A, 54, 135 15, 16

Haworth T. J., Harries T. J., Acreman D. M., 2012, MNRAS, 426, 203 215

Hayashi M., Itoh Y., Oasa Y., 2012, PASJ, 64, 96 218, 219

Heger M. L., 1922, Lick Observatory Bulletin, 10, 337, 146 189

Heiderman A., Evans Neal J. I., Allen L. E., Huard T., Heyer M., 2010, ApJ, 723, 2, 1019 144

Heiles C., 1967, ApJS, 15, 97 57, 64

Heiles C., 2000, AJ, 119, 923 xlvii, lii, 72, 74, 133, 259

Heitsch F., Mac Low M.-M., Klessen R. S., 2001a, ApJ, 547, 280 4

REFERENCES

Heitsch F., Zweibel E. G., Mac Low M.-M., Li P., Norman M. L., 2001b, ApJ, 561, 800 138

Hennebelle P., 2013, A&A, 556, A153 123, 124

Hennebelle P., Inutsuka S.-i., 2019, Frontiers in Astronomy and Space Sciences, 6, 5 217

Henney W. J., Arthur S. J., de Colle F., Mellema G., 2009, MNRAS, 398, 157 7, 228

Henning T., Wolf S., Launhardt R., Waters R., 2001, ApJ, 561, 871 16

Herbig G. H., 1960, ApJS, 4, 337 10, 147, 178, 197

Herbig G. H., 1995, ARA&A, 33, 19 194

Herbig G. H., 1998, ApJ, 497, 2, 736 181, 185

Herbig G. H., Jones B. F., 1983, AJ, 88, 1040 181

Hernández J., Calvet N., Hartmann L., Briceño C., Sicilia-Aguilar A., Berlind P., 2005, AJ, 129, 2, 856 24, 178, 181

Heyer M., Dame T. M., 2015, ARA&A, 53, 583 74, 177

Heyer M., Goldsmith P. F., Yıldız U. A., Snell R. L., Falgarone E., Pineda J. L., 2016, MNRAS, 461, 4, 3918 124

Hildebrand R. H., Dragovan M., Novak G., 1984, ApJ, 284, L51 133

Hill T., Motte F., Didelon P., et al., 2011, A&A, 533, A94 123

Hillenbrand L. A., Carpenter J. M., Kim J. S., et al., 2008, ApJ, 677, 1, 630 178

Hillenbrand L. A., Strom S. E., Vrba F. J., Keene J., 1992, ApJ, 397, 613 10, 11

Hiltner W. A., 1949a, ApJ, 109, 471 17

Hiltner W. A., 1949b, Science, 109, 165 16, 17

Hilton J., Lahulla J. F., 1995, A&AS, 113, 325 63

Hirota T., Bushimata T., Choi Y. K., et al., 2008, PASJ, 60, 37 181

Hirota T., Honma M., Imai H., et al., 2011, PASJ, 63, 1, 1 181

Hobbs L. M., Blitz L., Magnani L., 1986, ApJ, 306, L109 63

Hobbs L. M., York D. G., Thorburn J. A., et al., 2009, ApJ, 705, 1, 32 194

Hodapp K. W., Kaiser N., Aussel H., et al., 2004, Astronomische Nachrichten, 325, 6, 636 53

Hollenbach D. J., Yorke H. W., Johnstone D., 2000, in Protostars and Planets IV, edited by V. Mannings, A. P. Boss, S. S. Russell, 401–428 188

Hosokawa T., Yorke H. W., Omukai K., 2010, ApJ, 721, 1, 478 12

Hosoya K., Itoh Y., Oasa Y., Gupta R., Sen A. K., 2020, arXiv e-prints, arXiv:2006.00219 217, 218, 219

Hu E. M., 1981, ApJ, 248, 119 57

Hu J. Y., The P. S., de Winter D., 1989, A&A, 208, 213 10, 147

Hubble E., 1934, ApJ, 79, 8 57

Hubrig S., Ilyin I., Schöller M., Lo Curto G., 2013, Astronomische Nachrichten, 334, 10, 1093 12

Iffrig O., Hennebelle P., 2017, A&A, 604, A70 124

Ikeda H., Sugitani K., Watanabe M., et al., 2008, AJ, 135, 2323 216, 217, 218, 219

Indebetouw R., Zweibel E. G., 2000, ApJ, 532, 361 4

Inutsuka S.-i., Inoue T., Iwasaki K., Hosokawa T., 2015, A&A, 580, A49 124

Ishida K., 1970, PASJ, 22, 277 232

Itoh Y., Tamura M., Tokunaga A. T., 2002, PASJ, 54, 561 114

Jacoby G. H., Hunter D. A., Christian C. A., 1984, ApJS, 56, 257 xlviii, 87, 88, 260

Jain S. K., Bhatt H. C., Sagar R., 1990, A&AS, 83, 237 133

Jeong I.-G., Kang H., Jung J., et al., 2019, Journal of Korean Astronomical Society, 52, 227 128

Jijina J., Adams F. C., 1996, ApJ, 462, 874 13

Jiménez-Serra I., Caselli P., Fontani F., et al., 2014, MNRAS, 439, 2, 1996 123

REFERENCES

Jones B. F., 1997, Mem. Soc. Astron. Italiana, 68, 833 165, 229

Joshi U. C., Deshpande M. R., Kulshrestha A. K., 1987, in Circumstellar Matter, edited by I. Appenzeller, C. Jordan, vol. 122, 135–136 225

Kahn F. D., 1954, Bull. Astron. Inst. Netherlands, 12, 187 216

Kaiser N., Burgett W., Chambers K., et al., 2010, in Ground-based and Airborne Telescopes III, vol. 7733 of Proc. SPIE, 77330E 53

Kauffmann J., Bertoldi F., Bourke T. L., Evans II N. J., Lee C. W., 2008, A&A, 487, 993 63

Kenyon S. J., Hartmann L., 1987, ApJ, 323, 714 189

Kenyon S. J., Hartmann L., 1995, ApJS, 101, 117 185

Kirk H., Klassen M., Pudritz R., Pillsworth S., 2015, ApJ, 802, 2, 75 123

Kirk H., Myers P. C., Bourke T. L., Gutermuth R. A., Hedden A., Wilson G. W., 2013, ApJ, 766, 2, 115 123

Kirk J. M., Ward-Thompson D., Di Francesco J., et al., 2009, ApJS, 185, 198 xlvi, 58, 59, 67, 79, 80, 81, 89, 93, 102, 107, 111, 117, 118, 125, 145, 152

Klessen R. S., Heitsch F., Mac Low M.-M., 2000, ApJ, 535, 887 123

Knude J., Hog E., 1998, A&A, 338, 897 72, 226

Koch P. M., Tang Y.-W., Ho P. T. P., 2013, ApJ, 775, 1, 77 124

Koch P. M., Tang Y.-W., Ho P. T. P., et al., 2014, ApJ, 797, 2, 99 124

Koenig X., Hillenbrand L. A., Padgett D. L., DeFelippis D., 2015, AJ, 150, 100 218

Koenig X. P., Leisawitz D. T., 2014, ApJ, 791, 131 xlix, lvii, 92, 161, 162

Koenigl A., 1991, ApJ, 370, L39 15

Kounkel M., Covey K., Suárez G., et al., 2018, AJ, 156, 3, 84 217, 218, 219, 221, 232

Kroto H., 1988, Science, 242, 4882, 1139 194

Krumholz M. R., 2006, ApJ, 641, 1, L45 13

Krumholz M. R., Klein R. I., McKee C. F., Offner S. S. R., Cunningham A. J., 2009, Science, 323, 5915, 754 13

Kuhn M. A., Medina N., Getman K. V., et al., 2017, AJ, 154, 3, 87 234

Kun M., 1998, ApJS, 115, 59 57, 58, 64, 65, 67, 152, 168

Kun M., 2007, in Triggered Star Formation in a Turbulent ISM, edited by B. G. Elmegreen, J. Palous, vol. 237 of IAU Symposium, 119–123 168

Kun M., Balog Z., Kenyon S. J., Mamajek E. E., Gutermuth R. A., 2009, ApJS, 185, 451 l, lviii, 58, 67, 70, 71, 79, 80, 93, 94, 95, 102, 111, 112, 113, 114, 115, 116, 117, 118, 119, 125, 144, 149, 152, 156, 157, 168

Kun M., Kiss Z. T., Balog Z., 2008, Star Forming Regions in Cepheus, 136 57, 58, 67

Kun M., Vinkó J., Szabados L., 2000, MNRAS, 319, 3, 777 149, 163

Lada C. J., 1987, in Star Forming Regions, edited by M. Peimbert, J. Jugaku, vol. 115 of IAU Symposium, 1–17 7, 8, 79, 148

Lada C. J., Black J. H., 1976, ApJ, 203, L75 264

Lada C. J., Lada E. A., 2003, ARA&A, 41, 57 13, 147

Lada E. A., Lada C. J., 1995, AJ, 109, 1682 185

Lamzin S. A., 1998, Astronomy Reports, 42, 322 84

Lamzin S. A., 1999, Astronomy Letters, 25, 430 84

Larson R. B., 1978, MNRAS, 184, 69 14

Larson R. B., 2003, Reports on Progress in Physics, 66, 1651 2

Law C. Y., Li H. B., Leung P. K., 2019, MNRAS, 484, 3, 3604 144

Lazarian A., 2003, J. Quant. Spec. Radiat. Transf., 79, 881 132

Lazarian A., 2007, J. Quant. Spec. Radiat. Transf., 106, 225 18

Lee H. M., Draine B. T., 1985, ApJ, 290, 211 132

Lefloch B., Lazareff B., 1994, A&A, 289, 559 6, 215

REFERENCES

Leger A., D'Hendecourt L., Verstraete L., Schmidt W., 1988, A&A, 203, 1, 145 194

Leung C. M., 1985, in Protostars and Planets II, edited by D. C. Black, M. S. Matthews, 104–136 2, 6

Levenhagen R. S., Leister N. V., 2006, MNRAS, 371, 1, 252 205

Li A., Mann I., 2012, in Astrophysics and Space Science Library, edited by I. Mann, N. Meyer-Vernet, A. Czechowski, vol. 385 of Astrophysics and Space Science Library, 5 1

Li H.-B., Blundell R., Hedden A., Kawamura J., Paine S., Tong E., 2011, MNRAS, 411, 2067 124

Li H.-b., Dowell C. D., Goodman A., Hildebrand R., Novak G., 2009, ApJ, 704, 891 125

Li H.-b., Fang M., Henning T., Kainulainen J., 2013, MNRAS, 436, 4, 3707 124, 143

Li H. B., Goodman A., Sridharan T. K., et al., 2014, in Protostars and Planets VI, edited by H. Beuther, R. S. Klessen, C. P. Dullemond, T. Henning, 101 124

Li H.-B., Jiang H., Fan X., Gu Q., Zhang Y., 2017, Nature Astronomy, 1, 0158 143, 144, 145, 260

Li W., Evans II N. J., Harvey P. M., Colome C., 1994, ApJ, 433, 199 98

Lindegren L., 2018, Re-normalising the astrometric chi-square in Gaia DR2, GAIA-C3-TN-LU-LL-124 71, 152, 180, 220

Lindegren L., Lammers U., Hobbs D., O'Mullane W., Bastian U., Hernández J., 2012, A&A, 538, A78 98, 99

Liu Q. Z., van Paradijs J., van den Heuvel E. P. J., 2000, A&AS, 147, 25 204

Loinard L., Torres R. M., Mioduszewski A. J., et al., 2007, ApJ, 671, 546 64

Loinard L., Torres R. M., Mioduszewski A. J., Rodríguez L. F., 2008, ApJ, 675, L29 64

Lombardi M., Lada C. J., Alves J., 2008, A&A, 480, 785 65

Lombardi M., Lada C. J., Alves J., 2010, A&A, 512, A67 181

Looney L. W., Tobin J. J., Fields B. D., 2006, ApJ, 652, 2, 1755 147

López-Santiago J., Caballero J. A., 2008, A&A, 491, 3, 961 85

Lorenzetti D., Giannini T., Antoniucci S., et al., 2015, The Astronomer's Telegram, 7935, 1 161

Lorenzetti D., Giannini T., Larionov V. M., et al., 2011, ApJ, 732, 2, 69 225

Lu X., Zhang Q., Liu H. B., et al., 2018, ApJ, 855, 1, 9 123

Luhman K. L., 2018, AJ, 156, 271 80

Luhman K. L., Allen P. R., Espaillat C., Hartmann L., Calvet N., 2010, ApJS, 186, 1, 111 189

Luhman K. L., Herrmann K. A., Mamajek E. E., Esplin T. L., Pecaut M. J., 2018, AJ, 156, 76 80

Luhman K. L., Mamajek E. E., Allen P. R., Cruz K. L., 2009, ApJ, 703, 1, 399 221

Lynden-Bell D., Pringle J. E., 1974, MNRAS, 168, 603 12

Lynds B. T., 1962, ApJS, 7, 1 57, 58, 124, 149

Mackey J., Lim A. J., 2011, MNRAS, 412, 2079 7, 228

Maddalena R. J., Morris M., Moscowitz J., Thaddeus P., 1986, ApJ, 303, 375 265

Magakian T. Y., 2003, A&A, 399, 141 149

Magakian T. Y., Movsesian T. A., 2001, Astrophysics, 44, 4, 419 159

Maheswar G., Bhatt H. C., 2006, MNRAS, 369, 4, 1822 63

Maheswar G., Lee C. W., Bhatt H. C., Mallik S. V., Dib S., 2010, A&A, 509, A44 63, 64, 65

Maheswar G., Manoj P., Bhatt H. C., 2004, MNRAS, 355, 1272 63

Makovoz D., Marleau F. R., 2005, PASP, 117, 1113 81

Malfait K., Waelkens C., Waters L. B. F. M., Vand enbussche B., Huygen E., de Graauw M. S., 1998, A&A, 332, L25 10

Malkov O. Y., Tessema S. B., Kniazev A. Y., 2015, Baltic Astronomy, 24, 395 204

REFERENCES

Manoj P., Bhatt H. C., Maheswar G., Muneer S., 2006, ApJ, 653, 657 24, 58, 125, 149, 178

Manoj P., Maheswar G., Bhatt H. C., 2002, MNRAS, 334, 2, 419 179

Manset N., Bastien P., Ménard F., Bertout C., Le van Suu A., Boivin L., 2009, A&A, 499, 1, 137 225

Marigo P., Girardi L., Bressan A., et al., 2017, ApJ, 835, 77 l, lvi, 94, 95, 155, 158, 245

Martín E. L., 1998, AJ, 115, 1, 351 79

Mathew B., Manoj P., Bhatt B. C., Sahu D. K., Maheswar G., Muneer S., 2017, AJ, 153, 5, 225 79

Matsuyanagi I., Itoh Y., Sugitani K., Oasa Y., Mukai T., Tamura M., 2006, PASJ, 58, L29 216

Matter A., Labadie L., Kreplin A., et al., 2014, A&A, 561, A26 24, 199

Matthaeus W. H., Pouquet A., Mininni P. D., Dmitruk P., Breech B., 2008, Phys. Rev. Lett., 100, 8, 085003 124

Matthews B. C., McPhee C. A., Fissel L. M., Curran R. L., 2009, ApJS, 182, 143 123

Matthews H. I., 1979, A&A, 75, 345 235

McClure M. K., Furlan E., Manoj P., et al., 2010, ApJS, 188, 1, 75 79, 148

McKee C. F., Tan J. C., 2002, Nature, 416, 6876, 59 13

McKee C. F., Tan J. C., 2003, ApJ, 585, 2, 850 13

McKee C. F., Zweibel E. G., Goodman A. A., Heiles C., 1993, in Protostars and Planets III, edited by E. H. Levy, J. I. Lunine, 327 3

Meeus G., Waters L. B. F. M., Bouwman J., van den Ancker M. E., Waelkens C., Malfait K., 2001, A&A, 365, 476 11, 148

Megier A., Strobel A., Bondar A., et al., 2005, ApJ, 634, 451 63

Mel'nik A. M., Dambis A. K., 2017, MNRAS, 472, 4, 3887 166, 167

Ménard F., Duchêne G., 2004, A&A, 425, 973 228

Ménard F. C., 2005, in Astronomical Polarimetry: Current Status and Future Directions, edited by A. Adamson, C. Aspin, C. Davis, T. Fujiyoshi, vol. 343 of Astronomical Society of the Pacific Conference Series, 128 217

Mendigutía I., Calvet N., Montesinos B., et al., 2011, A&A, 535, A99 188, 199

Mendigutía I., Mora A., Montesinos B., et al., 2012, A&A, 543, A59 24, 199

Mennella A., Bersanelli M., Butler R. C., et al., 2011, A&A, 536, A3 55

Merrill P. W., 1936, ApJ, 83, 126 194

Merrill P. W., Wilson O. C., 1938, ApJ, 87, 9 194

Meyer M. R., Calvet N., Hillenbrand L. A., 1997, AJ, 114, 288 114

Miao J., White G. J., Nelson R., Thompson M., Morgan L., 2006, MNRAS, 369, 143 6

Miao J., White G. J., Thompson M. A., Nelson R. P., 2009, ApJ, 692, 382 215

Millan-Gabet R., Schloerb F. P., Traub W. A., 2001, ApJ, 546, 358 98

Miniati F., Jones T. W., Ryu D., 1999, ApJ, 517, 242 145

Miroshnichenko A. S., Bergner Y. K., Kuratov K. S., 1997, Astronomy Letters, 23, 1, 97 163

Molina F. Z., Glover S. C. O., Federrath C., Klessen R. S., 2012, MNRAS, 423, 3, 2680 123

Molinari S., Swinyard B., Bally J., et al., 2010, A&A, 518, L100 123

Montmerle T., Grosso N., Tsuboi Y., Koyama K., 2000, ApJ, 532, 1097 84

Montmerle T., Koch-Miramond L., Falgarone E., Grindlay J. E., 1983, ApJ, 269, 182 84

Mora A., Merín B., Solano E., et al., 2001, A&A, 378, 116 163, 203

Morales-Calderón M., Stauffer J. R., Rebull L., et al., 2009, ApJ, 702, 1507 218

REFERENCES

Morgan L. K., Thompson M. A., Urquhart J. S., White G. J., Miao J., 2004, A&A, 426, 535 216, 232

Motoyama K., Yoshida T., 2003, MNRAS, 344, 461 7

Mottram J. C., Vink J. S., Oudmaijer R. D., Patel M., 2007, MNRAS, 377, 3, 1363 200, 202

Mouschovias T. C., 1991, ApJ, 373, 169 3

Mouschovias T. C., Ciolek G. E., 1999, in NATO ASIC Proc. 540: The Origin of Stars and Planetary Systems, edited by C. J. Lada, N. D. Kylafis, 305 3

Muzerolle J., Calvet N., Hartmann L., 2001, ApJ, 550, 2, 944 197

Muzerolle J., D'Alessio P., Calvet N., Hartmann L., 2004, ApJ, 617, 1, 406 198

Muzerolle J., Hartmann L., Calvet N., 1998, AJ, 116, 1, 455 158

Myers P. C., 2009, ApJ, 700, 2, 1609 125

Myers P. C., Lazarian A., 1998, ApJ, 507, L157 3, 4

Nagai T., Inutsuka S.-i., Miyama S. M., 1998, ApJ, 506, 1, 306 123, 124

Nakagawa Y., Nakazawa K., Hayashi C., 1981, Icarus, 45, 3, 517 189

Nakamura F., Li Z.-Y., 2008, ApJ, 687, 1, 354 124

Nakano T., 1984, Fund. Cosmic Phys., 9, 139 3

Nakano T., 1998, ApJ, 494, 587 4

Nakano T., Hasegawa T., Norman C., 1995, ApJ, 450, 183 13

Natta A., Grinin V. P., Tambovtseva L. V., 2000, ApJ, 542, 1, 421 197

Natta A., Prusti T., Neri R., Wooden D., Grinin V. P., Mannings V., 2001, A&A, 371, 186 197

Nazé Y., Petit V., Rinbrand M., et al., 2014, ApJS, 215, 10 xlvii, 84, 85

Neha S., Maheswar G., Soam A., Lee C. W., 2018, MNRAS, 476, 4, 4442 123

Neha S., Maheswar G., Soam A., Lee C. W., Tej A., 2016, A&A, 588, A45 65, 123

Nielsen A. S., Jønch-Sørensen H., Knude J., 2000, A&A, 358, 1077 63

Ogura K., 2006, Bulletin of the Astronomical Society of India, 34, 111 xlv, 7

Ogura K., Sugitani K., Pickles A., 2002, AJ, 123, 2597 217, 218, 219

Olano C. A., Meschin P. I., Niemela V. S., 2006, MNRAS, 369, 2, 867 57, 168

Onaka P., Tonry J. L., Isani S., et al., 2008, in Ground-based and Airborne Instrumentation for Astronomy II, vol. 7014 of Proc. SPIE, 70140D 54

Oort J. H., 1954, Bull. Astron. Inst. Netherlands, 12, 177 216

Ortiz-León G. N., Loinard L., Dzib S. A., et al., 2018, ApJ, 865, 1, 73 181, 182, 183

Ostriker E. C., Stone J. M., Gammie C. F., 2001, ApJ, 546, 980 17, 138

Oudmaijer R. D., Drew J. E., 1999, MNRAS, 305, 1, 166 12

Oudmaijer R. D., van der Veen W. E. C. J., Waters L. B. F. M., Trams N. R., Waelkens C., Engelsman E., 1992, A&AS, 96, 625 10, 147

Padoan P., Juvela M., Goodman A. A., Nordlund Å., 2001, ApJ, 553, 1, 227 123

Padoan P., Nordlund Å., 2002, ApJ, 576, 2, 870 123

Palmeirim P., André P., Kirk J., et al., 2013, A&A, 550, A38 124

Panwar N., Chen W. P., Pandey A. K., et al., 2014, MNRAS, 443, 1614 217, 218, 219

Pecaut M. J., Mamajek E. E., 2013, ApJS, 208, 1, 9 114

Pelkonen V. M., Juvela M., Padoan P., 2009, A&A, 502, 3, 833 128

Peretto N., Fuller G. A., André P., et al., 2014, A&A, 561, A83 123

Peterson D. E., Clemens D. P., 1998, AJ, 116, 881 63

Pfalzner S., Kaczmarek T., 2013, A&A, 559, A38 165

Pilbratt G. L., Riedinger J. R., Passvogel T., et al., 2010, A&A, 518, L1 123

Planck Collaboration, Adam R., Ade P. A. R., et al., 2016a, A&A, 594, A1 55, 126

Planck Collaboration, Adam R., Ade P. A. R., et al., 2016b, A&A, 586, A133 126

REFERENCES

Planck Collaboration, Ade P. A. R., Aghanim N., et al., 2014, A&A, 571, A1 126

Planck Collaboration, Ade P. A. R., Aghanim N., et al., 2015, A&A, 576, A104 56, 126

Planck Collaboration, Ade P. A. R., Aghanim N., et al., 2016c, A&A, 586, A138 124, 135, 143

Planck HFI Core Team, Ade P. A. R., Aghanim N., et al., 2011, A&A, 536, A4 55

Poeckert R., 1975, ApJ, 196, 777 12

Poeckert R., Marlborough J. M., 1976, ApJ, 206, 182 199

Pokhrel R., Gutermuth R., Ali B., et al., 2016, MNRAS, 461, 1, 22 144

Prabhu T. P., Anupama G. C., 2010, in Astronomical Society of India Conference Series, vol. 1 of Astronomical Society of India Conference Series 26

Preibisch T., 2004, Ap&SS, 292, 631 84

Preibisch T., Brown A. G. A., Bridges T., Guenther E., Zinnecker H., 2002, AJ, 124, 1, 404 179

Preibisch T., Kim Y.-C., Favata F., et al., 2005, ApJS, 160, 401 84

Prisinzano L., Damiani F., Guarcello M. G., et al., 2018, A&A, 617, A63 233

Pudritz R. E., Klassen M., Kirk H., Seifried D., Banerjee R., 2014, in Magnetic Fields throughout Stellar Evolution, edited by P. Petit, M. Jardine, H. C. Spruit, vol. 302 of IAU Symposium, 10–20 16

Qiu K., Zhang Q., Menten K. M., Liu H. B., Tang Y.-W., Girart J. M., 2014, ApJ, 794, 1, L18 123

Ramaprakash A. N., Gupta R., Sen A. K., Tandon S. N., 1998, A&AS, 128, 369 40, 66

Ramirez S. V., Depoy D. L., Frogel J. A., Sellgren K., Blum R. D., 1997, AJ, 113, 1411 114

Rautela B. S., Joshi G. C., Pandey J. C., 2004, Bulletin of the Astronomical Society of India, 32, 159 xlvi, 27, 28, 65, 219

Rayner J. T., Toomey D. W., Onaka P. M., et al., 2003, PASP, 115, 805, 362 30

Rayner T. S. M., Griffin M. J., Schneider N., et al., 2017, A&A, 607, A22 123

Reach W. T., Faied D., Rho J., et al., 2009, ApJ, 690, 1, 683 218

Reach W. T., Rho J., Young E., et al., 2004, ApJS, 154, 1, 385 218

Rebull L. M., Johnson C. H., Gibbs J. C., et al., 2013, AJ, 145, 15 217, 218, 232

Rebull L. M., Padgett D. L., McCabe C.-E., et al., 2010, ApJS, 186, 259 xlviii, xlix, 89, 90, 91, 92, 94, 96, 97

Rector T. A., Schweiker H., 2013, AJ, 145, 35 58, 102, 125

Reed B. C., 2000, AJ, 120, 314 74, 177

Reipurth B., Bally J., Devine D., 1997, AJ, 114, 2708 265

Reynolds R. J., Ogden P. M., 1979, ApJ, 229, 942 235

Rigliaco E., Natta A., Testi L., et al., 2012, A&A, 548, A56 24

Riviere-Marichalar P., Merín B., Kamp I., Eiroa C., Montesinos B., 2016, A&A, 594, A59 163

Robitaille T. P., Whitney B. A., Indebetouw R., Wood K., 2007, ApJS, 169, 328 79, 148

Romano G., 1975, Ap&SS, 33, 487 59

Rosen S. R., Webb N. A., Watson M. G., et al., 2016, A&A, 590, A1 85

Rosino L., Romano G., 1962, Contributi dell'Osservatorio Astrofisica dell'Universita di Padova in Asiago, 127, 1 115, 116, 117

Sadavoy S. I., Di Francesco J., André P., et al., 2014, ApJ, 787, 2, L18 179

Sagar R., Kumar B., Omar A., 2013, ArXiv e-prints 25

Saha P., Gopinathan M., Kamath U., et al., 2020, MNRAS, 494, 4, 5851 57, 125, 138, 144, 149, 150, 151, 157, 158, 164, 169

Sandell G., Knee L. B. G., 2001, ApJ, 546, L49 7

Sato S., 1988, Progress of Theoretical Physics Supplement, 96, 37 217

REFERENCES

Sato S., Tamura M., Nagata T., et al., 1988, MNRAS, 230, 321 123

Savage B. D., Mathis J. S., 1979, ARA&A, 17, 73 185

Schlafly E. F., Green G., Finkbeiner D. P., et al., 2014, ApJ, 786, 1, 29 63, 181

Schmidt G. D., Elston R., Lupie O. L., 1992, AJ, 104, 1563 41, 66, 127, 219, 220

Schneider N., Csengeri T., Bontemps S., et al., 2010, A&A, 520, A49 123

Seaton M. J., 1979, MNRAS, 187, 73 185

Seifried D., Walch S., 2015, MNRAS, 452, 2410 16, 123, 143

Sellgren K., 1983, AJ, 88, 985 116, 117, 118

Sharma E., Gopinathan M., Soam A., et al., 2020, A&A, 639, A133 125, 141, 145, 149

Sharma S., Pandey A. K., Borissova J., et al., 2016, AJ, 151, 126 217, 218, 219

Sharpless S., 1959, ApJS, 4, 257 264

Shetty R., Ostriker E. C., 2006, ApJ, 647, 2, 997 123

Shevchenko V. S., Ibragimov M. A., Yakubov S. D., 1989, SvA, 33, 487 64, 65

Shimajiri Y., André P., Palmeirim P., et al., 2019, A&A, 623, A16 123

Shu F. H., Adams F. C., Lizano S., 1987, ARA&A, 25, 23 3, 13

Sicilia-Aguilar A., Hartmann L., Calvet N., et al., 2006a, ApJ, 638, 897 218

Sicilia-Aguilar A., Hartmann L. W., Fürész G., Henning T., Dullemond C., Brandner W., 2006b, AJ, 132, 2135 218

Sicilia-Aguilar A., Hartmann L. W., Hernández J., Briceño C., Calvet N., 2005, AJ, 130, 188 218

Sicilia-Aguilar A., Henning T., Hartmann L. W., 2010, ApJ, 710, 1, 597 218

Sicilia-Aguilar A., Kim J. S., Sobolev A., Getman K., Henning T., Fang M., 2013, A&A, 559, A3 218

Sicilia-Aguilar A., Patel N., Fang M., Roccatagliata V., Getman K., Goldsmith P., 2019, A&A, 622, A118 233

290

Skrutskie M. F., Cutri R. M., Stiening R., et al., 2006, AJ, 131, 1163 54, 150, 220

Snow T. P. J., York D. G., Welty D. E., 1977, AJ, 82, 113 194

Snow T. P., McCall B. J., 2006, ARA&A, 44, 1, 367 194

Soam A., Kwon J., Maheswar G., Tamura M., Lee C. W., 2015a, ApJ, 803, 2, L20 123

Soam A., Lee C. W., Andersson B. G., et al., 2019, ApJ, 883, 1, 9 125

Soam A., Maheswar G., Bhatt H. C., Lee C. W., Ramaprakash A. N., 2013, MNRAS, 432, 2, 1502 66

Soam A., Maheswar G., Lee C. W., et al., 2015b, A&A, 573, A34 66

Soam A., Maheswar G., Lee C. W., Neha S., Andersson B. G., 2017, MNRAS, 465, 1, 559 66

Soam A., Pattle K., Ward-Thompson D., et al., 2018, ApJ, 861, 1, 65 124

Soler J. D., 2019, A&A, 629, A96 124, 143

Soler J. D., Alves F., Boulanger F., et al., 2016, A&A, 596, A93 135

Soler J. D., Hennebelle P., 2017, A&A, 607, A2 124

Soler J. D., Hennebelle P., Martin P. G., Miville-Deschênes M. A., Netterfield C. B., Fissel L. M., 2013, ApJ, 774, 2, 128 124, 143

Sriram S., Kumar A., Surya A., et al., 2018, in Proc. SPIE, vol. 10702 of Society of Photo-Optical Instrumentation Engineers (SPIE) Conference Series, 107026K xlvi, 29, 30

Stahler S. W., Palla F., 2005, The Formation of Stars xlv, 19

Steenbrugge K. C., de Bruijne J. H. J., Hoogerwerf R., de Zeeuw P. T., 2003, A&A, 402, 587 179

Stein W., 1966, ApJ, 144, 318 17

Stone J. M., Ostriker E. C., Gammie C. F., 1998, ApJ, 508, 1, L99 124

Straizys V., 1991, in Precision Photometry: Astrophysics of the Galaxy, edited by A. G. D. Philip, A. R. Upgren, K. A. Janes, 341 63

REFERENCES

Straizys V., Cernis K., Kazlauskas A., Meistas E., 1992, Baltic Astronomy, 1, 149 63, 64, 65, 72, 226

Strom K. M., Strom S. E., Edwards S., Cabrit S., Skrutskie M. F., 1989, AJ, 97, 1451 178

Strom S. E., 1977, in Star Formation, edited by T. de Jong, A. Maeder, S. B. Pikel'Ner, vol. 75, 179 217

Strom S. E., Strom K. M., Carrasco L., 1974, PASP, 86, 798 185

Stubbs C. W., Doherty P., Cramer C., et al., 2010, ApJS, 191, 2, 376 54

Sugitani K., Fukui Y., Ogura K., 1991, ApJS, 77, 59 215, 216, 221

Sugitani K., Nakamura F., Tamura M., et al., 2010, ApJ, 716, 299 123

Sugitani K., Nakamura F., Watanabe M., et al., 2011, ApJ, 734, 63 124

Sugitani K., Ogura K., 1994, ApJS, 92, 163 215, 216

Sugitani K., Tamura M., Ogura K., 1995, ApJ, 455, L39 216

Tachihara K., Onishi T., Mizuno A., Fukui Y., 2002, A&A, 385, 909 125

Takami M., Chrysostomou A., Bailey J., Gledhill T. M., Tamura M., Terada H., 2002, ApJ, 568, 1, L53 199

Tamura M., Hashimoto J., Kandori R., et al., 2011, in Astronomical Society of the Pacific Conference Series, edited by P. Bastien, N. Manset, D. P. Clemens, N. St-Louis, vol. 449 of Astronomical Society of the Pacific Conference Series, 207 123

Testi L., Palla F., Natta A., 1998, A&AS, 133, 81 148, 149

Testi L., Palla F., Natta A., 1999, A&A, 342, 515 100, 148

Testi L., Palla F., Natta A., 2001, The Onset of Cluster Formation Around Intermediate-Mass Stars, vol. 243 of Astronomical Society of the Pacific Conference Series, 377 100

Testi L., Palla F., Prusti T., Natta A., Maltagliati S., 1997, A&A, 320, 159 148, 201

The P. S., de Winter D., Perez M. R., 1994, A&AS, 104, 315 10, 58, 86, 94, 96, 125, 147, 149, 157, 159, 179

Thompson M. A., Urquhart J. S., White G. J., 2004, A&A, 415, 627 216, 233

Tognelli E., Prada Moroni P. G., Degl'Innocenti S., 2011, A&A, 533, A109 lii, 114, 116

Treviño-Morales S. P., Fuente A., Sánchez-Monge Á., et al., 2019, A&A, 629, A81 123

Tritsis A., Tassis K., 2016, MNRAS, 462, 4, 3602 124

Trullols E., Jordi C., 1997, A&A, 324, 549 185

Vacca W. D., Cushing M. C., Rayner J. T., 2003, PASP, 115, 389 45

van den Ancker M. E., Bouwman J., Wesselius P. R., Waters L. B. F. M., Dougherty S. M., van Dishoeck E. F., 2000, A&A, 357, 325 148

van den Ancker M. E., de Winter D., Tjin A Djie H. R. E., 1998, A&A, 330, 145 64, 65, 98

van den Ancker M. E., The P. S., Feinstein A., Vazquez R. A., de Winter D., Perez M. R., 1997a, A&AS, 123, 63 10

van den Ancker M. E., The P. S., Tjin A Djie H. R. E., et al., 1997b, A&A, 324, L33 197

van Leeuwen F., 2007, A&A, 474, 653 64, 65, 98

Van Loo S., Keto E., Zhang Q., 2014, ApJ, 789, 1, 37 123, 124

Vázquez-Semadeni E., Banerjee R., Gómez G. C., Hennebelle P., Duffin D., Klessen R. S., 2011, MNRAS, 414, 3, 2511 124

Vieira S. L. A., Corradi W. J. B., Alencar S. H. P., et al., 2003, AJ, 126, 6, 2971 204

Vink J. S., 2015, Ap&SS, 357, 2, 98 199

Vink J. S., Drew J. E., Harries T. J., Oudmaijer R. D., 2002, MNRAS, 337, 1, 356 12, 199, 200, 205

293

REFERENCES

Vink J. S., Drew J. E., Harries T. J., Oudmaijer R. D., 2003, in Galactic Star Formation Across the Stellar Mass Spectrum, edited by J. M. De Buizer, N. S. van der Bliek, vol. 287 of Astronomical Society of the Pacific Conference Series, 319–324 12, 199

Vink J. S., Drew J. E., Harries T. J., Oudmaijer R. D., Unruh Y., 2005a, MNRAS, 359, 3, 1049 lxii, 224, 225

Vink J. S., Harries T. J., Drew J. E., 2005b, A&A, 430, 213 12, 199

Vioque M., Oudmaijer R. D., Baines D., Mendigutía I., Pérez-Martínez R., 2018, A&A, 620, A128 94, 148, 157

Viotti R., 1969, Mem. Soc. Astron. Italiana, 40, 75 64, 65

Vrba F. J., Strom S. E., Strom K. M., 1976, AJ, 81, 958 123

Wade Jr. C. M., 1958, A 21-CM Study of an Expanded Hydrogen II Region., Ph.D. thesis, HARVARD UNIVERSITY. 264

Wahhaj Z., Cieza L., Koerner D. W., et al., 2010, ApJ, 724, 2, 835 86, 94, 96, 157

Wang K., Zhang Q., Wu Y., Zhang H., 2011, ApJ, 735, 1, 64 13

Wang S., Looney L. W., 2007, ApJ, 659, 2, 1360 148

Ward-Thompson D., 2002, Science, 295, 76 4

Ward-Thompson D., Kirk J. M., Crutcher R. M., Greaves J. S., Holland W. S., André P., 2000, ApJ, 537, L135 123

Ward-Thompson D., Sen A. K., Kirk J. M., Nutter D., 2009, MNRAS, 398, 394 125

Wareing C. J., Pittard J. M., Falle S. A. E. G., Van Loo S., 2016, MNRAS, 459, 2, 1803 124

Waters L. B. F. M., Waelkens C., 1998, ARA&A, 36, 233 10, 147, 148

Watt G. D., Burton W. B., Choe S. U., Liszt H. S., 1986, A&A, 163, 194 132

Weston E. B., 1953, AJ, 58, 48 59, 125

White R. J., Basri G., 2003, ApJ, 582, 2, 1109 79

Whittet D. C. B., 2005, Polarization Observations of Molecular Clouds, vol. 343 of Astronomical Society of the Pacific Conference Series, 321 132

Whittet D. C. B., Prusti T., Franco G. A. P., et al., 1997, A&A, 327, 1194 72, 226

Wichittanakom C., Oudmaijer R. D., Fairlamb J. R., Mendigutía I., Vioque M., Ababakr K. M., 2020, MNRAS, 493, 1, 234 148

Wilking B. A., Vrba F. J., Sullivan T., 2015, ApJ, 815, 2 221

Williams G. M., Peretto N., Avison A., Duarte-Cabral A., Fuller G. A., 2018, A&A, 613, A11 123

Williams J. P., Cieza L. A., 2011, ARA&A, 49, 1, 67 188

Williams J. P., de Geus E. J., Blitz L., 1994, ApJ, 428, 693 101

Williams J. P., Myers P. C., 2000, ApJ, 537, 891 4

Wolf M., 1923, Astronomische Nachrichten, 219, 7, 109 63

Wright E. L., Eisenhardt P. R. M., Mainzer A. K., et al., 2010, AJ, 140, 1868 54, 94, 150, 220, 224

Yamaguchi R., Saito H., Mizuno N., et al., 1999, PASJ, 51, 791 233, 235

Yasui C., Kobayashi N., Tokunaga A. T., Saito M., 2014, MNRAS, 442, 3, 2543 180, 187, 188, 189, 261

Yonekura Y., Dobashi K., Mizuno A., Ogawa H., Fukui Y., 1997, ApJS, 110, 21 57, 141, 149, 164

Yorke H. W., Bodenheimer P., 1999, ApJ, 525, 1, 330 13

Yorke H. W., Sonnhalter C., 2002, ApJ, 569, 2, 846 13

Young K. E., Young C. H., Lai S.-P., Dunham M. M., Evans Neal J. I., 2015, AJ, 150, 2, 40 181

Yuan J.-H., Wu Y., Li J. Z., Yu W., Miller M., 2013, MNRAS, 429, 954 59, 67, 79, 80, 102, 111, 125, 152

Yun J. L., Clemens D. P., 1990, ApJ, 365, L73 63

REFERENCES

Zacharias N., Monet D. G., Levine S. E., Urban S. E., Gaume R., Wycoff G. L., 2004, in American Astronomical Society Meeting Abstracts, vol. 205 of American Astronomical Society Meeting Abstracts, 48.15 185

Zamora-Avilés M., Ballesteros-Paredes J., Hartmann L. W., 2017, MNRAS, 472, 1, 647 124

Zdanavičius K., Zdanavičius J., Straižys V., Maskoliūnas M., 2009, Baltic Astronomy, 18, 33 64, 65

Zinnecker H., 1982, Annals of the New York Academy of Sciences, 395, 226 14

Zinnecker H., Yorke H. W., 2007, ARA&A, 45, 1, 481 12, 13, 147, 178

Zonca A., Singer L., Lenz D., et al., 2019, Journal of Open Source Software, 4, 35, 1298 126